Surface Studies and Density Functional Theory Analysis of Ruthenium Polypyridyl Complexes

Noel M. O'Boyle, B.Sc.

Thesis presented to Dublin City University for the degree of Doctor of Philosophy

Supervised by Prof. Johannes G. Vos,
School of Chemical Sciences

Sept 2004

I hereby certify that this material, which I now submit for assessment on the programme of study leading to the award of Doctor of Philosophy by research and thesis, is entirely my own work and has not been taken from work of others, save and to the extent that such work has been cited within the text of my work.

Signed:_____

Noel O'Boyle

I.D. No.: **51167301**

Date:_____

Abstract

Surface Studies and Density Functional Theory Analysis of Ruthenium Polypyridyl Complexes

Noel M. O'Boyle

In recent years, the computational method Density Functional Theory (DFT) has become more and more important as an effective tool for studying inorganic complexes. This thesis describes computational studies on ruthenium polypyridyl-type complexes using DFT. An introduction to the theory behind DFT is presented in the first chapter, as well as a review of previous DFT studies on ruthenium polypyridyl-type complexes.

The second chapter describes the details of the computational studies. This includes a description of the basis set, functional, and integration grid. This chapter also describes two pieces of in-house software: GaussSum written to process the output of the computational package Gaussian, and GauStock, which is used to calculate Hirshfeld atomic charges.

Chapter 3 examines the electronic structure of a series of complexes related to $[Ru(bpy)_2(pytrz)]^+$. The calculated electronic structure is compared with results from experiment. Partial density of states (PDOS) spectra are used to visualise the results. Linkage isomerism and methylation reactions are examined using thermodynamics and, in the case of methylation reactions, also with kinetics.

Chapter 4 compares the electronic structure of dinuclear complexes with their corresponding mononuclear analogues. PDOS spectra are used to highlight the changes that occur on addition of a second metal centre.

The quality of the predicted Raman frequencies of $[Ru(bpy)_3]^{2+}$ is the focus of Chapter 5. The effect of basis set size, grid size and the inclusion of solvent effects is discussed. The results are compared with the experimental values.

Chapter 6 presents the first DFT study of an osmium complex attached to a surface, in this case, to a gold (111) surface. A cluster model is used for the surface. The effect of adsorption on the energy levels of the complex is studied. The effect of oxidation on the adsorbate-substrate bond is also examined.

Chapter 7 is an overview of the information available from DFT calculations. DFT is a very useful tool for examining the electronic structure of ruthenium polypyridyl complexes. PDOS spectra highlight changes in electronic structure between related complexes. Trends in oxidation potential are reproduced by the position of the metal PDOS peak. Predicted Raman frequencies agree well with experiment, although a scaling factor is required. Adsorption of an osmium complex on a gold surface causes molecular orbitals close to the surface to shift, while the relative positions of other molecular orbitals remain unchanged. The oxidised complex binds more strongly, due to the change in the nature of the frontier orbitals.

To Avril, for everything.

To Eddie and Mary, for everything else.

Acknowledgements

First of all, thanks Han for taking me on, and keeping me going all these years. Of course, the trips abroad helped, but you've always emphasised the plus side of my work, and been able to look forward to a successful end. In short, thanks for being positive, when I was negative (the ying to my yang?). Thanks in particular for making the leap of faith to become a computational chemist – especially since I really worry whether you'll be able to cope with Word now that I'm gone.

A big thanks to all the members of the inorganic lab over the last couple of years – I couldn't have done it without ye (in order of increasing height, some values estimated): Stefania (thank you very *muuch*), Sabine ("safe home" – are you sure you're not Irish?), Helen (whose Black Books DVD almost tempted me to use my computer for non-thesis-related activity – shame on you), Clare (go easy on the sherry), Tony (matrix mechanic), Mohammed (my partner in crime – I mean, in computational chemistry), Bernhard (keep the ears straight), Eric (watch that betting problem), Fiona Lynch (chemist, forensic scientist and Gaelgeoir), Johnny (is there any music you *don't* like??), Invisible Scary Skeleton (don't worry – I didn't tell anyone), Kevin and Dec (two of the most easy going guys on the planet), Fiona Frehill ("grand"), Bill (we'll always have Brussels), Marco (of sartorial splendour), Johan (you made working with TiO_2 a pleasure – well, almost), Adrian (remember, power corrupts, but we *need* electricity), Andy (owner of the coolest lab glasses ever), Wes (thanks for an insight into "seat-of-the-pants" chemistry, but how many cm^3 did you say?), Karl (the shadow on the Han Vos Research Group – that is, on the group photograph).

In relation to the work contained in this thesis, I'd especially like to thank (this time in order of name length):
Dr. Tim Albrecht – for STM info, and proof reading the chapter on the gold cluster
Wes – for your help with the experimental work, wedding gift of a laptop, having me do calculations on your dimer and sending me tons of papers
Andy – for giving me the confidence to do computational chemistry
Bill – for the help with the Raman, and sending me tons of papers (my advice, next time don't tell me you're going to RAL)
Prof. Jens Ulstrup – for the motivation to study osmium on gold

Prof. John McGarvey and Dr. Kate Ronayne – for help with Raman measurements in Belfast

Dr. Roma Oakes – for a very useful Gaussian tutorial

Avril – for proof-reading everything (!), help on statistics and sending me tons of papers

Fiona (L) – for the electrochemistry on the pytrzBr complex

Johan – for your help with all things TiO_2-related

Prof. Luisa De Cola – for a helpful introduction to photophysical measurements, and the use of transient techniques

Adrian – for the "we need this yesterday" syntheses of deuterated trisbpy, and having me do calculations on your dimer

Claire – for your "hot-off-the-press" results on pyrazine methylation

Dr. Egbert Figgemeier – for the TiO_2 slides

A.N.Other – Apologies to anyone I've missed out – so many people have helped me throughout the course of my PhD that I know I'm going to miss someone. Sorry!

A special word of thanks to the technicians, who went the extra kilometre in everything they did.

For making my other childhood dream come true (I got to visit Dublin Zoo years ago) thanks to the members of the Ketones (Dave, Damian^2, and Leon) – a truly, if I may say, homologous series.

Thanks to Jorge Cham of www.phdcomics.com for keeping me sane, and the readers of the Computational Chemistry mailing list (www.ccl.net) for all their help.

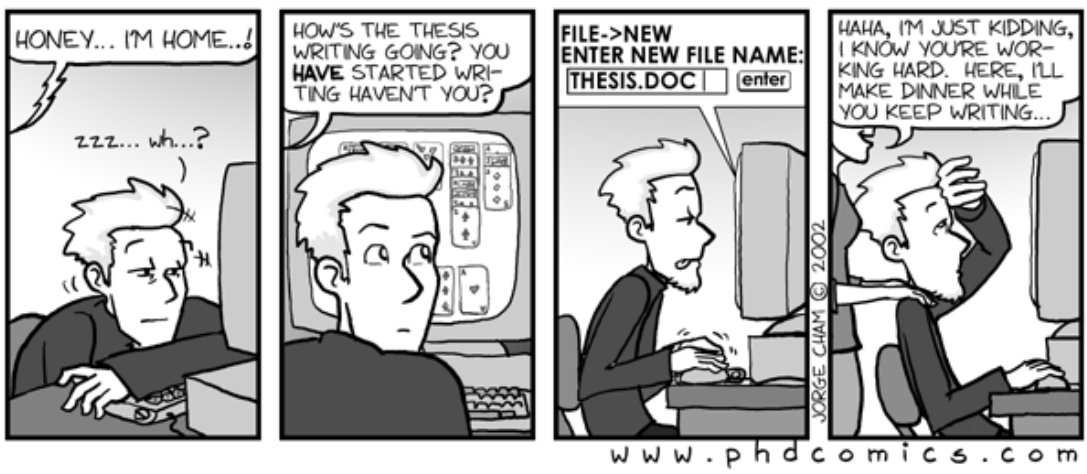

Table of Contents

List of Abbreviations

6-31G(d) – A valence double-zeta basis set

ACM – Adiabatic Connection Method

B3LYP – Becke's 3-parameter hybrid exchange functional and the correlation functional of Lee, Yang and Parr

BLMO – Bridging-Ligand Molecular Orbital

bpy – 2,2'-bipyridine

CC – Coupled-Cluster

ccp – cubic close-packed

CNDO – Complete Neglect of Differential Overlap

COOP – Crystal Orbital Overlap Population

COSMO – COnductor-like Screening MOdel

CT – Creutz-Taube

DFT – Density Functional Theory

DOS – Density of States

DSSC – Dye-Sensitised Solar Cell

ECP – Effective Core Potential or pseudopotential

EDDM – Electron Density Difference Map

ESP – ElectroStatic Potential

FMO – Frontier Molecular Orbital

GGA – Generalised Gradient Approximation

GTO – Gaussian-Type Orbital

HF – Hartree-Fock

HOMO – Highest Occupied Molecular Orbital

HPA – Hirshfeld Population Analysis

HPLC – High-Performance Liquid Chromatography

Hpytrz – 1*H*-pyridyl-1,2,4-triazole

Hpztrz – 1*H*-pyrazyl-1,2,4-triazole

IEF-PCM – Integral Equation Formalism of the Polarisable Continuum Model

INDO – Intermediate Neglect of Differential Overlap

ILCT – InterLigand Charge Transfer

KS – Kohn-Sham

LanL2DZ – A valence double-zeta basis set that includes ECPs for heavy atoms

LanL2MB – A minimal basis set that includes ECPs for heavy atoms

LC – Ligand-Centred state

LCAO – Linear Combination of Atomic Orbitals

LDA – Local Density Approximation

LSDA – Local Spin Density Approximation

LUMO – Lowest Unoccupied Molecular Orbital

MC – Metal-Centred state

MLCT – Metal-to-Ligand Charge Transfer

MP – Møller-Plesset perturbation theory

MPA – Mulliken Population Analysis

MSK – Merz-Singh-Kollman

OPDOS – Overlap Population Density of States

P0P – 4,4'-bipyridine

P2P – 1,2-bis(4-pyridyl)ethane

PCM – Polarisable Continuum Model

PDOS – Partial Density of States

PES – Potential Energy Surface

PW91 – The correlation functional of Perdew and Wang

QCA – Quantum dot Cellular Automata

RMSD – Root Mean Squared Deviation

SCE – Saturated-Calomel Electrode

SCF – Self-Consistent Field

SCRF – Self-Consistent Reaction Field

SFG – Sum Frequency Generation

SOMO – Singly-Occupied Molecular Orbitals

SQM-FF – Scaled Quantum Mechanical Force Field

STM – Scanning Tunnelling Microscopy

STO – Slater-Type Orbital

STO-3G – A minimal basis set

TD-DFT – Time Dependent Density Functional Theory

Trisbpy – $[Ru(2,2'\text{-bipyridyl})_3]^{2+}$

VWN – The correlation functionals of Vosko, Wilk and Nusair

$w_{½}$ – Full width at half maximum

WLS – Wavenumber Linear Scaling

ZINDO – Zerner's Intermediate Neglect of Differential Overlap

ZPE – Zero-Point Energy

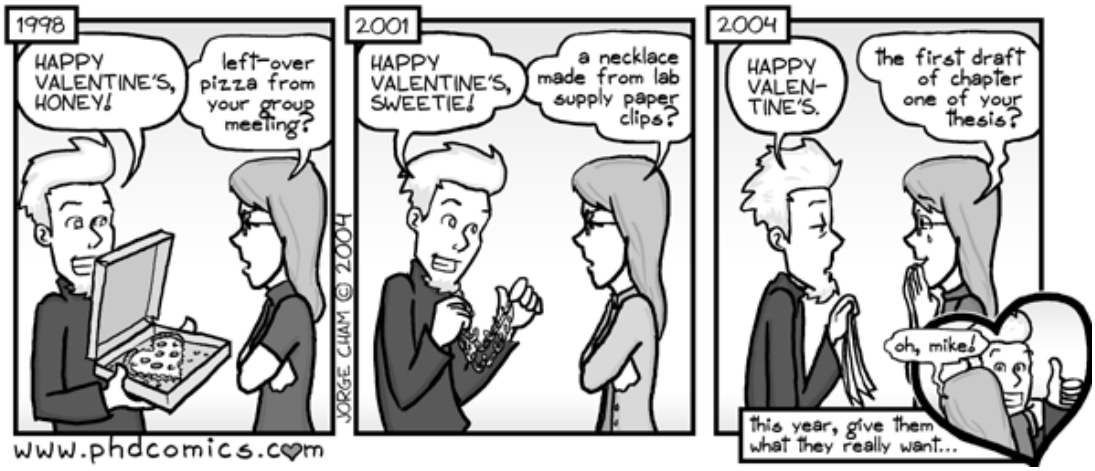
1998
HAPPY VALENTINE'S, HONEY!
left-over pizza from your group meeting?
2001
HAPPY VALENTINE'S, SWEETIE!
a necklace made from lab supply paper clips?
2004
HAPPY VALEN-TINE'S.
the first draft of chapter one of your thesis?
oh, mike!
this year, give them what they really want...
JORGE CHAM © 2004
www.phdcomics.com

Chapter 1
Density Functional Theory

The goal of computational chemists is to accurately model a chemical system. Unfortunately, modelling any multielectron system necessarily involves a number of approximations. The theoretical basis and inherent limitations of DFT are discussed in Section 1.1. The success of any model is measured by how well it predicts the characteristics of the system under study. Section 1.2 presents an overview of the published literature on DFT calculations of ruthenium polypyridyl complexes. Particular attention is given to the quality of the results obtained. The final section describes the aims of this thesis.

1.1 The theoretical basis of DFT[1]

One of the postulates of quantum mechanics (Section 1.1.1) is that the wavefunction contains all the information needed to accurately model a chemical system. The wavefunction is found by solving the Schrödinger equation. Unfortunately, it is not possible to find the exact solution of the Schrödinger equation for any system with more than one electron. As a result, a number of different quantum mechanical methods, or theories, have arisen.

Hartree-Fock (HF) theory gives rise to so-called *ab initio* methods (Section 1.1.2). By ignoring the effect of electron correlation in multi-electron systems, they allow the electronic structure to be calculated. Semi-empirical methods, including ZINDO, use more severe approximations and/or empirical data to increase the speed of calculations (Section 1.1.3). In the last 15 years, methods based upon density functional theory (DFT) have become available (Section 1.1.4). DFT treats electron correlation exactly, but exchange correlation is only treated approximately.

1.1.1 Introduction to quantum mechanics

Molecular orbital theory is based upon quantum mechanics. In the first few decades of the twentieth century, the mathematical basis of quantum mechanics was developed as it became increasingly clear that classical or Newtonian mechanics could not account for the properties of microscopic systems. These properties included quantisation of energy, and the wavelike properties of matter.

The fundamental postulate of quantum mechanics is that the state of a quantum mechanical system is completely described by a 'wave function', Ψ. The wave function has the property that the product of its complex conjugate and the wave function has units of probability density. In order to determine the observable properties of a system we need to apply a function called an 'operator', to Ψ:

$$\hat{\mathbf{A}}\Psi = a\Psi \qquad (1.1)$$

where $\hat{A}$ is an operator and a is an allowed value for the corresponding observable. By analogy with matrix algebra, Ψ is often called an eigenfunction and a an

eigenvalue. The average value of an observable corresponding to $\hat{A}$, or 'expectation value' <*A*> may be found as follows:

$$\langle A \rangle = \int \Psi \hat{\mathbf{A}} \Psi d\mathbf{r} \tag{1.2}$$

where the integral is over all space.

The operator which returns the energy of the system, *E*, is called the Hamiltonian operator, *H*. This means we can write the following eigenvalue equation:

$$H\Psi = E\Psi \tag{1.3}$$

which is the time-independent Schrödinger equation. *H* is made up of terms for the potential and kinetic energy of the system. In the case of a molecular system, it may be written as follows:

$$H = -\sum_{\mathrm{i}} \frac{\hbar^2}{2m_{\mathrm{e}}} \nabla_i^2 - \sum_k \frac{\hbar^2}{2m_k} \nabla_k^2 - \sum_i \sum_k \frac{e^2 Z_k}{r_{ik}} + \sum_{i<j} \frac{e^2}{r_{ij}} + \sum_{k<l} \frac{e^2 Z_k Z_l}{r_{kl}} \tag{1.4}$$

where *i* and *j* run over electrons, *k* and *l* run over nuclei, m_e is the mass of an electron, m_k is the mass of nucleus *k*, ∇^2 is the Laplacian operator, *e* is the charge on an electron, $\hbar$ is Planck's constant divided by 2π, Z_k is the atomic number of nucleus *k* and r_{ik} is the distance between particles *i* and *k*. The terms represent respectively the kinetic energy of the electrons, the kinetic energy of the nuclei, the attraction between the electrons and the nucleus, the interelectronic repulsion and the internuclear repulsion.

The expression for *H* in Eq. 1.4 can be simplified somewhat by use of the Born-Oppenheimer approximation[2]. This states that since electron motion is so rapid compared to nuclear motion, we can regard the electrons as moving in an average field generated by fixed nuclei. This allows us to separate the Hamiltonian into a nuclear and electronic part: the former being a constant for a fixed nuclear position (leading to the idea of a potential energy surface or PES), the latter having the nuclear coordinates as parameters and the electronic coordinates as independent variables. From now on, all reference to *H*, unless stated otherwise, is to the electronic Hamiltonian:

$$H = -\frac{1}{2}\sum_i \nabla_i^2 - \sum_i \sum_k \frac{Z_k}{r_{ik}} + \sum_{i<j} \frac{1}{r_{ij}} \tag{1.5}$$

where the notation is as in Eq. 1.4 except for the use of 'atomic units'. In atomic units, m_e, e and $\hbar$ are all defined to be 1. This results in clearer equations.

If we make an approximate guess for the wave function, Φ, of a system, then the following inequality may be shown to be true:

$$\frac{\int \Phi H \Phi d\mathbf{r}}{\int \Phi^2 d\mathbf{r}} \geq E_0 \tag{1.6}$$

where E_0 is the energy of the ground state. This is referred to as the variational principle. If Φ is the actual wave function of the ground state, computing the integral on the left-hand side will give E_0. In every other case, the value found will be larger than E_0. This suggests a method for finding the correct wave function: keep trying candidate wave functions until the value of the integral is at a minimum.

1.1.2 Hartree-Fock theory

If for the moment we consider a system Φ consisting of a single electron, we can ignore electron correlation. We can express the wave function Φ of the system as a linear combination of the atomic wave functions ψ of the atoms in the system. This approach is known as the linear combination of atomic orbitals (LCAO) method:

$$\Phi = \sum_{i=1}^{N} a_i \psi_i \tag{1.7}$$

where N is the number of atomic wave functions.

Substituting this expression into Eq. 1.6 gives:

$$E = \frac{\sum_{ij} a_i a_j \int \psi_i H \psi_j d\mathbf{r}}{\sum_{ij} a_i a_j \int \psi_i \psi_j d\mathbf{r}} = \frac{\sum_{ij} a_i a_j H_{ij}}{\sum_{ij} a_i a_j S_{ij}} \tag{1.8}$$

where we have used the shorthand notation H_{ij} and S_{ij} for the integrals in the numerator and denominator, respectively. H_{ij} is referred to as a 'resonance integral' and S_{ij} as an 'overlap integral'. We want to choose the coefficients a_i in Eq. 1.7 so as to minimise the energy as given by Eq. 1.8. At a minimum the derivative of the energy with respect to each of the coefficients must be zero. Applying this, we end up with the following series of N equations:

$$\sum_{i=1}^{N} a_i (H_{ki} - ES_{ki}) = 0 \qquad \forall k \tag{1.9}$$

These N equations (over k) have N unknowns, the a_i. This has a non-trivial solution if, and only if, the determinant formed from the coefficients of the unknowns is equal to zero. This gives the following equation, known as a secular equation:

$$\begin{vmatrix} H_{11} - ES_{11} & H_{12} - ES_{12} & \cdots & H_{1N} - ES_{1N} \\ H_{21} - ES_{21} & H_{22} - ES_{22} & \cdots & H_{2N} - ES_{2N} \\ \vdots & \vdots & \ddots & \vdots \\ H_{N1} - ES_{N1} & H_{N2} - ES_{N2} & \cdots & H_{NN} - ES_{NN} \end{vmatrix} = 0 \tag{1.10}$$

A similar method is used to deal with multi-electron systems. It was developed by Fock who built upon an earlier approach by Hartree. Hartree-Fock or HF theory makes the fundamental assumption that in a multi-electron system, we can imagine each electron interacting with a static field of all of the other electrons. In other words, the effect of electron correlation is neglected. This allows us to separate the Hamiltonian into a series of one-electron operators, called Fock operators:

$$f_i = -\frac{1}{2}\nabla_i^2 - \sum_{k}^{\text{nuclei}} \frac{Z_k}{r_{ik}} + V_i^{\text{HF}}\{j\} \tag{1.11}$$

The final term in Eq. 1.11 consists of an operator for the classical interelectronic repulsion and another accounting for quantum mechanical exchange.

This treatment gives rise to a secular equation analogous to that in Eq. 1.10 except that the resonance integrals H_{ij} are replaced by a matrix element F_{ij} which consists of two one-electron integrals and N^2 two-electron integrals. The two-electron integrals are weighed by elements of a 'density matrix' **P**. The elements of **P** are computed using the orbital coefficients, but the orbital coefficients are obtained by solving the secular equation. This paradox is resolved by use of a 'self-consistent field' or SCF method. This is an iterative procedure that begins by estimating the orbital coefficients, then uses these to calculate **P**, solves the secular equation and finds the orbital coefficients. The procedure is repeated until the difference between a newly determined set and the previous set is below a certain threshold criteria.

The calculated energy according to HF theory is always higher than the exact energy due to the neglect of electron correlation. In the limit of a complete basis set, the results are referred to as the Hartree-Fock limit.

1.1.3 Semiempirical methods and ZINDO

The computational bottleneck in the HF SCF method is calculation of the two-electron integrals. There are N^4 of these integrals to calculate, where N is the basis set size. Furthermore, numerical solution of these integrals is difficult. The common notation and form for one of these two-electron integrals is:

$$\left(\mu\nu\middle|\lambda\sigma\right) = \int\int \phi_\mu(1)\phi_\nu(1)\frac{1}{r_{12}}\phi_\lambda(2)\phi_\sigma(2)d\mathbf{r}(1)d\mathbf{r}(2) \qquad (1.12)$$

Semi-empirical methods increase the speed of computation by estimating the values of some of these integrals and setting others to zero. In addition, by fitting to experimentally derived data, they can account in an average way for the effects of electron-correlation.

Pople *et al.*[3] developed a method referred to as the complete neglect of differential overlap (CNDO) method. The basis set consisted of the valence atomic orbitals. The overlap matrix element S_{ij} was defined as unity where $i=j$ and zero otherwise. The two-electron integrals were set to zero if μ and ν were different orbitals, or λ and σ different orbitals. Otherwise their values were computed using a simple algebraic expression incorporating the ionisation potential and electron affinity of the atoms, and the interatomic distance (if μ and λ were on different atoms). Overall the number

of two-electron integrals having non-zero values is reduced to N^2 using this method. The one-electron integrals were also computed using easily evaluated formulae.

One of the deficiencies of CNDO was that it did not distinguish between different types of atomic orbitals. Pople *et al.*[4] modified CNDO to use different values for the one-centre two-electron integrals. This method is referred to as INDO, intermediate neglect of differential overlap. In terms of a basis set of s and p orbitals there are five integrals to consider:

$$\begin{gathered}(ss|ss) = G_{ss} \qquad (ss|pp) = G_{sp} \qquad (pp|pp) = G_{pp} \\ (pp|p'p') = G_{pp'} \qquad (sp|sp) = L_{sp}\end{gathered} \tag{1.13}$$

where the values of *G* and *L* are estimated from spectroscopic data. Valence-bond angles tend to be predicted much more accurately with INDO than with CNDO. Ridley and Zerner[5] parameterised INDO specifically for spectroscopic problems. This model is referred to as INDO/S or ZINDO/S. It is very successful for d→d transitions in transition metal complexes.

1.1.4 Density Functional Theory

Density functional theory or DFT is a quantum mechanical method that tries to calculate the electron density directly, without first finding the wave function. In this way it differs from the semi-empirical and *ab initio* methods described earlier. In DFT the problem of finding the wave function of a system is replaced by the similar problem of finding the electron density.

The potential energy of a system may be defined in terms of the electron density, *ρ*. Classical electrostatics gives us the relevant equations. The attraction between the density and the nuclei is referred to as the external potential and is given by:

$$V_{\mathrm{ne}}[\rho(\mathbf{r})] = \sum_{k}^{\mathrm{nuclei}} \int \frac{Z_k}{|\mathbf{r} - \mathbf{r}_k|} \rho(\mathbf{r}) d\mathbf{r} \tag{1.14}$$

while the electron-electron repulsion is given by the classical equation for the self-repulsion of an electric field:

$$V_{\mathrm{ee}}[\rho(\mathbf{r})] = \frac{1}{2} \iint \frac{\rho(\mathbf{r}_1)\rho(\mathbf{r}_2)}{|\mathbf{r}_1 - \mathbf{r}_2|} d\mathbf{r}_1 d\mathbf{r}_2 \tag{1.15}$$

Density functional theory derives its name from expressions such as those in Eqs. 1.14 and 1.15, where the energy is a function of the electron density, which is itself a function of three-dimensional spatial coordinates. A functional is a function of a function, and thus the expressions above are 'density functionals'.

In 1964 Hohenberg and Kohn[6] established the theoretical foundations of DFT as applied to molecular systems when they proved that for any ground-state electron density, there exists a unique external potential. This means that the electron density unambiguously determines the Hamiltonian. Thus, for a given electron density, there is a particular wave function and value for the energy of the system.

In the same paper[6], Hohenberg and Kohn also proved that ρ obeys a variational principle. If we have a candidate density, and determine the corresponding candidate wave function and Hamiltonian, we can evaluate the energy expectation value. By the variational principle of MO theory, this must be greater than or equal to the true ground-state energy:

$$\left\langle \Psi_{cand} \middle| H_{cand} \middle| \Psi_{cand} \right\rangle = E_{cand} \geq E_0 \tag{1.16}$$

In 1965 Kohn and Sham[7] provided a practical method for determining ρ. They considered a system of *non-interacting* electrons that have for their ground-state density the *same* density as the system of interest where the electrons *do* interact. The energy functional for this system may be written as:

$$E[\rho(\mathbf{r})] = T_{\mathrm{ni}}[\rho(\mathbf{r})] + V_{\mathrm{ne}}[\rho(\mathbf{r})] + V_{\mathrm{ee}}[\rho(\mathbf{r})] + \Delta T[\rho(\mathbf{r})] + \Delta V_{\mathrm{ee}}[\rho(\mathbf{r})] \tag{1.17}$$

where the terms on the r.h.s. refer, respectively, to the kinetic energy of the non-interacting electrons, the nuclear-electron interaction (Eq. 1.14), the classical electron-electron repulsion (Eq. 1.15), the correction to the kinetic energy due to the interacting nature of the electrons, and all non-classical corrections to the electron-electron repulsion energy. By considering a system of non-interacting electrons, the expression for the kinetic energy is considerably simplified:

$$T_{\mathrm{ni}}[\rho(\mathbf{r})] = \sum_{i}^{N} \left\langle \chi_i \middle| -\frac{1}{2}\nabla_i^2 \middle| \chi_i \right\rangle \tag{1.18}$$

where we use an orbital expression for the density in terms of the eigenfunctions of the non-interacting system.

According to the variational principle (see Eq. 1.6), if we find the set of orbitals χ_i that minimises the energy functional in Eq. 1.17, we can calculate the exact electron density. These orbitals are called the Kohn-Sham or KS orbitals. They can be determined using an approach similar to that of HF theory. They are expressed in terms of a basis set of functions φ_i whose coefficients are found by solving a secular equation. The matrix elements are computed from the density, but the density is determined using the orbitals found by solving the secular equation. This problem is solved in the same manner as in HF theory: an iterative SCF procedure is used.

So far, the theory of DFT is exact. It does not contain any approximations. The only problem is the last two terms of Eq. 1.17. These are usually added together to give a term referred to as the exchange-correlation energy, E_{xc}. This term accounts for the effects of quantum mechanical exchange and correlation, the correction for the classical self-interaction energy, and the difference in kinetic energy between the fictitious non-interacting system and real one. If the exact expression for this functional were known, the electron density and energy of the system could be solved exactly. Unfortunately, the form of this expression as a function of ρ is unknown. This means that approximate functionals must be used for E_{xc}.

The local density approximation (LDA) is a method for accounting for E_{xc}. It considers an electronic distribution of an infinite number of electrons moving in an infinite volume of a space that is characterised by a uniformly distributed positive charge. This is referred to as the uniform electron gas. It is assumed that in the case of a molecule, the exchange-correlation functional at every point in space is the same as it would be for the uniform electron gas having the same density as at that position. The advantage of this approach is that the exchange functional can be accurately derived for this system:

$$E_x[\rho(\mathbf{r})] = -\frac{9\alpha}{8}\left(\frac{3}{\pi}\right)^{1/3}\int \rho^{4/3}(\mathbf{r})d\mathbf{r} \qquad (1.19)$$

where α is ⅔ for the uniform electron gas. Other models use different values for α: Slater uses a value of 1, and the Xα model takes α as ¾. The local spin density approximation (LSDA) is an extension of LDA to account for systems including spin polarisation (e.g. open-shell systems). Unfortunately, analytical derivation of the correlation functional has not proven possible. However, Vosko, Wilk and Nusair[8]

have fit numerical solutions of the correlation energy of several different uniform electron gases with functionals. These functionals are referred to as VWN.

The LDA approach depends only on the density at a particular point. A number of other approaches have been developed which also take into account the gradient of the density. These functionals are often referred to as 'non-local', 'gradient-corrected' or the 'generalised gradient approximation' (GGA). They are usually constructed by addition of a correction term to the LDA functional. The most popular GGA exchange functional is that developed by Becke[9] (B) as a correction to the LSDA exchange energy. This makes use of an empirical parameter which was obtained by fitting to exactly known exchange energies of the six noble gas atoms He to Rn. One of the widely-used GGA correlation functionals is that of Lee, Yang and Parr[10] (LYP) which contains four empirical parameters fit to the helium atom. The correlation functional of Perdew and Wang[11] (PW91) is also very popular and is a correction to the LSDA energy.

The GGA differs from the LDA in its dependence on the derivative of ρ. Truly non-local effects are not included, unlike with the use of the exchange operator in the HF approach (see Eq. 1.11). Hybrid methods were developed in order to combine both methodologies. These are based upon the adiabatic connection method (ACM) which relies on the following expression for the exchange-correlation energy:

$$E_{\mathrm{xc}} = \int_0^1 \left\langle \Psi(\lambda) \middle| \mathbf{V}_{\mathrm{xc}}(\lambda) \middle| \Psi(\lambda) \right\rangle d\lambda \qquad (1.20)$$

where *λ* describes the extent of interelectronic interaction ranging from 0 (none) to 1 (exact). Visually the integral may be represented as shown in Figure 1.1. In the limit where there the electrons are not interacting, there is no correlation energy and the exchange energy can be exactly calculated just as in HF calculations to give E_x^{HF}. This gives the area of rectangle A. The area B is some fraction, *z*, of a rectangle whose height can be approximated by the exchange-correlation energy from the LSDA or the GGA, E_{xc}^{DFT}. In this way, Eq. 1.20 may be written as:

$$E_{\mathrm{xc}} = E_{\mathrm{x}}^{\mathrm{HF}} + z(E_{\mathrm{xc}}^{\mathrm{DFT}} - E_{\mathrm{x}}^{\mathrm{HF}}) \qquad (1.21)$$

which is usually expressed in terms of *a*, where $a = 1 - z$:

$$E_{\mathrm{XC}} = (1-a)E_{\mathrm{xc}}^{\mathrm{DFT}} + aE_{\mathrm{x}}^{\mathrm{HF}} \qquad (1.22)$$

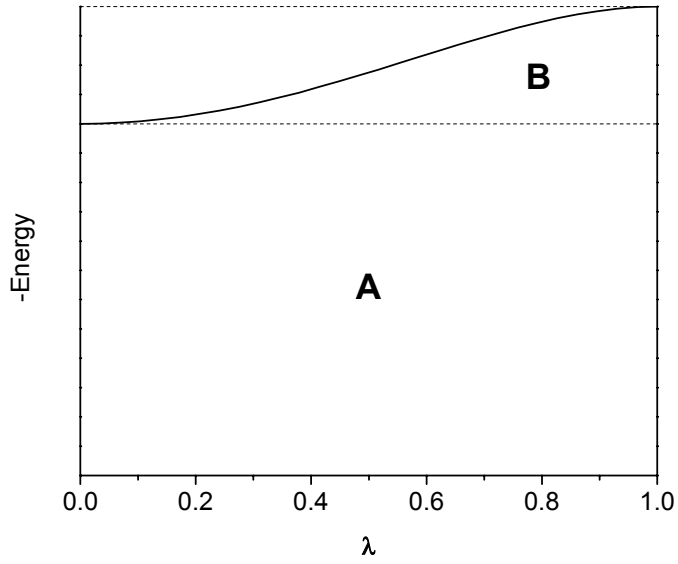

Figure 1.1 – Geometric diagram of the integral in Eq. 1.20. The area under the curve has been broken down into rectangle A and region B. The area of A may be computed exactly, while that of B is approximated under the Adiabatic Connection Method (ACM).

Becke[12] extended this expression to use 3 parameters, whose values were optimised. The result was one of the most popular functionals to date, B3LYP:

$$E_{\mathrm{xc}}^{\mathrm{B3LYP}} = (1-a)E_{\mathrm{x}}^{\mathrm{LSDA}} + aE_{\mathrm{x}}^{\mathrm{HF}} + b\Delta E_{\mathrm{x}}^{\mathrm{B}} + (1-c)E_{\mathrm{c}}^{\mathrm{LSDA}} + cE_{\mathrm{c}}^{\mathrm{LYP}} \qquad (1.23)$$

1.1.5 Advantages and limitations of DFT

When compared to HF techniques, DFT has several advantages. Density functional theory treats electron correlation exactly while HF neglects it completely. Although post-HF methods such as MP (Møller-Plesset) and CC (coupled-cluster) can be used to take into account electron correlation, DFT gives results of comparable or better quality at a computational cost similar to HF.

In terms of computational efficiency, in principle DFT scales as N^3, where N is the number of basis functions used to represent the KS orbitals. This compares with N^4 for HF. Slater-type orbitals (STOs) may be used instead of contracted Gaussian-type orbitals (GTOs), thus reducing the number of orbitals necessary. The original motivation to use GTOs was to allow analytical integration of four-centre two-

electron integrals, but this is not necessary in DFT calculations. Furthermore, convergence with respect to basis-set size tends to be more rapid than for HF techniques.

DFT has the ability to provide formal expressions for quantities of chemical interest, most of which are not easily defined in HF theory.[13] These include electronegativity, global hardness and softness, local hardness and softness, and the Fukui function. These can be used to rationalise trends in reactivity, site specificity, etc.

One of the problems with DFT is that it is necessary to use approximate functionals to calculate E_{xc}. In addition, it is not clear how to improve a functional. There is no progression in levels of theory which allows the calculation of molecular properties with increasing accuracy, thus allowing extrapolation to the exact answer, as is possible with HF and post-HF methods. Weak interactions such as van der Waals-type interactions are poorly described by current functionals, although hydrogen bonding is reasonably well accounted for.

The Kohn-Sham (KS) orbitals (see Section 1.1.4) that arise in DFT calculations represent the molecular orbitals of a fictitious system of non-interacting electrons. It is not universally accepted that it is valid to discuss the KS orbitals as physically meaningful orbitals, although the KS orbitals have been shown to be very similar to the molecular orbitals calculated from HF theory.[14] In addition, it has been proven that for the exact density functionals the eigenvalue of the highest occupied orbitals is equal to the first ionisation potential.[15] It should also be noted that DFT tends to favour delocalised structures over localised ones.[16]

1.2 DFT calculations on ruthenium polypyridyl complexes

This section serves as an overview of the literature on density functional theory (DFT) calculations on ruthenium polypyridyl-type complexes.† It is only in the last decade that such calculations have become practical due to advances in theory and application: better functionals (most notably B3LYP), more robust techniques for self-consistent field (SCF) convergence, faster computers, incorporation of common DFT methods into widely-used commercial software. Today such calculations are within the reach of any research group that can afford the necessary software and a medium-specification desktop computer.

The intention of this review is not to discuss every paper published in the field, but rather a selection of papers which I feel are of particular interest or significance. For example, Lever[17a-e], Pakkanen[18a-d] and Zheng[19a-f] have published widely on DFT calculations of ruthenium polypyridyl complexes, but only one paper of Lever will be discussed. First of all, some of the early papers in the field are reviewed. Next, papers are described which illustrate several different uses of DFT calculations. The final section deals with a series of DFT calculations on the same molecule.

1.2.1 Early papers

Before the advent of DFT, the semi-empirical modified-INDO method of Zerner (ZINDO) was the primary tool used to study the electronic structure and spectra of transition metal systems. Parameters for Ru complexes were available since 1990[20]. Daul, Baerends and Vernooijs[21] were the first to use density functional theory to investigate the electronic properties of a ruthenium polypyridyl-type complex. Baerends is one of the authors of the Amsterdam Density Functional (ADF) program package, which they used in this study. Using a crystal structure of D_3 symmetry, they predicted from first principles the energetic ordering of the components of the MLCT excited state manifold of $[Ru(bpy)_3]^{2+}$. The calculated transition energies showed an acceptable agreement with experiment, though not enough to unambiguously describe the fine structure of the MLCT manifold of $[Ru(bpy)_3]^{2+}$.

† A review of papers dealing with DFT calculations on ruthenium dinuclear complexes is left until Chapter 4.

$[Ru(bpy)_3]^{2+}$ was also the first ruthenium polypyridyl complex to be geometry-optimised using DFT. Buchs and Daul[22] used the ADF package with the Vosko, Wilk and Nusair (VWN) functional in the local density approximation (LDA). A comparison with the crystal structure of the geometries obtained using a GGA functional and the LDA functional showed the LDA to perform better. The largest difference was found for the Ru-N bond length: 2.056Å (X-ray), 2.050Å (LDA), 2.099Å (GGA). This tendency of the GGA to overestimate the metal-ligand distance had previously been found for other Werner complexes. The calculation correctly predicted a slight dihedral angle between the two rings of each bipyridine unit. The energy of the ^{3}MC was calculated, assuming the same geometry as the ground state. The result was 1.5 times the experimental value. The authors concluded that due to the long lifetime of the ^{3}MLCT, vibrational relaxation had time to occur before the ^{3}MC was populated. They noted that the energy of the MC transition was lowered when the calculation was repeated with increasing Ru-N bond lengths, as expected.

1.2.2 Comparison of ZINDO and DFT

A comparison of ZINDO and DFT results was made by Gorelsky and Lever[23] for the series of complexes, $[Ru(bqdi)_n(bpy)_{3-n}]^{2+}$, where bqdi=benzoquinonediimine. As well as comparing the ground state electronic structure (see Figure 1.2), Gorelsky and Lever compared the electronic spectrum predicted using ZINDO to that found using time-dependent DFT (TD-DFT). The B3LYP functional was used in conjunction with the LanL2DZ basis set and effective core potential. The HOMO-LUMO gap calculated using DFT is twice as small as that obtained with ZINDO. The energy order of the occupied orbitals were largely predicted to be the same by both methods, and where an interchange occurred, the orbitals differed by less than 0.1eV. In each case, DFT predicted a greater degree of covalency than ZINDO, based on the ligand character in the highest occupied molecular orbitals. The TD-DFT method gave a slightly more accurate UV-Vis spectrum than ZINDO, at a much higher computational cost. The authors note that since ZINDO is parameterised to reproduce experimental solution spectra (in most cases) it is possible that it would perform better than TD-DFT for complexes exhibiting strong solvatochromic effects. It may also be the explain why TD-DFT predicts a higher degree of covalency – in polar solution, ionic structures are stabilised.

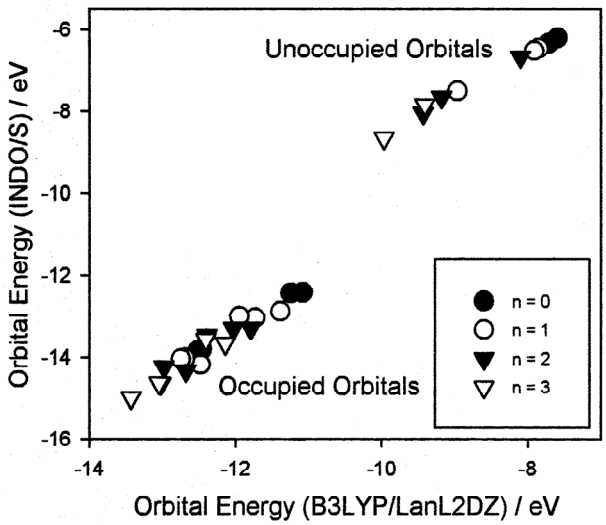

Figure 1.2 – Correlation between orbital energies calculated using ZINDO/S and DFT, for the series of complexes, $[Ru(bqdi)_n(bpy)_{3-n}]^{2+}$, where bqdi=benzoquinonediimine. Taken from Gorelsky and Lever.[23]

1.2.3 Redox potentials

The measurement of reduction and oxidation potentials is a key experimental technique for the investigation and characterisation of ruthenium complexes. Several researchers have noted a correlation between the HOMO and LUMO energies and the first oxidation and first reduction potentials, respectively. Stoyanov *et al.*[24] looked at 10 different complexes of ruthenium which used a combination of the ligands bipyridine, bipyrimidine and bipyrazine. A plot of the energy of the LUMO versus $E_{½}^{red}$ had a correlation coefficient of 0.937, while the HOMO versus $E_{½}^{ox}$ gave a value of 0.994.

Is it possible then to predict, purely from DFT, the redox potential of a ruthenium complex? This is the question that Baik and Friesner[25] addressed using DFT calculations on three series of related molecules: (a) simple organic molecules, (b) several metallocenes, and (c) the trisbpy complexes of Fe, Ru and Os as well as the hexacyano complexes of Fe and Ru. Geometry optimisations were performed at the B3LYP/6-31G(d,p) level, followed by single-point calculations at the cc-pVTZ(-f)++ level incorporating solvent effects through a self-consistent reaction field (SCRF). The results, especially for anionic species, were greatly improved through the use of the diffuse basis set. Very good correlation was obtained for series (a) and (b), with the former having an average error of 0.120V for the redox potentials. For series (c)

all the calculated redox potentials appeared to be systematically shifted. The authors attribute this to a systematic overestimation of the solvation energy due to a mismatch of the solvation model parameters with the systems studied. Nevertheless, the relative order of the redox potentials was correct, and in the case of $[Ru(bpy)_3]^n$, the four computed potentials formed a perfect line when correlated with experiment. The authors conclude by stressing the importance of a sophisticated and diffuse basis set for obtaining quantitative agreement with experimental redox potentials.

1.2.4 Basicities

Hamra *et al.*[26] studied the relative basicities of $[Ru(NH_3)_5pz]^{2+}$, $[Ru(CN)_5pz]^{3-}$ and pz using DFT. This involved calculating the proton affinities of each, which corresponds to the enthalpy changes accompanying the following equation:

$$BH^+ \rightarrow B + H^+ \qquad (1.24)$$

The change in entropy, ΔS, for the reaction was also found which allowed the free energy change in the gas phase, ΔG_{gp}, to be calculated using the relation:

$$\Delta G_{gp} = PA - T\Delta S \qquad (1.25)$$

They modelled solvent effects in three ways: first using a shell of hydrating water molecules, then using a continuum method (the Onsager reaction field model), and finally using a hybrid of the two. The relative basicities were ordered in agreement with experiment only when the hybrid method was used, although even in that case only qualitative agreement was obtained with experimentally-determined pK_a values.

1.2.5 Surface studies

While there are many cases where researchers have used DFT in surface studies involving organic molecules, this author could only find one involving a ruthenium polypyridyl-type molecule attached to a surface. Haukka and Hirva[27] looked at the interaction between *cis*(CO)-*trans*(I)-Ru(H_2dcb)$(CO)_2I_2$ and a TiO_2 (anatase) surface. This is a key interaction in dye-sensitised solar cells, involving formation of an ester linkage at the surface. The hybrid functional B1PW91 was used, with 6-31G(d) as the basis set for all elements except Ru and I, for which Huzinaga's bases were used. A cluster model was used for the surface (see Figure 1.3). An interaction

energy was calculated as the difference between the sum of the energy of the freely-optimised surface and the freely-optimised adsorbate, and the energy when the adsorbate is bound to the surface. Due to the size of the system, the structure of the cluster was held fixed at the geometry in bulk TiO_2 while the geometry of the adsorbate was optimised in several binding modes. Multidentate binding modes were found to be favoured over monodentate.

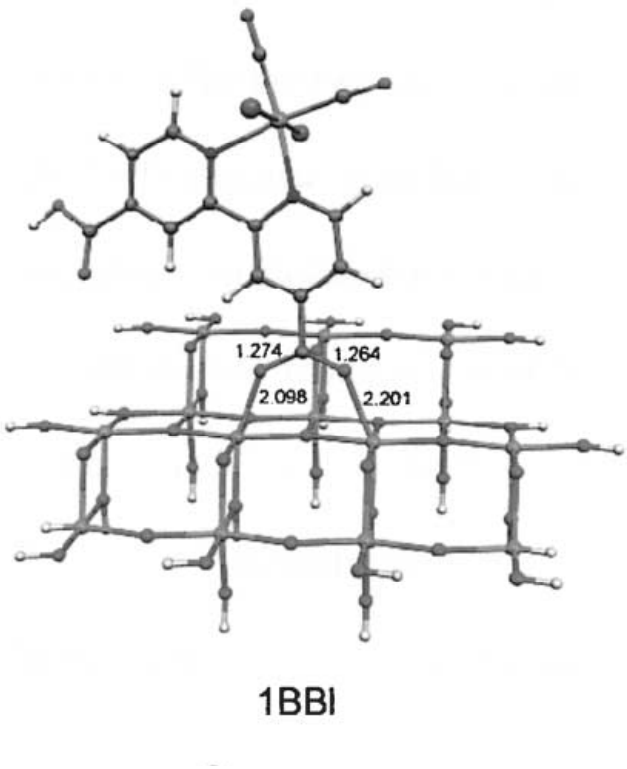

Figure 1.3 – A bidentate binding mode of $[Ru(H_2dcb)(CO)_2I_2]$ to a $Ti_{14}O_{42}H_{28}$ cluster representing the anatase (1 0 1) surface. Taken from Haukka *et al*.[27]

1.2.6 Normal coordinate analysis

The first normal coordinate analysis of a ruthenium polypyridyl complex was of $[Ru(bpy)_3]^{2+}$. Kincaid *et al.*[28] used an empirical force field which considered the complex as a single bpy ligand coordinated to a Ru^{II} atom and only dealt with in-plane vibrations. Alexander and Dines[29] recently carried out a scaled quantum mechanical force field (SQM-FF) investigation of the Ru^{II} tris homoleptic complexes of bipyrimidine and bipyrazine. They used DFT at the B3LYP/LanL2DZ level of theory and, unlike the earlier study, this analysis treated the ion as a whole and dealt with all 3N – 6 vibrational modes. Bands in the infrared and Raman spectra were assigned in terms of detailed mode descriptions and symmetry species. After

scaling the force constants involving hydrogen atoms by 0.90, and the others by 1.025, the authors report that a highly satisfactory fit to the experimental spectra was obtained (rmsd not reported).

1.2.7 Excited-state and photochemical studies

For ruthenium polypyridyl complexes, although absorption occurs to a singlet state, the lowest-energy excited state is a triplet state and it is from here that emission occurs. In general, most studies of ruthenium polypyridyl complexes deal with the ground state singlet structure. Formally, DFT may only be used to calculate the electronic structure of the lowest energy state of each irreducible representation of the molecular point group – this is a consequence of the Hohenberg-Kohn theorem upon which modern DFT is built.[6,30] For a ruthenium complex with C_1 symmetry, this means that formally only the singlet ground state (S_0) may be studied. However, recent studies[31,32,33] on ruthenium polypyridyl complexes show that calculation of the lowest energy triplet state (T_1) gives energies in good agreement with those from TDDFT (see below). In addition, since a spin-unrestricted formalism is required for triplet states, excited-state calculations require considerable additional computation compared to ground state calculations.

TD-DFT calculations can give the vertical excitation energy to the lowest energy singlet and triplet states. Amini *et al.*[34] found good agreement between calculation and experiment for the energy of the ^{3}MLCT state of $[Ru(terpy)_2]^{2+}$ (16365cm^{-1} versus 16920cm^{-1}). A study by Guillemoles *et al.*[31] compared the so-called ΔSCF approach to the TD-DFT approach in their ability to calculate the energy of the excited states of $M(bpy)_2(SCN)_2$ and $M(bpy)_2(CN)_2$ (M=Ru, Os). The ΔSCF approach involved calculation of the energy difference between the ground state S_0 and the triplet state T_1 at the ground state geometry. The difference was also calculated after optimisation of the triplet state geometry. In general, for T_1, the ΔSCF and TD-DFT approaches at the S_0 geometry gave results which differed by only about 0.1eV. This indicated the one-electron nature of the lowest energy excitations. After optimisation of T_1, the ΔSCF energy was reduced by between 0.1 and 0.2 eV. Inclusion of solvent effects (through PCM) increased the S_0/T_1 gap by about 0.6 eV. In the case of the Os complexes, where experimental values were available for the energy of the $S_0 \rightarrow T_1$ transition, the inclusion of solvent effects brought the predicted values into agreement with experiment.

Light-induced linkage isomerisation in $[Ru(bpy)(terpy)dmso]^{2+}$ was investigated by Ciofini, Daul and Adamo.[32] The S-linked isomer is converted to the O-linked isomer on irradiation at 442 nm, with an η^2 SO-linked species proposed as an intermediate by Rack, Winkler and Gray.[35] A transition state search performed on the S_0 potential energy surface found a transition state (see Figure 1.4) corresponding to the proposed intermediate at an energy 13.9 and 25.6 kcal/mol above the S- and O-linked isomers, respectively. Starting from this geometry, a transition state search on the T_1 potential energy surface gave a similar structure at 3.0 and 13.1 kcal/mol above the S- and O-linked isomers, respectively. The small barrier for S→O interconversion indicated that isomerism was possible in the T_1 state through a single-step mechanism, rather than the two-step mechanism involving an intermediate proposed by Rack *et al.* The ΔSCF method was used to calculate the energy of emission from the T_1 state. This involved calculating the difference between the energy of the optimised T_1 state and the S_0 state at the geometry of the T_1 state. The energies obtained were used to interpret the experimentally observed emission.

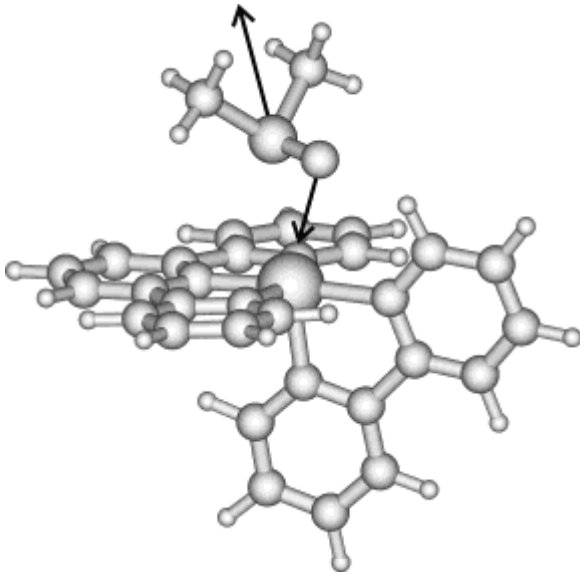

Figure 1.4 – Structure of the transition state for the S-linked → O-linked interconversion in the ground state of $[Ru(bpy)(terpy)dmso]^{2+}$. The arrows indicate the direction of the transition vector. Taken from Ciofini *et al.*[32]

1.2.8 The 'N3 dye': an example of a series of calculations

Certain ruthenium polypyridyl complexes in particular have attracted widespread attention due to their interesting or useful photophysical properties. In such cases a

number of DFT studies on the same molecule may appear, each trying to improve on the previous. An example of such a series of calculations gives an insight into the increasing levels of theory or complexity possible within the overall framework of DFT. The example dealt with here, the so-called 'N3 dye', $[Ru(H_2dcb)_2(NCS)_2]$ (see Figure 1.5), is one of the most widely studied ruthenium polypyridyl complexes due to its unmatched performance in dye-sensitised solar cells. In the solar cells, the carboxy groups of the complex attach to a TiO_2 surface through the formation of ester linkages.

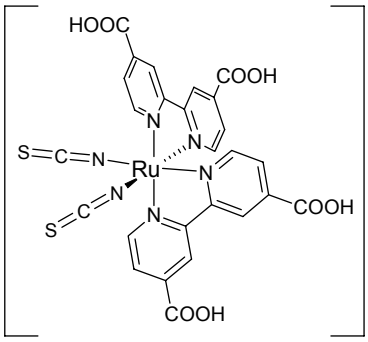

N3 dye

Figure 1.5 – The structure of the N3 dye

A paper by Guillemoles *et al.*[31] described itself as giving insight into a class of molecules used in dye-sensitised photoelectrochemical cells, but dealt with the computationally simpler *bis*bpy analogue of the N3 dye. Since the carboxy groups are expected to interact electronically with the bipyridines, and furthermore to play an important role in the electronic communication between the metal centre and the TiO_2 surface, this approach clearly has its deficiencies. A DFT study by Monat *et al.*[36] used the crystal structure of the N3 dye as the basis for single-point and TD-DFT calculations. The justification given was that the method employed (B3LYP) tended to overestimate the metal-ligand bond length. The HOMO was calculated to be 51% Ru with about 30% on the NCS ligands. The TD-DFT method gave very good agreement with experiment although the calculated spectrum appeared to be shifted to higher energy by 0.146eV (see Figure 1.6). The distance between the two peak maxima differed by only 0.057eV compared to the experimental spectrum.

Fantacci *et al.*[37] extended the previous study by including solvent effects in single-point and TD-DFT calculations using the Conductor-like Screening Model (COSMO). In addition, they first geometry optimised the structure. NCS was calculated to make

a much stronger contribution to the HOMO than reported in the previous study, although direct comparison is difficult due to the difference in the way the contributions are reported. The energies of the orbitals involving the metal and the NCS ligands were stabilised by up to 0.6eV by including the solvent. The dipole moment increased from 10.93 D *in vacuo* to 20.60 D in water, reflecting the more effective charge-separation favoured by the polar solvent. The TD-DFT calculations *in vacuo* show very poor agreement with experiment. Much better agreement is obtained by inclusion of solvent effects, although the calculated spectra are red-shifted by about 0.3eV with respect to experiment (see Figure 1.6). However, the interpeak distances (for the three peaks in the spectrum) are accurate to within 0.05eV. More recently, the same authors looked at the effect of pH on the predicted TD-DFT spectra.[38]

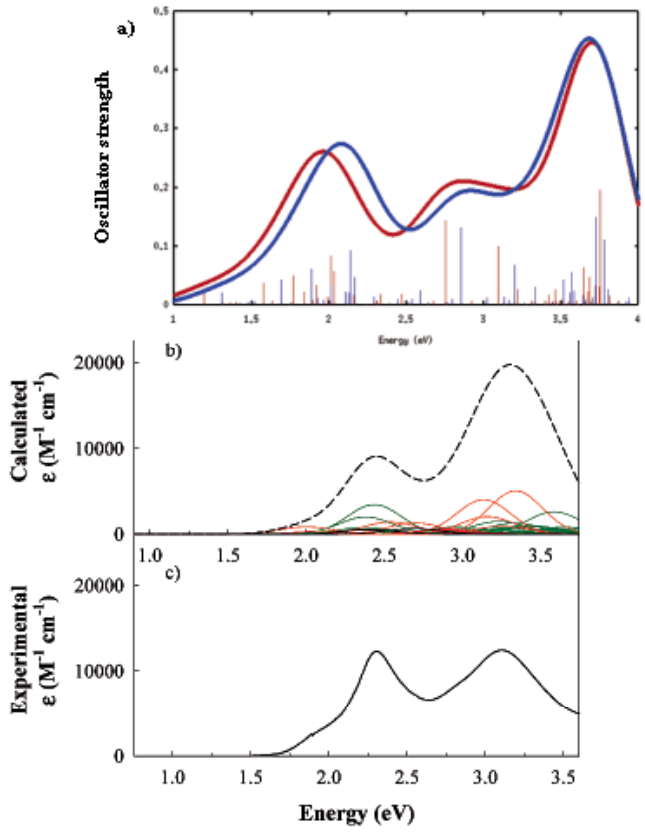

Figure 1.6 – Calculated and experimental spectra of the 'N3 dye': (a) in water and ethanol (BPW91/ADF IV) from Fantacci *et al.*[37], (b) gas phase (B3LYP/LanL2DZ) and (c) experimental from Monat *et al.*[36]

1.2.9 Future challenges

To a large degree, computing power determines the size of the problem which can currently be tackled by existing computational methods. DFT calculations formally scale as N^4 (where N is the number of basis set functions), although there are approaches which reduce this dependence to N^3. As the speed of computation increases in the coming years, we can expect to see calculations performed which today are computationally too expensive. Such technical challenges include unrestricted calculations: for example, the electronic structure of the triplet state of ruthenium dinuclear complexes and investigations of electrochemically oxidised and reduced species. In the area of surface studies, an investigation of the N3 dye attached to a TiO_2 surface is an obvious challenge – in addition, as computing power increases, this problem is open to investigation at a number of levels of theory. An ability to use more complete basis sets, as well as an all-electron basis set for ruthenium, will also arrive with an improvement in the speed of computers.

Some scientific challenges for the future include:

(1) more accurate prediction of UV-Vis spectra, perhaps by inclusion of spin-orbit coupling in TD-DFT and better solvent models
(2) an ability to accurately predict NMR spectra to aid in assignment of peaks
(3) rational design of anion sensors
(4) rational design of complexes with desired redox or basicity properties
(5) an ability to predict photochemistry

1.2.10 Scope of thesis

Chapter 1 has introduced Density Functional Theory (DFT), the computational method used throughout this thesis. In addition, a review was presented of DFT calculations on ruthenium polypyridyl complexes. Chapter 2 gives details of the computational method used in the thesis – for example, details of the basis set and functional used are given. In addition, a description is provided of in-house software developed to analyse the results of calculations.

Chapter 3 investigates the electronic structure of a series of complexes of type $[Ru(bpy)_2(pytrz)]^+$. Observed reactivity patterns are correlated with calculations. Chapter 4 compares the electronic structures of mononuclear and dinuclear ruthenium complexes.

The resonance Raman spectrum of $[Ru(bpy)_3]^{2+}$ is studied for the first time using DFT in Chapter 5. Parameters affecting the accuracy of the calculation are examined. The first DFT study of an osmium complex attached to a gold surface is presented in Chapter 6. The effect of adsorption on the energy levels of the system was investigated.

Chapter 7 presents an overview of the capabilities of DFT calculations on ruthenium polypyridyl complexes. Some suggestions are made for future work.

Finally, some appendices are attached. Appendix A describes experimental work on the effect of $LiClO_4$ concentration on the emission from ruthenium polypyridyl complexes attached to a nanocrystalline TiO_2 substrate. Since computational studies form the bulk of the thesis, it was decided to place this work in an appendix. Appendix B describes gives some tips for using Gaussian03 and GaussView to carry out DFT calculations. Appendix C lists some structures that have been geometry-optimised in the course of my thesis, but are not contained in this thesis. Appendix D contains contributions to publications during the course of my research.

1.3 References

1. Based on introductory chapters to HF and DFT in (a) Jensen, F., *Introduction to Computational Chemistry*, Wiley, **1999**. (b) Springborg, M., *Density-Functional Methods in Chemistry and Materials Science*, Wiley, **1997**. (c) Cramer, C.J., *Essentials of Computational Chemistry*, Wiley, **2002**.

2. Born, M. and Oppenheimer, J.R., *Ann. D. Physik Lpz.*, **1927**, *84*, 457.

3. (a) Pople, J.A., Santry, D.P. and Segal, G.A., *J. Chem. Phys.*, **1965**, *43*, S129. (b) Pople, J.A. and Segal, G.A., *J. Chem. Phys.*, **1965**, *43*, S136.

4. Pople, J.A., Beveridge, D.L. and Dobosh, P.A., *J. Chem. Phys.*, **1967**, *47*, 2026.

5. Ridley, J.E. and Zerner, M.C., *Theor. Chim. Acta*, **1973**, *32*, 111.

6. Hohenberg, P. and Kohn, W., *Phys. Rev.*, **1964**, *136*, B864.

7. Kohn, W. and Sham, L.J., *Phys. Rev.*, **1965**, *140*, A1133.

8. Vosko, S.H., Wilk, L. and Nusair, M., *Can. J. Phys.*, **1980**, *58*, 1200.

9. Becke, A.D., *Phys. Rev. A.*, **1988**, *33*, 8800.

10. Lee, C., Yang, W. and Parr, R.G., **1988**, *37*, 785.

11. (a) Perdew, J.P. and Wang, Y., *Phys. Rev. B*, **1992**, *45*, 13244. (b) Perdew, J.P., Chevary, J.A., Vosko, S.H., Jackson, K.A., Pederson, M.R., Singh, D.J. and Fiolhais, C., *Phys. Rev. B*, **1992**, *46*, 6671.

12. Becke, A.D., *J. Chem. Phys.*, **1993**, *98*, 5648.

13. Geerlings, P., De Proft, F. and Langenaeker, W., *Chem. Rev.*, **2003**, *103*, 1793.

14. Stowasser, R. and Hoffmann, R., *J. Am. Chem. Soc.*, **1999**, *121*, 3414.

15. Perdew, J.P., Parr, R.G., Levy, M. and Balduz, J.L.Jr., *Phys. Rev. Lett.*, **1982**, *49*, 1691.

16. Braun-Sand, S.B. and Wiest, O., *J. Phys. Chem. A*, **2003**, *107*, 285.

17. (a) Nazeeruddin, Md.K., Zakeeruddin, S.M., Humphry-Baker, R., Gorelsky, S.I., Lever, A.B.P. and Grätzel, M., *Coord. Chem. Rev.*, **2000**, *208*, 213. (b) Gorelsky, S.I., da Silva, S.C., Lever, A.B.P. and Franco, D.W., *Inorg. Chim. Acta.*, **2000**, *300-302*, 698. (c) da Silva, R.S., Gorelsky, S.I., Dodsworth, E.S., Tfouni, E. and Lever, A.B.P., *J. Chem. Soc., Dalton Trans.*, **2000**, 4078. (d) Gorlesky, S.I., Lever, A.B.P. and Ebadi, M., *Coord. Chem. Rev.*, **2002**, *230*, 97. (e) Renouard, T., Fallahpour, R.-A., Nazeeruddin, Md.K., Humphry-Baker, R., Gorelsky, S.I., Lever, A.B.P. and Grätzel, M., *Inorg. Chem*, **2002**, *41*, 367.

18. (a) Haukka, M., Hirva, P., Luukkanen, S., Kallinen, M., Ahlgrén, M. and Pakkanen, T.A., *Inorg. Chem.*, **1999**, *38*, 3182. (b) Luukkanen, S., Haukka, M. and Pakkanen, T.A., *Inorg. Chim. Acta*, **2000**, *309*, 155. (c) Kinnunen, T.-J.J., Haukka, M., Nousiainen, M., Patrikka, A. and Pakkanen, T.A., *J. Chem. Soc., Dalton Trans.*, **2001**, 2949. (d) Kinnunen, T.-J.J., Haukka, M. and Pakkanen, T.A., *J. Organomet. Chem.*, **2002**, *654*, 8.

19. (a) Zheng, K.C., Wang, J.P., Shen, Y., Kuang, D.B. and Yun, F.C., *Acta Chim. Sin.*, **2001**, *59*, 1283. (b) Zheng, K.C., Wang, J.P., Shen, Y., Peng, W.L. and Yun, F.C., *J. Chem. Soc., Dalton Trans.*, **2002**, 111. (c) Zheng, K.C., Wang, J.P., Peng, W.L., Shen,

Y. and Yun, F.C., *Inorg. Chim. Acta*, **2002**, *328*, 247. (d) Zheng, K.C., Shen, Y., J.P. Wang, Liu, X.W. and Yun, F.C., *Inorg. Chim. Acta*, **2002**, *335*, 100. (e) Zheng, K.C., Wang, J.P., Liu, X.W., Shen, Y. and Yun, F.C., *J. Mol. Struct. (Theochem)*, **2002**, *577*, 95. (f) Zheng, K.C., Wang, J.P., Peng, W.L., Liu, X.W. and Yun, F.C., *J. Mol. Struct. (Theochem)*, **2002**, *582*, 1.

20. Anderson, W.P., Cundari, T.R., Drago, R.S. and Zerner, M.C., *Inorg. Chem.* **1990**, *29*, 1.

21. Daul, C., Baerends, E.J. and Vernooijs, P., *Inorg. Chem.*, **1994**, *33*, 3538.

22. Buchs, M. and Daul, C., *Chimia*, **1998**, *52*, 163.

23. Gorelsky, S.I. and Lever, A.B.P., *J. Organomet. Chem.*, **2001**, *635*, 187.

24. Stoyanov, S.R., Villegas, J.M. and Rillema, D.P., *Inorg. Chem.*, **2002**, *41*, 2941.

25. Baik, M.-H. and Friesner, R.A., *J. Phys. Chem. A*, **2002**, *106*, 7407.

26. Hamra, O.Y., Slep, L.D., Olabe, J.A. and Estrin, D.A., *Inorg. Chem.*, **1998**, *37*, 2033.

27. Haukka, M. and Hirva, P., *Surf. Sci.*, **2002**, *511*, 373.

28. Strommen, D.P., Mallick, P.K., Danzer, G.D., Lumpkin, R.S. and Kincaid, J.R., *J. Phys. Chem.*, **1990**, *94*, 1357.

29. Alexander, B.D. and Dines, T.J., *Inorg. Chem.*, **2004**, *43*, 342.

30. (a) Gunnarson, O. and Lundqvist, B.I., *Phys. Rev. B*, **1976**, *13*, 4274. (b) Gunnarson, O. and Lundqvist, B.I., *Phys. Rev. B*, **1976**, *15*, 6006 (erratum).

31. Guillemoles, J.-F., Barone, V., Joubert, L. and Adamo, C., *J. Phys. Chem. A*, **2002**, *106*, 11354.

32. Ciofini, I., Daul, C.A. and Adamo, C., *J. Phys. Chem. A*, **2003**, *107*, 11182.

33. Pourtois, G., Beljonne, D., Moucheron, C., Schumm, S., Kirsch-De Mesmaeker, A., Lazzaroni, R. and Brédas, J.-L., *J. Am. Chem. Soc.*, **2004**, *126*, 683.

34. Amini, A., Harriman, A. and Mayeux, A., *Phys. Chem. Chem. Phys.*, **2004**, *6*, 1157.

35. Rack, J.J., Winkler, J.R. and Gray, H.B., *J. Am. Chem. Soc.*, **2001**, *123*, 2432.

36. Monat, J.E., Rodriguez, J.H. and McCusker, J.K., *J. Phys. Chem. A*, **2002**, *106*, 7399.

37. Fantacci, S., De Angelis, F. and Selloni, A., *J. Am. Chem. Soc.*, **2003**, *125*, 4381.

38. De Angelis, F., Fantacci, S. and Selloni, A., *Chem. Phys. Lett.*, **2004**, *389*, 204.

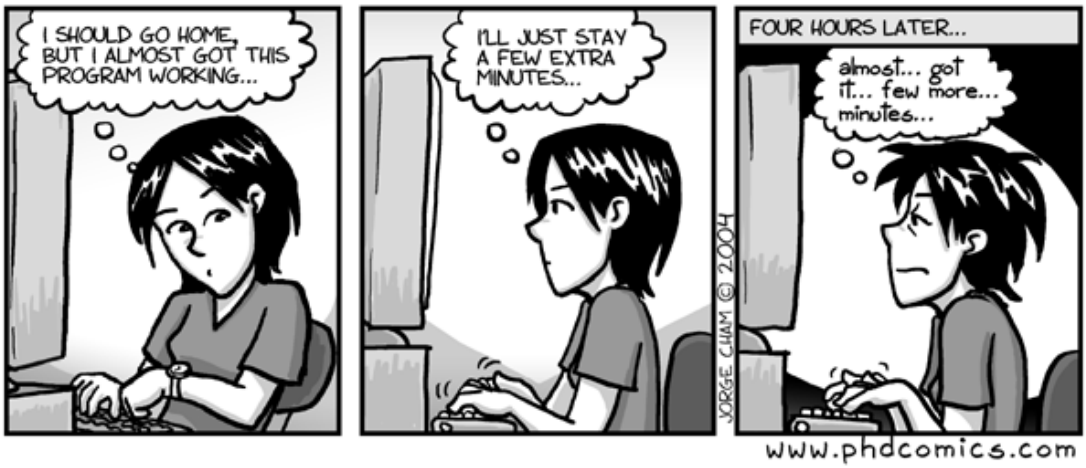
I SHOULD GO HOME, BUT I ALMOST GOT THIS PROGRAM WORKING...
I'LL JUST STAY A FEW EXTRA MINUTES...
FOUR HOURS LATER...
almost... got it... few more... minutes...
JORGE CHAM © 2004
www.phdcomics.com

Chapter 2
Computational Method

This chapter contains three sections. The first section describes the general experimental conditions for the DFT calculations carried out in this thesis. (For a practical introduction to carrying out DFT calculations, see Appendix II.) The second and third sections describe our own in-house software which have been used to obtain data included in this thesis. GaussSum is a multifunctional program capable of monitoring the progress of calculations, extracting data from the Gaussian output file, convoluting spectra and performing various calculations. GauStock calculates the partial atomic charge using Hirshfeld Population Analysis.

2.1 Hardware and software

Calculations were carried out on an Intel Pentium IV 2.8GHz desktop computer with 1GB DDR RAM running Windows XP. Gaussian 03W[1] was used to carry out all DFT calculations. Jobs were prepared and results were inspected using GaussView 3.0[2]. GaussSum[3] was used to monitor jobs, calculate density of states spectra, convolute UV-Vis and Raman spectra, calculate group contributions to molecular orbitals, and prepare electron density difference maps. GauStock[4] was used to calculate partial atomic charges using Hirshfeld Population Analysis.

2.2 Calculation details

2.2.1 Density functional

Becke's 3-parameter hybrid functional[5] was used along with the correlation functional of Lee, Yang and Parr[6,7]. This combination is denoted by B3LYP (see Section 1.1.4). The functional is described by the following equation:

$$E_{\mathrm{xc}}^{\mathrm{B3LYP}} = (1-a)E_{\mathrm{x}}^{\mathrm{LSDA}} + aE_{\mathrm{x}}^{\mathrm{HF}} + b\Delta E_{\mathrm{x}}^{\mathrm{B}} + (1-c)E_{\mathrm{c}}^{\mathrm{LSDA}} + cE_{\mathrm{c}}^{\mathrm{LYP}} \qquad (2.1)$$

Becke chose values for a, b and c (0.20, 0.72, and 0.81) that minimised the least-squares fit to 56 atomisation energies, 42 ionisation potentials and 8 proton affinities of the G1 set of atoms and molecules. Although in his original paper Becke used the correlation functional PW91[8], Stevens *et al.*[9] modified Becke's functional to use LYP instead, while retaining the original values of a, b and c.

2.2.2 Basis set

Most modern computational codes use the 'Basis Set Approximation' to solve the Schrödinger equation. This involves expressing the molecular orbitals as a linear combination of a set of mathematical functions called the basis set. An infinite basis set will give the best possible result for a given level of theory although, in practice, only a finite basis set is possible.

A larger and more flexible basis set is better able to describe the electron density of a molecule, and hence gives more accurate results. Generally, a trade-off between speed and accuracy is necessary, as there is an N^4 dependence on the basis set size. In a system of the size of a ruthenium polypyridyl complex, a reasonable

compromise is to use the LanL2DZ basis set and electron-core potential of Dunning, Hay and Wadt.

For the atoms C, H and N, LanL2DZ uses the Dunning/Huzinaga[10] valence double-ζ basis set. Following the usual notation for basis sets, H, C and N are described by (10s5p/4s)[3s2p/2s].

The treatment of heavy atoms (third row and lower) by LanL2DZ involves the use of a pseudopotential or effective core potential (ECP) for the core electrons[11]. The ECP is an analytical function which is used to account for the effect of the combined nuclear-electronic core on the remaining electrons. This approach is justified by the fact that the inner electrons of a heavy atom are unimportant, in a chemical sense – their spatial distribution and energies are largely unchanged when they form a chemical bond. In addition, relativistic effects, which are important for atoms as heavy as ruthenium, can be 'folded in' to the ECP. These effects would otherwise be neglected. The LanL2DZ ECP accounts for the innermost 28 electrons of Ru ([Ar]$3d^{10}$)and the innermost 60 electrons of Os ([Kr]$4d^{10}4f^{14}$). In both cases the remaining 16 electrons ($4s^2 4p^6 4d^7 5s^1$ for Ru, and $5s^2 5p^6 5d^7 6s^1$ for Os) are treated using a double-ζ basis set. The name LanL2DZ comes from the fact that it uses the Los Alamos National Laboratory (LANL) ECPs along with a double-ζ (DZ) basis set.

For some calculations in Chapter 6, the LanL2MB basis set and ECP was used instead. This uses a minimal basis set for C, H and N (STO-3G[12]) and the outermost 16 electrons of Ru and Os. The resulting basis set is thus smaller.

The 6-31G(d) (or 6-31G*) basis set is used in Chapter 5 for C, H and N. This implies the 6-31G valence double-ζ basis set,[13] (10s4p/4s)[3s2p/2s], with an additional set of 6 d functions on C and N to allow for polarisation of the p orbitals.

2.2.3 Symmetry

Except where otherwise noted, the highest possible symmetry was used in the calculations. For example, D_3 symmetry was imposed on $[Ru(bpy_3)]^{2+}$ and dinuclear complexes were set up as either C_2 or C_i. The use of symmetry has advantages. The symmetry detected by Gaussian at the start of a geometry optimisation will be retained throughout the calculation, thus reducing the effective degrees of freedom of the molecule and hence the number of steps required for the geometry to

converge. Calculation of the energy is faster, since some integrals will be equal due to symmetry, and others will be zero because of the orthogonality of irreducible representations. TD-DFT calculations (used to calculate electronic transitions; see Chapter 4 on dinuclear complexes) use the fact that transitions between orbitals of the same symmetry are forbidden in a molecule with a centre of symmetry.

2.2.4 Geometry optimisation

The Berny algorithm is the default geometry optimisation algorithm for Gaussian. This algorithm is based upon a program by Schlegel[14], although it has been considerably enhanced (see under keyword *OPT* in Ref. 15, and references therein). The optimisation takes place in redundant internal coordinates regardless of the input format (Z-matrix or Cartesian coordinates). Redundant internal coordinates include all sets of internal coordinates (bond distances, angles and torsions) between atoms within bonding distance. In general, the number of such internal coordinates will be greater than the minimum of 3N-6 required to specify the structure of the molecule – hence the name 'redundant'.

After each calculation of the energy, the algorithm moves the atoms slightly, based upon an analysis of the gradient vector (the vector of first derivatives of the energy with respect to each of the internal coordinates) and the Hessian (the matrix of second derivatives of the energy with respect to internal coordinates). The energy is calculated again, and the cycle continues until a local minimum is found. Gaussian 03 concludes that a local minimum has been found if each of the following four criteria is met:

(1) the maximum force is less than 0.000450 hartrees/bohr
(2) the RMS force is less than 0.000300 hartrees/bohr
(3) the maximum displacement is less than 0.001800 bohr
(4) the RMS displacement is less than 0.001200 bohr

Alternatively, if the forces are two orders of magnitude smaller than the threshold value, the geometry is considered to have converged irrespective of criteria 3 and 4. This facilitates optimisation of large molecules which may have a very flat potential energy surface around the minimum.

The threshold values listed above for each of the criteria are the defaults. It is possible to specify tighter thresholds (Gaussian keyword *OPT=TIGHT*) for which the

values are 0.000015 hartrees/bohr, 0.000010 hartrees/bohr, 0.000060 bohr and 0.000040 bohr respectively. Use of the tighter thresholds is recommended for calculation of low frequency vibrational modes.[15] When tight thresholds are specified for DFT calculations an ultrafine grid should also be used (see Section 2.2.5).

Difficulties in geometry convergence are often due to a poor guess for the Hessian, or force constant, matrix. In this case, calculation of the force constants by means of a frequency calculation can greatly reduce the number of steps required to reach an energy minimum. The Gaussian keywords, *OPT=CALCFC* (calculate the force constants for the initial geometry optimisation step), *OPT=CALCALL* (calculate the force constants before every step), and *OPT=READFC* (read in the force constants from a frequency calculation, usually at a lower level of theory) are useful in this regard.

2.2.5 Integration grid

The exchange-correlation energy is calculated numerically by integration using a quadrature grid. The default, or 'fine', grid was used in most instances. This is a pruned (75,302) grid; that is, it is equivalent to having 75 radial shells and 302 angular points per shell. Pruned grids are optimised to use the minimal number of points required to achieve a given level of accuracy – this grid uses about 7000 points per atom (instead of about 23000).

In some cases, either where the SCF or geometry had difficulty in converging or where tight thresholds were used for the geometry optimisation, an 'ultrafine' grid was used (Gaussian keyword *INT=ULTRAFINE*). This is a pruned (99,590) grid, recommended for computing very low frequency modes of systems (see the discussion of *OPT=TIGHT* in Section 2.2.4).

The same integration grid should be used when comparing the energies of two molecules, and also when performing frequency calculations after a geometry optimisation.

2.3 GaussSum

GaussSum is a program written to parse the output of two popular computational chemistry programs, Gaussian[1] and GAMESS[16]. In addition to rearranging the computed data into a more accessible format, it performs calculations on the data and can convolute spectra. GaussSum provides a graphical user interface to all of its functions and runs on Windows, Linux and MacOSX. It is written in Python and uses the plotting program Gnuplot[17] for drawing graphs. GaussSum is open-source and is available for free from http://gausssum.sourceforge.net. Since January 2004, there have been more than one thousand downloads of GaussSum 0.8.

GaussSum may be used to:

- monitor the progress of the self-consistent field (SCF) convergence
- monitor the progress of geometry optimisation
- display all lines in the log file containing a particular phrase
- extract molecular orbital information
- calculate contributions of groups of atoms to each molecular orbital using Mulliken Population Analysis
- plot the density of states spectrum (and the partial density of states, in the case of groups of atoms)
- calculate and plot the crystal orbital overlap population (COOP)
- extract information on electronic transitions and plot the UV-Vis spectra
- calculate the change in the charge density corresponding to a particular UV-Vis transition
- create an electron density difference map, which can be used to visualise the change in electron density corresponding to a particular UV-Vis transition
- extract information on IR and Raman vibrations
- plot the IR and Raman spectra, which may be scaled using general or individual scaling factors

The following sections discuss some of these features in detail.

The next version of GaussSum will include a new module to handle calculated NMR data. This module is being developed in collaboration with Prof. Ulrich Siehl of the University of Ulm, Germany.

2.3.1 Progress of SCF convergence and geometry optimisation

GAMESS and Gaussian monitor the progress of SCF convergence and geometry optimisation by using a number of criteria. Once these criteria are fulfilled, the SCF or geometry is regarded as having converged. For example, for SCF convergence using Gaussian, there are three criteria to be met: each of 'RMS density matrix', 'maximum density matrix', and energy must differ by less than a certain amount upon successive iterations. The convergence threshold values depend on whether tight convergence is being used (Gaussian keyword *SCF=TIGHT*). The geometry convergence criteria for Gaussian are discussed in Section 2.2.4.

For each step in the SCF convergence or geometry optimisation, GaussSum calculates a progress value. For each of the unfulfilled criteria, the current value is divided by the threshold value, and the log is taken of the result. These values are then added together to give the progress value. GaussSum creates a plot of procedure step versus progress value. When the progress value equals zero, the procedure is completed.

In general, the progress value decreases by about the same amount for each step. In this way, it is possible to estimate how many more steps are required for convergence. This is in contrast to a plot of procedure step versus energy, which tends to decrease exponentially.

2.3.2 Mulliken Population Analysis

It is often useful to describe molecular orbitals in terms of fragment orbitals – for example, to find out what fragments (that is, basis functions, atoms or ligands) contribute to the highest occupied molecular orbital (HOMO). Population analysis schemes partition all the electrons of a molecule among fragments according to a set of rules. If the same partitioning method can be applied to a particular molecular orbital, it may be used to calculate the contribution of a particular fragment to that molecular orbital. GaussSum uses Mulliken Population Analysis (MPA)[18] to calculate contributions of fragments to molecular orbitals.

Gaussian expresses each of the *P* molecular orbitals, Ψ_n, as a linear combination of *P* normalised basis functions, ϕ_x. In order to make the formulae clearer, let us consider a system where *P* is 2:

$$\Psi_n = \sum_i^P c_{in}\phi_i = c_{1n}\phi_1 + c_{2n}\phi_2 \tag{2.2}$$

where c_{xn} is the coefficient of ϕ_x in Ψ_n. The square of the wavefunction gives the probability density corresponding to an electron in the orbital. Its integral over space is equal to one (the electron must be somewhere):

$$\begin{aligned} 1 &= \int \Psi_n^2 \\ &= \int c_{1n}^2\phi_1^2 + \int c_{2n}^2\phi_2^2 + 2\int c_{1n}c_{2n}\phi_1\phi_2 \\ &= c_{1n}^2\int \phi_1^2 + c_{2n}^2\int \phi_2^2 + 2c_{1n}c_{2n}\int \phi_1\phi_2 \\ &= c_{1n}^2 + c_{2n}^2 + 2c_{1n}c_{2n}S_{12} \end{aligned} \tag{2.3}$$

where **S** is the overlap matrix, which defines the extent of the overlap between any two basis functions. It is symmetric, that is, $S_{ij}=S_{ji}$, and the diagonal elements are all 1, $S_{ii}=1$.

The total number of electrons in a molecule, *N*, is a sum of the electrons in each orbital:

$$\begin{aligned} N &= \sum_i^P n_i \int \Psi_i^2 \\ &= \sum_i^P n_i (c_{1i}^2 + c_{2i}^2 + 2c_{1i}c_{2i}S_{12}) \\ &\text{or in general} \\ &= \sum_i^P n_i \sum_j^P c_{ji}^2 + \sum_i^P n_i \sum_{j,k<j}^P 2c_{ji}c_{ki}S_{jk} \end{aligned} \tag{2.4}$$

where n_i is the electron occupation (0, 1 or 2 electrons) of Ψ_i.

Mulliken defined the net electronic population of basis function ϕ_x as those electrons belonging exclusively to ϕ_x:

$$N_{\text{NET}}(\phi_x) = \sum_i^P n_i c_{xi}^2 \tag{2.5}$$

The remaining electrons are shared between basis functions due to overlap, and are called the overlap electronic population. In the case of two basis functions, the overlap population is:

$$N_{\mathrm{OVERLAP}} = \sum_{i}^{P} 2 n_i c_{1i} c_{2i} S_{12} \tag{2.6}$$

In order to divide the total electronic population among basis functions, Mulliken divided the overlap population equally between each pair of basis functions contributing to the overlap. This gives the following equation for the gross electronic population on basis function ϕ_1:

$$\begin{aligned} N_{\mathrm{GROSS}}(\phi_1) &= N_{\mathrm{NET}}(\phi_1) + \tfrac{1}{2} \sum_{i}^{P} 2 n_i c_{1i} c_{2i} S_{12} \\ &= \sum_{i}^{P} n_i c_{1i}^2 + \sum_{i}^{P} n_i c_{1i} c_{2i} S_{12} \\ &= \sum_{i}^{P} n_i \sum_{j}^{P} c_{1i} c_{ji} S_{1j} \\ &\text{or in general for } \phi_x \\ &= \sum_{i}^{P} n_i \sum_{j}^{P} c_{xi} c_{ji} S_{xj} \end{aligned} \tag{2.7}$$

using the fact that S_{ii}=1.

The Mulliken partial atomic charge of atom A is defined as:

$$q(A) = N_0(A) - N_{\mathrm{GROSS}}(A) \tag{2.8}$$

where N_0(A) is the total number of electrons in the ground state of the free neutral atom A.

The expression in Equation 2.7 for the gross electronic population describes how to partition the electron population of the whole molecule among basis functions. If we consider only the electrons of a particular molecular orbital, the same expression may be used to calculate the fractional contribution, C_{xn}, of basis function ϕ_x to Ψ_n:

$$C_{xn} = \sum_{j}^{P} c_{xn} c_{jn} S_{xj} \tag{2.9}$$

GaussSum calculates the fractional contribution of larger fragments (for example, an atom or a ligand) to each molecular orbital. This is simply the sum of the contributions of the basis functions of all of the atoms in the fragment.

2.3.3 Convolution of spectra

In order to relate calculated IR frequencies, Raman frequencies and electronic transitions to experimental data it is often necessary to convolute the results to create a graph. Furthermore, the creation of Density of States (DOS) and Crystal Orbital Overlap Population (COOP) spectra from molecular orbital data require the energy levels to be convoluted (see Sections 2.3.4 and 2.3.5).

GaussSum uses Gaussian curves to convolute the electronic transitions and energy levels. A Gaussian curve of height *N* has an equation of the form (Figure 2.1):

$$y = Ne^{-(ax)^2} \tag{2.10}$$

It is useful to be able to control the full width at half maximum ($w_{½}$). Since $w_{½}$ is $(2\sqrt{\ln 2})/a$ for the Gaussian curve in Equation 2.10, this implies:

$$a = \frac{2\sqrt{\ln 2}}{w_{1/2}} \tag{2.11}$$

Substitution of this expression into Equation 2.10 allows the full width at half maximum to be controlled.

Lorentzian curves are used to convolute the vibrational frequencies. A Lorentzian curve of unit height has the form:

$$y = \frac{a}{x^2 + a} \tag{2.12}$$

This has a $w_{½}$ of $2\sqrt{a}$, which implies:

$$a = \frac{w_{1/2}^{\ 2}}{4} \tag{2.13}$$

By substituting this expression into Equation 2.12, the $w_{½}$ of the curve can be controlled.

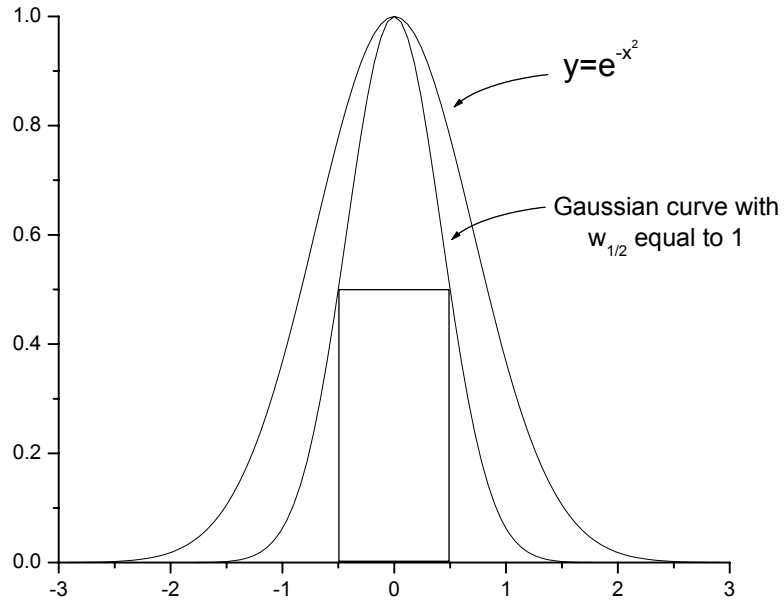

Figure 2.1 – Gaussian curves corresponding to Equation 2.10.

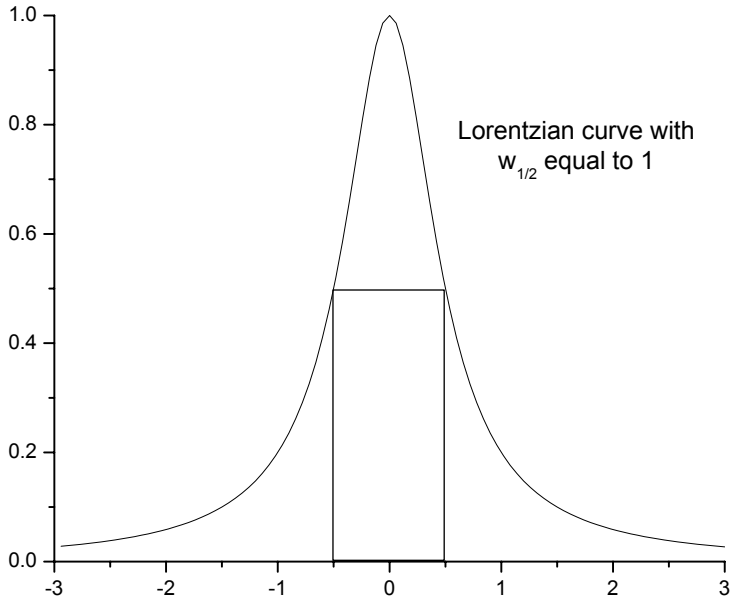

Figure 2.2 – Lorentzian curve corresponding to Equation 2.12.

The oscillator strength is a measure of the 'allowedness' of an electronic transition. In UV-Vis spectroscopy, it can be experimentally measured by integrating the molar extinction coefficient (ε) due to a particular transition. Specifically, the oscillator strength, f, is calculated as follows:

$$f = \frac{4m_e c^2 \varepsilon_0}{N_A e^2} \ln 10 \int \varepsilon(\nu) d\nu \qquad (2.14)$$

where m_e is the mass of an electron, e is the charge on an electron, N_A is Avogadro's constant, c is the speed of light and ε_0 is the permittivity of free space.

Time dependent DFT calculations (TD-DFT) may be used to calculate the energy and oscillator strength of electronic transitions. This data can be convoluted with gaussian curves of a particular $w_{½}$ to give a simulated UV-Vis spectrum of $\varepsilon(\nu)$ versus ν. The equation used to convolute the UV-Vis spectrum is (for the full derivation, see Ref. 19):

$$\varepsilon(\nu) = \frac{N_A e^2 f}{2m_e c^2 \varepsilon_0 \ln(10) w_{1/2}} \sqrt{\frac{\ln 2}{\pi}} \exp\left[-\left(\frac{2\sqrt{\ln 2}}{w_{1/2}} (\nu' - \nu) \right)^2 \right]$$
$$= \frac{2.175 \cdot 10^8 L \cdot mol \cdot cm^{-2}}{w_{1/2}} f \exp\left[-2.772 \left(\frac{\nu' - \nu}{w_{1/2}} \right)^2 \right] \quad (2.15)$$

2.3.4 Density of States and Partial Density of States spectra

A Density of States (DOS) spectrum is a representation of the number of energy levels in a section along the energy axis of width dE.[20] Typically, each energy level is convoluted with a Gaussian curve of unit height and a given full width at half maximum ($w_{½}$) (see Section 2.3.3). Where there are many energy levels close together, the curves overlap and the spectrum has a peak. Thus the density of the energy levels, the 'density of states', is indicated by the height of the curve. This procedure is illustrated in Figure 2.3 where the density of states spectrum (b) is convoluted with Gaussian curves of $w_{½}$ of 0.5eV from the energy level diagram (a).

The resulting spectra, DOS spectra, can be related to the spectra obtained from photoelectron spectroscopy (PES). This experimental technique involves bombarding a sample with a beam of high-energy X-rays. This causes valence and core electrons to be knocked out of the sample with a kinetic energy equal to the difference between the energy of the X-rays and the binding energy of the orbital it was removed from. A plot of the binding energy of the emitted electrons versus intensity gives a spectrum equivalent to a density of states spectrum (see, for example, Ref. 21).

Equation 2.9 can be used to calculate the contribution to each molecular orbital of a particular group or atom.[22] This information can be shown visually if the DOS spectrum is convoluted with Gaussian curves of heights equal to the calculated contributions for each orbital. The resulting spectrum is referred to as a Partial Density of States (PDOS) spectrum, since it shows only the portion of the DOS that is due to a particular group. The spectra from different groups within the molecule may be stacked to show how the DOS spectrum is divided, as in Figure 2.3 (c); or they may be unstacked, which facilitates comparison between different PDOS spectra, as in Figure 2.3 (d).

PDOS spectra give a better overview of the contributions from different group than a table of values does. Where neighbouring orbitals are closely spaced, the spectrum allows them to overlap so that a single peak is seen. Thus, at a glance, molecular orbitals of a particular character (for example, metal-based orbitals) are seen to cluster in a certain energy region. In general, a value for $w_{½}$ of 0.3eV was used. This value was chosen based on a visual comparison of PDOS of different $w_{½}$, and maintains the maximum amount of information about individual energy levels while allowing sufficient overlap to create a single peak from neighbouring related energy levels (for example, the ruthenium-based orbitals in the highest occupied molecular orbitals).

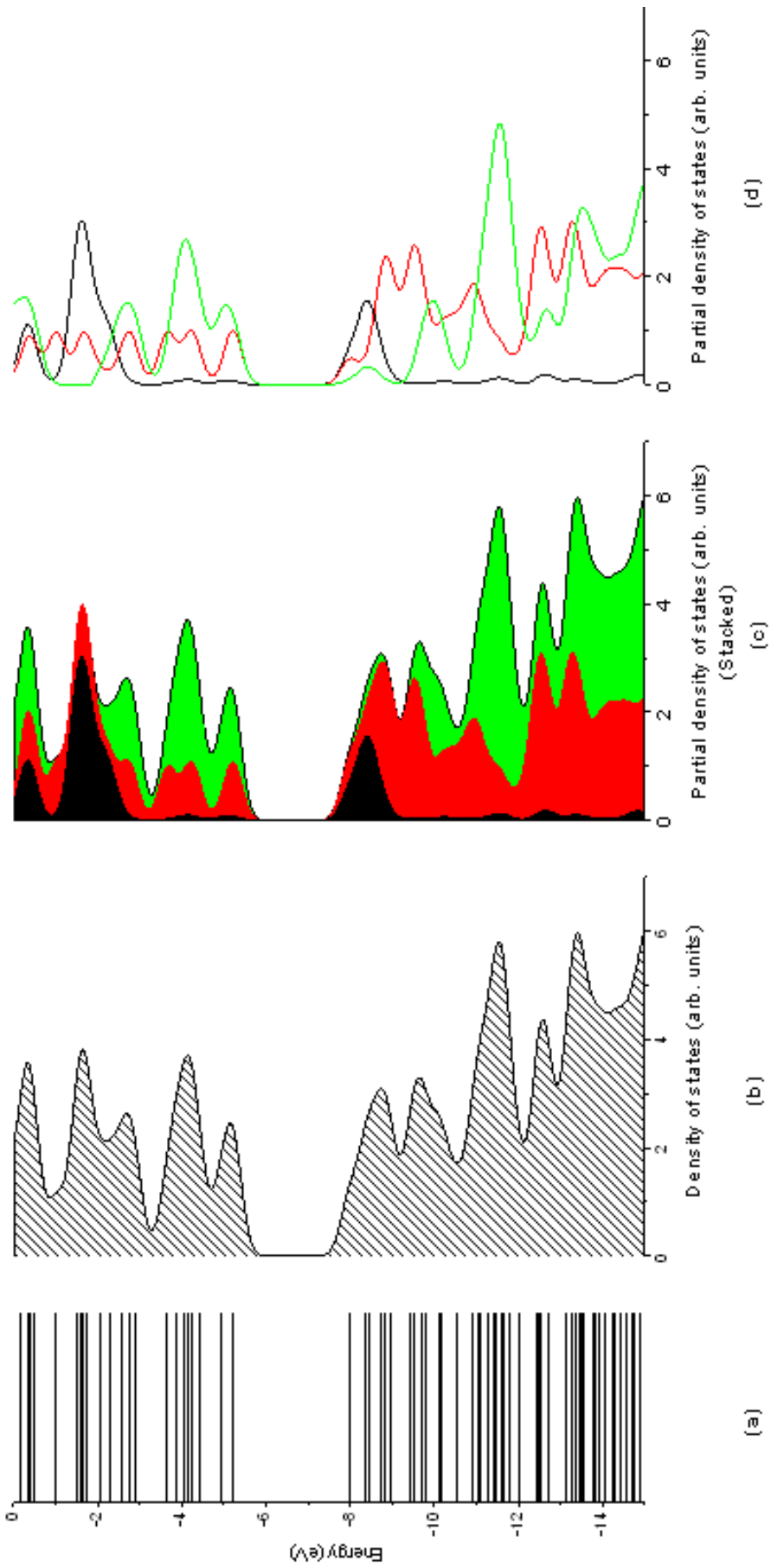

Figure 2.3 – A density of states (DOS) spectrum (b) can be created from an energy level diagram (a). If contributions are calculated from groups within the molecule, partial density of states (PDOS) spectra can be created, either (c) stacked or (d) unstacked.

2.3.5 Calculation of crystal orbital overlap population (COOP)

The overlap electronic population, given by Equation 2.6, can be partitioned among pairs of basis functions ϕ_x and ϕ_y, as follows:

$$N_{\mathrm{OVERLAP}}(\phi_x, \phi_y) = \sum_i^P 2 n_i c_{xi} c_{yi} S_{xy} \qquad (2.16)$$

Mulliken[18, 23] interpreted the sign of this overlap as a measure of whether the overlap interaction between ϕ_x and ϕ_y could be considered bonding (positive) or antibonding (negative). Furthermore, he interpreted the magnitude of the overlap as a measure of the strength of bonding or antibonding.

Hughbanks and Hoffmann[24] were the first to calculate the value of this overlap for each molecular orbital and plot the resulting spectrum after convolution with Gaussian curves. They were carrying out calculations on an extended solid, and named their spectra the Crystal Orbital Overlap Population (COOP). It is also sometimes referred to as Overlap Population Density of States (OPDOS). The spectrum is created in a similar manner as the normal DOS spectrum (see Section 2.3.4), except that instead of using Gaussian curves of unit height, the curves have a height (positive or negative) equal to the overlap population given by Equation 2.16.

GaussSum uses Equation 2.16 to calculate the overlap population between molecular fragments (atoms or groups of atoms). In this case, the total overlap population is the sum of the overlap populations between all of the basis functions in one fragment, and all of the basis functions in the other fragment.

2.3.6 Creation of electron density difference maps (EDDMs)

Gaussian 03 may be used to calculate the energy and oscillator strength of electronic transitions using Time Dependent DFT (using the *TD* keyword). The calculated transitions are described in terms of a linear combination of single electron transitions between ground state energy levels. If the energy levels are broken down in terms of percent contributions from different groups within the molecule (see Section 2.3.2), it is possible to calculate the change in the percent contribution of a particular group when the molecule undergoes a particular electronic transition. This allows a transition to be characterised as ligand-centred

(LC), metal-centred (MC), metal-to-ligand charge transfer (MLCT), and so on. GaussSum automates this process for TD-DFT calculations.

In addition, it automates the creation of electron density difference maps (EDDMS). These correspond to the difference in the charge density between the ground and excited state, when the molecule undergoes an electronic transition. Each EDDM is created using the data on singly-excited configurations in the output of a TD-DFT calculation.

2.3.7 Example: 1,4-divinyl-benzene

The structure of 1,4-divinyl-benzene (Figure 2.4) was optimised at the B3LYP/STO-3G level of theory using Gaussian 03.

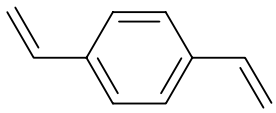

1,4-divinyl-benzene

Figure 2.4 – The structure of 1,4-divinyl-benzene.

The geometry optimisation proceeded smoothly towards a local minimum in 4 steps (see Figure 2.5).

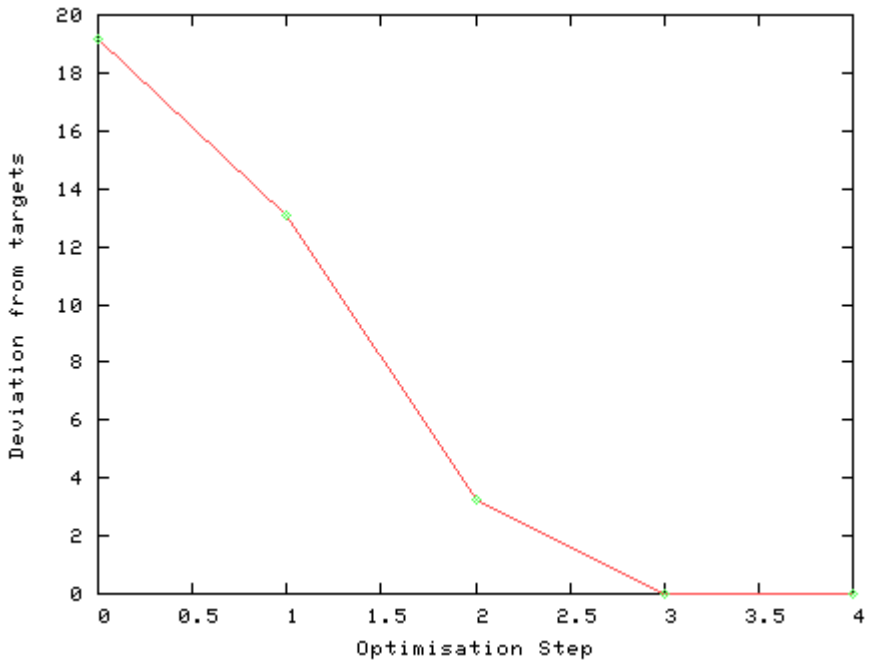

Figure 2.5 – Graph created by GaussSum showing the progress of geometry optimisation.

GaussSum was used to describe the molecular orbitals in terms of their contribution to two groups: C_6H_4, the benzene ring, and $C{=}C$, the two vinyl substituents. Data for the frontier orbitals are shown in Table 2.1. This data was plotted as a PDOS using GaussSum (Figure 2.6).

MO		eV	Symmetry	C_6H_4	C=C
38	L+2	3.01	BG	17	83
37	L+1	2.46	AU	100	0
36	LUMO	1.02	AU	54	46
35	HOMO	-4.17	BG	54	46
34	H-1	-5.31	BG	100	0
33	H-2	-5.78	AU	15	85

Table 2.1 – Molecular orbital contributions for the frontier orbitals of divinylbenzene. Data as presented in the output file of GaussSum.

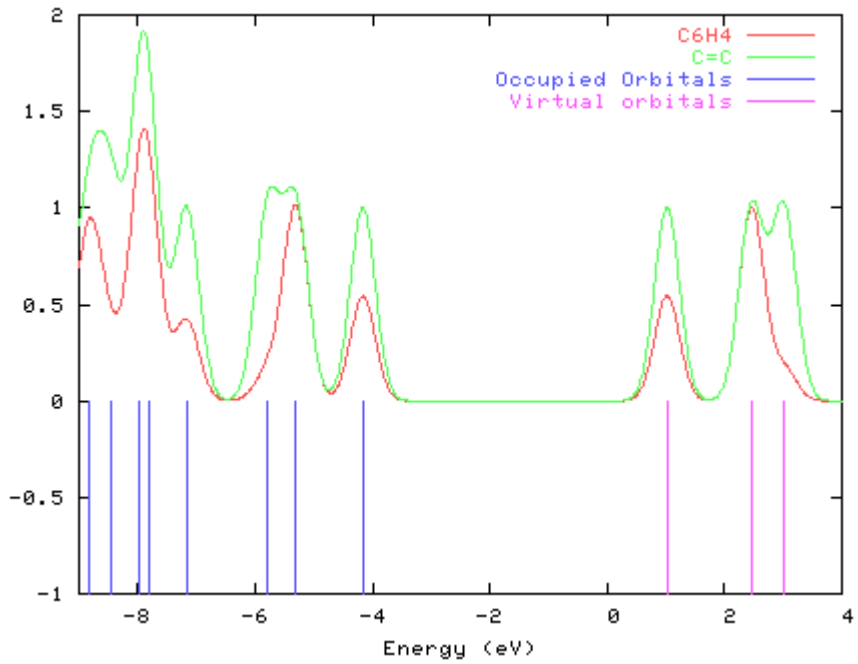

Figure 2.6 – The partial density of states (PDOS) diagram produced by GaussSum for 1,4-divinyl-benzene, using the results of a Mulliken population analysis calculation.

The five lowest-energy singlet electronic transitions were calculated by Gaussian 03 using Time Dependent DFT (TD-DFT). GaussSum was used to convolute the spectrum (Figure 2.7).

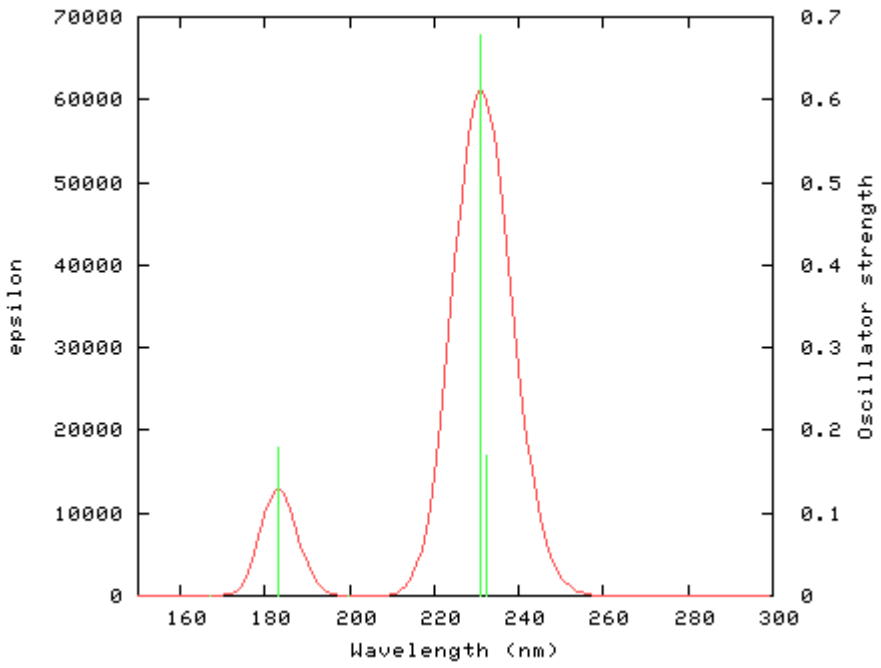

Figure 2.7 – The convoluted UV-Vis spectrum created by GaussSum after calculation of the five lowest energy singlet electronic transitions by Gaussian 03.

No.	Energy (eV)	λ (nm)	Osc. Strength	Symmetry	Major contributions	C_6H_4	C=C
1	5.3351	232.39	0.1695	Singlet-BU	H-1->LUMO (47%) HOMO->LUMO (-15%) HOMO->L+1 (36%)	76-->71 (-5)	24-->29 (5)

Table 2.2 – The major single-electron transitions contributing to the lowest energy singlet electronic transition in 1,4-divinyl-benzene. Also shown is the change in the electron density associated with the *C_6H_4* and *C=C* moieties described in the text.

For every transition, the output file lists its symmetry, energy (in eV), wavelength (in nm) and oscillator strength. Next it lists the major singly-excited configurations contributing to the electronic transition. GaussSum takes these data and creates a rearranges them into a more useful form. In addition, it can combine this information with the molecular orbital contributions. The result of this is shown in Table 2.2 for the lowest energy singlet electronic transition. It is clear that a substantial movement of electron density does not happen, since only small changes occur in the electron density on the *C_6H_4* and *C=C* moieties. In order to visualise the change in electron density, GaussSum was used to create an electron density difference map corresponding to this transition (Figure 2.8).

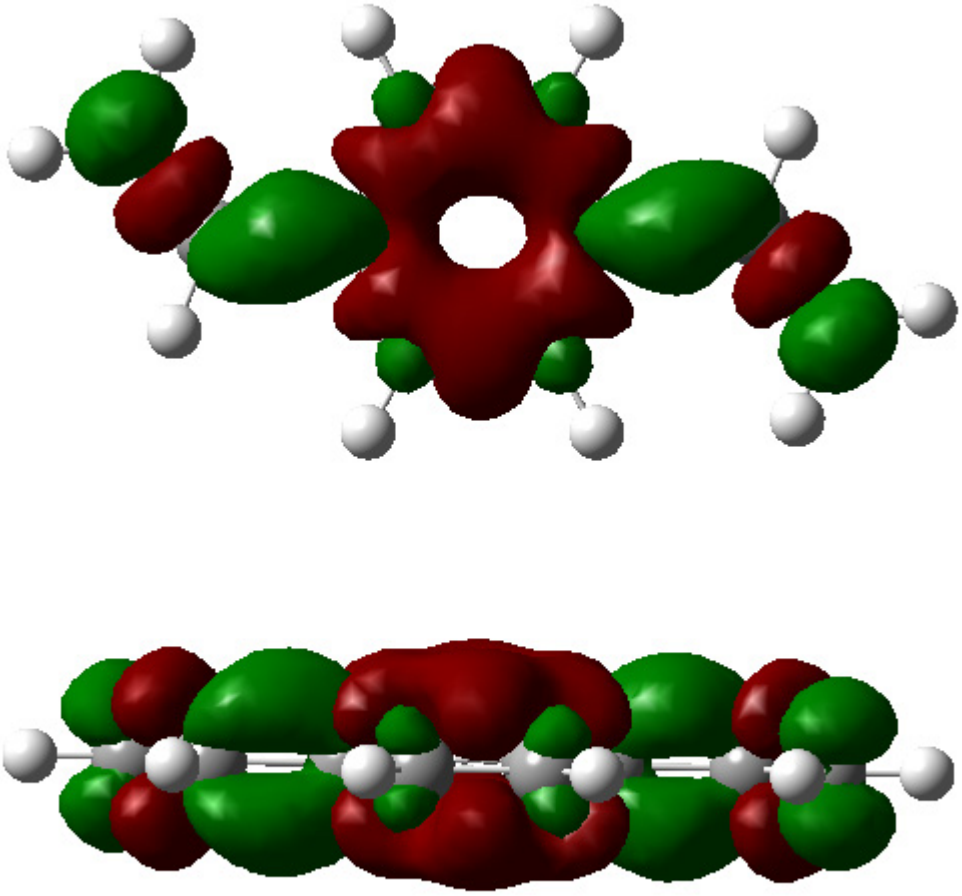

Figure 2.8 – Electron density difference map (EDDM) for 1,4-divinyl-benzene, corresponding to the lowest energy electronic transition to a singlet state. Red indicates a decrease in the electron density and green indicates an increase.

The frequencies of the harmonic vibrational modes and their associated IR activity were calculated by Gaussian 03 (using the *FREQ* keyword). GaussSum was used to convolute the spectrum with Lorentzian curves of $w_{½}$ of 5cm^{-1}. A general scaling factor of 0.98 was applied. Figure 2.9 illustrates the ability of GaussSum to apply individual scaling factors to vibrational modes (modes above 2500cm^{-1} are scaled by 0.80).

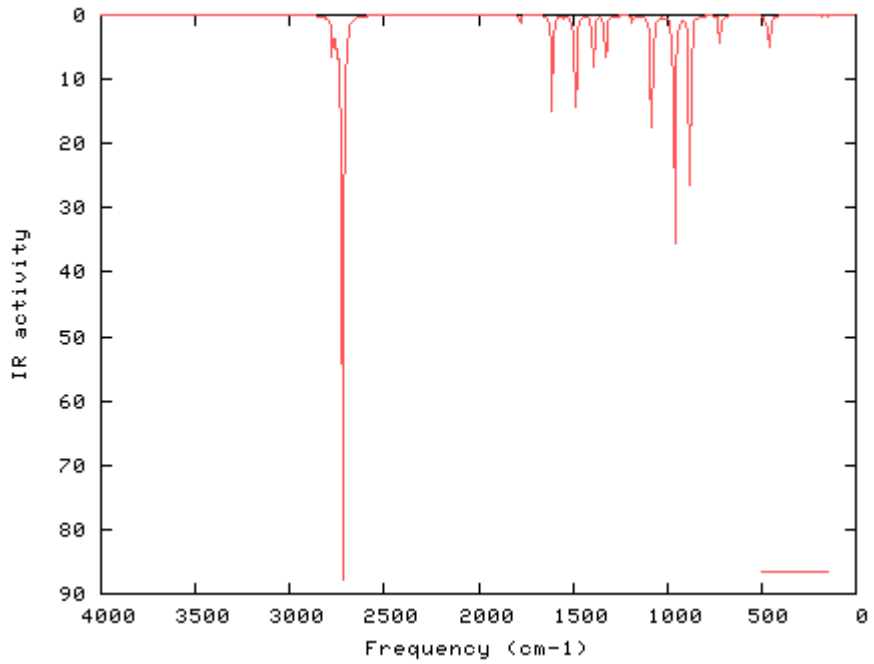

Figure 2.9 – The calculated IR spectrum of 1,4-divinyl-benzene convoluted by GaussSum, using Lorentzian curves of $w_{½}$ of 5cm^{-1}. The diagram was created by GaussSum using a scaling factor of 0.98 for all frequencies under 2000cm^{-1}, and 0.80 for all frequencies above (scaling factors chosen for illustrative purposes).

The graphs shown in this section were created by GaussSum using Gnuplot, and should be used as a quick preview of the data. The data needed to create the graph is written to an output file so that other graphing software (for example, Excel or Origin) may be used instead to create production quality graphs.

2.4 GauStock – Hirshfeld Population Analysis for Gaussian

In his 1977 paper, Hirshfeld[25] described a method for calculating partial atomic charges based on a partitioning of the electron density. This method is referred to as Hirshfeld Population Analysis (HPA) or Stockholder Partitioning. I have written a program, GauStock, that implements this method for Gaussian03 output files.

2.4.1 Introduction to Hirshfeld Population Analysis

The population analysis method of Hirshfeld is based upon the concept of 'atoms-in-molecules' – that is, that a good description of a molecule can be gained from considering the difference between the free atoms and the atoms in the molecule. Specifically, Hirshfeld's method considers the difference in the electron density around each atom in the molecule compared to the electron density around the free atom. This difference is the partial atomic charge on that atom.

The electron density around the free atom is simply the spherically-averaged ground-state density for the isolated atom. In order to find the electron density around each atom in the molecule, it is necessary to partition the molecular electron density among the atoms. Hirshfeld Population Analysis (HPA) divides the molecular electron density at each point in space among the atoms based on the contribution of each atom to the 'promolecule' at that point in space. The promolecule, $\rho^{\mathrm{pro}}(\mathbf{r})$, is defined as the sum of the electron densities of all of the free atoms:

$$\rho^{\mathrm{pro}}(\mathbf{r}) = \sum_{i=1}^{N} \rho_i^{\mathrm{at}}(\mathbf{r}) \qquad (2.17)$$

where N is the number of atoms in the molecule, and $\rho_i^{\mathrm{at}}(\mathbf{r})$ is the electron density of the free atom i. Electron density is a function of each point in space, $\mathbf{r}$.

The sharing function for atom i, $w_i(\mathbf{r})$, describes the contribution of atom i to the promolecule:

$$w_i(\mathbf{r}) = \rho_i^{\mathrm{at}}(\mathbf{r}) / \rho^{\mathrm{pro}}(\mathbf{r}) \qquad (2.18)$$

This sharing function is used to partition the molecular density among the atoms, giving the bonded atom density, $\rho_i^{\mathrm{b.a.}}(\mathbf{r})$:

$$\rho_i^{\mathrm{b.a.}}(\mathbf{r}) = w_i(\mathbf{r})\rho^{\mathrm{mol}}(\mathbf{r}) \qquad (2.19)$$

If the density of the free atom is then subtracted from the density of the bonded atom, the atomic deformation density, $\delta\rho_i(\mathbf{r})$, is obtained:

$$\delta\rho_i(\mathbf{r}) = \rho_i^{\text{b.a.}}(\mathbf{r}) - \rho_i^{\text{at}}(\mathbf{r}) \tag{2.20}$$

The atomic deformation density is integrated over space to give the atomic charge, q_i:

$$q_i = -\int \delta\rho_i(\mathbf{r})dv \tag{2.21}$$

An interesting feature of HPA is that it is the partitioning scheme that retains the most information about the unbonded atoms (using arguments from information theory[26]). In addition, It shows less basis set dependence than partitioning schemes based on the molecular orbitals or electrostatic potential.

2.4.2 Implementation of HPA using GauStock

GauStock is a series of scripts written in Python, which use two Gaussian utilities, *cubman* and *cubegen*, for some of the computation. All calculations are carried out using cube files. This is the standard file format used by Gaussian for electron densities. A cube file contains the values of the electron density at regularly-spaced grid points throughout a volume of space. The spacing of the grid points along the x, y and z axes can be controlled.

The first step in using GauStock is to choose the settings for the cube file. Accurate evaluation of the integral in Equation 2.21 requires a grid spacing of about 0.1Å. The volume of space enclosed by the cube must encompass the majority of the electron density of the atom of interest. A cube of side 10Å was found to be sufficient for most calculations.

GauStock requires three more parameters: the name of an output file from a single point or geometry optimisation calculation; the atom of interest in the molecule; and the required level of theory. With this information, GauStock creates Gaussian job files (.gjf) for the whole molecule and each of the atoms in the molecule, runs the jobs using Gaussian03, formats the checkpoint files (using *formchk*), and creates electron density cube files for each (using *cubegen*). The cube files are centred on the specified atom of interest.

A complication arises during calculation of the electron densities of the free atoms. Spherically-averaged ground-state densities are required for each atom. The spectroscopic ground state of a hydrogen atom is calculated using an unrestricted calculation and a multiplicity of 2. A similar procedure is used for nitrogen, carbon and ruthenium atoms, whose ground states have multiplicities of 4, 3 and 5, respectively. However, for both C and Ru, the calculation results in a electron density which is biased along a unique axis, the z axis. This is due to the degeneracy of symmetrically-equivalent orbitals. As a result two extra calculations are required for both C and Ru, which involve swapping a pair of orbitals so that the electron density is biased along the x or y axis instead (using the Gaussian keyword *GUESS=ALTER*). The cube files with the x-, y- and z-biased electron densities are then added together (using *cubman*) and divided by 3, resulting in a spherically-averaged density.

The promolecule is created by summing the cube files for each of the atoms (using *cubman*). Next, a Python script uses the atomic density, promolecule density and molecular density to calculate the atomic deformation density according to Equation 2.20. The integral of the atomic deformation density (see Equation 2.21) is approximated by a summation of the electron density values at each of the grid positions in the cube, multiplied by the volume described by each grid position.

The whole process is automated by the Python scripts. Care must be taken to ensure that each of the Gaussian calculations completes successfully. In addition, considerable disk space may be required if fine grid spacing or large cube volumes are required, particularly in the case of large molecules. For example, to calculate the Hirshfeld charge on an atom in a ruthenium polypyridyl complex, using a cube volume of 12x12x12 $Å^3$ and a grid spacing of 0.075Å, requires about 13GB of disk space.

2.4.3 Example: HCN

GauStock was used to calculate Hirshfeld atomic charges for each atom of HCN (see Figure 2.10) at the B3LYP/cc-pVDZ level of theory. The three charges were calculated simultaneously using the same cube volume (10x10x12 $Å^3$, with the long axis aligned with the molecular axis). A grid spacing of 0.075Å was used.

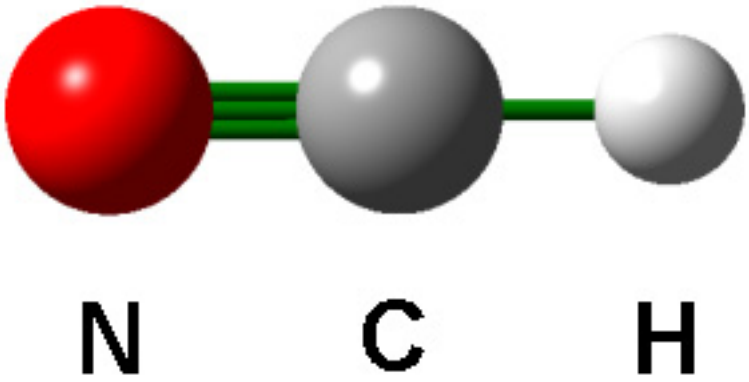

Figure 2.10 – The structure of HCN

The free atom density, bonded atom density and atomic deformation density for the carbon atom in HCN are shown in Figure 2.11.

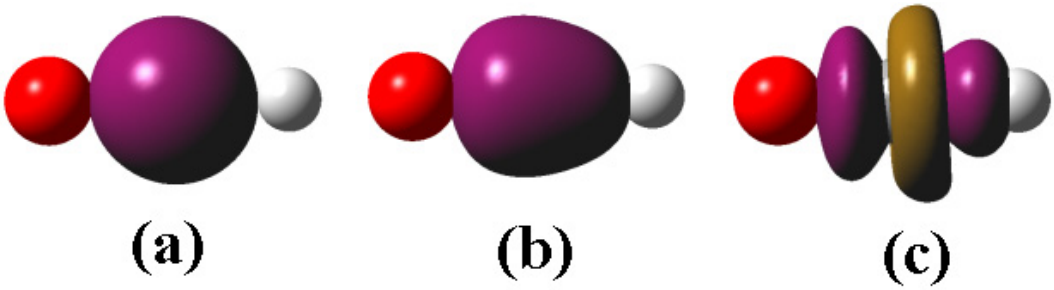

Figure 2.11 – The free atom density (a), bonded atom density (b) and atomic deformation density (c) of the C atom in HCN. Isosurfaces were drawn at a value of 0.08 for (a) and (b), and at 0.008 for (c). The positive isosurface is coloured purple and the negative isosurface is brown.

The promolecule, actual molecular density and molecular deformation density are shown in Figure 2.12.

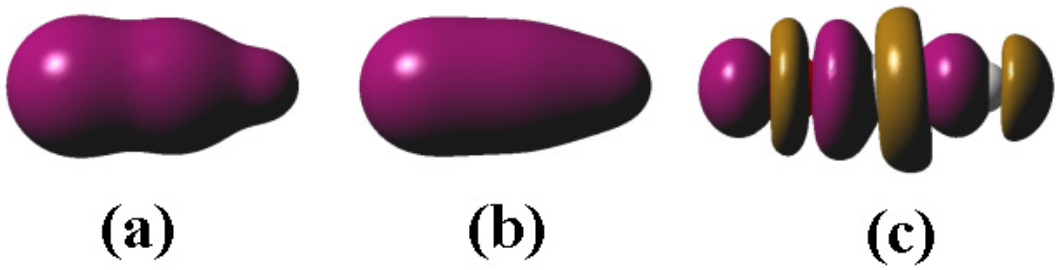

Figure 2.12 – The promolecule (a), the molecular density (b) and the molecular deformation density (c) for HCN. Isosurfaces were drawn at a value of 0.08 for (a) and (b), and at 0.008 for (c). The positive isosurface is coloured purple and the negative isosurface is brown.

Hirshfeld atomic charges calculated using GauStock for H, C and N were 0.120, 0.041 and –0.165. These compare well with the Hirshfeld charges calculated by Alsenoy[27] at the same level of theory: 0.125, 0.041 and –0.166.

2.5 References

1. Gaussian 03, Revision B.04, M. J. Frisch, G. W. Trucks, H. B. Schlegel, G. E. Scuseria, M. A. Robb, J. R. Cheeseman, J. A. Montgomery, Jr., T. Vreven, K. N. Kudin, J. C. Burant, J. M. Millam, S. S. Iyengar, J. Tomasi, V. Barone, B. Mennucci, M. Cossi, G. Scalmani, N. Rega, G. A. Petersson, H. Nakatsuji, M. Hada, M. Ehara, K. Toyota, R. Fukuda, J. Hasegawa, M. Ishida, T. Nakajima, Y. Honda, O. Kitao, H. Nakai, M. Klene, X. Li, J. E. Knox, H. P. Hratchian, J. B. Cross, C. Adamo, J. Jaramillo, R. Gomperts, R. E. Stratmann, O. Yazyev, A. J. Austin, R. Cammi, C. Pomelli, J. W. Ochterski, P. Y. Ayala, K. Morokuma, G. A. Voth, P. Salvador, J. J. Dannenberg, V. G. Zakrzewski, S. Dapprich, A. D. Daniels, M. C. Strain, O. Farkas, D. K. Malick, A. D. Rabuck, K. Raghavachari, J. B. Foresman, J. V. Ortiz, Q. Cui, A. G. Baboul, S. Clifford, J. Cioslowski, B. B. Stefanov, G. Liu, A. Liashenko, P. Piskorz, I. Komaromi, R. L. Martin, D. J. Fox, T. Keith, M. A. Al-Laham, C. Y. Peng, A. Nanayakkara, M. Challacombe, P. M. W. Gill, B. Johnson, W. Chen, M. W. Wong, C. Gonzalez, and J. A. Pople, Gaussian, Inc., Pittsburgh PA, **2003**.

2. GaussView 3.0, Gaussian, Inc., Pittsburgh PA, **2003**.

3. O'Boyle, N.M. and Vos, J.G., GaussSum 0.8, Dublin City University, **2004**. Available at http://gausssum.sourceforge.net.

4. O'Boyle, N.M. and Vos, J.G., GauStock, Dublin City University, **2004**.

5. Becke, A.D., *J. Chem. Phys.*, **1993**, *98*, 5648.

6. Lee, C., Yang, W. and Parr, R.G., *Phys. Rev. B*, **1988**, *37*, 785.

7. Miehlich, B., Savin, A., Stoll, H. and Preuss, H., *Chem. Phys. Lett.*, **1989**, *157*, 200.

8. (a) Perdew, J.P. and Wang, Y., *Phys. Rev. B*, **1992**, *45*, 13244. (b) Perdew, J.P., Chevary, J.A., Vosko, S.H., Jackson, K.A., Pederson, M.R., Singh, D.J. and Fiolhais, C., *Phys. Rev. B*, **1992**, *46*, 6671.

9. Stevens, P.J., Devlin, J.F., Chabalowski, C.F. and Frisch, M.J., *J. Phys. Chem.*, **1994**, *98*, 11623.

10. Dunning Jr., T.H. and Hay, P.J., *Modern Theoretical Chemistry*, Ed. Schaefer III, H.F., Vol. 3, p. 1-28, Plenum, New York, **1976**.

11. (a) Hay, P.J. and Wadt, W.R, *J. Chem. Phys.*, **1985**, *82*, 270. (b) Wadt, W.R. and Hay, P.J., *J. Chem. Phys.*, **1985**, *82*, 284. (c) Hay, P.J. and Wadt, W.R, *J. Chem. Phys.*, **1985**, *82*, 299.

12. (a) Hehre, W.J., Stewart, R.F. and Pople, J.A., *J. Chem. Phys.*, **1969**, *51*, 2657. (b) Collins, J.B., Schleyer, P.v.R., Binkley, J.S. and Pople, J.A., *J. Chem. Phys.*, **1976**, *64*, 5142.

13. (a) Ditchfield, R., Hehre, W.J. and Pople, J.A., *J. Chem. Phys.*, **1971**, *54*, 724. (b) Hehre, W.J., Ditchfield, R. and Pople, J.A., *J. Chem. Phys.*, **1972**, *56*, 2257. (c) Hariharan, P.C. and Pople, J.A., *Mol. Phys.*, **1974**, *27*, 209. (d) Gordon, M.S., *Chem. Phys. Lett.*, **1980**,

76, 163. (e) Hariharan, P.C. and Pople, J.A., *Theo. Chim. Acta*, **1973**, *28*, 213. (f) Blaudeau, J.-P., McGrath, M.P., Curtiss, L.A. and Radom, L., *J. Chem. Phys.*, **1997**, *107*, 5016. (g) Francl, M.M., Pietro, W.J., Hehre, W.J., Binkley, J.S., DeFrees, D.J., Pople, J.A. and Gordon, M.S., *J. Chem. Phys.*, **1982**, *77*, 3654. (h) Binning Jr., R.C. and Curtiss, L.A., *J. Comp. Chem.*, **1990**, *11*, 1206. (i) Rassolov, V.A., Pople, J.A., Ratner, M.A. and Windus, T.L., *J. Chem. Phys.*, **1998**, *22*, 976. (j) Rassolov, V.A., Ratner, M.A., Pople, J.A., Redfern, P.C. and Curtiss, L.A., *J. Comp. Chem.*, **2001**, *22*, 976.

14. Schlegel, H.B., *J. Comp. Chem.*, **1982**, *3*, 214.

15. Frisch, A., Frisch, M.J. and Trucks, G.W., *Gaussian 03 User's Reference*, Gaussian, Inc., Carnegie, PA., **2003**.

16. Schmidt, M.W., Baldridge, K.K., Boatz, J.A., Elbert, S.T., Gordon, M.S., Jensen, J.H., Koseki, S., Matsunaga, N., Nguyen, K.A., Su, S., Windus, T.L., Dupuis, M. and Montgomery, J.A., *J. Comput. Chem.*, **1993**, *14*, 1347.

17. Gnuplot – An interactive plotting program, Version 3.7.3, Williams, T. and Kelley, C., http://www.gnuplot.info/.

18. Mulliken, R.S., *J. Chem. Phys.*, **1955**, *23*, 1833.

19. Serr, A., *Calculations of the spatial and electronic structure of ground and singly excited states for ruthenium complexes containing aza-aromatic ligands with ZINDO methods*, **2002**, Report on research work, Dublin City University.

20. It should be noted that the density of states (DOS) spectra discussed here are *not* the same as the DOS spectra used in solid-state physics.

21. Rensmo, H., Södergren, S., Patthey, L., Westermark, K., Vayssieres, L., Kohle, O., Brühwiler, P.A., Hagfeldt, A. and Siegbahn, H., *Chem. Phys. Lett.*, **1997**, *274*, 51.

22. An examiner has pointed out that contributions based on Natural Atomic Orbitals would be less basis-set dependent. Gaussian 03 may be used to calculate these.

23. Mulliken, R.S., *J. Chem. Phys.*, **1955**, *23*, 1841.

24. Hughbanks, T. and Hoffmann, R., *J. Am. Chem. Soc.*, **1983**, *105*, 3528.

25. Hirshfeld, F.L., *Theoret. Chim. Acta (Berl.)*, **1977**, *44*, 129.

26. Nalewajski, R.F. and Parr, R.G., *Proc. Nat. Acad. Sci.*, **2000**, *97*, 8879.

27. Rousseau, B., Peeters, A. and Van Alsenoy, C., *Chem. Phys. Lett.*, **2000**, *324*, 189.


P-PROF. VOS ..?
I DIDN'T SLEEP ALL WEEK, BUT I FINISHED THE PAPER FOR THAT CONFERENCE IN ITALY...
HUH? WHAT CONFERENCE?
WH..? UM... I-I THOUGHT YOU SAID IF I FINISHED THESE TESTS EARLY YOU WOULD PAY FOR FEES, PASSAGE AND ROOM IN PISA FOR THE MEETING
UH, NO... I SAID I'D PAY FOR A CHEESE, SAUSAGE AND MUSHROOM PIZZA FOR EATING...
OH. IS IT OK IF I TAKE A QUICK NAP ON YOUR RUG, SIR?
JORGE CHAM ©THE STANFORD DAILY

Chapter 3
$[Ru(bpy)_2(pytrz)]^+$
– comparison of theory with experiment

DFT is used to investigate the electronic structure of a series of complexes of type $[Ru(bpy)_2(pytrz)]^+$. The results are visualised using partial density of states (PDOS) spectra, allowing identification of metal- and ligand-centred orbitals, and assessment of σ-donor strength of coordinated ligands. Linkage isomerism in $[Ru(bpy)_2(pytrz)]^+$ and $[Ru(bpy)_2(pytrzMe)]^+$ is examined using thermodynamics. Reactivity indices and thermodynamics are used to investigate the regioselectivity of methylation reactions on $[Ru(bpy)_2(pytrz)]^+$ and $[Ru(bpy)_2(pztrz)]^+$.

3.1 Introduction

Density functional theory has been effectively used to accurately predict heats of formation and other thermodynamic properties for a wide range of molecules. One of the aims of this chapter is investigate whether accurate energies are computed at the B3LYP/LanL2DZ level of theory for ruthenium complexes. Computational results on the series $[Ru(bpy)_2(pytrz)]^+$ are compared with a number of key experimental results obtained by other members of our group.

"The real strength of computational chemistry is the ability to generate data from which a human may gain *insight*, and thereby rationalize the behaviour of a large class of molecules," according to Jensen.[1] It is with this in mind that molecular orbital data from DFT calculations is analysed here using partial density of states (PDOS) spectra (see Chapter 2). These spectra create a link between the calculated data and a more intuitive picture of the energy levels within a complex.

The abbreviation 'Hpytrz' refers to 1*H*-pyridyl-1,2,4-triazole, and 'Hpztrz' will be used for 1*H*-pyrazyl-1,2,4-triazole, as shown in Figure 3.1. The numbering system shown in Figure 3.1 will be used to refer to the positions of atoms in each ligand.

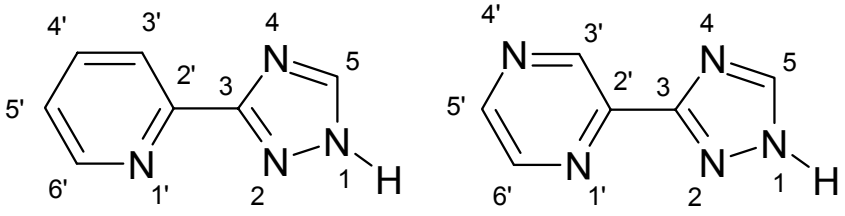

Figure 3.1 – Abbreviations and numbering systems used for pyridyltriazole and pyrazyltriazole.

Figure 3.2 shows the abbreviations used for the $[Ru(bpy)_2(pytrz)]^+$ derivatives studied in this chapter. **1** to **4** involve a series of substitutions of the H at the C5 position of the triazole. The triazole moiety of pytrz and pztrz has two possible

binding sites: the N2 position or the N4 position (see Figure 3.1). All of the structures except for **5**, **6** and **10** involve the N2-bound triazole. **5**, **6** and **10** are derivatives of the N4-bound triazole. **7**, **11** and **12** have a pyrazine group instead of a pyridine group. If **1** is methylated at the free nitrogens, **8** and **9** are obtained. In the same way, **10** is derived from **5**, and **11** and **12** are derived from **7**. Since pytrz is a negatively-charged ligand, and the metal centre is Ru^{II}, all of the complexes carry a single positive charge, except for the N-methylated complexes, **8** to **12**, which have a 2+ charge.

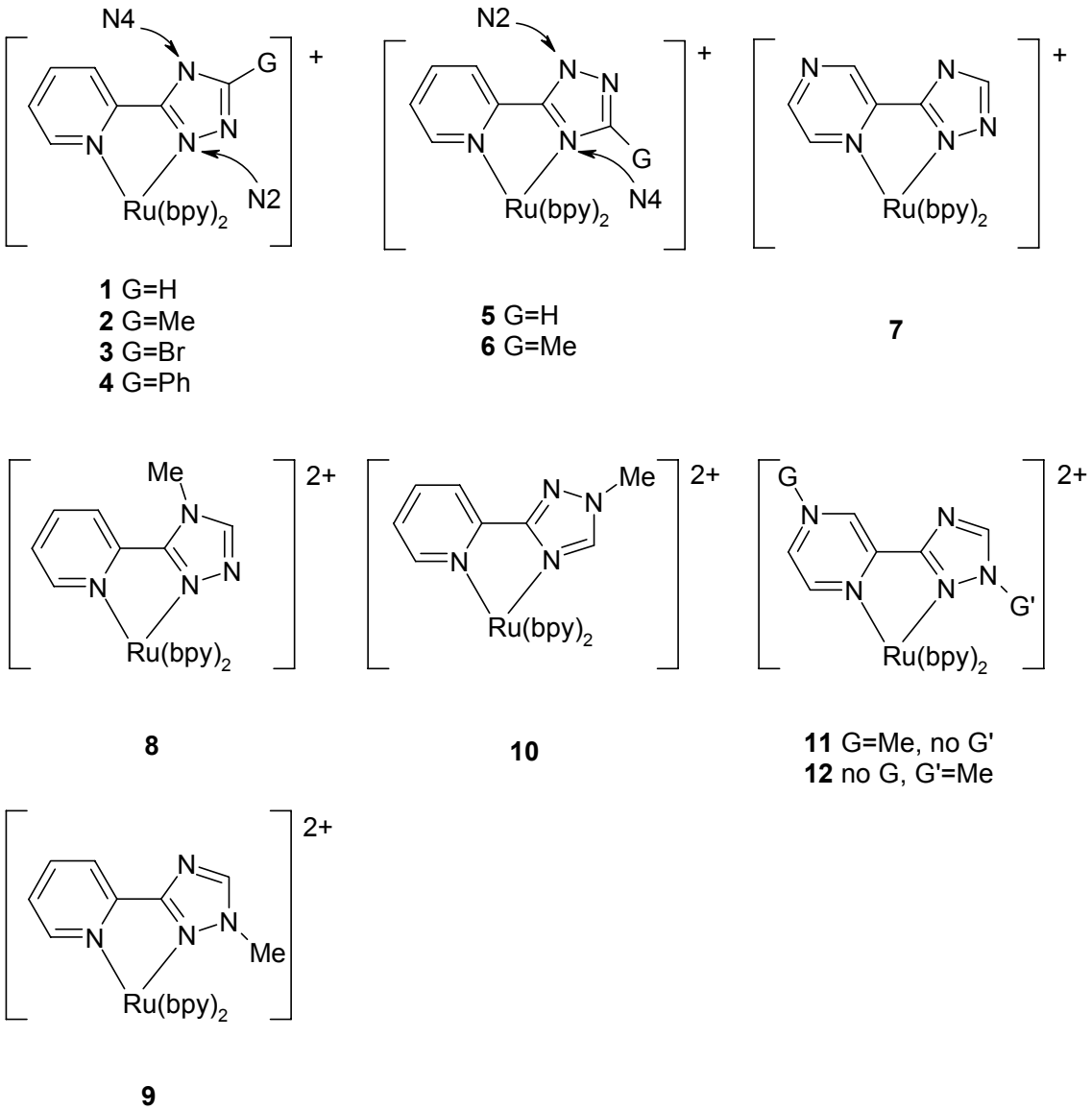

Figure 3.2 – Abbreviations for the $[Ru(bpy)_2(pytrz)]^+$ derivatives studied in this chapter.

3.1.1 Pyridyltriazole as a ligand in ruthenium complexes

Although $[Ru(bpy)_3]^{2+}$ is the prototype for photophysical studies of ruthenium polypyridyl-type complexes, substitution of one of the bipyridine ligands by a bidentate nitrogen-donor ligand L-L offers more possibilities for varying the properties of the complex. Pytrz is an ideal candidate for such studies since it has a protonation site, is asymmetric, forms stable complexes, and its properties can be tuned by substitution at several positions.[2,3,4,5]

The asymmetry of pytrz is of interest when we consider the different electronic properties of pyridine and triazole as coordinating ligands.[5] Triazole is a stronger σ-donor than pyridine, but a weaker π-acceptor. However, when the triazole is in its protonated state, its σ-donor properties are reduced, making it more 'pyridine-like'.

There are two binding sites on the triazole moiety of pytrz, at the N2 position and at the N4 position (see Figure 3.1). As a result, there are two possible linkage isomers for $[Ru(bpy)_2(pytrz)]^+$ (see **1** and **5** in Figure 3.2). This offers further possibilities for tuning the properties of the complex, since the N2-coordinated triazole is the better σ-donor.[4]

3.1.2 Thermochemistry

The relative stability of two isomers can be calculated by finding the change in Gibbs free energy, *ΔG*, for the following reaction at the desired temperature:

$$\text{Isomer A} \longrightarrow \text{Isomer B} \tag{3.1}$$

Assuming that the formation of the two isomers is under thermodynamic control, the relative proportion of each should follow the Boltzmann distribution:

$$\frac{n_B}{n_A} = e^{-\frac{\Delta G}{RT}} \tag{3.2}$$

where n_A indicates the number of moles of isomer A formed.

In order to calculate *ΔG*, it is necessary to calculate the vibrational frequencies of both isomers. This is because the Gibbs free energy for each isomer is calculated using:

$$G = H - TS \tag{3.3}$$

and both the entropy, *S*, and the enthalpy, *H*, have contributions from rotational and vibrational motions. The formulas used are only valid at a geometry which is optimised with respect to all normal coordinates. The frequency calculation also computes the zero-point energy (ZPE) correction, which accounts for the effects of molecular vibrations at 0K.

Since vibrational frequencies are consistently overestimated by B3LYP,[6] a scale factor must be applied. The use of a scale factor affects the calculation of the ZPE as well as the Gibbs free energy.

There are several DFT studies on ruthenium polypyridyl complexes that have used energy differences to rationalise experimental results: Armstrong *et al.*[7] looked at the energy difference between the *mer* and *fac* isomers of a tris homoleptic ruthenium complex; Kinnunen *et al.*[8] compared the structures and energies of (n,n'-COOEt-2,2'-bpy)$Ru(CO)_2Cl_2$ where n=3,4,5 or 6; Haukka *et al.*[9] studied a set of reactions involving the synthesis of carbonyl-containing ruthenium mono(bipyridine) complexes.

3.1.3 Predicting regiospecificity

Ideally, where a reaction can give a number of products, it should be possible to predict or explain which is favoured. A number of qualitative theories have been proposed to predict regiospecificity. Frontier Molecular Orbital (FMO) theory, which is based on work by Fukui,[10] uses the atomic charges and frontier orbital coefficients as local reactivity descriptors. For polar species, the reaction is seen as being charge controlled and, for example, electrophilic attack will occur at the atom with the most negative atomic charge. For non-polar molecules, for example a soft electrophile, attack would occur at the site with the largest HOMO coefficient.

Density functional theory gave reactivity descriptors a more rigorous theoretical foundation. Parr and Yang[11] defined the 'Fukui function' as:

$$f(\mathbf{r}) = \left[\frac{\delta\rho(\mathbf{r})}{\delta N} \right]_v \qquad (3.4)$$

where *N* is the number of electrons, *v* is the potential due to the nuclei, *ρ* is the electron density, and the vector **r** represents a point in space. As a consequence of the fact that the electron density as a function of *N* has slope discontinuities,[12] Equation 3.4 provides three reactivity indices – one for electrophilic attack:

$$f^{-}(\mathbf{r}) = \left[\frac{\delta\rho(\mathbf{r})}{\delta N}\right]^{-}_{\nu} \tag{3.5}$$

another for nucleophilic attack:

$$f^{+}(\mathbf{r}) = \left[\frac{\delta\rho(\mathbf{r})}{\delta N}\right]^{+}_{\nu} \tag{3.6}$$

and a third for radical attack:

$$f^{0}(\mathbf{r}) = \left[\frac{\delta\rho(\mathbf{r})}{\delta N}\right]^{0}_{\nu} \tag{3.7}$$

Evaluation of the Fukui function is made easier by use of the finite difference method[13], where $f^{+}(\mathbf{r})$ is approximated as follows:

$$f^{+}(\mathbf{r}) \approx \rho_{N+1}(\mathbf{r}) - \rho_{N}(\mathbf{r}) \tag{3.8}$$

and $f^{-}(\mathbf{r})$ as follows:

$$f^{-}(\mathbf{r}) \approx \rho_{N}(\mathbf{r}) - \rho_{N-1}(\mathbf{r}) \tag{3.9}$$

where $\rho(\mathbf{r})_{N+1}$ and $\rho(\mathbf{r})_{N-1}$ are the electron densities of the reduced and oxidised species evaluated at the geometry of the ground state. This can be visualised using an isosurface of the electron density that just encloses the van der Waals volumes. The appropriate reactivity index is mapped onto this surface and colour-coded to indicate the values.[14] It is worth noting that $f^{-}(\mathbf{r})$ in Equation 3.9 can be approximated (using a frozen-core approximation) by the electron density due to the HOMO. This shows that FMO theory is, in fact, a limiting case of the use of Fukui functions.[15]

Yang and Mortier[16] introduced the idea of using a condensed-to-atoms form of the Fukui function. This involves partitioning the function to give values for each atom, similar to the procedure used in population analysis. Combined with the finite difference approximation, this gives the following working equations:

$$f_A^{+} = q_A(N+1) - q_A(N) \tag{3.10}$$

$$f_A^{-} = q_A(N) - q_A(N-1) \tag{3.11}$$

where $q_A(N)$ is the electronic population of atom A in the system with N electrons. Work by Roy and co-workers[17a-e] has established Hirshfeld's stockholder partitioning technique[18] as the most reliable method for performing the population analysis required to evaluate Equations 3.10 and 3.11. Using this method, the molecular charge density at each point in space is divided up between the atoms based on the contribution of each atom to the sum of the molecular charge densities of the free

atoms, at that point in space (see Section 2.4.1). Our own in-house software, GauStock[19], was used to evaluate Hirshfeld charges (Section 2.4).

3.2 Method

All calculations were carried out at the B3LYP/LanL2DZ level of theory. The structures were fully optimised. The default integration grid was used in most cases. Where the geometry had difficulty converging, an ultrafine grid was employed. Where the energies of two isomers are compared, the same integration grid has been used for both.

Frequency calculations were carried out at the optimised geometry and with the same integration grid as used for the optimisation. A scaling factor of 0.977 (see Section 5.3.4) was used for the vibrational frequencies calculated using the default integration grid. A scaling factor of 0.978 (see Section 5.3.4) was used for calculations involving an ultrafine grid. Since the reactions were carried out by refluxing in ethanol/water, the thermochemical analysis is carried out at 78°C.

Partial density of states (PDOS) spectra were created using GaussSum[20] using Gaussian curves of full width at half maximum ($w_{½}$) of 0.3eV.

3.3 Results

3.3.1 Geometry optimisation

Selected bond lengths and bite angles for the pytrz complexes are shown in Table 3.1, and for the pztrz complexes in Table 3.2. The calculated geometry for **2** agrees very well with the crystal structure, although the Ru-N bond lengths, in particular Ru-N_{py}, are slightly overestimated. Compounds **1** to **4** have identical Ru-N bond lengths and bite angles. The Ru-N_{trz} bond length increases for the N-4 bound triazoles, **5** and **6**. These also have larger pytrz bite angles.

The calculated geometry for **7** also agrees very well with the crystal structure of the phenyl derivative (Figure 3.3), although again the Ru-N bond lengths are slightly overestimated. Methylation at the N-1 position of a N-2 bound triazole (that is, compounds **9** and **12**) causes an increase in the Ru-N_{trz} bound length. The Ru-$N_{py/pz}$

distance is almost identical for all of the complexes, except for **11**, where it is slightly shorter.

	Crystal[a]	**1**	**2**	**3**	**4**	**5**	**6**	**8**	**9**	**10**
Ru-N_{bpy}[b]	2.05	2.08	2.08	2.08	2.08	2.09	2.09	2.09	2.09	2.09
Ru-N_{py}	2.09	2.14	2.14	2.14	2.14	2.14	2.14	2.14	2.14	2.13
Ru-N_{trz}	2.05	2.06	2.06	2.06	2.06	2.08	2.10	2.06	2.13	2.10
∠bpy[b]	79.1	78.7	78.7	78.7	78.6	78.6		78.5	78.6	78.6
∠pytrz	78.0	78.0	78.0	78.0	78.0	78.7	78.9	77.0	77.2	78.9
trz-C5-R	1.49		1.50	1.92	1.47		1.50			
N-Me								1.48	1.47	1.50

Table 3.1 – Selected bond lengths and bite angles for compounds 1 **to** 6**, and** 8 **to** 10**, compared with the crystal structure of** 2**. All angles are in degrees and all distances are in Å. [a]Crystal structure of** 2**, [Ru(bpy)$_2$(pytrzMe)]PF$_6$.4H$_2$O, taken from Ref. 4. [b]Values averaged.**

	Crystal[a]	**7**	**11**	**12**
Ru-N_{bpy}[b]	2.05	2.09	2.10	2.10
Ru-N_{pz}	2.11	2.13	2.08	2.13
Ru-N_{trz}	2.03	2.06	2.05	2.13
∠bpy[b]	78.9	78.6	78.4	78.5
∠pztrz	78.2	78.1	78.9	77.4
N-Me			1.50	1.47

Table 3.2 – Selected bond lengths and bite angles for compounds 7**,** 11 **and** 12**, compared with the crystal structure of [Ru(bpy)$_2$(pztrzph)]$^{2+}$. All angles are in degrees and all distances are in Å. [a]Crystal structure of [Ru(bpy)$_2$(pztrzph)]PF$_6$.CH$_3$OH, taken from Ref. 21. [b]Values averaged.**

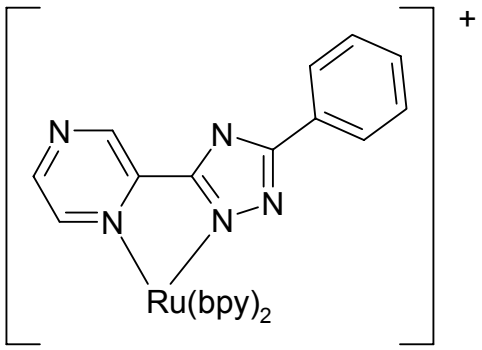

[Ru(bpy)$_2$(pztrzph)]$^+$

Figure 3.3 – The structure of [Ru(bpy)$_2$(pztrzph)]$^+$

3.3.2 Electronic structure

The HOMO and LUMO for each of the twelve complexes are shown in Figure 3.27, Figure 3.28 and Figure 3.29 from page 99 to page 101.

3.3.2.1 $[Ru(bpy)_2(pytrz)]^+$, 1 (Figure 3.10 and Table 3.7, page 82)

The prototype for this series of complexes is $[Ru(bpy)_2(pytrz)]^+$, **1**, where the triazole is bound to the metal at the N2 position. An N4 linkage isomer (**5**) is also possible and will be discussed below. The highest occupied molecular orbitals of **1** have a large component centred on the Ru centre – specifically this component is found in the HOMO, H-1 and H-2, and to a lesser extent, in the H-3. This is the typical situation for Ru polypyridyl-type complexes. In a simplistic molecular orbital treatment, the HOMO can be thought of as consisting of the t_{2g} metal orbitals (in an octahedral environment), with the ligand π orbitals lower in energy.

Since all of the molecules featured in this section are of C_1 symmetry, the two bipyridine ligands are not equivalent. However, they make almost the same contributions to the molecular orbitals throughout the frontier region. This fact is not clear from the tabulated data and only becomes evident when the data are plotted as PDOS spectra. The bipyridine ligands contribute little to the highest occupied molecular orbitals, whereas the lowest unoccupied molecular orbitals are largely bipyridine-based.

It is interesting to note that although part of the same ligand, the pyridine and triazole moieties of the pyridyltriazole ligand contribute to different molecular orbitals. This is somewhat to be expected since a simplistic view of the negatively-charged ligand has the negative charge based on the triazole moiety. The pyridine moiety could be expected to behave similarly to the bipyridine ligands. This is largely the case: the pyridine moiety contributes little to the highest occupied molecular orbitals (although more than the bipyridines), and makes a strong contribution to the lowest unoccupied molecular orbitals (mainly L+3 and L+4). The triazole π and π* orbitals appear at higher energy than those for pyridine. This is consistent with the negative charge being based on the triazole moiety, making the triazole electron rich (higher π orbitals) and a poor π-acceptor (higher π* orbitals). As a result the triazole moiety contributes to the highest occupied molecular orbitals, unlike the pyridine and bipyridine ligands.

The overall order of molecular orbitals with increasing energy is bpy, pyridine, triazole, ruthenium for the occupied orbitals, and bpy, pyridine, ruthenium, triazole for the unoccupied orbitals. Based on these ground states orbital energies, the lowest energy transition is a metal-to-ligand charge transfer (MLCT) from the metal centre to the bipyridine ligands.

3.3.2.2 $[Ru(bpy)_2(py\text{-}N4\text{-}trz)]^+$, 5 (Figure 3.16 and Table 3.12, page 88)

The electronic structure of the N4 linkage isomer of $[Ru(bpy)_2(pytrz)]^+$, **5**, is almost identical to that of **1**. The PDOS of the ruthenium, the bipyridines and the pyridine are very similar for both – the change in the triazole moiety of pytrz does not perturb the electronic structure of the other components significantly. However, a substantial difference occurs for the triazole moiety itself in the frontier region of the occupied orbitals. Compared to the N2-bound triazole of **1**, the N4-bound triazole of **5** has a much greater involvement in the highest occupied molecular orbitals, and equals the contribution of the ruthenium centre itself.

The peak for the Ru PDOS in the highest occupied molecular orbitals occurs at slightly lower energy for **5** than for **1** (by about 0.04eV). This indicates a decrease in the electron density on the metal centre for **5**, suggesting that the N4-coordinated triazole of **5** is a weaker σ-donor than the N2-coordinated triazole of **1**.

3.3.2.3 $[Ru(bpy)_2(pytrzBr)]^+$, 3 (Figure 3.14 and Table 3.17, page 94)

Complex **3,** $[Ru(bpy)_2(pytrzBr)]^+$, is the same as **1** except for the replacement of a proton with a bromine at the C5 position of the triazole. Since bromine is an electron-withdrawing group, the electron-donating ability of the triazole ligand is expected to reduce. This should result in an decrease in the energy of the ruthenium t_{2g} orbitals. The character of the orbitals is very similar for both **1** and **3**. The lowest unoccupied molecular orbitals are almost identical, although the highest occupied molecular orbitals have slightly more triazole character in the case of **3**.

If we consider only the HOMO of **1** and **3**, which both contain considerable Ru character, there is almost no difference in the energy. However, a different picture results from examination of the peak of the ruthenium PDOS in the highest occupied molecular orbitals: the peak shifts from –8.31eV for **1** to –8.48eV for **3**, indicating that it is easier to remove electrons from **1**.

3.3.2.4 $[Ru(bpy)_2(pytrzMe)]^+$, 2 (Figure 3.13 and Table 3.16, page 92)

The methyl group is a weak electron donating group. As a result, its effect on the energy levels of **2** should be opposite to that of the Br atom in **3**.

Although the energy of the HOMO increases with respect to **1**, inspection of the Ru peak in the frontier occupied region shows only a negligible increase. In addition, the PDOS spectra of **1** and **2** are identical throughout the frontier region. This indicates that the electron donating ability of the methyl group does not noticeably increase the σ-donor ability of the triazole moiety. This is understandable, since the triazole moiety is already supporting a negative charge and methyl is only a weak electron donating group.

3.3.2.5 $[Ru(bpy)_2(py\text{-}N4\text{-}trzMe)]^+$, 6 (Figure 3.17 and Table 3.13, page 89)

When comparing **1** and **5** it was found that the orbital energies and triazole PDOS differed significantly. Nevertheless, the effect of the substitution of the C5 hydrogen with a methyl group should be similar for both. As with **2**/**1**, the energy of the HOMO increases for **6**/**5**. However, there is a negligible decrease in the energy of the Ru PDOS peak (this compares with a negligible increase for **2**/**1**). The methyltriazole moiety of **6** contributes slightly more to the highest occupied molecular orbitals than in **5**, but apart from this, the PDOS spectra of **5** and **6** are identical throughout the frontier region. The same conclusion is made as for **2** – the electron donating ability of the methyl group does not noticeably increase the σ-donor ability of the triazole moiety.

3.3.2.6 $[Ru(bpy)_2(pztrz)]^+$, 7 (Figure 3.18 and Table 3.14, page 90)

All of the other molecules discussed so far have involved modification of the triazole moiety of the pyridyltriazole ligand. In contrast, the molecule $[Ru(bpy)_2(pztrz)]^+$, **7**, is formed from **1** by replacing the pyridyl moiety by a pyrazyl. In this case, we expect to see the former pyridyl molecular orbitals perturbed to a greater extent than those of the triazole. Pyrazine is known to be a better π-acceptor than pyridine, and hence a weaker σ donor. As a result, the peak of the ruthenium PDOS in the highest occupied molecular orbitals is shifted to lower energy on going from **1** to **7** (from –8.31eV to –8.55eV).

The PDOS of the bipyridines are almost unchanged in the frontier region. They still contribute little to the highest occupied molecular orbitals, but feature strongly in the lowest unoccupied molecular orbitals. Indeed, the LUMO and L+1 are almost

entirely bipyridine-based. Furthermore, the calculated contributions of the various groups are almost identical compared with the LUMO and L+1 of **1**.

The shape and magnitude of the triazole PDOS for **7** is identical with that of the triazole in **1**. Indeed, the calculated contributions of the various groups are identical for the HOMO to H-4. This once again emphasises the fact the two moieties of the pyridyl-/pyrazyl-triazole are electronically independent.

From the H-5 down and from the L+2 up, the contributions are different. This is because the pyrazine molecular orbitals start to appear. Among the frontier region of the occupied molecular orbitals, the pyrazine orbitals make a strong contribution to the H-5. In contrast, the first major contribution of pyridine in **1** occurred at H-9. The overall order of the molecular orbitals in this region is still the same as for **1**, but the pyrazine/pyridine orbital has been shifted to higher energy. In the unoccupied region, the stronger π-acceptor nature of the pyrazine ligand is reflected in a shift to lower energy of the pyrazine peak in **7**, compared to that of pyridine in **1**. Pyrazine makes a strong contribution to L+2, whereas pyridine's major contribution is centred on L+4.

3.3.2.7 $[Ru(bpy)_2(pytrzph)]^+$, 4 (Figure 3.15 and Table 3.11, page 87)

Substitution of the C5 hydrogen of **1** with a phenyl group gives $[Ru(bpy)_2(pytrzph)]^+$, **4**. Like the methyl group, phenyl is a weak electron donating group. The methyl group of **2** resulted in a negligible shift to higher energy of the ruthenium PDOS peak. The phenyl group also has a negligible effect on the peak, although the shift this time is to lower energy. Apart from that, the size and shape of the ruthenium PDOS is identical with that of **2**.

4 is the first complex discussed where the metal centre does not make a strong contribution to the HOMO, or even to the H-1. The H-1 is completely phenyl-based whereas the HOMO is largely phenyl-based but with a large contribution also from the triazole. Both **2** and **4** have identical PDOS for the bipyridines – once again the LUMO is bipyridine-based. The lowest energy transition may thus be expected to have substantial interligand charge-transfer character. For pyridine, some small differences might be expected, but in the frontier region the PDOS are almost identical. This is another example that the different moieties of the ligand largely behave independently.

Each of **1**, **2** and **3** has very similar triazole behaviour in the highest occupied molecular orbitals. **4** breaks this trend – the triazole makes a large contribution to the phenyl-dominated HOMO. This is an indication that an electronic interaction exists between the phenyl ring and the triazole. That is, that the phenyl and triazole moieties of pytrzph are not completely independent.

3.3.2.8 $[Ru(bpy)_2(Hpytrz)]^{2+}$, H1, $[Ru(bpy)_2(pytrz\text{-}N4\text{-}Me)]^{2+}$, 8, and $[Ru(bpy)_2(pytrz\text{-}N1\text{-}Me)]^{2+}$, 9 (Figure 3.11, Figure 3.12 and Table 3.8, pages 83 and 84; Figure 3.20, Figure 3.21, and Table 3.16, pages 92 and 93; Figure 3.22, Figure 3.23 and Table 3.17, pages 94 and 95)

The energy levels of **H1**, **8** and **9** are shifted to lower energy, by about 3eV, compared to **1**. This is due to the increased charge on the molecule (2+ versus 1+) and the resulting increase in the difficulty of removing an additional electron.

If we compare the parent molecule, **1**, to one of the N-methylated complexes, **8**, the PDOS spectra appear quite different, except for the bipyridines, which are identical apart from the shift in energy. The highest occupied molecular orbitals are completely Ru-based in **8**, while there is considerable triazole character in **1**. Throughout the energy levels of **8**, the PDOS for both the triazole and pyridine moieties have peaks at the same energy. Now that the formal negative charge on the triazole has been neutralised, the two moieties of the pyridyltriazole are very alike and perhaps share delocalised energy levels.

With this in mind, the PDOS spectra were recalculated taking the pyridyltriazole ligand as a single moiety. Surprisingly, the PDOS for the combined pytrz moiety is very similar to that of the bipyridines. In the highest occupied molecular orbitals, the order of the metal and ligand energy levels is Ru>bpy>pytrz. This implies that the methylated pytrz is a poorer σ-donor than bpy. In the lowest unoccupied molecular orbitals, the situation is not as clear: pytrz seems to be a better π-acceptor than bipyridine, but the difference is very small.

The features of the PDOS of **9** are largely the same as for **8**, except that they are shifted to lower energy by about 0.25eV. This indicates that the N4-methylated ligand is a better σ-donor than its N1-methylated isomer. The PDOS for the bpy1 and bpy2 are identical for **9** – in every other molecule discussed so far, there was always a slight difference between the PDOS for bpy1 and bpy2, due to the asymmetry of the pytrz ligand. The PDOS for the combined pytrz ligand is shifted to

higher energy relative to the Ru and bipyridine PDOS. The order of the metal and ligand occupied energy levels is now Ru>bpy=pytrz. In the lowest unoccupied molecular orbitals, bipyridine is a slightly better π-acceptor than pytrz.

H1 has a very similar PDOS to that of **9**. The bipyridine PDOS is identical, although the ruthenium PDOS is shifted to slightly lower energy by about 0.1eV. This is due to the weaker σ-donor properties of the proton compared to the methyl group, due to the reduction in electron density on the Hpytrz ligand. This reduction is also evident looking at the PDOS of Hpytrz, which is shifted to lower energy in the PDOS of **H1** compared to that of **9**. This means that the order of the metal and ligand occupied energy levels is now Ru>bpy>Hpytrz, although the bpy-Hpytrz difference is small. In the lowest unoccupied molecular orbitals, bipyridine is a slightly better π-acceptor than Hpytrz, although the difference is small.

3.3.2.9 $[Ru(bpy)_2(py\text{-}N4\text{-}trz\text{-}N1\text{-}Me)]^{2+}$, 10 (Figure 3.24 and Table 3.18, page 96)

10 is the N4-bound isomer of **9**. For the other N2/N4 isomer pairs already discussed (**1** and **5**, **2** and **6**), a shift to lower energy was observed for the peak of the Ru PDOS in the occupied frontier region. This is consistent with the reduced σ donor abilities of the N4-bound triazole. In the case of **10**, however, the N4-bound triazole appears to be a better σ donor. There are additional effects to be considered in this case: in **9**, the nitrogen beside the bound nitrogen is methylated, whereas in **10** the methylated nitrogen is one atom further away. **8**, like **9**, is N2-bound but the methylated nitrogen is two atoms away from the bound nitrogen. Comparing **8** and **10** shows the N2-bound triazole to be the better σ donor.

3.3.2.10 $[Ru(bpy)_2(pztrz\text{-}N1\text{-}Me)]^{2+}$, 12 and $[Ru(bpy)_2(Hpztrz)]^{2+}$, H7 (Figure 3.26 and Table 3.20, page 98; Figure 3.19 and Table 3.15, page 91)

The comparison of $[Ru(bpy)_2(pytrz)]^+$, **1**, and its pyrazine analogue **7**, above, showed that only the PDOS of the pyridine/pyrazine moiety was affected by the change. A similar result is found when comparing the N1-methylated pytrz complex, **9**, and its pyrazine analogue, **12**. The highest occupied molecular orbitals are almost completely Ru-based, like the other N-methylated complexes discussed. Both pyrazine and bipyridine contribute strongly to the lowest unoccupied molecular orbitals, similar to the results obtained for **8** with pyridine.

The weaker σ-donor ability of pyrazine (compared to pyridine) is again shown by the shift to lower energy of the Ru PDOS peak in the occupied frontier region (from –11.36eV to –11.64eV). Unlike the py and trz moieties of **8**, **9** and **10**, which contribute to the same molecular orbitals, the pyrazine and triazole moieties of **12** behave independently of each other.

The PDOS spectra of **H7** is very similar to that of **12**. The Ru PDOS peak of **H7** in the frontier region of the occupied orbitals is shifted slightly to lower energy (0.06eV) compared to that of **12**. This is a very small shift, but may reflect a decrease in the σ-donor strength of the pztrz ligand on replacement of the electron-donating group methyl, with a proton. A similar effect, although with a slightly larger shift (0.1eV) was observed for the pyridine analogues (**H1** and **9**). The decrease in electron density on the pztrz ligand also results in a shift to lower energy of the trz PDOS, although the pz PDOS does not shift to the same extent. The nature of the frontier orbitals is largely unchanged, although pztrz contributes slightly more to the lowest unoccupied orbitals due to the shift to lower energy: the LUMO is based on Hpztrz for **H7**, whereas pztrz contributed to the LUMO+2 for **12**.

3.3.2.11 $[Ru(bpy)_2(Mepztrz)]^{2+}$, 11 (Figure 3.25 and Table 3.19, page 97)

If **7** were methylated at the N'4 position of the pyrazine, $[Ru(bpy)_2(Mepztrz)]^{2+}$, **11**, would be obtained. Apart from the shift to lower energy due to the increased charge, the PDOS for Ru, the bipyridines and the triazole moiety are largely unchanged.

The most significant, and interesting, difference occurs for the pz moiety. An additional shift to lower energy occurs for the pz PDOS which means that pz does not contribute to the occupied frontier region. On the other hand, the LUMO is completely pyrazine-based. A significant gap of 1.13eV occurs before the bipyridine-based L+1.

3.3.3 Linkage isomerism of $[Ru(bpy)_2(pytrz)]^+$ and $[Ru(bpy)_2(pytrzMe)]^+$

There are two coordination sites on the triazole moiety of pytrz, the N2 position and the N4 position (see Figure 3.1). This means that there are two possible linkage isomers for $[Ru(bpy)_2(pytrz)]^+$, one that binds through the N2 position, **1**, and another that uses the N4 position, **5**. Similarly for $[Ru(bpy)_2(pytrzMe)]^+$, there are two isomers – the N2 isomer, **2**, and the N4 isomer, **6**.

The structures of the linkage isomers of $[Ru(bpy)_2(pytrz)]^+$ and $[Ru(bpy)_2(pytrzMe)]^+$ were geometry-optimised at the B3LYP/LanL2DZ level of theory. The energies of the isomers were calculated at the stationary point by means of a frequency calculation. Two sets of thermodynamic data were calculated. The first set was at 298.15K. The second set was at 373.15K, and the zero-point energy and contributions from vibrational frequencies were scaled using the scaling factors determined in Chapter 5.

1 was found to be 30.9kJ/mol more stable than **5**, for both sets of calculations. A Boltzmann distribution of products would give 100% of **1**.

2 was calculated to be 38.0kJ/mol more stable than **6** at 298.15K, and 38.7kJ/mol more stable at 373.15K (scaled). This corresponds to a Boltzmann distribution with 100% of **2**.

Molecule	Energy (a.u.)	
	Unscaled (298.15K)	Scaled (373.15K)
1	-1572.7405	-1572.7745
2	-1612.0328	-1612.0686
5	-1572.7287	-1572.7627
6	-1612.0183	-1612.0539
9	-1612.3345	-1612.3710
8	-1612.3370	-1612.3736
10	-1612.3467	-1612.3771
11	-1628.3386	-1628.3745
12	-1628.3532	-1628.3889

Table 3.3 – The calculated energies of several complexes discussed in the text. Two sets of values are shown. The unscaled values are calculated at standard temperature and pressure. The other set of values were calculated for 373.15K. In addition, the zero-point energy and contributions from vibrational frequencies were scaled using the scaling factors determined in Chapter 4.

Lower energy	Higher energy	Difference (kJ/mol)		Boltzmann distribution	
		Unscaled (298.15)	Scaled (373.15)	Unscaled (298.15)	Scaled (373.15)
8	**9**	6.8	6.7	94:6	90:10
1	**5**	30.9	30.9	100:0	100:0
2	**6**	38.0	38.7	100:0	100:0
12	**11**	38.2	37.7	100:0	100:0
10	**9**	32.2	15.9	100:0	99:1

Table 3.4 – Comparison of the relative energies of structurally-related isomers.

3.3.4 Methylation of $[Ru(bpy)_2(pytrz)]^+$, 1

The preparation of an N-methylated derivative of $[Ru(bpy)_2(pytrz)]^+$ can follow one of two routes: either the methylated ligand is prepared first and used to form the complex (Scheme 3.1), or a precursor complex is directly methylated (Scheme 3.2). Due to availability of two methylation sites, and the possibility of linkage isomerism,

there are three possible products: the N-2 linkage isomer methylated at the N-1 and N-4 positions (**8** and **9**), and the N-4 linkage isomer methylated at the N-1 position (**10**).

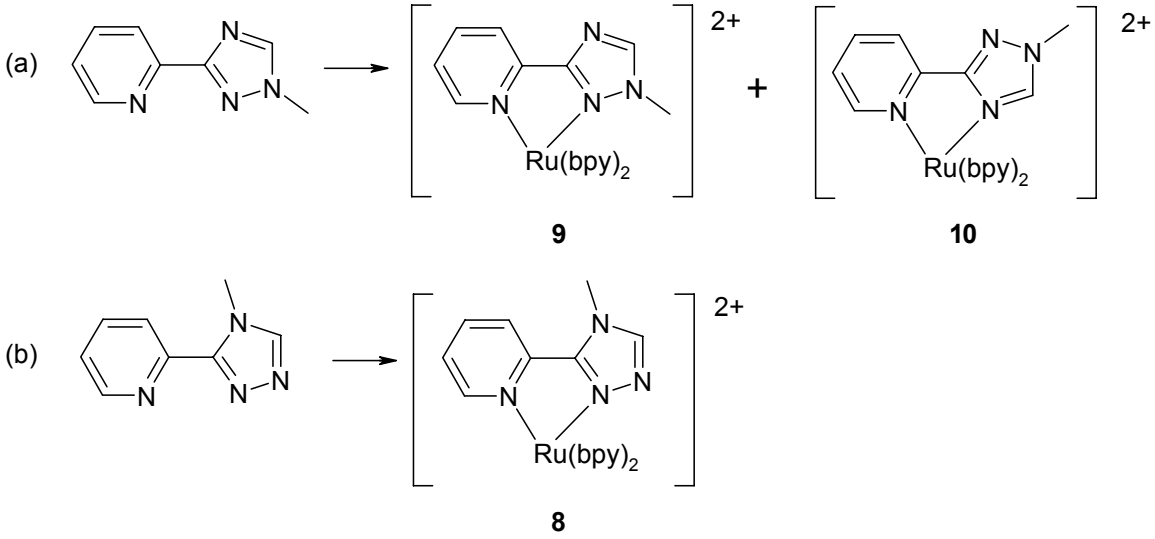

Scheme 3.1 – (a) Two products are possible when N1-methylated pytrz is used to form a *bis*bpy ruthenium complex. (b) Only one product is possible for the N4-methylated ligand.

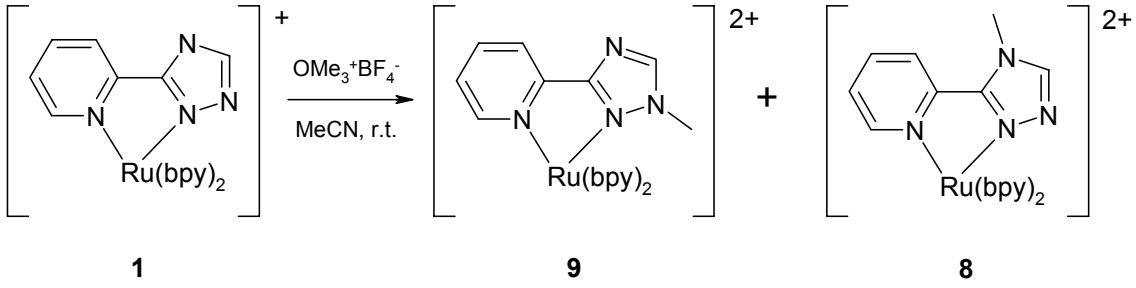

Scheme 3.2 – Direct methylation of 1 **gives two possible products:** 8 **and** 9**.**

The products of the reactions shown in Scheme 3.1a and Scheme 3.2 were investigated using DFT at the B3LYP/LanL2DZ level of theory. Frequency calculations were carried out at the optimised geometry. Two sets of thermodynamic data were calculated. The first set was at 298.15K. The second set was at 373.15K, and the zero-point energy and contributions from vibrational frequencies were scaled using the scaling factors determined in Chapter 5.

10 was calculated to be 32.2kJ/mol more stable than **9** at 298.15K, and 15.9kJ/mol more stable at 373.15K (scaled). This corresponds to a Boltzmann distribution with 100% of **10** at 298.15K (99% at 373.15K).

8 was found to be 6.8 kJ/mol more stable than **9** at 298.15K, and 6.7 kJ/mol more stable at 373.15K (scaled). A Boltzmann distribution of products would give a ratio of **8**:**9** of 94:6 at 285.15K, and 90:10 at 373.15K.

The electrostatic potential (ESP), square of the HOMO, and Fukui function have all been used in the literature to rationalise reactivity. Following the method of Bartolotti and Flurchick[14], they were mapped onto an isosurface of the electron density that just covers the van der Waals radii. This type of surface shows the values for the indices that an attacking molecule will experience at its closest approach. The resulting diagrams for **1** are shown in Figure 3.4, Figure 3.5 and Figure 3.6, where red indicates the areas of greatest reactivity.

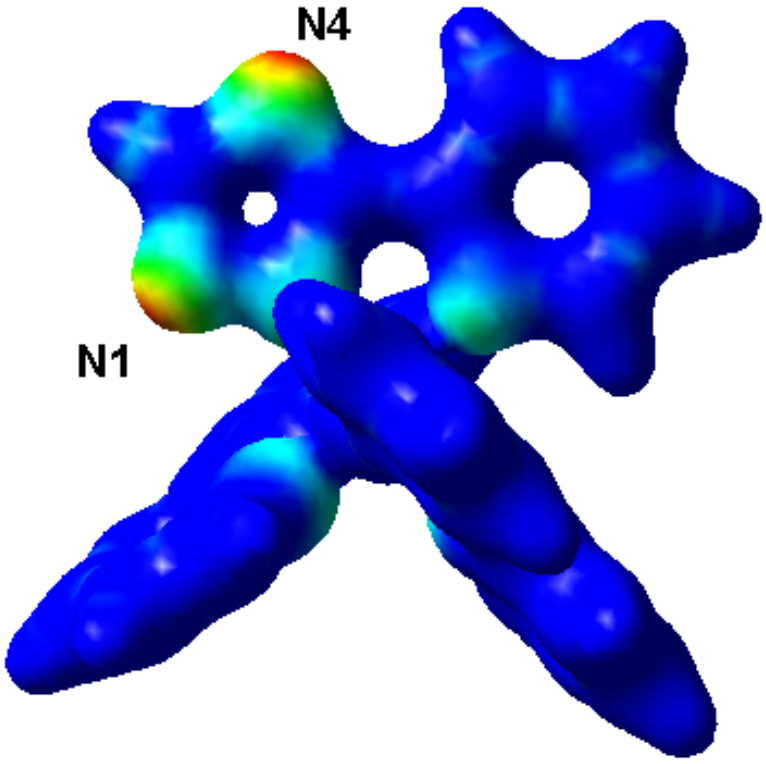

Figure 3.4 – Electrostatic potential (ESP) of 1 **mapped onto an isosurface of the electron density.**

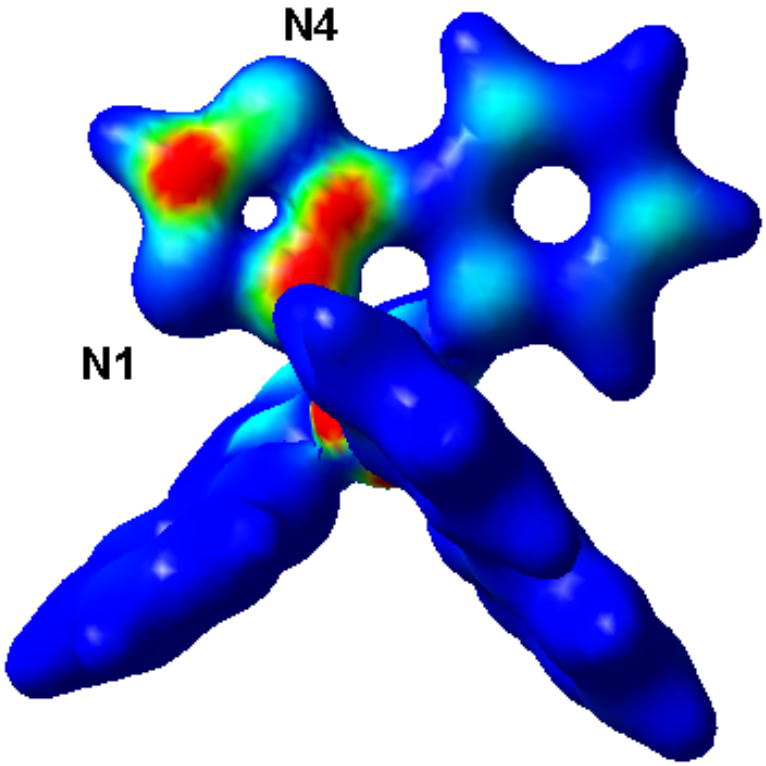

Figure 3.5 – HOMO squared of 1 **mapped onto an isosurface of the electron density.**

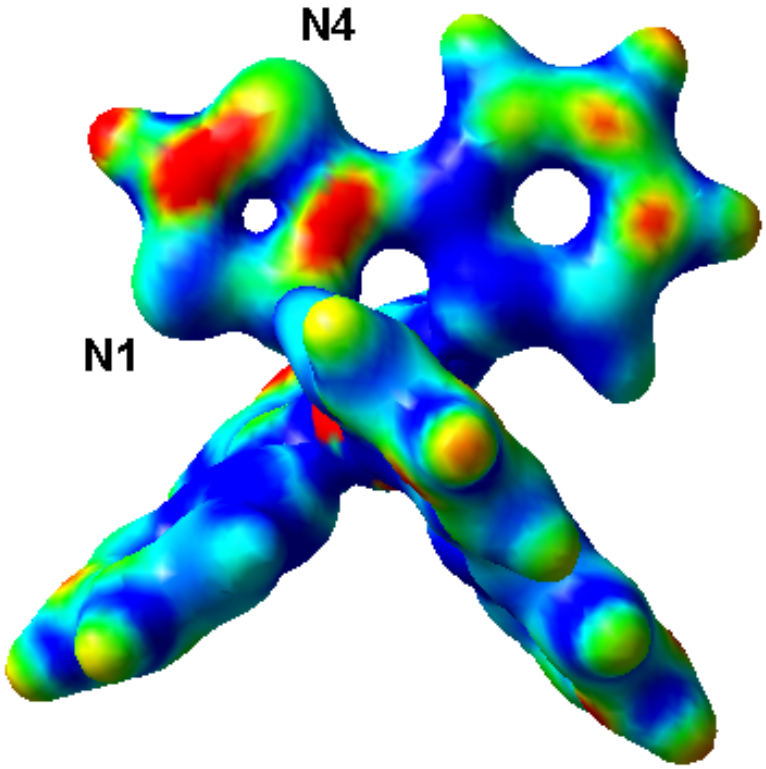

Figure 3.6 – Fukui function of 1 **mapped onto an isosurface of the electron density.**

An attempt was made to calculate atomic charges using the Merz-Singh-Kollman (MSK) method[22] (Gaussian keyword *POP=MK*). This method involves calculating values for the charges so as to reproduce the electrostatic potential. In order to do this, Gaussian requires a 'Merz-Kollman radius' for each atom in the molecule. No radius was available for ruthenium. Charges were calculated for $[Ru(bpy)_3]^{2+}$ with a number of different Merz-Kollman radii, but the results were not encouraging: the six nitrogens had significantly different charges although they are related by symmetry. In addition, the charges showed a large dependence on the ruthenium radius used. MSK charges for the atoms in this inorganic complex appear to be ill-defined.

GaussSum was used to calculate the % contribution of the N1 and N4 atoms to the HOMO. The calculation is carried out within the framework of Mulliken population analysis. N4 makes a larger contribution to the HOMO than N1 (2.3% versus 0.5%).

A numerical value for the Fukui function was calculated using the condensed-to-atoms approximation (Equation 3.11). GauStock was used to calculate the electronic population on N1 and N4 using Hirshfeld population analysis (HPA) for the N electron and N-1 electron complexes (Table 3.5). The more reactive site is predicted to be N4 (f^-_A is 0.039 versus 0.021 for N1).

	$q_A(N)$	$q_A(N-1)$	f^-_A
N1	0.180	0.159	0.021
N4	0.260	0.221	0.039

Table 3.5 – Comparison of the electronic populations on N1 and N4 in 1 **and in its oxidised form at the same geometry, $q_A(N)$ and $q_A(N-1)$, and the electrophilic Fukui function (f^-_A) for N1 and N4. Note that the atomic charge is the negative of the electronic population (following the convention that electrons are negatively-charged).**

3.3.5 Methylation of $[Ru(bpy)_2(pztrz)]^+$, 7

Methylation of the pyrazine analogue of **1**, $[Ru(bpy)_2(pztrz)]^{2+}$ (**7**), can result in a third isomer, apart from the N1- and N4-methylated isomers discussed earlier. The additional reactive site is the pyrazine N'4:

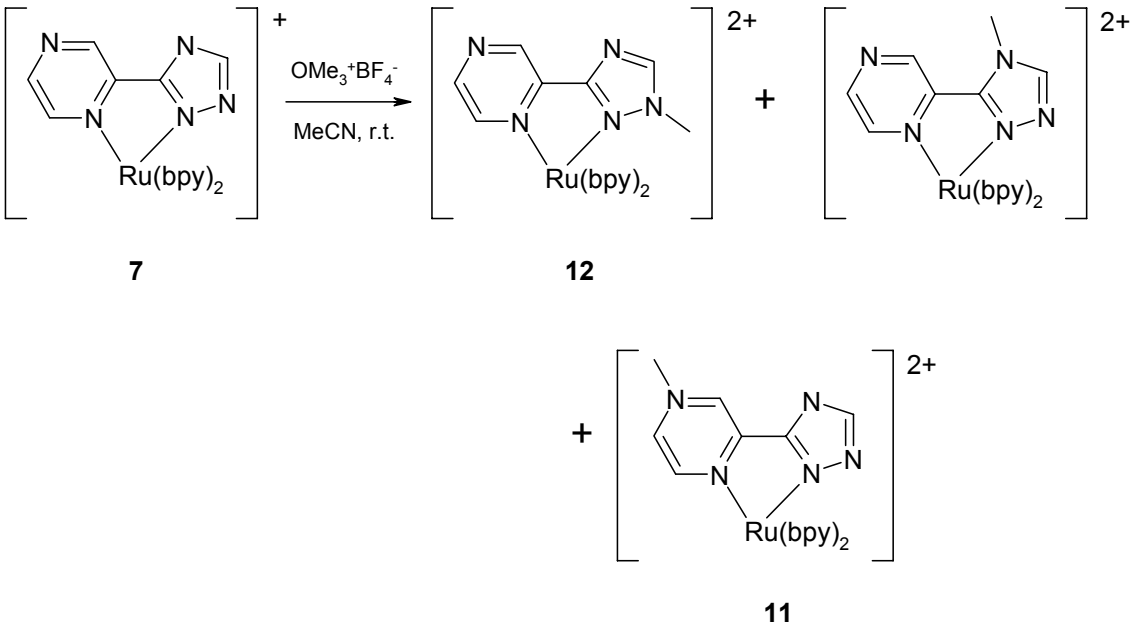

Scheme 3.3 – Methylation of 7 **can result in three isomers.**

As with the pyridine analogue already discussed, the products of the reaction were investigated using DFT at the B3LYP/LanL2DZ level of theory. Only the pz-methylated (**11**) and the trz-N1-methylated (**12**) products were examined. Frequency calculations were carried out at the optimised geometry. Two sets of thermodynamic data were calculated. The first set was at 298.15K. The second set was at 373.15K, and the zero-point energy and contributions from vibrational frequencies were scaled using the scaling factors determined in Chapter 5.

12 was calculated to be 38.2kJ/mol more stable than **11** at 298.15K, and 37.7kJ/mol more stable at 373.15K (scaled). In both cases, this corresponds to a Boltzmann distribution with 100% of **12**.

In order to investigate kinetic factors affecting regioselectivity, reactivity indices were mapped onto an isosurface of the electron density that just covered the van der Waals radii of the atoms. The results, for the electrostatic potential (ESP), square of the HOMO, and Fukui function, are shown in Figure 3.7, Figure 3.8 and Figure 3.9, respectively. In these diagrams, red indicates the areas of greatest reactivity.

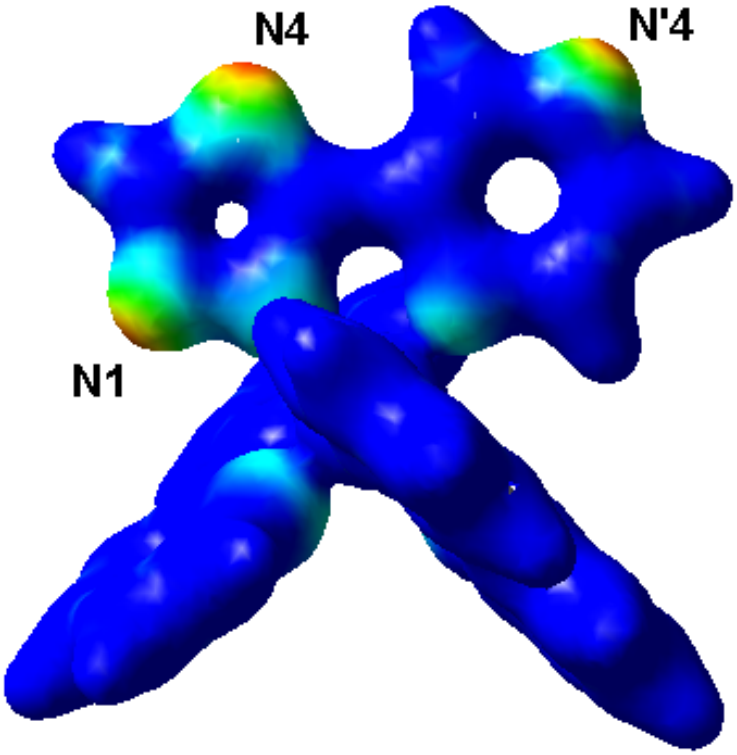

Figure 3.7 – Electrostatic potential (ESP) of 7 mapped onto an isosurface of the electron density.

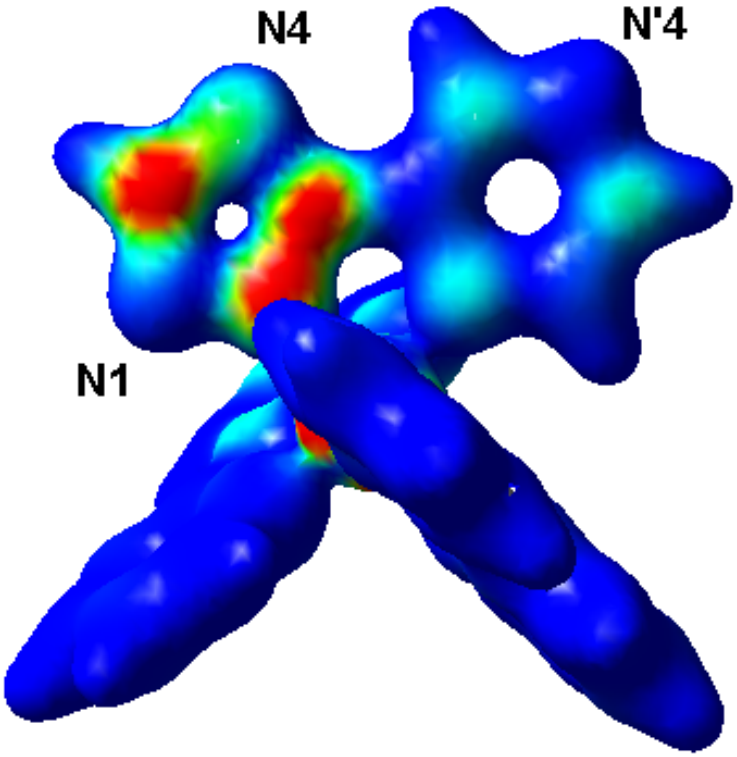

Figure 3.8 – HOMO squared of 7 mapped onto an isosurface of the electron density.

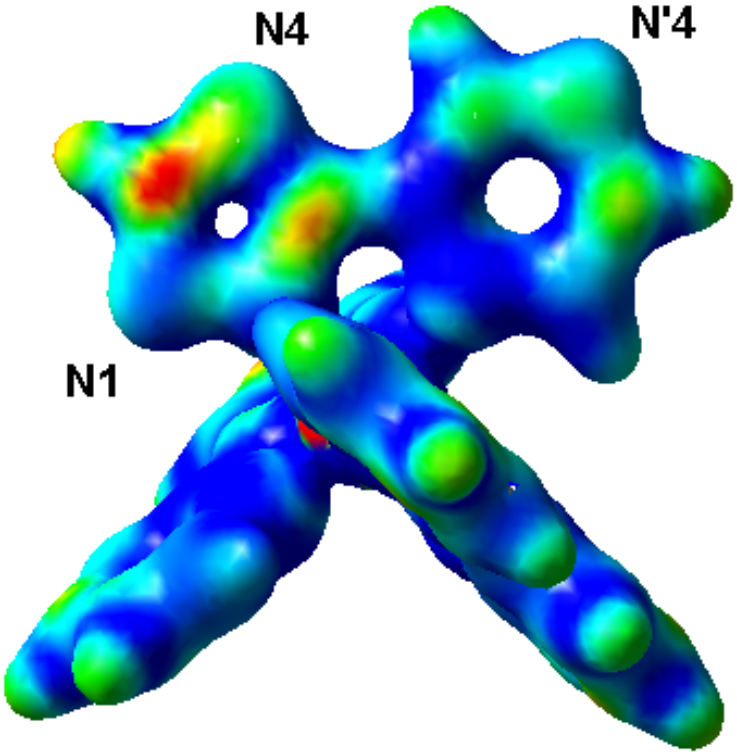

Figure 3.9 – Fukui function of 7 mapped onto an isosurface of the electron density.

GaussSum was used to calculate the % contribution of the N1, N4 and N'4 atoms to the HOMO. The calculation is carried out within the framework of Mulliken population analysis. N4 makes a larger contribution to the HOMO than either N1 or N'4 (2.5% versus 0.4% and 0.0%, respectively).

A numerical value for the Fukui function was calculated using the condensed-to-atoms approximation (Equation 3.11). GauStock was used to calculate the electronic population on N1 and N'4 using Hirshfeld population analysis (HPA) for the N electron and N-1 electron complexes (Table 3.6). The more reactive site is predicted to be N'4 (f^-_A is 0.038 versus 0.023 for N1), in agreement with Figure 3.9.

	$q_A(N)$	$q_A(N-1)$	f^-_A
N1	0.189	0.166	0.023
N'4	0.125	0.087	0.038

Table 3.6 – Comparison of the electronic populations on N1 and N'4 in 7 and in its oxidised form at the same geometry, $q_A(N)$ and $q_A(N-1)$, and the electrophilic Fukui function (f^-_A) for N1 and N'4. Note that the atomic charge is the negative of the

electronic population (following the convention that electrons are negatively-charged).

3.4 Partial Density of States spectra and frontier orbital information for complexes 1 to 12

This section contains partial density of states (PDOS) spectra and frontier orbital information on the geometry-optimised structures of complexes **1** to **12**. Frontier orbital information was extracted from the Gaussian output file using GaussSum. Molecular orbital contributions were calculated for various moieties within each molecule: *Ru* indicates the metal centre; *bpy1* and *bpy2* indicates each of the bipyridine ligands; *py* or *pz* indicate the pyridine or pyrazine moiety of the triazole ligand; *trz* or *trzMe* indicates the triazole moiety, including any methyl substituent; *ph* indicates a phenyl substituent on the triazole.

Partial density of states (PDOS) spectra were convoluted from the molecular orbital contributions using GaussSum with Gaussian curves of full-width at half maximum ($w_{½}$) of 0.3eV.

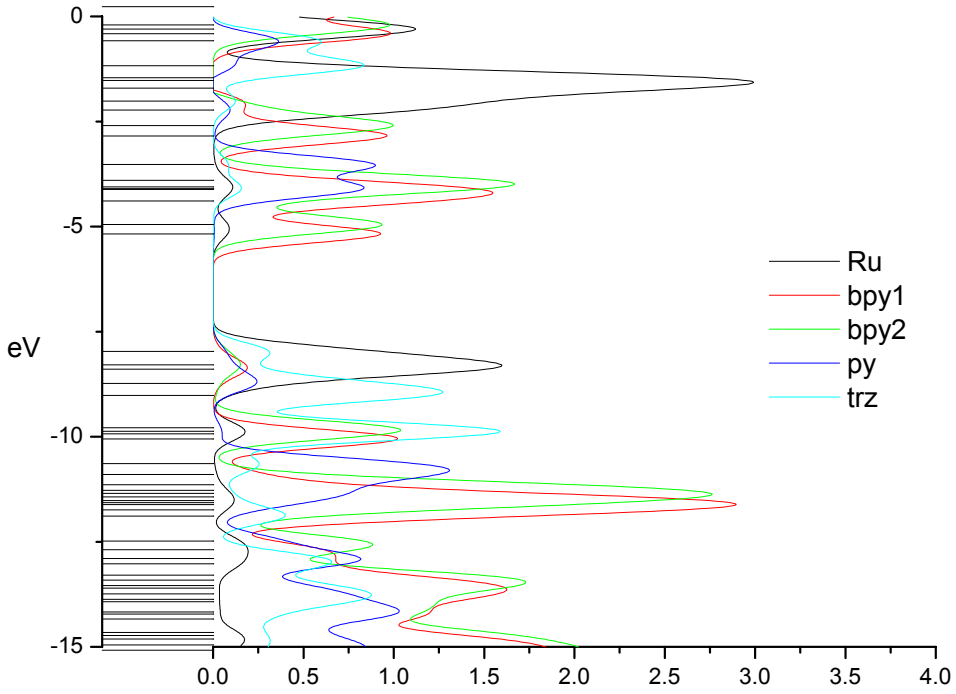

Figure 3.10 – PDOS diagram for $[Ru(bpy)_2(py\text{-}N2\text{-}trz)]^+$, 1.

MO		eV	Ru	bpy1	bpy2	Py	Trz
138	L+10	-2.23	67	6	17	9	1
137	L+9	-2.60	0	7	92	0	0
136	L+8	-2.84	1	93	6	0	0
135	L+7	-3.52	1	1	3	87	8
134	L+6	-3.90	2	4	92	1	0
133	L+5	-4.06	4	19	65	10	3
132	L+4	-4.09	4	15	16	55	10
131	L+3	-4.11	1	78	5	14	2
130	L+2	-4.39	1	79	17	3	0
129	L+1	-4.95	5	3	91	0	0
128	LUMO	-5.18	5	91	3	1	0
127	HOMO	-7.97	58	3	5	5	29
126	H-1	-8.29	77	6	10	3	4
125	H-2	-8.39	70	12	4	7	7
124	H-3	-8.73	19	2	2	22	55
123	H-4	-9.01	1	0	1	0	98
122	H-5	-9.79	5	1	46	1	46
121	H-6	-9.87	4	2	45	1	47
120	H-7	-9.93	9	4	14	2	71
119	H-8	-10.05	1	97	2	0	1
118	H-9	-10.64	0	1	1	74	24
117	H-10	-10.90	1	14	3	80	2

Table 3.7 – Frontier orbital information for $[Ru(bpy)_2(py\text{-}N2\text{-}trz)]^+$, 1.

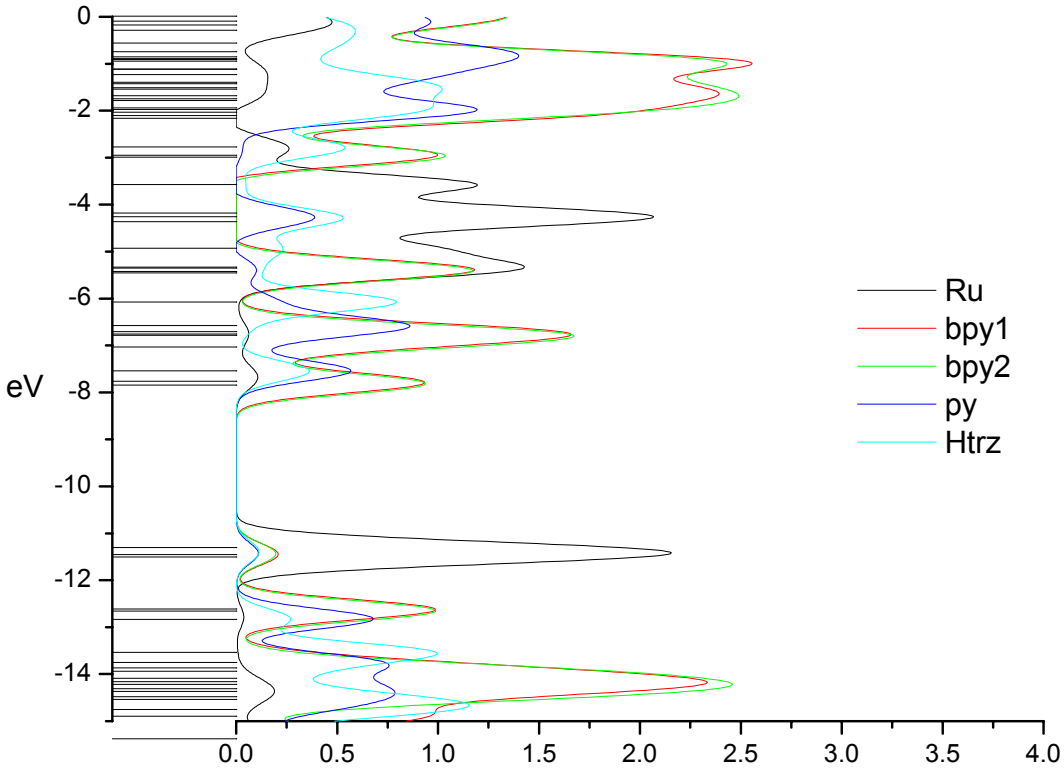

Figure 3.11 – PDOS diagram for $[Ru(bpy)_2(Hpytrz)]^{2+}$, H1.

MO		eV	Ru	bpy1	bpy2	py	Htrz
138	L+10	-5.42	63	15	8	5	9
137	L+9	-5.46	1	38	61	0	0
136	L+8	-6.07	1	1	1	19	79
135	L+7	-6.58	1	8	7	77	7
134	L+6	-6.70	1	81	16	2	0
133	L+5	-6.76	2	14	75	8	0
132	L+4	-6.78	2	49	48	1	0
131	L+3	-7.03	1	44	49	5	1
130	L+2	-7.54	5	2	1	56	36
129	L+1	-7.76	6	60	34	0	0
128	LUMO	-7.85	1	34	61	2	1
127	HOMO	-11.30	81	5	6	3	5
126	H-1	-11.45	76	6	6	7	5
125	H-2	-11.50	76	11	10	2	2
124	H-3	-12.61	0	74	26	0	0
123	H-4	-12.66	1	25	70	3	1
122	H-5	-12.83	3	1	5	66	26
121	H-6	-13.53	0	3	4	1	92
120	H-7	-13.75	0	33	1	63	3
119	H-8	-13.87	0	37	55	2	6
118	H-9	-13.94	0	21	52	5	22
117	H-10	-14.09	1	62	35	2	0

Table 3.8 – Frontier orbital information for $[Ru(bpy)_2(Hpytrz)]^{2+}$, H1.

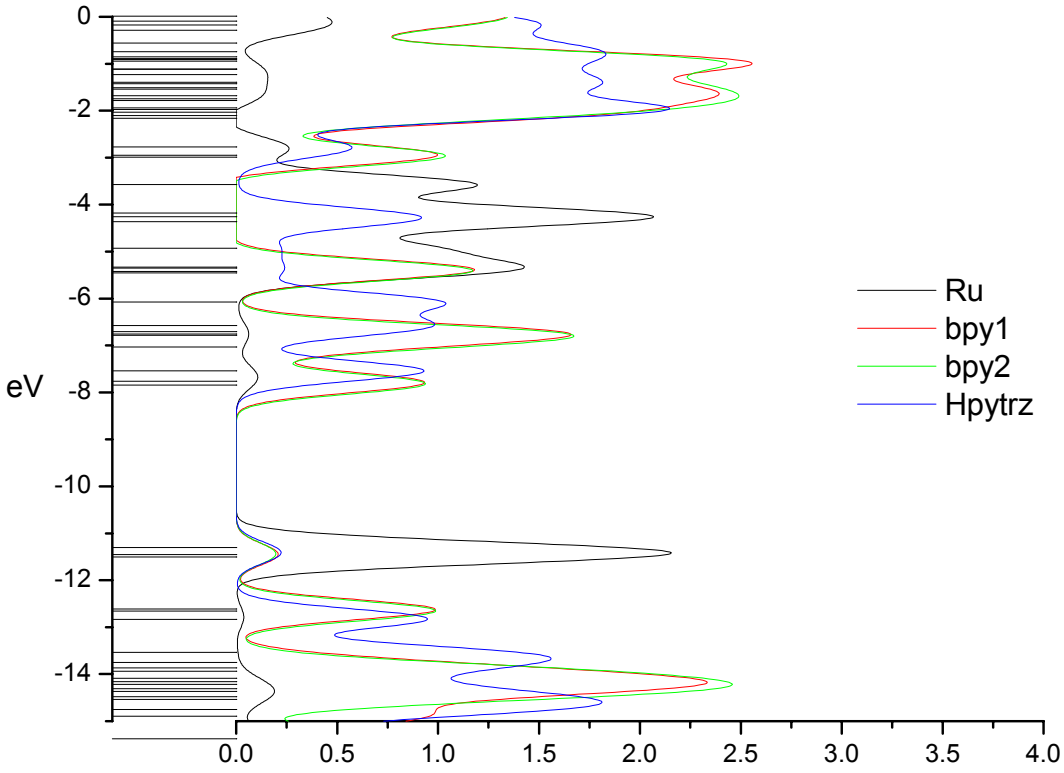

Figure 3.12 – Alternative PDOS diagram for $[Ru(bpy)_2(Hpytrz)]^{2+}$, H1, created by summing the *py* and *Htrz* moieties in Figure 3.11.

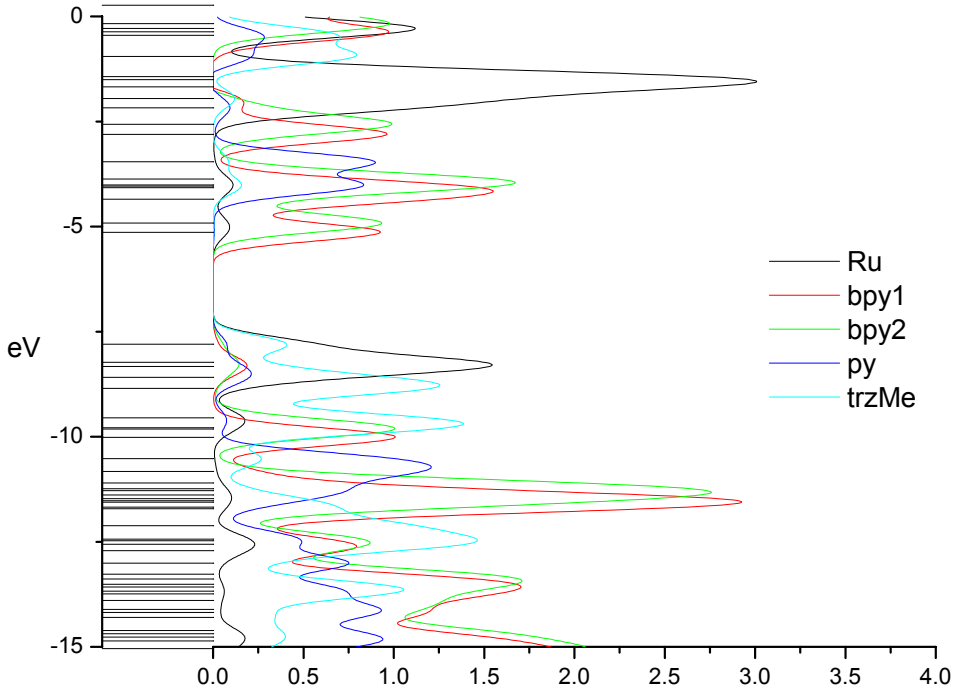

Figure 3.13 – PDOS diagram for $[Ru(bpy)_2(py\text{-}N2\text{-}trz\text{-}Me)]^+$, 2.

MO		eV	Ru	bpy1	bpy2	py	trzMe
142	L+10	-2.17	67	6	17	9	1
141	L+9	-2.56	0	7	92	0	0
140	L+8	-2.81	1	93	7	0	0
139	L+7	-3.46	1	1	2	87	8
138	L+6	-3.87	2	4	92	1	0
137	L+5	-4.01	5	10	29	46	10
136	L+4	-4.04	2	14	48	31	5
135	L+3	-4.07	1	88	8	3	0
134	L+2	-4.35	1	78	17	3	0
133	L+1	-4.91	6	3	91	0	0
132	LUMO	-5.14	5	91	4	1	0
131	HOMO	-7.80	47	2	4	7	40
130	H-1	-8.23	77	7	10	3	4
129	H-2	-8.33	67	11	3	7	11
128	H-3	-8.58	31	3	4	16	47
127	H-4	-8.85	1	0	1	0	98
126	H-5	-9.55	13	1	9	6	71
125	H-6	-9.78	4	3	9	2	82
124	H-7	-9.82	2	2	87	1	8
123	H-8	-10.01	1	98	1	0	0
122	H-9	-10.52	0	1	1	72	26
121	H-10	-10.83	1	14	2	81	2

Table 3.9 – Frontier orbital information for $[Ru(bpy)_2(py\text{-}N2\text{-}trz\text{-}Me)]^+$, 2.

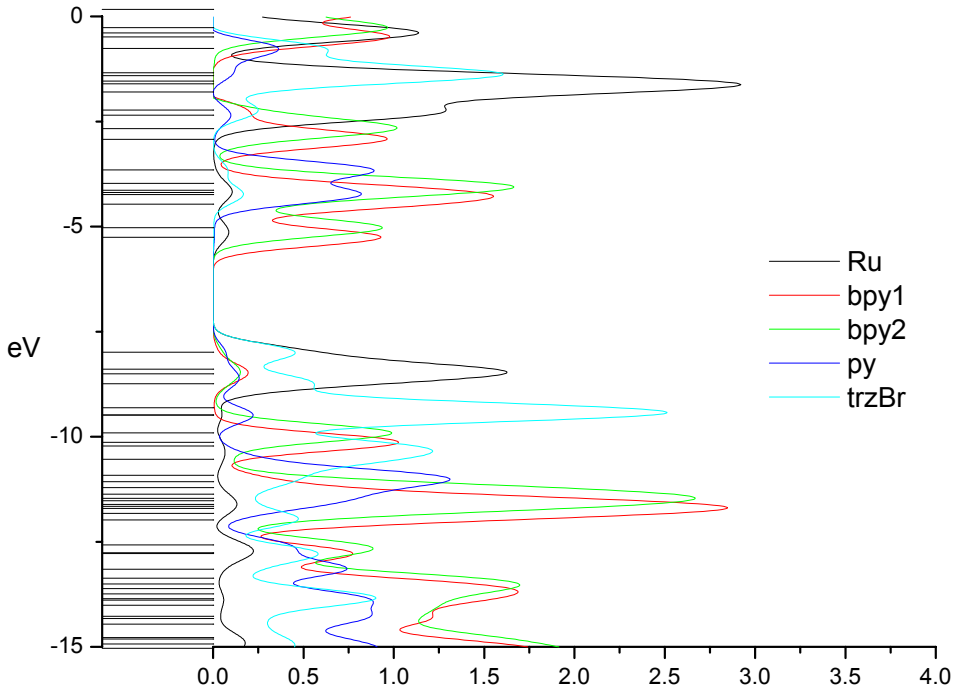

Figure 3.14 – PDOS diagram for $[Ru(bpy)_2(py\text{-}N2\text{-}trz\text{-}Br)]^+$, 3.

MO		eV	Ru	bpy1	bpy2	py	trzBr
141	L+10	-2.35	66	5	16	10	4
140	L+9	-2.67	0	6	93	0	0
139	L+8	-2.92	1	93	6	0	0
138	L+7	-3.65	1	2	3	87	8
137	L+6	-3.97	2	4	92	2	0
136	L+5	-4.14	3	19	76	2	1
135	L+4	-4.19	2	85	9	2	1
134	L+3	-4.24	3	8	0	73	15
133	L+2	-4.47	1	78	16	4	0
132	L+1	-5.02	5	3	91	0	0
131	LUMO	-5.26	5	91	3	1	0
130	HOMO	-7.99	44	2	4	6	44
129	H-1	-8.39	77	7	9	3	4
128	H-2	-8.50	72	12	4	6	6
127	H-3	-8.74	36	2	5	8	48
126	H-4	-9.31	0	0	0	0	99
125	H-5	-9.48	1	0	0	1	98
124	H-6	-9.49	4	0	1	21	74
123	H-7	-9.91	0	1	97	0	1
122	H-8	-10.13	0	98	1	0	1
121	H-9	-10.22	4	5	2	2	87
120	H-10	-10.54	4	1	9	16	70

Table 3.10 – Frontier orbital information for $[Ru(bpy)_2(py\text{-}N2\text{-}trz\text{-}Br)]^+$, 3.

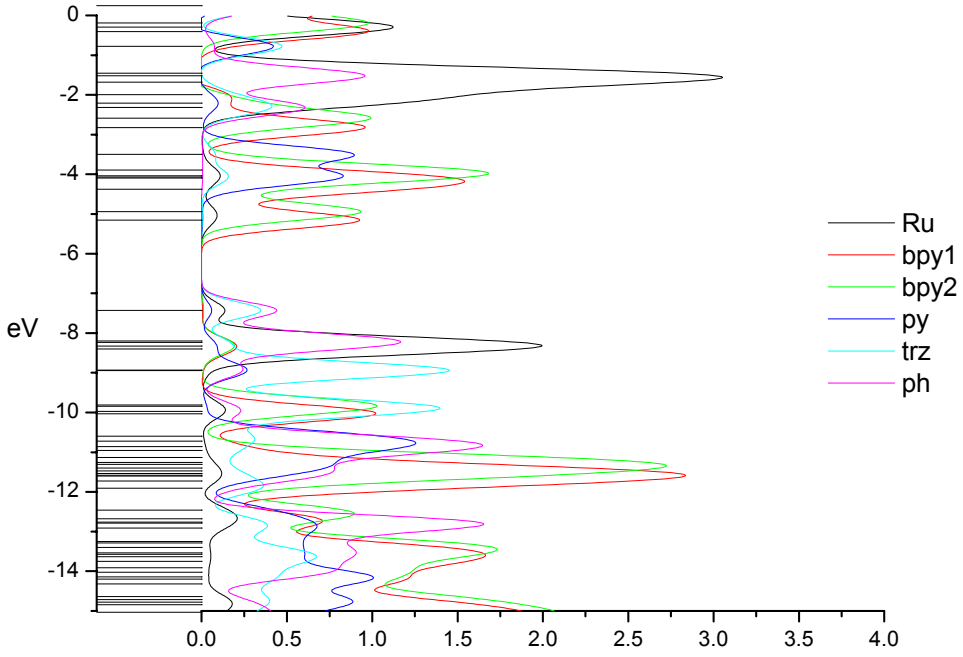

Figure 3.15 – PDOS diagram for $[Ru(bpy)_2(py\text{-}N2\text{-}trz\text{-}Ph)]^+$, 4.

MO		eV	Ru	bpy1	bpy2	py	trz	ph
158	L+10	-2.32	2	0	0	0	37	60
157	L+9	-2.59	0	7	92	0	0	0
156	L+8	-2.83	1	92	7	0	0	0
155	L+7	-3.50	1	1	3	87	8	1
154	L+6	-3.90	2	4	92	1	0	0
153	L+5	-4.04	4	17	54	20	5	0
152	L+4	-4.07	3	11	26	50	9	0
151	L+3	-4.09	1	84	5	8	1	0
150	L+2	-4.37	1	78	17	3	0	0
149	L+1	-4.94	6	3	91	0	0	0
148	LUMO	-5.16	5	91	4	1	0	0
147	HOMO	-7.43	14	1	1	6	35	44
146	H-1	-8.20	7	1	1	0	3	89
145	H-2	-8.24	72	6	6	2	3	11
144	H-3	-8.33	61	4	7	3	10	14
143	H-4	-8.40	71	11	6	4	2	6
142	H-5	-8.93	3	1	0	24	53	20
141	H-6	-8.95	1	0	1	3	92	4
140	H-7	-9.81	1	2	76	0	18	3
139	H-8	-9.84	3	4	17	1	72	3
138	H-9	-9.98	9	7	11	1	55	17
137	H-10	-10.04	1	92	2	0	3	1

Table 3.11 – Frontier orbital information for $[Ru(bpy)_2(py\text{-}N2\text{-}trz\text{-}Ph)]^+$, 4.

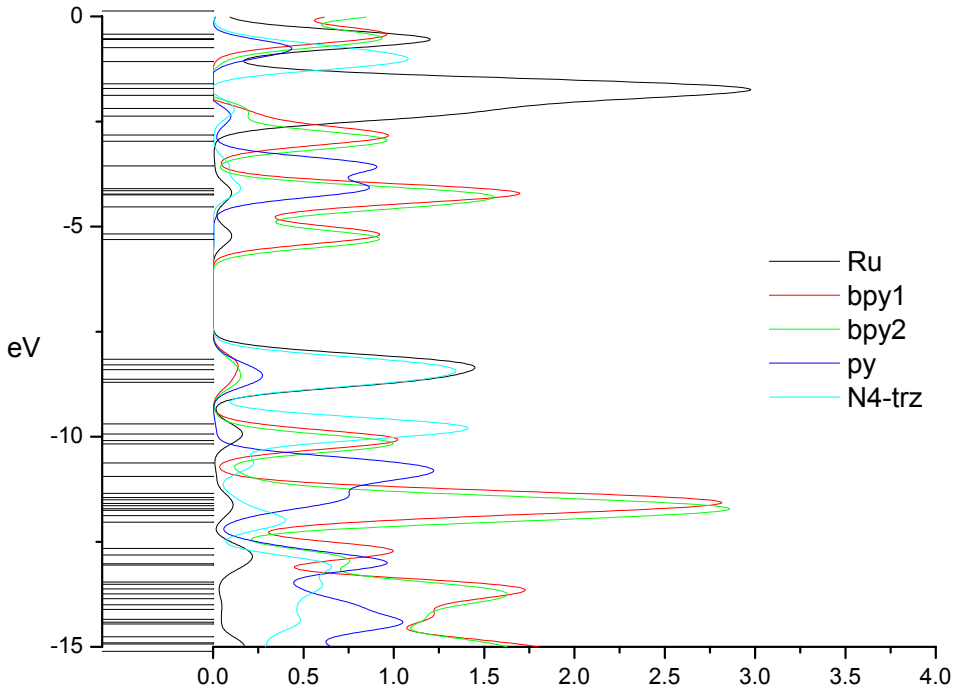

Figure 3.16 – PDOS diagram for $[Ru(bpy)_2(py\text{-}N4\text{-}trz)]^+$, 5.

MO		eV	Ru	bpy1	bpy2	py	N4-trz
138	L+10	-2.37	67	16	6	10	1
137	L+9	-2.82	0	82	17	1	0
136	L+8	-2.97	1	16	83	0	0
135	L+7	-3.55	1	2	1	87	8
134	L+6	-4.10	3	1	1	81	14
133	L+5	-4.15	2	90	7	1	0
132	L+4	-4.22	2	6	92	0	0
131	L+3	-4.24	4	68	28	0	0
130	L+2	-4.53	1	29	67	2	0
129	L+1	-5.17	7	80	13	0	0
128	LUMO	-5.31	4	14	82	0	0
127	HOMO	-8.16	63	5	3	4	25
126	H-1	-8.29	38	6	3	1	52
125	H-2	-8.41	42	2	5	13	38
124	H-3	-8.63	36	3	3	12	46
123	H-4	-8.70	46	5	8	7	34
122	H-5	-9.70	3	1	3	1	92
121	H-6	-9.93	12	18	1	1	68
120	H-7	-10.09	3	82	7	0	8
119	H-8	-10.17	1	7	92	0	0
118	H-9	-10.63	0	1	1	77	21
117	H-10	-10.94	2	2	13	82	2

Table 3.12 – Frontier orbital information for $[Ru(bpy)_2(py\text{-}N4\text{-}trz)]^+$, 5.

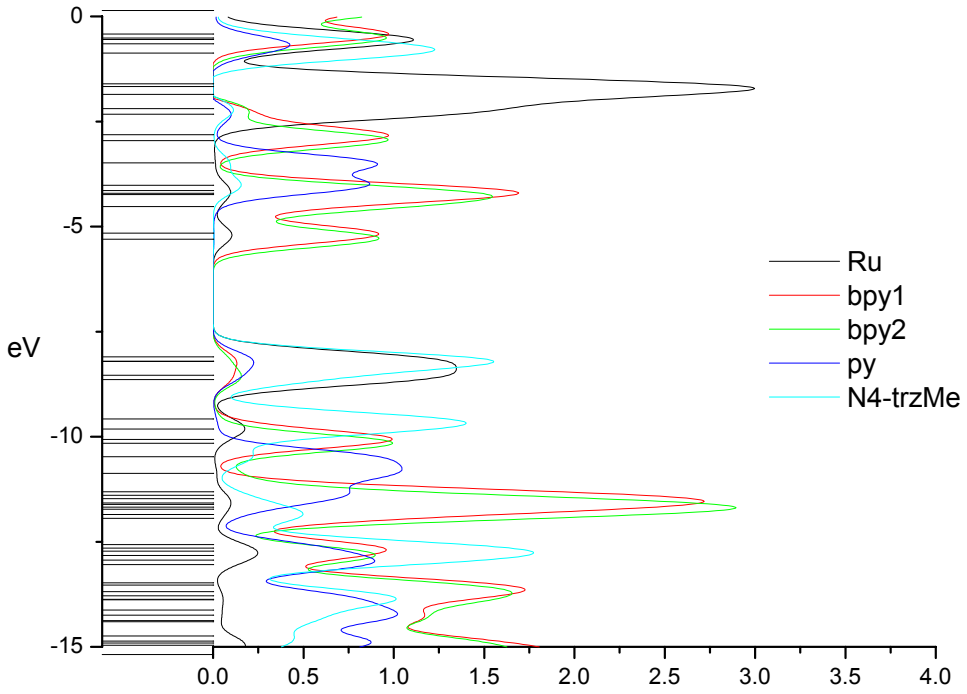

Figure 3.17 – PDOS diagram for $[Ru(bpy)_2(py\text{-}N4\text{-}trz\text{-}Me)]^+$, 6.

MO		eV	Ru	bpy1	bpy2	py	N4-trzMe
142	L+10	-2.33	68	15	5	10	2
141	L+9	-2.82	0	84	15	1	0
140	L+8	-2.95	1	15	84	0	0
139	L+7	-3.49	1	2	1	87	9
138	L+6	-4.02	3	1	1	81	15
137	L+5	-4.14	2	93	5	1	0
136	L+4	-4.21	2	7	91	0	0
135	L+3	-4.24	4	65	31	0	0
134	L+2	-4.52	1	29	68	2	0
133	L+1	-5.16	7	79	14	0	0
132	LUMO	-5.30	4	15	80	0	0
131	HOMO	-8.10	50	4	3	8	35
130	H-1	-8.20	20	1	3	10	66
129	H-2	-8.21	41	6	2	2	48
128	H-3	-8.54	57	3	6	9	24
127	H-4	-8.64	55	6	9	3	27
126	H-5	-9.58	3	1	3	1	92
125	H-6	-9.82	15	11	1	2	71
124	H-7	-10.07	1	88	5	1	4
123	H-8	-10.16	1	5	94	0	0
122	H-9	-10.48	0	1	1	77	20
121	H-10	-10.88	2	1	12	83	2

Table 3.13 – Frontier orbital information for $[Ru(bpy)_2(py\text{-}N4\text{-}trz\text{-}Me)]^+$, 6.

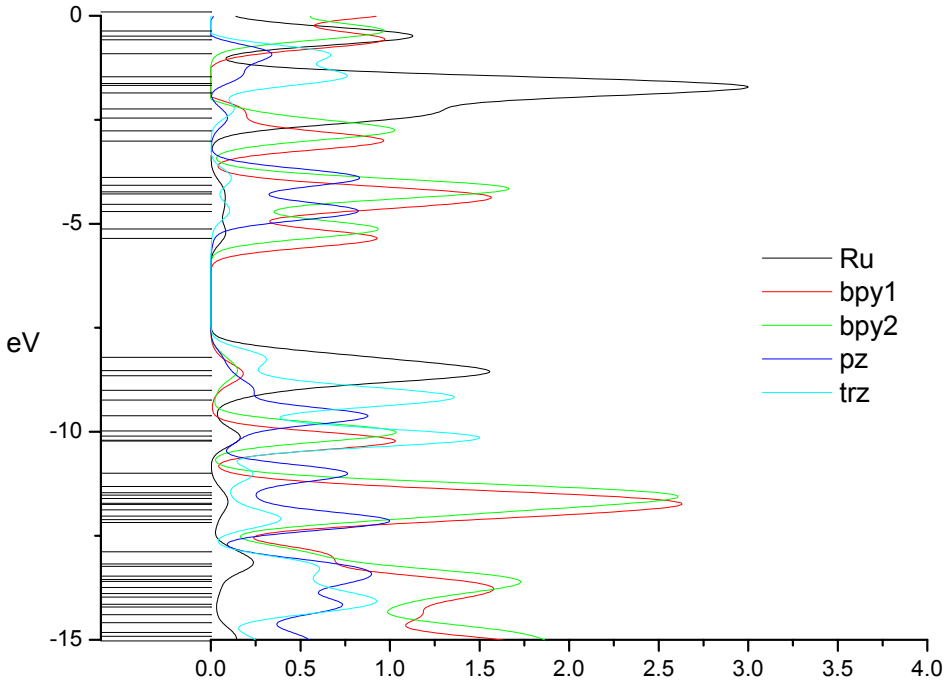

Figure 3.18 – PDOS diagram for $[Ru(bpy)_2(pztrz)]^+$, 7.

MO		eV	Ru	bpy1	bpy2	pz	trz
138	L+10	-2.46	67	7	17	9	1
137	L+9	-2.76	0	7	93	0	0
136	L+8	-3.01	1	93	6	0	0
135	L+7	-3.89	1	2	6	80	11
134	L+6	-4.07	2	3	90	4	1
133	L+5	-4.23	3	21	74	1	0
132	L+4	-4.28	2	89	9	0	0
131	L+3	-4.53	3	73	14	9	2
130	L+2	-4.71	4	8	4	76	9
129	L+1	-5.12	5	3	91	1	0
128	LUMO	-5.35	4	91	3	1	0
127	HOMO	-8.21	59	3	5	5	28
126	H-1	-8.53	75	7	10	2	5
125	H-2	-8.65	69	11	3	7	10
124	H-3	-9.01	20	2	2	21	54
123	H-4	-9.24	1	0	1	0	99
122	H-5	-9.62	2	1	1	87	10
121	H-6	-9.98	2	1	81	0	16
120	H-7	-10.11	9	2	24	4	61
119	H-8	-10.20	5	8	1	10	76
118	H-9	-10.22	1	92	2	0	5
117	H-10	-11.00	0	1	1	75	23

Table 3.14 – Frontier orbital information for $[Ru(bpy)_2(pztrz)]^+$, 7.

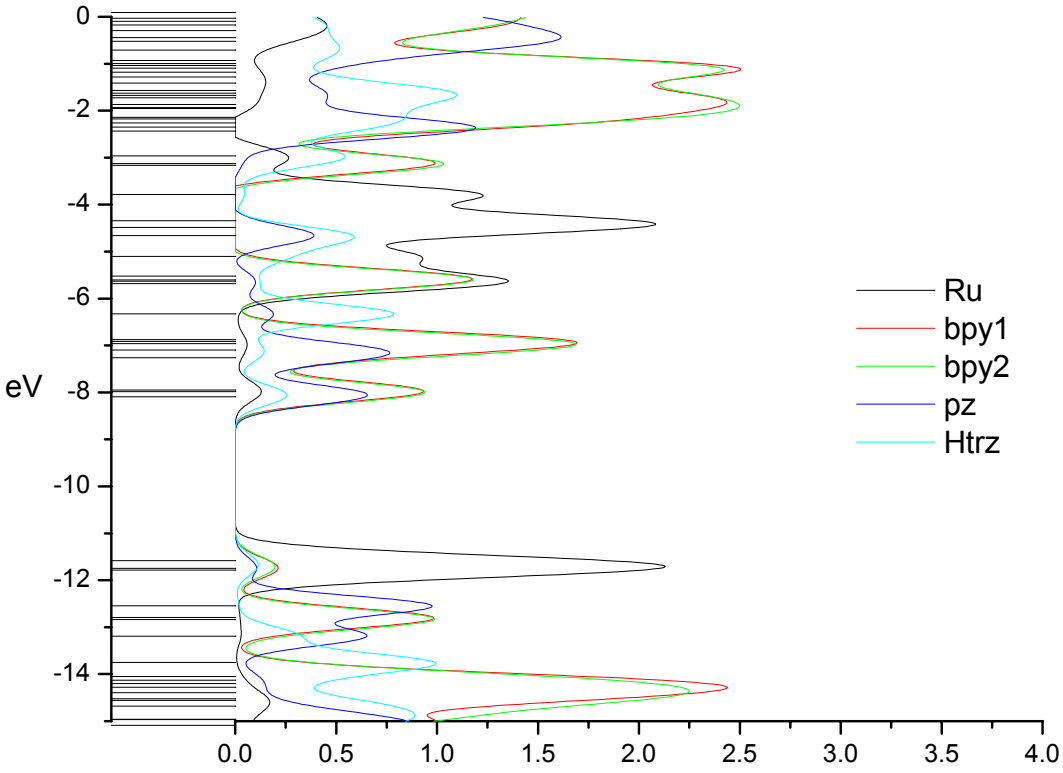

Figure 3.19 – PDOS diagram for $[Ru(bpy)_2(Hpztrz)]^{2+}$, H7.

MO		eV	Ru	bpy1	bpy2	pz	Htrz
138	L+10	-5.63	4	42	53	1	0
137	L+9	-5.68	66	13	7	4	10
136	L+8	-6.33	1	1	1	19	78
135	L+7	-6.88	1	58	39	1	1
134	L+6	-6.91	2	50	44	3	1
133	L+5	-6.96	2	47	51	0	0
132	L+4	-7.09	1	9	36	44	9
131	L+3	-7.26	1	32	27	36	5
130	L+2	-7.95	6	66	26	2	1
129	L+1	-7.98	6	12	52	22	8
128	LUMO	-8.09	2	18	19	44	18
127	HOMO	-11.58	80	5	7	2	6
126	H-1	-11.75	76	6	10	4	5
125	H-2	-11.78	76	12	5	5	1
124	H-3	-12.55	1	0	1	97	2
123	H-4	-12.79	0	68	31	0	0
122	H-5	-12.84	1	30	68	1	0
121	H-6	-13.19	3	0	3	64	30
120	H-7	-13.75	0	2	4	1	92
119	H-8	-14.05	0	48	48	1	3
118	H-9	-14.13	1	16	57	5	21
117	H-10	-14.20	2	78	12	6	2

Table 3.15 – Frontier orbital information for $[Ru(bpy)_2(Hpztrz)]^{2+}$, H7.

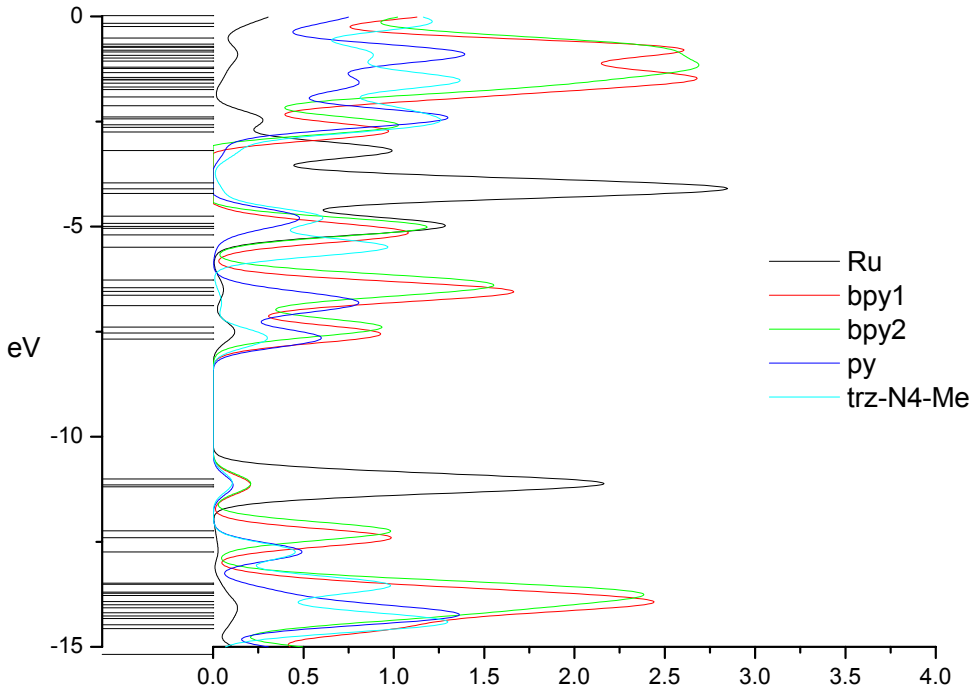

Figure 3.20 – PDOS diagram for $[Ru(bpy)_2(py\text{-}N2\text{-}trz\text{-}N4\text{-}Me)]^{2+}$, 8.

MO		eV	Ru	bpy1	bpy2	py	trz-N4-Me
142	L+10	-5.04	64	10	17	8	1
141	L+9	-5.19	2	86	9	1	2
140	L+8	-5.49	1	2	1	1	95
139	L+7	-6.27	2	6	92	0	0
138	L+6	-6.45	2	62	35	1	0
137	L+5	-6.54	2	52	46	0	0
136	L+4	-6.63	2	53	13	31	2
135	L+3	-6.88	1	24	11	61	3
134	L+2	-7.39	5	1	90	2	1
133	L+1	-7.54	6	78	0	10	5
132	LUMO	-7.68	2	17	6	50	25
131	HOMO	-11.00	82	5	6	2	5
130	H-1	-11.15	75	6	12	3	5
129	H-2	-11.19	76	11	4	7	2
128	H-3	-12.24	1	1	97	0	0
127	H-4	-12.41	1	97	1	0	0
126	H-5	-12.74	2	1	3	49	45
125	H-6	-13.48	1	27	71	1	1
124	H-7	-13.51	2	6	6	2	85
123	H-8	-13.70	1	10	76	3	9
122	H-9	-13.72	1	62	11	22	3
121	H-10	-13.78	1	18	75	1	6

Table 3.16 – Frontier orbital information for $[Ru(bpy)_2(py\text{-}N2\text{-}trz\text{-}N4\text{-}Me)]^{2+}$, 8.

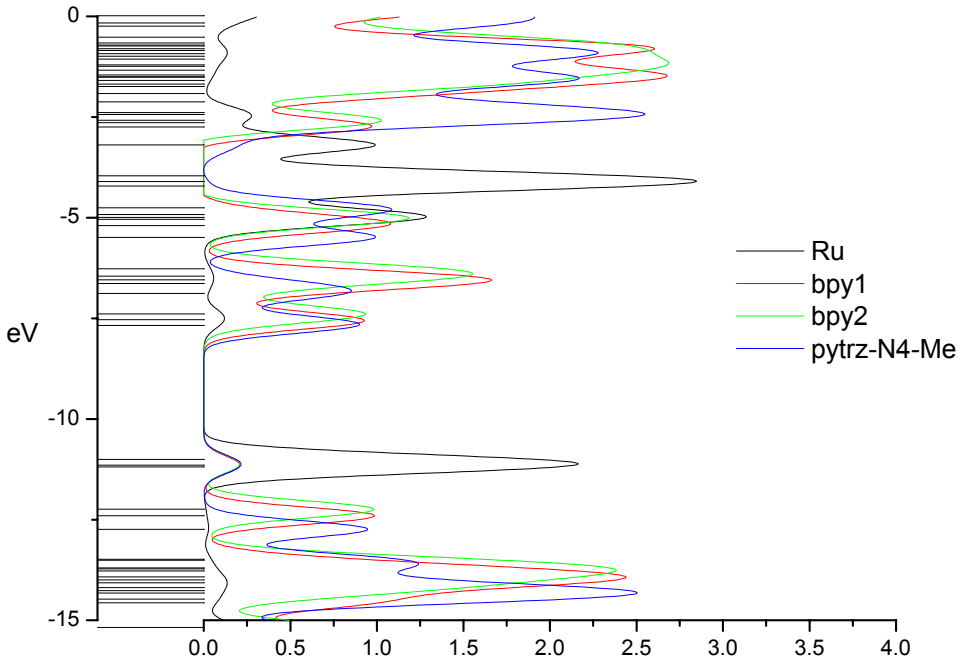

Figure 3.21 – Alternative PDOS diagram for $[Ru(bpy)_2(py\text{-}N2\text{-}trz\text{-}N4\text{-}Me)]^{2+}$, 8, created by summing the *py* and *trz-N4-Me* moieties in Figure 3.20.

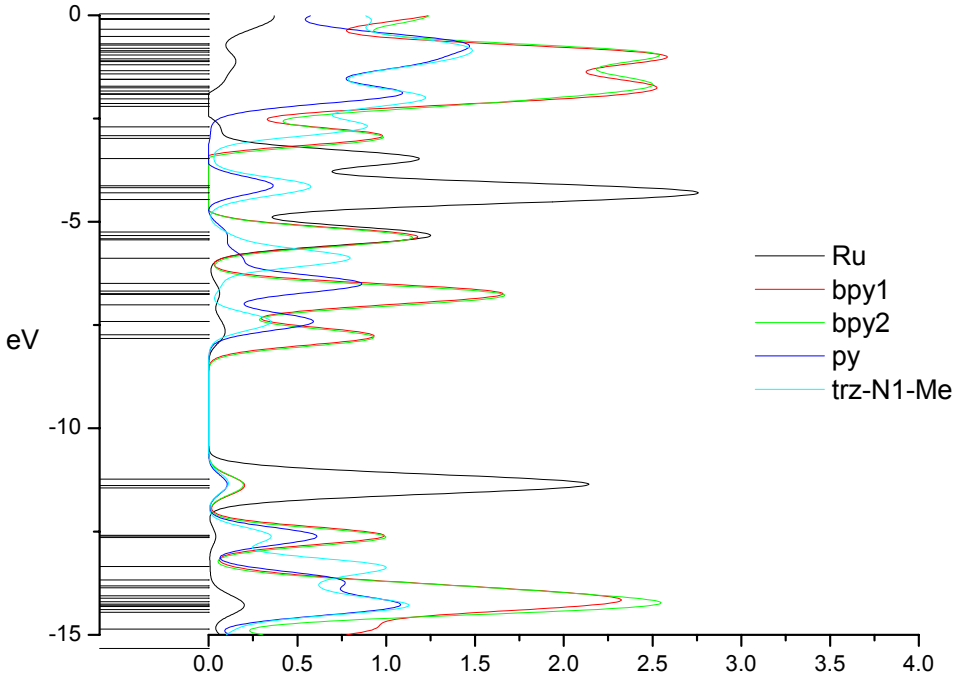

Figure 3.22 – PDOS diagram for $[Ru(bpy)_2(py\text{-}N2\text{-}trz\text{-}N1\text{-}Me)]^{2+}$, 9.

MO		eV	Ru	bpy1	bpy2	py	trz-N1-Me
142	L+10	-5.41	63	18	6	4	9
141	L+9	-5.44	1	34	63	0	1
140	L+8	-5.88	1	0	2	18	79
139	L+7	-6.49	2	6	4	83	6
138	L+6	-6.68	1	79	19	1	0
137	L+5	-6.74	2	17	78	3	0
136	L+4	-6.76	2	52	44	1	0
135	L+3	-7.01	1	43	51	4	0
134	L+2	-7.42	5	1	1	58	35
133	L+1	-7.73	6	62	31	0	0
132	LUMO	-7.83	2	32	64	1	1
131	HOMO	-11.23	81	5	6	3	5
130	H-1	-11.38	77	6	6	6	5
129	H-2	-11.44	76	11	10	2	2
128	H-3	-12.59	1	79	17	2	2
127	H-4	-12.61	2	0	16	53	29
126	H-5	-12.65	2	20	67	6	4
125	H-6	-13.35	1	2	2	1	95
124	H-7	-13.67	0	25	3	66	6
123	H-8	-13.82	0	21	54	2	23
122	H-9	-13.86	0	41	39	4	15
121	H-10	-14.05	1	60	33	3	3

Table 3.17 – Frontier orbital information for $[Ru(bpy)_2(py\text{-}N2\text{-}trz\text{-}N1\text{-}Me)]^{2+}$, 9.

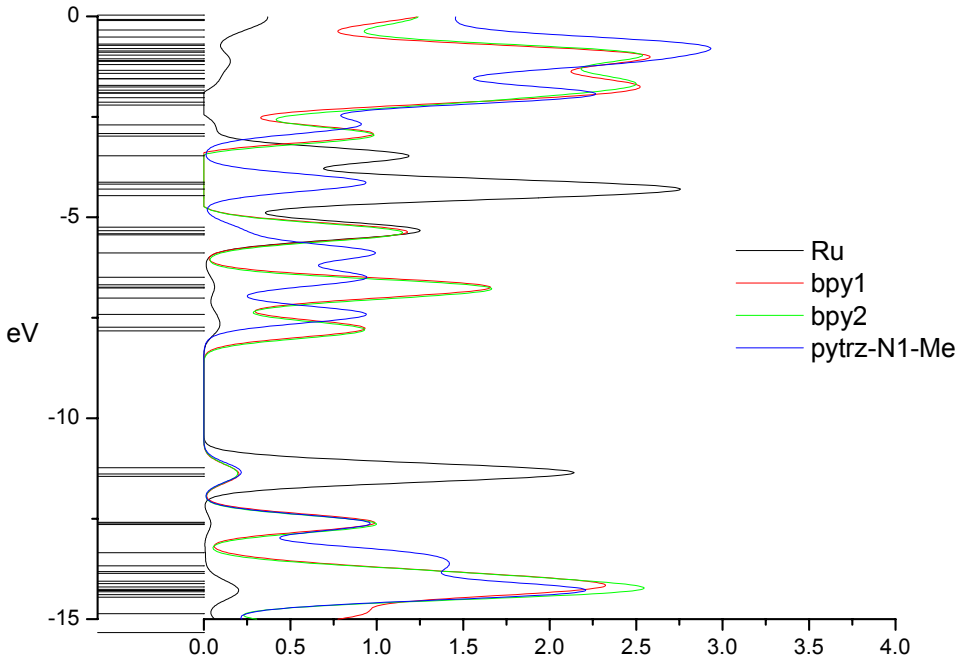

Figure 3.23 – Alternative PDOS diagram for $[Ru(bpy)_2(py\text{-}N2\text{-}trz\text{-}N1\text{-}Me)]^{2+}$, 9, created by summing the *py* and *trz-N1-Me* moieties in Figure 3.22.

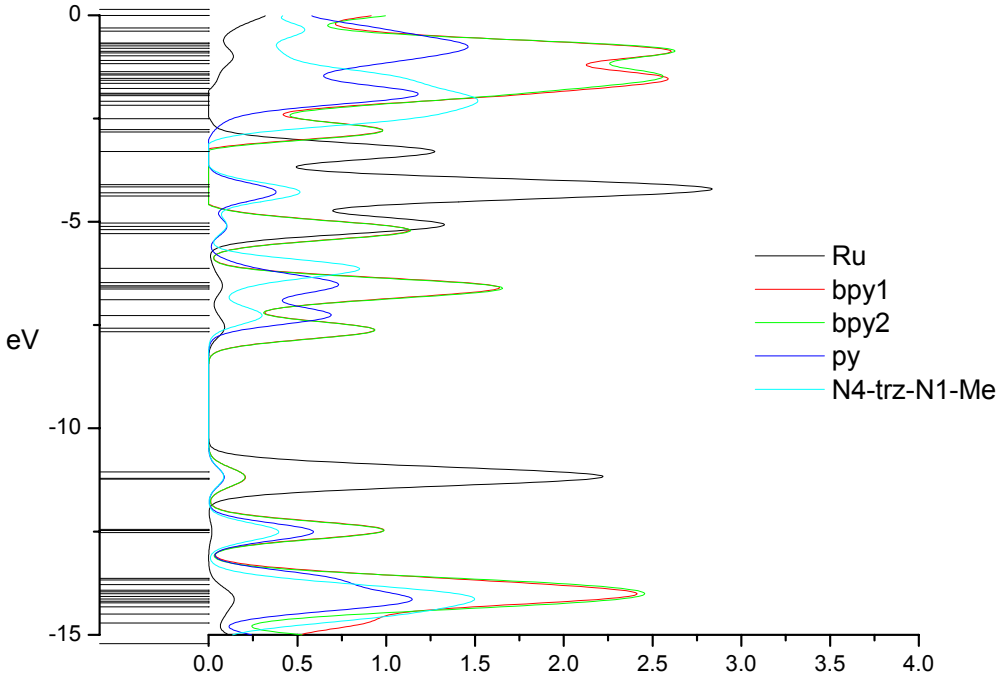

Figure 3.24 – PDOS diagram for $[Ru(bpy)_2(py\text{-}N4\text{-}trz\text{-}N1\text{-}Me)]^{2+}$, 10.

MO		eV	Ru	bpy1	bpy2	py	N4-trz-N1-Me
142	L+10	-5.19	3	49	47	1	0
141	L+9	-5.29	1	47	51	0	0
140	L+8	-6.12	2	1	1	14	82
139	L+7	-6.47	2	21	29	39	8
138	L+6	-6.55	2	85	10	2	2
137	L+5	-6.58	1	1	65	29	4
136	L+4	-6.63	2	46	51	0	0
135	L+3	-6.89	1	43	41	12	3
134	L+2	-7.27	3	1	1	66	29
133	L+1	-7.58	6	50	44	0	0
132	LUMO	-7.66	2	45	51	1	1
131	HOMO	-11.06	83	6	6	2	3
130	H-1	-11.21	78	6	6	5	4
129	H-2	-11.23	76	10	10	2	2
128	H-3	-12.45	0	60	39	0	0
127	H-4	-12.47	0	28	41	19	12
126	H-5	-12.52	1	12	19	41	27
125	H-6	-13.63	0	43	2	54	1
124	H-7	-13.67	0	39	52	5	5
123	H-8	-13.78	1	4	70	1	24
122	H-9	-13.92	1	59	38	1	2
121	H-10	-13.96	2	36	10	15	37

Table 3.18 – Frontier orbital information for $[Ru(bpy)_2(py\text{-}N4\text{-}trz\text{-}N1\text{-}Me)]^{2+}$, 10.

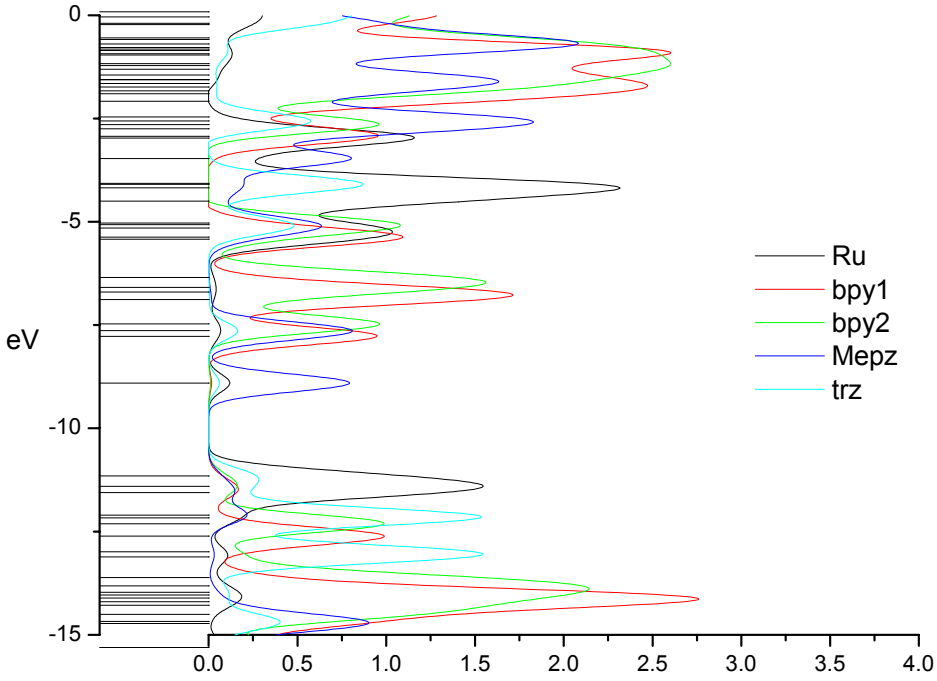

Figure 3.25 – PDOS diagram for $[Ru(bpy)_2(pztrz\text{-}N'4\text{-}Me)]^{2+}$, 11.

MO		eV	Ru	bpy1	bpy2	Mepz	trz
142	L+10	-5.15	39	9	5	25	22
141	L+9	-5.37	29	56	10	4	0
140	L+8	-5.42	35	46	12	6	1
139	L+7	-6.35	2	3	95	0	0
138	L+6	-6.59	2	17	81	0	0
137	L+5	-6.70	1	90	9	0	0
136	L+4	-6.88	1	86	11	1	0
135	L+3	-7.48	4	1	95	0	0
134	L+2	-7.64	1	7	0	76	15
133	L+1	-7.77	4	89	1	5	1
132	LUMO	-8.90	12	2	1	79	6
131	HOMO	-11.15	65	3	5	5	23
130	H-1	-11.41	74	8	11	3	4
129	H-2	-11.56	64	9	4	11	13
128	H-3	-12.10	17	3	4	21	55
127	H-4	-12.17	0	0	2	0	97
126	H-5	-12.31	1	1	94	0	3
125	H-6	-12.61	1	97	1	0	0
124	H-7	-12.99	3	5	5	1	85
123	H-8	-13.11	8	1	13	2	76
122	H-9	-13.61	2	19	75	0	3
121	H-10	-13.81	1	3	95	0	1

Table 3.19 – Frontier orbital information for $[Ru(bpy)_2(pztrz\text{-}N'4\text{-}Me)]^{2+}$, 11.

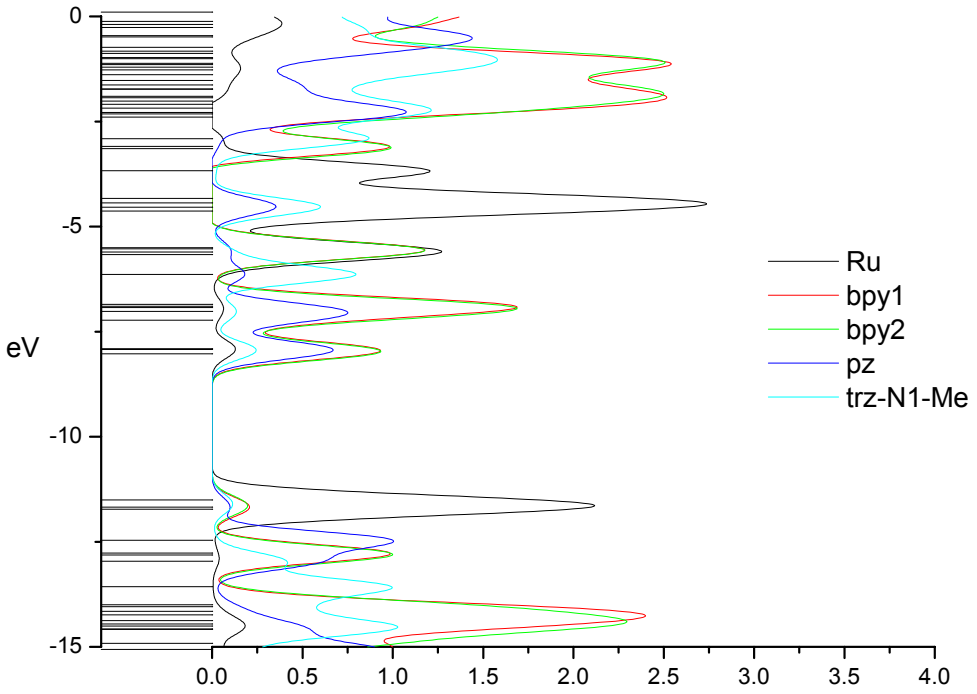

Figure 3.26 – PDOS diagram for $[Ru(bpy)_2(pztrz\text{-}N1\text{-}Me)]^{2+}$, 12.

MO		eV	Ru	bpy1	bpy2	pz	trz-N1-Me
142	L+10	-5.61	1	42	56	0	1
141	L+9	-5.66	66	14	7	3	10
140	L+8	-6.14	2	1	2	18	79
139	L+7	-6.85	1	56	39	3	1
138	L+6	-6.89	2	54	37	5	2
137	L+5	-6.93	2	47	49	2	0
136	L+4	-7.02	1	2	36	52	9
135	L+3	-7.22	1	37	35	23	3
134	L+2	-7.90	7	29	3	45	16
133	L+1	-7.92	5	36	52	5	2
132	LUMO	-8.03	1	31	41	19	8
131	HOMO	-11.50	81	5	7	2	6
130	H-1	-11.68	76	6	9	4	5
129	H-2	-11.72	76	12	6	5	2
128	H-3	-12.46	1	0	1	96	2
127	H-4	-12.77	0	71	28	0	0
126	H-5	-12.81	1	28	71	1	0
125	H-6	-12.96	3	1	2	56	39
124	H-7	-13.57	0	2	1	2	95
123	H-8	-14.00	0	29	56	1	13
122	H-9	-14.04	0	30	40	3	27
121	H-10	-14.15	2	77	10	9	1

Table 3.20 – Frontier orbital information for $[Ru(bpy)_2(pztrz\text{-}N1\text{-}Me)]^{2+}$, 12.

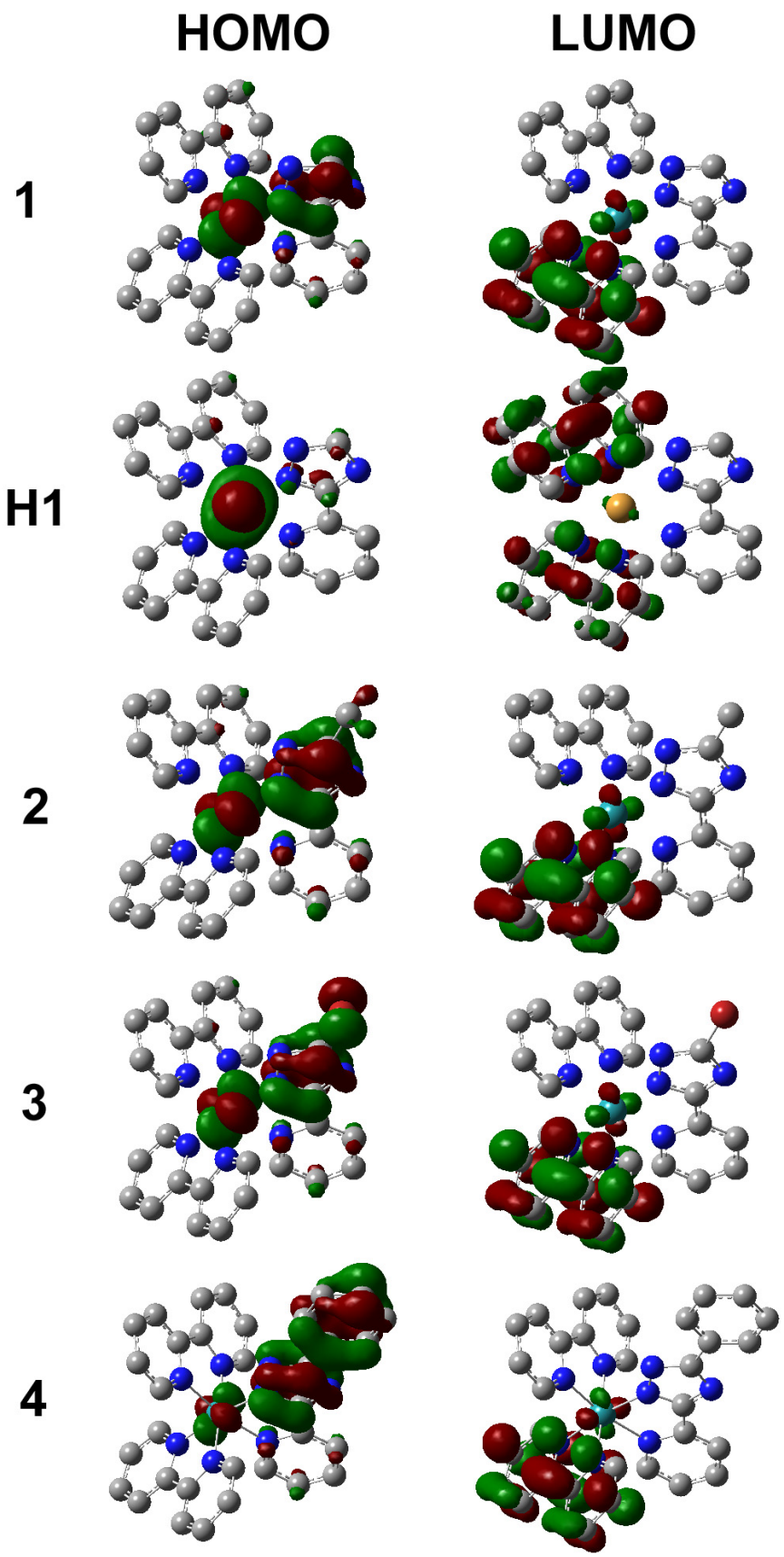

Figure 3.27 – Isosurfaces of the HOMO and LUMO of 1 to 4. Isosurfaces drawn at 0.04e/bohr^3.

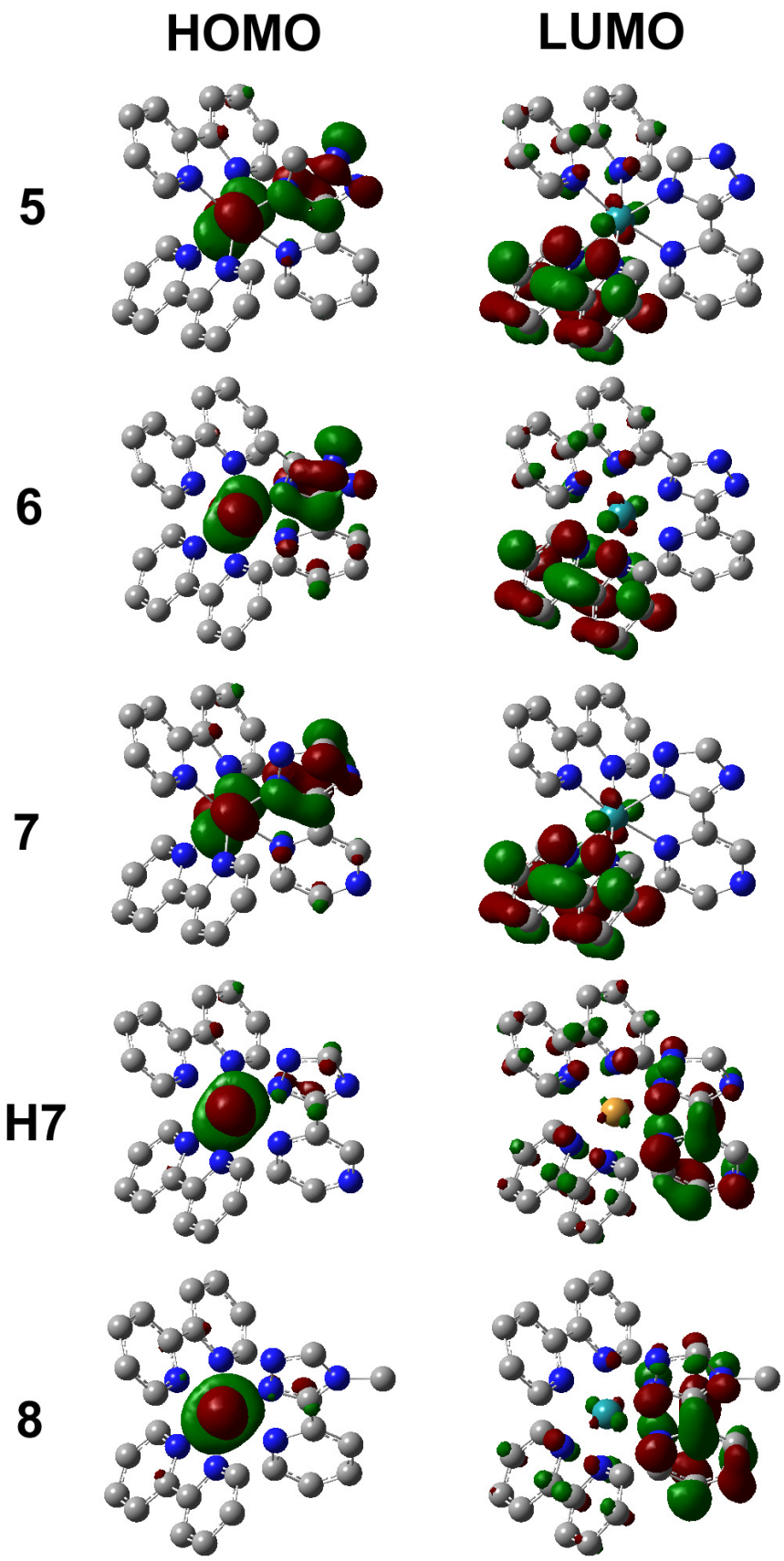

Figure 3.28 – Isosurfaces of the HOMO and LUMO of 5 to 8. Isosurfaces drawn at 0.04e/bohr^3.

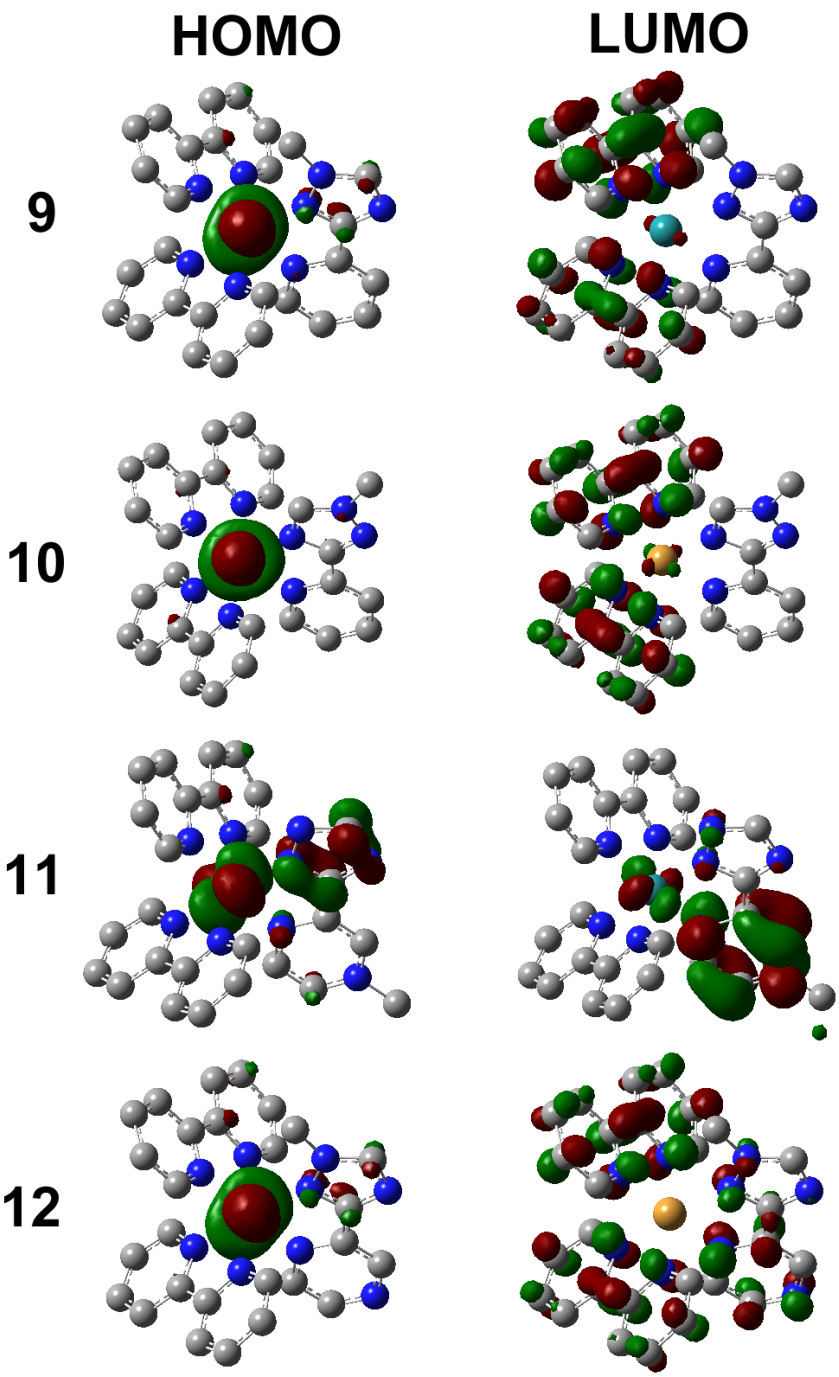

Figure 3.29 – Isosurfaces of the HOMO and LUMO of 9 **to** 12**. Isosurfaces drawn at 0.04e/bohr^3.**

3.5 Discussion

3.5.1 Electronic structures

The photophysical properties of **1** and **H1** have been studied by Hage *et al.*[3] and Buchanan *et al.*[4] Oxidation occurs at the metal centre in each case. The fact that **1** is a stronger acid in the excited state, as well as evidence from electrochemical data,[3] suggested that the emitting state in **1** is bipyridine-based. This was confirmed in a later study by Keyes *et al.*[23] who showed that deuteration of the bipyridine ligands lead to a doubling of the emission lifetime, whereas deuteration of pytrz had no effect. The location of the excited state in **H1** is not as clear. The lifetime of the excited state was too short to be accurately measured. This is due to deactivation by population of a metal-centred state.

The DFT calculations on **1** agree with the experimental results. The PDOS spectra show that the highest occupied molecular orbitals are Ru-based, while the lowest unoccupied orbitals are bipyridine-based. For **H1**, the highest occupied molecular orbitals are also metal-based. The experimental results do not clearly show the position of the emitting state. The bipyridine PDOS in the lowest unoccupied molecular orbitals occurs at slightly lower energy than the Hpytrz PDOS. However, the difference is very small.

The series of complexes, **1** to **4**, provide an excellent test for the ability of DFT to predict trends in metal oxidation potentials, without calculation of the oxidised species. The oxidation potentials of these complexes are (all in MeCN versus SCE): 0.83V for **1**[24], 0.79V for **2**[3], 0.95V for **3** (measured by Fiona Lynch, Dublin City University), and 0.81V for **4** (measured by Dr. Wesley Browne, University of Groningen). If experimental error is +/- 0.01V, then the order of the oxidation potentials is **3**>**1**>(**4**)>**2**, but the oxidation potential of **4** could be equal to that of either **1** or **2**. These values reflect an increase in the σ-donor strength of pytrz as the C5 bromine atom is replaced with stronger electron donating groups/atoms. This causes an increase in the electron density on the ruthenium atom, and hence makes it easier (lower $E_{1/2}$(ox)) to oxidise the metal centre. The fact that **2** is a slightly weaker acid than **1** also indicates the electron-donating nature of the methyl group.[4]

The location of the peak of the ruthenium PDOS in the frontier region of the highest occupied molecular orbitals is a measure of the relative electron density on the

metal centre in related complexes. This occurs at -8.31eV for **1**, -8.30eV for **2**, –8.48eV for **3**, and -8.33eV for **4**. This gives an ordering of **3**>**1**=**2**=**4**. This method does not give the correct order where the differences in oxidation potential are less than 0.05V. However, the relatively large difference between the oxidation potentials of **1** and **3** (0.12V) is reflected by a large difference (0.17eV) between the Ru peaks in the PDOS. An alternative method of estimating the relative ordering of the oxidation potentials of these complexes is to simply use the energy of the HOMO. However, this does not even give the correct ordering of **1** and **3**: **1**=**3** > **2** > **4**.

The spectroscopic and electrochemical properties of **8** are discussed by Hage *et al.*[3] According to them, the data indicate that the methylated pytrz ligand is a weaker π-acceptor than bpy. However, the electrochemical data show that methylated pytrz has a σ-donor strength comparable to that of bpy (the metal oxidation for **8** occurs at 1.21V versus SCE, compared to 1.22V for $[Ru(bpy)_3]^{2+}$). The DFT calculations show the LUMO to be based on the methylated pytrz, although the difference between the bpy-based orbitals and those based on pytrz is very small. It would be interesting to see whether further experimental studies (for example, resonance Raman measurements) show the emitting state to be pytrz- or bpy-based.

An electrochemical study of **1** and **5** by Buchanan *et al.*[24] showed that the N4-coordinated triazole is a weaker σ-donor than the N2 isomer. This was confirmed in a later study (Buchanan *et al.*[4]) by the fact that the triazole N-H proton of **1** is two orders of magnitude more acidic than that of **5**. Complex **6** has not been synthesised, so a similar comparison cannot be made for **2** and **6**. Although both complexes **9** and **10** have been synthesised, electrochemical data is only available for **10**. However, studies of the linkage isomers of the pytrz complexes of $Ru(phen)_2$ and $Ru(diMebpy)_2$ also show the N4-coordinated isomer to be a weaker σ-donor than the N2 isomer.[29]

The DFT calculations for **1** and **5**, and for **2** and **6**, show an increase in the electron density on the metal centre for the N2-coordinated isomer, compared to the N4 isomer. This is based on the shift of the ruthenium PDOS in the highest occupied molecular orbitals – a shift of -0.04eV is observed for **1**/**5**, and a shift of -0.06eV for **2**/**6**. However, a shift of +0.18eV is observed for **9**/**10** – that is, the N2 isomer is a weaker σ-donor than the N4 isomer. The reason for this is unclear, although it may be due to the position of the electron-withdrawing methyl group relative to the coordinating nitrogen. For **8** and **10**, the methyl group is equally distant from the

coordinating nitrogen, and a shift of -0.06eV is observed for the Ru peak of **10** compared to that of **8**.

Nieuwenhuis *et al.*[25] have investigated the photophysical and electrochemical properties of **7** and **H7**. These indicate that pztrz is a weaker σ-donor than pytrz, although it is still stronger than bpy. Similarly, Hpztrz is a weaker σ-donor than Hpytrz, but in this case Hpztrz is also weaker than bpy. For **H7**, the first reduction potential is Hpztrz-based, unlike for **7** and **1** where it is bpy-based. They concluded that the emitting state in **H7** is likely to be Hpztrz-based, where that of **7** is bpy-based. This conclusion was supported by a analysis of the acid-base properties of **7** by Hage *et al.*[26]. Keyes *et al.*[27] have shown that **7** exhibits dual emission – that is, emission occurs from two weakly coupled excited states over a wide temperature range. The higher energy state is attributed to a pyrazine-based MLCT, whereas the lower energy emitting state is a bipyridine-based MLCT. In its protonated state, normal single emission is observed for **H7**. In a later study, Keyes *et al.*[23] found that deuteration of Hpztrz increased the emission lifetime of **H7**, whereas deuteration of bpy had no effect. The emission lifetime of **7** was insensitive to deuteration, but time-resolved resonance Raman showed that the emitting state was bpy-based.

The DFT calculations on **7** agree with the experimental picture. Compared to pytrz (in **1**), pztrz is shown to be a weaker σ-donor (the Ru peak in the PDOS is shifted to lower energy, indicating that there is less electron density on the metal centre), but a stronger π-acceptor (the PDOS of pztrz in **7** is shifted to lower energy compared to the PDOS of pytrz in **1**). In fact, to be accurate, it is the PDOS of *pz* that is shifted relative to the PDOS of *py* – the PDOS of trz is the same for **1** and **7**. This emphasises the fact that the two moieties of py-/pztrz should be considered independently. The lowest unoccupied molecular orbitals are bpy-based, in agreement with the experimental results. The energy difference between the LUMO (bpy-based) and the LUMO+2 (pz-based) is about 0.64eV or 5000cm^{-1}. However, this is the twice the value of the proposed energy difference between the dual emitting pz- and bpy-based states of **7** (2400cm^{-1}, from Keyes *et al.*[27]). For **H7**, the calculations do not clearly indicate the location of the excited state. Although the LUMO is based on Hpztrz, in agreement with the experimental results, the energy difference between the Hpztrz-based orbitals and the bpy-based orbitals is only about 0.05eV.

Experimental results on **12** are not available. However, they are available for an isomer of **12**, where the triazole is bound to the metal centre through the N4 position (in **12** the triazole is bound to the metal centre through the N2 position). Nieuwenhuis *et al.*[25] found the photochemical and electrochemical properties of this complex to be very similar to those of **H7**. That is, the first reduction potential is based on pztrz, and the lowest energy absorption is a ^{1}MLCT based on pztrz. The calculations show the lowest unoccupied molecular orbitals of **12** to be equally pztrz- and bpy-based. Coordination isomers can have quite different photophysical properties, as has been shown for the coordination isomers of pytrz complexes (see above).

3.5.2 Linkage isomerism in $[Ru(bpy)_2(pytrz)]^+$ and $[Ru(bpy)_2(pytrzMe)]^+$

Hage *et al.*[3] were the first to synthesise the complexes $[Ru(bpy)_2(pytrz)]^+$ and $[Ru(bpy)_2(pytrzMe)]^+$, by reacting equimolar amounts of the appropriate ligand with *cis*-$[Ru(bpy)_2Cl_2]$. In the case of the methyl derivative, proton n.m.r. showed that it was likely to be the N2-bound isomer, **2** (this was later confirmed by a crystal structure[4]). No unambiguous assignment could be made for the unsubstituted pytrz complex.

This issue was further investigated by Buchanan *et al.*[28] who developed a HPLC method to separate the coordination isomers of these two complexes. For the methyl derivative a single peak is observed, which is attributed to the N2-bound isomer **2** on the basis of the previous study. However, two peaks are observed for $[Ru(bpy)_2(pytrz)]^+$, corresponding to the two linkage isomers, **1** and **5**. The authors describe the ratio of the isomers as 1:1, suggesting that there is no preference for coordination at either position. Although the heights of the peaks obtained are almost equal, the peak with the longer retention time has about twice the area of the other peak, indicating a ratio closer to 2:1 than 1:1. In a later study, Buchanan *et al.*[24] used preparative HPLC to obtain up to 100mg of each of the pure linkage isomers, **1** and **5**. The identity of the isomers was established using proton n.m.r. and nuclear Overhauser effect experiments.

It is interesting to note that for the *bis* phenanthroline and *bis* 4,4'-dimethylbpy analogues, similar results were obtained by Ryan *et al.*[29] Using HPLC, a 1:1 ratio of isomers was found for the pytrz complex, although two isomers were also obtained

for the pytrzMe complex, in a ratio of approximately 10%:90%. After using semi-preparative HPLC to separate the isomers, proton n.m.r. was used to identify the first isomer as the N4-bound isomer and the second as the N2-bound isomer.

For both complexes, the N2 isomer is the more stable, by 30.9kJ/mol in the case of the pytrz complex, and by 38.7kJ/mol for the methyl derivative. This is in qualitative agreement with the experimental results. The energy difference is expected to be more for the methyl derivative due to unfavourable steric interactions with a bipyridine. Quantitatively, a thermodynamic distribution of the isomers would yield exclusively the N2 isomer in both cases. Experimentally, only one isomer is found for the methyl derivative, but a ratio of approximately 1:2 of complexes **5** and **1** is found for the pytrz. Such a ratio would be consistent with an energy difference of closer to 2kJ/mol.

Either energy calculations using B3LYP/LanL2DZ are very inaccurate, or perhaps thermodynamic factors do not play such a large role in the distribution of the isomers. Experimentally, the linkage isomers of pytrz have quite different physical properties – this is consistent with the fact that they have quite different energies. Solvation energy for the two isomers may differ considerably due to difference in solvent accessibility for the triazole nitrogens for the linkage isomers. Alternatively, kinetic factors may dominate in the synthesis of the complex, in which case both the N2 and N4 sites must be supposed to have similar reactivities based on the experimental results. Further studies are needed before this question can be answered conclusively.

3.5.3 Methylation of $[Ru(bpy)_2(pytrz)]^+$, 1

The methylation route depicted in Scheme 3.1 was investigated by Hage *et al.*[3] Only one isomer was formed when the N1-methylated ligand was used (Scheme 3.1a). This product was shown to be **10**, based on proton n.m.r. The lack of formation of **9** was explained by an unfavourable steric interaction between the N1-methyl and a neighbouring bipyridine. In addition, Fanni *et al.*[30] found that **9** photoisomerises to give the N4-bound isomer, **10**, which is photostable.

The DFT calculations agree with these results. The N4-linkage isomer **10** is the only product formed, based on a thermodynamic distribution of the products. A significant energy difference is expected between **9** and **10**, given the unfavourable steric

interaction between the N1-methyl and a neighbouring bipyridine for **9**. It is worth noting that the calculated energy difference between **9** and **10** (16 kJ/mol) is about half that between **1** and **5** (another pair of linkage isomers), but that for **1**/**5** the N2-linkage isomer **1** is favoured.

Fanni *et al.*[30] showed that direct methylation of **1** (Scheme 3.2) gave a mixture of **8** and **9** in a ratio of 10:90 (based on proton n.m.r.). That is, the sterically-hindered complex, **9**, was favoured. Similar results were found for other derivatives of the complex. The authors reasoned that the nucleophilicity of the N1 site was the determining factor in this reaction, and not thermodynamics. This was supported by the photochemical studies mentioned above, which showed that **9** photoisomerises to give the N4-bound isomer, **10**, which is photostable.

The DFT calculations show that thermodynamic arguments, based on B3LYP/LanL2DZ energies, cannot be used to explain the reactivity pattern. A thermodynamic distribution of the products gives a ratio of **8**:**9** of 10:90, the exact opposite, in fact, of what is observed. Based on these calculations, Fanni *et al.* were correct to attribute the reactivity pattern to kinetic factors, rather than thermodynamics.

The relative reactivities of the N1 and N4 positions of the triazole towards electrophilic attack were assessed by comparing the electrostatic potential (ESP), square of the HOMO, and Fukui function at the two sites. This was done visually by mapping the values onto an isosurface of the electron density, and also numerically for the square of the HOMO (by calculation of the fractional contribution of N1 and N4 to the HOMO) and the Fukui function (Hirshfeld charges were calculated for **1** and the oxidised complex).

Visually, the ESP does not allow a judgement to be made between N1 and N4 – each appears equally reactive. On the other hand, the diagrams and numerical values for both the Fukui function and the square of the HOMO indicate that the N4 position should be the more reactive. Since this is the opposite of the experimental result, it seems that neither kinetic arguments nor thermodynamics can explain the observed reactivity pattern for the methylation of **1**. It is not known whether this is due to the limitations of the basis set and functional, or whether it may be a general problem with the methods employed.

To this author's knowledge, there are no other examples of the use of local reactivity indices for ruthenium polypyridyl complexes. However, the global reactivity indices of electrophilicity (ω) and donor-acceptor hardness (η_{DA}) were used by Adamo and co-workers[31] to rationalise trends in reactivity among a series of Ru and Os polypyridyl complexes. They found that these indices accurately predict reactivity trends, provided that solvent effects were included in the calculation.

3.5.4 Methylation of $[Ru(bpy)_2(pztrz)]^+$, 7

The methylation of **7** was studied by Fanni *et al.*[30], who found that methylation occurred exclusively on the triazole moiety, resulting in an isomer ratio of 70:30 of N1-methylated (**12**):N4-methylated isomers. However, recent work by Claire Brennan[32] suggests that the pyrazine is exclusively methylated (giving **11**), rather than the triazole.

According to the calculations, **12** is more stable than **11** (by 38 kJ/mol). A thermodynamic distribution of these two products would yield **12** exclusively, in disagreement with the experimental results. However, as discussed earlier in relation to the methylation of **1**, thermodynamics is not a major factor in the determination of the relative ratios of the isomers resulting from the methylation of these complexes. Kinetic factors involving the relative nucleophilicity of the reactive sites are expected to play a more important role.

As was done earlier for the methylation of **1**, the relative reactivities towards electrophilic attack of the N1 position of the triazole and the N'4 position of the pyrazine were assessed by comparing the electrostatic potential (ESP), square of the HOMO, and Fukui function at the two sites.

The ESP of **5** is very similar to that of **1**, except for the additional reactivity of the N'4 of the pyrazine. However, again it is not possible to predict relative reactivities of the N1 and N'4 sites using Figure 3.7, as both sites appear equally reactive. On the other hand, once again both the square of the HOMO and the Fukui function favour the N4 position of the triazole, in preference to either the N'4 position of the pyrazine or the N1 position of the triazole. Of the latter two, the Fukui function shows the N'4 position to be favoured, while the square of the HOMO does not show a clear difference in reactivity.

The results again show that predicting the reactivity patterns of ruthenium polypyridyl complexes is not straightforward. In this study, neither thermodynamic nor kinetic arguments using the results of DFT calculations agree with the experimental results.

3.6 Conclusion

Electronic structure calculations produce a large amount of information in the form of numbers and tables. The conversion of this information into partial density of states (PDOS) spectra allows these results to be easily visualised. Comparisons between PDOS spectra of related compounds can highlight unusual or distinguishing features. Such spectra allow a more comprehensive view of the nature of the frontier orbitals than is available from simply considering a picture of the HOMO and LUMO – for example, the relative ordering of metal-centred and ligand-centred (π and π*) orbitals is available at a glance.

The position of the peak of the metal PDOS in the highest occupied molecular orbitals can be used as an indication of the electron density on the metal centre, and hence to give the relative σ-donor strength of a coordinated ligand. This method has been shown to be more reliable than to simply consider the energy of the HOMO, which may contain large contributions from moieties which are not involved in the first oxidation potential.

Reactivity indices hold the promise to a wealth of information. They may be used to explain regioselectivity of reactions, and more usefully, to predict and control the isomeric distribution of products. However, as results from this chapter show, they must be used with caution, and correlation with known experimental results is essential, before they can be used to predict future results. Accurate prediction of reactivity may require a large basis set, better functionals or systems where electron correlation is not very important (for example, simple organic molecules). Solvent effects may also be important.

To this author's knowledge, this is the first study carried out on ruthenium polypyridyl complexes using local reactivity indices to predict or explain experimental results. Although the results of this study are somewhat disappointing, it is expected that as

more accurate functionals become available and calculations using more complete basis sets become feasible, prediction of reactivity using the methods described here will become more accurate.

3.7 References

1. Jensen, F., *Introduction to Computational Chemistry*, p. xiv, Wiley: Chichester, 1999.

2. Wang, R., Vos, J.G., Schmehl, R.H. and Hage, R., *J. Am. Chem. Soc.*, **1992**, *114*, 1964.

3. Hage, R., Prins, R., Haasnoot, J.G., Reedijk, J. and Vos, J.G., *J. Chem. Soc., Dalton Trans.*, **1987**, 1389.

4. Buchanan, B.E., Vos, J.G., Kaneko, M., van der Putten, W.J.M., Kelly, J.M., Hage, R., de Graaff, R.A.G., Prins, R., Haasnoot, J.G. and Reedijk, J., *J. Chem. Soc., Dalton Trans.*, **1990**, 2425.

5. Fanni, S., Keyes, T.E., O'Connor, C.M., Hughes, H., Wang, R. and Vos, J.G., *Coord. Chem. Rev.*, **2000**, *208*, 77.

6. Stephens, P.J., Devlin, F.J., Chabalowski, C.F. and Frisch, M.J., *J. Phys. Chem.*, **1994**, *98*, 11623.

7. Armstrong, E.A.P., Brown, R.T., Sekwale, M.S., Fletcher, N.C., Gong, X.-Q. and Hu, P., *Inorg. Chem.*, **2004**, *43*, 1714.

8. Kinnunen, T.-J.J., Haukka, M. and Pakkanen, T.A., *J. Organomet. Chem.*, **2002**, *654*, 8.

9. Haukka, M., Hirva, P., Luukkanen, S., Kallinen, M., Ahlgrén, M. and Pakkanen, T.A., *Inorg. Chem.*, **1999**, *38*, 3182.

10. (a) Fukui, K., Yonezawa, T. and Shingu, H., *J. Chem. Phys.*, **1952**, *20*, 722. (b) Fukui, K., *Theory of orientation and stereoselection*, **1972**, Springer, New York.

11. (a) Parr, R.G. and Yang, W., *J. Phys. Chem.*, **1984**, *106*, 4049. (b) Ayers, P.W. and Levy, M., *Theor. Chem. Acc.*, **2000**, *103*, 353.

12. Perdew, J.P., Parr, R.G., Levy, M. and Balduz Jr., J.L., *Phys. Rev. Lett.*, **1982**, *49*, 1691.

13. Geerlings, P., De Proft, F. and Langenaeker, W., *Chem. Rev.*, **2003**, *103*, 1793.

14. (a) Bartolotti, L.J. and Flurchick, K., In *Reviews in Computational Chemistry*, Vol VII, p. 187; Lipkowitz, K.B. and Boyd, D.B., Eds; VCH: New York, **1996**. (b) Flurchick, K. and Bartolotti, L., *J. Mol. Graph.*, **1995**, *13*, 10.

15. Kato, S., *Theor. Chim. Acta*, **2000**, *103*, 219.

16. Yang, W. and Mortier, W.J., *J. Am. Chem. Soc.*, **1986**, *108*, 5708.

17. (a) Roy, R.K., Pal, S. and Hirao, K., *J. Chem. Phys.*, **1999**, *110*, 8236. (b) Roy, R.K., Hirao, K. and Pal, S., *J. Chem. Phys.*, **2000**, *113*, 1372. (c) Roy, R.K., Hirao, K., Krishnamurty, S. and Pal, S., *J. Chem. Phys.*, **2001**, *115*, 2901. (d) Roy, R.K., Tajima, N. and Hirao, K., *J. Phys. Chem.*, **2001**, *105*, 211. (e) Roy, R.K., *J. Phys. Chem. A*, **2003**, *107*, 10428.

18. Hirshfeld, F.L., *Theor. Chim. Acta*, **1977**, *44*, 129.

19. GauStock, O'Boyle, N.M. and Vos, J.G., Dublin City University, **2004**.

20. GaussSum 0.8, O'Boyle, N.M. and Vos, J.G., **2004**, Dublin City University.

21. Browne, W.R., Hesek, D., Gallagher, J.F., O'Connor, C.M., Killeen, J.S., Aoki, F., Ishida, H., Inoue, Y., Villani, C. and Vos, J.G., *J. Chem. Soc., Dalton Trans.*, **2003**, 2597.

22. (a) Singh, U.C. and Kollman, P.A., *J. Comp. Chem.*, **1984**, *5*, 129. (b) Besler, B.H., Merz, K.M. and Kollman, P.A., *J. Comp. Chem.*, **1990**, *11*, 431.

23. Keyes, T.E., O'Connor, C.M., O'Dwyer, U., Coates, C.G., Callaghan, P., McGarvey, J.J. and Vos, J.G., *J. Phys. Chem. A*, **1999**, *103*, 8915.

24. Buchanan, B.E., Wang, R., Vos, J.G., Hage, R., Haasnoot, J.G. and Reedijk, J., *Inorg. Chem.*, **1990**, *29*, 3263.

25. Nieuwenhuis, H.A., Haasnoot, J.G., Hage, R., Reedijk, J., Snoeck, T.L., Stufkens, D.J. and Vos, J.G., *Inorg. Chem.*, **1991**, *30*, 48.

26. Hage, R., Haasnoot, J.G., Nieuwenhuis, H.A., Reedijk, J., Wang, R. and Vos, J.G., *J. Chem. Soc., Dalton Trans.*, **1991**, 3271.

27. Keyes, T.E., O'Connor, C. and Vos, J.G., *Chem. Commun.*, **1998**, 889.

28. Buchanan, B.E., McGovern, E., Harkin, P. and Vos, J.G., *Inorg. Chim. Acta*, **1988**, *154*, 1.

29. Ryan, E.M., Wang, R., Vos, J.G., Hage, R. and Haasnoot, J.G., *Inorg. Chim. Acta*, **1993**, *208*, 49.

30. Fanni, S., Murphy, S., Killeen, J.S. and Vos, J.G., *Inorg. Chem.*, **2000**, *39*, 1320.

31. (a) Joubert, L., Guillemoles, J.-F. and Adamo, C., *Chem. Phys. Lett.*, **2003**, *371*, 378. (b) Ciofini, I., Hazebroucq, S., Joubert, L. and Adamo, C., *Theor. Chem. Acc.*, **2004**, *111*, 188.

32. Brennan, C., personal communication, **2004**.


UH, HONEY..? THE PLACE HAS NEVER LOOKED CLEANER, BUT... THIS IS THE FOURTH TIME THIS WEEK YOU CLEAN UP... HOW'S THAT THESIS COMING?
JORGE CHAM © 2002
www.phdcomics.com

Chapter 4
Comparison of electronic structures of mononuclear and dinuclear ruthenium polypyridyl complexes

This chapter reports DFT studies of several dinuclear ruthenium complexes of type $[(Ru(bpy)_2)_2(LL)]^{(4+n)+}$*, where LL is a bridging ligand with charge n. A review is presented of previous DFT calculations on ruthenium-ruthenium dinuclear complexes. The geometry and electronic structure of the dinuclear complexes are compared with the corresponding mononuclear complexes, and with the available experimental data. The results of electronic structure and Time Dependent DFT calculations are visualised using Partial Density of States spectra and electron density difference maps. The description of LL in terms of its component moieties provides a more detailed picture of the shifts of energy levels on binding of a second metal centre. For dinuclear complexes without internuclear communication, the electronic structure of the mononuclear complex is shown to be a good model for the dinuclear complex.*

4.1 Introduction

All of the dinuclear complexes discussed in this chapter consist of two $Ru(bpy)_2$ moieties connected by a bridge. The bridges are composed of phenyl (ph), pyridine (py), pyrazine (pz), triazole (trz) and fused imidazole (imid) units (see Figure 4.1). The structures and abbreviations for the mononuclear and dinuclear complexes discussed in this chapter are shown in Figure 4.2.

The protonated complexes were also studied in the case of some of the complexes containing a trz moiety. The additional proton(s) are added at the N-1 position of the triazole (see Chapter 3 for the numbering of triazoles).

The remainder of the introduction briefly describes dinuclear complexes, focusing on DFT calculations of ruthenium-ruthenium dinuclear complexes and on stereoisomerism. Section 4.2 describes the method used for the DFT calculations. This is followed by the results section (4.3), which describes the geometry and electronic structure of each of the complexes studied. The discussion of the results (Section 4.4) is followed by conclusions and suggestions for further work (Section 4.5).

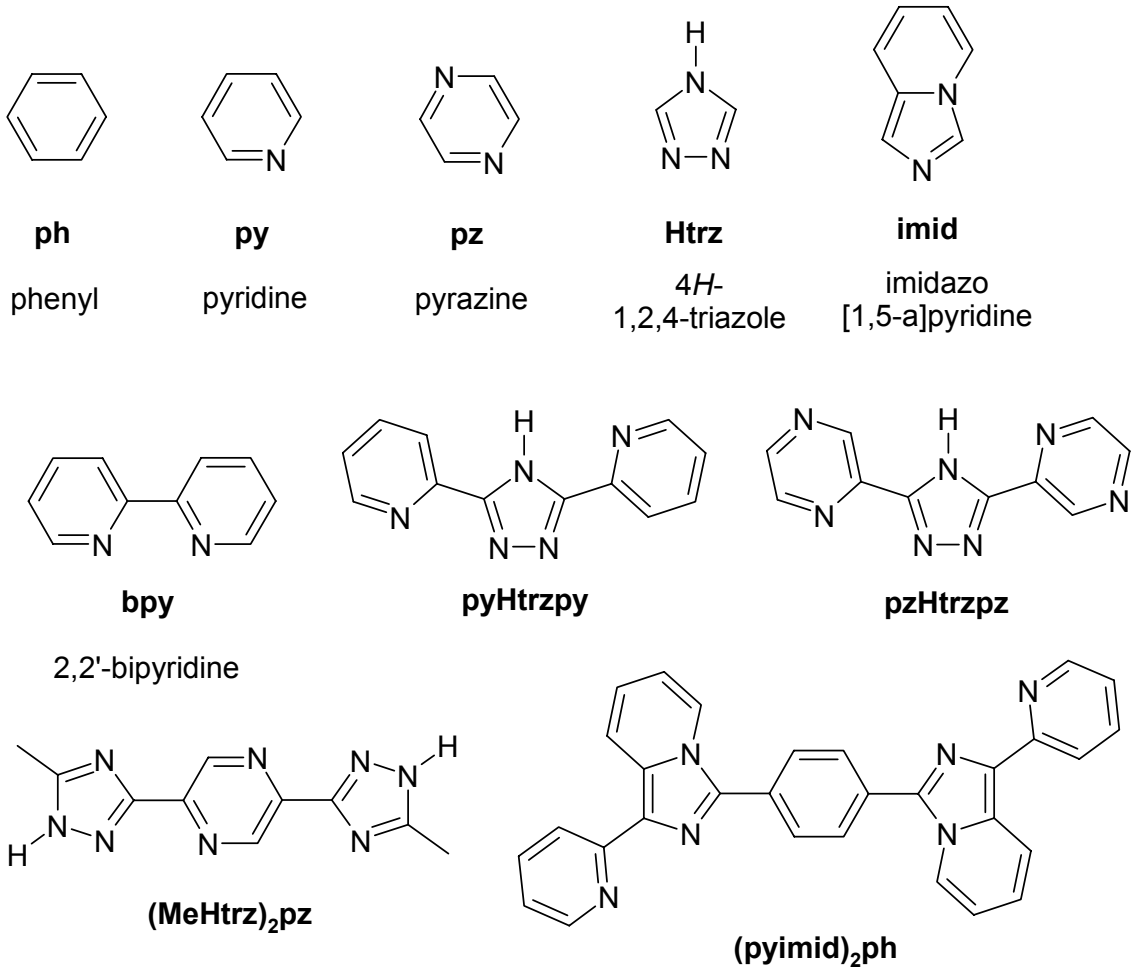

Figure 4.1 – Abbreviations for ligand moieties and bridges of complexes discussed in this chapter.

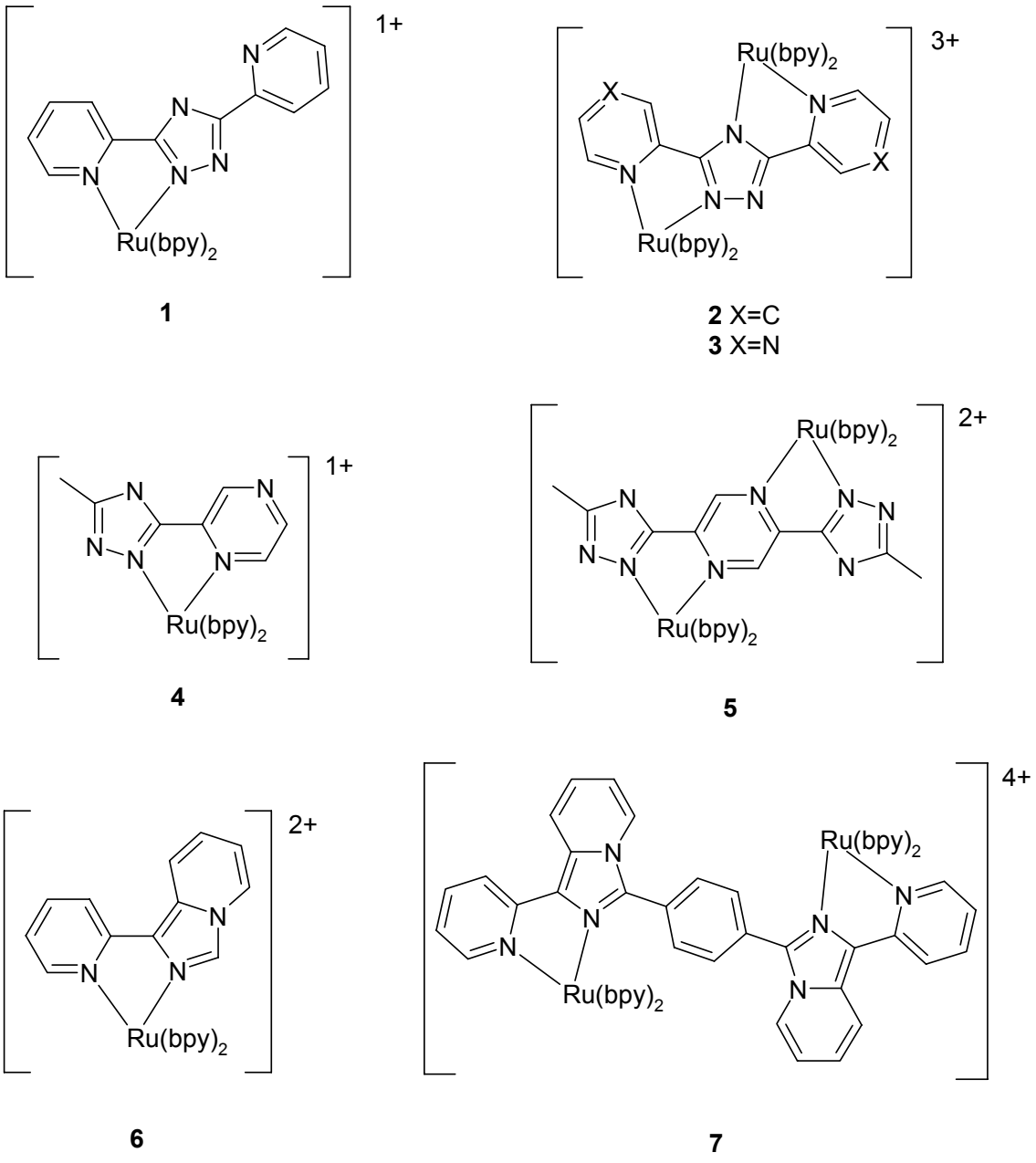

Figure 4.2 – Structures and abbreviations for the mononuclear and dinuclear complexes discussed in this chapter.

4.1.1 Dinuclear complexes

Dinuclear complexes are complexes containing two metal centres. Where there exists an interaction between the two metal centres, there is a potential for supramolecular chemistry[12] – that is, the photophysical properties of the dinuclear complex are not just a simple summation of the properties of its component mononuclear moieties. Such supermolecules are of great interest to theorists, since

they allow studies of the degree of interaction between metal centres which are separated by a known distance. Studies of energy transfer between the metal centres in dinuclear complexes are of great practical interest due to their potential applications in dye-sensitised solar cells,[3,4] and as antenna complexes to harvest energy.[5]

Dinuclear complexes are also of interest from the point of view of studying electron transfer. In this regard, mixed valence $Ru^{II}Ru^{III}$ complexes are of particular interest.[6,7] Such complexes may find application as quantum-dot cellular automata (QCA) in molecular computing.[8] The classic example is the Creutz-Taube ion[9], $[(NH_3)_5Ru\text{-}(\mu\text{-pyrazine})\text{-}Ru(NH_3)_5]^{5+}$, Figure 4.3. Hush[10], Robin and Day[11] and Creutz *et al.*[12] have developed a theoretical basis for the study of such systems. The classification scheme of Robin and Day[11] is very useful for describing the degree of internuclear communication in a mixed-valence dinuclear complex:

Class I: complete valence trapping (negligible electronic coupling)

Class II: valence trapping (weak electronic coupling)

Class III: delocalised valency (strong electronic coupling)

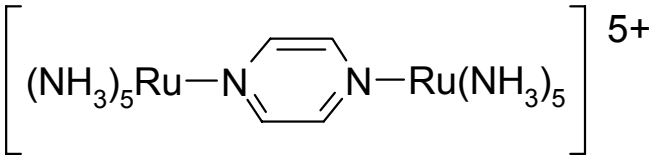

Figure 4.3 – The structure of the Creutz-Taube ion.

DFT computational studies of ruthenium-ruthenium dinuclear complexes have focused on the Creutz-Taube (CT) ion or derivatives thereof. The CT ion is thought to be a Class III complex. Both Bencini *et al.*[13] and Hardesty *et al.*[14] looked at the mixed valence state of the CT ion using DFT, but imposed C_{2v} symmetry. The use of symmetry in these studies has the effect of delocalising the singly-occupied molecular orbital (SOMO) equally across both Ru atoms, thus preventing the development of a localised state. Bencini *et al.*[13] overcame this disadvantage by investigating the potential energy surface associated with the symmetric and antisymmetric stretch of the pyrazine between the Ru atoms. The presence of a single minimum indicated that the CT ion belongs to Class III. This information was used to calculate the frequency of this vibration, which is of importance in vibronic coupling models. The study by Chen *et al.*[15] also focused on this vibration, and the

imposed C_s symmetry did not enforce a delocalised SOMO. They concluded that the CT ion is a borderline Class II/III complex.

A study by Braun-Sand and Wiest[8] optimised the geometry of the CT ion without imposing any symmetry, although the very small basis set 3-21G was used, even for the ruthenium atom. They compared its electronic structure to those of RuRu dinuclear complexes belonging to each of the other Robin and Day classes (I and II), and deduced some simple rules for the identification of the Class of a mixed valence complex. The SOMO of Class III complexes contains significant contributions from both metal atoms, whereas that of Class II complexes is centred on a single metal atom. In both cases, the LUMO is on the bridging ligand. In Class I complexes, instead of the LUMO, the SOMO is located on the bridging ligand. The energy gap between the SOMO and the molecular orbital of the bridging ligand (BLMO) increases as the complex becomes more localised.

A study by Albano *et al.*[16] used a mononuclear complex as a model for a dinuclear complex, by assuming that there was no communication between the metal centres in the dinuclear complex. This approach should be only be used where experimental results indicate the absence of internuclear communication, or where the nature of the bridge precludes internuclear communication. In this study, the two mononuclear units were separated by a bridge containing a saturated spacer, adamantane, which prevented internuclear communication.

4.1.2 Stereoisomers

A six-coordinate centre surrounded by 3 bidentate ligands gives rise to two enantiomers, Δ (Delta) and Λ (Lambda), whose relative configurations are shown in Figure 4.4 for a ruthenium polypyridyl-type complex. Although enantiomers have non-superimposable structures, they have the same physical and chemical properties (in a non-chiral environment) and the same electronic structure.

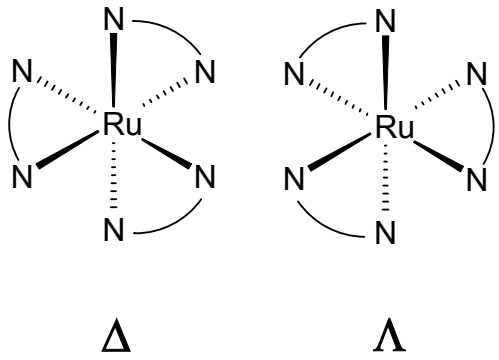

Figure 4.4 – Two enantiomers (Δ and Λ) are possible when there are 3 bidentate ligands around a 6-coordinate centre.

For a dinuclear complex, the existence of two different configurations around each Ru centre gives rise to 4 possible combinations of stereoisomer: two homochiral dinuclear complexes, ΔΔ and ΛΛ, and two heterochiral dinuclear complexes, ΔΛ and ΛΔ. If the bridge connecting the two Ru centres has a centre of symmetry, the two heterochiral dinuclear complexes are identical (and the molecule as a whole has a centre of symmetry), while the two homochiral dinuclear complexes are enantiomers of each other (and each molecule has a C_2 axis). This is the case for dinuclear complexes **5** and **7**. The pytrzpy bridge of dinuclear complex **2** and the pztrzpz bridge of **3**, on the other hand, do not have a centre of symmetry: the two heterochiral dinuclear complexes are enantiomers of each other, and the two homochiral dinuclear complexes are enantiomers of each other. Such dinuclear complexes cannot have symmetry greater than C_1.

Since enantiomers have the same electronic structure, it is only necessary to study one of each enantiomer. Furthermore, since the electronic structure of each diastereomer is expected to be quite similar, a single structure for each dinuclear complex was examined (see Method below). This is supported by work by Browne *et al.*,[17] who separated and characterised the four stereoisomers of **2**. The absorption and emission maxima for each of the four were equal within experimental error, even when a chiral solvent was used.

4.2 Method

All of the structures studied were geometry-optimised at the B3LYP/LanL2DZ level of theory. Time Dependent Density Functional Theory (TDDFT) calculations were

carried out on some of the complexes to calculate the energies and nature of the lowest energy singlet electronic transitions.

Due to the size of the structures, C_i symmetry was imposed on the dinuclear complexes **5** (and **$H_2$5**), and C_2 symmetry was imposed on the dinuclear complex **7**. Dinuclear complexes **2** and **3** have C_1 symmetry. The heterochiral isomers of **2**, **3** and **5** were studied, while the homochiral ΔΔ isomer of **7** was studied. The crystal structure of **2** is the heterochiral isomer. The crystal structure of **7** is also the heterochiral isomer. However, since the symmetry of the bridge was close to C_2 in the crystal structure, the homochiral isomer was studied instead. No crystal structure is available for **3** or **5**.

Partial density of states (PDOS) spectra were convoluted from the molecular orbital data using Gaussian curves of full width at half maximum ($w_{½}$) of 0.3eV. Calculated UV-Vis spectra were convoluted from TDDFT results using Gaussian curves of $w_{½}$ of 3000cm^{-1}.

4.3 Results

4.3.1 Geometry

The optimised geometries of **1**, **2**, **H1** and **H2** are compared with the crystal structures of **1** and **2** in Table 4.1. Values for **1** and **2** are in good agreement with their respective crystal structures, apart from a slight overestimation of the Ru-N bond length. Note that both the calculated and crystal structures of the dinuclear complex agree that the Ru-N_{trz} bond length is significantly longer in the case of the N4-bound ruthenium centre. However, the calculated geometry predicts quite different bite angles for N2 and N4 bound pytrz (76.8° versus 78.7°), but the crystal structure has similar bite angles for each (77.6° and 77.2°). For each of the structures listed in Table 4.1, the pytrzpy bridge is planar.

H1 is predicted to have a slightly longer Ru-N_{trz} bond length than **1**, and a reduction in the bite angles of both the pytrz ligand and the bipyridines. This trend is also observed for **H2**, except that the bipyridine bite angle is the same as for **2**.

	Crystal **1**[a]	**1**	**H1**	Crystal **2**[b]		**2**		**H2**	
				N2Ru	*N4Ru*	*N2Ru*	*N4Ru*	*N2Ru*	*N4Ru*
Ru-N_{bpy}[c]	2.05	2.08	2.10	2.06	2.05	2.10	2.09	2.11	2.10
Ru-N_{py}	2.11	2.14	2.13	2.06	2.10	2.12	2.13	2.13	2.12
Ru-N_{trz}	2.03	2.06	2.10	2.03	2.11	2.07	2.20	2.08	2.25
∠bpy[c]	79	78.6	77.0	79.1	79.1	78.5	78.5	78.3	78.5
∠pytrz	78	78.1	77.1	77.6	77.2	76.8	78.7	75.8	77.7

Table 4.1 – Selected bond lengths and bite angles for 1**,** 2**,** H1 **and** H2**, compared with the crystal structure of** 2**. Both the calculated and crystal structures of the dinuclear complex are described in terms of two 'mononuclear units': the unit containing a Ru bound to N2 of the triazole (*N2Ru*), and that containing a Ru bound to N4 of the triazole (*N4Ru*). All angles are in degrees and all distances are in Å. [a]Crystal structure of** 1**, $[Ru(bpy)_2(pytrzpy)]PF_6$.[18] [b]Crystal structure of** 2**, $[(Ru(bpy)_2)_2(pytrzpy)](CF_3SO_3)_3.4H_2O$.[19] [c]Values averaged.**

The optimised geometries of **3**, **4**, **5**, **H4** and **$H_2$5** are compared with the crystal structure of $[Ru(bpy)_2(pztrzph)]^+$ in Table 4.2. The chemical structure of $[Ru(bpy)_2(pztrzph)]^+$ is shown in Figure 4.5. The geometry of **3** is in good agreement with the crystal structure, although the Ru-N_{bpy} and Ru-N_{trz} bond lengths are slightly overestimated. The calculated structure has a significantly longer Ru-N_{trz} bond length in the case of the N4-bound ruthenium centre; this was also observed for **2**. The calculations underestimate the pztrz bite angle.

Except for slightly overestimated Ru-N bond lengths, the geometries of **4** and **5** are in good agreement with the crystal structure. The geometries of the protonated complexes, **H4** and **$H_2$5**, have slightly longer Ru-N_{trz} bonds and smaller pztrz bite angle. The trzpztrz bridge is planar in both **5** and **$H_2$5**.

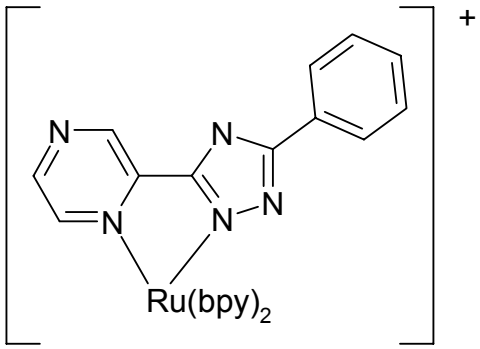

$[Ru(bpy)_2(pztrzph)]^+$

Figure 4.5 – The structure of $[Ru(bpy)_2(pztrzph)]^+$

	Crystal[a]	3		4	5	H4	$H_2$5
		N2Ru	*N4Ru*				
Ru-N_{bpy}[b]	2.05	2.10	2.10	2.09	2.09	2.10	2.10
Ru-N_{pz}	2.11	2.11	2.11	2.13	2.12	2.13	2.13
Ru-N_{trz}	2.03	2.07	2.20	2.06	2.07	2.10	2.10
∠bpy[b]	78.9	78.4	78.5	78.5	78.5	77.0	78.4
∠pztrz	78.2	77.1	78.6	78.1	78.2	77.1	77.0
trz-C5-R	1.49			1.50	1.50	1.49	1.49

Table 4.2 – Selected bond lengths and bite angles for 3**,** 4**,** 5**,** H4 **and** $H_2$5**, compared with the crystal structure of [Ru(bpy)$_2$(pztrzph)]$^+$. The calculated structure of** 3 **is described in terms of two 'mononuclear units': the unit containing a Ru bound to N2 of the triazole (*N2Ru*), and that containing a Ru bound to N4 of the triazole (*N4Ru*). All angles are in degrees and all distances are in Å. [a]Crystal structure of [Ru(bpy)$_2$(pztrzph)]PF_6.CH_3OH.[20] [b]Values averaged.**

The optimised geometries of **6** and **7** are compared with their crystal structures in Table 4.3. The crystal structure of **7** is of the heterochiral isomer, connected by a bridge with C_2 pseudosymmetry. It is impossible for this structure to have a symmetry greater than C_1, since chiral centres are related by a centre of inversion. Calculations on this structure would be computationally too expensive. As a result, the structure studied was the homochiral isomer, with overall C_2 symmetry. The Ru-N bond lengths are slightly overestimated in each case, but otherwise the agreement is very good.

7 is the only dinuclear complex studied in this chapter with a bridging ligand that is not planar. It is worth noting that the dihedral angle between the pyridine and imidazole moieties of pyimid varies between the two halves of the crystal structure of **7** (13.3° versus 1.8°). The calculated value is close to 2° for both **6** and **7**, in agreement with the *Ru2* moiety of the crystal. The dihedral angle between the imidazole and phenyl moieties of the bridging ligand also varies between the halves (65.0° versus 57.2°). The calculated value of 66.4° agrees well with that of *Ru1* of the crystal.

The geometry of **7** is very similar to that of **6** except for an increase in the bond length of Ru-N_{imid} in **7**. This is due to steric crowding in **7** in the region between the metal centres, where the bridging ligand and two bipyridines are close together. The

extra bond length is required to keep the bipyridines away from the bridge. This was especially clear during the progress of the geometry optimisation.

	Crystal **6**[a]	**6**	Crystal **7**[b] (*Ru1*)	Crystal **7**[b] (*Ru2*)	**7**
Ru-N_{bpy}[c]	2.06	2.10	2.06	2.05	2.10
Ru-N_{py}	2.09	2.12	2.08	2.08	2.11
Ru-N_{imid}	2.06	2.09	2.07	2.08	2.15
∠bpy[c]	78.6	78.5	79.1	78.9	78.4
∠pyimid	78.4	78.1	78.6	78.8	78.9
∠py∠imid	(unknown)	2.2	13.3	1.8	2.3
∠imid∠ph			65.0	57.2	66.4

Table 4.3 – Selected bond lengths, bite angles (∠) and dihedral angles (∠ ∠) for 6 **and** 7**, compared with the crystal structures of** 6 **and** 7**. The crystal structure of** 7 **is described in terms of two 'mononuclear units': *Ru1* and *Ru2*. All angles are in degrees and all distances are in Å. [a]Crystal structure of $[Ru(bpy)_2(pyimid)](PF_6)_2$.[21] [b]Crystal structure of $[(Ru(bpy)_2(pyimid)_2ph](PF_6)_4$.[21] [c]Values averaged.**

4.3.2 $[Ru(bpy)_2(pytrzpy)]^+$, 1 and $[(Ru(bpy)_2)_2(pytrzpy)]^{3+}$, 2

The partial density of states (PDOS) spectra for the mononuclear complex $[Ru(bpy)_2(pytrzpy)]^+$, **1**, are shown in Figure 4.16. *freePy* refers to the unbound pyridine ring, whereas *RuPy* is the bound pyridine of the pytrzpy ligand. Molecular orbital information for **1** is listed in Table 4.4.

1 is similar to the series of $[Ru(bpy)_2(pytrz)]^+$ complexes studied in Chapter 3. In particular, it is almost identical to $[Ru(bpy)_2(pytrzph)]^+$, referred to as '**4**' in Chapter 3, and which will be referred to as **4Chap3** here. The only difference between the two molecules is the replacement of the phenyl ring of **4Chap3** with a pyridine ring. Both molecules have almost identical PDOS spectra for the metal centre, the bipyridines, *RuPy* and *trz*. However, the PDOS for *freePy* is shifted to higher energy compared to that for *ph* in **4Chap3**. As discussed in Chapter 3, the peak of the Ru PDOS in the frontier region of the occupied orbitals indicates the ease of oxidation of the metal centre. The peak for $[Ru(bpy)_2(pytrzMe)]^+$ ('**2'** in Chapter 3) occurs at –8.30eV, while that for **1** occurs at –8.36eV. This indicates that *freePy* is a weak electron-withdrawing group. A much larger shift was observed for the strong electron-withdrawing group bromine, $[Ru(bpy)_2(pytrzBr)]^+$ ('**3**' in Chapter 3), which has a Ru peak at –8.48eV.

It is interesting to compare the PDOS spectra for *RuPy* and *freePy* in **1**. Both of these moieties refer to pyridine attached to triazole – however, the pyridine of *RuPy* is also bound to the metal centre. *RuPy* donates electron density to the Ru – as a result, its PDOS is shifted to lower energy compared to *freePy*.

The PDOS spectra of the RuRu dinuclear complex, **2**, are shown in Figure 4.18. Molecular orbital data for the dinuclear complex is listed in Table 4.6. The two rutheniums are distinct, due to lack of central symmetry of the bridging ligand. The ruthenium bound to the N2 position of the triazole is referred to as *N2-Ru*, while the other ruthenium, bound to N4, is *N4-Ru*. The bipyridines attached to *N2-Ru* are referred to as *N2Ru-bpy*, and the pyridine moiety of the triazole ligand attached to *N2-Ru* is *py(N2Ru)*.

The PDOS spectra of **2** are shifted to lower energy by about 4eV compared to those of **1**. This is consistent with the increase in the charge on the molecule, from +1 to +3, which makes it more difficult to remove an electron. As discussed in Chapter 3, the N2 position of the triazole is a stronger σ-donor than the N4 position. As a result, the Ru PDOS peak in the highest occupied molecular orbitals occurs at slightly higher energy for *N2-Ru* than for *N4-Ru*. The peak for the bipyridines bound to the *N2-Ru* also occurs at slightly higher energy than for those bound to *N4-Ru*.

The highest occupied molecular orbitals of **2** are almost completely Ru-based. This contrasts with **1**, which has a large contribution from *freePy* and *trz* in the same region. In **2**, both pyridines are bound to a metal centre, and so have peaks in their PDOS at around the same energy. These peaks are shifted to lower energy with respect to **1**. This is as a result of the lower electron density on the bridge, due to donation to the extra ruthenium. The same effect causes the PDOS peak of the triazole to shift to lower energy – instead of donating electrons to just one metal centre, now it donates to two. The lowest unoccupied molecular orbitals of **1** are based completely on the bipyridines. This is also largely true for **2**, but the pyridine moieties of the bridging ligand also make a small contribution.

The PDOS peaks for *RuPy*, *trz* and *freePy* in **1** seem to occur independently of each other. However, the PDOS peaks for *py(N2Ru)*, *trz* and *py(N4Ru)* in **2** all occur in the same region. This indicates an electronic interaction between these moieties – that is, that molecular orbitals are delocalised across the entire bridge.

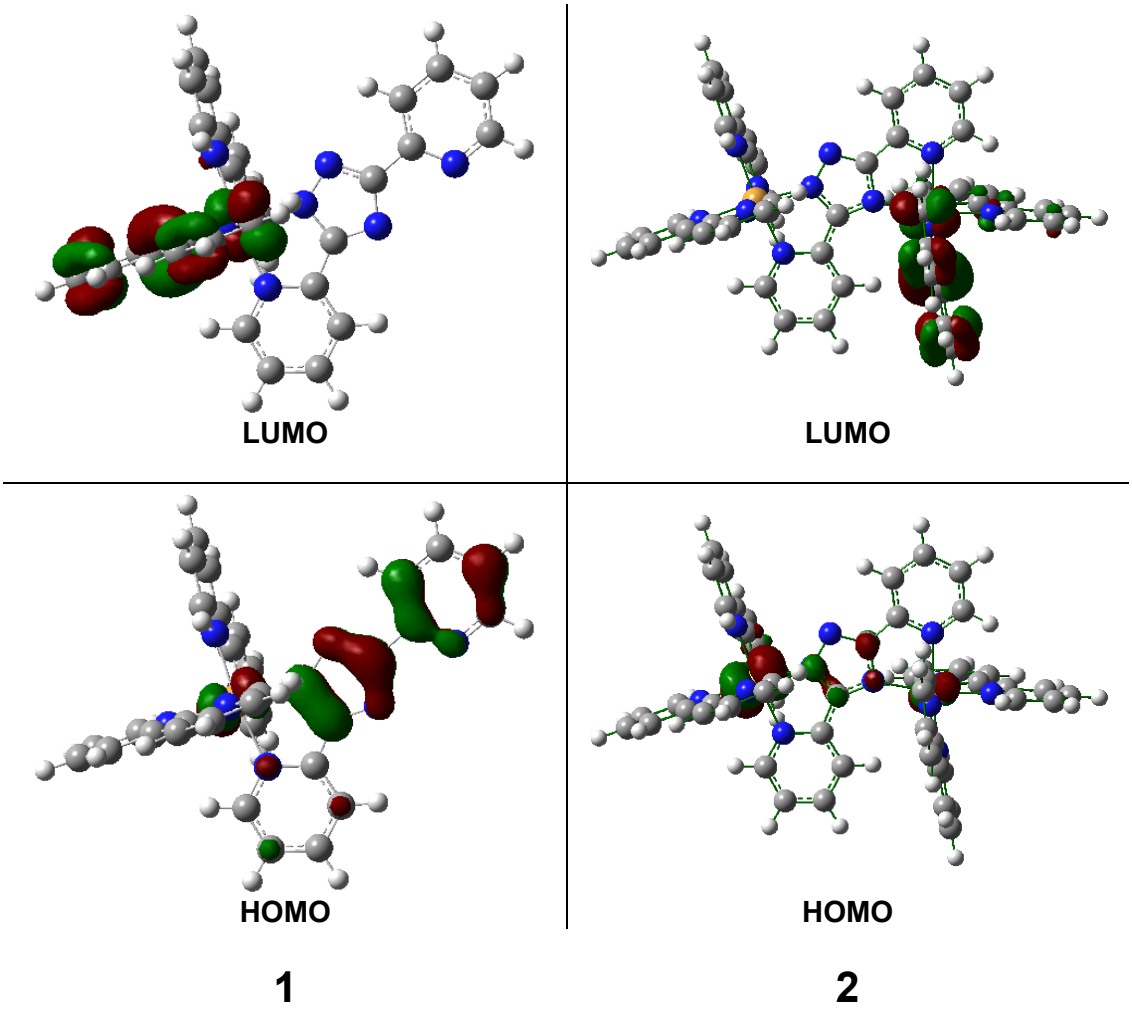

Figure 4.6 – Isosurfaces of the HOMO and LUMO of 1 **and** 2 **drawn at 0.04e/bohr^3.**

4.3.3 $[(Ru(bpy)_2)_2(pyHtrzpy)]^{4+}$, H2 and $[Ru(bpy)_2(pyHtrzpy)]^{2+}$, H1

The PDOS spectra for the protonated mononuclear complex, **H1**, are shown in Figure 4.17, and molecular orbital data are listed in Table 4.5. The PDOS spectra for the protonated dinuclear complex, **H2**, are shown in Figure 4.19 and molecular orbital data are listed in Table 4.7.

The effect of protonation is to shift the PDOS to lower energy by about 2.7eV in the case of **2** and 3.4eV in the case of **1**. Protonation has less of an effect on the dinuclear complex since the formal negative charge on the triazole is shared between two ruthenium centres.

In the mononuclear complex **H1**, the PDOS for *freePy* is shifted to slightly lower energy. This means that there is a change in the nature of the highest occupied molecular orbitals, from mainly *freePy* to mainly ruthenium. Neutralisation of the negative charge on the triazole has caused the *trz* peak to become more 'pyridine-like' and shift to lower energy. *Trz* has peaks in the same regions where *RuPy* has peaks, suggesting the delocalisation of orbitals across both moieties. The lowest unoccupied molecular orbitals are still largely bipyridine-based, although the LUMO+2 is based on the *RuPy/trz* portion of the pytrzpy ligand.

For the dinuclear complex **H2**, neutralisation of the triazole charge means that there is little difference between the σ-donor abilities of the N2 and N4 positions of the triazole. As a result, the PDOS spectra for *N2-Ru* and *N4-Ru*, *N2Ru-bpy* and *N4Ru-bpy*, and *py(N2Ru)* and *py(N4Ru)* are almost identical. The peaks of the triazole moiety of the bridging ligand occur in line with the pyridine peaks, suggesting delocalisation of molecular orbitals across the entire bridge. The highest occupied molecular orbitals are completely metal-based. The lowest unoccupied molecular orbitals of **2** had a small contribution from the components of the bridging ligand, while for **H2** the LUMO and LUMO+1 are entirely based on the bridge.

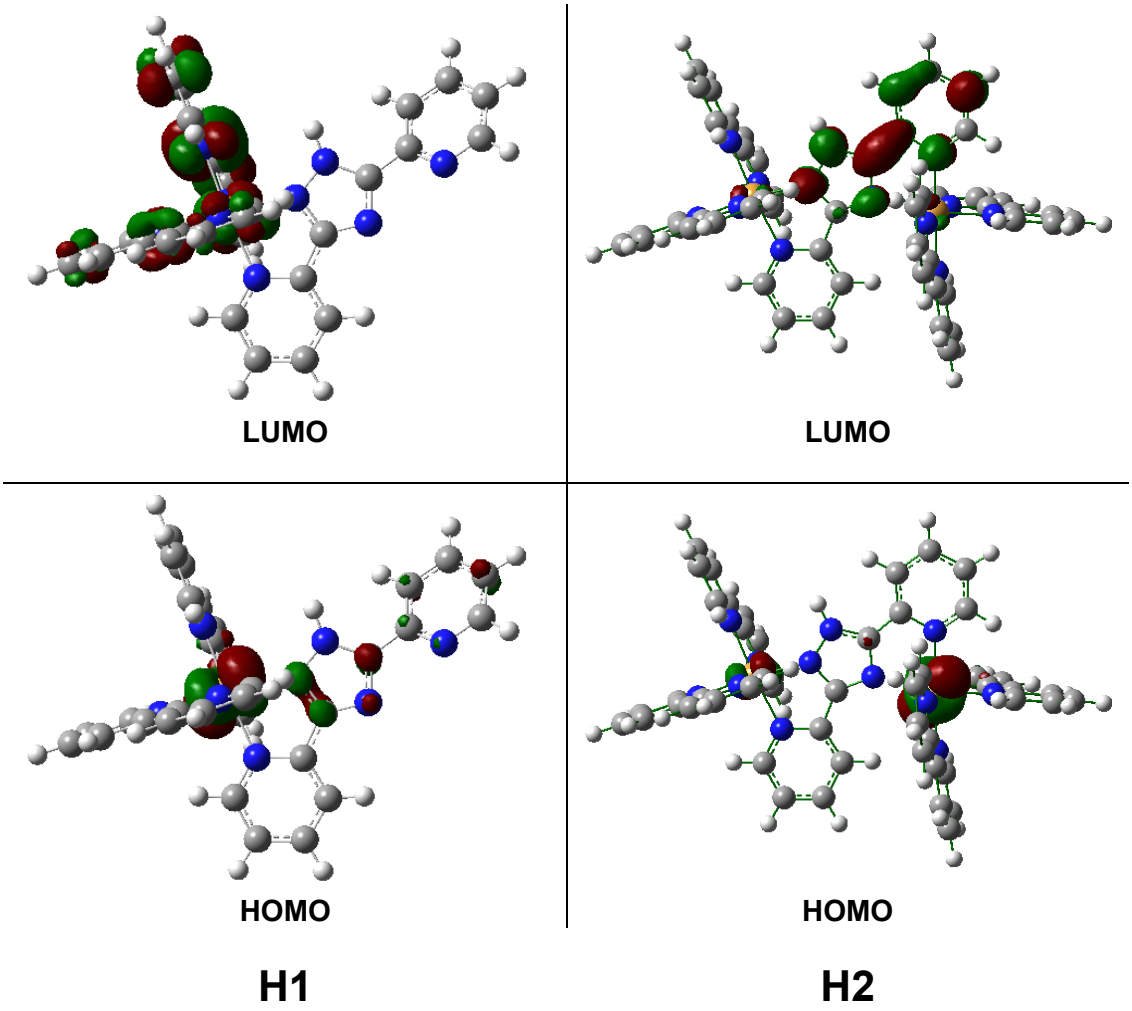

Figure 4.7 – Isosurfaces of the HOMO and LUMO of H1 **and** H2 **drawn at 0.04e/bohr^3.**

4.3.4 $[(Ru(bpy)_2)_2(pztrzpz)]^{3+}$, 3

The PDOS spectra of **3** are shown in Figure 4.20, and molecular orbital data are listed in Table 4.8. The DOS is described in terms of the same moieties as used for **2**, earlier.

$[Ru(bpy)_2(pztrz)]^+$ is a close analogue of the mononuclear complex of **3**. Its electronic structure is discussed in Chapter 3, where it is referred to as '**7**' – here it will be referred to as **7Chap3**. The main difference between the PDOS of **3** and **7Chap3** is the position of the triazole and pyrazine PDOS – both are shifted to lower energy in **3**, due to donation to the extra ruthenium atom. The triazole PDOS is shifted more than that of the pyrazine, due to the fact that it is coordinated to both metal centres.

Pyrazine is a poorer σ-donor than pyridine. This is evident from a comparison of the PDOS of **2** and **3**. The Ru PDOS occurs at a higher energy in **2**, due to the increase in electron density on the ruthenium. On the other hand, pyrazine is a better π-acceptor than pyridine. The LUMO to LUMO+3 were almost completely bipyridine-based in **2**, but for **3** the LUMO is based on the pyrazine bound to *N2-Ru*. Overall, the lowest unoccupied molecular orbitals of **3** appear to be based equally on the bipyridines and the pyrazines (it should be noted that each bipyridine PDOS corresponds to two bipyridines). The composition of the highest occupied molecular orbitals is identical for **2** and **3**. The HOMO and LUMO for **2** and **3** are compared in Figure 4.8.

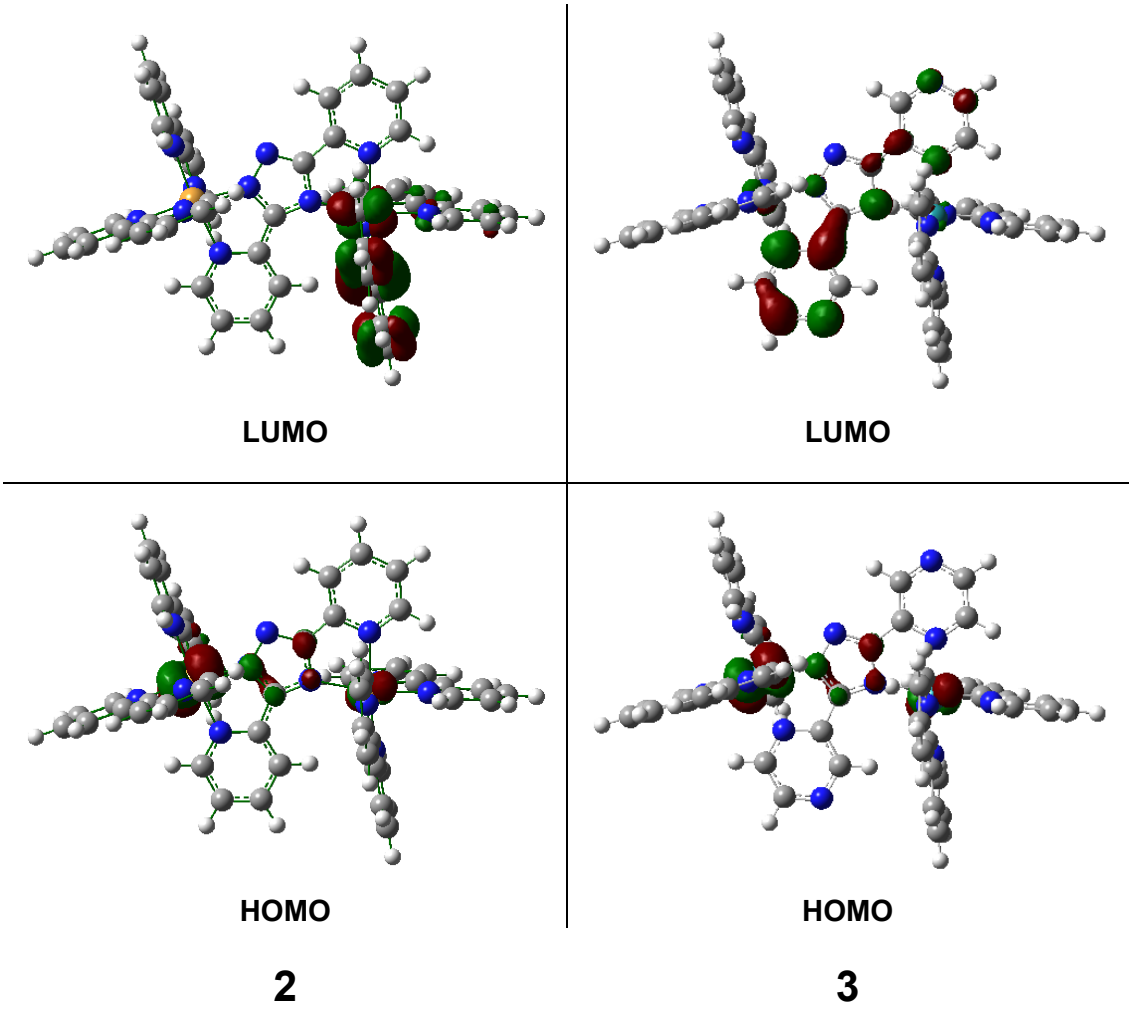

Figure 4.8 – Isosurfaces of the HOMO and LUMO of 2 **and** 3 **drawn at 0.04e/bohr^3.**

4.3.5 $[Ru(bpy)_2(5\text{-}Metrzpz)]^+$, 4 and $[(Ru(bpy)_2(5\text{-}Metrz))_2pz]^{2+}$, 5

The PDOS spectra for the mononuclear complex, $[Ru(bpy)_2(5\text{-}Metrzpz)]^+$, **4**, are shown in Figure 4.21. The 5-Metrzpz ligand is described in terms of two moieties, *Metrz* and *pz*. Molecular orbital information for **4** is listed in Table 4.9.

4 is a derivative of the $[Ru(bpy)_2(pztrz)]^+$ complex studied in Chapter 3. This complex, referred to as '**7**' in Chapter 3, will be referred to as **7Chap3** here. Both **4** and **7Chap3** have almost identical PDOS spectra throughout the frontier region. There is a slight shift to higher energy of the triazole PDOS for **4**, due to the weak electron-donating ability of the methyl group. Since the highest occupied molecular orbitals are partly *Metrz*, this has resulted in the HOMO shifting to higher energy by about 0.2eV for **4**, compared to **7Chap3**. However, the Ru PDOS peak of **4** in the frontier occupied region only shifts slightly (to lower energy), indicating that the electron density on the metal centre has not changed significantly.

The overall characteristics of the PDOS spectra of **4** are the same as for **7Chap3**. The highest occupied molecular orbitals are largely metal-based, but also have a substantial contribution from *Metrz*. The LUMO and LUMO+1 are bipyridine-based, while the LUMO+2 has a large contribution from *pz*.

The PDOS spectra of the RuRu dinuclear complex, **5**, are shown in Figure 4.23. Molecular orbital data are listed in Table 4.11. Since the molecule has a centre of symmetry, the two 'mononuclear units' of **5** are identical, both structurally and electronically. For the purposes of describing the electronic structure, the molecule has been divided into five moieties (Figure 4.9): *Ru* (the two metal centres), *pz* (the central pyrazine), *Metrz* (the two 5-Me-triazoles), *flatbpy* (the two bipyridines with a pyridine moiety trans to *pz*), and *orthobpy* (the two bipyridines with a pyridine moiety trans to *Metrz*).

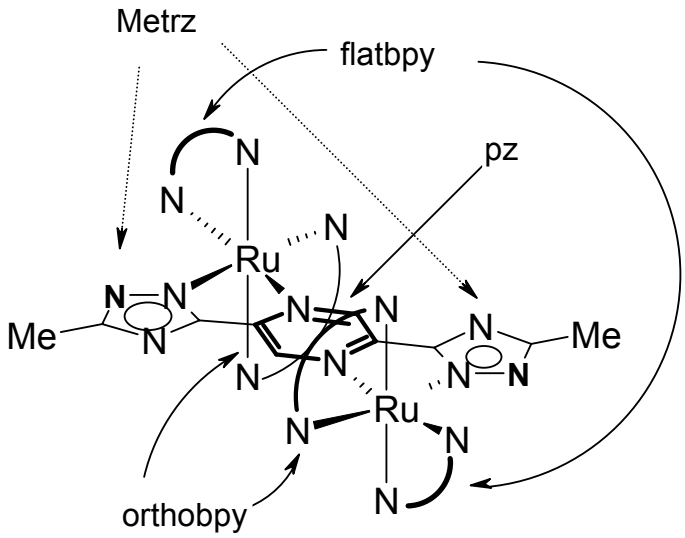

5

Figure 4.9 – The naming system used for the moieties of 5**.**

The PDOS spectra of **5** are shifted to lower energy by about 1.3eV compared to **4**. This is consistent with the increase in positive charge on the dinuclear complex (2+) compared to the mononuclear complex (1+). Apart from this overall shift and a doubling of the height of the peaks, the PDOS spectra for *Ru*, the bipyridines, and *Metrz* are very similar for **4** and **5**. The highest occupied molecular orbitals of **5** are still based mainly on the metal centres, but also have a contribution from *Metrz*.

However, the PDOS for *pz* has shifted to lower energy in **5**, both in the occupied and unoccupied regions. *pz* contributes considerably to the LUMO+2 of **4**, but the LUMO and LUMO+1 are bipyridine-based and at lower energy (0.4eV). In **5**, the LUMO to LUMO+4 are clustered closely together, and both the LUMO and LUMO+2 have a strong contribution from *pz*. The same shift occurs in the frontier region of the occupied orbitals – the *pz* contribution is shifted from HOMO-5 in **4** to HOMO-22 in **5**. This shift is not unexpected – the pyrazine donates electrons to two metal centres in the dinuclear complex, but to only one metal centre in the mononuclear complex. The same effect was noted earlier for the *trz* moiety of **2**. In that case also, the bridging group moves to lower energy on formation of the dinuclear complex.

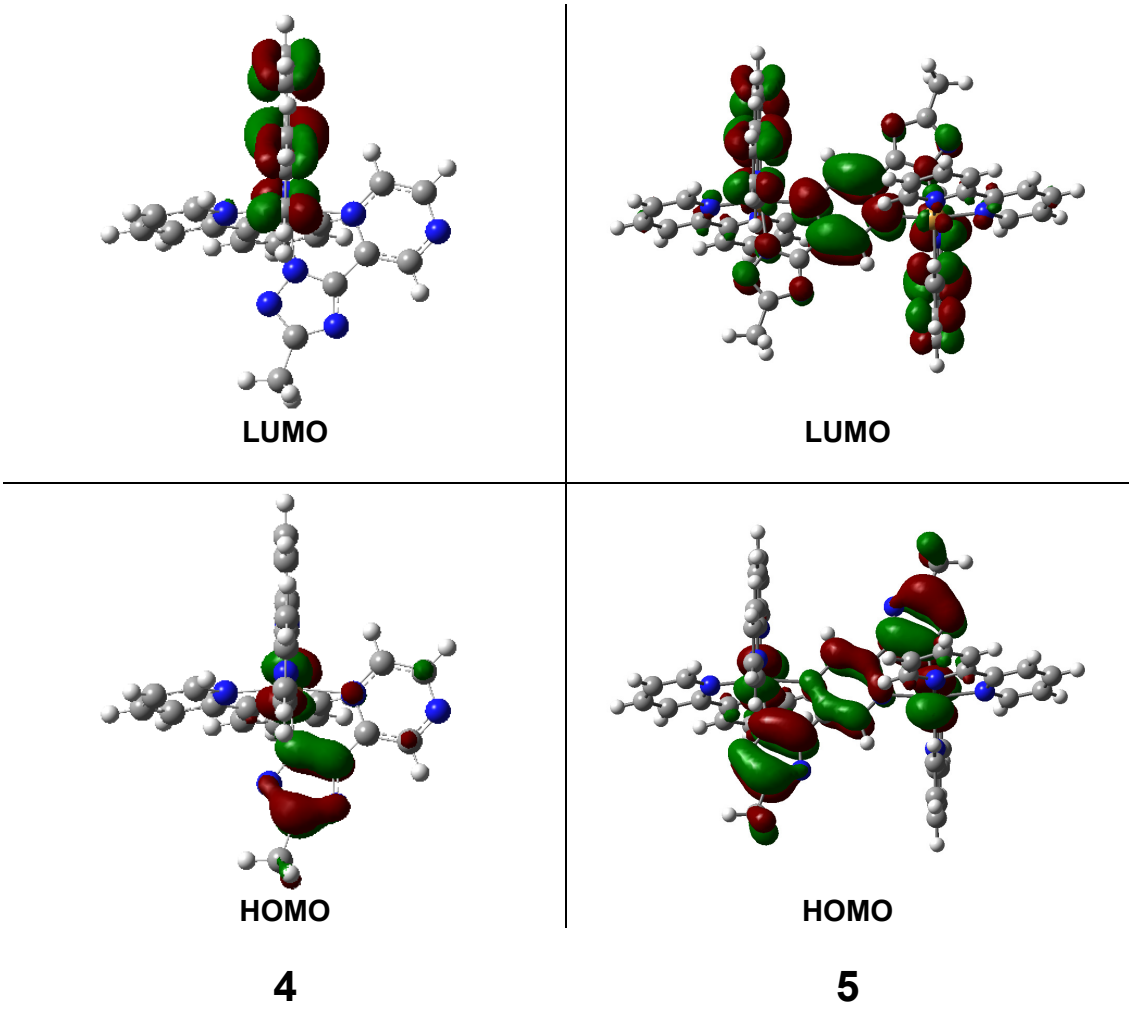

Figure 4.10 – Isosurfaces of the HOMO and LUMO of 4 and 5 drawn at 0.04e/bohr^3.

Using Time Dependent Density Functional Theory (TDDFT), the 35 lowest energy singlet electronic transitions of **5** were calculated (Table 4.15). The lowest energy transition is mainly HOMO→LUMO (83%). Electron density moves from the Ru centres and *Metrz* to *orthobpy* and *pz*. This is illustrated by the electronic density difference map (EDDM) in Figure 4.11 for the this transition.

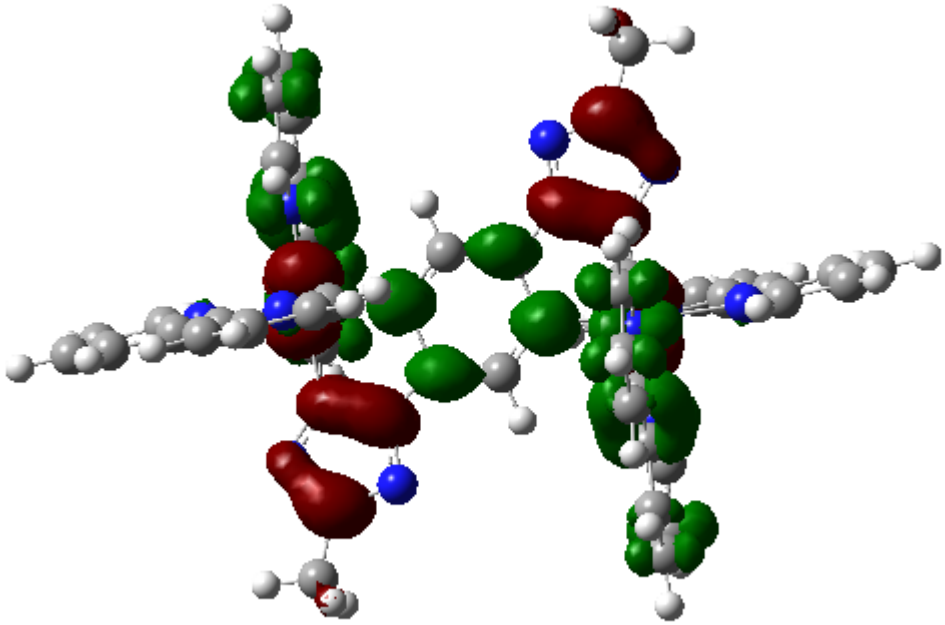

Figure 4.11 – Electron density difference map (EDDM) for the lowest energy singlet electronic transition of 5**. Red indicates a decrease in charge density, and green indicates an increase.**

4.3.6 $[Ru(bpy)_2(1H\text{-}5\text{-}Metrzpz)]^{2+}$, H4 and $[(Ru(bpy)_2(1H\text{-}5\text{-}Metrz))_2pz]^{4+}$, $H_2$5

The PDOS spectra for the protonated mononuclear complex, **H4**, are shown in Figure 4.22, and molecular orbital data are listed in Table 4.10. The PDOS spectra for the protonated dinuclear complex, **$H_2$5**, are shown in Figure 4.24, and molecular orbital data are listed in Table 4.12.

Protonation shifts the PDOS of **4** to lower energy by about 3.4eV – a shift of the same magnitude was observed earlier for the protonation of **1**. The PDOS of **5** is shifted to lower energy by about 5.2eV upon protonation – the larger value compared to **4** is due to the addition of two protons to **5**, rather than just one.

Protonation causes a decrease in the σ-donor ability of the triazole, and the PDOS of *Metrz* shifts to lower energy. For both **H4** and **$H_2$5**, this means that the highest

occupied molecular orbitals no longer have a strong contribution from *Metrz* – these orbitals are now almost completely metal-based.

The *pz* moiety is also affected by the protonation of *Metrz*. In both **H4** and **$H_2$5**, the *pz* PDOS has been shifted to lower energy. For the mononuclear complex, this means that the lowest unoccupied orbitals are based equally on *pz* and bipyridine. For the dinuclear complex, the lowest unoccupied orbitals are almost completely *pz*-based.

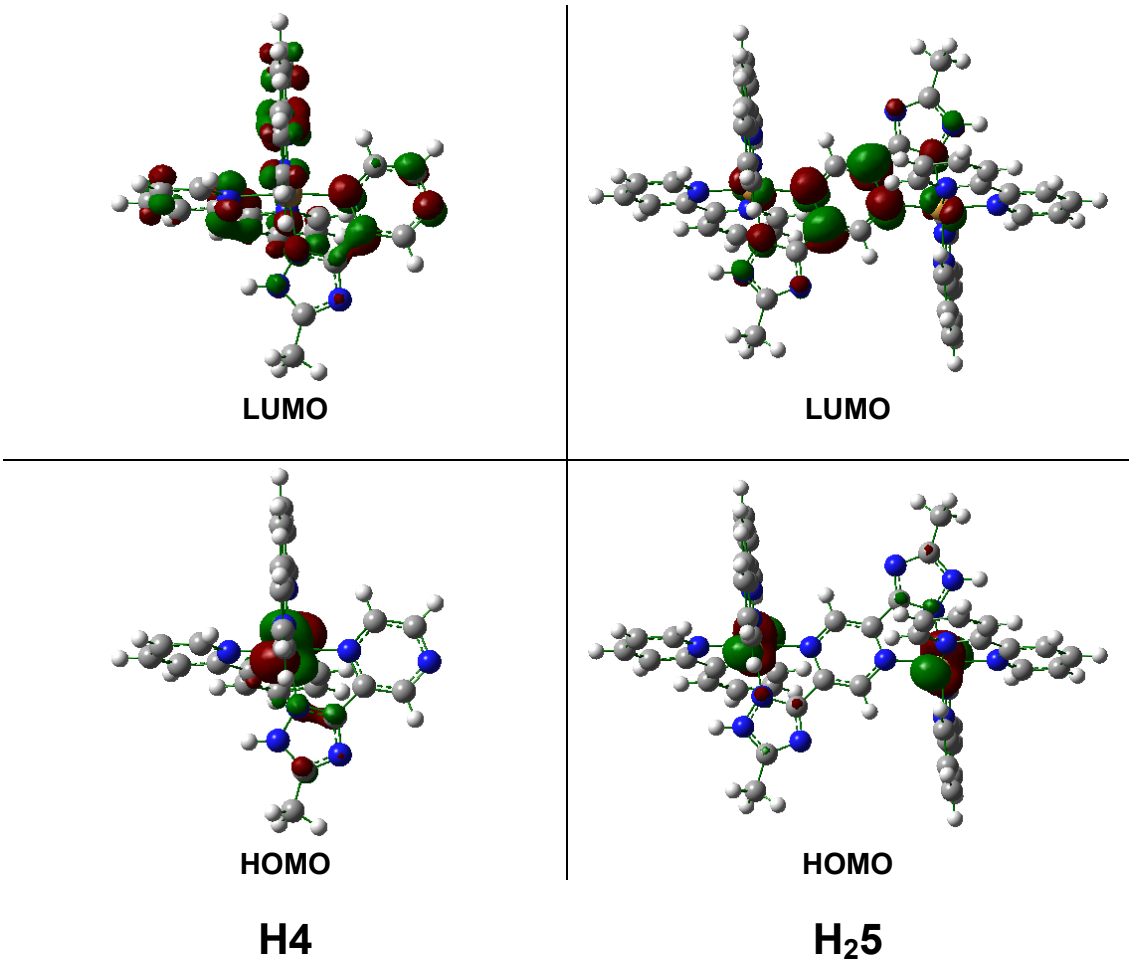

Figure 4.12 – Isosurfaces of the HOMO and LUMO of H4 **and** $H_2$5 **drawn at 0.04e/bohr^3.**

Using Time Dependent Density Functional Theory (TDDFT), the 35 lowest energy singlet electronic transitions of **$H_2$5** were calculated (Table 4.16). The lowest energy transition is mainly HOMO→LUMO (93%). Electron density moves from the Ru centres to *MeHtrz* and *pz*. This is illustrated by the electronic density difference map (EDDM) in Figure 4.13 for this transition.

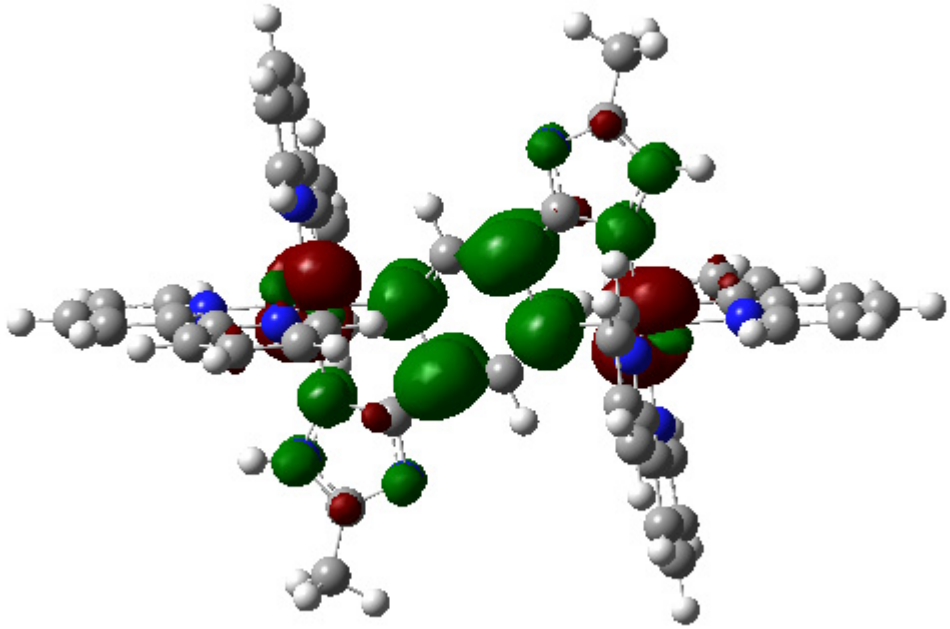

Figure 4.13 – Electron density difference map (EDDM) for the lowest energy singlet electronic transition of $H_2$5. Red indicates a decrease in charge density, and green indicates an increase.

4.3.7 $[Ru(bpy)_2(pyimid)]^{2+}$, 6 and $[(Ru(bpy)_2(pyimid))_2ph]^{2+}$, 7

The PDOS spectra of **6** are shown in Figure 4.25, and molecular orbital data are listed in Table 4.13. For the purposes of describing the electronic structure of **6**, the pyimid ligand is broken into two moieties: the pyridine moiety, *py*, and the fused imidazole/pyridine ring, *imid*.

The highest occupied molecular orbitals are based on the metal centres and also on the imidazole. The lowest unoccupied molecular orbitals are based on bipyridine. Although both moieties of the pyimid ligand contribute to the LUMO+2, there is a gap of 0.4eV between the LUMO+1 and LUMO+2. The two moieties of pyimid are electronically independent. This is clear from the PDOS spectra around –13.6eV: here, *py* makes a large contribution, whereas there is a valley in the PDOS spectrum of *imid*.

The PDOS spectra of the dinuclear complex, **7**, are shown in Figure 4.27, and molecular orbital data are listed in Table 4.14. Since both 'mononuclear units' of **7** are related through a C_2 symmetry axis, they are identical structurally and electronically. The PDOS spectra are described in terms of *Ru*, the two ruthenium centres, *pyimid*, the pyridine and fused imidazole/pyridine moieties of the bridging ligand, *bpy1*, the bipyridines with a moiety trans to the fused imidazole moiety of pyimid, *bpy2*, the bipyridines with a moiety trans to the pyridine moiety of pyimid, and *ph*, the phenyl moiety of the bridging ligand.

For the purposes of comparison with the PDOS of **7**, the PDOS spectra for **6** were recreated by summing the PDOS for *py* and *imid* to make *pyimid*. The new PDOS spectra are shown in Figure 4.26.

The PDOS spectra for **7** are shifted to lower energy by about 2.6eV compared to that of **6**. This is due to the increased charge on the molecule (from +2 to +4). The PDOS spectra for *Ru*, *pyimid* and *bpy1* are almost identical for **6** and **7**. The PDOS of *bpy2* is shifted to lower energy by about 0.3eV relative to *bpy1*. In **6** both bipyridines had identical PDOS spectra. The difference must therefore be due to the proximity of *bpy2* to the additional *ph* in **7**.

There seems to be little evidence for any electronic communication between the two centres in **7**: the *imid*/*ph* dihedral angle is about 114°; the *pyimid* PDOS is

unperturbed on formation of the dinuclear complex; and the peaks of the PDOS of *ph* and *pyimid* do not coincide.

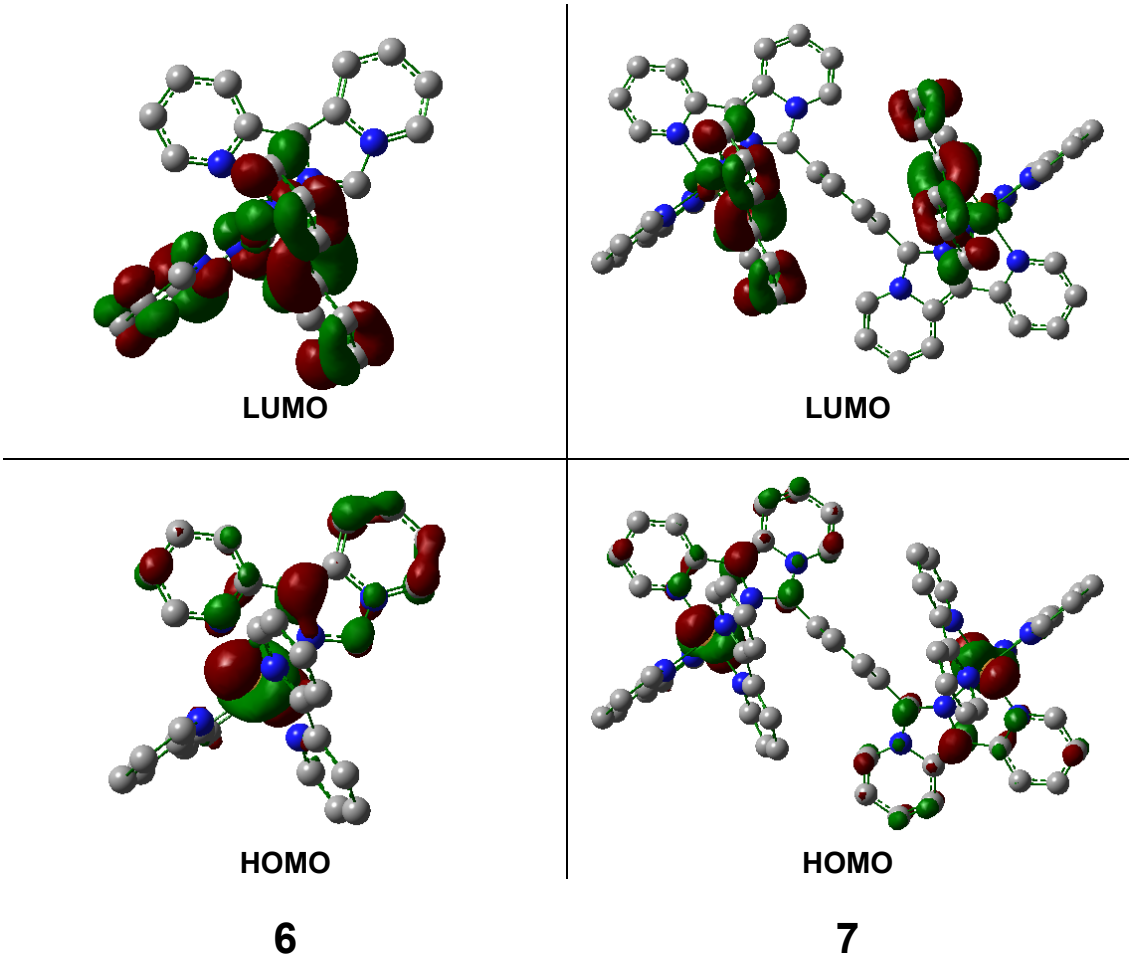

Figure 4.14 – Isosurfaces of the HOMO and LUMO of 6 and 7 drawn at 0.03e/bohr^3. Hydrogens omitted for clarity.

The nature of the lowest energy singlet electronic transition was investigated using TDDFT. The predicted energy for this transition was 2.44eV (509nm), with an oscillator strength of 0.0007. The character of the transition was mainly HOMO→LUMO (69%) but with significant contribution from HOMO→LUMO+1 (17%). The change in the contribution of each of the moieties was calculated using GaussSum: the *Ru* contribution changed from 62%→3%, *pyimid* changed from 29%→2%, *bpy1* changed from 4%→53% and *bpy2* changed from 5%→42%. An electron density difference map (EDDM) was created using GaussSum to visualise the change in charge density accompanying the transition. The transition can be

classified as a metal-to-ligand charge transfer (MLCT) from the Ru to the bipyridines, with some interligand charge transfer (ILCT) from pyimid to the bipyridines.

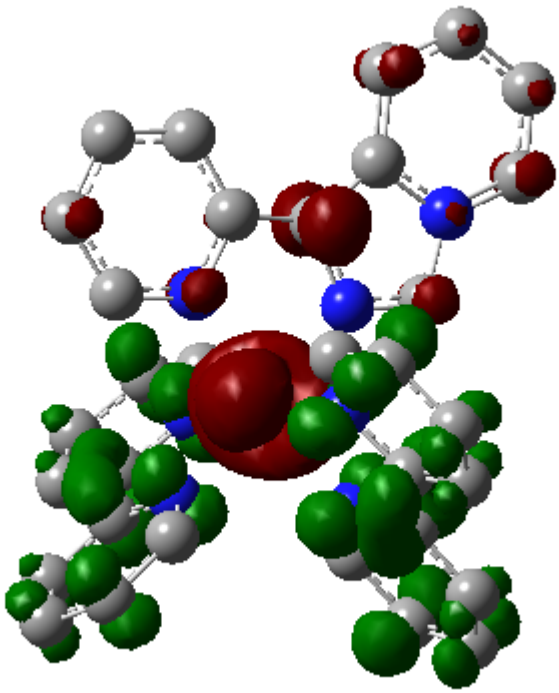

Figure 4.15 – Electron density difference map (EDDM) for the lowest energy singlet electronic transition of 6**. Red indicates a decrease in charge density, and green indicates an increase. The hydrogen atoms are not shown for clarity.**

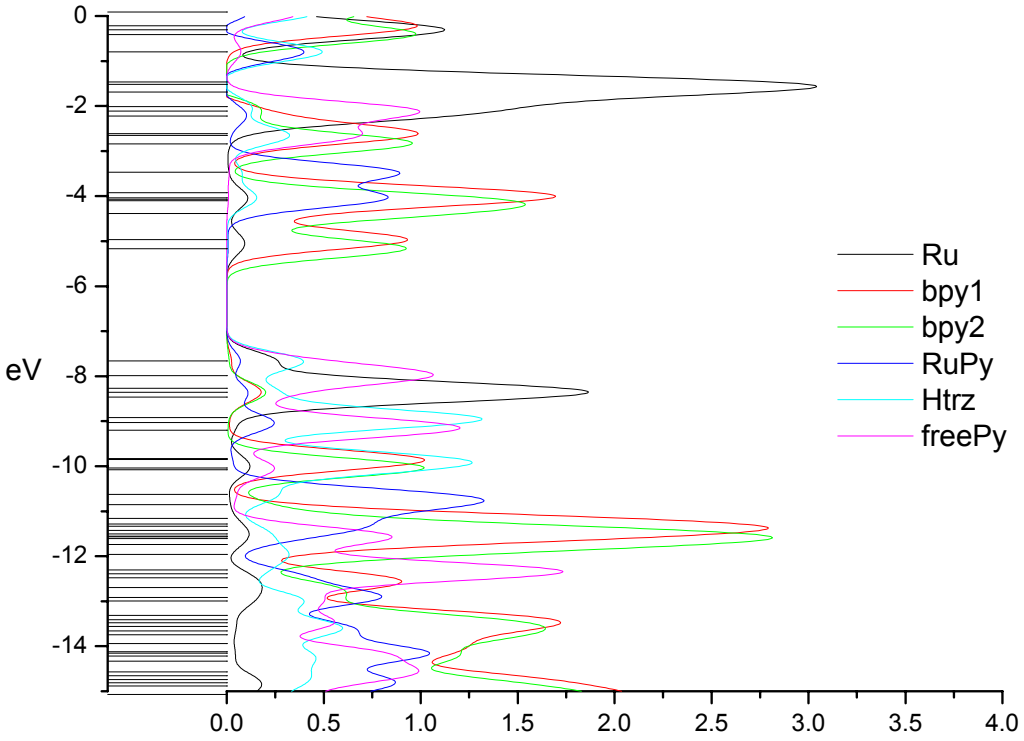

Figure 4.16 – Partial density of states spectra for $[Ru(bpy)_2(pytrzpy)]^+$, 1.

MO		EV	Ru	bpy1	bpy2	RuPy	trz	freePy
158	L+10	-2.61	0	91	8	1	0	0
157	L+9	-2.65	1	0	2	1	32	64
156	L+8	-2.84	1	8	89	0	1	1
155	L+7	-3.47	1	2	1	87	7	1
154	L+6	-3.93	2	92	5	1	0	0
153	L+5	-4.04	5	10	4	67	13	1
152	L+4	-4.07	2	65	20	11	2	0
151	L+3	-4.10	2	8	88	2	0	0
150	L+2	-4.39	1	19	77	3	0	0
149	L+1	-4.96	6	90	4	0	0	0
148	LUMO	-5.17	5	4	90	1	0	0
147	HOMO	-7.66	25	2	1	7	38	27
146	H-1	-7.99	0	0	0	0	5	94
145	H-2	-8.27	76	8	7	2	4	3
144	H-3	-8.36	63	4	8	6	14	5
143	H-4	-8.46	60	7	7	3	8	16
142	H-5	-8.92	1	1	0	0	94	4
141	H-6	-9.03	2	0	0	22	37	38
140	H-7	-9.20	2	1	0	2	7	88
139	H-8	-9.83	4	9	4	2	77	3
138	H-9	-9.85	0	86	1	0	11	1
137	H-10	-10.04	1	1	88	1	7	3

Table 4.4 – Molecular orbital data for $[Ru(bpy)_2(pytrzpy)]^+$, 1.

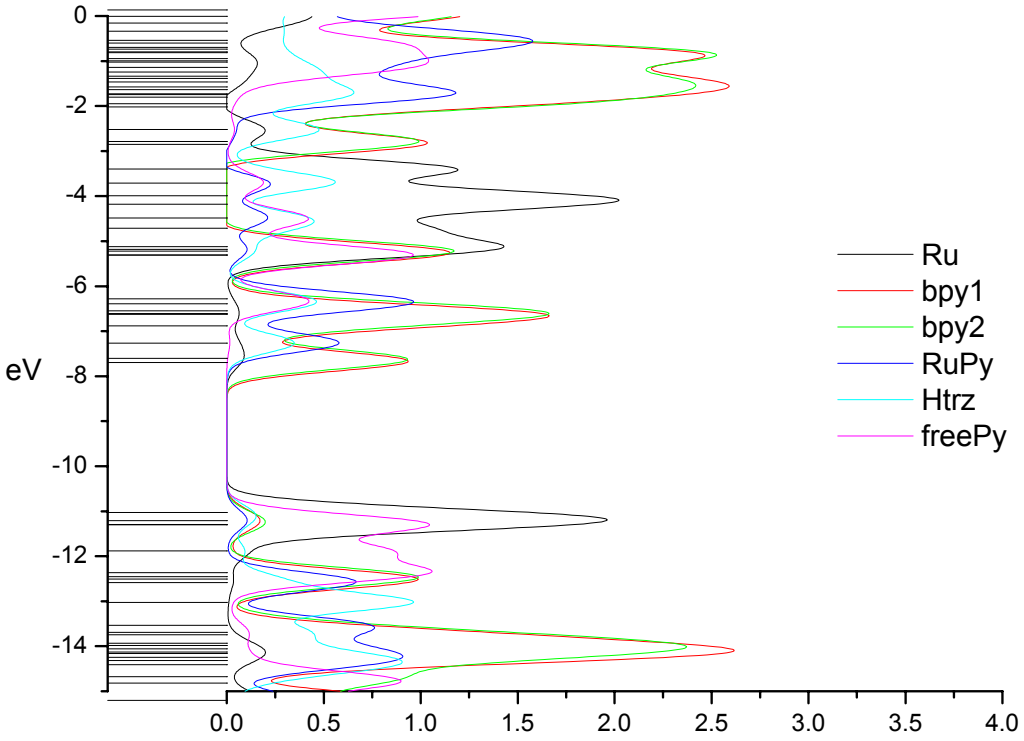

Figure 4.17 – Partial density of states spectra for $[Ru(bpy)_2(pyHtrzpy)]^{2+}$, H1.

MO		eV	Ru	bpy1	bpy2	RuPy	Htrz	freePy
158	L+10	-5.31	1	8	4	0	3	83
157	L+9	-5.31	1	61	25	0	1	12
156	L+8	-6.29	1	4	4	46	22	24
155	L+7	-6.39	1	1	3	51	25	20
154	L+6	-6.55	1	11	86	1	1	0
153	L+5	-6.61	2	80	14	4	0	0
152	L+4	-6.63	2	47	50	1	0	0
151	L+3	-6.88	1	54	41	4	1	0
150	L+2	-7.26	5	1	1	57	34	1
149	L+1	-7.60	6	27	67	0	0	0
148	LUMO	-7.70	2	69	28	1	1	0
147	HOMO	-11.03	71	6	3	2	10	7
146	H-1	-11.21	74	5	7	6	3	5
145	H-2	-11.29	58	6	9	2	2	24
144	H-3	-11.31	20	3	3	1	2	72
143	H-4	-11.88	11	2	1	0	9	77
142	H-5	-12.37	1	1	0	1	2	96
141	H-6	-12.46	0	13	87	0	0	0
140	H-7	-12.51	0	70	10	12	5	2
139	H-8	-12.58	2	17	2	54	21	3
138	H-9	-13.03	1	1	1	1	93	2
137	H-10	-13.54	0	2	25	66	5	2

Table 4.5 – Molecular orbital data for $[Ru(bpy)_2(pyHtrzpy)]^{2+}$, H1.

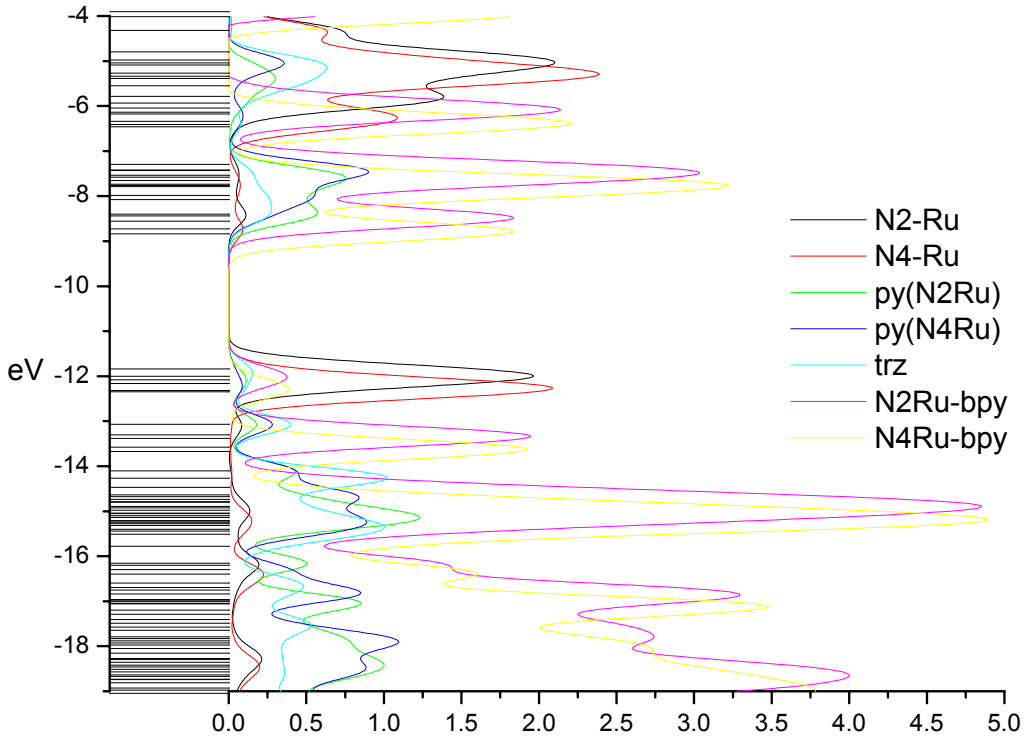

Figure 4.18 – Partial density of states spectra for $[(Ru(bpy)_2)_2(pytrzpy)]^{3+}$, 2.

MO		eV	N2-Ru	N4-Ru	py(N2Ru)	py(N4Ru)	trz	N2Ru-bpy	N4Ru-bpy
247	L+10	-7.65	0	1	1	1	0	0	97
246	L+9	-7.74	1	1	7	10	3	52	27
245	L+8	-7.76	0	2	0	3	0	3	92
244	L+7	-7.79	1	1	12	4	3	12	68
243	L+6	-7.99	1	1	10	21	7	3	57
242	L+5	-8.07	1	2	19	22	12	5	38
241	L+4	-8.40	4	1	32	16	14	31	1
240	L+3	-8.44	5	0	10	3	5	76	0
239	L+2	-8.56	1	0	9	1	4	84	0
238	L+1	-8.72	0	6	0	1	0	0	93
237	LUMO	-8.84	0	3	0	0	0	0	96
236	HOMO	-11.84	67	9	2	3	11	9	1
235	H-1	-12.00	70	8	3	0	3	14	1
234	H-2	-12.08	72	5	5	0	1	16	1
233	H-3	-12.17	9	73	1	4	1	2	11
232	H-4	-12.32	5	72	3	4	4	1	12
231	H-5	-12.35	6	71	1	1	3	1	18
230	H-6	-13.07	7	2	18	28	39	6	1
229	H-7	-13.30	1	0	0	1	1	97	0
228	H-8	-13.38	1	0	0	0	0	98	0
227	H-9	-13.58	0	1	0	0	0	0	99
226	H-10	-13.67	0	1	0	1	0	0	98

Table 4.6 – Molecular orbital data for $[(Ru(bpy)_2)_2(pytrzpy)]^{3+}$, 2.

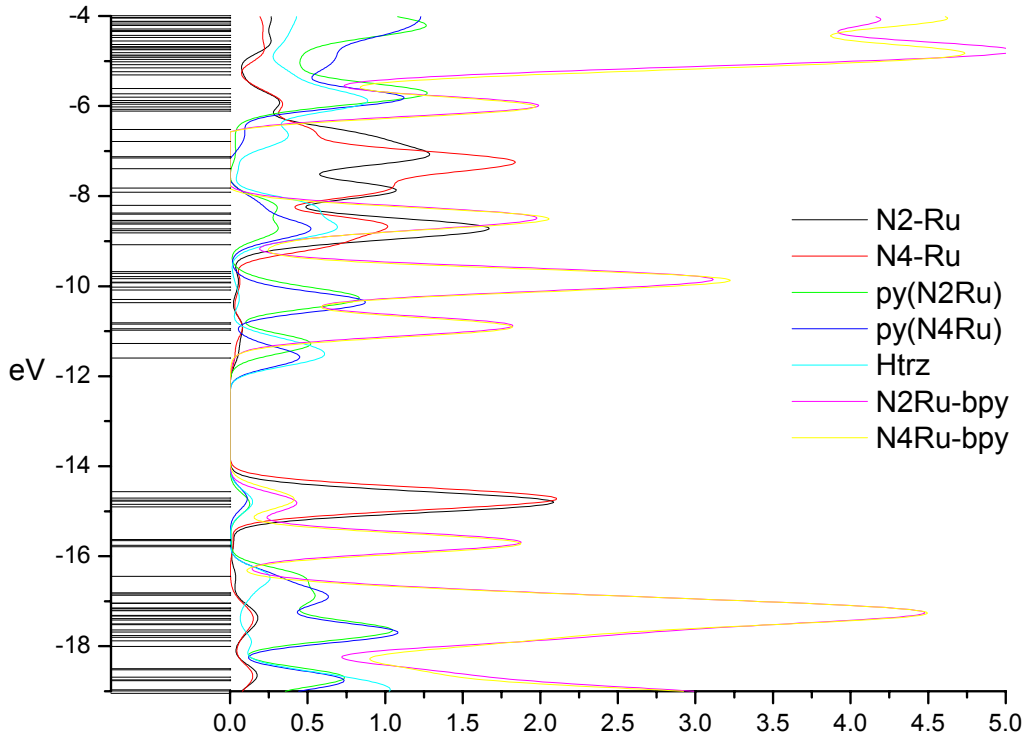

Figure 4.19 – Partial density of states spectra for $[(Ru(bpy)_2)_2(pyHtrzpy)]^{4+}$, H2.

MO		eV	N2-Ru	N4-Ru	py(N2Ru)	py(N4Ru)	Htrz	N2Ru-bpy	N4Ru-bpy
247	L+10	-9.92	1	0	0	0	0	94	4
246	L+9	-10.02	1	1	15	4	1	49	28
245	L+8	-10.09	1	2	0	4	0	35	58
244	L+7	-10.29	1	0	74	0	3	15	6
243	L+6	-10.37	0	1	2	84	2	0	11
242	L+5	-10.82	4	0	0	0	0	95	0
241	L+4	-10.84	0	4	0	0	0	0	95
240	L+3	-10.94	3	0	1	0	1	94	1
239	L+2	-10.98	0	3	0	0	0	1	95
238	L+1	-11.28	4	2	51	9	32	3	1
237	LUMO	-11.60	3	2	2	42	48	1	1
236	HOMO	-14.57	10	72	0	3	2	1	11
235	H-1	-14.71	71	9	3	1	3	11	2
234	H-2	-14.75	16	61	1	1	2	3	16
233	H-3	-14.78	10	68	1	6	2	2	12
232	H-4	-14.85	70	5	2	0	2	20	1
231	H-5	-14.91	49	25	6	1	5	9	5
230	H-6	-15.63	1	0	0	0	0	98	0
229	H-7	-15.65	0	1	0	0	0	0	99
228	H-8	-15.76	1	0	0	0	0	98	0
227	H-9	-15.79	0	1	0	0	0	0	99
226	H-10	-16.45	3	0	42	24	24	6	1

Table 4.7 – Molecular orbital data for $[(Ru(bpy)_2)_2(pyHtrzpy)]^{4+}$, H2.

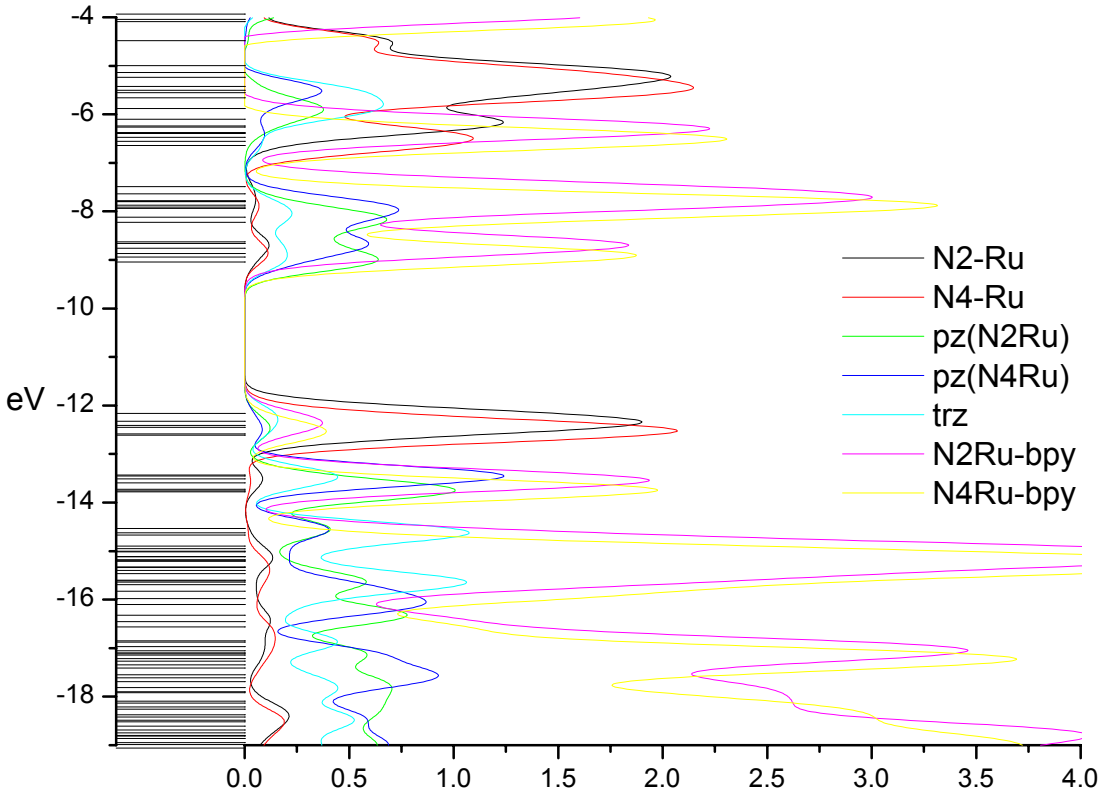

Figure 4.20 – Partial density of states spectra for $[(Ru(bpy)_2)_2(pztrzpz)]^{3+}$, 3.

MO		eV	N2-Ru	N4-Ru	pz(N2Ru)	pz(N4Ru)	trz	N2Ru-bpy	N4Ru-bpy
247	L+10	-7.87	1	1	6	14	2	59	17
246	L+9	-7.91	0	2	1	0	0	15	82
245	L+8	-7.94	0	1	3	34	8	12	42
244	L+7	-8.12	1	1	30	7	9	6	46
243	L+6	-8.23	0	1	32	24	5	5	31
242	L+5	-8.63	5	1	12	14	4	64	0
241	L+4	-8.66	4	2	15	30	8	40	1
240	L+3	-8.76	3	1	1	9	2	84	1
239	L+2	-8.87	0	6	1	0	0	0	92
238	L+1	-8.94	0	2	4	0	1	1	92
237	LUMO	-9.05	3	1	53	17	15	5	5
236	HOMO	-12.16	61	15	1	2	10	8	2
235	H-1	-12.33	67	11	3	0	2	15	2
234	H-2	-12.41	47	32	3	1	2	10	5
233	H-3	-12.45	29	49	3	3	2	6	9
232	H-4	-12.59	2	75	0	4	1	0	18
231	H-5	-12.61	22	55	5	1	4	4	9
230	H-6	-13.44	3	1	10	36	24	25	1
229	H-7	-13.45	1	1	2	78	6	11	1
228	H-8	-13.51	4	1	4	8	12	71	1
227	H-9	-13.60	1	0	2	1	2	94	0
226	H-10	-13.73	0	0	3	1	0	0	95

Table 4.8 – Molecular orbital data for $[(Ru(bpy)_2)_2(pztrzpz)]^{3+}$, 3.

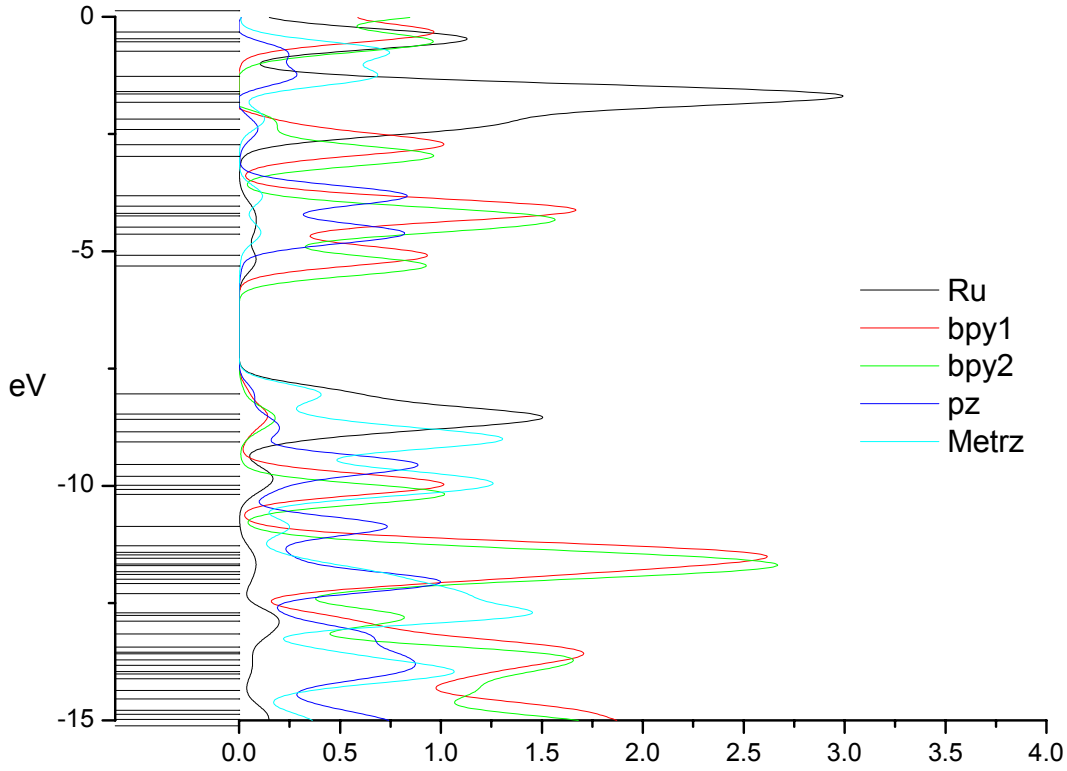

Figure 4.21 – Partial density of states spectra for $[Ru(bpy)_2(5\text{-Metrzpz})]^+$, 4.

MO		eV	Symmetry	Ru	bpy1	bpy2	pz	Metrz
142	L+10	-2.40	A	67	17	7	9	0
141	L+9	-2.73	A	0	93	7	0	0
140	L+8	-2.97	A	1	6	93	0	0
139	L+7	-3.81	A	1	5	2	81	11
138	L+6	-4.04	A	2	91	4	3	0
137	L+5	-4.20	A	3	74	22	1	0
136	L+4	-4.24	A	2	10	88	0	0
135	L+3	-4.49	A	3	13	69	12	3
134	L+2	-4.64	A	3	4	12	72	8
133	L+1	-5.09	A	5	91	3	1	0
132	LUMO	-5.31	A	4	4	91	1	0
131	HOMO	-8.04	A	48	4	2	7	39
130	H-1	-8.47	A	76	10	7	2	5
129	H-2	-8.58	A	66	3	10	7	14
128	H-3	-8.85	A	34	3	3	15	45
127	H-4	-9.06	A	1	1	0	0	98
126	H-5	-9.54	A	2	1	1	85	11
125	H-6	-9.80	A	12	13	1	6	68
124	H-7	-9.99	A	2	91	1	1	5
123	H-8	-10.08	A	4	1	3	13	79
122	H-9	-10.18	A	1	1	98	0	0
121	H-10	-10.87	A	0	2	1	73	24

Table 4.9 – Molecular orbital data for $[Ru(bpy)_2(5\text{-Metrzpz})]^+$, 4.

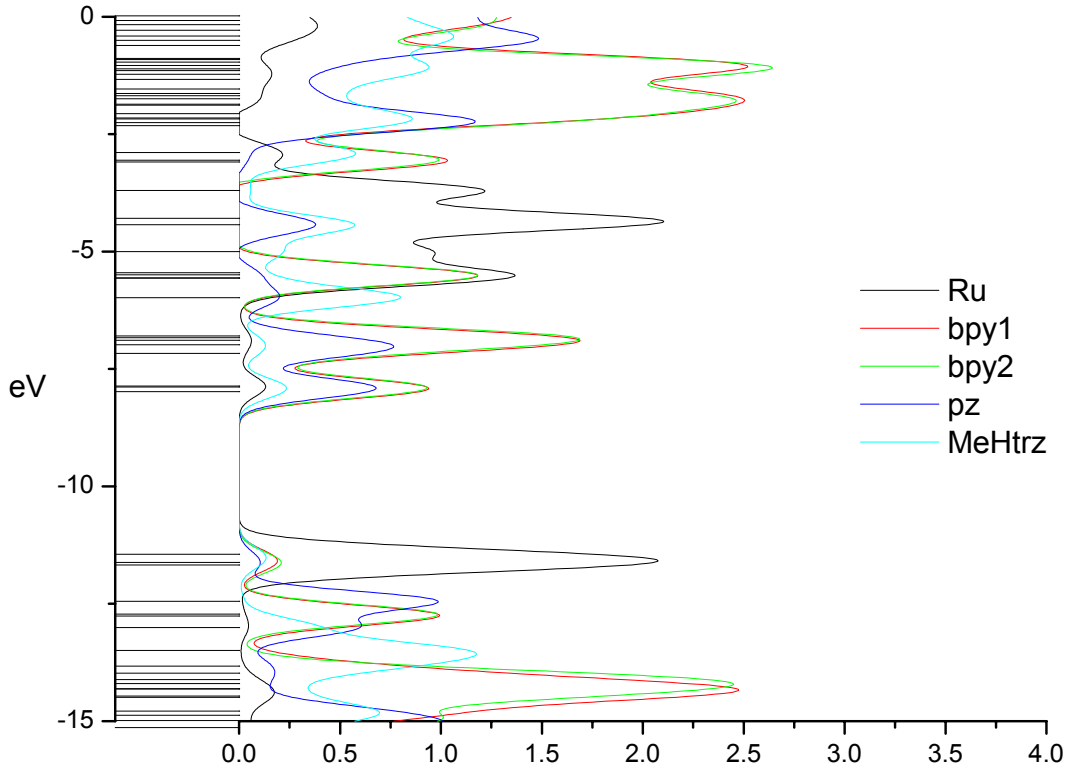

Figure 4.22 – Partial density of states spectra for $[Ru(bpy)_2(1H\text{-}5\text{-}Metrzpz)]^{2+}$, H4.

MO		eV	Ru	bpy1	bpy2	pz	MeHtrz
142	L+10	-5.56	5	49	45	1	1
141	L+9	-5.57	62	13	11	4	9
140	L+8	-5.98	2	1	1	19	78
139	L+7	-6.80	1	44	51	3	1
138	L+6	-6.83	2	35	57	4	1
137	L+5	-6.89	2	50	47	1	0
136	L+4	-6.99	1	34	4	52	9
135	L+3	-7.17	1	33	37	25	3
134	L+2	-7.86	7	5	61	20	7
133	L+1	-7.88	6	56	4	26	9
132	LUMO	-7.98	1	35	32	24	9
131	HOMO	-11.44	79	7	4	2	8
130	H-1	-11.62	76	9	6	4	5
129	H-2	-11.67	76	6	12	5	1
128	H-3	-12.44	1	1	0	96	2
127	H-4	-12.72	0	33	66	0	0
126	H-5	-12.76	1	65	32	1	1
125	H-6	-13.01	4	4	1	56	35
124	H-7	-13.49	0	2	2	2	94
123	H-8	-13.83	1	29	1	12	57
122	H-9	-13.98	0	38	58	1	2
121	H-10	-14.12	2	11	79	7	1

Table 4.10 – Molecular orbital data for $[Ru(bpy)_2(1H\text{-}5\text{-}Metrzpz)]^{2+}$, H4.

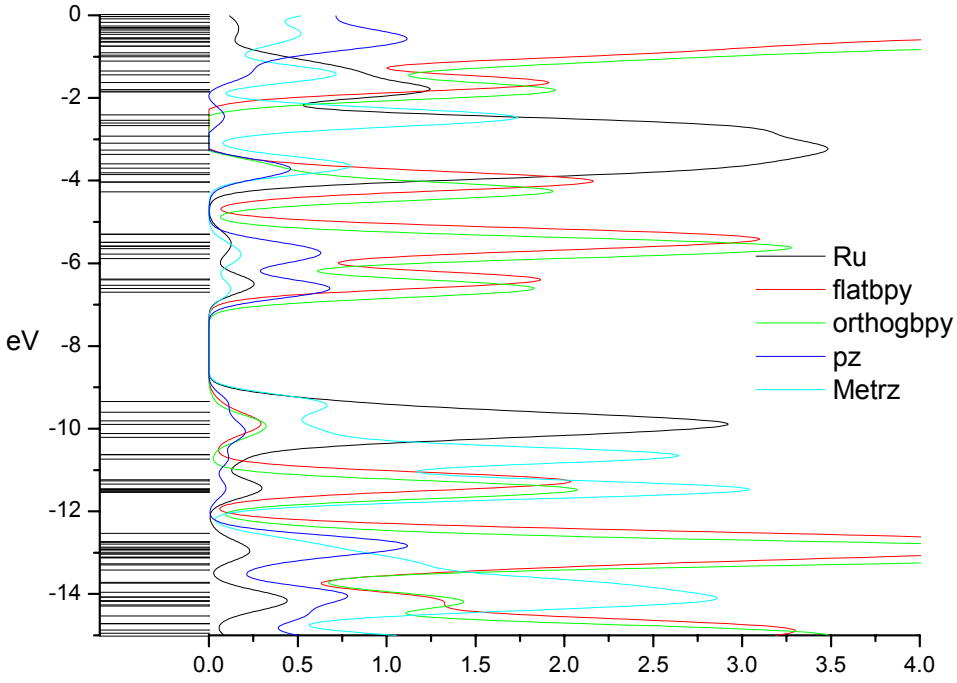

Figure 4.23 – Partial density of states spectra for $[(Ru(bpy)_2(5\text{-Metrz}))_2pz]^{2+}$, 5.

MO		eV	Symmetry	Ru	flatbpy	orthobpy	Metrz	pz
252	L+10	-5.49	AG	2	47	51	0	0
251	L+9	-5.58	AU	1	31	57	3	8
250	L+8	-5.59	AG	2	38	60	0	0
249	L+7	-5.64	AU	2	7	55	6	29
248	L+6	-5.77	AG	2	18	80	0	0
247	L+5	-5.89	AU	2	13	37	12	36
246	L+4	-6.38	AU	6	87	1	1	5
245	L+3	-6.40	AG	5	92	2	0	0
244	L+2	-6.53	AU	10	3	49	5	33
243	L+1	-6.61	AG	5	3	92	0	0
242	LUMO	-6.70	AU	2	6	47	8	37
241	HOMO	-9.34	AG	37	3	1	49	9
240	H-1	-9.60	AU	63	6	3	26	3
239	H-2	-9.81	AG	80	7	6	3	4
238	H-3	-9.89	AU	76	11	8	4	2
237	H-4	-9.90	AG	69	6	11	10	4
236	H-5	-10.12	AG	42	5	3	40	9
235	H-6	-10.21	AU	72	3	11	7	7
234	H-7	-10.62	AU	0	1	0	99	0
233	H-8	-10.63	AG	1	0	0	98	0
232	H-9	-10.73	AU	15	3	1	70	10
231	H-10	-11.24	AG	3	68	1	28	1

Table 4.11 – Molecular orbital data for $[(Ru(bpy)_2(5\text{-Metrz}))_2pz]^{2+}$, 5.

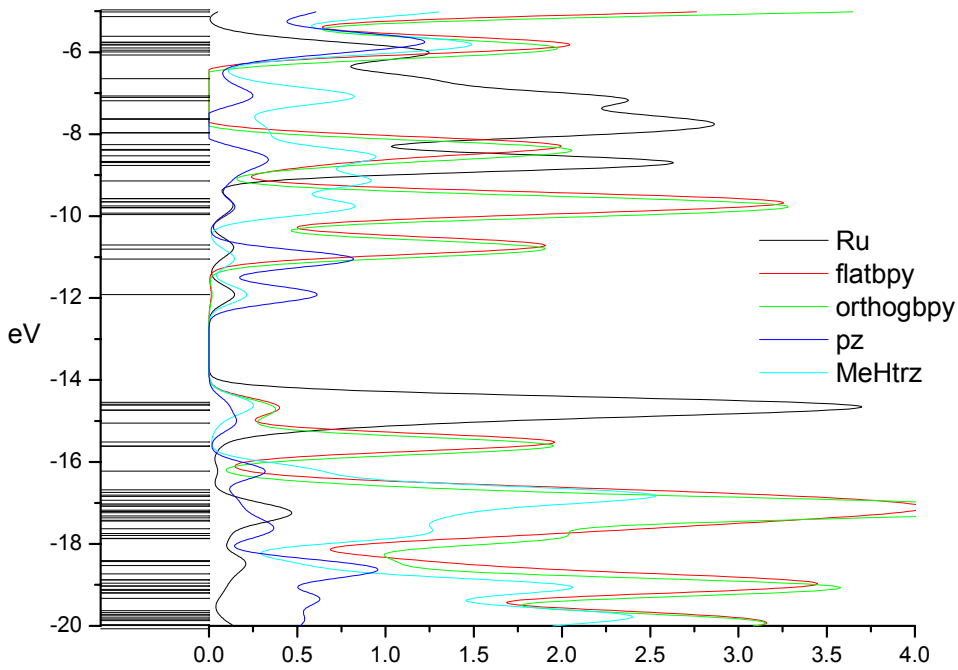

Figure 4.24 – Partial density of states spectra for $[(Ru(bpy)_2(1H\text{-}5\text{-}Metrz))_2pz]^{4+}$, H_25.

MO		eV	Symmetry	Ru	flatbpy	orthobpy	MeHtrz	pz
252	L+10	-9.75	AG	5	16	5	64	10
251	L+9	-9.79	AU	1	52	46	0	0
250	L+8	-9.80	AG	1	39	45	12	2
249	L+7	-9.93	AU	2	31	65	1	1
248	L+6	-9.96	AG	1	29	63	5	1
247	L+5	-10.70	AU	4	85	11	0	0
246	L+4	-10.70	AG	4	83	12	0	0
245	L+3	-10.80	AU	3	12	85	0	0
244	L+2	-10.81	AG	2	13	84	0	0
243	L+1	-11.05	AU	2	1	2	14	81
242	LUMO	-11.91	AU	14	1	2	21	61
241	HOMO	-14.54	AG	78	7	4	8	2
240	H-1	-14.59	AG	79	5	8	5	4
239	H-2	-14.62	AU	79	8	4	8	1
238	H-3	-14.73	AG	74	11	11	2	1
237	H-4	-14.74	AU	74	12	10	3	1
236	H-5	-15.05	AU	67	3	13	4	14
235	H-6	-15.51	AG	1	92	7	0	0
234	H-7	-15.52	AU	1	92	6	0	0
233	H-8	-15.61	AG	1	6	92	0	0
232	H-9	-15.62	AU	2	6	91	0	0
231	H-10	-16.22	AG	5	8	1	55	32

Table 4.12 – Molecular orbital data for $[(Ru(bpy)_2(1H\text{-}5\text{-}Metrz))_2pz]^{4+}$, H_25.

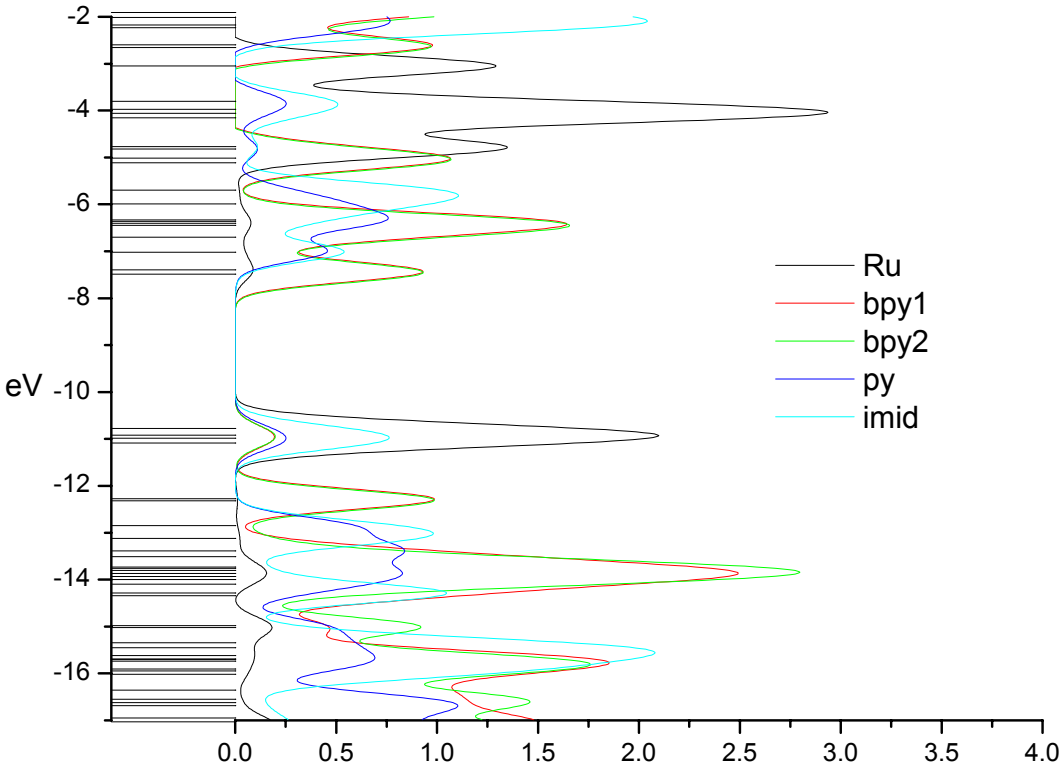

Figure 4.25 – Partial density of states spectra for $[Ru(bpy)_2(pyimid)]^{2+}$, 6.

MO		eV	Ru	bpy1	bpy2	py	imid
151	L+10	-5.11	1	40	58	1	1
150	L+9	-5.70	2	1	1	16	80
149	L+8	-5.99	1	2	2	37	58
148	L+7	-6.33	2	17	18	39	24
147	L+6	-6.36	1	84	6	6	3
146	L+5	-6.40	2	5	74	17	3
145	L+4	-6.45	2	46	50	2	1
144	L+3	-6.70	1	43	47	7	2
143	L+2	-7.02	3	1	1	43	53
142	L+1	-7.40	6	56	37	0	0
141	LUMO	-7.49	2	39	58	1	1
140	HOMO	-10.77	64	4	4	8	20
139	H-1	-10.92	61	6	5	5	24
138	H-2	-10.98	75	5	11	2	6
137	H-3	-11.09	38	6	2	15	40
136	H-4	-12.27	0	72	27	0	0
135	H-5	-12.32	1	27	72	0	0
134	H-6	-12.85	0	0	1	48	51
133	H-7	-13.12	2	1	9	21	68
132	H-8	-13.39	0	33	2	63	1
131	H-9	-13.51	0	48	48	2	1
130	H-10	-13.73	2	25	67	2	3

Table 4.13 – Molecular orbital data for $[Ru(bpy)_2(pyimid)]^{2+}$, 6.

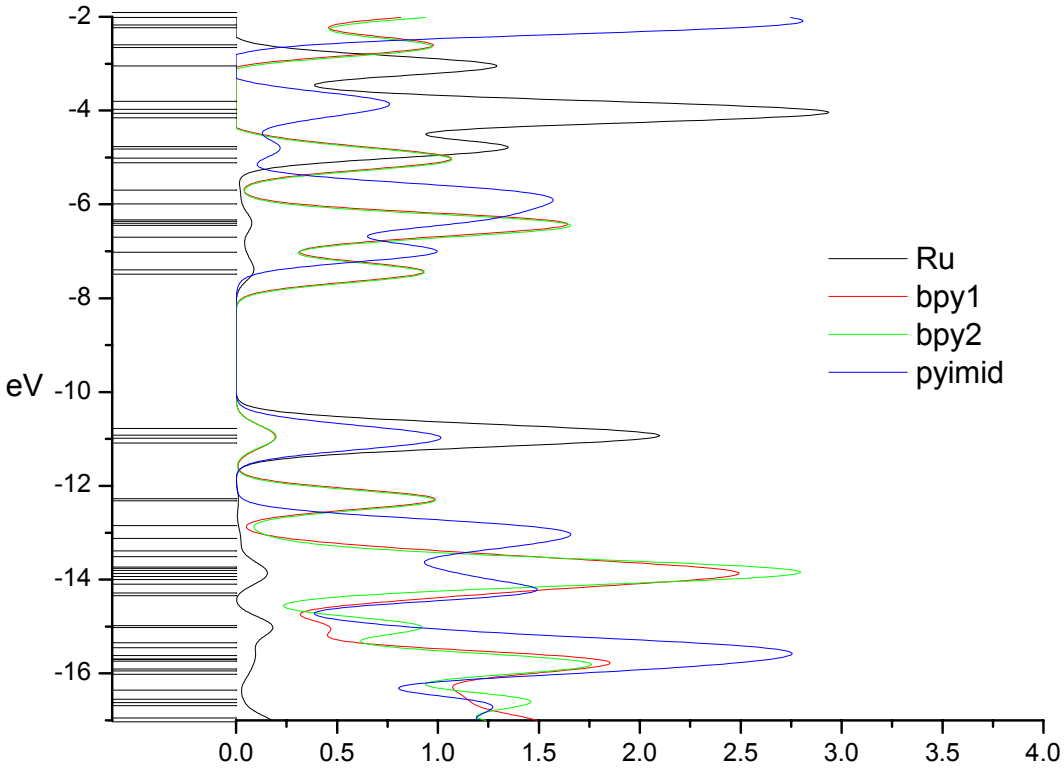

Figure 4.26 – Alternative partial density of states spectra for $[Ru(bpy)_2(pyimid)]^{2+}$, 6.

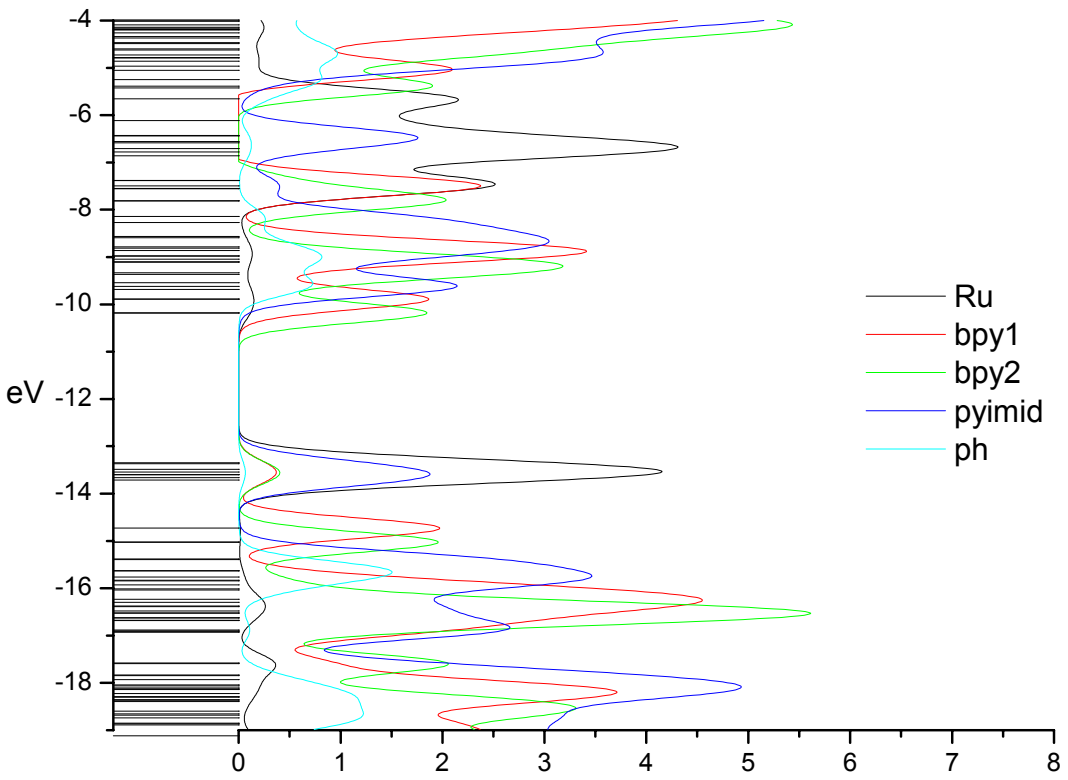

Figure 4.27 – Partial density of states spectra for $[(Ru(bpy)_2(pyimid))_2ph]^{2+}$, 7.

MO		eV	Symmetry	Ru	bpy1	bpy2	pyimid	ph
310	L+10	-9.10	B	2	1	94	2	1
309	L+9	-9.11	A	2	1	94	2	1
308	L+8	-9.33	B	2	11	84	3	0
307	L+7	-9.36	A	2	10	81	2	5
306	L+6	-9.54	B	0	0	3	56	41
305	L+5	-9.62	A	3	1	1	95	0
304	L+4	-9.68	B	3	2	1	64	29
303	L+3	-9.89	A	5	91	3	1	0
302	L+2	-9.89	B	4	90	2	2	0
301	L+1	-10.18	B	4	3	91	1	1
300	LUMO	-10.19	A	4	4	91	1	0
299	HOMO	-13.35	A	56	5	3	35	1
298	H-1	-13.37	B	68	5	5	22	0
297	H-2	-13.49	A	61	5	5	27	2
296	H-3	-13.55	B	68	8	5	17	1
295	H-4	-13.60	A	76	5	11	8	0
294	H-5	-13.60	B	76	4	10	10	0
293	H-6	-13.66	A	45	7	3	44	1
292	H-7	-13.71	B	25	4	3	66	2
291	H-8	-14.73	A	1	98	1	0	0
290	H-9	-14.73	B	1	98	1	0	0
289	H-10	-15.02	B	1	1	97	1	1

Table 4.14 – Molecular orbital data for $[(Ru(bpy)_2(pyimid))_2ph]^{2+}$, 7.

No.	λ (nm)	Osc. Strength	Symmetry	Major contributions	*Ru*	*flatbpy*	*orthobpy*	*Metrz*	*pz*
1	621.42	0.0358	A_U	HOMO→LUMO (83%)	40-→2 (-38)	3-→7 (4)	2-→50 (48)	47-→7 (-40)	8-→34 (26)
2	606.52	0	A_G	H-1→LUMO (15%), H-1→L+2 (-13%), HOMO→L+1 (66%)	45-→5 (-40)	4-→4 (0)	2-→78 (76)	42-→2 (-40)	7-→10 (3)
3	598.99	0.0129	A_U	H-1→L+1 (-21%), HOMO→L+2 (68%)	44-→9 (-35)	4-→4 (0)	2-→58 (56)	43-→4 (-39)	7-→25 (18)
4	569.61	0	A_G	H-1→LUMO (60%), H-1→L+2 (31%)	62-→5 (-57)	6-→7 (1)	3-→47 (44)	26-→7 (-19)	3-→34 (31)
5	543.31	0	A_G	H-1→L+4 (26%), HOMO→L+3 (60%)	47-→5 (-42)	4-→88 (84)	2-→5 (3)	40-→0 (-40)	7-→2 (-5)
6	542.57	0.0214	A_U	H-1→L+3 (25%), HOMO→L+4 (61%)	48-→6 (-42)	4-→86 (82)	2-→3 (1)	39-→1 (-38)	7-→4 (-3)
7	521.47	0.0099	A_U	H-3→L+1 (25%), H-2→LUMO (40%), H-2→L+2 (-20%)	76-→5 (-71)	8-→5 (-3)	7-→62 (55)	6-→4 (-2)	3-→24 (21)
8	521.1	0	A_G	H-3→LUMO (10%), H-3→L+2 (-18%), H-2→L+1 (54%)	76-→6 (-70)	8-→4 (-4)	7-→75 (68)	6-→2 (-4)	3-→13 (10)
9	515.12	0.0543	A_U	H-4→LUMO (14%), H-4→L+2 (17%), H-2→LUMO (29%), H-2→L+2 (27%)	74-→7 (-67)	7-→7 (0)	8-→48 (40)	8-→6 (-2)	4-→33 (29)
10	505.76	0	A_G	H-3→LUMO (65%), H-3→L+2 (25%)	75-→5 (-70)	10-→7 (-3)	8-→47 (39)	5-→7 (2)	2-→35 (33)
11	500.05	0.0157	A_U	H-1→L+1 (54%), HOMO→L+2 (19%)	57-→5 (-52)	5-→4 (-1)	3-→72 (69)	30-→3 (-27)	5-→15 (10)
12	497.91	0	A_G	H-1→LUMO (-16%), H-1→L+2 (43%), HOMO→L+1 (25%)	57-→7 (-50)	5-→5 (0)	3-→62 (59)	30-→4 (-26)	5-→22 (17)
13	487.76	0.2226	A_U	H-4→LUMO (53%), H-2→LUMO (-10%)	68-→3 (-65)	6-→8 (2)	9-→53 (44)	13-→6 (-7)	4-→30 (26)
14	468.43	0	A_G	H-4→L+1 (18%), H-3→L+4 (17%), H-2→L+3 (20%), HOMO→L+3 (15%)	67-→6 (-61)	7-→63 (56)	7-→26 (19)	16-→1 (-15)	4-→5 (1)
15	467.06	0.0881	A_U	H-3→L+3 (16%), H-2→L+4 (26%), H-1→L+3 (-11%), HOMO→L+4 (20%)	65-→6 (-59)	7-→75 (68)	6-→11 (5)	18-→1 (-17)	4-→6 (2)
16	460.56	0	A_G	H-6→L+4 (-14%), H-4→L+3 (-22%), H-2→L+3 (31%)	72-→5 (-67)	6-→69 (63)	9-→20 (11)	9-→1 (-8)	5-→4 (-1)
17	458.4	0.0131	A_U	H-6→L+3 (17%), H-4→L+4 (33%), H-2→L+4 (-22%), H-1→L+3 (-11%)	70-→6 (-64)	6-→81 (75)	8-→6 (-2)	12-→1 (-11)	5-→5 (0)
18	456.16	0	A_G	H-4→L+1 (17%), H-4→L+3 (-12%), H-1→L+4 (30%), HOMO→L+3 (-16%)	63-→6 (-57)	6-→61 (55)	6-→27 (21)	21-→1 (-20)	4-→6 (2)
19	450.12	0.0999	A_U	H-4→L+2 (-13%), H-4→L+4 (11%), H-1→L+3 (25%), HOMO→L+4 (-10%)	63-→6 (-57)	6-→58 (52)	6-→22 (16)	21-→2 (-19)	5-→11 (6)
20	441.7	0.0389	A_U	H-1→L+3 (11%), HOMO→L+5 (43%)	51-→4 (-47)	5-→31 (26)	4-→32 (28)	34-→7 (-27)	7-→25 (18)
21	439.07	0	A_G	H-4→L+3 (16%), H-3→L+4 (18%), H-1→L+4 (24%)	67-→6 (-61)	7-→69 (62)	7-→16 (9)	15-→2 (-13)	4-→8 (4)
22	430.18	0.0436	A_U	H-5→LUMO (54%)	54-→3 (-51)	6-→15 (9)	5-→47 (42)	29-→6 (-23)	7-→28 (21)
23	426.94	0	A_G	H-6→LUMO (14%), H-4→L+1 (11%), H-3→LUMO (-10%), H-3→L+2 (18%), H-2→L+1 (15%), H-1→L+5 (12%)	68-→5 (-63)	7-→7 (0)	7-→62 (55)	14-→5 (-9)	4-→22 (18)
24	424.16	0.0086	A_U	H-4→L+2 (32%), H-3→L+1 (33%)	69-→7 (-62)	7-→6 (-1)	8-→63 (55)	12-→4 (-8)	4-→21 (17)
25	423.36	0	A_G	H-6→LUMO (23%), H-4→L+1 (-24%), H-1→L+5 (17%)	66-→4 (-62)	5-→9 (4)	8-→61 (53)	16-→5 (-11)	5-→21 (16)

No.	λ (nm)	Osc. Strength	Symmetry	Major contributions	*Ru*	*flatbpy*	*orthobpy*	*Metrz*	*pz*
26	419.29	0	A_G	H-6→LUMO (11%), H-5→L+1 (30%), HOMO→L+6 (23%)	54-→4 (-50)	5-→9 (4)	4-→72 (68)	30-→3 (-27)	7-→12 (5)
27	419.14	0.0399	A_U	H-5→LUMO (-10%), H-5→L+2 (12%), H-2→L+2 (11%), HOMO→L+5 (19%)	55-→5 (-50)	6-→16 (10)	4-→51 (47)	29-→5 (-24)	6-→23 (17)
28	411.14	0	A_G	H-5→L+1 (36%), HOMO→L+6 (-33%)	47-→4 (-43)	4-→13 (9)	3-→76 (73)	38-→1 (-37)	8-→6 (-2)
29	408.22	0.0511	A_U	H-5→L+2 (48%), HOMO→L+7 (14%)	47-→7 (-40)	5-→10 (5)	4-→52 (48)	36-→5 (-31)	8-→27 (19)
30	399.19	0.1895	A_U	H-1→L+6 (11%), HOMO→L+7 (40%)	49-→4 (-45)	4-→22 (18)	4-→49 (45)	36-→5 (-31)	7-→21 (14)
31	397.13	0	A_G	H-6→LUMO (-17%), H-6→L+2 (12%), H-1→L+5 (23%)	61-→4 (-57)	5-→17 (12)	6-→51 (45)	23-→5 (-18)	6-→22 (16)
32	394.96	0	A_G	H-5→L+3 (11%), H-4→L+3 (-12%), H-3→L+4 (12%), H-1→L+9 (-10%), HOMO→L+8 (28%)	55-→3 (-52)	5-→56 (51)	5-→34 (29)	30-→1 (-29)	6-→5 (-1)
33	394.86	0.0055	A_U	H-6→L+1 (43%), H-4→L+4 (-11%)	66-→5 (-61)	5-→33 (28)	8-→53 (45)	15-→1 (-14)	6-→7 (1)
34	394.03	0.0272	A_U	H-6→L+1 (16%), H-1→L+8 (-10%), HOMO→L+9 (43%)	52-→3 (-49)	4-→32 (28)	4-→56 (52)	32-→2 (-30)	7-→7 (0)
35	393.09	0	A_G	H-4→L+3 (10%), H-3→L+4 (-21%), HOMO→L+8 (24%)	58-→4 (-54)	6-→55 (49)	5-→34 (29)	25-→1 (-24)	5-→6 (1)

Table 4.15 – The 35 lowest energy singlet transitions of 5, calculated using TDDFT.

No.	λ (nm)	Osc. Strength	Symmetry	Major contributions	*Ru*	*flatbpy*	*orthobpy*	*MeHtrz*	*pz*
1	707.56	0.0001	A_U	HOMO→LUMO (93%)	78-->14 (-64)	7-->1 (-6)	4-->2 (-2)	8-->22 (14)	2-->61 (59)
2	682.09	0	A_G	H-2→LUMO (93%)	78-->14 (-64)	8-->1 (-7)	5-->2 (-3)	7-->22 (15)	1-->61 (60)
3	632.98	0.0035	A_U	H-3→LUMO (90%)	75-->15 (-60)	10-->1 (-9)	11-->2 (-9)	2-->21 (19)	2-->61 (59)
4	626.95	0	A_G	H-4→LUMO (93%)	74-->15 (-59)	11-->1 (-10)	10-->2 (-8)	3-->21 (18)	1-->61 (60)
5	561.32	0.3784	A_U	H-1→LUMO (74%)	78-->13 (-65)	6-->4 (-2)	8-->3 (-5)	5-->20 (15)	4-->60 (56)
6	469.97	0	A_G	H-5→LUMO (67%), H-2→L+1 (20%)	69-->12 (-57)	5-->2 (-3)	11-->2 (-9)	5-->20 (15)	11-->64 (53)
7	444	0.0842	A_U	H-1→L+1 (-18%), HOMO→L+1 (72%)	77-->3 (-74)	7-->2 (-5)	5-->3 (-2)	8-->14 (6)	3-->79 (76)
8	439	0.1372	A_U	H-1→L+1 (75%), HOMO→L+1 (14%)	77-->3 (-74)	6-->3 (-3)	7-->3 (-4)	6-->14 (8)	4-->78 (74)
9	432.47	0	A_G	H-2→L+1 (60%)	76-->4 (-72)	8-->4 (-4)	6-->15 (9)	7-->12 (5)	3-->64 (61)
10	429.29	0.0023	A_U	H-2→L+2 (37%), HOMO→L+3 (49%)	78-->3 (-75)	8-->18 (10)	4-->76 (72)	8-->1 (-7)	2-->2 (0)
11	428.8	0	A_G	H-2→L+1 (-13%), H-2→L+3 (31%), HOMO→L+2 (42%)	78-->3 (-75)	8-->16 (8)	5-->65 (60)	8-->3 (-5)	2-->13 (11)

No.	λ (nm)	Osc. Strength	Symmetry	Major contributions	*Ru*	*flatbpy*	*orthobpy*	*MeHtrz*	*pz*
12	420.52	0.0516	A_U	H-3→L+1 (88%)	75-->2 (-73)	10-->5 (-5)	11-->5 (-6)	3-->13 (10)	2-->75 (73)
13	420.24	0	A_G	H-4→L+1 (87%)	74-->3 (-71)	11-->4 (-7)	9-->3 (-6)	4-->13 (9)	2-->76 (74)
14	414.23	0.0057	A_U	H-2→L+4 (34%), HOMO→L+5 (45%)	78-->4 (-74)	8-->73 (65)	5-->17 (12)	7-->1 (-6)	2-->4 (2)
15	414.21	0	A_G	H-2→L+5 (34%), HOMO→L+4 (44%)	78-->4 (-74)	8-->72 (64)	5-->18 (13)	7-->1 (-6)	2-->4 (2)
16	406.09	0	A_G	H-4→L+3 (-21%), H-3→L+2 (-11%), H-1→L+2 (51%)	76-->3 (-73)	7-->19 (12)	9-->76 (67)	4-->0 (-4)	4-->1 (-3)
17	405.85	0.0048	A_U	H-4→L+2 (-22%), H-3→L+3 (-11%), H-1→L+3 (49%)	76-->3 (-73)	7-->19 (12)	9-->76 (67)	4-->0 (-4)	4-->1 (-3)
18	398.99	0.0068	A_U	H-6→LUMO (96%)	1-->14 (13)	89-->1 (-88)	9-->2 (-7)	0-->21 (21)	0-->61 (61)
19	398.21	0	A_G	H-7→LUMO (96%)	2-->14 (12)	89-->1 (-88)	8-->2 (-6)	0-->21 (21)	0-->61 (61)
20	391.71	0	A_G	H-5→L+5 (12%), H-1→L+2 (14%), H-1→L+4 (52%)	75-->4 (-71)	6-->65 (59)	10-->28 (18)	4-->1 (-3)	5-->2 (-3)
21	391.11	0.0013	A_U	H-8→LUMO (53%), H-1→L+5 (23%)	34-->10 (-24)	8-->30 (22)	54-->13 (-41)	2-->12 (10)	2-->35 (33)
22	390.68	0.0038	A_U	H-8→LUMO (-42%), H-1→L+5 (35%)	44-->9 (-35)	6-->44 (38)	44-->11 (-33)	3-->9 (6)	3-->27 (24)
23	390.49	0	A_G	H-9→LUMO (91%)	6-->14 (8)	8-->4 (-4)	85-->3 (-82)	0-->20 (20)	1-->59 (58)
24	386.26	0	A_G	H-4→L+3 (20%), H-3→L+2 (29%), H-1→L+4 (-17%)	73-->4 (-69)	9-->34 (25)	12-->58 (46)	3-->1 (-2)	3-->3 (0)
25	385.14	0.1888	A_U	H-4→L+2 (21%), H-3→L+3 (28%), H-1→L+3 (11%), H-1→L+5 (-12%)	74-->4 (-70)	9-->33 (24)	11-->61 (50)	3-->1 (-2)	3-->1 (-2)
26	375.57	0	A_G	H-5→L+1 (77%)	67-->3 (-64)	5-->13 (8)	13-->4 (-9)	4-->12 (8)	12-->68 (56)
27	364.82	0	A_G	H-4→L+5 (25%), H-3→L+4 (27%)	72-->5 (-67)	10-->56 (46)	11-->24 (13)	4-->5 (1)	3-->11 (8)
28	364.37	0.0123	A_U	H-4→L+4 (26%), H-3→L+5 (27%)	73-->5 (-68)	10-->58 (48)	10-->30 (20)	5-->3 (-2)	2-->4 (2)
29	362.22	0	A_G	H-2→L+3 (55%), HOMO→L+2 (-41%)	78-->3 (-75)	8-->14 (6)	4-->83 (79)	8-->0 (-8)	2-->0 (-2)
30	362.13	0.0008	A_U	H-2→L+2 (48%), HOMO→L+3 (-39%)	78-->3 (-75)	8-->16 (8)	5-->80 (75)	7-->0 (-7)	2-->1 (-1)
31	347.91	0.0007	A_U	H-2→L+4 (54%), HOMO→L+5 (-41%)	78-->4 (-74)	8-->83 (75)	4-->13 (9)	8-->0 (-8)	2-->0 (-2)
32	347.86	0	A_G	H-2→L+5 (54%), HOMO→L+4 (-41%)	78-->4 (-74)	8-->83 (75)	5-->13 (8)	8-->0 (-8)	2-->0 (-2)
33	345.75	0.0006	A_U	H-4→L+2 (48%), H-3→L+3 (-46%)	74-->3 (-71)	11-->13 (2)	10-->84 (74)	3-->0 (-3)	2-->0 (-2)
34	345.67	0	A_G	H-4→L+3 (49%), H-3→L+2 (-45%)	75-->3 (-72)	11-->14 (3)	10-->83 (73)	3-->0 (-3)	2-->0 (-2)
35	338.54	0.0005	A_U	H-2→L+18 (32%), HOMO→L+19 (30%)	76-->62 (-14)	9-->12 (3)	6-->16 (10)	7-->7 (0)	2-->3 (1)

Table 4.16 – The 35 lowest energy singlet electronic transitions of $H_2$5.

4.4 Discussion

The aim of these electronic structure calculations is to assess their ability to predict experimental results, in particular the location of the excited state and the degree of internuclear interaction. In this section, the results from DFT calculations are compared with available experimental data.

Complexes **1** and **2** have been extensively studied by Vos and co-workers.[17,22,23,24,25,26,27,28] Hage *et al.*[28] have shown that the first oxidation occurs on a metal centre in the case of **1**, **2**, **H1** and **H2**. This is in agreement with the PDOS of **2**, where the highest occupied molecular orbitals are metal-based. However, according to the PDOS spectra of **1**, the highest occupied molecular orbitals are based on the free pyridine of pytrzpy (the HOMO-1 is 94% *freePy*, while the HOMO is 27% *freePy* and 38% triazole). This highlights the fact that electrochemical oxidation does not always occur at the site indicated by the HOMO. A better way of finding the oxidation site might be to calculate the electron density of **1** in the oxidised form (overall charge 2+), and subtract it from the electron density of **1**. This would give the instantaneous change in the electron density on oxidation, and would highlight the areas where electron density changed the most.

Barigeletti *et al.*[23] examined the photophysical properties of **1** and **2**. They found that absorption and emission showed that pytrzpy is a better σ-donor and poorer π-acceptor than bipyridine. Resonance Raman studies of **1** and **2** at 458nm and 514.5nm showed only bpy vibrations. These results are in agreement with the PDOS of **1** and **2**, which show the LUMO to be bpy-based. They also state that, based on the stronger σ-donor abilities of the N2 position of the triazole ring[22] (versus the N4 position), the lowest energy ^{3}MLCT of **2** (which is of Ru→bpy nature) is expected to be on the 'mononuclear unit' attached to the N2 position of the triazole. Our calculations show that the PDOS of N2-bound Ru is at higher energy than that of N4-bound Ru. However, the bipyridines attached to the ruthenium centres have also shifted by equal amounts, so that the LUMO is based on the bipyridines attached to N4-bound Ru (see Figure 4.6). This would indicate that the lowest energy transition would involve charge transfer from the N2-bound Ru to the bipyridines attached to the N4-bound Ru. This is not a purely theoretical issue: Hughes and Vos[25] explain the photochemistry of **2** in terms of the assumed relative ordering of the ^{3}MLCT states. To find a more accurate answer for this question, a TDDFT calculation could be performed to calculate the change in electron density

associated with the lowest energy electronic transition (to ^{1}MLCT), or alternatively the electronic structure of the triplet excited state could be calculated directly, although this is computationally expensive.

A point worth noting is that experimental studies of **1** and **2** talk in terms of the π* of the pytrzpy ligand. In contrast, here we have used PDOS spectra to describe the molecular orbitals of the complexes in terms of separate pyridine and triazole units. Although the PDOS of these units coincide in the case of $\mathbf{H_2 2}$, this is not the case in general. For instance, the *freePy* unit of **1** has a PDOS at higher energy than that of *RuPy*, and this point is not considered when the bridge is discussed in terms of a single unit.

The location of the excited state in the protonated dinuclear complex **H2** has not been studied in the literature. One reason for this may be that, experimentally, protonation of **2** is quite difficult: unlike the mononuclear complex **1**, which has a pK_a of 4.0, **2** has a pK_a of around –0.6.[28] The PDOS spectra for **H2** indicate a change in the nature of the excited state on protonation: the excited state location changes from bipyridine to pytrzpy. Resonance Raman measurements on the protonated complex would show whether this is correct.

Hage *et al.*[29] used electrochemical and resonance Raman measurements to show that the π* level of the pztrzpz ligand in **3** was lower than those of the bipyridines. In a further study, Coates *et al.*[30] investigated the location of the excited state in complex **3** using ground state and excited state resonance Raman spectroscopy. They also concluded that the ^{3}MLCT state was based on a pyrazine. Our DFT calculations on **3** agree with this result, as they show that the LUMO is pyrazine-based.

The photophysical and electrochemical properties of **4** and **H4** were studied by Nieuwenhuis *et al.*[31], who found that the LUMO of **4** is bipyridine-based, whereas that of **H4** is pyrazine-based. The DFT calculations on **4** are in agreement with these results. However, the calculations on **H4** show that the lowest unoccupied molecular orbitals are based equally on pyrazine and bipyridine. The exact location of the excited state might be available from a TDDFT calculation of the lowest energy electronic transition.

Data from experimental studies on **5** and **$H_2$5** have been combined with the DFT calculations in this chapter in order to describe their ground and excited state structures.[32] The first electrochemical oxidation occurs on one of the ruthenium centres, in agreement with the picture from the PDOS spectra. Spectroscopic and electrochemical measurements show that the LUMO in both **5** and **$H_2$5** is pyrazine-based. Computational predictions for **$H_2$5** agree: the PDOS for **$H_2$5** predicts the LUMO to be completely pyrazine-based. However, the PDOS for **5** shows an equal contribution of *pz* and bipyridine to the lowest unoccupied orbitals. TDDFT calculations were carried out to find the nature of the lowest singlet excited state. The corresponding EDDMs (Figure 4.11 and Figure 4.13) give the same result: the lowest energy ^{1}MLCT for **$H_2$5** is from the ruthenium centres to the bridge, mainly *pz*, but the lowest energy ^{1}MLCT for **5** is from *Ru* and *Metrz* to both *pz* and *orthobpy*.

The results from TDDFT calculations on **5** and **$H_2$5** (see Table 4.15 and Table 4.16) were convoluted with Gaussian curves of $w_{½}$ of 3000cm^{-1} to create the predicted UV-Vis spectra shown in Figure 4.28. Figure 4.28 also shows the experimental spectra measured in MeCN and H_2O.[32] This compound exhibits a strong solvatochromic effect, so it is expected that gas-phase calculations would have problems reproducing the experimental spectrum. However, the calculated and experimental spectra of **$H_2$5** are in quite good agreement, although for **5** the λ_{max} of absorption is predicted to occur at a shorter wavelength (by 60nm) than is experimentally observed.

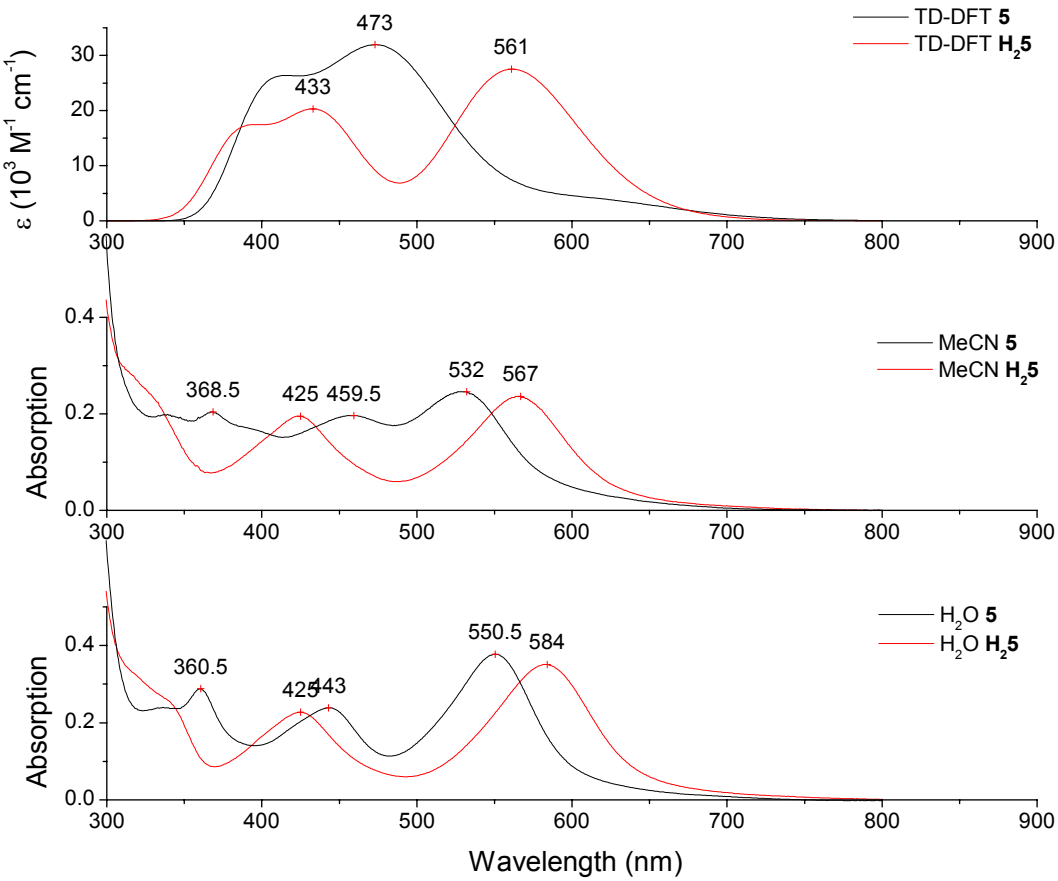

Figure 4.28 – Calculated UV-Vis spectra of 5 **and** $H_2$5 **(top) compared with the experimental spectra in MeCN (middle) and H_2O (bottom). The experimental spectra were measured by Dr. Wesley Browne, University of Groningen, the Netherlands.**

Complexes **6** and **7** have been experimentally studied by Dr. Adrian Guckian, Dublin City University.[21] A paper describing the experimental and computational results on **7** is currently in press.[33] Electrochemical and photophysical measurements on **7** have shown that there is no interaction between the metal centres. The calculated and predicted geometries of **7** show a dihedral angle of about 60° between the phenyl and fused imidazole moieties of the bridging ligand. This would make it difficult, if not unlikely, for a delocalised molecular orbital to span the bridge. Furthermore, the PDOS of **7** is identical to that of **6**, except for a doubling of the intensity of the peaks, and the additional phenyl moiety. If there was internuclear communication between the metal centres of **7**, the PDOS of **7** would be expected to show some additional changes.

The first electrochemical oxidation of both **6** and **7** is based on the metal centre, in agreement with the PDOS of **6** and **7**, which show the highest occupied molecular

orbitals to be mainly metal-based, although with a significant contribution from pyimid. In fact, the second oxidation of **7** (irreversible) is based on the bridging ligand. Photophysical measurements show the excited state of both **6** and **7** to be bipyridine-based, in agreement with the PDOS of **6** and **7**. The lowest energy singlet electronic transition for **6** was calculated using TDDFT, and the corresponding EDDM created (Figure 4.15). The transition can be classified as a metal-to-ligand charge transfer (MLCT) from the Ru to the bipyridines, with some interligand charge transfer (ILCT) from pyimid to the bipyridines. This confirms the location of the excited state as bipyridine-based.

As discussed in the introduction to this chapter regarding Albano *et al.*[16], it may be possible to use mononuclear complexes as models for dinuclear complexes, if there is no internuclear communication. The results for **6** and **7** support this conclusion.

As discussed in Chapter 3, the position of the peak of the ruthenium PDOS in the highest occupied molecular orbitals is a measure of the ease of oxidation of the metal centre. Experimentally, it is easier to oxidise $[Ru(bpy)_2(pytrzMe)]^+$, '**2**' in Chapter 3, than **1** (0.79V[34] versus 0.87V[28]). The calculated position of the ruthenium peak is 0.06eV lower for **1**, in agreement with the experimental results. On the other hand, the oxidation potentials of $[Ru(bpy)_2(pztrz)]^+$, '**7**' in Chapter 3, and **4** are equal within experimental error (0.95V versus 0.92V[31]). A negligible shift is observed for the Ru PDOS peak.

Although this is by no means a comprehensive study, by comparing the results for the dinuclear complexes **2**, **3** and **5**, where internuclear communication exists, and those for **7**, where there is no internuclear communication, a number of points can be made relating to prediction of the existence of internuclear communication. There is probably no internuclear communication if:

(1) the PDOS spectra of the mononuclear complex are identical to those of the dinuclear complex (apart from an overall shift)
(2) the optimised structure for the dinuclear complex contains a bridge whose moieties have substantial dihedral angles with respect to each other

It is likely that internuclear communication exists if:

(1) the PDOS spectra of bridge moieties are shifted to lower energy relative to the other PDOS spectra
(2) the optimised structure contains a planar bridge

(3) if the peaks in the PDOS spectra of the bridge moieties coincide

4.5 Conclusions and further work

Investigating and controlling the degree of internuclear interaction is an important aspect of the study of dinuclear complexes. The results from DFT calculations on the homovalent $Ru^{II}Ru^{II}$ dinuclear complex give a qualitative view of this interaction in terms of its effect on the energy levels of the bridge. Partial density of states spectra can be effectively used to compare the electronic structure of the dinuclear complex to a suitable mononuclear complex. Where internuclear communication exists, a relative shift to lower energy is observed for the moieties of the bridge.

If symmetry can be exploited, calculations on the ground state of dinuclear complexes are not much more computationally expensive than calculations on mononuclear complexes. Furthermore, in cases where there is no internuclear communication between the metal centres, it is possible to model the electronic structure of the dinuclear complex very accurately by calculating the electronic structure of the mononuclear complex (for example, for **6** and **7**).

Although it is conceptually useful to think in terms of the orbitals of the bridging ligand as a whole, this picture is too simplistic. The different moieties of the bridging ligand can be electronically independent. The part of the bridge that is directly between the metal centres should be thought of as distinct from those parts at the periphery, since the PDOS of the bridge centre shifts more to lower energy than does the PDOS of the periphery.

Further work on RuRu dinuclear complexes like those studied in this chapter should involve studies of the triplet state and mixed valence states. However, such calculations are computationally quite expensive, requiring unrestricted calculations and C_1 symmetry. Nevertheless they have the potential to show the location of the excited state and provide information regarding the correct Robin and Day classification of the complex.[8]

4.6 References

1. Balzani, V. and Scandola F., *Supramolecular Photochemistry*, **1991**, Horwood, Chichester, UK.

2. Lehn, J.-M., *Angew. Chem. Int. Ed. Engl.*, **1988**, *27*, 89.

3. Lees, A.C., Kleverlaan, C.J., Bignozzi, C.A. and Vos, J.G., *Inorg. Chem.*, **2001**, *40*, 5343.

4. Argazzi, R., Bignozzi, C.A., Heimer, T.A. and Meyer, G.J., *Inorg. Chem.*, **1997**, *36*, 2.

5. Bignozzi, C.A., Schoonover, J.R. and Scandola, F., *Prog. Inorg. Chem.*, **1997**, *44*, 1.

6. Brunschwig, B.S., Creutz, C. and Sutin, N., *Chem. Soc. Rev.*, **2002**, *31*, 168.

7. Evans, C.E.B., Naklicki, M.L., Rezvani, A.R., White, C.A., Kondratiev, V.V. and Crutchley, R.J., *J. Am. Chem. Soc.*, **1998**, *120*, 13096.

8. Braun-Sand, S.B. and Wiest, O., *J. Phys. Chem. A*, **2003**, *107*, 285.

9. Creutz, C. and Taube, H., *J. Am. Chem. Soc.*, **1969**, *91*, 3988.

10. Hush, N.S., *Prog. Inorg. Chem.*, **1967**, *8*, 391.

11. Robin, M.P. and Day, P., *Adv. Inorg. Chem. Radiochem.*, **1967**, *10*, 247.

12. Creutz, C., Newton, M.D. and Sutin, N., *J. Photochem. Photobio. A*, **1994**, *82*, 47.

13. Bencini, A., Ciofini, I., Daul, C.A. and Ferretti, A., *J. Am. Chem. Soc.*, **1999**, *121*, 11418.

14. Hardesty, J., Goh, S.K. and Marynick, D.S., *J. Mol. Struct. (THEOCHEM)*, **2002**, *588*, 223.

15. Chen, Z., Bian, J., Zhang, L. and Li, S., *J. Chem. Phys.*, **1999**, *111*, 10926.

16. Albano, G., Belser, P. and Daul, C., *Inorg. Chem.*, **2001**, *40*, 1408.

17. Browne, W.R., O'Connor, C.M., Villani, C. and Vos, J.G., *Inorg. Chem.*, **2001**, *40*, 5461.

18. Hage, R., de Graaff, R.A.G., Haasnoot, J.G., Turkenburg, J.P., Reedijk, J. and Vos, J.G., *Acta Cryst. C*, **1989**, *45*, 381.

19. Hage, R., Haasnoot, J.G., Nieuwenhuis, H.A., Reedijk, J., De Ridder, D.J.A. and Vos, J.G., *J. Am. Chem. Soc.*, **1990**, *112*, 9245.

20. Browne, W.R., Hesek, D., Gallagher, J.F., O'Connor, Killeen, J.S., Aoki, F., Ishida, H., Inoue, Y., Villani, C. and Vos, J.G., *J. Chem. Soc., Dalton Trans.*, **2003**, 2597.

21. Guckian, A.L., PhD Thesis, **2002**, Dublin City University.

22. Buchanan, B.E., Wang, R., Vos, J.G., Hage, R., Haasnoot, J.G. and Reedijk, J., *Inorg. Chem.*, **1990**, *29*, 3263.

23. Barigelletti, F., De Cola, L., Balzani, V., Hage, R., Haasnoot, J.G., Reedijk, J. and Vos, J.G., *Inorg. Chem.*, **1989**, *28*, 4344.

24. Hage, R., Haasnoot, J.G., Stufkens, D.J., Snoeck, T.L., Vos, J.G. and Reedijk, J., *Inorg. Chem.*, **1989**, *28*, 1413.

25. Hughes, H.P. and Vos, J.G., *Inorg. Chem.*, **1995**, *34*, 4001.

26. Keyes, T.E., Weldon, F., Müller, E., Pechy, P., Grätzel, M. and Vos, J.G., *J. Chem. Soc., Dalton Trans.*, **1995**, 2705.

27. Coates, C.G., Keyes, T.E., McGarvey, J.J., Hughes, H.P., Vos, J.G. and Jayaweera, P.M., *Coord. Chem. Rev.*, **1998**, *171*, 323.

28. Hage, R., Dijkhuis, A.H.J., Haasnoot, J.G., Prins, R., Reedijk, J., Buchanan, B.E. and Vos, J.G., *Inorg. Chem.*, **1988**, *27*, 2185.

29. Hage, R., Haasnoot, J.G., Reedijk, J., Wang, R. and Vos, J.G., *Inorg. Chem.*, **1991**, *30*, 3263.

30. Coates, C.G., Keyes, T.E., Hughes, H.P., Jayaweera, P.M., McGarvey, J.J. and Vos, J.G., *J. Phys. Chem. A*, **1998**, *102*, 5013.

31. Nieuwenhuis, H.A., Haasnoot, J.G., Hage, R., Reedijk, J., Snoeck, T.L., Stufkens, D.J. and Vos, J.G., *Inorg. Chem.*, **1991**, *30*, 48.

32. Browne, W.R., O'Boyle, N.M., Henry, W., Guckian, A.L., Horn, S., Fett, T., O'Connor, C.M., Duati, M., De Cola, L., Coates, C.G., Ronayne, K., McGarvey, J.J. and Vos, J.G., manuscript in preparation.

33. Guckian, A.L., Doering, M., Ciesielski, M., Walter, O., Hjelm, J., O'Boyle, N.M., Henry, W., Browne, W.R., McGarvey, J.J. and Vos, J.G., *J. Chem. Soc., Dalton Trans.*, **2004**, in press.

34. Hage, R., Prins, R., Haasnoot, J.G., Reedijk, J. and Vos, J.G., *J. Chem. Soc., Dalton Trans.*, **1987**, 1389.


we now return to our feature documentary: "The Grad Student: Call of the Wild"...
THOUGH A SIMPLE CREATURE, THE GRAD STUDENT HAS A COMPLEX FEEDING CYCLE...
ALWAYS HUNGRY, THE GRAD STUDENT PREYS UPON THE OCCASIONAL HERD OF PEOPLE CHATTING, SIGNIFYING WHAT ARE KNOWN AS "HAPPY HOURS" OR "SOCIAL EVENTS."
A MASTER OF CAMOUFLAGE, THE GRAD STUDENT EASILY BLENDS IN AND GORGES ON ITS SOLE SOURCE OF NUTRITION: A SUBSTANCE CALLED "FREE FOOD."
HAVING FEASTED, THE GRAD STUDENT ENTERS A LETHARGIC STATE CALLED "RESEARCHING", IN ANTICIPATION OF THE NEXT FREE MEAL.
when we return: the Grad Student's Mating Habits!
HTTP://phd.stanford.edu
JORGE CHAM ©THE STANFORD DAILY

Chapter 5

Density Functional Theory study of the Raman frequencies of $[Ru(2,2'\text{-bipyridyl})_3]^{2+}$

This chapter examines the dependence of calculated Raman frequencies on basis set size, integration grid, and solvent model. The prototype ruthenium polypyridyl complex, $[Ru(2,2'\text{-bipyridyl})_3]^{2+}$, is used for these studies. The effect of deuteration on the Raman frequencies is also investigated and a novel technique is presented for correlating peaks in the spectrum of an undeuterated complex and its perdeuterated analogue. The larger 6-31G(d) basis set did not give results significantly different from the LanL2DZ basis set, although the calculation took 1.5 times as long. The use of the default 'FineGrid' in Gaussian03 gave results almost identical to those obtained using the 'Ultrafine' grid, although the calculation took 1.5 times as long. Although the Onsager model may be used for molecules with a dipole moment, the use of more sophisticated treatments for solvent effects is not a straightforward process for ruthenium polypyridyl complexes.

5.1 Introduction

Density functional theory has been shown to be a major aid in the study of the properties of a variety of molecules. In particular, it scales well with the size of the system, thus allowing study of large molecules where the traditional *ab initio* approach is prohibitively expensive. Density functional theory is of particular interest to the inorganic chemist, as it can accurately calculate electronic transitions by means of a time-dependent approach. For example, it can provide information on the nature of charge transitions between metal centres and ligands.

Much less studied, however, is its ability to calculate Raman frequencies. In this study, the Raman frequencies of $[Ru(2,2'\text{-bipyridyl})_3]^{2+}$, **trisbpy** (Figure 5.1), are calculated using the DFT functional B3LYP. The B3LYP hybrid functional has been shown to obtain accurate vibrational frequencies. In a study[1] of calculated vibrational frequencies for 122 organic molecules using a variety of computational methods, B3LYP, B3PW91 and HF using 6-31G(d) outperformed the other methods. In other studies on furan and thiophene[2], and triazole and tetrazole[3], B3LYP gave the lowest average error.

Trisbpy is one of the most widely studied inorganic complexes and its photophysical and photochemical properties are well understood. Although an earlier study[4] successfully assigned the Raman frequencies of trisbpy using an empirical force field, this is the first work to calculate the Raman frequencies of trisbpy using DFT. More recently, Alexander and Dines[5] performed the first full 'Scalable Quantum Mechanics – Force Field' (SQM-FF) normal coordinate analysis of a ruthenium tris-α-diimine, when they studied the tris complexes of 2,2'-bipyrazine and 2,2'-bipyrimidine using B3LYP/LanL2DZ.

We investigate the factors which affect the accuracy of a Raman calculation on a molecule of this size: the size of the integration grid, the basis set, and the inclusion of solvent effects. Deuteration of ligands is a powerful tool for investigating photophysical properties, especially when combined with Raman techniques. The ability of DFT calculations to yield information on the Raman shifts accompanying deuteration will also be examined.

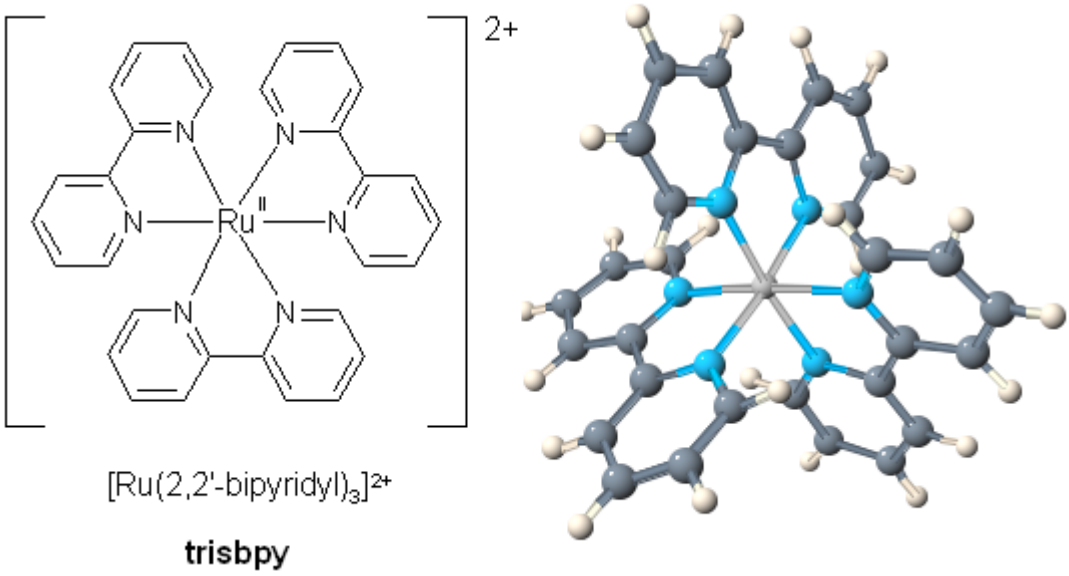

Figure 5.1 – The structure of $[Ru(2,2'\text{-bipyridyl})_3]^{2+}$, trisbpy.

5.1.1 Raman scattering

Raman spectroscopy is based upon Raman scattering, the inelastic scattering of electromagnetic radiation by molecules or atoms in solids, liquids or gases. Raman scattering occurs when photons of light passing through a sample collide with molecules. Two types of Raman transition can then occur (Figure 5.2):

(1) The photons give up some of their energy to the molecules and are scattered in all directions at a lower frequency. This is the Stokes radiation.

(2) The photons receive some energy from excited molecules and emerge at a higher frequency. This is the anti-Stokes radiation.

Since the Stokes radiation is always more intense than the anti-Stokes radiation, it is the Stokes region of the Raman spectrum that is generally studied. The difference between the energy of the incident light and the Raman scattered light is referred to as the Raman shift and is usually reported in wavenumbers, cm^{-1}.

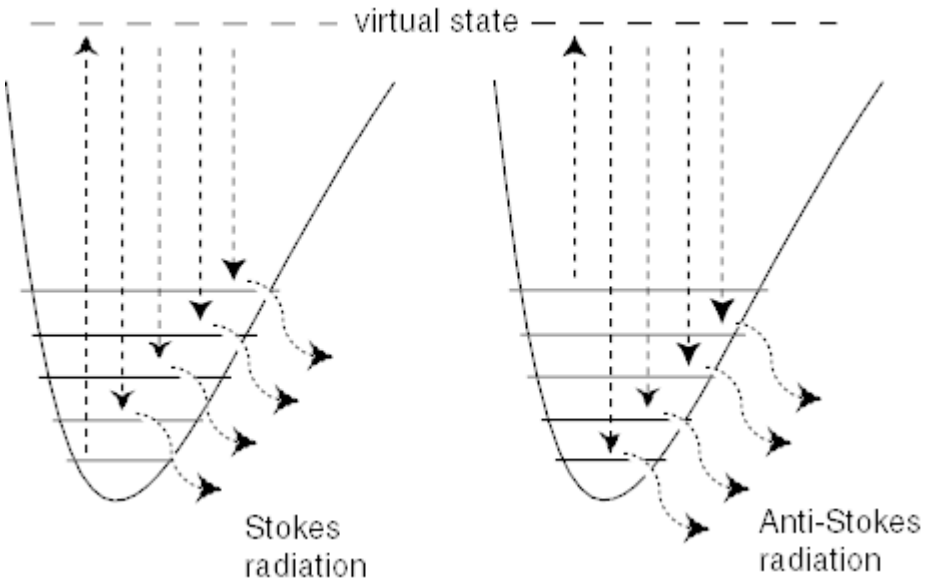

Figure 5.2 – The diagram shows the process by which Raman scattering occurs. Molecules in the vibrational ground state (left) give rise to Stokes radiation, whereas vibrationally-excited molecules (right) give rise to anti-Stokes radiation.

The molecular energy levels involved are vibrational energy levels. The selection rules for Raman transitions are:

(1) a change in the molecular polarisability must occur. The molecular polarisability, α, is a measure of the extent to which an electric dipole can be induced by the electric field of electromagnetic radiation:

$$\mu_i = \alpha E_0 \cos \omega_L t \qquad (5.1)$$

where μ_i is the induced dipole moment, E_0 is the amplitude of the electric field oscillations and ω_L is the frequency of those oscillations.

(2) Raman transitions can only occur between neighbouring vibrational energy levels. That is, they must satisfy $\Delta v = \pm 1$.

5.1.2 Calculation of Raman frequencies and intensities

Vibrational frequencies are calculated by taking the second derivative of the energy with respect to the nuclear coordinates. This method only works at the equilibrium geometry – otherwise, imaginary frequencies are found, corresponding to nuclear displacements that reduce the energy. Calculated harmonic frequencies often differ from experimental vibrational frequencies by a fixed ratio or scaling factor, whose value depends on the basis set used. This is due to consistent underestimation of

bond lengths, for example, and neglect of anharmonicity. Analytical expressions for the second derivative of the energy are used in Gaussian.[6]

If we approximate the potential energy by a second-order Taylor expansion around the stationary geometry in terms of the normal coordinates (**x**), we have:

$$V(\mathbf{x}) \approx V(\mathbf{x}_0) + \left(\frac{dV}{d\mathbf{x}}\right)^t (\mathbf{x}-\mathbf{x}_0) + \frac{1}{2}(\mathbf{x}-\mathbf{x}_0)^t \left(\frac{d^2V}{d\mathbf{x}^2}\right)(\mathbf{x}-\mathbf{x}_0) \qquad (5.2)$$

Since $\mathbf{x}_0$ is a stationary point, the first derivative of the energy (the gradient) is zero. If we take the energy of the expansion point itself to be zero, the energy expression simplifies to:

$$V(\Delta\mathbf{x}) = \tfrac{1}{2}\Delta\mathbf{x}^t\mathbf{F}\Delta\mathbf{x} \qquad (5.3)$$

where **F** is the matrix of force constants, the second derivative of the energy with respect to each of the normal coordinates.

The matrix **F** is then converted to mass-weighted coordinates. Diagonalisation of the resulting matrix gives eigenvectors $\mathbf{q}_i$, the vibrational normal coordinates, and eigenvalues ε_i, related to the vibrational frequencies by:

$$\nu_i = \frac{1}{2\pi}\sqrt{\varepsilon_i} \qquad (5.4)$$

The intensity of an IR absorption is approximately proportional to the change in the dipole moment with respect to a geometry displacement along a normal coordinate. Similarly, Raman intensities depend upon the derivative of the polarisability with respect to a normal coordinate. Since the polarisability is itself the second derivative of the energy with respect to an applied electric field, the Raman intensity is a third derivative property. Gaussian evaluates Raman intensities analytically.[7]

5.1.3 Inclusion of solvent effects

Typically, electronic structure calculations are performed on isolated molecules in the gas-phase. Unfortunately, experimental studies typically involve molecules in solution or in the solid phase. The nature of the solvent can dramatically affect experimental results – for example, solvatochromic shifts of UV-Vis absorption bands. Experimentally, Raman shifts do not show a strong solvent dependence (see, for example, Reiher *et al.*[8]). However, it is important to know whether the

inclusion of solvent effects in Raman frequency calculations improves the accuracy of prediction.

There are a number of approaches to incorporating solvent effects into theoretical calculations. Molecular dynamics methods include explicit solvent molecules, but because of the size of the system, molecular dynamics simulations require the use of force field methods. A less expensive approach would be to explicitly include a small number of solvent molecules, for example, the first solvent shell. This method has a dependence on the number and position of the solvent molecules included.

The most widespread approach is to use a continuum solvent model. No explicit solvent molecules are included. Instead, the solvent is treated as a continuous polarisable medium outside the solvent accessible surface. The Self-Consistent Reaction Field (SCRF) model places the molecule inside a suitably-shaped hole in the medium. The dipole moment of the molecule acts upon the medium, which in turn acts back on the molecule. This process is repeated until the reaction field is self-consistent.

SCRF models differ on how they define the cavity in the medium. The simplest model uses a spherical cavity. This is the Onsager model.[9,10,11] In Gaussian, the molecular volume is computed as the volume inside a contour of 0.001 electrons/bohr^3 density. The recommended radius for the cavity is 0.5Å greater than the radius corresponding to the computed volume, in order to account for the van der Waals radii of the surrounding solvent molecules. The other only required parameter is the dielectric constant of the medium, ε, which is the ratio of the attractive force between two point charges in vacuum and in the medium.

The polarisable continuum model[12] (PCM) allows the construction of cavities with more complicated shapes. The cavities are constructed from overlapping atomic spheres with radii 20% larger than their van der Waals radii. In this way, the shape of the cavity represents the molecular shape much more accurately. The method used in Gaussian03 is referred to as the integral equation formalism of PCM (IEF-PCM) due to the computational method used.[13]

5.2 Method

5.2.1 Calculations

Density functional calculations were carried out using Gaussian03W. The hybrid B3LYP functional was used for all calculations. Two sets of calculations were performed, which will be referred to as **B1** and **B2**. Both **B1** and **B2** used the LanL2DZ basis set and pseudopotential for the Ru atom. For the other atoms, **B1** used the LanL2DZ basis set while **B2** used the 6-31G(d) basis set. An ultrafine quadrature grid was used in both cases (keyword *INT=ULTRAFINE*). Another set of calculations were performed using the same basis set as for **B1**, but using the default fine quadrature grid: these calculations will be referred to as **B1coarse**.

The $[Ru(bpy)_3]^{2+}$ structure was constrained to D_3 symmetry and optimised under tight geometry convergence criteria (keyword *OPT=TIGHT*). Raman frequencies were obtained at the optimised geometry using the same basis set and integration grid as for the geometry optimisation. No imaginary frequencies were found, confirming that, in each case, the geometry was at a minimum. Solvent effects were included for **B2** by carrying out a frequency calculation at the optimised **B2** gas phase geometry using the Onsager model. The solvent used was H_2O, as in the experimental measurements, and a molecular volume of 6.20Å was used (calculated by Gaussian using the *VOLUME* keyword). Results obtained using this method will be referred to as **B2water**.

Frequency calculations were repeated using the *FREQ(READISO,READFC)* keyword to calculate the corresponding vibrational frequencies for the perdeuterated complex, $[Ru([D]_8\text{-}2,2'\text{-bipyridyl})_3]^{2+}$ ($[D_{24}]$-trisbpy). The same force constant matrix was used for both deutomers.

GaussSum[14] was used to extract Raman details and convolute the spectra. The spectra were convoluted using Lorentzian curves of full-width at half maximum of 5 cm^{-1}. The values for the calculated peaks reported in Table 5.5 were taken from the unscaled convoluted spectra.

5.2.2 Scaling of predicted vibrational frequencies

The prediction of vibrational frequencies by either *ab initio* or density-functional methods typically gives harmonic vibrational frequencies larger than the

fundamentals observed experimentally.[15] This is due to the neglect of anharmonicity, the incomplete incorporation of electron correlation, and the use of finite basis sets. Fortunately, for hybrid functionals such as B3LYP, the overestimation of the frequencies is relatively uniform, allowing the use of an empirical scaling factor to correct for this effect.[1]

The scale factor is the ratio of the observed wavenumbers to the calculated wavenumbers, v_{obs}/v_{calc}. Two different methods were used for scaling: a single scale factor for all the wavenumbers[1] (Eq. 5.5), and scale factors which are linearly-dependent on the wavenumbers[16,17,18] (wavenumber-linear scaling method, WLS) (Eq. 5.6):

$$v_{obs} / v_{calc} = c \tag{5.5}$$

$$v_{obs} / v_{calc} = c + d * v_{calc} \tag{5.6}$$

where *c*, *d* are constants.

The best fit of v_{obs} to v_{calc} was obtained by choosing values of *c* and *d* which minimise the root mean-square deviation of v_{obs} from v_{scaled}. This was carried out using the Solver module in Microsoft Excel.

Pulay *et al.*[19] recommend weighting the mean-square deviations by the inverse of the corresponding wavenumber. They describe this method as a compromise between the assumption that every predicted wavenumber has the same absolute error (which would require equal weights) and that they have the same relative error (which would require weights proportional to v^{-2}). For our data, we assumed that the data had the same absolute error. After application of the scaling method, there was no indication that this assumption was invalid.

5.2.3 Experimental

The synthesis of the perdeuterated complex was carried out by Dr. Adrian Guckian, Complex Solutions, Dublin City University.

Ground state Raman measurements were carried out by Mr. William Henry (Dublin City University), with the help of Dr. Kate Ronayne (Queens University of Belfast) and Prof. John J. McGarvey (Queens University of Belfast).

5.3 Results

5.3.1 Geometry and electronic structure

The geometries of the structures were optimised with D_3 symmetry. The optimised Ru-N_{bpy} distance is 2.10Å for **B1** and 2.12Å for **B2**. These values are slightly overestimated compared to the experimental value of 2.06Å found by Rillema *et al.*[20] for $[Ru(2,2'\text{-bipyridyl})_3](PF_6)_2$. A comparison of key geometrical values is shown in Table 5.1. Both the **B1** and **B2** structures are in good agreement with the experimental values, although the pyridine-pyridine dihedral angle is underestimated (1.7° for both **B1** and **B2**, versus 5.9° for the crystal structure).

	Ru-N	N-C	C-C	∠N-Ru-N	∠N-C-C	∠N-C-C-N
Crystal[20]	2.06	1.35	1.47	78.7	114.6	5.9
B1	2.10	1.38	1.48	78.4	115.3	1.7
B2	2.12	1.36	1.48	77.6	115.6	1.7

Table 5.1 – Comparison of selected molecular parameters for the B1 **and** B2 **trisbpy structures and the crystal structures from Ref. 20 (values averaged). All distances are in Å, and all angles are in degrees. N-C, C-C, ∠N-C-C and ∠N-C-C-N are taken from the bridge between two bonded pyridines.**

The electronic structure of **B1** and **B2** trisbpy are shown in Table 5.2 and Table 5.3. These data were convoluted with Gaussian curves of $w_{½}$ of 0.3eV to create the partial density of states (PDOS) spectra in Figure 5.3 and Figure 5.4.

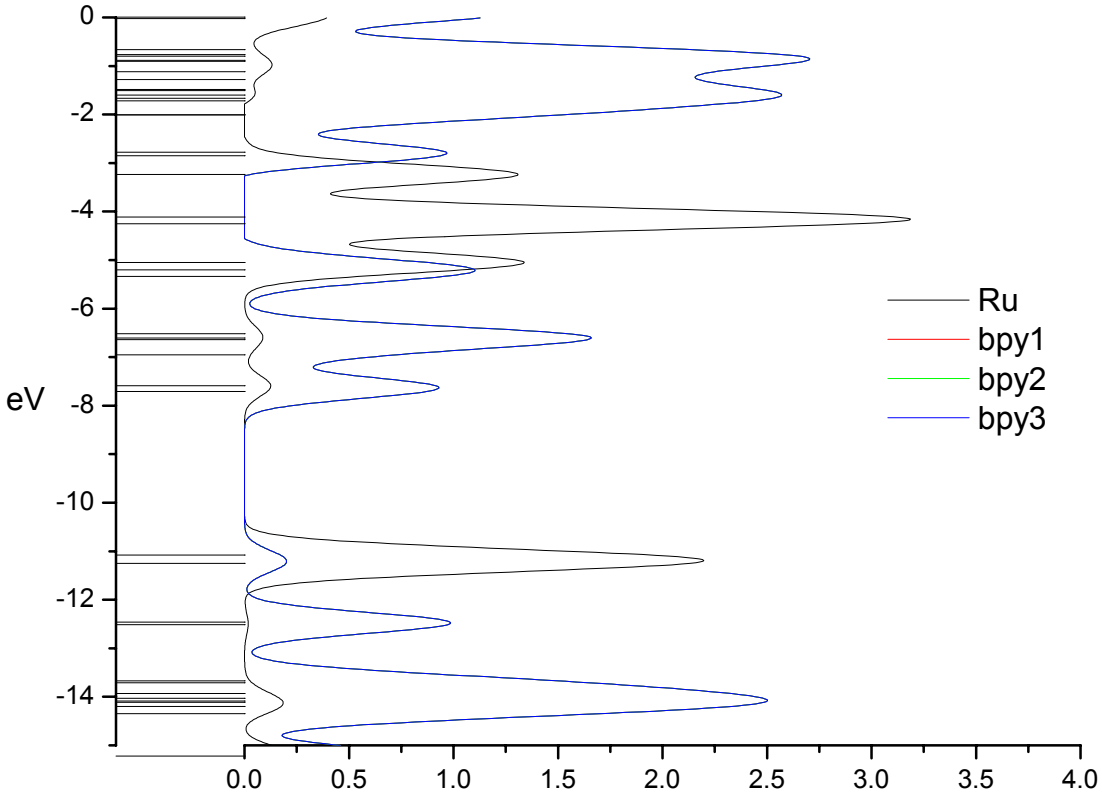

Figure 5.3 – Partial density of states (PDOS) spectra of B1 **trisbpy. PDOS curves for *bpy1* and *bpy2* are underneath the *bpy3* curve, and are not visible as a result.**

Molecular orbital		eV	Symmetry	Ru	bpy1	bpy2	bpy3
141	L+10	-5.20	E	1	0	49	49
140	L+9	-5.34	A1	1	33	33	33
139	L+8	-6.52	E	2	14	42	42
138	L+7	-6.52	E	2	52	23	23
137	L+6	-6.61	A1	3	32	32	32
136	L+5	-6.64	E	2	51	24	24
135	L+4	-6.64	E	2	15	42	42
134	L+3	-6.95	A2	1	33	33	33
133	L+2	-7.59	E	6	62	16	16
132	L+1	-7.59	E	6	0	47	47
131	LUMO	-7.71	A2	0	33	33	33
130	HOMO	-11.08	A1	83	6	6	6
129	H-1	-11.25	E	76	4	10	10
128	H-2	-11.25	E	76	12	6	6
127	H-3	-12.46	E	0	0	50	50
126	H-4	-12.46	E	0	66	17	17
125	H-5	-12.52	A1	1	33	33	33
124	H-6	-13.67	E	0	9	45	45
123	H-7	-13.67	E	0	57	21	21
122	H-8	-13.71	A2	0	33	33	33
121	H-9	-13.93	E	0	1	49	49
120	H-10	-13.93	E	0	65	17	17

Table 5.2 – Molecular orbital data for B1 **trisbpy.**

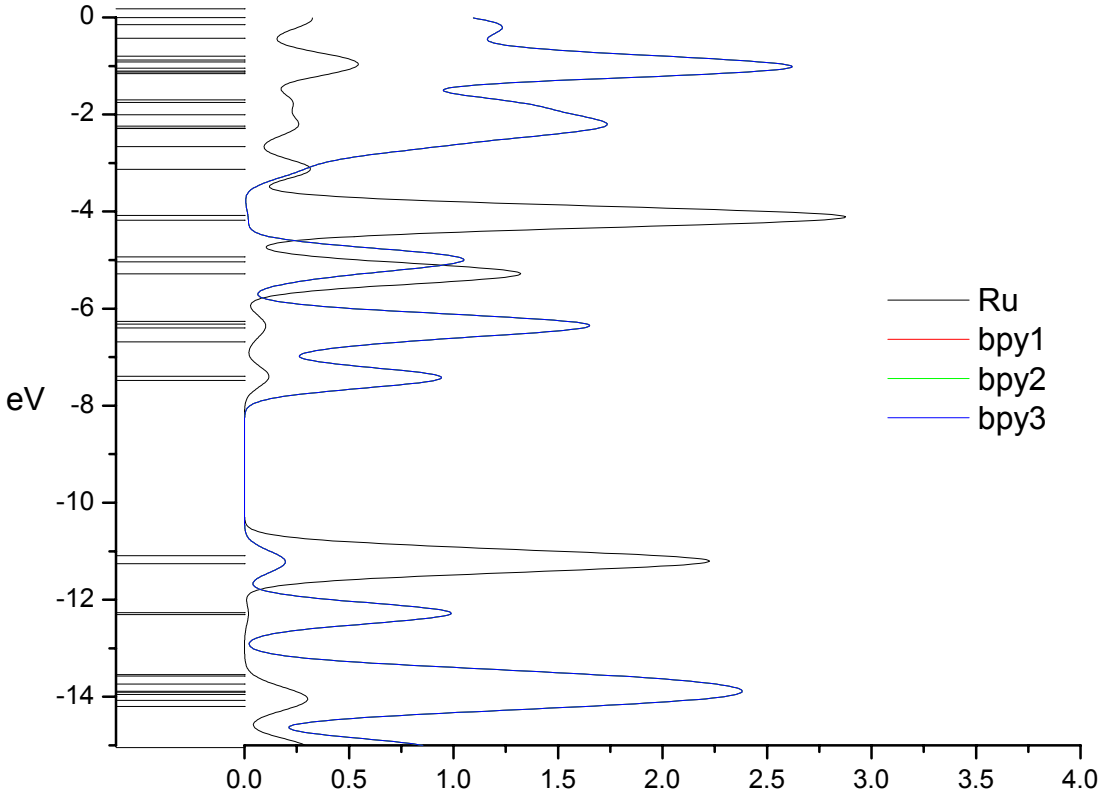

Figure 5.4 – Partial density of states (PDOS) spectra for B2 **trisbpy. PDOS curves for *bpy1* and *bpy2* are underneath the *bpy3* curve, and are not visible as a result.**

Molecular orbital		eV	Symmetry	Ru	bpy1	bpy2	bpy3
141	L+10	-5.28	E	66	12	17	6
140	L+9	-5.28	E	66	11	6	17
139	L+8	-6.26	E	2	32	52	14
138	L+7	-6.26	E	2	34	13	51
137	L+6	-6.32	A1	2	33	33	33
136	L+5	-6.40	E	2	30	52	16
135	L+4	-6.40	E	2	35	13	49
134	L+3	-6.69	A2	2	33	33	33
133	L+2	-7.39	E	5	30	59	5
132	L+1	-7.39	E	5	33	4	58
131	LUMO	-7.48	A2	1	33	33	33
130	HOMO	-11.09	A1	84	5	5	5
129	H-1	-11.26	E	77	7	11	5
128	H-2	-11.26	E	77	8	4	10
127	H-3	-12.26	E	0	27	64	8
126	H-4	-12.26	E	0	39	2	58
125	H-5	-12.31	A1	1	33	33	33
124	H-6	-13.54	E	0	36	51	12
123	H-7	-13.54	E	0	30	15	54
122	H-8	-13.58	A2	0	33	33	33
121	H-9	-13.73	E	1	32	60	7
120	H-10	-13.73	E	1	34	7	59

Table 5.3 – Molecular orbital data for B2 **trisbpy.**

5.3.2 Experimental Raman spectra

Ground state Raman frequencies were obtained for $[Ru(bpy)_3]^{2+}$ and its perdeuterated analogue in H_2O, using a laser wavelength of 457.9nm. The measurements were repeated three times, in order to identify artefacts due to cosmic rays. The spectra obtained are shown in Figure 5.5, and the peaks are listed in Table 5.5. The peaks discussed in this chapter are labelled as in Mallick *et al.*[4], where the same label is used for peaks that correspond to each other.

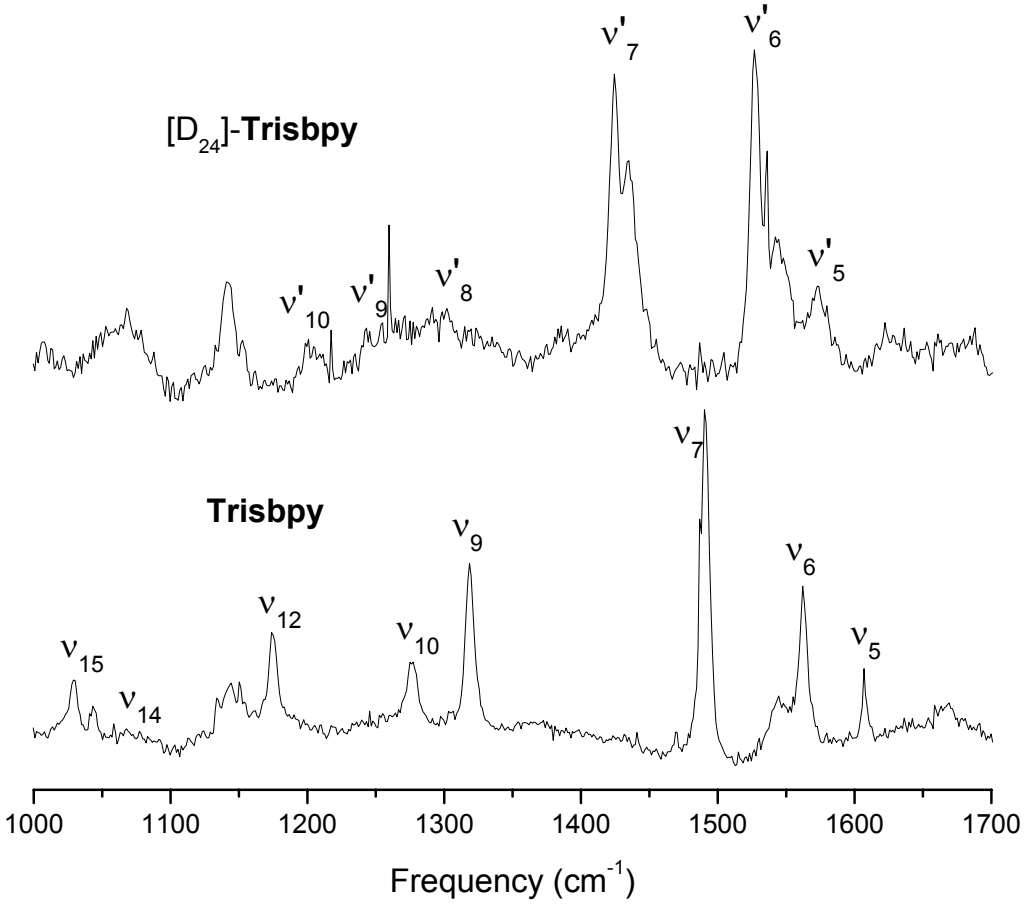

Figure 5.5 – The experimental resonance Raman spectrum of undeuterated and perdeuterated trisbpy. A laser wavelength of 457.9nm was used. The peaks are labelled as in Mallick *et al.*[4]

5.3.3 Group theory analysis

Trisbpy is a molecule of 61 atoms. Since it has 3N-6 vibrational degrees of freedom, there are 177 normal modes of vibration. Using standard group theory methods (see Box 5.1), these modes can be decomposed in terms of the irreducible

representations of the relevant point group. The normal modes of trisbpy, which is of D_3 symmetry, can be broken down as follows:

$$\Gamma_{D_3} = 30\mathrm{A}_1 + 29\mathrm{A}_2 + 59\mathrm{E} \qquad (5.7)$$

Of these, the A_1 and E modes are Raman active, while the A_2 and E modes are IR active.

The vibrational modes of a molecule are found by considering the effect of the symmetry operations on the Cartesian displacement coordinates of each atom of the molecule.

(1) For each of the operations of the point group, the number of unshifted atoms is counted: E, 61; C_3, 1; C_3^2, 1; $3C_2$, 1.
(2) Each of these is then multiplied by a number (E, 3; C_3, 0; C_3^2, 0; $3C_2$, -1) representing the effect of a particular symmetry operation on the combined Cartesian displacement coordinates of an unshifted atom: E, 183; C_3, 0; C_3^2, 0; $3C_2$, -1.
(3) The resulting reducible representation is broken down into a linear combination of reducible representations using the projection operator: $30A_1 + 31A_2 + 61E$.
(4) The translational and rotational degrees of freedom ($2A_2 + 2E$) are subtracted (the reducible representations that these belong to are shown in the point group table by x, y, z and R_x, R_y, R_z respectively): $30A_1 + 29A_2 + 59E$.
(5) The Raman active modes (A_1 and E) are those that transform as xy, yz, xz, x^2, y^2, z^2 or a linear combination thereof (as shown in the point group table): $30A_1 + 61E$.
(6) The IR active modes (A_2 and E) are those that transform as x, y or z: $31A_2 + 61E$.

Box 5.1 – Steps in the calculation of the number and symmetries of the Raman active modes of trisbpy, which has D_3 symmetry.

5.3.4 Predicted Raman frequencies

Predicted harmonic frequencies using **B1** and **B2** are shown in Table 5.5. Fitting constants, *c* and *d*, for the various scaling methods and basis sets, are shown in Table 5.4.

The uniform scaling method uses a single scaling factor for all wavenumbers (Section 5.2.2) and due to its simplicity has been widely used (see for example, ref. 1). When we applied the uniform scaling method to the results obtained using the **B1** and **B2** basis sets, the RMSD was 4.8cm^{-1} for **B1** and 6.1cm^{-1} for **B2**.

Unexpectedly, the smaller **B1** basis set had a better RMSD. The maximum deviation was 12cm^{-1} for **B1** and 11cm^{-1} for **B2**. Almost the same scaling factor was found in each case: 0.978 and 0.974. This value is comparable to that found by Scott and Radom[1], 0.9614, for B3LYP/6-31G(d). The scaled spectra are shown in Figure 5.6 and Figure 5.7, compared to the experimental spectra.

The wavenumber-linear scaling (WLS) can improve the accuracy of scaled frequencies if there is a linear dependence of the scaling factor on the wavenumber (Section 5.2.2). For the **B1** basis set, the following expression gave the lowest RMSD:

$$\nu_{obs} / \nu_{calc} = 0.970 + 5.229 * 10^{-6} * \nu_{calc} \quad (5.8)$$

The scaled frequencies are shown in Table 5.5. This corresponds to a range of scaling factors from 0.975 to 0.979 for the range of wavenumbers 1000cm^{-1} to 1650cm^{-1}. The effect of this more flexible scaling method was a negligible reduction of the RMSD from 4.8cm^{-1} to 4.6cm^{-1}.

Application of the WLS method to the harmonic frequencies calculated with the **B2** basis set gave the following expression for the scaling factors:

$$\nu_{obs} / \nu_{calc} = 0.984 - 6.910 * 10^{-6} * \nu_{calc} \quad (5.9)$$

The scaled frequencies are shown in Table 5.5. The absolute value of *d* (Eq. 5.6) for **B2** is about the same as that for **B1**, but this time it is negative: the best fit is obtained when larger scaling factors are used for lower frequencies (from 0.977 to 0.972 for the range 1000cm^{-1} to 1650cm^{-1}). Again, the RMSD is only slightly reduced by using the WLS instead of a single scaling factor: from 6.1cm^{-1} to 5.7cm^{-1}.

Scaling method	Basis set	Grid	c	d / 10^{-6}
Linear scaling	**B1**	Ultrafine	0.978	–
	B2	Ultrafine	0.974	–
Wavelength linear scaling (WLS)	**B1**	Ultrafine	0.970	5.229
	B2	Ultrafine	0.984	-6.910

Table 5.4 – The best fit values for the scaling factors *c* (Eq. 5.5 and 5.6) and *d* (Eq. 5.6) for the frequencies calculated using B1 **and** B2**.**

	Experimental		Predicted		Linear scaling		Wavelength linear scaling	
		Labels[a]	**B1**	**B2**	**B1**	**B2**	**B1**	**B2**
$[H]_{24}$	1607	ν_5	1641	1651	1604	1608	1606	1605
	1563	ν_6	1596	1616	1560	1574	1562	1571
	1490	ν_7	1526	1531	1492	1491	1493	1490
	1320	ν_9	1357	1344	1327	1309	1326	1309
	1276	ν_{10}	1309	1305	1280	1271	1279	1272
	1175	ν_{12}	1214	1211	1187	1179	1186	1181
	1067	ν_{14}	1093	1092	1069	1063	1067	1066
	1028	ν_{15}	1046	1050	1023	1022	1021	1025
$[D]_{24}$	1574	ν'_5	1605	1610	1569	1568	1571	1566
	1526	ν'_6	1558	1576	1523	1535	1524	1533
	1424	ν'_7	1459	1458	1426	1420	1427	1419
	1304	ν'_8	1330	1345	1300	1310	1300	1310
	1255	ν'_9	1284	1293	1255	1259	1254	1260
	1201	ν'_{10}	1224	1231	1197	1199	1195	1200
	RMSD		31.4	37.1	4.8	6.1	4.6	5.7

Table 5.5 – Comparison of calculated and experimental peaks in the Raman spectrum of $[Ru(2,2'\text{-bipyridyl})_3]^{2+}$. All values are in cm^{-1}. The $[H]_{24}$ section lists peaks for undeuterated trisbpy, while the $[D]_{24}$ section lists peaks for perdeuterated trisbpy. [a]Labels taken from Mallick *et al.*[4]

For comparison with the experimental spectra, the calculated spectra using **B1** and **B2** are shown in Figure 5.6 and Figure 5.7. The calculated spectra are scaled by their respective uniform scaling factors: 0.978 for **B1** and 0.974 for **B2**.

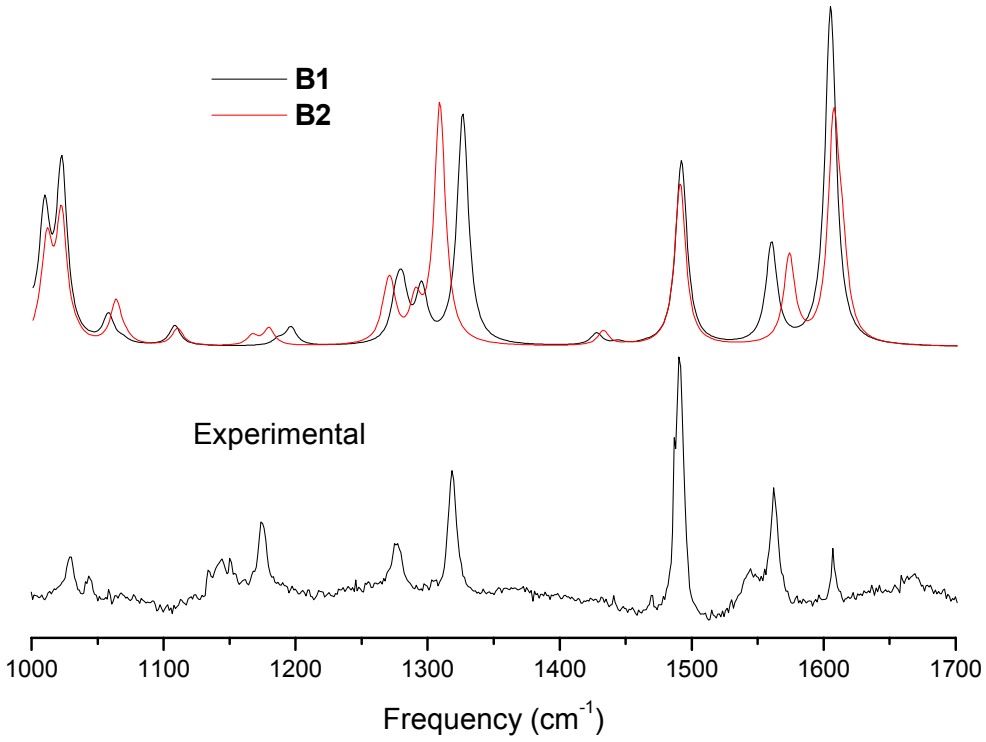

Figure 5.6 – The experimental Raman spectrum of trisbpy compared with the Raman spectra calculated using B1 **and** B2**, scaled by 0.978 and 0.974, respectively.**

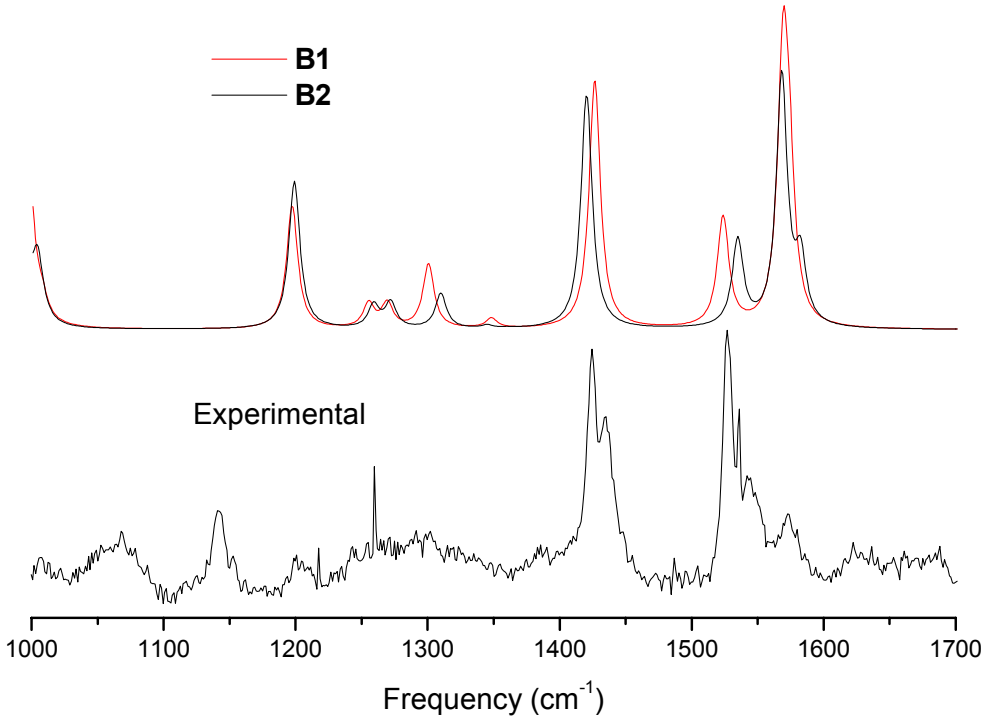

Figure 5.7 – The experimental Raman spectrum of [D_{24}]-trisbpy compared with the Raman spectra calculated using B1 **and** B2**, scaled by 0.978 and 0.974, respectively.**

5.3.5 Effect of deuteration on Raman frequencies

In order to investigate the effect of deuteration on the predicted Raman frequencies of trisbpy, vibrational frequencies using the **B1** basis set were calculated for hypothetical molecules whose hydrogen atoms were replaced with atoms of weight intermediate between hydrogen and deuterium. These atoms are referred to as $^{1.2}$H to $^{1.8}$H in Figure 5.8, where the number in superscript indicates the mass of the atom relative to ^{1}H. This process makes it easy to identify at a glance those peaks in the spectrum of the perdeuterated complex that correspond to particular peaks in the spectrum of the undeuterated complex.

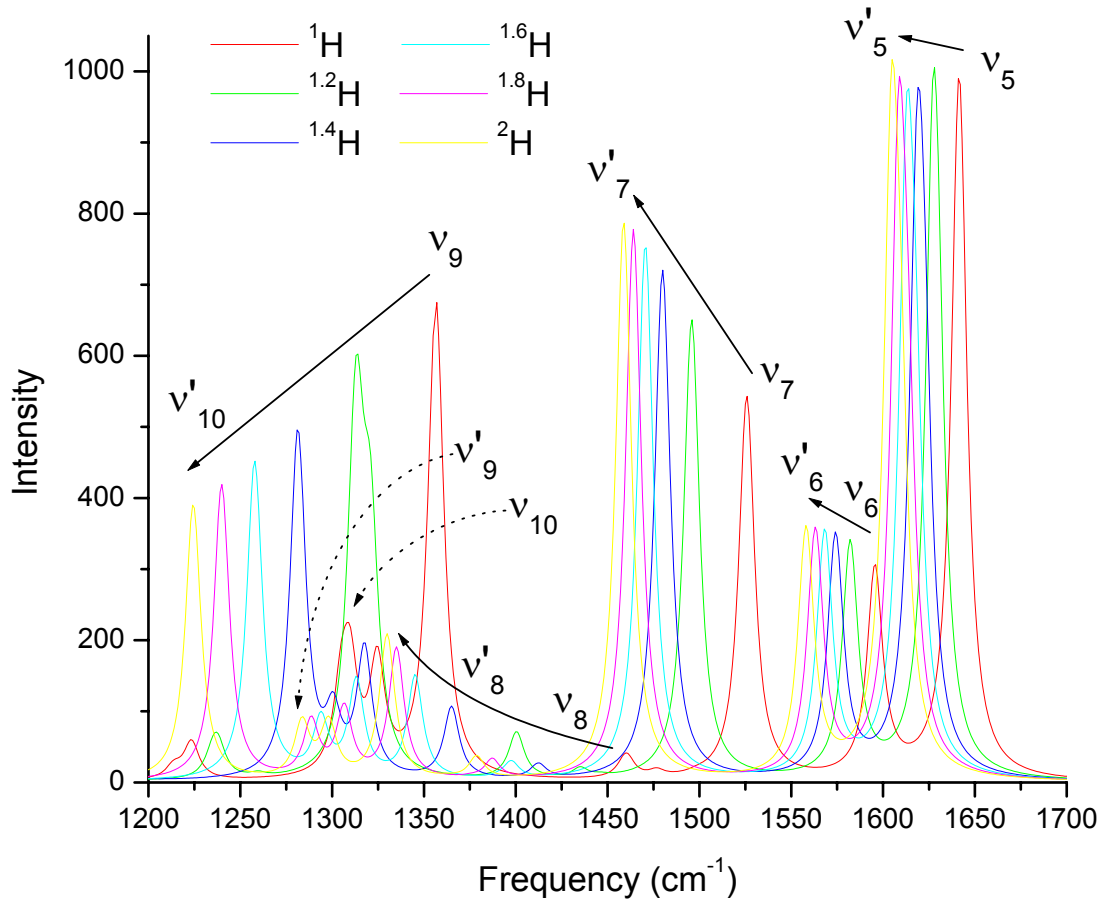

Figure 5.8 – Calculated Raman spectrum for trisbpy created by replacing the hydrogen atoms with atoms of mass intermediate between hydrogen and deuterium. The arrows indicate the shift in intensity and frequency associated with some of the peaks of the undeuterated complex, on replacement of the hydrogen atoms with atoms of increasing mass. The frequencies are unscaled. The peaks are labelled as in Mallick *et al.*[4], with the peaks for the deuterated complex marked by an apostrophe.

Diagrams of the normal mode displacement vectors were created for each of the normal modes corresponding to a peak in the experimental (using the method described in Box 5.2). The results for undeuterated trisbpy are shown in Figure 5.9, and for the deuterated complex in Figure 5.10.

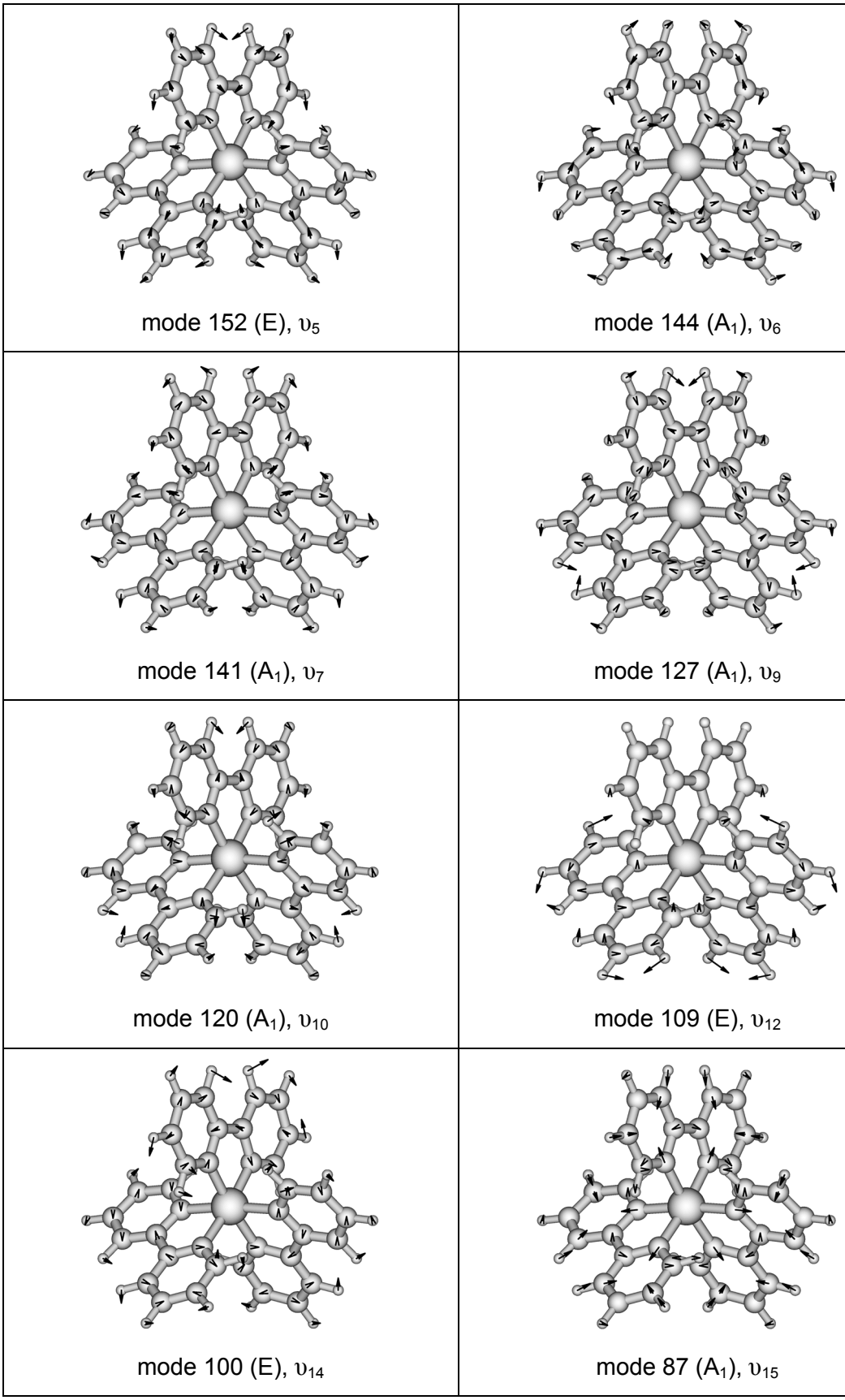

Figure 5.9 – Normal mode displacement vectors for [H_{24}]-trisbpy (calculated using B1**).**

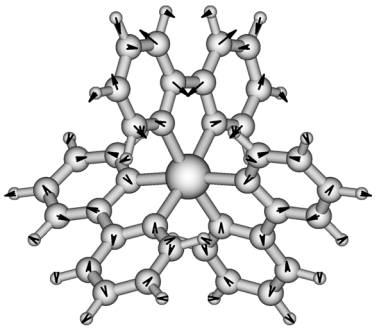

mode 148 (E), υ'_5

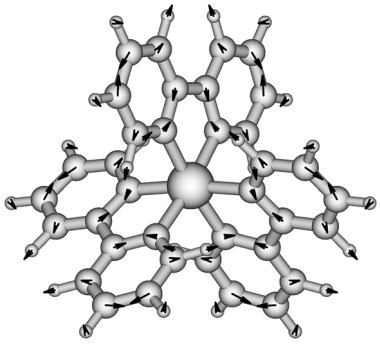

mode 144 (A_1), υ'_6

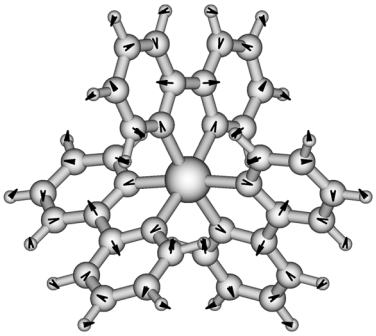

mode 141 (A_1), υ'_7

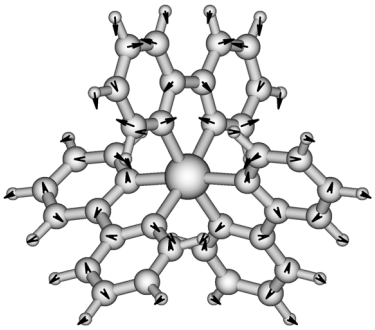

mode 130 (E), υ'_8

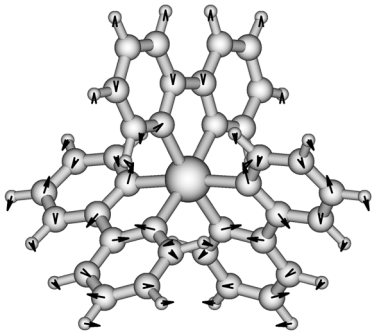

mode 124 (E), υ'_9

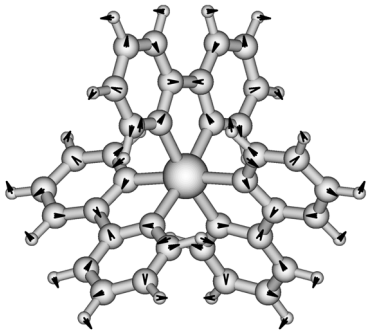

mode 121 (A_1), υ'_{10}

Figure 5.10– Normal mode displacement vectors for [D_{24}]-trisbpy (calculated using B1**).**

The output file of a frequency calculation using Gaussian03 was used to create diagrams of the vibrations using the following steps:

1. dos2unix was used to convert the carriage-returns at the end of each line from DOS format to Unix format. If this step is not carried out, every third vibrational mode is not recognised.
2. The file was opened with Molden 3.9[21] using the following command-line (this applies a scaling factor of 4.0 to all to the normal mode displacements, and only displays arrows for displacements greater than 0.1):

```
molden -y0.1 -s4.0 RuBpy3_freq.out
```

3. Click on Solid/"Ball and Stick".
4. Click on Shade.
5. Click on Normal Mode, close the spectrum window, and chose the appropriate normal mode.
6. Click on Normal Mode again to close the normal mode window.
7. Click on Postscript/Mono and write a filename including the .ps extension.
8. Open the postscript file in Ghostview, File/Convert/pnggray/resolution=300.
9. Click okay, and choose a filename including the .png extension.

Box 5.2 – The method used to create the vibrational diagrams shown in Figure 5.9 and Figure 5.10.

5.3.6 Effect of an increase of the grid size on predicted frequencies

Evaluation of exchange-correlation integrals (see Sections 1.1.4 and 2.2.5) cannot be carried out analytically[22]. In Gaussian03, they are integrated numerically using a quadrature grid. The default quadrature grid is 'FineGrid', a grid defined as having 75 radial shells and 302 angular points per shell. The Gaussian manual[23] recommends use of the 'UltraFine' grid for computing very low frequency modes of molecules. This has 99 radial shells and 590 angular points per shell.

Figure 5.11 shows the Raman spectra calculated with (**B1**), and without (**B1coarse**), the use of an ultrafine grid.

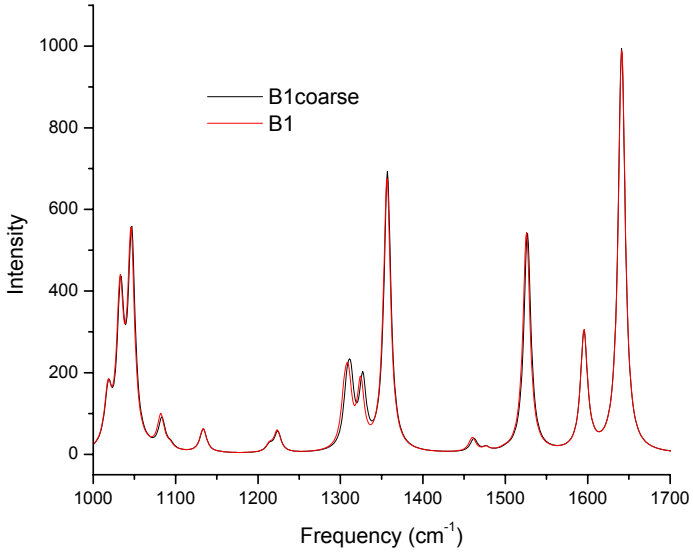

Figure 5.11 – The effect of an ultrafine integration grid on the calculated Raman spectrum (B1**) compared to the default integration grid (**B1coarse**). Frequencies are unscaled.**

Peak values for **B1coarse** are shown in Table 5.7, compared to those for **B1**. Table 5.6 shows the fitting constants for these frequencies.

Scaling method	Basis set	Grid	c	d / 10^{-6}
Linear scaling	**B1coarse**	Fine	0.977	–
	B1	Ultrafine	0.978	–
Wavelength linear scaling (WLS)	**B1coarse**	Fine	0.968	6.552
	B1	Ultrafine	0.970	5.229

Table 5.6 – The best fit values for the scaling factors *c* (Eq. 5.5 and 5.6) and *d* (Eq. 5.6) for the frequencies calculated using B1 **and** B1coarse**.**

		Predicted		Linear scaling		Wavelength linear scaling	
	Labels[a]	**B1coarse**	**B1**	**B1coarse**	**B1**	**B1coarse**	**B1**
$[H]_{24}$	ν_5	1641	1641	1604	1604	1606	1606
	ν_6	1596	1596	1560	1560	1562	1562
	ν_7	1527	1526	1492	1492	1493	1493
	ν_9	1357	1357	1326	1327	1326	1326
	ν_{10}	1311	1309	1281	1280	1280	1279
	ν_{12}	1214	1214	1187	1187	1185	1186
	ν_{14}	1094	1093	1069	1069	1067	1067
	ν_{15}	1047	1046	1023	1023	1021	1021
$[D]_{24}$	ν_5	1605	1605	1569	1569	1571	1571
	ν_6	1558	1558	1523	1523	1524	1524
	ν_7	1459	1459	1426	1426	1426	1427
	ν_8	1330	1330	1300	1300	1299	1300
	ν_9	1284	1284	1255	1255	1254	1254
	ν_{10}	1225	1224	1197	1197	1196	1195
RMSD		31.8	31.4	4.8	4.8	4.6	4.6

Table 5.7 – Comparison of calculated Raman peaks for B1 **and** B1coarse **for trisbpy. All values are in cm^{-1}. The $[H]_{24}$ section lists peaks for undeuterated trisbpy, while the $[D]_{24}$ section lists peaks for perdeuterated trisbpy. [a]Labels taken from Mallick *et al.*[4]**

Assuming **B1** to be the more accurate of the two methods, the error due to **B1coarse** is shown in Figure 5.12 plotted against the **B1** frequencies. A scaling factor of 0.977 was used for **B1coarse** and 0.978 for **B1**. The mean difference, including all of the calculated frequencies, is $0.62cm^{-1}$, which is within experimental error. The largest difference found was just over $2cm^{-1}$.

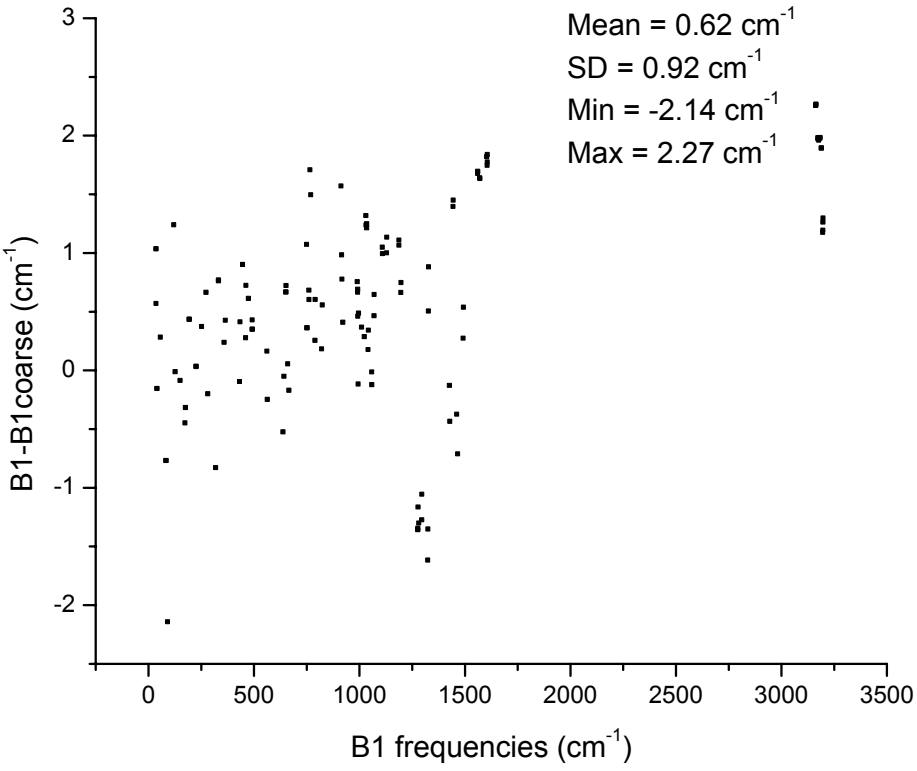

Figure 5.12 – The deviation between the scaled frequencies calculated using B1 **and those calculated using** B1coarse**, plotted against the scaled** B1 **frequencies.**

When comparing normal modes, the assumption was made that the order of the normal modes was the same for **B1** as for **B1coarse**. Comparison of the symmetries of the normal modes showed one instance where neighbouring A1 and A2 vibrational modes had exchanged positions. The effect of this assumption is that the error due to **B1coarse** may have been slightly underestimated.

5.3.7 Inclusion of solvent effects

A frequency calculation was carried out using the **B2** basis set at the optimised geometry in the gas phase, using the Onsager model for modelling the solvent, water. The Onsager model places the solute in a spherical cavity within the solvent reaction field. A molecular volume of diameter 6.20Å was used for the solute, as calculated by Gaussian03 using the VOLUME keyword. This method will be referred to as **B2water**. Figure 5.13 shows the effect of including the solvent on the calculated Raman spectrum.

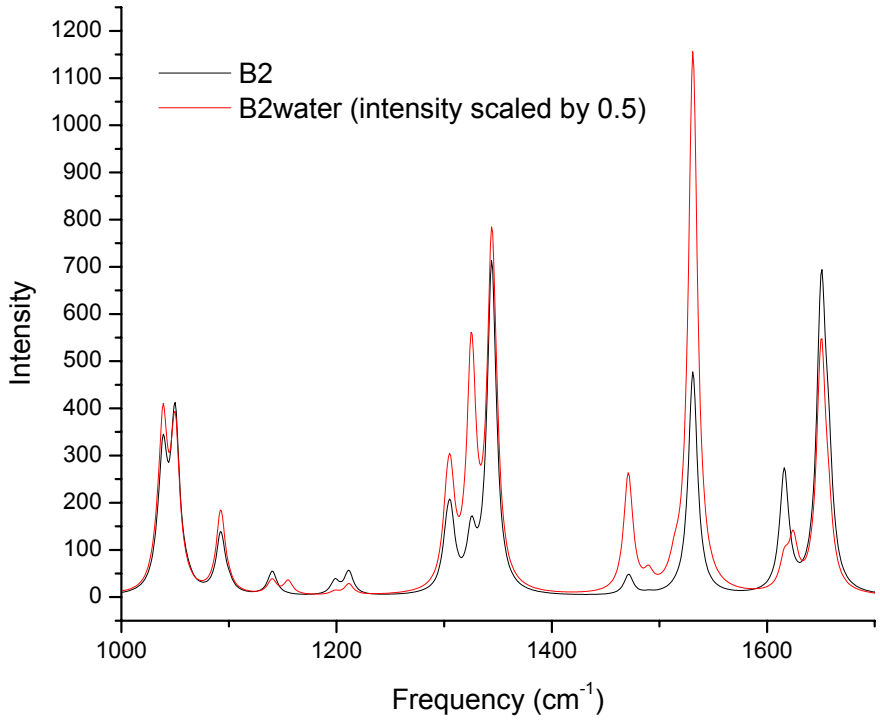

Figure 5.13 – The effect of including solvent effects with the Onsager model on the Raman spectrum calculated using B2

Although the intensities of the peaks have changed dramatically, the frequencies remain largely unchanged. The deviation between the **B2** and **B2water** frequencies is shown in Figure 5.14. They are in excellent agreement – the median (a more robust measurement of the average than the mean, in the case of a skewed distribution) is 0.005cm^{-1}, and even the maximum deviation, 1.1cm^{-1}, is within experimental error.

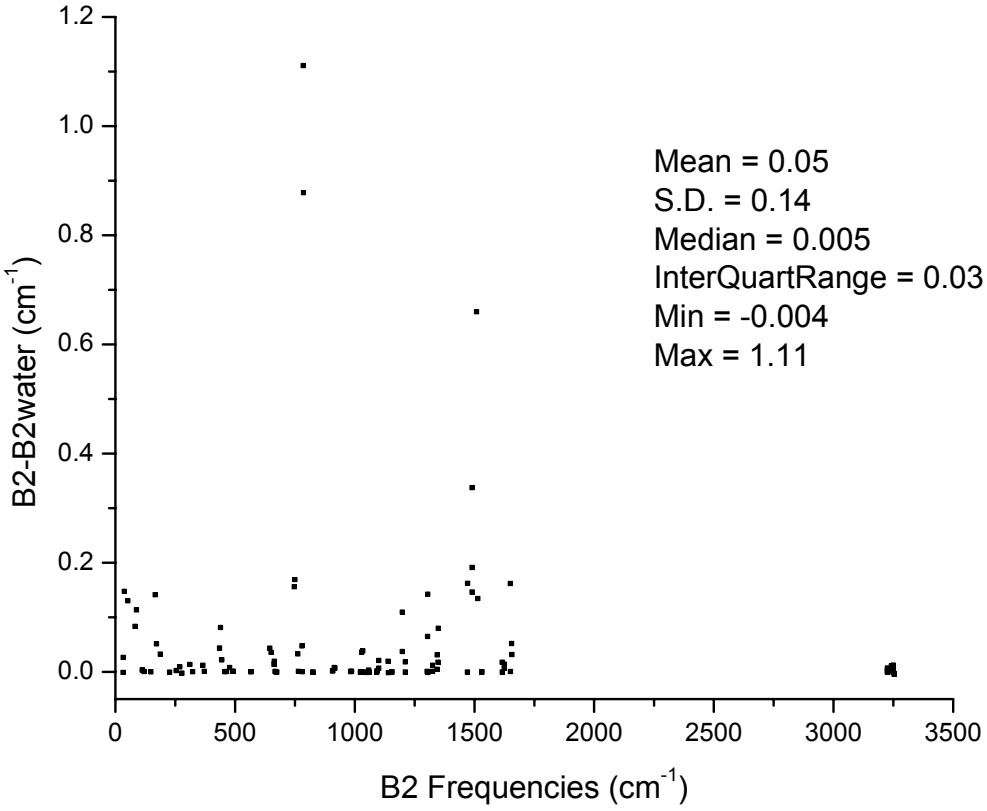

Figure 5.14 – A comparison of the frequency values calculated with and without including solvent effects.

A Raman frequency calculation was also performed using the more sophisticated polarisable continuum model (PCM). The calculation exited with a memory allocation error when the larger basis set **B2** was used, but successfully completed when the smaller basis set **B1** was used, and when the number of tessarae used to approximate the spheres was set to 25 (*TSNUM*=25). However, four imaginary frequencies were found at the gas-phase optimised geometry, indicating that the structure was not at a minimum with respect to the normal coordinates. A geometry optimisation was then carried out using PCM, but it did not reach a minimum – every time the energy appeared to be levelling off, it increased again (see Figure 5.15). In case there was some problem with the guess for the Hessian (for example, if the potential energy surface around the minimum was a long narrow valley), the calculation was continued but with the force constants calculated analytically at each step (keyword *OPT=CALCFC*). Despite this, the same behaviour was observed during the course of the geometry optimisation. As a result, it was not possible to calculate the Raman frequencies using the PCM model.

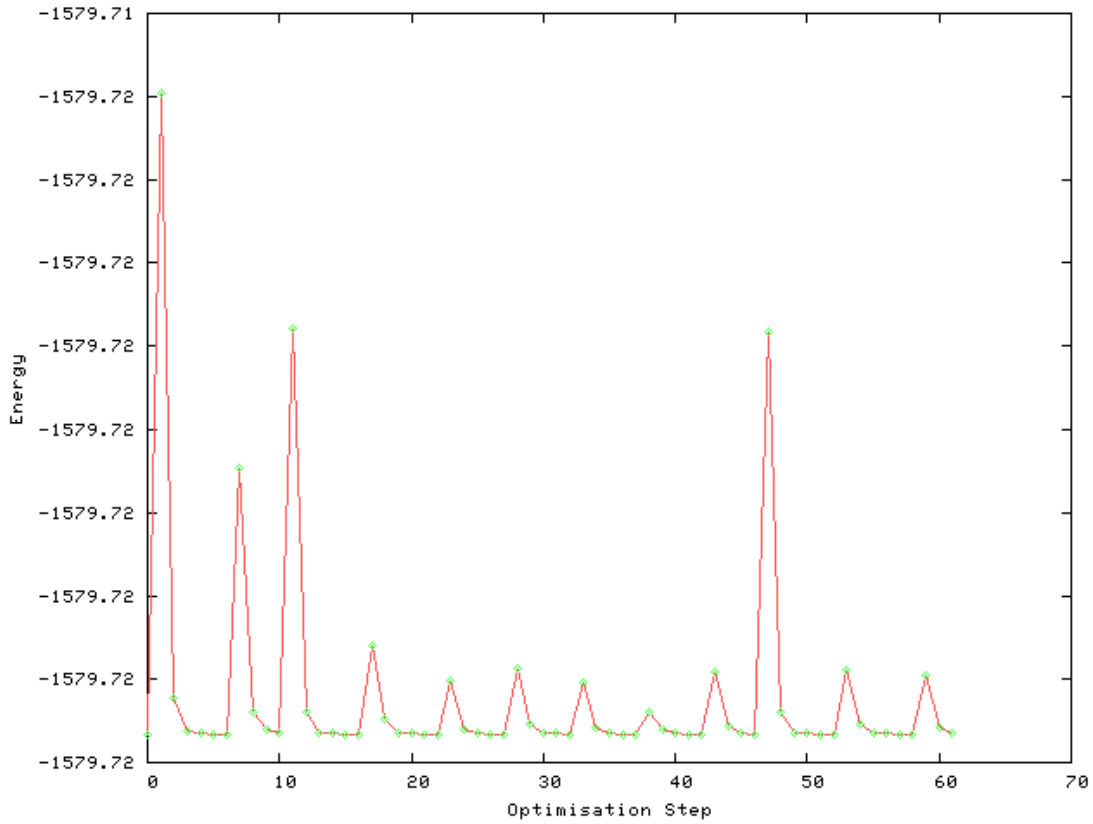

Figure 5.15 – The progress of the geometry optimisation of trisbpy using the PCM model.

5.4 Discussion

5.4.1 Geometry and electronic structure

The optimised geometry for **B1** trisbpy agrees with that found by Gorelsky and Lever[24] who also used **B1** (B3LYP/LanL2DZ). In addition, their molecular orbital data is identical to that obtained by us. The Ru-N_{bpy} distance is slightly overestimated (0.04Å for **B1**, 0.06Å for **B2**) compared to the crystal structure, but is otherwise in very good agreement.

The three bipyridine ligands are equivalent due to the D_3 symmetry – as a result, only a single curve for bpy is visible in the PDOS spectrum (Figure 5.3 and Figure 5.4). Note that this equivalence is not immediately clear from the molecular orbital information (Table 5.2). The HOMO, HOMO-1 and HOMO-2 are all metal-based,

whereas the lowest unoccupied molecular orbitals are bipyridine-based. As a result, the lowest-energy electronic transition is expected to be a metal-to-ligand charge transfer (MLCT). The PDOS for both basis sets are very similar, the only noticeable difference being a slight shift to lower energy (less than 0.2eV) of the bipyridine peaks in the case of **B1**.

5.4.2 Experimental Raman frequencies

The experimental spectra obtained (Figure 5.5) are ground state resonance Raman spectra. The resonance Raman effect occurs when the frequency of the incident laser light is at the same energy as an electronic transition of the molecule. The intensity of vibrations involving the chromophore may be increased by up to 10^6 times.

Trisbpy absorbs at the laser wavelength of 457.9nm, and as a result, a resonance Raman spectrum is obtained. It might be expected the intensity of all of the ligand-based Raman vibrations would be enhanced equally, since they all involve the chromophore. However, as Mallick *et al.*[4] point out, the relative intensities of the peaks are different when the sample is excited by 363.8nm laser light, compared to 457.9nm light. Since the calculations do not take into account the resonance Raman effect, it is expected that even in the limit of a complete basis set, the calculated intensities will not agree with the experimental intensities.

The experimental Raman frequencies for the undeuterated and fully deuterated complexes listed in Table 5.5 agree with those found by Dallinger and Woodruff[25], and Kincaid *et al.*[4,26,27]. Correlated peaks (peaks due to the same normal mode) in the two spectra show a shift to lower frequency for the deuterated complex. This effect to due to the increased mass of the deuterium atom compared to the hydrogen atom. This is discussed further below.

5.4.3 Effect of basis set on predicted Raman frequencies

Raman frequencies were calculated using two different basis sets: **B1** and **B2**. Both **B1** and **B2** use the LanL2DZ basis set and pseudopotential for the ruthenium atom. For all other atoms, **B2** used 6-31G(d) while **B1** uses the Dunning/Huzinaga basis set. These basis sets are described in Chapter 2. They are both valence double-zeta, although 6-31G(d) is slightly larger: in this study, **B1** consists of 394 basis

functions composed of 1046 primitive gaussians while **B2** uses 574 basis functions composed of 1154 primitive gaussians. The frequency calculations using **B2** took 1.5 times those using **B1**.

The combination of B3LYP/6-31G(d) is recommended for the calculation of vibrational frequencies.[1] On the other hand, the **B1** basis set has been widely used in the theoretical study of Ru polypyridyl molecules. For example, several groups have successfully used B3LYP/LanL2DZ calculations to model the electronic transitions of Ru complexes.[28,29,30]

After scaling with a single scaling factor (0.978 for **B1** and 0.974 for **B2**, Table 5), the calculated peaks agreed well with the experimental peaks (Table 5): the RMSD was 4.8cm^{-1} for **B1** and 6.1cm^{-1} for **B2**. A statistical analysis of the **B1** and **B2** frequencies was carried out with the help of Dr. Avril Coghlan, University College Dublin. The hypothesis was that the correlation between the scaled **B2** frequencies and experiment (correlation coefficient r=0.9997), was different than the correlation between the scaled **B1** frequencies and experiment (r=0.9995). The difference was not found to be significant (P=0.7) using Steiger's t-test[31] for comparing non-independent correlations. However, the power of the statistical test was low due to the small sample size of 14 points.

Neither the **B1** frequencies nor the **B2** frequencies show a strong linear dependence on the wavenumber. However, the fact that **B1** frequencies and **B2** frequencies have opposite signs for the wavenumber dependence suggested that the mean of the predicted frequencies might scale better than either on their own. The RMSD of the means was 3.6 cm^{-1}, a significant improvement on both **B1** and **B2**, with a scaling factor of 0.976. However, since using two basis sets takes twice as long as using only one, this approach is not very practical.

DFT methods converge more quickly than *ab initio* methods with respect to basis set size. This means that a modest basis set size is usually sufficient to obtain accurate results using DFT. Studies on the effect of basis set size on calculated vibrational frequencies have shown that the size of the basis set has only a small effect, even when the basis set size is increased from 6-31G(d,p) to aug-cc-pVDZ[3], and from 6-31G(d) to TZ2P.[32] However, when the basis set is reduced to 3-21G, the predicted frequencies are of much poorer quality.[32] Our results agree with the results of these

studies: the predicted frequencies obtained using the larger **B2** basis set are not significantly different than those obtained using **B1**.

The only other study this author could find that calculated the vibrational frequencies of a ruthenium polypyridyl complex using DFT is a scaled quantum mechanical normal coordinate analysis by Alexander and Dines[5] on the vibrational frequencies of $[Ru(2,2'\text{-bipyrazine})_3]^{2+}$ and $[Ru(2,2'\text{-bipyrimidine})_3]^{2+}$. The functional used was B3LYP and the basis set was LanL2DZ – this is equivalent to the **B1** basis set used in our study. A scale factor of 0.90 was applied to force constants involving motion of hydrogen atoms, and a value of 1.025 applied to all other force constants. Application of a single scale factor, *x*, to all of the force constants is the same as scaling the resulting frequencies by $\sqrt{x}$. This means that if the force constant scaling factors 0.90 and 1.025 were applied to all of the vibrations, the frequencies would be scaled by 0.95 and 1.012, respectively (compared to a value of 0.978 found in our study). The authors do not report the resulting RMSD, although they declare the fit to be highly satisfactory. However, using the data given in the paper, it is possible to calculate the RMSD as 12.8cm^{-1} for the bipyrazine complex, more than twice that obtained in our study using **B1**.

5.4.4 Effect of deuteration on Raman frequencies

The replacement of protons with deuterons leads to a decrease in the vibrational frequencies associated with the movement of these atoms. This is a consequence of the increased mass of the atom. However, as shown by Figure 5.8, the size of the decrease varies for different normal modes. For the shifts highlighted in Figure 5.8, the magnitude varies from 36cm^{-1} to 133cm^{-1}.

The variation in the magnitude of the shifts has lead to some incorrect assignments in the past. The labels used in Figure 5.5 for the Raman frequencies are those used by Mallick *et al.*[4] Figure 5.8 shows that ν_5, ν_6 and ν_7 in the undeuterated and deuterated spectra correspond to each other. However, ν_9 in the undeuterated spectrum corresponds with the peak labelled ν'_{10} in the deuterated spectrum. Knowledge of the correspondence of the peaks for different isotopomers is necessary in order to carry out normal coordinate analysis incorporating data from the different isotopomers.

Examination of the normal mode displacements in Figure 5.9 and Figure 5.10 leads to the same conclusion. Although the displacements of the atoms for ν_5, ν_6 and ν_7 correspond to each other for the undeuterated and deuterated complex, ν_9 does not correspond to ν'_9. In fact, it corresponds to ν'_{10} instead (note that in the diagrams, all of the arrows are pointing in the opposite direction for ν'_{10} compared to ν_9). Furthermore, the symmetry of the ν_9 vibration is A_1, whereas that of ν'_9 is E; ν'_{10} has the correct symmetry (A_1).

5.4.5 Effect of an increase of the grid size on predicted frequencies

The use of the default 'FineGrid' (**B1coarse**) gave fitting constants and peak values almost identical to those obtained using the ultrafine grid (**B1**), although the frequencies show a slightly higher linear dependence on the wavenumber. Nevertheless, the same RMSD is found in both instances. A comparison of all of the calculated frequencies showed that on average the **B1coarse** frequencies were 0.6cm^{-1} larger than the **B1** frequencies, and the maximum difference between the two sets of frequencies was just over 2cm^{-1}.

These results agree with those found by Scott and Radom[1]. They compared a grid with 50 radial shells and 194 angular points with the 'FineGrid' (75 radial shells and 302 points per shell) and found that increasing the size and extent of the grid did not significantly modify either the scaling factor or the RMSD.

The Gaussian manual[23] recommends the use of an ultrafine grid for calculating very low frequency modes. Unless these are of interest, we recommend use of the default quadrature grid. The Raman frequency calculation using the ultrafine grid took 1.5 times as long, and the calculated frequencies were almost identical.

5.4.6 Inclusion of solvent effects

Attempts were made to include solvent effects using either the Onsager model or the more sophisticated polarisable continuum model (PCM). The intensities of the peaks changed dramatically using the Onsager model, but frequencies remained largely unchanged (median increase is 0.005cm^{-1}). No imaginary frequencies were found, which indicated that the structure of the molecule was at a minimum on the potential energy surface (PES). This seemed unusual, since solvation is expected to

perturb the PES. We learnt, after completing these calculations, that an inherent limitation of the Onsager SCRF model is that it only has an effect on molecules with a permanent electric dipole moment.[33] However, only molecules belonging to the point groups C_n, C_{nv} and C_s can have a dipole moment[34]. Unfortunately, as a result the Onsager model does not have an effect on trisbpy, which has D_3 symmetry.

It was not possible to calculate the Raman frequencies of trisbpy using the polarisable continuum model (PCM), due to problems converging the geometry to an energy minimum. The reason for this is unclear. In order to keep the size of the problem as small as possible, the number of tessarae used to approximate the spheres was set to 25 (*TSNUM=25*). This reduced the total number of tessarae from around 4600 to around 1200 (thus requiring less memory). This reduction in the number of tessarae may have been too severe, with the result that the geometry optimisation procedure was unable to converge. Another possible cause of the geometry optimisation problem is that the PCM used a radius of 1.5Å for the ruthenium atom, which is probably an underestimation of the correct value (a value of 1.8Å was used for nitrogen).

Further work needs to be carried out in order to assess whether the use of a solvent model improves the quality of predicted frequencies for ruthenium polypyridyl complexes. Such improvements have been observed by other workers – in the study of the vibrational frequencies of sulfamic acid by Wong *et al.*[11], substantially better agreement with experiment occurred when the Onsager model was used.

5.4.7 Raman intensities and IR intensities

Although the focus of this chapter is on the accuracy of the calculated Raman frequencies, it is worth noting a few points regarding the calculated Raman intensities.

The graphs in Figure 5.6 and Figure 5.7 show that calculation of accurate Raman intensities is difficult. First of all, the calculations fail to take into account the resonance effect, which can increase the intensity of Raman transitions by up to 10^6. In addition, there is a strong basis set effect. In order to adequately describe the polarisability of a molecule, a basis set containing diffuse orbitals is required. The first derivative of the polarisability, which is directly related to the Raman intensity, has an even stronger dependence on the use of such a basis set.

Despite these shortcomings, the peaks in the experimental spectrum are, in general, accompanied by peaks in the calculated spectrum. It must be borne in mind that there are a large number of calculated peaks (about 70) in the range covered by Figure 5.6, and yet only a handful have appreciable intensity.

The use of the Onsager model has a strong effect on the Raman intensities. A plot of the Raman activities of the normal modes of **B2** versus those of **B2water** shows a very low correlation between the two sets (Figure 5.16). Points above the line indicate a larger activity value was obtained for **B2water**. For vibrations 78, 79, 85 and 86, the Raman activity increased 500 times. For other vibrations the Raman activity decreased on going from **B2** to **B2water**: for example, a decrease of almost 120 times was observed for vibrations 4 and 5. Further studies are necessary to investigate whether the use of solvent models improves the intensity of the calculated peaks.

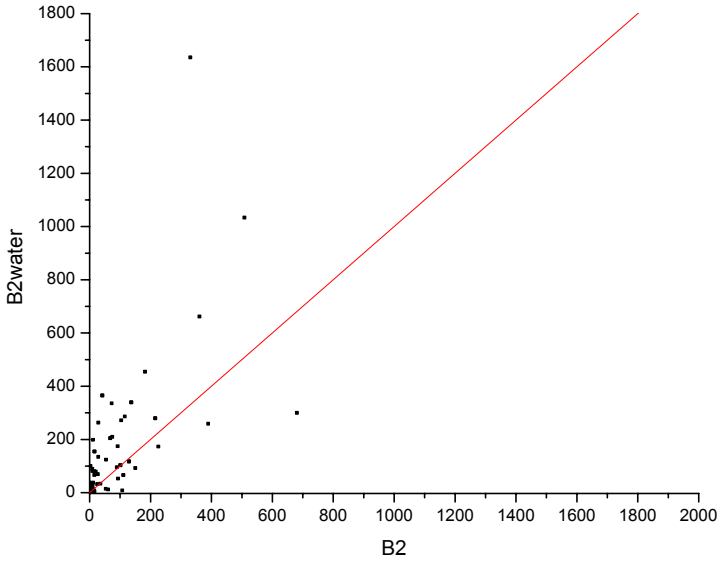

Figure 5.16 – A plot of the Raman activities obtained using B2 **versus those obtained using** B2water

Calculated IR intensities, particularly those calculated using **B2**, seem in much better agreement with experiment than Raman intensities. Figure 5.17 shows the predicted IR spectra using **B1** and **B2**, compared to an experimental spectrum taken from Mallick *et al.*[4]

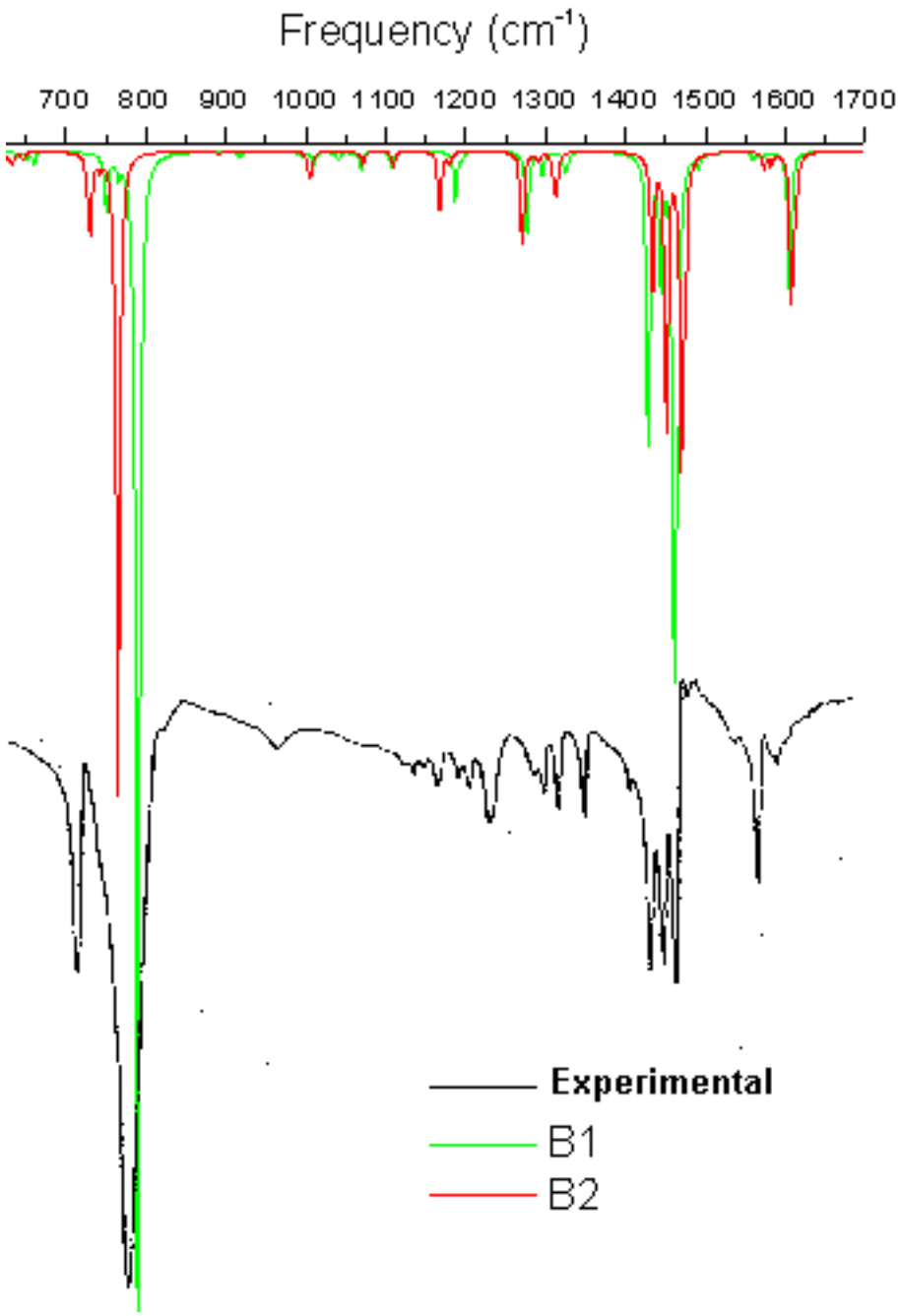

Figure 5.17 – The predicted IR spectra calculated using B1 **and** B2**, compared with the experimental spectrum (taken from Mallick *et al.*[4]).**

5.5 Conclusions

This study creates a baseline for further studies, which will investigate whether the trends observed for Raman frequency calculations on the prototype Ru polypyridyl complex, $[Ru(2,2'\text{-bipyridyl})_3]^{2+}$, are generally applicable to related complexes.

Raman calculations on $[Ru(2,2'\text{-bipyridyl})_3]^{2+}$ give results which agree well with experiment. Although scaling is required, a single scaling factor is sufficient for calculations that use either the LanL2DZ or 6-31G(d) basis sets for the ligands. Although the use of an ultrafine grid and a larger basis set should give better results, the improvement in accuracy was not found to be significant and certainly not worth the extra computation involved. Thus, Raman frequency calculations using the default integration grid and the LanL2DZ basis set for all atoms are recommended for future work.

Further work is required to assess the effect of a solvent model on the computed harmonic frequencies. It should be remembered that the Onsager model is only suitable for molecules with a dipole moment, and that more sophisticated solvent models are memory-intensive.

The related peaks in the Raman spectra of an undeuterated complex and its deuterated analogue can be identified by means of calculations using atoms of fractional masses intermediate between hydrogen and deuterium. This assignment can be confirmed by examination of the symmetries and displacement vectors of the corresponding normal modes.

5.6 References

1. Scott, A.P. and Radom, L., *J. Phys. Chem.*, **1996**, *100*, 16502.
2. El-Azhary, A.A. and Suter, H.U., *J. Phys. Chem.*, **1996**, *100*, 15056.
3. El-Azhary, A.A., Suter, H.U. and Kubelka, J., *J. Phys. Chem.*, **1998**, *102*, 620.
4. Mallick, P.K., Danzer, G.D., Strommen, D.P. and Kincaid, J.R., *J. Phys. Chem.*, **1988**, *92*, 5628.
5. Alexander, B.D. and Dines, T.J., *Inorg. Chem.*, **2004**, *43*, 342.
6. Johnson, B.G. and Frisch, M.J., *J. Chem. Phys.*, **1994**, *100*, 7429.
7. Frisch, M.J., Yamaguchi, Y., Gaw, J.F., Schaefer III, H.F. and Binkley, J.S., *J. Chem. Phys.*, **1986**, *84*, 531.
8. Reiher, M., Brehm, G., and Schneider, S., *J. Phys. Chem. A*, **2004**, *108*, 734.
9. Onsager, L., *J. Am. Chem. Soc.*, **1936**, *58*, 1486.
10. Wong, M.W., Frisch, M.J. and Wiberg, K.B., *J. Am. Chem. Soc.*, **1991**, *113*, 4776.
11. Wong, M.W., Wiberg, K.B. and Frisch, M.J., *J. Am. Chem. Soc.*, **1992**, *114*, 523.
12. Miertus, S., Scrocco, E. and Tomasi, J., *Chem. Phys.*, **1981**, *55*, 117.
13. Cancès, M. T., Mennucci, B. and Tomasi, J., *J. Chem. Phys.*, **1997**, *107*, 3032.
14. GaussSum 0.6, O'Boyle, N.M. and Vos, J.G., **2003**, Dublin City University.
15. Pople, J.A., Schlegel, H.B., Krishnan, R., Defrees, D.J., Binkley, J.S., Frisch, M.J., Whiteside, R.A., Hout, R.F. and Hehre, W.J., *Int. J. Quantum Chem. Symp.*, **1981**, *15*, 269.
16. Kudos, S., Takayangi, M. and Nakata, M., *Chem. Phys. Lett.*, **2000**, *322*, 363.
17. Yoshida, H., Ehara, A. and Matsuura, H., *Chem. Phys. Lett.*, **2000**, *325*, 477.
18. Yoshida, H., Takeda, K., Okamura, J., Ehara, A. and Matsuura, H., *J. Phys. Chem. A*, **2002**, *106*, 3580.
19. Pulay, P., Fogarasi, G., Pongor, G., Boggs, J.E. and Vargha, A., *J. Am. Chem. Soc.*, **1983**, *105*, 7037.
20. Rillema, D.P., Jones, D.S. and Levy, H.A., *J. Chem. Soc., Chem. Commun.*, **1979**, 849.
21. Molden 3.9, Schaftenaar, G. and Noordik, J.H., *J. Comput.-Aided Mol. Design*, **2000**, *14*, 123.
22. Becke, A.D., *J. Chem. Phys.*, **1988**, *88*, 4.
23. Frisch, A., Frisch, M.J. and Trucks, G.W., Gaussian 03 User's Reference, Gaussian, Inc, Carnegie, USA.
24. Gorelsky, S.I. and Lever, A.B.P., *J. Organomet. Chem.*, **2001**, *635*, 187.
25. Dallinger, R.F. and Woodruff, W.H., *J. Am. Chem. Soc.*, **1979**, *101*, 4391.
26. McClanahan, S., Hayes, T. and Kincaid, J., *J. Am. Chem. Soc.*, **1983**, *105*, 4486.
27. Strommen, D.P., Mallick, P.K., Danzer, G.D., Lumpkin, R.S. and Kincaid, J.R., *J. Phys. Chem.*, **1990**, *94*, 1357.
28. Monat, J.E., Rodriguez, J.H. and McCusker, J.K., *J. Phys. Chem. A*, **2002**, *106*, 7399.

29. Zheng, K.C., Wang, J.P., Shen, Y., Peng, W.L. and Yun, F.C., *J. Chem. Soc., Dalton Trans.*, **2002**, 111.

30. Gorelsky, S.I., Lever, A.B.P. and Ebadi, M., *Coord. Chem. Rev.*, **2002**, *230*, 97.

31. Steiger, J.H., *Psych. Bull.*, **1980**, *87*, 245.

32. Stephens, P.J., Devlin, F.J., Chabalowski, C.F. and Frisch, M.J., *J. Phys. Chem.*, **1994**, *98*, 11623.

33. Foresman, J.B. and Frisch, A., *Exploring Chemistry with Electronic Structure Methods*, 2nd Ed., **1996**, Gaussian, Inc., Pittsburgh, USA.

34. Atkins, P.W., *Physical Chemistry*, 6th Ed., **1998**, Oxford University Press, Oxford.


NOEL THESE ARE INTERESTING RESULTS. WE SHOULD TAKE THIS DATA AND TURN IT INTO A PAPER.
REALLY? WE SHOULD?
YES, AND WE SHOULD DO IT SOON, TOO.
GREAT! LET'S DO IT HAN!
BY "WE" YOU ACTUALLY MEAN ME, DON'T YOU?
YES, AND BY "SOON" I ACTUALLY MEAN NOW. SO GET GOING.
JORGE CHAM © 2004
www.phdcomics.com

Chapter 6

DFT study of the adsorption of osmium polypyridyl complexes on a Au (111) surface

This chapter presents the first density functional theory study of an osmium polypyridyl complex attached to a Au (111) surface. The surface is modelled by a cluster of 28 gold atoms. We investigate the nature of the interaction between the complex and the surface, and the effect of adsorption on the electronic energy levels of the osmium complex. Insights from these calculations will help to develop a theoretical model for the current-voltage relationship in in situ *scanning tunnelling microscopy.*

6.1 Introduction

The miniaturisation of electronic components has allowed the semiconductor industry to produce smaller, faster and more efficient components year after year. However, as existing 'top-down' technologies for construction of electronic circuits approach a limit where quantum effects start to interfere, there has been increasing interest in a 'bottom-up' approach, the area of molecular electronics. This refers to controlling charge transfer at the nanoscale level[1], typically by using single or small groups of molecules as components in electronic devices. This idea was first proposed by Aviram and Ratner[2] in 1974. Conventional (*ex situ*) scanning tunnelling microscopy (STM) may be used to measure the current-voltage characteristics of such systems.

In situ STM is a more recent technique that allows an extra degree of control over the redox state of the molecules – the ability to change the potential of the surface with respect to the redox potential of the molecules. It is a scanning probe technique that can be thought of as a combination of a three-electrode electrochemical cell and conventional (*ex situ*) Scanning Tunnelling Microscopy (Figure 6.1). Scanning Tunnelling Microscopy (STM) in general is a surface analysis technique that involves scanning a probe tip across the surface of a conducting sample. The tip does not touch the surface – instead, a current is measured which is created by electrons tunnelling across the gap between the tip and the surface. The direction and magnitude of the tunnelling current are functions of the bias voltage (the potential difference between the sample and the tip) and the distance between sample and tip. The distance between the surface and the tip can be adjusted to keep the tunnelling current constant as the surface is scanned. This allows information on local conductivity to be obtained, which may reflect the topology of the surface.

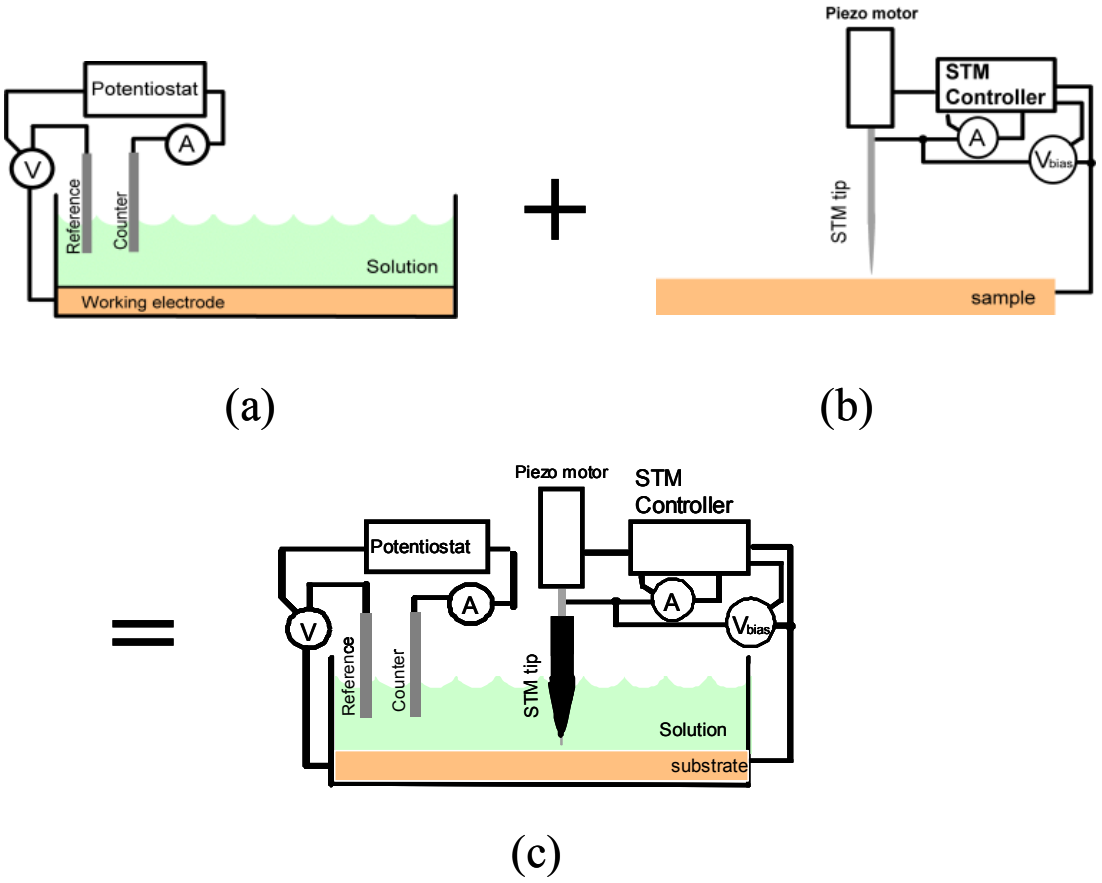

Figure 6.1 – *In situ* STM (c) can be thought of as a combination of a standard electrochemical cell (a) and a conventional (*ex situ*) STM (b). Diagram reproduced from Zhang *et al.*[3d]

In situ STM is performed in a conducting solvent, and the potential of the substrate (the working electrode) can be controlled relative to a fixed potential (the reference electrode). Of particular interest are systems involving assemblies of redox-active molecules attached to the substrate surface, in which case the molecular redox level mediates the electron tunnelling between the tip and substrate[3,4,5]. Ulstrup and Kuznetsov[6,7,8] have developed and extended electron transfer theory to explain the characteristics of tunnelling in such a three-level system (tip Fermi level, molecular redox potential and surface Fermi level).

Our collaborators Prof. Jens Ulstrup and Dr. Tim Albrecht of the Technical University of Denmark are carrying out *in situ* STM studies of a number of osmium polypyridyl complexes. The work described in this chapter describes density functional theory studies of two of these osmium complexes: $[Os(bpy)_2(P0P)Cl]^+$ (**OsP0P**) and

$[Os(bpy)_2(P2P)Cl]^+$ (**OsP2P**), where P0P is 4,4'-bipyridine and P2P is 1,2-Bis(4-pyridyl)ethane (see Figure 6.2). P*n*P will be used to indicate both P0P and P2P.

These complexes are able to form stable monolayers with high coverage on the gold surface. They adsorb through the free nitrogen of the pendant 4-pyridyl of the P*n*P ligand and the monolayers are stable in both the oxidised and reduced forms (Os^{II} and Os^{III}). In addition, their redox potentials are within the stability range of the Au surface and the tip (either W or 80:20 Pt/Ir).

Although the two complexes are structurally and electronically very similar (see below), it is expected that the coupling between the metal centre and the surface will be different for the two complexes, due to the difference in the distance between the metal centre and the surface. In addition, the P0P ligand provides a delocalised π-system for electronic connection between the Os and the surface, whereas the two pyridine rings of P2P are separated by two sp^3-hybridised carbons. As a result, calculations on these molecules should give insight into the mechanism of the electron tunnelling through the molecule.

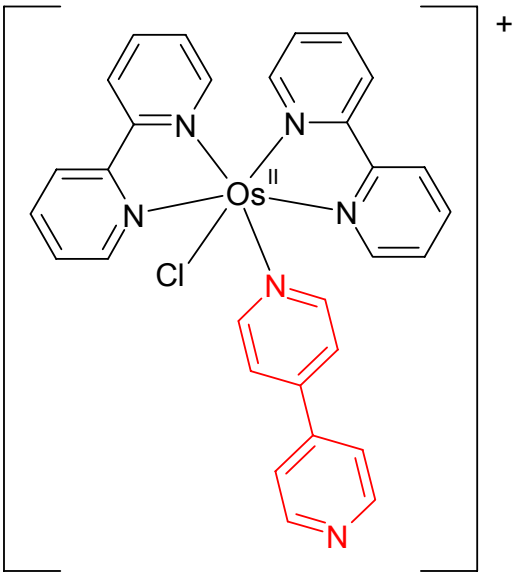

$[Os(bpy)_2(P0P)Cl]^+$

OsP0P

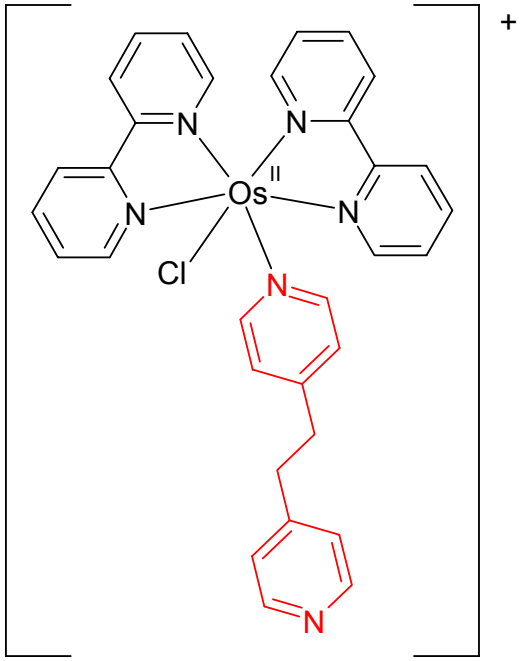

$[Os(bpy)_2(P2P)Cl]^+$

OsP2P

Figure 6.2 – The structures of the two osmium complexes studied in this chapter, OsP0P **and** OsP2P**.**

The results and discussion in this chapter are divided into three sections. The first section deals with the optimisation of the gold cluster (Section 6.2). The next section focuses on the oxidised and reduced forms of the osmium complexes (Section 6.3). Section 6.4 investigates the complexes adsorbed on the gold surface. Finally, some conclusions are presented in Section 6.5.

6.2 The gold cluster

6.2.1 Method

The crystalline form of gold is a cubic close-packed (ccp) structure. The (111) surface cuts along the close-packed planes. In a ccp structure, the planes are arranged ABCABC… (see Figure 6.4). Each atom on the surface is surrounded by 6 atoms on the same plane, and three atoms on the plane below.

A surface can be thought of as the termination of a solid that is infinite along the x and y axes and the negative direction of the z axis, but is finite along the positive direction of the z axis. Some computational chemistry programs deal with the problem of infinite surfaces by using cells of atoms that are repeated infinitely in one or more directions – this is referred to as 'periodic boundary conditions'. The Vienna Ab initio Simulation Package[9] (VASP) and CRYSTAL98[10] are examples of programs that use this method. The problem of an infinite basis set size is tackled using plane-wave basis sets (for example in VASP) or Bloch functions modulated over an infinite lattice (in CRYSTAL98).

This was the approach used by Bilić, Reimers and Hush[11] who investigated the absorption of pyridine on Au(111) using VASP to perform DFT calculations. They applied periodic boundary conditions in all three Cartesian directions to create an infinite array of periodically repeated slabs separated by regions of vacuum. The slabs used were 4 atomic layers thick separated by vacuum with a thickness of 10 atomic layers wide. A pyridine molecule was placed on both sides of the slab, in the centre of a 3 gold atom x 3 gold atom cell which was repeated along the x and y directions. The top and bottom layers of the slab were allowed to relax while the inner layers were held at the bulk positions. The optimised geometry was not reported. In an earlier paper by the same authors[12] on NH_3 adsorption on Au(111)

they use a similar model for the gold surface and report that very little relaxation was observed for the top and bottom surfaces.

Although the latest version of Gaussian, Gaussian03, supports periodic boundary conditions, their use is not straightforward, especially if hybrid functionals are required. As a result, the only viable method for modelling surfaces is to use a 'cluster model'[13]. This is simply a cluster of atoms that is used to represent a portion of the surface and the bulk. Although the cluster model only gives a limited description of the surface band structure, it can be used to investigate local aspects of surface chemistry, including adsorbate-surface interactions.

Gomes and Illas[14] investigated the adsorption of nitromethane and methylnitrite on Au (111). For the surface, they used a cluster model of 22 gold atoms, arranged as two layers of 14 and 8 atoms respectively (Figure 6.3). The LanL2DZ basis set was used for the central 4 atoms of the top layer and 3 atoms from the second layer, while LanL2MB was used for the others. The geometry of the cluster was held fixed at the bulk value.

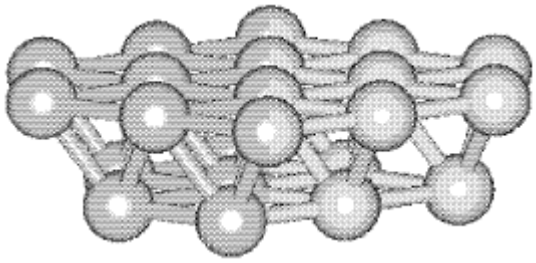

Figure 6.3 – The cluster model used by Gomes and Illas for the Au (111) surface. Taken from Gomes and Illas[14a].

Pluchery *et al.*[15] looked at the adsorption of 4-cyanopyridine on Au (111) using a combination of voltammetry, sum frequency generation (SFG) and DFT calculations. The gold surface was modelled as a cluster of 28 atoms of three layers: 13 atoms in the first layer, 12 in the second and 3 in the final. The internuclear distance was set at 2.884Å and held fixed throughout the calculation. The basis sets and electron core potentials (ECPs, see Section 2.2.2) of the Stuttgart group[16] were used for gold atoms. The central atom of the first layer was modelled with a small core ECP of 60 electrons (similar to LanL2DZ and LanL2MB, see Section 2.2.2), while the other

atoms were modelled with a large core ECP of 78 electrons (leaving only one valence electron).

In an INDO/S study, Reimers *et al.*[17] found little charge rearrangement for the third and subsequent layers after adsorption of $C_2H_2S_2$ on a 143-atom 5-layer gold cylinder. However, significant charge rearrangements were observed for the second layer. On the other hand, according to Bagus and Illas[13], even minimal clusters containing only a small number of substrate atoms are able to properly describe many properties. They state that there is no simple rule for choosing the cluster size, especially if accurate chemisorption energies are required.

Our approach to modelling the gold surface involved the same gold cluster used by Pluchery *et al.*[15]: a Au_{28} cluster consisting of three layers, A, B and C of 13,12 and 3 atoms (Figure 6.4). Clearly, this cluster is of limited size (see Figure 6.7): only one atom has the nine-fold coordination of a surface atom (the central atom of layer A), and there are no atoms with the twelve-fold coordination of bulk gold atoms (although there are 3 with 11-fold coordination). However, in terms of a trade-off between speed and accuracy, this cluster size was considered the minimum necessary to obtain a meaningful result (within a reasonable length of time).

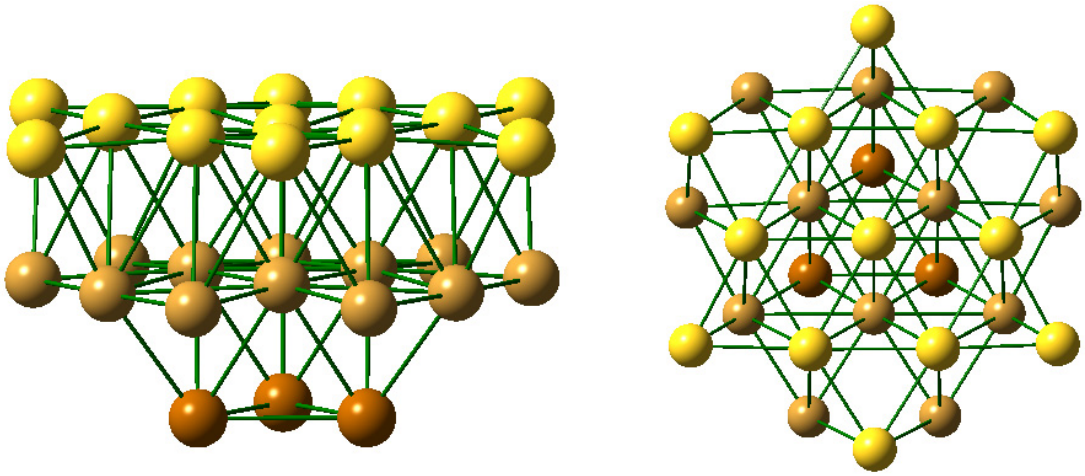

Figure 6.4 – (Left) The structure of the gold cluster used in our analysis, showing the three layers A (yellow), B (brown) and C (brick red) of 13, 12 and 3 atoms, respectively. (Right) The same structure viewed from directly above layer A.

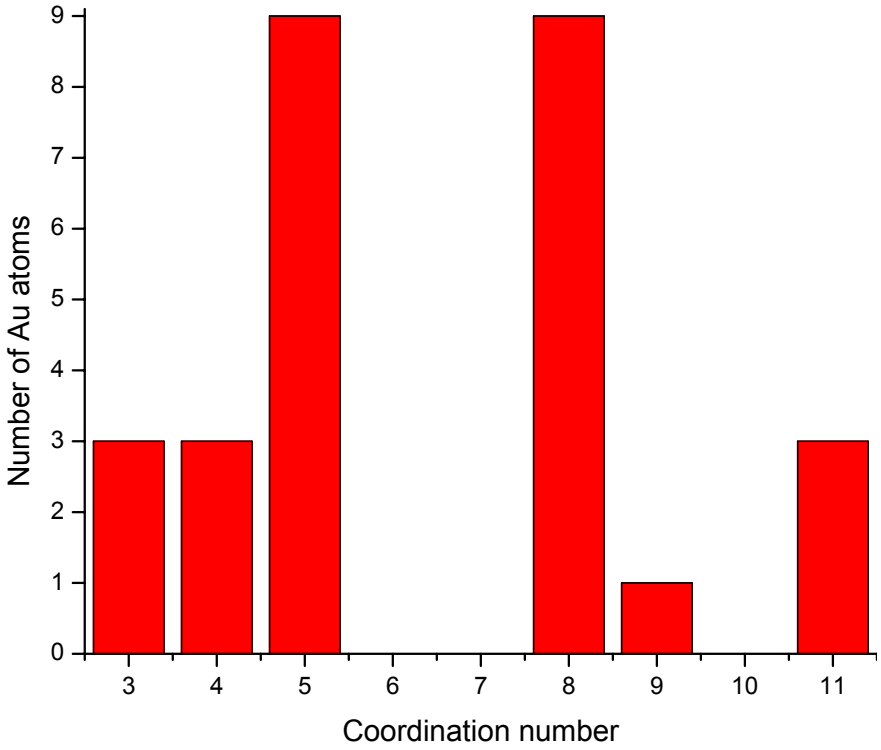

Figure 6.5 – The height of the bar indicates the number of atoms in the Au_{28} cluster which have a particular coordination number (the number of nearest neighbours). Due to the C_{3v} symmetry of the cluster, the height of each bar is a multiple of 3 except for the central atom of layer A, which lies on the C_{3v} axis and has a coordination number of 9.

Since the Au atoms at the centre of layer A will play the most important role in the adsorption process, the LanL2DZ basis and ECP were used for the central atom of layer A and its nearest neighbours (6 from layer A and 3 from layer B, see Figure 6.6). The LanL2MB basis set and ECP were used for all other Au atoms. The difference between the two basis sets is that although both use an ECP for the 60 innermost core electrons, the valence electrons are treated with a double-zeta basis set for LanL2DZ but only a minimum basis for LanL2MB (see also Section 2.2.2). This basis set is similar to that used by Gomes *et al.*[14] and significantly larger than that of Pluchery *et al.*[15].

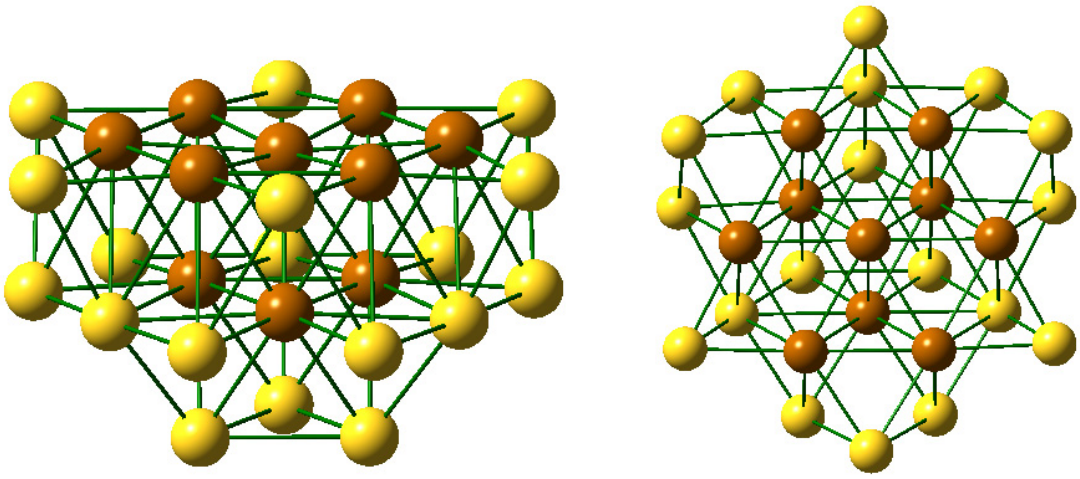

Figure 6.6 – (Left) In our analysis, a larger basis set (LanL2DZ) was used for the valence electrons of the central atom of layer A and its neighbouring atoms (coloured brick red). For the other atoms (coloured yellow), the smaller LanL2MB basis set was used. (Right) The same structure, viewed from directly above layer A.

The structure of the cluster was optimised using B3LYP under C_{3v} symmetry. This differs from the approach of both Pluchery *et al.*[15] and Gomes *et al.*[14], who kept the geometry of the cluster fixed at that of the bulk. Their approach results in the use of a highly strained nanocluster to represent the bulk and surface. Although it takes some time, partial optimisation (that is, within the constraints of C_{3v} symmetry) removes much of the strain and allows the electronic structure of the nanocluster to be represented as accurately as possible within the constraints of the chosen DFT functional and basis set. It is for the same reason that gas-phase electronic structure calculations are carried out on geometry-optimised structures, and not crystal structures.

6.2.2 Results and Discussion

The experimental distance between Au atoms in bulk gold is 2.88Å[18]. The calculated distance between neighbouring atoms in our gold cluster ranges from 2.78Å to 3.14Å, with an average of 2.99Å (see Figure 6.7). This overestimation is partly due to deficiencies in the DFT functional and basis set, but is also due to the low coordination numbers of the atoms (see Figure 6.5), which mean that deviation from results for bulk Au atoms is expected.

Garzón *et al.*[19] found an average nearest-neighbour distance of 2.77Å for a 38-atom gold cluster using DFT within the local density approximation (LDA, see Section 1.1.4). For the same size cluster, Häberlen *et al.*[20] found a value of 2.78Å using LDA, and 2.86Å within the generalised gradient approximation (GGA, see Section 1.1.4). They found a strong correlation between the average coordination number and the average nearest-neighbour distance for a series of clusters of increasing size. The largest cluster studied by Häkkinen and Landman[21] using GGA was Au_{10} for which the average bond length was 2.81Å. Wang, Wang and Zhao[22] looked at trends in the geometrical and electronic structures of gold clusters with 2 to 20 atoms using GGA. They found the average nearest neighbour distance in Au_{20} to be about 2.80Å.

During the course of the geometry optimisation, some movement of the atoms occurred, with the result that neither layer A nor B remained a perfect plane. Although the procedure resulted in a slight dimpling of both of these layers, the overall cluster structure was largely unchanged. This change, from a completely regular lattice to a more disordered structure, is shown in Figure 6.7 by the broadening of each of the histograms peaks. This indicates that the original values of the bond lengths and angles, which were the same for all of the atoms, have been replaced by a spread of values, distributed as shown in Figure 6.7.

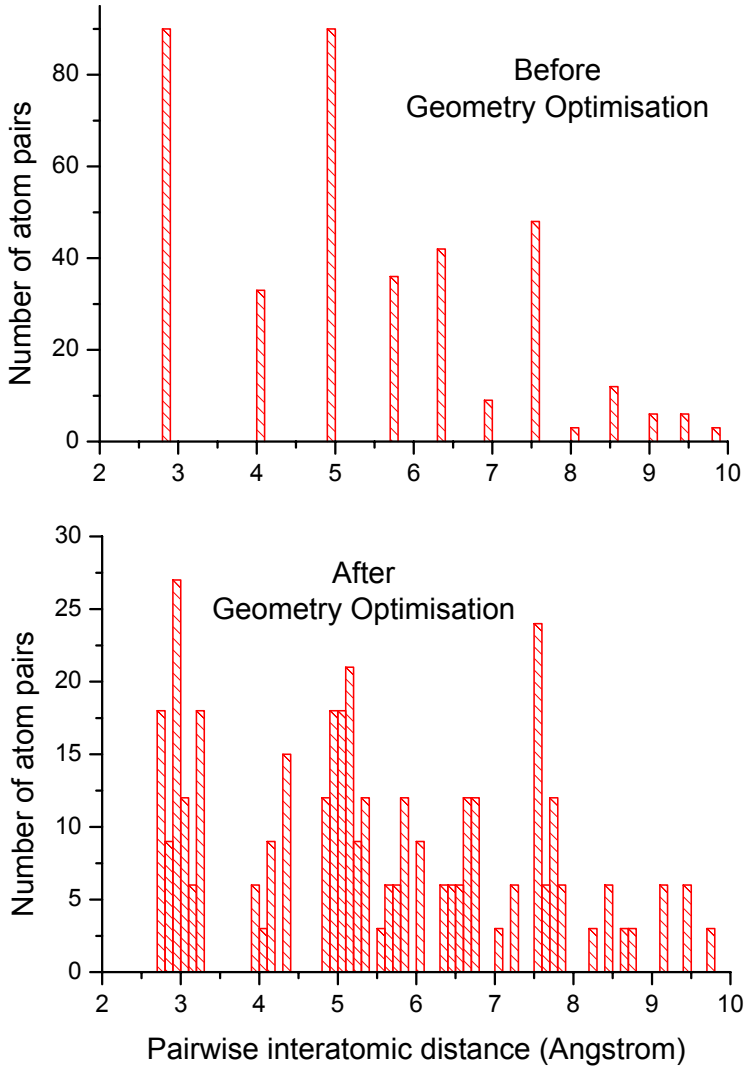

Figure 6.7 – The distribution of pairwise interatomic distances within the gold cluster before (above) and after (below) geometry optimisation. The histogram was constructed using bin sizes of 0.1Å.

The electronic structure and density of states (DOS) spectrum of Au_{28} is shown in Figure 6.8. Bulk metals have a band structure of molecular orbitals. The evolution of this band structure is evident in the occupied portion of the molecular orbitals between about –7eV and –11eV. However, a number of discrete energy levels still exist, especially near the frontier region. A gold cluster of 28 atoms is a nanocrystal, and has electronic properties different from the bulk.[23] Häberlen *et al.*[20] found that, in general, the HOMO/LUMO gap decreased with increasing cluster size. In bulk gold, the HOMO and LUMO converge to the Fermi level, and there is no HOMO/LUMO gap. For our Au_{28} cluster, a HOMO/LUMO gap of 1.0eV was found. This compares with a value of 0.7eV for a gold cluster of 55 atoms studied by Häberlen *et al.*[20].

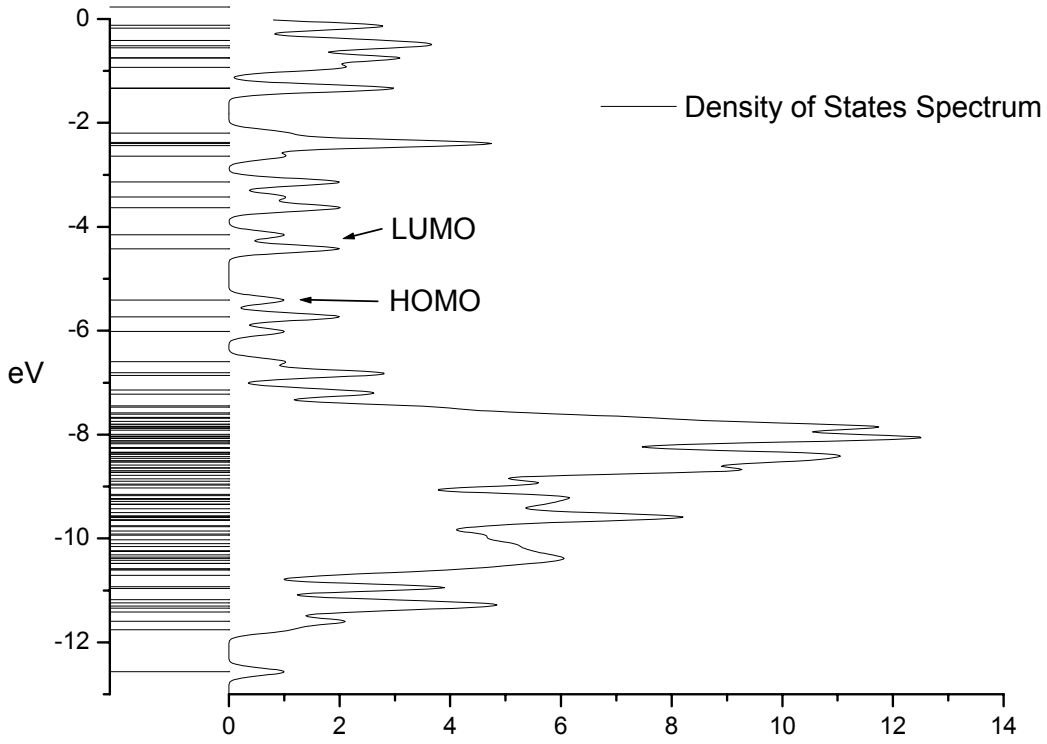

Figure 6.8 – Density of states spectrum for the optimised Au_{28} cluster. Spectrum convoluted with gaussian curves of full-width at half-maximum of 0.1eV.

6.3 The osmium complexes

6.3.1 Geometry optimisation

The structures of the complexes **OsP0P** and **OsP2P** and their oxidised analogues, **OsP0Pox** and **OsP2Pox**, were optimised at the B3LYP/LanL2DZ level of theory. Restricted DFT calculations were carried out on **OsP0P** and **OsP2P**, which both have an even number of electrons. Due to the odd number of electrons in the oxidised species, it was necessary to perform unrestricted calculations for **OsP0Pox** and **OsP2Pox**.

Figure 6.9 shows the optimised structures of **OsP0P** and **OsP2P**. The structures are very similar except for the P*n*P ligand. There is a dihedral angle of 29° between the two pyridines of P0P. For P2P the two pyridines are almost parallel, although displaced from the same plane by the two intervening methylenes.

A crystal structure of **OsP0P**, $[Os(bpy)_2(P0P)Cl](BF_4)$, has recently been obtained by Ryabov *et al*.[24] In addition, two crystal structures are available for the ruthenium

analogue of the **OsP0P** complex: Hesek *et al.*[25] and Du *et al.*[26] have both reported the crystal structure of $[Ru(bpy)_2(P0P)Cl](PF_6).H_2O$. The average Os-$N_{bpy}$ distance is 2.05Å (the same as for both Ru-N_{bpy}). The Os-N_{P0P} distance is 2.10Å (2.12Å for both Ru-N_{pop}). The Os-Cl distance is 2.42Å (2.43Å for both Ru-Cl). The pyridine-pyridine P0P dihedral angle is 24° for the osmium complex, 20° in the case of Hesek *et al.* and only 8° for Du *et al*. This indicates that rotation is not strongly hindered, at least within this range of angles.

Table 6.1 shows a selection of geometrical parameters calculated for the osmium complexes. For the optimised **OsP0P** complex, the average Os-N_{bpy} distance is 2.06Å. The Os-N_{P0P} distance is 2.12Å while Os-Cl is 2.50Å. These values agree very well with the experimental values. The pyridine-pyridine P0P dihedral angle at 29° is somewhat larger than the experimental value of 24°. However, since the structures of the ruthenium analogues indicate that quite a large deviation is possible for this angle, we can conclude that the structure of **OsP0P** is quite reasonably predicted. (Note: the starting point for the optimisation of **OsP0P** was an optimised structure for $[Ru(bpy)_2(P0P)_2]^{2+}$, where the P0P dihedral angle changed from 0° to 29° during the course of the geometry optimisation.)

The calculated parameters for the P2P complexes are almost identical to those for the P0P complexes, apart from those concerning the internal structure of the P*n*P ligand. This indicates that any differences in the electronic behaviour of the two complexes are not due to structural effects.

	Crystal OsP0P[a]	**OsP0P**	**OsP2P**	**OsP0Pox**	**OsP2Pox**
Os-Cl	2.42	2.50	2.50	2.43	2.43
Os-N_{PnP}	2.10	2.12	2.13	2.14	2.14
Os-N_{bpy1}(trans to PnP)	2.05	2.06	2.06	2.09	2.09
Os-N_{bpy1}	2.06	2.07	2.07	2.09	2.09
Os-N_{bpy2}(trans to Cl)	2.02	2.07	2.07	2.10	2.10
Os-N_{bpy2}	2.06	2.04	2.04	2.08	2.08
py-py_{PnP} dihedral	24°	29°	0°	27°	5°

Table 6.1 – Calculated geometrical parameters for osmium complexes studied. All distances are in Å. [a]Crystal structure of $[Os(bpy)_2(P0P)Cl](BF_4)$, from Ryabov *et al.*[24]

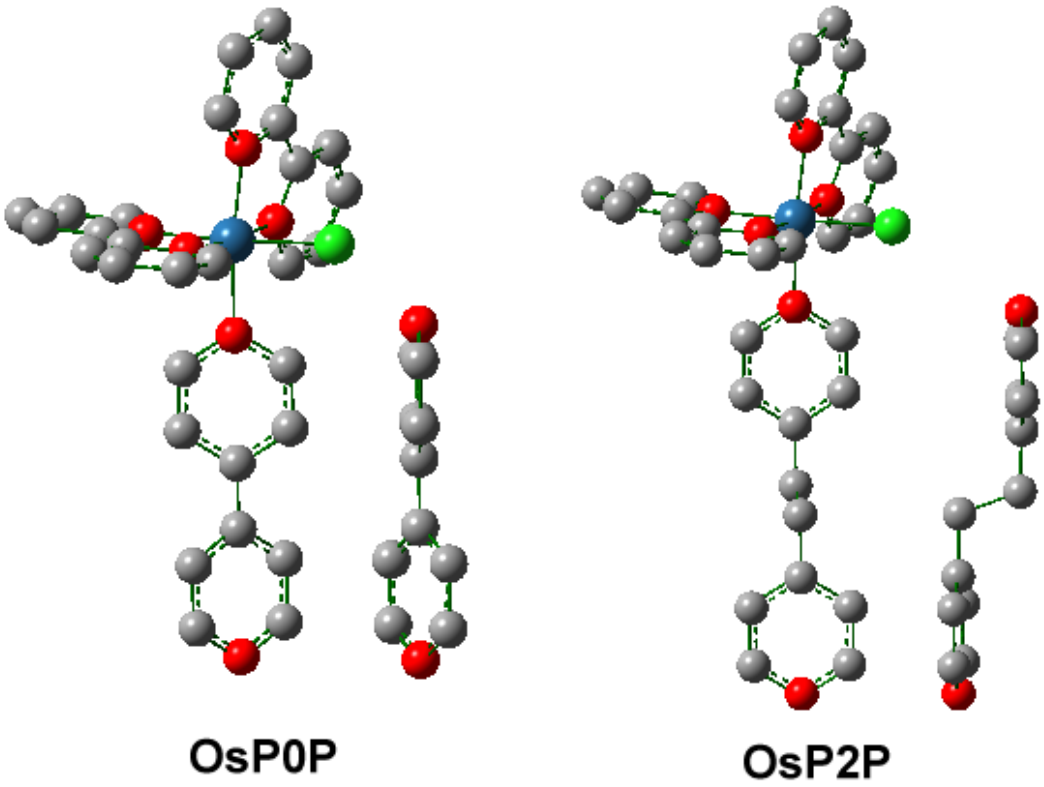

Figure 6.9 – The geometry optimised structures of OsP0P **and** OsP2P **(hydrogen atoms not shown for clarity). A side view of the P*n*P ligand in the complex emphasises the dihedral angle between the pyridine rings.**

6.3.2 Electronic structure

The HOMO and LUMO of each of the four complexes **OsP0P**, **OsP2P** and their oxidised forms, are shown in Figure 6.10. GaussSum[27] was used to describe the molecular orbitals in terms of contributions from the Os centre, the P*n*P ligand, and the two 2,2'-bipyridines. The molecular orbital information for each of the complexes is shown in Table 6.2 to Table 6.5, and is plotted in Figure 6.11 and Figure 6.12.

For both **OsPnP** and **OsPnPox**, both the P0P and P2P complexes have almost identical HOMOs and LUMOs. Figure 6.11 shows that this similarity extends to the HOMO-1 and HOMO-2, and the LUMO+1. However, beyond these orbitals, differences start to appear. Of the frontier occupied orbitals, the HOMO-3, HOMO-4 and HOMO-5 of **OsP2P** are all P2P-based, whereas only the HOMO-3 of **OsP0P** is based on the P0P ligand. The LUMO+2 of **OsP0P** is P0P-based, but that of **OsP2P**

is based on the 2,2'-bipyridines. The lowest energy transition in **OsPnP** is a MLCT from the Os to the bpy ligands.

An interesting question to ask is what is the effect of oxidation on the order and nature of the molecular orbitals? A naïve picture is that oxidation removes an electron from the HOMO, so that the LUMO of the oxidised species is similar to the original HOMO, and the new HOMO is either the singly-occupied original HOMO or the original HOMO-1. A comparison of the images of the HOMOs and LUMOs in Figure 6.10 shows that this simple idea has some merit. The LUMOs of the oxidised species are indistinguishable from the HOMOs of the reduced species. However, it does not correctly predict the location of the HOMO of the oxidised species. Figure 6.11 compares the electronic structures of **OsP0P** and **OsP0Pox**. By comparing the contributions of the various moieties, it is clear that the LUMO of **OsP0Pox** is spatially very similar to the HOMO of **OsP0P**, as also shown by Figure 6.10. However, the HOMO of the oxidised complex is P0P-based, similar to the HOMO-3 of **OsP0P**. It seems that a substantial rearrangement of the occupied orbitals has occurred on oxidation, which means that a simple picture of the oxidation process is not valid for osmium polypyridyl complexes such as **OsP0P** and **OsP2P**.

To further investigate these issues, PDOS spectra were created for the complexes using GaussSum. The contribution from the PnP ligand was divided in two – the half of the ligand closest to the metal centre, *PnP_Os*, and the half further away, *PnP_free*. The resulting spectra are shown in Figure 6.13 to Figure 6.16.

The peak in the Os PDOS spectrum in the occupied frontier region for **OsP2P** is shifted to slightly higher energy (0.04eV) compared to that of **OsP0P**. This indicates that P2P is a stronger σ-donor than P0P. This agrees with the relative electrochemical oxidation potentials of **OsP0P** (0.47V) and **OsP2P** (0.43V).[28] Apart from this shift, the Os, bpy and Cl PDOS spectra are identical for **OsP0P** and **OsP2P**. The *P2P_free* PDOS is shifted to higher energy relative to *P0P_free*, although the bound moiety, *PnP_Os*, does not seem to shift (however, its shape changes somewhat). This may indicate that the increased σ-donor strength of the ligand is due to the influence of *P2P_free*, rather than *P2P_Os*.

On oxidation of **OsP0P**, the PDOS spectra shift to lower energy by about 3eV (for bpy), due to the increased difficulty of removing an electron. If the two sets of spectra are aligned using the bpy PDOS (whose shape is unchanged on oxidation),

a shift to higher energy is observed for the *P0P_free* PDOS (which retains the same shape) and a shift to lower energy occurs for the Os PDOS. As shown in Figure 6.10, this has the effect of changing the nature of the HOMO from Os-based to P0P-based. Based on the PDOS spectra, the lowest energy transition in **OsP0Pox** is a LMCT from the P0P ligand to Os. The PDOS spectra for **OsP2Pox** shows a shift to higher energy for the PnP PDOS. This has the effect of reducing the HOMO-LUMO gap from 1.3eV for **OsP0Pox** to 0.3eV for **OsP2Pox**.

OsP0P	OsP2P
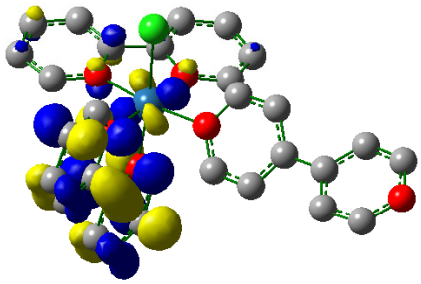	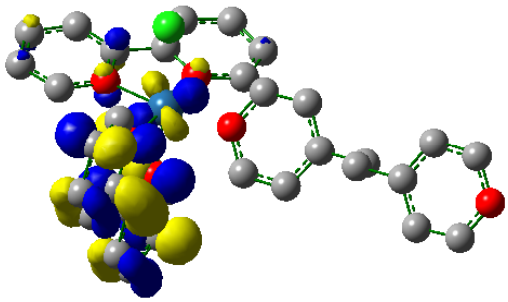
LUMO	LUMO
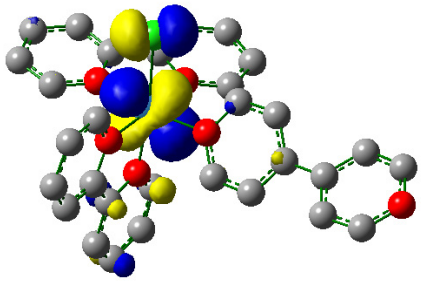	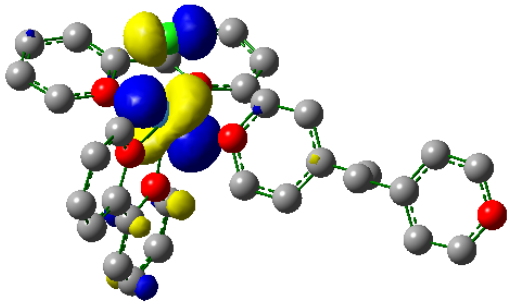
HOMO	HOMO

OsP0Pox	OsP2Pox
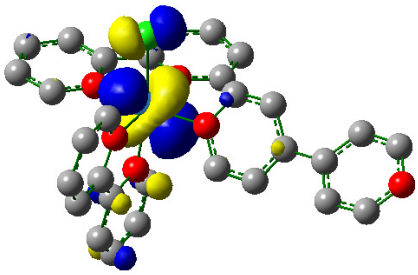	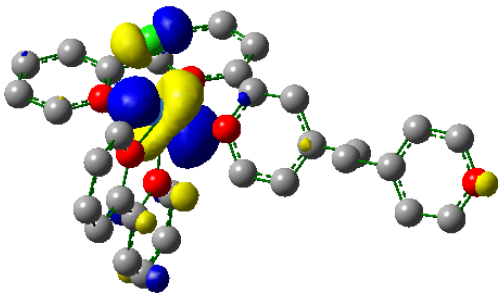
LUMO	LUMO
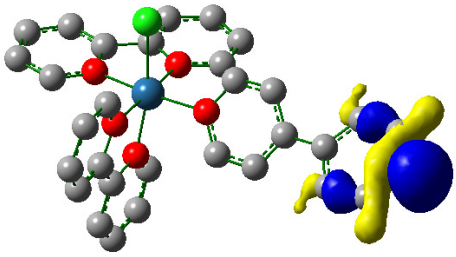	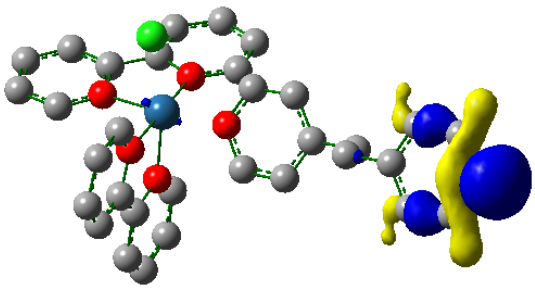
HOMO	HOMO

Figure 6.10 – Highest occupied molecular orbitals (HOMOs) and lowest unoccupied molecular orbitals (LUMOs) of OsP0P, OsP2P, OsP0Pox **and** OsP2Pox**. Isosurfaces drawn at 0.04e/bohr^3. Hydrogen atoms not shown for clarity.**

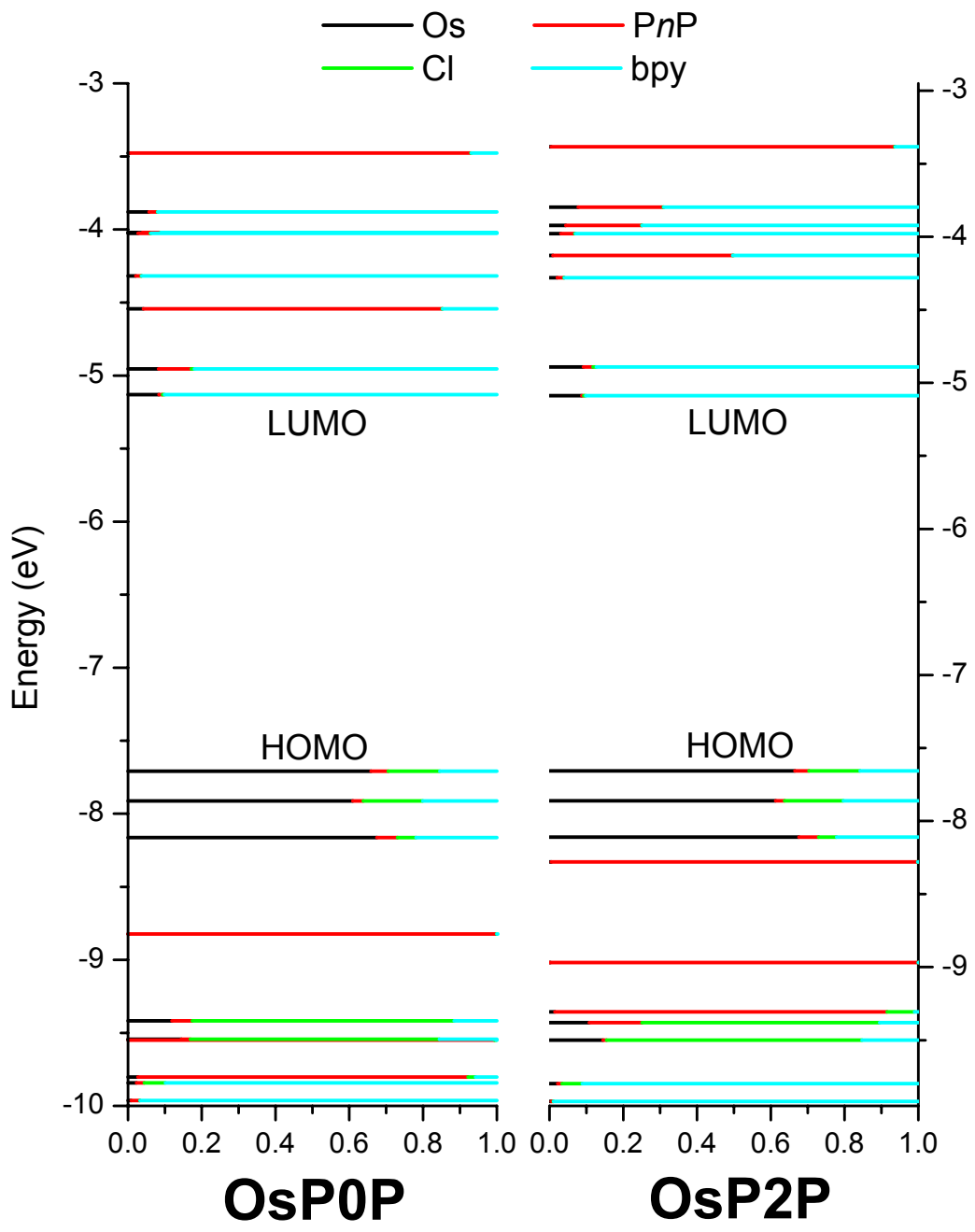

Figure 6.11 – Comparison of the energies and fractional contributions of the molecular orbitals of OsP0P **and** OsP2P**.**

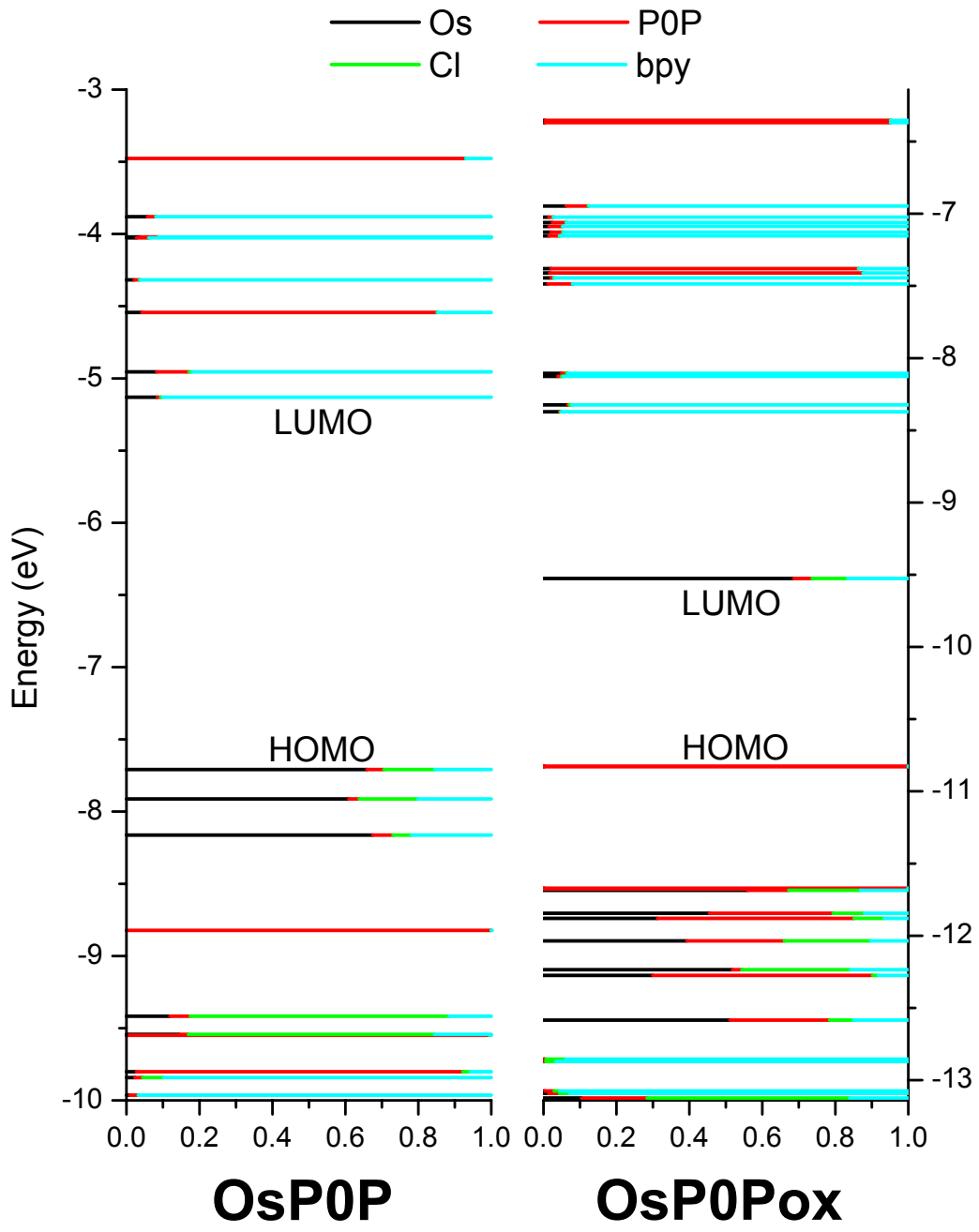

Figure 6.12 – Comparison of the energies and fractional contributions of the molecular orbitals of OsP0P**, with those of the spinorbitals (each containing only a single electron) of** OsP0Pox**.**

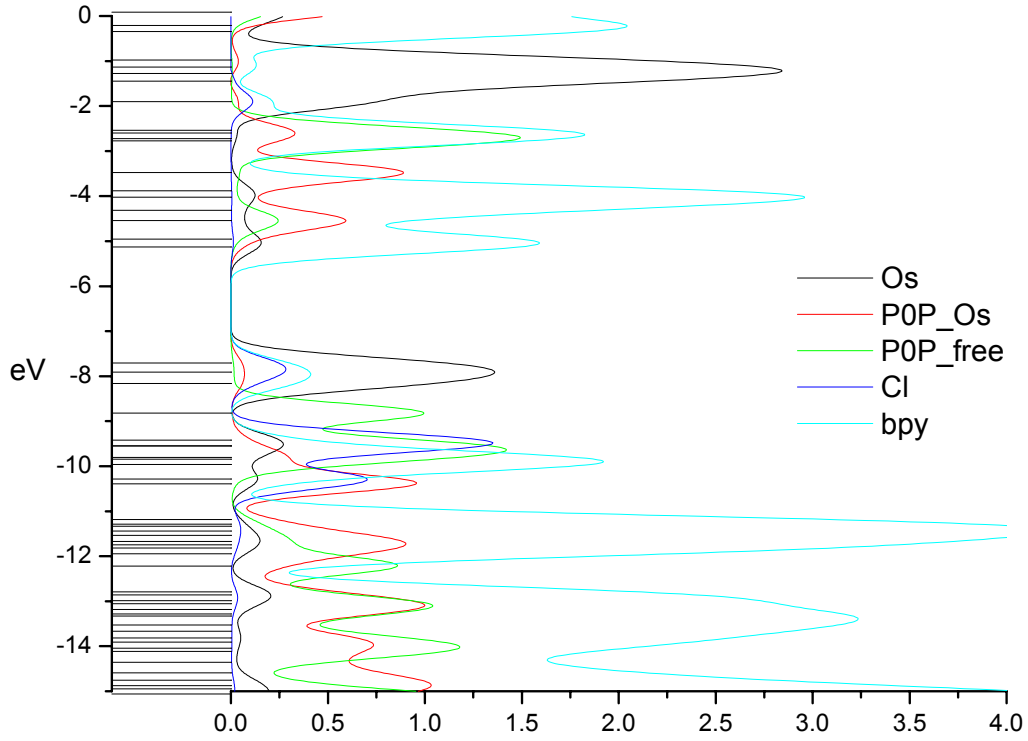

Figure 6.13 – PDOS spectra of OsP0P

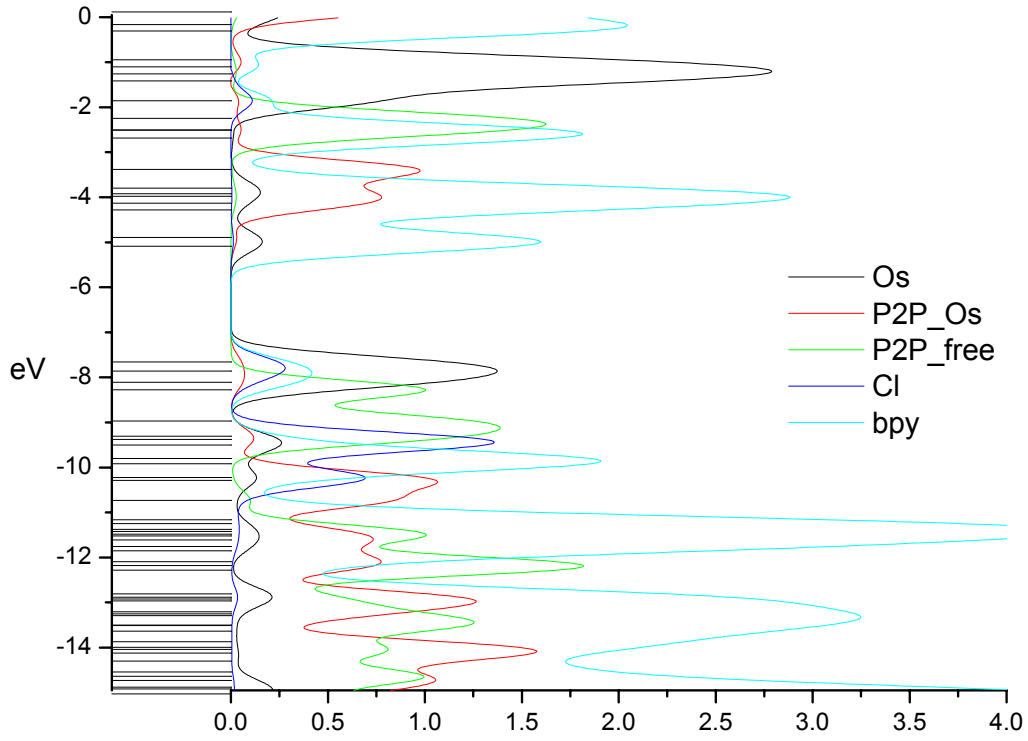

Figure 6.14 – PDOS spectra of OsP2P

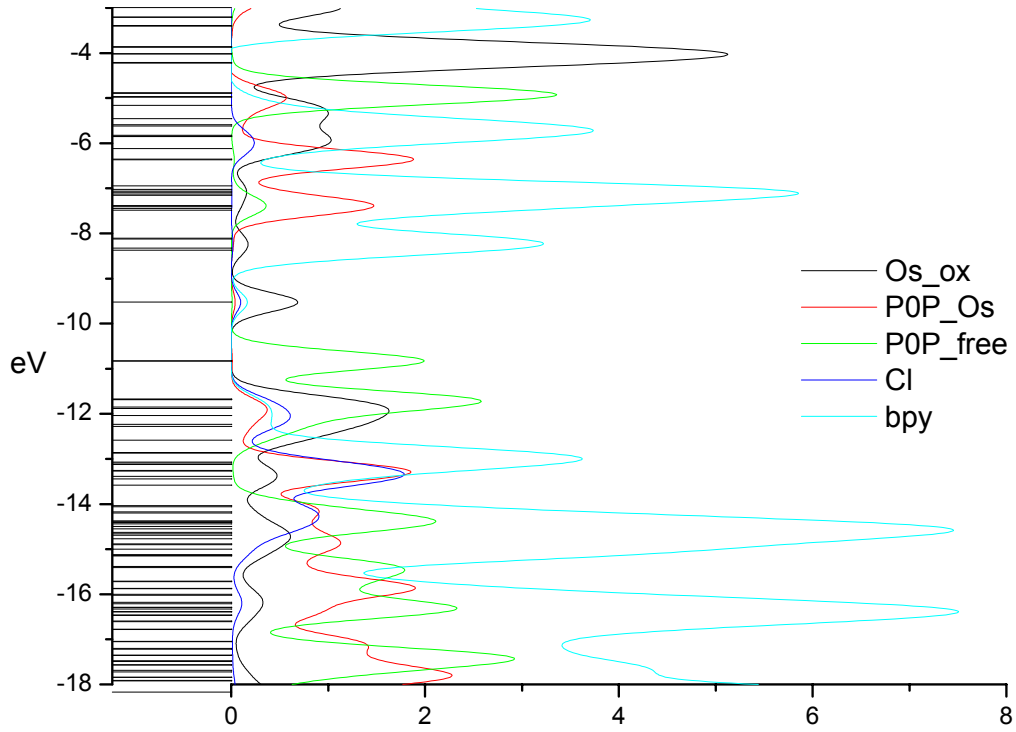

Figure 6.15 – PDOS spectra of OsP0Pox

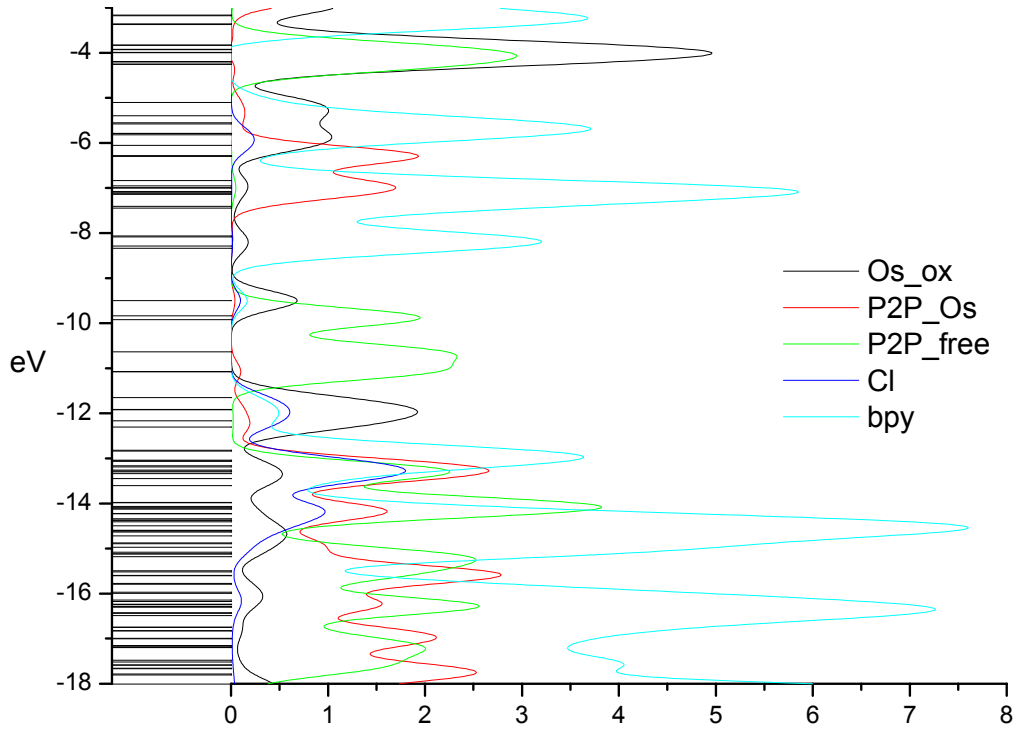

Figure 6.16 – PDOS spectra of OsP2Pox

MO		eV	Os	P0P	Cl	bpy
145	L+10	-2.6	2	83	0	16
144	L+9	-2.72	1	1	0	98
143	L+8	-2.77	0	99	0	1
142	L+7	-3.48	0	92	0	7
141	L+6	-3.88	6	2	0	92
140	L+5	-4.02	4	5	0	91
139	L+4	-4.03	3	3	0	94
138	L+3	-4.32	2	1	0	96
137	L+2	-4.54	4	81	0	15
136	L+1	-4.95	8	9	1	82
135	LUMO	-5.13	8	1	1	90
134	HOMO	-7.71	66	5	14	15
133	H-1	-7.91	61	3	16	20
132	H-2	-8.16	67	6	5	22
131	H-3	-8.82	0	100	0	0
130	H-4	-9.42	12	6	71	12
129	H-5	-9.54	14	2	67	16
128	H-6	-9.55	0	99	1	0
127	H-7	-9.8	3	90	2	6
126	H-8	-9.84	2	2	6	90
125	H-9	-9.96	1	2	0	97
124	H-10	-10.29	11	13	61	15

Table 6.2 – Molecular orbital information for OsP0P**.**

MO		eV	Os	P2P	Cl	bpy
153	L+10	-2.5	0	36	0	64
152	L+9	-2.51	0	65	0	35
151	L+8	-2.68	1	0	0	99
150	L+7	-3.38	0	93	0	6
149	L+6	-3.8	8	23	0	69
148	L+5	-3.92	4	21	0	75
147	L+4	-3.98	3	4	0	93
146	L+3	-4.13	1	49	0	50
145	L+2	-4.28	2	2	0	96
144	L+1	-4.89	9	3	1	87
143	LUMO	-5.09	9	1	1	90
142	HOMO	-7.66	67	4	14	16
141	H-1	-7.86	61	2	16	20
140	H-2	-8.11	68	5	5	22
139	H-3	-8.28	0	99	0	0
138	H-4	-8.97	0	100	0	0
137	H-5	-9.31	1	90	7	1
136	H-6	-9.38	11	14	64	10
135	H-7	-9.5	15	1	69	15
134	H-8	-9.8	2	1	5	91
133	H-9	-9.92	0	1	0	99
132	H-10	-10.22	10	23	53	14

Table 6.3 – Molecular orbital information for OsP2P**.**

MO		eV	Os	P0P	Cl	bpy
144(Beta)	L+20	-5.83	1	0	0	99
143(Beta)	L+19	-5.84	61	4	14	21
144(Alpha)	L+18	-5.85	1	0	0	99
143(Alpha)	L+17	-6.12	59	3	15	22
142(Beta)	L+16	-6.35	0	95	0	5
142(Alpha)	L+15	-6.37	0	95	0	5
141(Beta)	L+14	-6.95	6	6	0	88
141(Alpha)	L+13	-7.02	1	1	0	97
140(Beta)	L+12	-7.06	2	4	0	94
140(Alpha)	L+11	-7.09	2	4	0	95
139(Beta)	L+10	-7.13	2	3	0	95
139(Alpha)	L+9	-7.15	1	3	0	96
138(Beta)	L+8	-7.38	2	84	0	14
138(Alpha)	L+7	-7.41	2	86	0	12
137(Beta)	L+6	-7.44	2	1	0	97
137(Alpha)	L+5	-7.49	1	7	0	92
136(Beta)	L+4	-8.10	5	1	0	93
136(Alpha)	L+3	-8.13	4	1	0	95
135(Beta)	L+2	-8.32	7	0	1	92
135(Alpha)	L+1	-8.37	4	0	0	95
134(Beta)	LUMO	-9.53	69	5	10	17
134(Alpha)	HOMO	-10.83	0	100	0	0
133(Beta)	H-1	-10.83	0	100	0	0
132(Beta)	H-2	-11.67	0	100	0	0
133(Alpha)	H-3	-11.68	0	100	0	0
131(Beta)	H-4	-11.69	56	11	20	13
130(Beta)	H-5	-11.84	45	34	9	12
132(Alpha)	H-6	-11.88	31	54	8	7
131(Alpha)	H-7	-12.04	39	27	24	10
130(Alpha)	H-8	-12.23	52	3	30	16
129(Beta)	H-9	-12.27	30	60	2	8
129(Alpha)	H-10	-12.58	51	27	7	15
128(Beta)	H-11	-12.85	0	0	5	94
128(Alpha)	H-12	-12.87	0	0	3	97
127(Beta)	H-13	-13.07	0	3	2	95
127(Alpha)	H-14	-13.09	1	3	3	93
126(Beta)	H-15	-13.12	10	18	56	16
126(Alpha)	H-16	-13.26	5	75	10	10
125(Beta)	H-17	-13.27	8	42	36	14
124(Beta)	H-18	-13.38	8	40	36	15
125(Alpha)	H-19	-13.44	13	20	44	23
124(Alpha)	H-20	-13.58	15	7	46	32

Table 6.4 – Molecular orbital information for OsP0Pox**.**

MO		eV	Os	P2P	Cl	bpy
152(Beta)	L+20	-5.79	61	3	14	22
151(Beta)	L+19	-5.79	1	0	0	98
152(Alpha)	L+18	-5.82	1	0	0	99
151(Alpha)	L+17	-6.06	59	3	15	22
150(Beta)	L+16	-6.28	0	95	0	5
150(Alpha)	L+15	-6.30	0	95	0	5
149(Beta)	L+14	-6.84	8	44	0	48
149(Alpha)	L+13	-6.95	2	47	0	51
148(Beta)	L+12	-6.99	2	16	0	82
148(Alpha)	L+11	-7.00	2	15	0	83
147(Beta)	L+10	-7.08	2	12	0	85
147(Alpha)	L+9	-7.09	2	20	0	78
146(Beta)	L+8	-7.13	1	25	0	74
146(Alpha)	L+7	-7.14	1	17	0	82
145(Beta)	L+6	-7.41	2	1	0	97
145(Alpha)	L+5	-7.45	1	1	0	98
144(Beta)	L+4	-8.06	5	1	0	94
144(Alpha)	L+3	-8.09	4	1	0	95
143(Beta)	L+2	-8.29	7	0	1	92
143(Alpha)	L+1	-8.34	4	0	0	95
142(Beta)	LUMO	-9.50	68	6	10	17
141(Beta)	HOMO	-9.84	1	98	0	0
142(Alpha)	H-1	-9.92	0	100	0	0
141(Alpha)	H-2	-10.64	0	100	0	0
140(Beta)	H-3	-10.64	0	100	0	0
139(Beta)	H-4	-11.07	0	100	0	0
140(Alpha)	H-5	-11.08	0	100	0	0
138(Beta)	H-6	-11.65	59	2	24	15
139(Alpha)	H-7	-11.91	55	2	29	14
137(Beta)	H-8	-11.92	69	9	5	17
138(Alpha)	H-9	-12.17	56	3	24	17
137(Alpha)	H-10	-12.31	58	16	13	13
136(Beta)	H-11	-12.82	0	0	6	94
136(Alpha)	H-12	-12.83	0	1	3	97
135(Beta)	H-13	-13.04	1	12	9	78
135(Alpha)	H-14	-13.05	1	7	2	90
134(Beta)	H-15	-13.06	9	18	43	31
134(Alpha)	H-16	-13.16	4	78	7	11
133(Beta)	H-17	-13.19	5	55	28	12
132(Beta)	H-18	-13.26	8	48	33	11
133(Alpha)	H-19	-13.28	3	85	8	4
131(Beta)	H-20	-13.30	2	87	8	4

Table 6.5 – Molecular orbital information for OsP2Pox**.**

6.4 The adsorbed complex

6.4.1 Optimisation of the structure

There are a number of possible adsorption sites and orientations for positioning the complex on the surface: the angle of the P*n*P ligand may be varied with respect to the surface, the dihedral angle between two atoms of the ligand and two atoms of the surface can also be altered, and the nitrogen of the P*n*P ligand can be positioned over an atom (the "on-top" configuration), a hollow (between 3 atoms) or a bridging site (between 2 atoms). Due to the large size of the problem, it is outside the scope of this study to investigate the many possibilities. However, this issue has been previously addressed by a number of studies that involved smaller systems.

Pluchery *et al.*[15] found that the largest adsorption energy for cyanopyridine attached to Au(111) was obtained for the 'on-top' position with the C_2 axis of pyridine perpendicular to the surface. Similar results were found by Bilić *et al.* for pyridine[11] and ammonia[12]. If the C_2 axis of pyridine is perpendicular to the surface, then depending on the dihedral angle between the σ_h plane of the pyridine and two neighbouring gold atoms on the surface, there are two possible energy minima: staggered and eclipsed (see Figure 6.17). These were found to give almost the same adsorption energy[11].

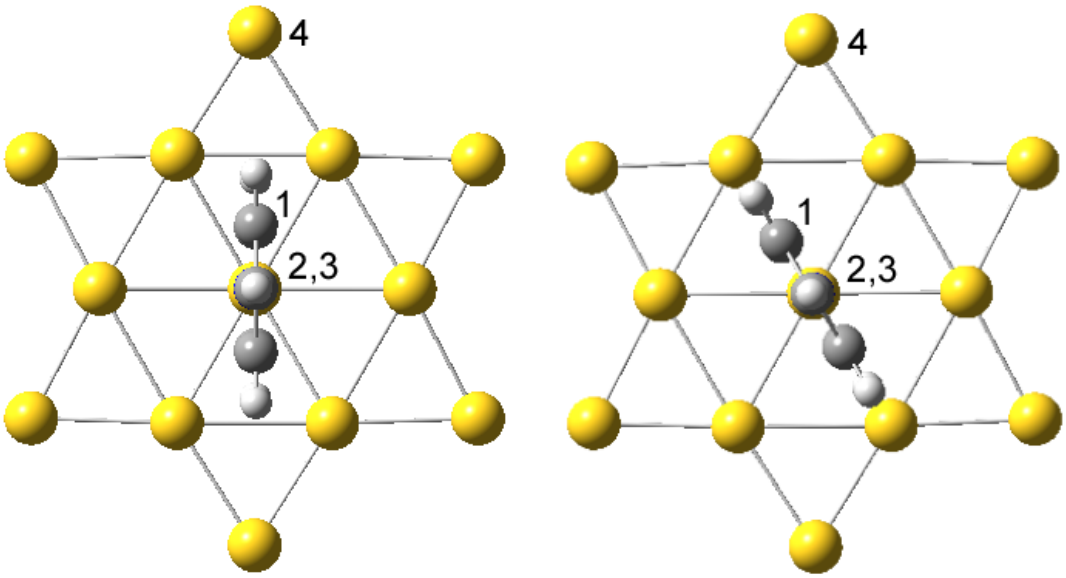

Figure 6.17 – Two possible energy minima for pyridine binding to Au(111) in the "on top" position. The two configurations shown have different values for the dihedral angle between atoms 1 and 2 of the pyridine and atoms 3 and 4 of the surface. The

diagram on the left corresponds to the "staggered" configuration (dihedral angle is 0°), while the diagram on the right shows an "eclipsed" configuration (dihedral angle is 30°).

In our study, each osmium complex was placed on the surface such that the long axis of the P*n*P ligand was perpendicular to layer C of the gold cluster. The initial distance between the central gold atom in layer A and the nitrogen of the P*n*P (the distance 2 to 3 in Figure 6.18) was set to 2.32Å for **OsP0P**, and 2.58Å for **OsP0Pox** and **OsP2P**. The initial distance of 2.32Å was the optimised distance found by Pluchery *et al.*[15] for cyanopyridine on Au(111), whereas 2.58Å was the optimised distance found for our own Au_{28}/**OsP0P** calculation (see below). The dihedral angle formed by the four atoms 1 to 4 in Figure 6.18 was initially set to 0° – this is the staggered conformation (see Figure 6.17).

Box 6.1 describes the practical details of preparing an input file for Gaussian03 for an adsorbate/substrate calculation.

(1) The optimised Z-matrix of the gold surface was modified to include a dummy atom, X, in the centre of layer C, by adding the following line:

```
X,26,1.68389402,27,30.0,28,0.0
```

where 26, 27 and 28 are the atoms of layer C. Atom X will be used to position the complex. Note that layer A cannot be used for this purpose since the optimised atoms are not perfectly in the same plane.

(2) The optimised structure of the osmium complex was opened in GaussView and saved as a Cartesian-coordinate Gaussian job file. The atoms to be used in the alignment with the surface were reordered to the start of the file. The nitrogen atom to be adsorbed was placed first, then the neighbouring carbon, followed by the next carbon along the ring. This file was opened in GaussView and saved in the default Z-matrix format. Atoms 1, 2 and 3 at the start of the Z-matrix are now the atoms that were moved to the start of the Cartesian-coordinate file.

(3) Each of the atom numbers in the Z-matrix of the complex was increased by 29, which is the number of atoms in the Z-matrix of the Au surface. Each reference to a variable must also be modified so that it will not clash with the variables used by the Au Z-matrix. This can be accomplished by prefixing each variable name by the letter 'N', for example. Both of these tasks were automated using a Python script.

(4) The Z-matrix of the complex was appended to the Z-matrix of the surface, to create a new Z-matrix for the adsorbed complex. The additional variables used by the complex were appended to the existing list of variables. Six internal coordinates were required to complete the new Z-matrix (shown in bold below). The values chosen for these determined the position and orientation of the complex on the Au surface.

```
N,29,7.18658,26,90.0,27,-90.0
C,30,NB1,29,121.27849,26,0.0
C,31,NB2,30,NA1,29,180.0
```

The first line listed above fixes the N1 of the complex (now N30 of the adsorbed complex) 7.187Å above the dummy atom X in layer C, that is, 2.322Å above the central atom in layer A. The following line ensures that the P0P as a whole is perpendicular to layer C and turns the complex to reduce unfavourable steric interactions with the surface. The value for the angle is 180 minus 58.72151, the angle between C1 of the complex, the neighbouring nitrogen, and the nitrogen at the other end of the ligand. If a value less than 180° is used for the final missing internal coordinate (on the third line), the complex will be tilted with respect to the surface.

(5) The dummy atom was deleted using GaussView.

Box 6.1 – Preparation of a Gaussian job file for a molecule adsorbed on a surface.

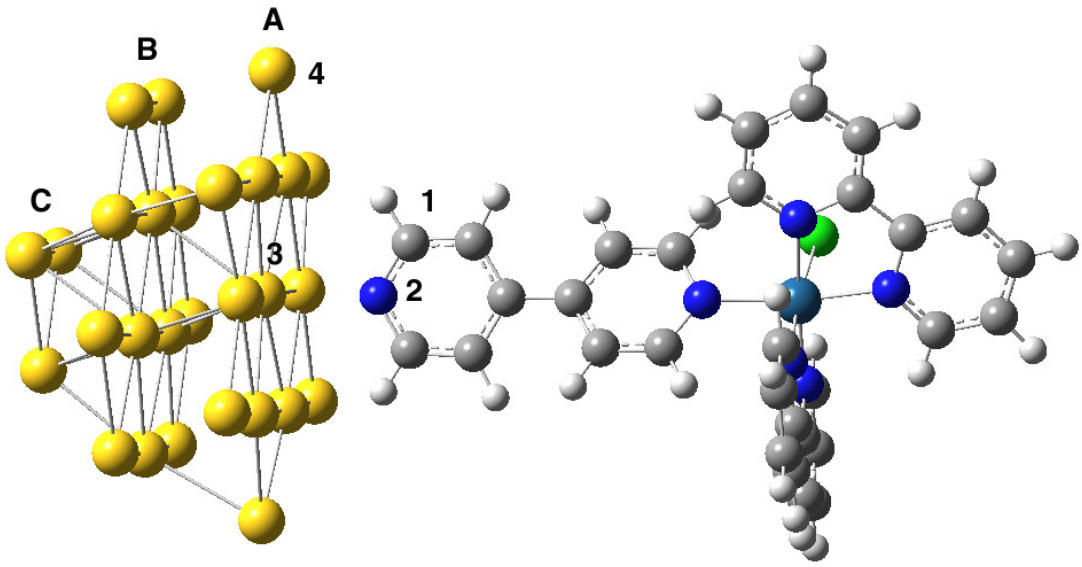

Figure 6.18 – The optimised structure of OsP0P **adsorbed on the surface of the gold cluster. The numbers indicate atoms referred to in the text.**

The desired basis set for the atoms of the adsorbed complex was equivalent to the basis sets used for the corresponding atoms of the constituent systems (see above for details). However, a test run showed that the SCF procedure suffered from extremely large energy oscillations. In order to improve the initial guess for the wavefunction, a single point energy calculation was carried out using a small basis set, STO-3G, for all atoms– except for Au, Os and Cl, for which the LanL2MB basis set and ECP were used. SCF convergence was achieved within 23 steps, during the first 17 of which very large oscillations occurred with respect to the targets. The converged wavefunction was used as an initial guess for the wavefunction for a single point energy calculation using the desired basis set. SCF convergence was achieved in 6 steps without any oscillatory behaviour.

The geometry of the adsorbed complex was optimised with two degrees of freedom: the distance between the complex and the surface (the distance from 2 to 3 in Figure 6.18), and the dihedral angle between the P*n*P ligand and two gold atoms on the surface (the dihedral angle formed by 1-2-3-4 in Figure 6.18).

6.4.2 Results and Discussion

The optimised distance between the complex and the surface was 2.58Å for Au_{28}/**OsP0P** and 2.54Å for Au_{28}/**OsP2P**, while the dihedral angle remained unchanged at 0°, keeping the complex in the staggered conformation.

The adsorption energy, E_{ads}, for Au_{28}/**OsP0P** was calculated using the following formula:

$$E_{\text{ads}} = E(\text{Au}_{28}) + E(\mathbf{OsP0P}) - E(\text{Au}_{28}/\mathbf{OsP0P}) \qquad (6.1)$$

where E(Au_{28}/**OsP0P**) indicates the energy of the system shown in Figure 6.18. E_{ads} for **OsP0P** on Au_{28} was found to be 9.2 kcal mol^{-1}, while that for **OsP2P** was 10.1 kcal mol^{-1}.

These results compare well with those found by Bilić *et al.*[11] for the absorption of pyridine on Au(111). Their equilibrium bond length was 2.46Å with E_{ads} equal to 7.3 kcal mol^{-1}. Pluchery *et al.*[15] found a much higher adsorption energy of 1.453 eV (33.5 kcal mol^{-1}) for the binding of cyanopyridine to Au(111). Their optimised Au-N bond length was 2.32Å.

Figure 6.19 shows the change in electron density associated with the adsorption of **OsP0P** to the gold surface. This diagram was created by summing the electron density of the complex and the surface, which were calculated separately at their geometry in the adsorbed system, and then subtracting the electron density of the adsorbed system. Electron density has decreased in the area between the N and the central gold atom. There is a corresponding increase in electron density on the N and on the gold atom. Bilić *et al.* created similar diagrams for the adsorption of pyridine[11] and ammonia[12] on Au(111). They noted that the change in charge density is very low in magnitude. As regards the bonding interaction, they noted that there is no evidence for covalent bonding effects since charge density *decreases* in the area between the adsorbate and the surface. The major effect appears to be internal charge redistribution, or polarisation, rather than charge transfer. These conclusions also apply to the system shown in Figure 6.19.

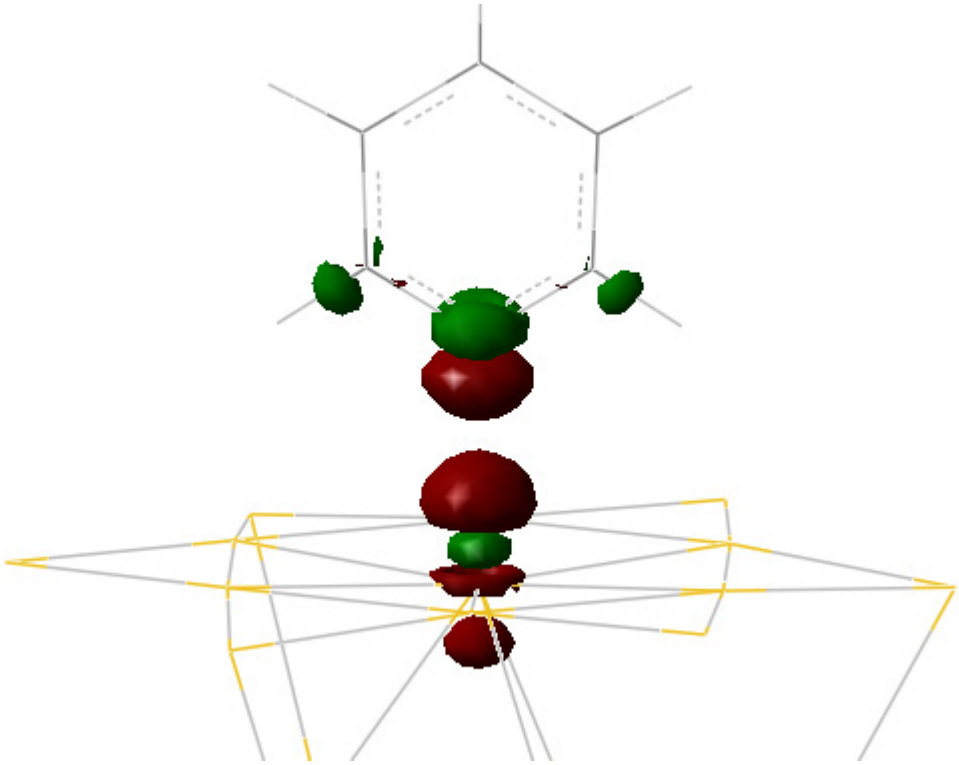

Figure 6.19 – Isosurface of the difference in the electron density between OsP0P**/Au_{28} and the sum of the electron densities of** OsP0P **and Au_{28}. Green indicates an increase in the electron density while red indicates a decrease. The isosurface is drawn at 0.004e/bohr^3.**

The electronic structures of **OsP0P**/Au_{28} and **OsP2P**/Au_{28} are shown in Figure 6.20 and Figure 6.21 respectively, compared to those of the isolated surface and isolated complex. A comparison of the energy levels for isolated **OsP0P** and for **OsP0P**/Au_{28} shows that adsorption has resulted in a slight shift to lower energy of 0.05eV (0.03eV for **OsP2P**). The shift to lower energy is larger for the isolated gold surface at 0.85eV for **OsP0P** and 0.75eV for **OsP2P**.

A full description of the conductivity of a molecule requires a treatment involving the complete density of states of the molecule. In general, though, the HOMO and LUMO play a key role, and their energy relative to the Fermi level of the surface can indicate whether electron transfer is mediated by the HOMO or by the LUMO.[1] For a true metal surface, it is expected that the Fermi level lies somewhere between the HOMO and LUMO of the Au_{28} nanocluster. Without any further calculations on larger systems, it is impossible to speculate on the relative energy of the HOMO or LUMO of the Os complex, and the Fermi level of the metal surface.

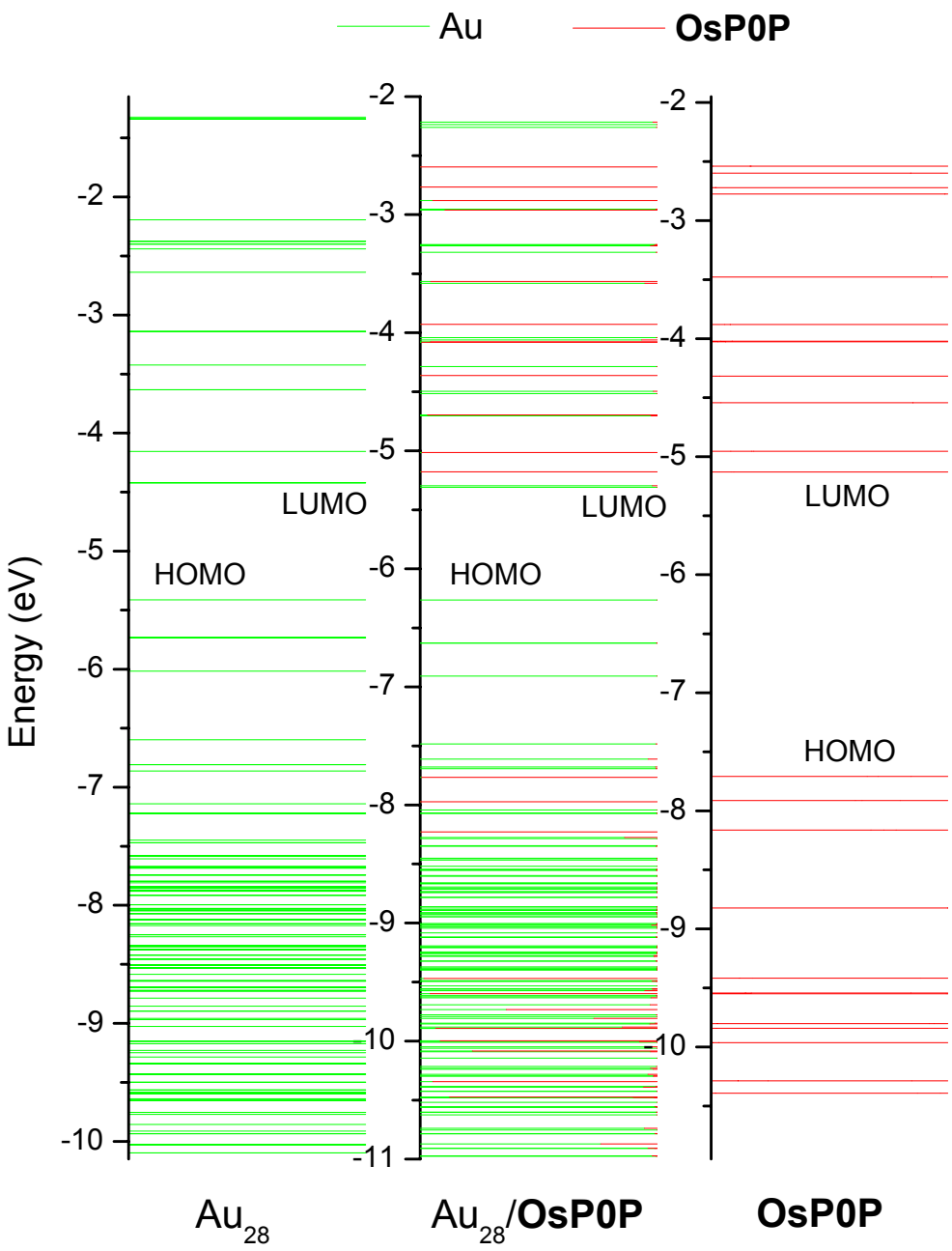

Figure 6.20 – The energy levels of the isolated Au_{28} cluster (left), the isolated OsP0P **complex (right), and the complex adsorbed on the surface (centre). Note that the axes have been shifted in order to line up the HOMOs and LUMOs.**

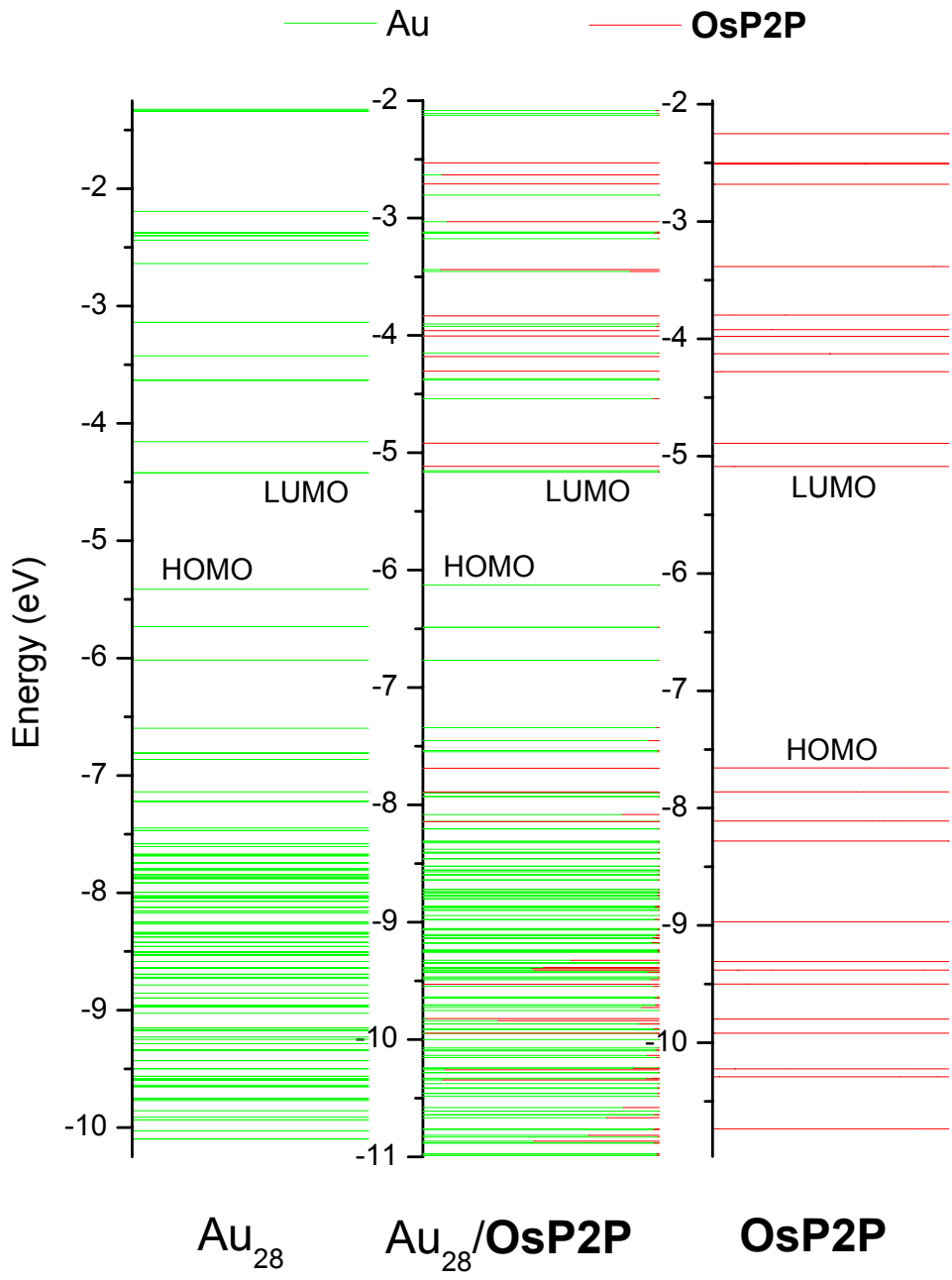

Figure 6.21 – The energy levels of the isolated Au_{28} cluster (left), the isolated OsP2P **complex (right), and the complex adsorbed on the surface (centre). Note that the axes have been shifted in order to line up the HOMOs and LUMOs.**

A comparison of the energy levels for **OsP0P**/Au_{28} and **OsP0P** shows that some of the **OsP0P** levels have shifted more than 0.05eV, and that others have mixed with energy levels from the gold. Indeed, the HOMO-3 seems to have disappeared on adsorption. This orbital is almost completely P0P-based (see Table 6.2), and so is expected to interact strongly with the gold surface.

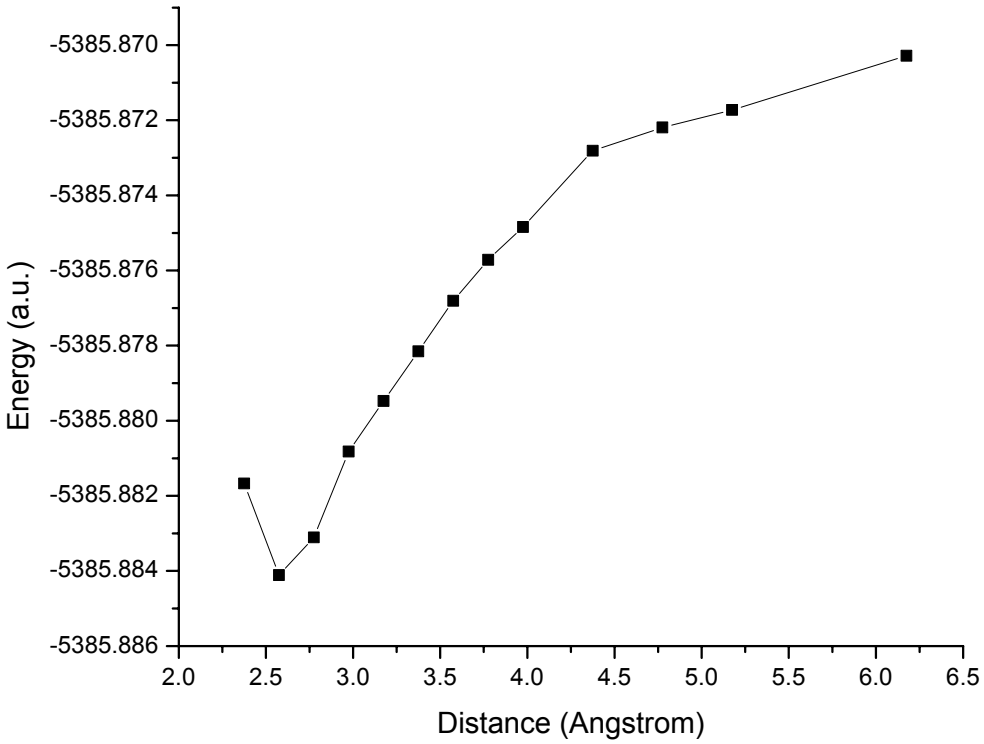

Figure 6.22 – A plot of electronic energy versus Au-N distance for Au_{28}/OsP0P.

In order to investigate this further, a series of single point energy calculations were performed for several values of the Au_{28}–**OsP0P** distance. A plot of the energy versus distance is shown in Figure 6.22. The energy of the system is at a minimum at 2.58Å – at shorter distances, repulsive forces outweigh the energy gain from absorption, and the stability of the system decreases.

Figure 6.23 shows the resulting energy levels for four different Au-N values. At a distance of 6.18Å, there is no mixing between the orbitals of the gold cluster and the complex. The HOMO-3 from the isolated **OsP0P** is marked with an asterisk (*) in Figure 6.23. As the molecule is moved closer to the surface, the HOMO-3 starts to split and mix with the gold energy levels, until there is no trace of it at the original energy.

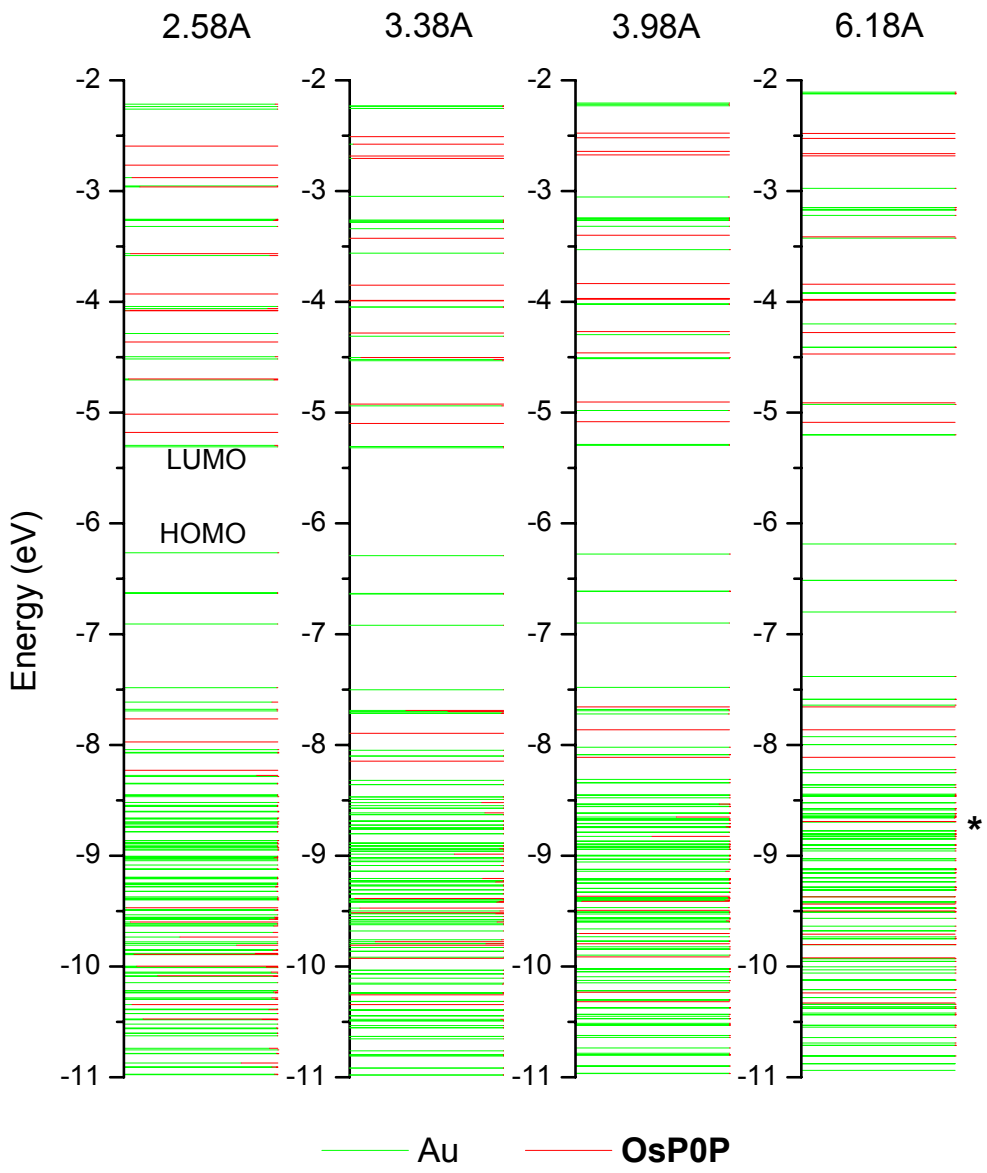

Figure 6.23 – The effect of an increase in the Au-N distance on the energy levels of Au_{28}/OsP0P. The Au-N distance is given in Å above each graph. The red energy level marked with an asterisk (*) at 6.18Å, is the HOMO–3 of isolated OsP0P**.**

From the point of view of modelling current-voltage relationships through a molecule, the interaction between the molecule and the surface is very important. This interaction is measured in terms of the exchange energy. Exchange is a purely quantum-mechanical interaction arising from the antisymmetry of the wavefunction. It is treated accurately within Hartree-Fock theory, but can only be approximated in DFT using current functionals. Hybrid functionals such as B3LYP, which incorporate a degree of HF exchange, have been found to treat exchange more accurately.

The Morokuma-Kituara energy decomposition scheme[29,30] breaks down the interaction between two fragments (for example, two molecules, or two moieties within a molecule) in terms of the electrostatic interaction energy (which can be attractive or repulsive), the polarisation and dispersion interaction energy (attractive), the exchange interaction energy (repulsive) and the charge transfer energy (attractive). Unfortunately, Gaussian03 does not implement this energy decomposition scheme.

On the other hand, this method *is* implemented by the computational chemistry program, PC-GAMESS[31], which is a version of the GAMESS (US)[32] quantum chemistry package. It is however restricted to Hartree-Fock wavefunctions. As a first test, we used PC-GAMESS to converge the wavefunction for $[Ru(bpy)_3]^{2+}$ with a minimal basis set and D_3 symmetry. The geometry used for $[Ru(bpy)_3]^{2+}$ was taken from a Gaussian03 geometry optimisation at the B3LYP/LanL2DZ level of theory. Next, an attempt was made to use the LanL2DZ basis set for the same calculation. However, the SCF did not converge within 1000 cycles. Unlike Gaussian03, there is no way to project the converged wavefunction using a minimal basis set onto the LanL2DZ basis set. As a result, no further calculations were attempted using PC-GAMESS. Thus, unfortunately, it was not possible to carry out energy decomposition analysis on Au_{28}/**OsP0P**.

6.4.3 Preliminary results on Au_{28}/OsP0Pox

At the time of writing, the geometry optimisation of Au_{28}/**OsP0Pox** had not yet completed. The preliminary results are presented here. These results should be qualitatively, if not quantitatively, equal to the final results. Figure 6.24 shows the progress of the geometry optimisation of Au_{28}/**OsP0Pox**, indicating that the lowest energy structure found so far should be close to the final answer.

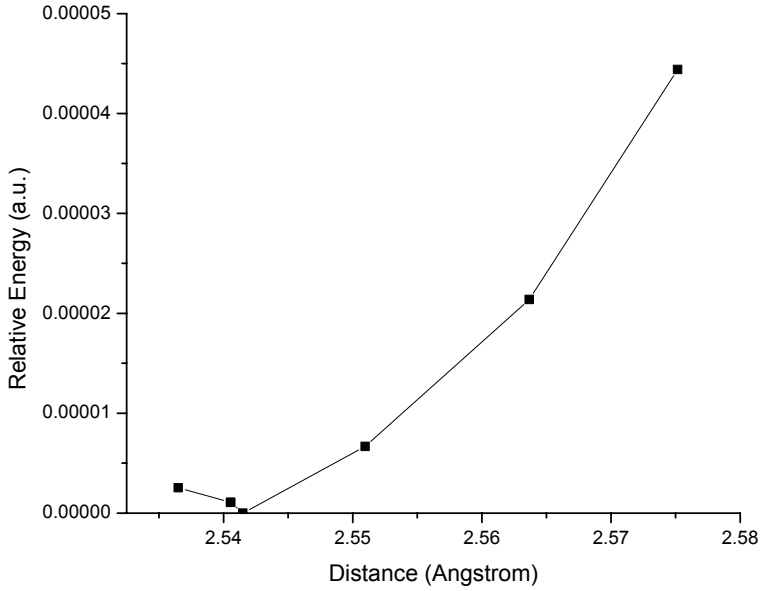

Figure 6.24 – A plot of electronic energy versus Au-N distance for Au_{28}/OsP0Pox.

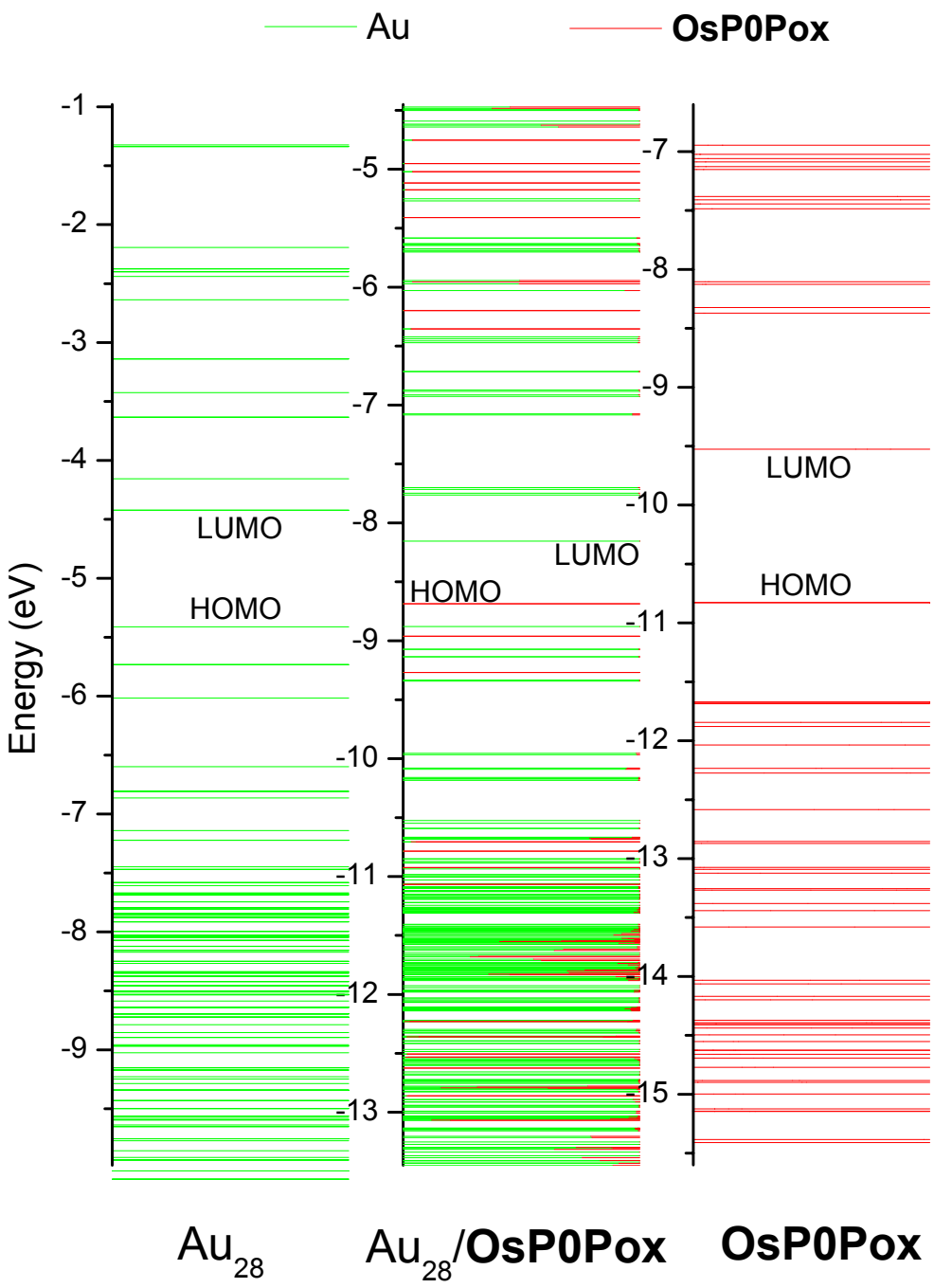

Figure 6.25 – The energy levels of the isolated Au_{28} cluster (left), each containing two electrons, are compared with the energy levels (each containing a single electron) of the isolated OsP0Pox **complex (right), and the complex adsorbed on the surface (centre). Note that the axes have been shifted in order to line up the HOMOs and LUMOs.**

OsP0Pox adsorbs much more strongly than either of **OsP0P** (9.1 kcal mol^{-1}) or **OsP2P** (10.1 kcal mol^{-1}), having an adsorption energy of 38.7 kcal mol^{-1}.

The Au-N bond length corresponding to the lowest energy structure found is equal to that of Au_{28}/**OsP2P** (2.54 Å), but slightly shorter than that of Au_{28}/**OsP0P**. The other degree of freedom, the dihedral angle, remained close to zero at 0.6°.

6.5 Conclusions

The first DFT calculations of an osmium complex attached to a gold surface were described in this chapter. Such calculations, although requiring a considerable length of time to carry out, are now technically feasible, due to the speed of current computers and software.

Oxidation of the osmium complexes involves a large reordering of the energy levels of the complex. The HOMO changes from metal-based to being based on the PnP ligand, specifically on the pyridine ring of PnP furthest away from the metal centre. The complex attaches to the surface through the nitrogen of this pyridine ring, and this rearrangement of the energy levels may explain why a much larger adsorption energy (38.7 kcal mol^{-1} versus 9.2 kcal mol^{-1}) is observed for **OsP0Pox** compared to **OsP0P**.

The interaction between the surface and the complex does not involve covalent bonding, but rather involves polarisation at the adsorbate/substrate interface. Apart from a general shift in energy, the orbitals of the complex and the gold surface are not perturbed by the adsorption process, except for those orbitals based on the PnP ligand. The size of the gold cluster employed, although adequate to describe bonding interaction, was found to reproduce the electronic structure of a nanocluster, rather than bulk gold. A HOMO-LUMO gap of 1.0eV was found, consistent with other calculations on gold clusters of comparable size.

6.6 References

1. Adams, D.M., Brus, L., Chidsey, C.E.D.,Creager, S., Creutz, C., Kagan, C.R., Kamat, P.V., Lieberman, M., Lindsay, S., Marcus, R.A., Metzger, R.M., Michel-Beyerle, M.E., Miller, J.R., Newton, M.D., Rolison, D.R., Sankey, O., Schanze, K.S., Yardley, J. and Zhu, X., *J. Phys. Chem. B*, **2003**, *107*, 6668.

2. Aviram, A. and Ratner, M.A., *Chem. Phys. Lett.*, **1974**, *29*, 277.

3. (a) Farver, O., Zhang, J., Chi, Q., Pecht, I. and Ulstrup, J., *Proc. Nat. Acad. Sci.*, **2001**, *98*, 4426. (b) Chi, Q., Zhang, J., Andersen, J.E.T. and Ulstrup, J., *J. Phys. Chem. B*, **2001**, *105*, 4669. (c) Brask, J., Wackerbarth, H., Jensen, K.J., Zhang, J., Chorkendorff, I. and Ulstrup, J., *J. Am. Chem. Soc.*, **2003**, *125*, 94. (d) Zhang, J., Chi, Q., Kuznetsov, A.M., Hansen, A.G., Wackerbarth, H., Christensen, H.E.M., Andersen, J.E.T. and Ulstrup, J., *J. Phys. Chem. B*, **2002**, *106*, 1131.

4. (a) Gittins, D.I., Bethell, D., Schiffrin, D.J. and Nichols, R.J., *Nature*, **2000**, *408*, 67. (b) Haiss, W., van Zalinge, H., Higgins, S.J., Bethell, D., Höbenreich, H., Schiffrin, D.J. and Nichols, R.J., *J. Am. Chem. Soc.*, **2003**, *125*, 15294.

5. (a) Tao, N.J., *Phys. Rev. Lett.*, **1996**, *76*, 4066. (b) Xiao, X., Xu, B. and Tao, N.J., *Nano Lett.*, **2004**, *4*, 267.

6. Kuznetsov, A.M. and Ulstrup, J., *J. Phys. Chem. A*, **2000**, *104*, 11531.

7. Kuznetsov, A.M. and Ulstrup, J., *Electrochim. Acta*, **2000**, *45*, 2339.

8. Zhang, J., Kuznetsov, A.M. and Ulstrup, J., *J. Electroanal. Chem.*, **2003**, *541*, 133.

9. (a) Kresse, G. and Hafner, J., *Phys. Rev. B*, **1993**, *47*, RC558. (b) Kresse, G. and Furthmüller, J., *Comput. Mater. Sci.*, **1996**, *6*, 15.

10. Dovesi, R., Saunders, V.R, Roetti, C., Causà, M., Harrison, N.M., Orlando, R. and Zicovich-Wilson, C.M., *CRYSTAL98 User's Manual*, University of Torino, **1998**.

11. Bilić, A., Reimers, J.R. and Hush, N.S., *J. Phys. Chem. B*, **2002**, *106*, 6740.

12. Bilić, A., Reimers, J.R., Hush, N.S. and Hafner, J., *J. Chem. Phys.*, **2002**, *116*, 8981.

13. Bagus, P.S. and Illas, F., in *Encyclopedia of Computational Chemistry*, Vol. 4, p. 2870, eds. Schleyer, P.V., Allinger, N.L., Clark, T., Gasteiger, J., Kollman, P.A., Schaefer III, H.F. and Schreiner, P.R., Wiley, Chichester, **1998**.

14. (a) Gomes, J.R.B. and Illas, F., *Catal. Lett.*, **2001**, *71*, 31. (b) Gomes, J.R.B. and Illas, F., *Int. J. Mol. Sci.*, **2001**, *2*, 211.

15. Pluchery, O., Tadjeddine, M., Flament, J.-P. and Tadjeddine, A., *Phys. Chem. Chem. Phys.*, **2001**, *3*, 3343.

16. (a) Andrae, D., Haeussermann, U., Dolg, M., Stoll, H. and Preuss, H., *Theoret. Chim. Acta*, **1990**, *77*, 123. (b) Fuentealba, P., Stoll, H., Szentpaly, L.V., Schwerdtfeger, P. and Preuss, H., *J. Phys. B*, **1983**, *16*, L323.

17. Reimers, J.R., Shapley, W.A., Lambropoulos, N. and Hush, N.S., *Ann. N.Y. Acad. Sci.*, **2002**, *960*, 100.

18. *CRC Handbook of Chemistry and Physics*, 64th ed., ed. Weast, R.C., CRC Press, Florida, **1983**.

19. Garzón, I.L., Michaelian, K., Beltrán, M.R., Posada-Amarillas, A., Ordejón, P., Artacho, E., Sánchez-Portal, D. and Soler, J.M., *Phys. Rev. Lett.*, **1998**, *81*, 1600.

20. Häberlen, O.D., Chung, S.-C., Stener, M. and Rösch, N., *J. Chem. Phys.*, **1997**, *106*, 5189.

21. Häkkinen, H. and Landman, U., *Phys. Rev. B*, **2000**, *62*, R2287.

22. Wang, J., Wang, G. and Zhao, J., *Phys. Rev. B*, **2002**, *66*, 035418.

23. Rao, C.N.R., Kulkarni, G.U., John Thomas, P. and Edwards, P.P., *Chem. Eur. J.*, **2002**, *8*, 29.

24. Ryabov, A.D., Roznyatovskaya, N.V., Suwinska, K., Revenco, M. and Ershov, A.Y., *J. Biol. Inorg. Chem.*, **2003**, *8*, 815.

25. Hesek, D., Hembury, G.A., Drew, M.G.B., Taniguchi, S. and Inoue, Y*., Inorg. Chem.*, **2001**, *40*, 2478.

26. Du, M., Ge, X.-J., Liu, H., Bu, X.-H., *J. Mol. Struct.*, **2002**, *610*, 207.

27. GaussSum 0.8, O'Boyle, N.M. and Vos, J.G., **2004**, Dublin City University.

28. Guckian, A.L., PhD Thesis, **2002**, Dublin City University.

29. (a) Morokuma, K., *J. Chem. Phys.*, **1971**, *55*, 1236. (b) Kituara, K. and Morokuma, K., *Int. J. Quantum Chem.*, **1976**, *10*, 325.

30. Gordon, M.S. and Jensen, J.H., in *Encyclopedia of Computational Chemistry*, Vol. 5, p. 3198, *ibid.*

31. The PC GAMESS, ver. 6.2, Granovsky, A.A., **2001**. Available at http://classic.chem.msu.su/gran/gamess/index.html

32. Schmidt, M.W., Baldridge, K.K., Boatz, J.A., Elbert, S.T., Gordon, M.S., Jensen, J.H., Koseki, S., Matsunaga, N., Nguyen, K.A., Su, S., Windus, T.L. Dupuis, M. and Montgomery Jr., J.A., *J. Comput. Chem.*, **1993**, *14*, 1347.

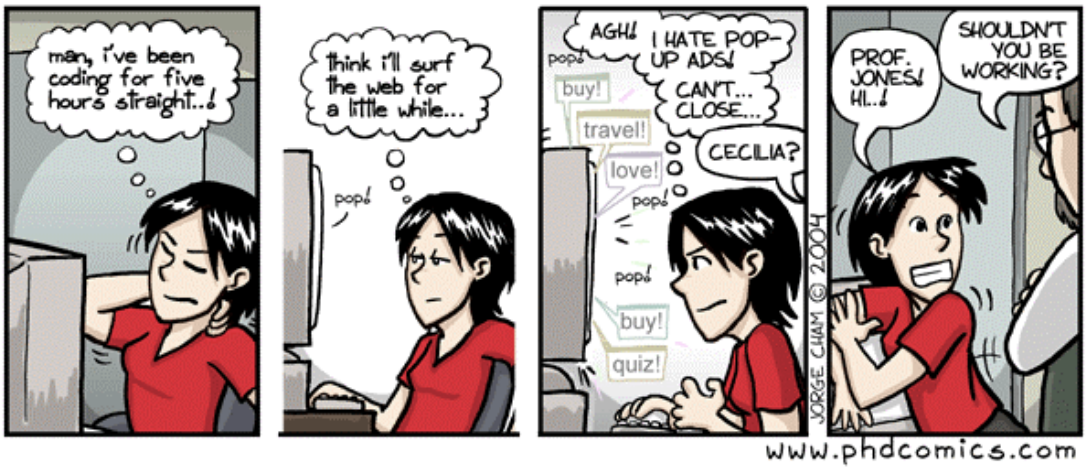
man, i've been coding for five hours straight..!
think i'll surf the web for a little while...
pop!
AGH! I HATE POP-UP ADS!
pops
buy!
travel!
love!
pop!
CAN'T... CLOSE...
CECILIA?
pop!
buy!
quiz!
PROF. JONES! HI..!
SHOULDN'T YOU BE WORKING?
JORGE CHAM © 2004
www.phdcomics.com

Chapter 7
Overview

An overview is presented of the information available from DFT calculations on ruthenium polypyridyl complexes. Some suggestions for further work are made.

7.1 Density Functional Theory as a tool for studying ruthenium polypyridyl complexes

One of the main aims of this thesis is to assess the usefulness of DFT as a tool for studying ruthenium polypyridyl complexes. This section summarises the information available from DFT calculations on ruthenium polypyridyl complexes.

The electronic structure of a complex is of great importance to an inorganic chemist. Photophysical, photochemical and electrochemical properties are directly related to the location and nature of excited states, and the location of the HOMO and the LUMO. DFT calculations produce a large amount of information regarding the molecular orbitals – the difficult part is to interpret this information to give insight into the nature of the electronic structure. Partial Density of States (PDOS) spectra are particularly useful for this purpose, as comparison of the PDOS spectra of related complexes highlights key differences in their electronic structure. PDOS spectra were used extensively throughout the work described in Chapters 3 and 4, which focus on electronic structures

If we consider electrochemistry first of all, it may reasonably be expected that DFT calculations on the ground state of an inorganic complex can (a) predict the sites of electrochemical oxidation and reduction, and (b) indicate which complexes are more easily oxidised/reduced than others. In Chapters 3 and 4, it is shown that ease of oxidation is directly correlated with the location of the peak of the Ru PDOS in the frontier occupied region. Furthermore, it is noted that the energy of the HOMO is poorly correlated with ease of oxidation. In fact, the location of the HOMO can be different from site of oxidation (see **4** in Chapter 3). In Further Work, below, an alternative strategy for the prediction of the site of electrochemical oxidation/reduction is outlined.

The location of the excited state, a ^{3}MLCT state, was found in general to coincide with the location of the lowest unoccupied orbitals. This is despite a number of assumptions: that the 'virtual' KS orbitals from the DFT calculations are equivalent to unoccupied orbitals; that the lowest energy transition is to the lowest unoccupied orbitals; and that the ^{1}MLCT state is located on the same ligand as the ^{3}MLCT state. However, in some cases, the calculations showed that the bipyridines and the third ligand, LL, made almost equal contributions to the lowest unoccupied molecular

orbitals, but the experimental results indicated that the excited state was based entirely on one ligand or the other. The example of **$H_2$5** in Chapter 4 illustrates the fact that even a TDDFT calculation of the lowest energy singlet transition does not always accurately identify the position of an excited state.

DFT at the B3LYP/LanL2DZ level does not yield quantitatively accurate thermodynamic information. However, qualitatively speaking, the results are in reasonable agreement with experiment. It should be noted that the calculations are for gas phase molecules, whereas the experimental results are obtained in solution. Where thermodynamics is not expected to be the driving force, for example, for the methylation reactions described in Chapter 3, we found that local reactivity indices do not provide the correct answer. Thus, care must be taken not to base predictions on reactivity indices that have not been tested extensively for the reaction under study.

The studies of homovalent $Ru^{II}Ru^{II}$ dinuclear complexes described in Chapter 4 provide useful information on the interaction between the metal centres, and on the difference in electronic structure between the dinuclear and mononuclear complex. In particular, if a dinuclear complex has internuclear communication, the PDOS spectra of the bridge moieties is shifted to lower energy on coordination of the second metal centre. The PDOS spectra of such complexes also reveal molecular orbitals that are delocalised across the bridge. These studies will form the basis for a more in-depth investigation of triplet excited states and of the electronic structures of the mixed-valence dinuclear complexes.

DFT calculations predict Raman frequencies quite well, although a scaling factor is required. This is despite the fact that it was not possible to include solvent effects. The positions of experimental peaks from resonance Raman measurements clearly coincide with peaks in the calculated spectrum, but the calculated intensities differ from their experimental values. These calculations provide information on the vibrations giving rise to each peak, as well as the effect of deuteration. Chapter 5 is a base upon which future Raman frequency calculations will build (see Further Work below).

Chapter 6 described a study of the adsorption of osmium complexes on a Au(111) surface. The only previous study of a Ru or Os polypyridyl complex adsorbed on a surface is described in Chapter 1. The potential of these studies, as well as their

current limitations, are highlighted by the work described in Chapter 6. The effect of adsorption on the energy levels of the complex, and in particular, the change in the adsorption energy on oxidation of the complex, are two of the most interesting aspects of this work. The main limitation with this type of study is the size of problem and the approximations required to keep the problem to a manageable size. It is necessary to use a cluster model, to reduce the size of the basis set on atoms that are distant from the adsorption site, and to use a partial optimisation of the degrees of freedom of the system. In particular, the study of the system with the oxidised complex is very computationally expensive.

It should be noted that all of the work described in this thesis used the B3LYP functional. It was outside the scope of this study to investigate the accuracy of results derived from other DFT functionals. The development of new functionals is an area of active research and attention should to paid to the current literature, especially where comparisons between functionals have been made for inorganic complexes.

In addition to the work described in this thesis, the literature described in Chapter 1 gives example of other information available from DFT calculations on ruthenium polypyridyl complexes, ranging from studies of basicities, to excited state calculations and calculation of redox potentials.

7.2 Further work

The studies described in this thesis focussed on ground state calculations, and some TDDFT studies of singlet transitions. Much of the interesting chemistry of ruthenium polypyridyl complexes relates to triplet states, or the mixed valence states of RuRu dinuclear complexes. These are two areas which have not been touched upon in this thesis, but which merit further investigation. For example, how good is the agreement between predicted and calculated emission values? Can DFT predict the Robin and Day Class of the dinuclear complexes discussed in Chapter 4?

Although briefly dealt with in Chapter 6, the effect of oxidation/reduction on the energy levels of ruthenium (or osmium) complexes has not been well studied using computational techniques. In addition the site of oxidation or reduction could be

identified by modelling the oxidised/reduced species, or by looking at the instantaneous change in electron density associated with oxidation/reduction.

Raman frequency calculations on heteroleptic complexes are the logical extension of the work described in Chapter 5. Are different scaling factors required for different ligands? or for the same ligand in different complexes? Does coupling occur between vibrations involving different ligands?

As mentioned at the end of Chapter 1, a DFT study of the N3 dye attached to a TiO_2 substrate would be of great interest to researchers working in the area of dye sensitised solar cells.


WELL, GENTLEMEN, LET'S STOP POST-PONING THE INEVI-TABLE, AND HEAD BACK TO THE LAB...
sigh... if we must.
COFFEE, ANYONE?
I'M IN.
I'M IN.
I'M IN.
ZZZZZ
JORGE CHAM © 2004
www.phdcomics.com

Appendix A
Control of the interaction between a surface and a molecular component

This appendix describes an experimental study of the effect of the $LiClO_4$ concentration on the interaction between an adsorbed ruthenium-based dye and a nanocrystalline TiO_2 substrate. The dyes used in this chapter are ruthenium polypyridyl complexes containing at least one H_2dcb ligand (where H_2dcb is 4,4'-dicarboxy-2,2'-bipyridine). Emission from adsorbed complexes is reduced by increasing the $LiClO_4$ concentration. This is due to a decrease in the energy of the TiO_2 conducting band, thus favouring electron injection over emission. The photophysical properties of a RuRu dimer and a RuOs dimer are examined at room temperature and at 77K. Preliminary studies indicate that the location of the emitting state in RuOs may be temperature-dependent. Emission only occurs from the Os centre at room temperature. At 77K, emission is also observed from the Ru centre.

A.1 Introduction

A.1.1 Dye-sensitised solar cells

Increasing concern over dwindling supplies of oil and coal, and the fact that conventional energy sources are a major contributor to air pollution and greenhouse gases, have led to a search for cleaner renewable sources of energy. Among these, solar power is a strong contender. The sun supplies $3x10^{24}$ J to the earth per year, 10000 times more than our present needs require.[1]

In 1991, O'Regan and Grätzel[2] developed the first dye-sensitised solar cell (DSSC) that used nanocrystalline TiO_2 (Figure A.1). The 'Grätzel' cell consisted of a nanocrystalline TiO_2 layer laid down on a conducting glass substrate. The surface of the TiO_2 was sensitised by a ruthenium complex, usually referred to as the dye. The nanostructured material had an internal surface area up to 1000 times the external area, allowing monolayer coverages of the dye to achieve large optical densities. A liquid electrolyte was used containing a redox mediator, I^-/I^{3-} in H_2O. When light was absorbed by the dye, it became excited and injected an electron into the conducting band of the semiconductor (see below). The electron was picked up at the back contact and passed through the external circuit to the counter electrode. The redox mediator reduced the oxidised dye and was in turn reduced at the counter electrode, thus regenerating the initial state of the cell.

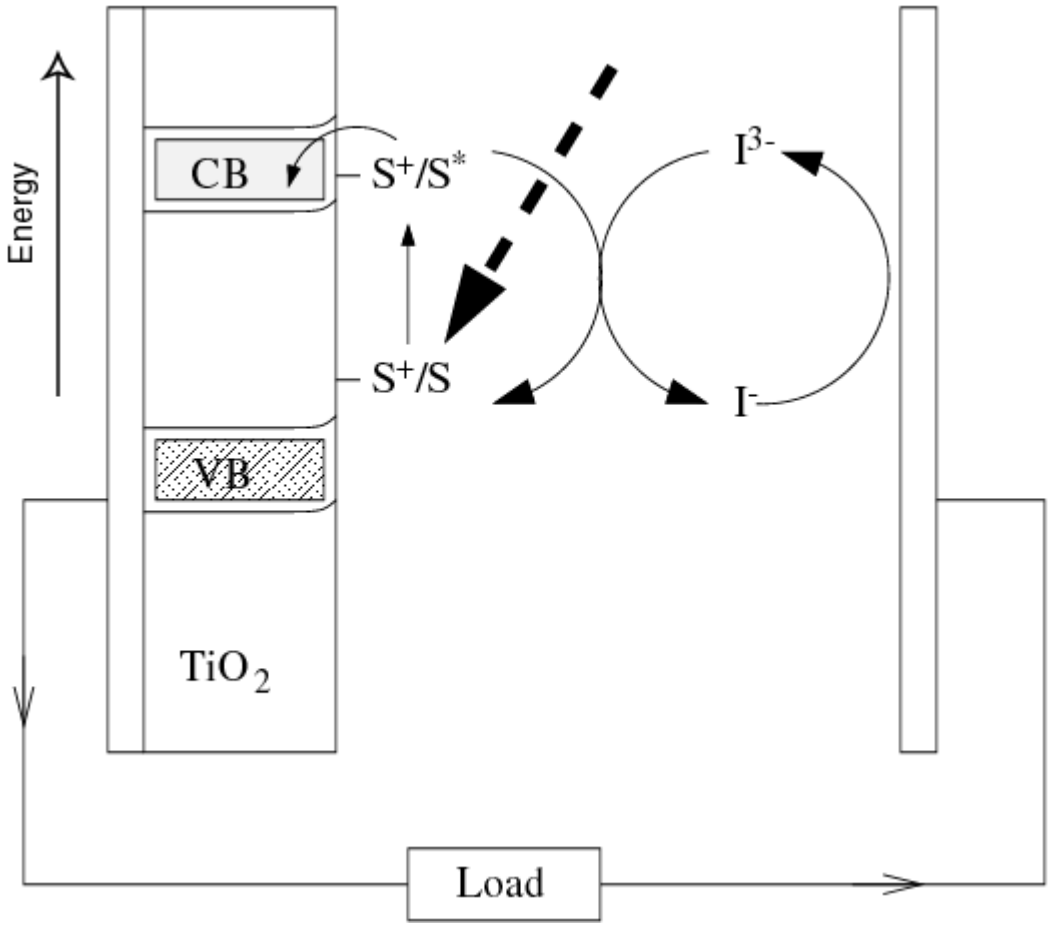

Figure A.1 – Schematic of the Grätzel cell. S^+/S indicates the redox level of the sensitiser. S+/S* indicates the redox level of the excited state of the sensitiser. CB and VB are the conducting band and valence band of the TiO_2, respectively (see below).

The dyes used in DSSCs are typically ruthenium polypyridyl type complexes, although studies on organic dyes such as porphyrins are also common. The ruthenium complexes bind to the surface through ester or phosphonate linkages. This chapter will focus on ruthenium complexes that bind through ester linkages.

A.1.2 Interfacial electron transfer

The key step in the DSSC is the injection of an electron into the TiO_2. This is referred to as the charge-separation step, since the previously neutral system now contains a substrate with a negative charge, and a dye with a positive charge. This step, of great importance in DSSCs, is also of interest in the area of molecular

devices and molecular electronics, where charge separation on a nanoscale is one of the key aims.

The relative energy levels of the TiO_2 and adsorbed dye play an important role in this process. Due to the extended 3-dimensional structure of crystals, the orbitals of the TiO_2 tend to occur in groups, or bands. The highest occupied band is called the valence band, while the lowest vacant band is called the conducting band (VB and CB, respectively, in Figure A.1). Semiconductors are classified as materials which have an energy gap (the band gap) between the valence band and the conducting band. TiO_2 is one of a number of wide band gap semiconductors. The anatase form of TiO_2 (which is used in DSSCs) has a band gap of 3.2eV. The valence band consists of orbitals derived from the filled 2p orbitals of O^{2-}, while the conduction band is based on the empty 3d orbitals of Ti^{4+}.

Charge separation on the surface of a dye-sensitised nanocrystalline TiO_2 film is achieved kinetically – that is, the rate of the charge injection process is greater than the rate of the charge recombination process. The relative rates of these processes have been extensively studied.[3,4,5,6,7] It suffices here to note that it is generally agreed that electron injection is an ultrafast process (femtosecond timescale), whereas the recombination process is in the Marcus inverted region and occurs on the microsecond timescale. Dinuclear complexes, or supramolecular dyads, have been developed which decrease the rate of back electron transfer (charge recombination) by increasing the distance over which the electron transfer must take place. The **RuRu** and **RuOs** dinuclear complexes described in this chapter (and first described by Lees *et al.*[8]) are examples of such systems.

In order for electron injection to be energetically favourable, the redox level of the excited state of the dye must be more negative than the conducting band of the TiO_2. Even then, deactivation of the excited state by radiative and non-radiative decay competes with electron injection. Little information is available on the competition between electron injection and emission. In a typical DSSC, the system is chosen so that the quantum efficiency of electron injection approaches unity. However, control over the relative rates of these processes is important for a molecular device.

The study described in this chapter involves the use of Li^+ to control the rate of charge injection. Li^+ is a potential-determining cation for TiO_2. In a non-aqueous

solvent, Li^+ ions control the level of the conducting and valence bands relative to the solvent. By increasing the concentration of Li^+, the energy of the conducting band is reduced, and electron injection is favoured over emission. Emission spectroscopy is thus a simple technique for monitoring this process. This technique was used in a study by Farzad *et al.*[9] who coadsorbed two dyes on a TiO_2 surface and investigated the rates of intermolecular energy transfer versus electron injection.

The complexes discussed in this chapter are composed of the ligands shown in Figure A.2. The complexes themselves are shown in Figure A.3.

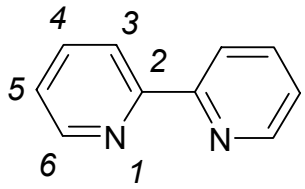

bpy
2,2'-bipyridine

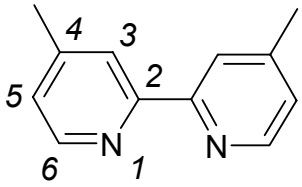

diMebpy
4,4'-dimethyl-2,2'-bipyridine

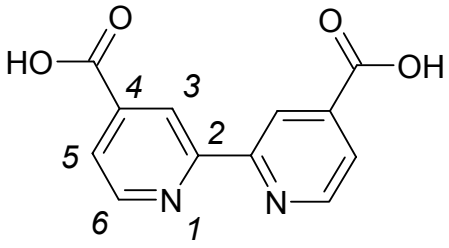

H_2dcb
4,4'-dicarboxy-2,2'-bipyridine

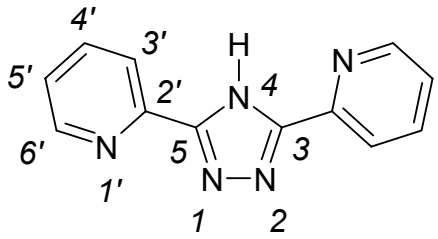

Hbpt
4*H* -3,5-bis(pyridin-2-yl)-1,2,4-triazole

Figure A.2 – Ligands discussed in this chapter, and the numbering system used.

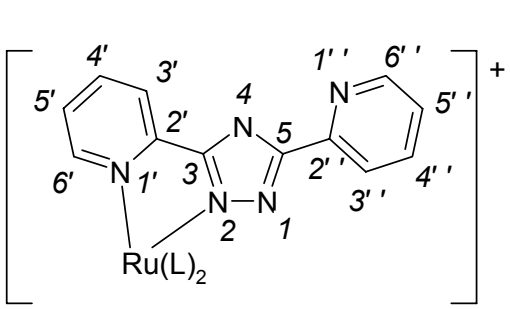

1 L=H_2dcb
d1 L=[d_6]-H_2dcb

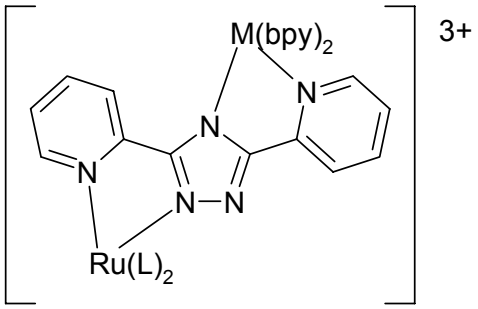

RuRu M=Ru, L=H_2dcb
RuOs M=Os, L=H_2dcb

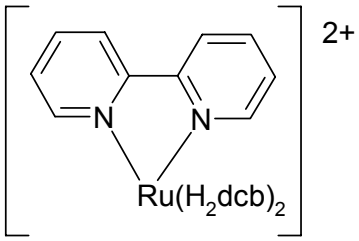

2 $[Ru(H_2dcb)_2(bpy)]^{2+}$

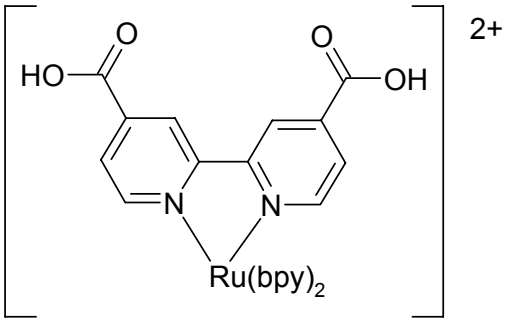

3 $[Ru(H_2dcb)(bpy)_2]^{2+}$

Figure A.3 – Complexes discussed in this chapter.

A.2 Experimental

All ^{1}H NMR and ^{1}H COSY NMR experiments were recorded on a Bruker Avance 400 NMR Spectrometer and the free induction decay (FID) profiles processed using XWIN-NMR software package. UV/Vis spectra were recorded on a Shimadzu UV/Vis/NIR 3100 spectrophotometer. Emission spectra were recorded on a Perkin-Elmer LS50 or LS50-B Luminescence spectrophotometer. Measurements at 77 K were carried out in a liquid nitrogen filled glass cryostat, with the sample held in a NMR tube. These samples were also measured at room temperature using the same apparatus. Emission spectra are uncorrected for photomultiplier response. pH titrations were carried out in Britton-Robinson buffer (0.04 M H_3BO_3, 0.04 M H_3PO_4, 0.04 M CH_3CO_2H). Elemental analysis of C, H and N was carried out at the Microanalytical Laboratory of University College Dublin (UCD) using an Exador analytical CE440.

TiO_2-coated glass slides were provided by Dr. Egbert Figgemeier of the University of Uppsala. The glass slides were rinsed with ethanol and air-dried before being left overnight in a 0.05M solution of the dye in MeCN. The solvent was rinsed from the slide using ethanol and the slide allowed to air-dry. Emission measurements required the use of a wide-top cuvette, and a wedge to fix the slide in place. The wedge used was a section from a Pasteur pipette. Pieces of a glass coverslip were often also used. The experimental setup is shown in Figure A.4. Note that the wedge does not interfere with the path of the light from source to detector. Due to the orientation of the glass slide in the cuvette, reflection of incident light from the glass surface is not a problem. Each slide was used for a single experiment, in order to ensure reproducibility.

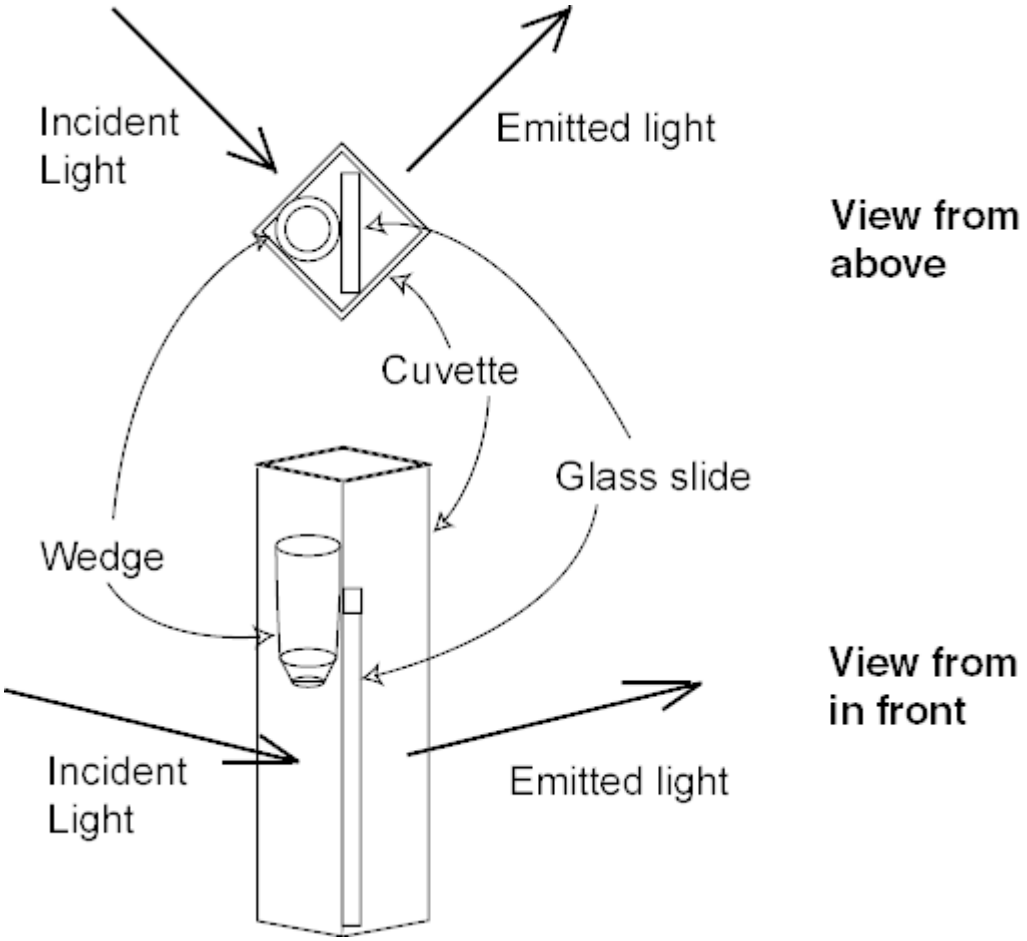

Figure A.4 – Experimental setup for measurement of emission from a TiO_2-coated glass slide.

A.3 Synthesis

All chemicals used were of reagent grade. Dr. W.R. Browne (Dublin City University) provided [D_6]-H_2dcb, [D_8]-bpy and complex **3**. See Figure A.2 for the structure and numbering scheme of the ligands.

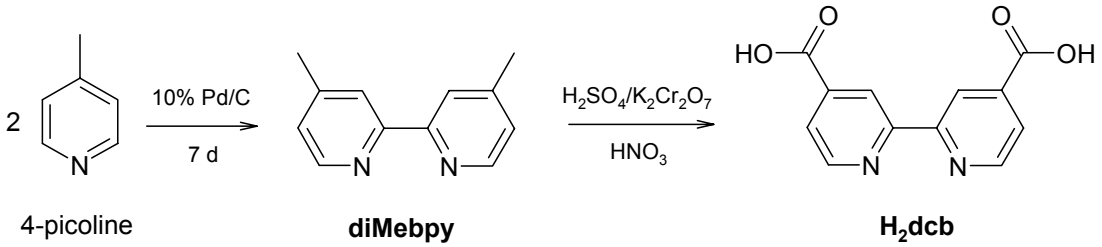

4-picoline **diMebpy** **H_2dcb**

Scheme A.1 – Synthesis of H_2dcb **from 4-picoline.**

Synthesis of 4,4'-dimethyl-2,2'-bipyridine, diMebpy **(Scheme A.1)**

Freshly distilled 4-picoline (~160 cm^3, 1.6 mol) was refluxed with 5 g 10% Pd/C for 7 d. Toluene (50 cm^3) was added and the mixture was refluxed for a further 0.5 h. The mixture was filtered while still warm to remove the catalyst and left at 4°C overnight. The precipitate of pale yellow crystals was recrystallised from ethyl acetate to give colourless crystals. Yield: 4.9 g, 26.7 mmol, 1.7%. ^{1}H NMR ([D_6]-DMSO): 8.53 (d, H6), 8.23 (s, H3), 7.28 (d_d, H5), 2.41 (s, Me).

Adapted from the methods of Sprintschnik *et al.*[10] and Ghosh and Spiro.[11]

Synthesis of 4,4'-dicarboxy-2,2'-bipyridine, H_2dcb **(Scheme A.1)**

DiMebpy (9.9 g, 53.8 mmol) was added to a stirring solution of H_2SO_4 (98%, 250 cm^3). Potassium dichromate (48.4 g, 164.5 mmol) was added in small portions with stirring using an ice-bath to keep the temperature between 70°C and 80°C. After the temperature fell below 40°C, the reaction mixture was poured into 1.6 L of ice water and stirred. The precipitate was filtered, washed with water and dried. The solid was then refluxed for 4 h in 68% HNO_3 (170 cm^3), poured over ice and diluted with water (800 cm^3). The chalky-white precipitate was filtered, washed with water (5x50 cm^3), acetone (2x20 cm^3) and dried. Yield: 12.0 g, 48.0 mmol, 91.1%. ^{1}H NMR ([D_6]-DMSO): 8.89 (d, H6), 8.84 (s, H3), 7.90 (d_d, H5).

The method of Oki and Morgan[12] was used.

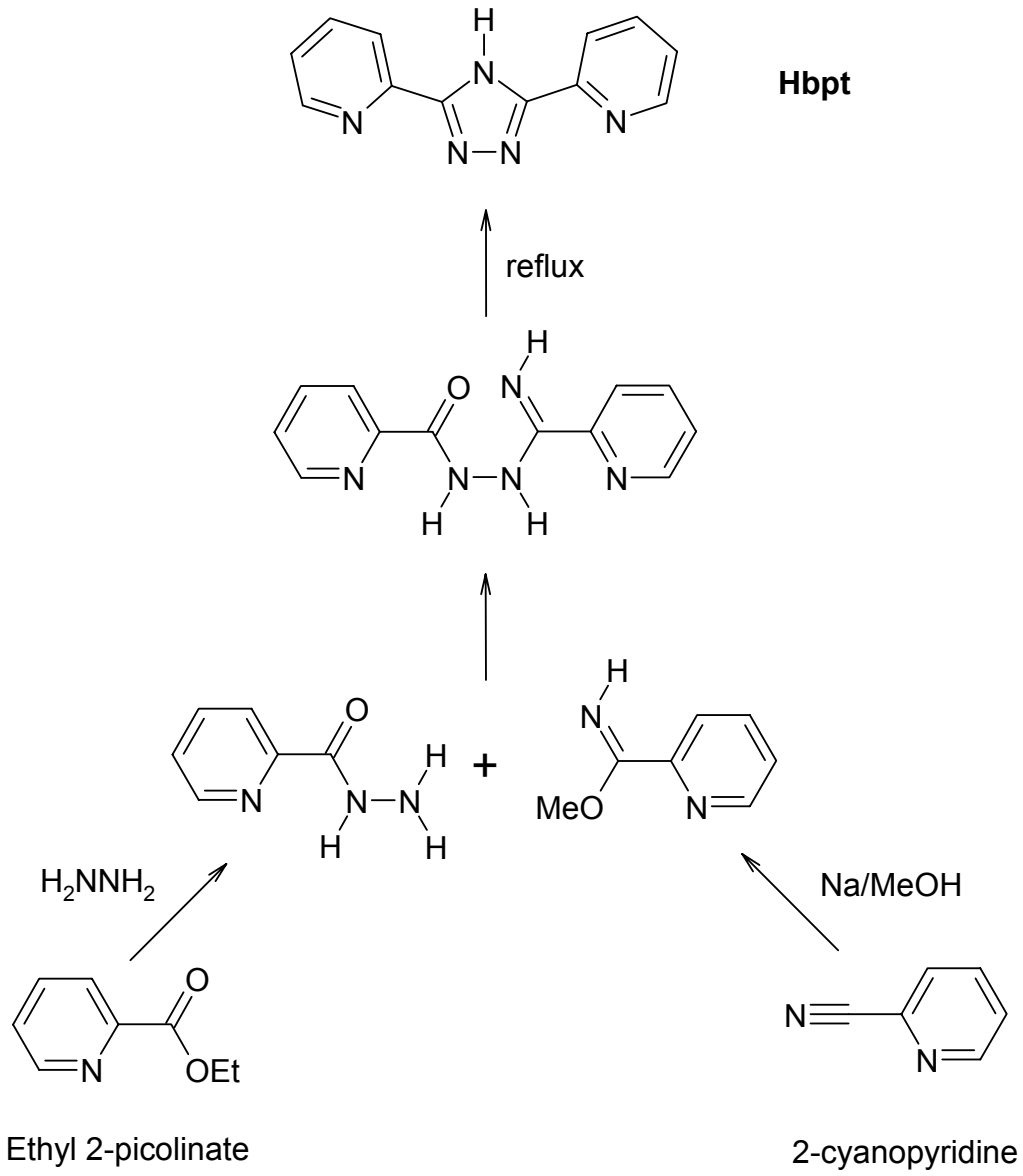

Scheme A.2 – Synthesis of Hbpt **from ethyl 2-picolinate and 2-cyanopyridine.**

Synthesis of 4*H*-3,5-bis(pyridin-2-yl)-1,2,4-triazole, Hbpt **(Scheme A.2)**

Hydrazine monohydrate (2 equiv. v/v) in ethanol (30 cm^3) was added to ethyl picolinate (10 cm^3, 74 mmol) with stirring, and left at –4°C overnight. The pyridylhydrazide was filtered, washed with 10 cm^3 diethyl ether, and dried. Sodium (0.7 g) was added to 2-cyanopyridine (equimolar to the pyridylhydrazide) in methanol (30 cm^3) and refluxed for 3 h to form the pyridylimidate. The pyridylhydrazide was added to the solution and heated for 15 min. The precipitate (a yellow intermediate) was heated under reflux for 1 h in a minimal quantity of ethylene glycol to yield the product. The product was recrystallised from hot ethanol

to give a white solid. Yield: 3.46 g, 15.5 mmol, 21%. ^{1}H NMR ([D_6]-DMSO): 8.70 (d_d, H6'), 8.16 (d, H3'), 7.97 (t_d, H4'), 7.48 (d_d, H5').

The general method used here is described in the theses of Dr. Wesley Browne[13] and Dr. Donal Hughes[14], both from Dublin City University.

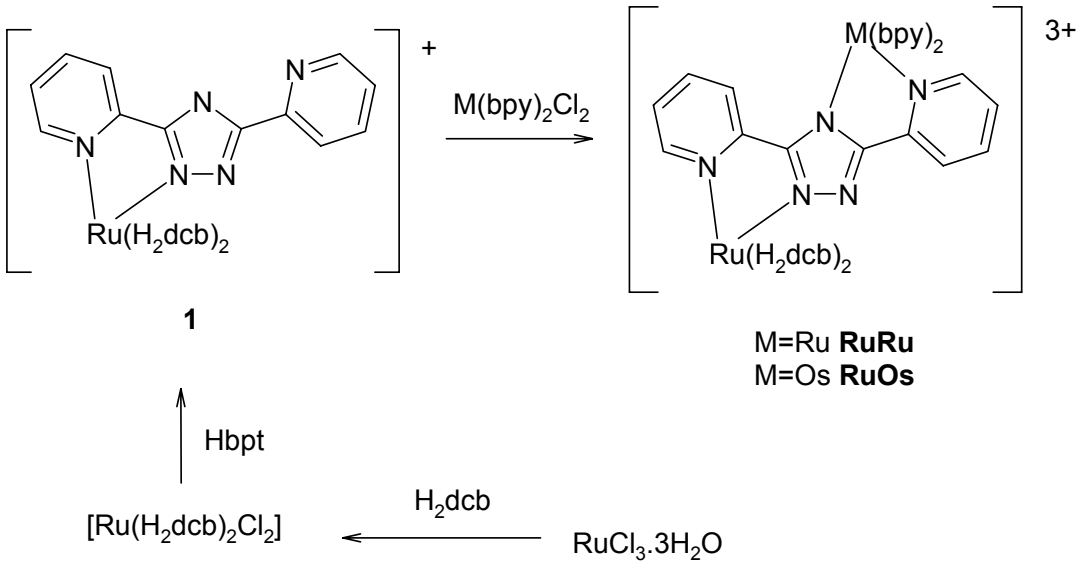

Scheme A.3 – Synthesis of 1**,** RuRu **and** RuOs**.**

Synthesis of [*cis*-Ru(H$_2$dcb)$_2$Cl$_2$].3H$_2$O (Scheme A.3)

A solution of $RuCl_3.3H_2O$ (687 mg, 2.63 mmol) and H_2dcb (1.283 g, 5.36 mmol) in dimethylformamide (20 cm^3) was microwaved at 240 W for 16 min. The solution was filtered to remove the tris byproduct and the solvent evaporated under reduced pressure. Acetone was added to precipitate the product, a black powder. The product was washed with acetone, then with diethyl ether and finally dried. Yield: 1.107 g, 1.550 mmol, 59%. ^{1}H NMR ([D_6]-DMSO): 10.12 (d, H6'), 9.09 (s, H3'), 8.92 (s, H3), 8.26 (d, H5'), 7.77 (d, H6), 7.53 (d_d, H5). See Figure A.6.

Adapted from the method described by Liska *et al.*[15]

Synthesis of [*cis*-Ru([D_6]-H_2dcb)$_2$$Cl_2$].3$H_2O$

[*cis*-Ru([D_6]-H_2dcb)$_2$$Cl_2$] was prepared in the same way as [*cis*-Ru(H_2dcb)$_2$$Cl_2$] from [$RuCl_3$] and [$D_6$]-$H_2$dcb.

Synthesis of Na_3[Ru(H_2dcb)$_2$bpt].3H_2O, 1 **(Scheme A.3)**

Hbpt (248 mg, 1.11 mmol) was heated under reflux in 2:1 ethanol/water (40 cm^3) to which [Ru(H_2dcb)$_2$$Cl_2$].3$H_2O$ (661 mg, 926 µmol) was added slowly over 3 h. After a further 3 h, the volume of the solution was reduced to ca. 10 cm^3 and the product precipitated using 0.2 M HCl. Purification of the product was achieved by dissolving the product in basic water and utilising column chromatography with Sephadex LH20 resin (neutral water). The product was isolated after chromatography by adjusting the pH with HCl as before. Yield: 318 mg, 341 µmol, 37%. ^{1}H NMR ([D_6]-DMSO): (bpt$^-$ resonances, numbered as shown in Figure A.3) 8.49 (d, H6''), 8.24 (d,H3'), 8.04 (t, H4'), 7.97 (d, H3''), 7.87 (m, H4''), 7.51 (d, H6'), 7.37 (m, H5''), 7.30 (t, H5'). See Figure A.7.

The method used was that of Lees *et al.*[8]

Synthesis of Na_3[Ru([D_6]-H_2dcb)$_2$bpt].3H_2O, d1

Na_3[Ru([D_6]-H_2dcb)$_2$bpt] was prepared in the same way as Na_3[Ru(H_2dcb)$_2$bpt] from [Ru([D_6]-H_2dcb)$_2$$Cl_2$].3$H_2O$ and Hbpt.

Synthesis of Na_4[Ru(H_2dcb)$_2$(bpt)Ru(bpy)$_2$].(PF_6)$_3$.3H_2O, RuRu **(Scheme A.3)**

Na_3[Ru(H_2dcb)$_2$bpt].3H_2O (339 mg, 363 µmol) and [Ru(bpy)$_2$$Cl_2$].3$H_2O$ (248 mg, 461 µmol) were heated under reflux in ethanol/water (40 cm^3, 2:1 v/v) for 12 h. The volume of the solution was reduced to ca. 10 cm^3 by rotary evaporation and the product precipitated by reducing the pH using 0.2 M HCl. Purification of the product was achieved by dissolving the product in basic water and utilising column chromatography with Sephadex LH20 resin (basic water). The product was isolated after chromatography by adjusting the pH with HCl as before, and isolating the complex as the PF_6 salt. Yield: 67 mg, 38 µmol, 10%. ^{1}H NMR ([D_6]-DMSO): see Figure A.8.

The method used was that of Lees *et al.*[8]

Synthesis of $Na_3[Ru(H_2dcb)_2(bpt)Os(bpy)_2].(PF_6)_2.3H_2O$, RuOs **(Scheme A.3)**

A small amount of zinc was added to a ethanol/water (40 cm^3, 2:1 v/v) solution containing $Na_3[Ru(H_2dcb)_2bpt].3H_2O$ (excess) and $[Os(bpy)_2Cl_2].2H_2O$ (150 mg, 246 μmol), and the mixture refluxed for 24 h. The zinc was removed by gravity filtration and the volume of the solution reduced to ca. 10 cm^3 by rotary evaporation. The pH was lowered by addition of 0.2M HCl (ca. 2 cm^3) and addition of a saturated solution of ammonium hexafluorophosphate (ca. 2 cm^3) yielded the product. Purification was achieved by dissolving the product in basic water and utilising column chromatography with Sephadex LH20 resin (basic water). The product was isolated after chromatography by adjusting the pH with HCl as before, and isolating the complex as the PF_6 salt. Yield: 72 mg, 42 μmol, 17%. ^1H NMR ($[D_6]$-DMSO): see Figure A.9.

The method used was that of Lees *et al.*[8]

Synthesis of $[Ru(H_2dcb)_2(bpy)]Cl_2$, 2

$[Ru(H_2dcb)_2Cl_2]$ (148 mg, 204 μmol) and bpy (45 mg, 287 μmol) were heated under reflux in ethanol/water (40 cm^3, 2:1 v/v) for 5 h. The volume of the solution was reduced to ca. 10 cm^3 by rotary evaporation. The pH of the solution was reduced by addition of 0.2 M HCl (ca. 2 cm^3). Addition of a saturated solution of ammonium hexafluorophosphate (ca. 2 cm^3) yielded the crude product. Purification was achieved by dissolving the product in basic water and utilising column chromatography with Sephadex LH20 resin (basic water). The product was isolated after chromatography by adjusting the pH with HCl as before. Yield: 65 mg, 80 μmol, 39%. ^1H NMR ($[D_6]$-DMSO):

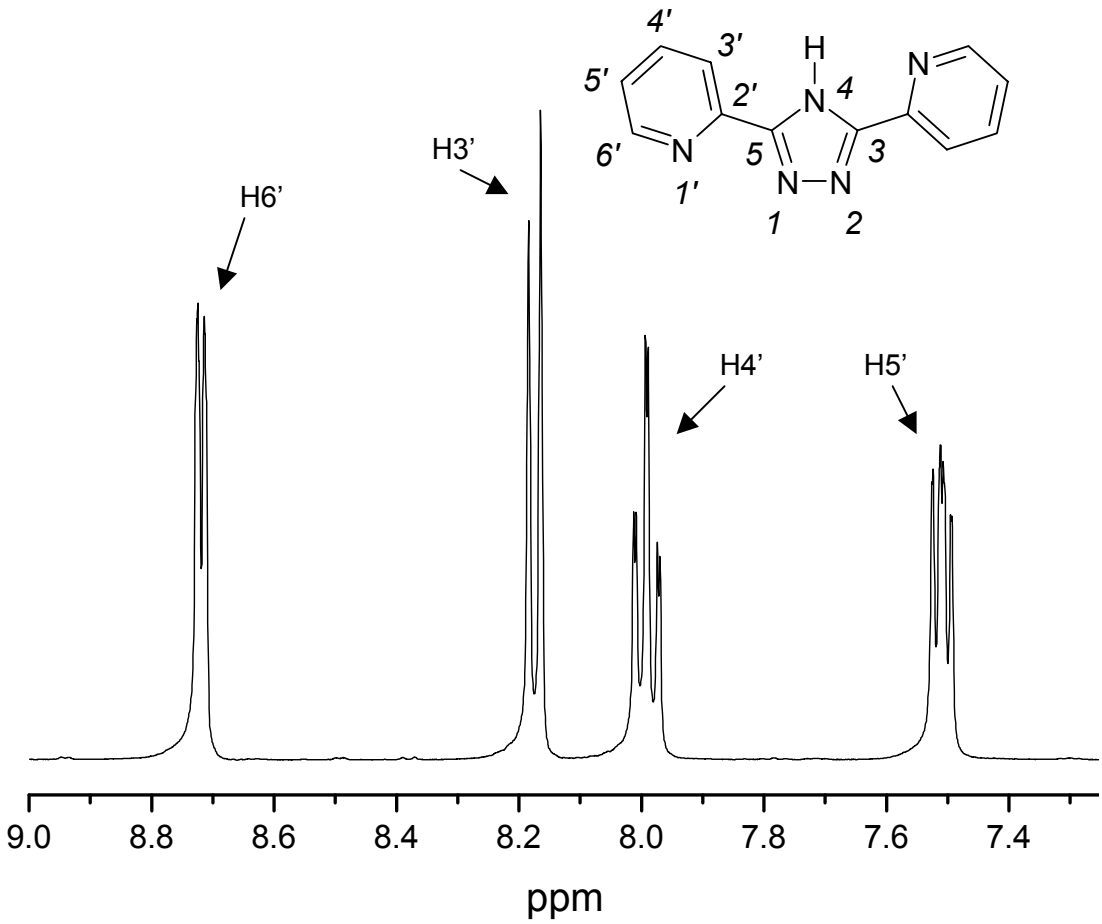

Figure 5 – ^{1}H NMR of Hbpt in [D_6]-DMSO.

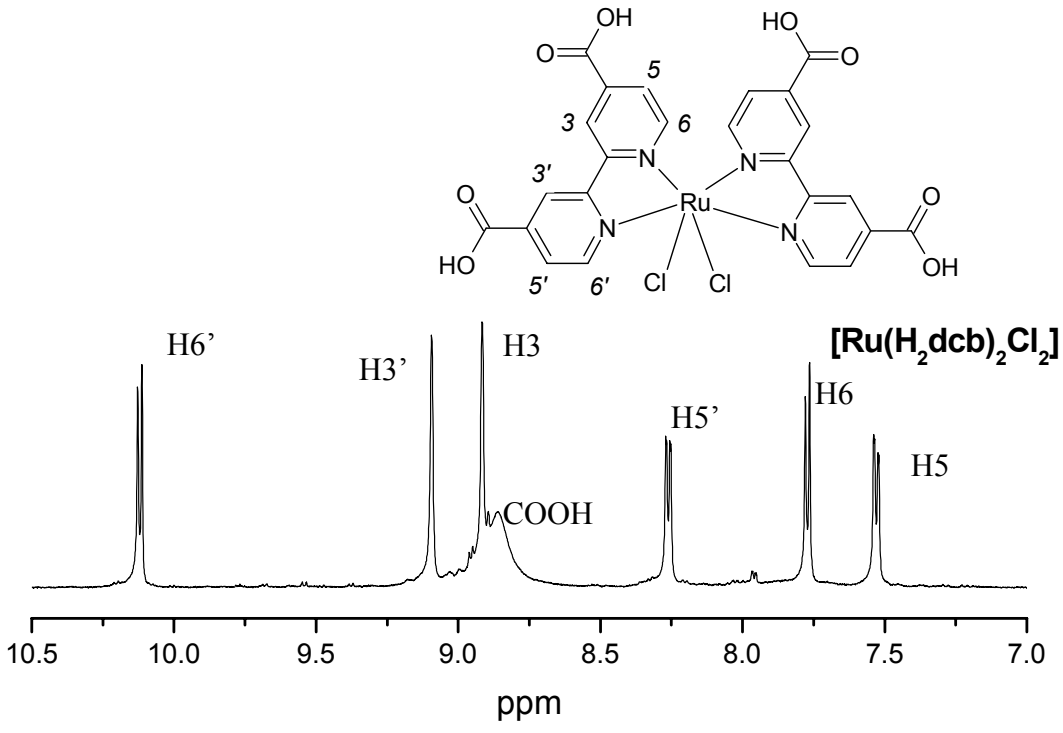

Figure A.6 – ^{1}H NMR of [Ru(H_2dcb)Cl_2] in [D_6]-DMSO.

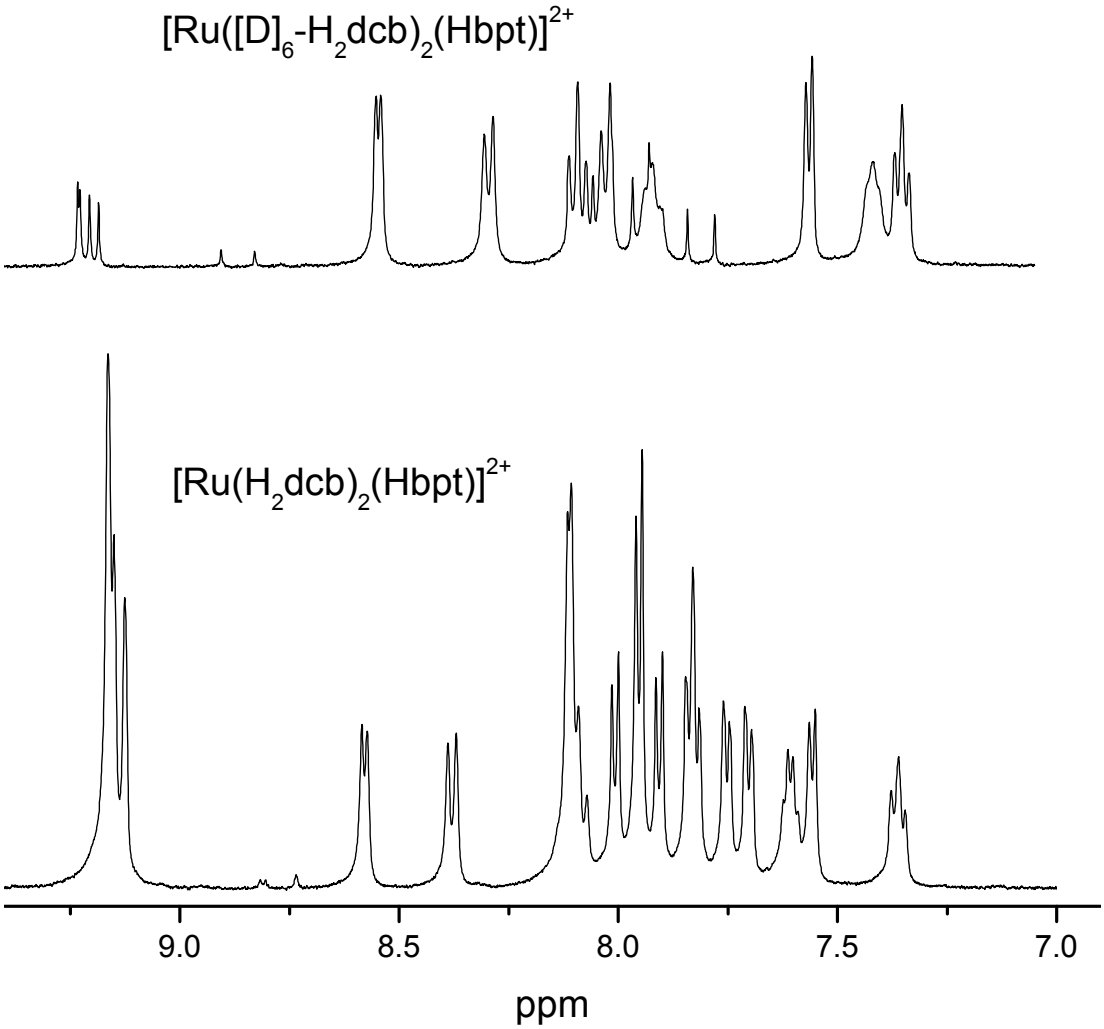

Figure A.7 – ^{1}H NMR of 1 **(bottom) and** d1 **(top) in [D_6]-DMSO.**

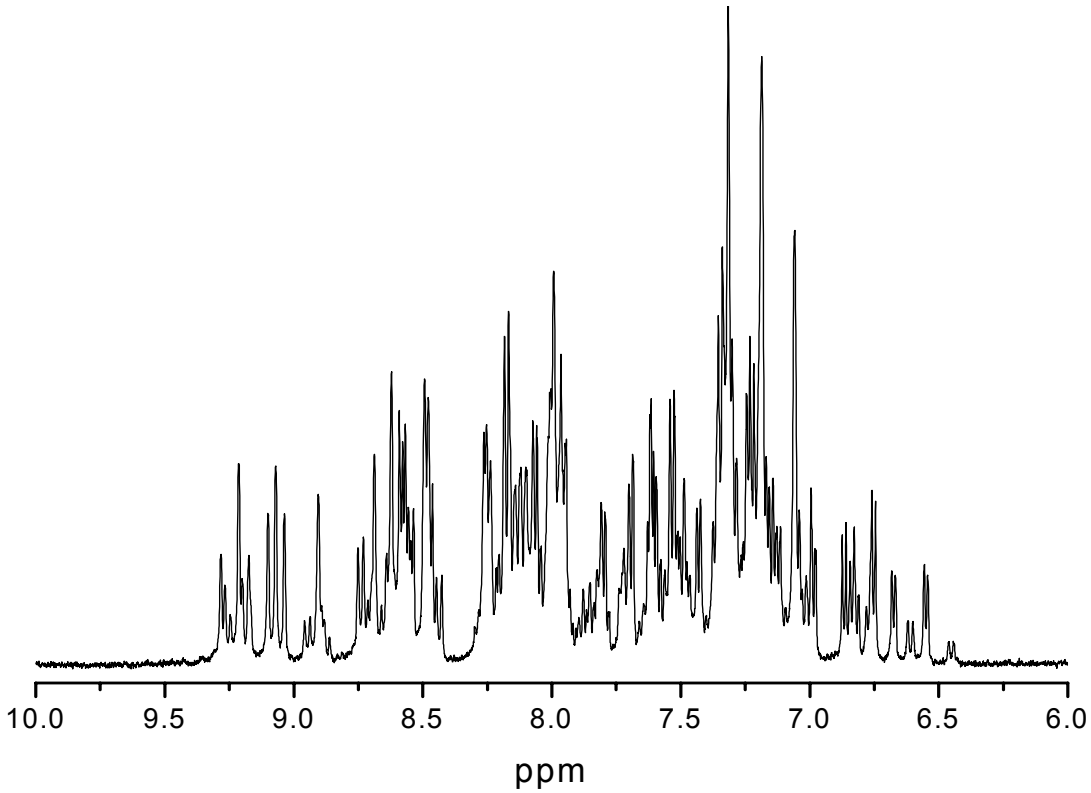

Figure A.8 – ^{1}H NMR of RuRu **in [D_6]-DMSO/NaOD.**

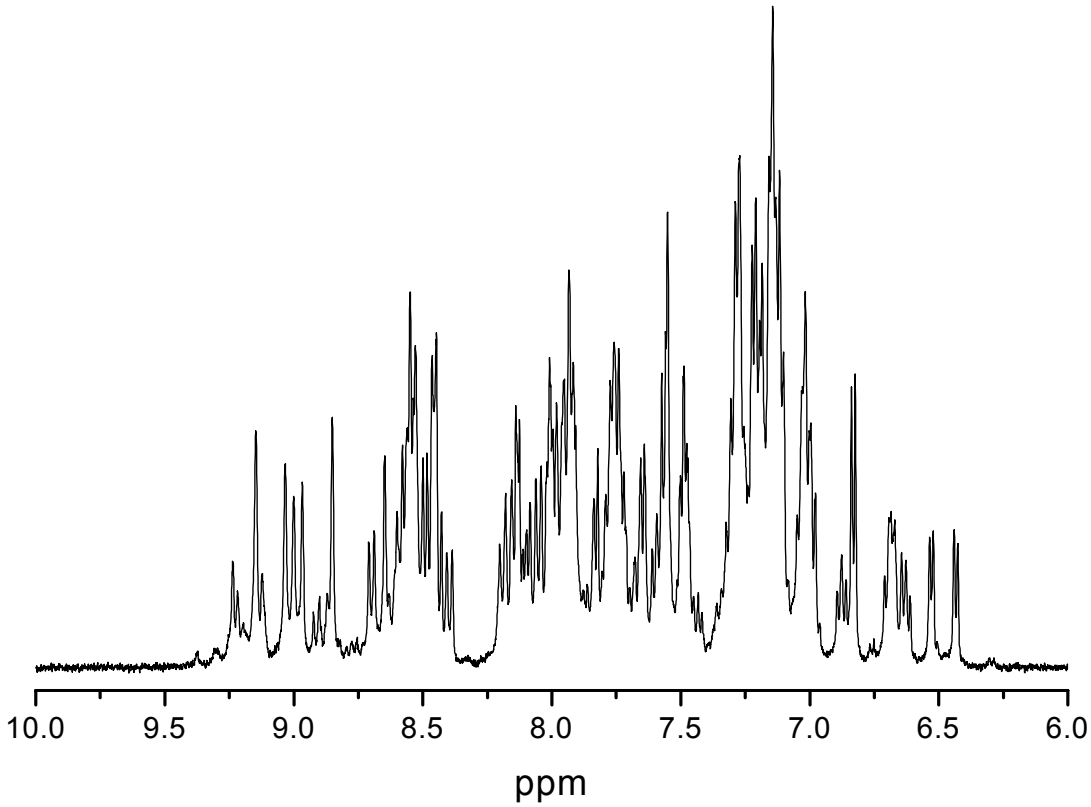

Figure A.9 – ^{1}H NMR of RuOs **in [D_6]-DMSO/NaOD.**

Note on syntheses

Initial synthesis of Hbpt using the method of Geldard and Lions[16] gave a product, LL, whose ^{1}H NMR spectrum was identical to a previously reported spectrum, although shifted somewhat. The product was used to synthesise $[Ru(bpy)_2(LL)]^+$, which emitted strongly, in contrast to the reported photophysical behaviour of $[Ru(bpy)2bpt]^+$. It was concluded that the synthesis had not proceeded beyond the final intermediate – which had an amino group attached at N4 of the triazole. The desired product, Hbpt, was then synthesised using the method described above.

The microwave synthesis of $[Ru(H_2dcb)Cl_2].3H_2O$ presents many advantages in comparison to the conventional method of heating under reflux. The reaction is complete within 16 minutes (at the power used) compared to several hours for the conventional method. A minimum amount of solvent is used. The microwave setup consists of a domestic microwave oven with a hole in the top through which a very long reflux condenser is passed. Even though the amount a solvent used is approx. 20 cm^3, a 500 cm^3 round-bottomed flask should be used to allow room for the solvent to boil, as this can be very vigorous. The progress of the reaction depended strongly on the length of time used for the microwave heating.

If a H_2dcb-containing complex was precipitated using acid, a very fine precipitate was obtained. This required filtering using a Grade 4 sintered frit.

Complexes containing H_2dcb were separated using Sephedex LH20. This column is designed for size-exclusion chromatography but worked well for purification of the complexes discussed in this chapter. The mechanism of separation is unclear, but it is not on the basis of size: compounds not containing H_2dcb were not separated on the column. The crude sample to be columned was divided into fractions of not more than approx. 200 mg. The portion that dissolved in basic water was filtered before being columned in neutral or basic water. A large number of bands were often visible after the initial columning, and fractions had to be recolumned in some cases to ensure separation. Fractions which moved very slowly were eluted using water acidified with a few drops of 0.1M HCl. The Sephedex LH20 could be reused several times, although organic solvents appeared to degrade it quickly.

There is an inherent problem determining the exact composition of complexes containing the H_2dcb ligand. These complexes are precipitated from solutions

(containing NH_4PF_6 in some cases) by reducing the pH using 0.1 M HCl (approx. 2 cm^3). In the solid state, the ligand may be present as either H_2dcb, $Hdcb^-$ or dcb^{2-}. The counter anion will be PF_6^- if present, otherwise Cl^-. However, Na^+ may also be present as a counter cation. According to Lees *et al.*,[8] the amount incorporated is not always the same and may depend on the manner in which the complex is precipitated. The solid-state structures described for the complexes were deduced by Lees *et al.* using mass spectrometry and CHN analyses. Despite this uncertainty in the solid-state composition, photophysical measurements in solution are not affected. In solution, the protonation state of the complexes are governed by the pH of the solution.

A.4 Photophysical studies in solution

Before investigating the emission properties of complexes attached to a solid substrate, it is important to look at their photophysical properties in solution. Figure A.10 shows the absorption and emission spectra of **2** in 0.1M NaOH at room temperature. Both absorption and emission occur at lower energy compared to trisbpy.

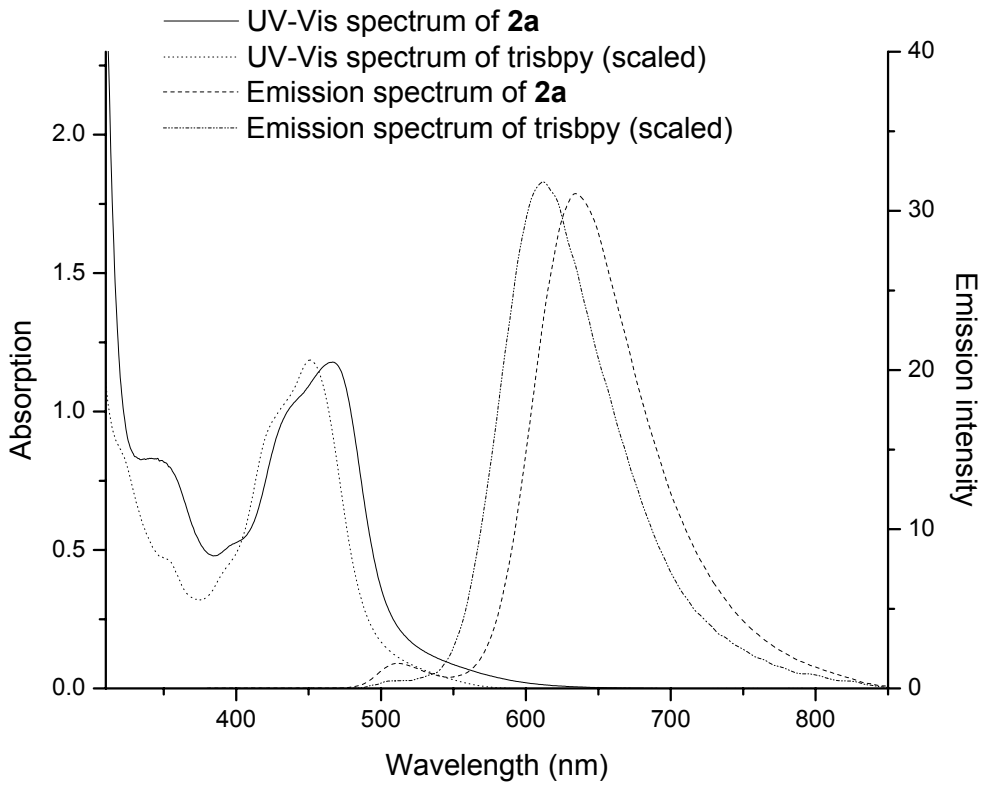

Figure A.10 – UV-Vis and emission spectra of 2 **in 0.1M NaOH, compared with those of trisbpy in MeCN. An excitation wavelength of 381nm was used for the emission spectra.**

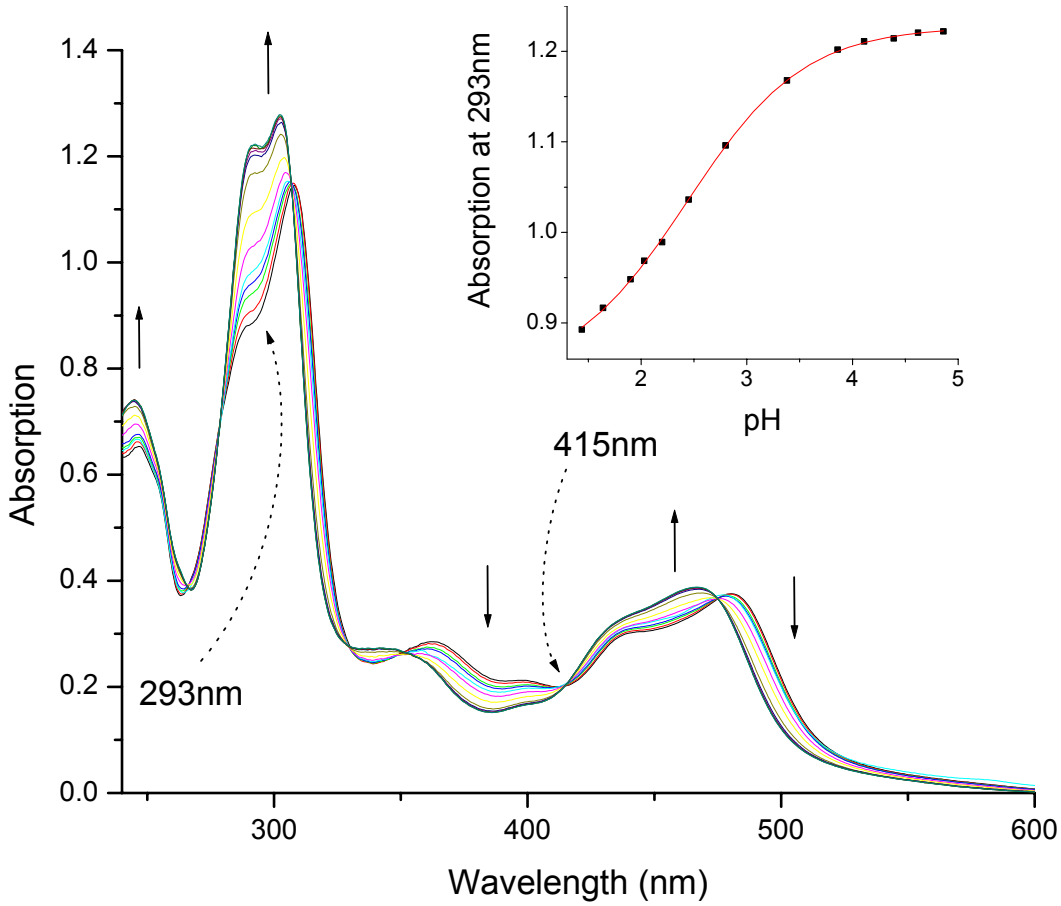

Figure A.11 – pH titration of the absorption spectrum of 2 **in Britton-Robinson buffer. The pH was adjusted using NaOH or sulphuric acid. The arrows indicate the direction of change as pH is increased. The pH values are (a) 1.44, (b) 1.64, (c) 1.80, (d) 1.90, (e) 2.03, (f) 2.20, (g) 2.45, (h) 2.80, (i) 3.38, (j) 3.86, (k) 4.11, (l) 4.39, (m) 4.62, and (n) 4.86. The inset shows a plot of absorption at 293nm versus pH. The data has been fitted with a sigmoidal curve.**

pH titrations of the absorption and emission spectra can yield useful information regarding the pK_a of the ground and excited state complexes, respectively. A pH titration was performed on **2** in Britton-Robinson buffer, using concentrated NaOH and H_2SO_4 to adjust the pH. The resulting absorption spectra is shown in Figure A.11, and the emission spectra are shown in Figure A.12. For the emission spectra, the sample was excited at an isosbestic point (415nm) in the absorption spectrum.

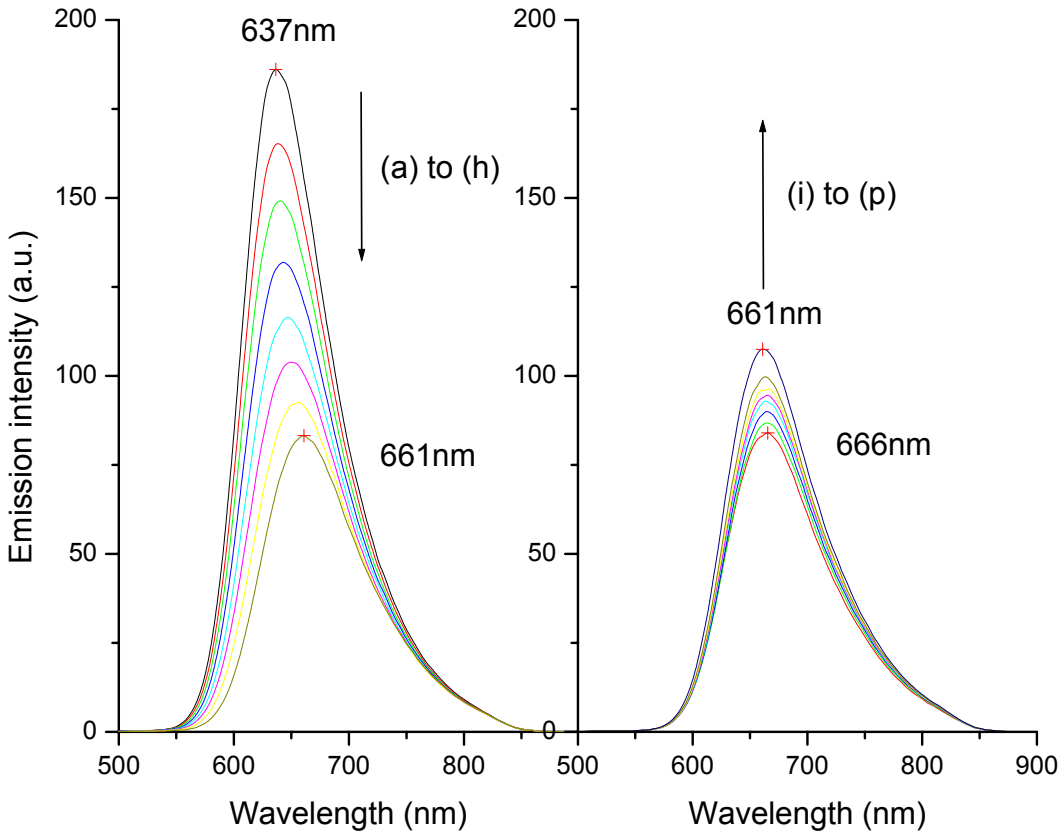

Figure A.12 – pH titration of the emission spectrum of 2**, with an excitation wavelength of 415nm. The measurements were carried out in Britton-Robinson buffer, and the pH was adjusted using sulphuric acid or NaOH. The arrows show the direction of change as the pH is decreased. The pH values are (a) 4.87, (b) 4.60, (c) 4.47, (d) 4.20, (e) 3.97, (f) 3.79, (g) 3.54, (h) 3.16, (i) 2.76, (j) 2.52, (k) 2.39, (l) 2.27, (m) 2.22, (n) 2.12, (o) 1.98 and (p) 1.79.**

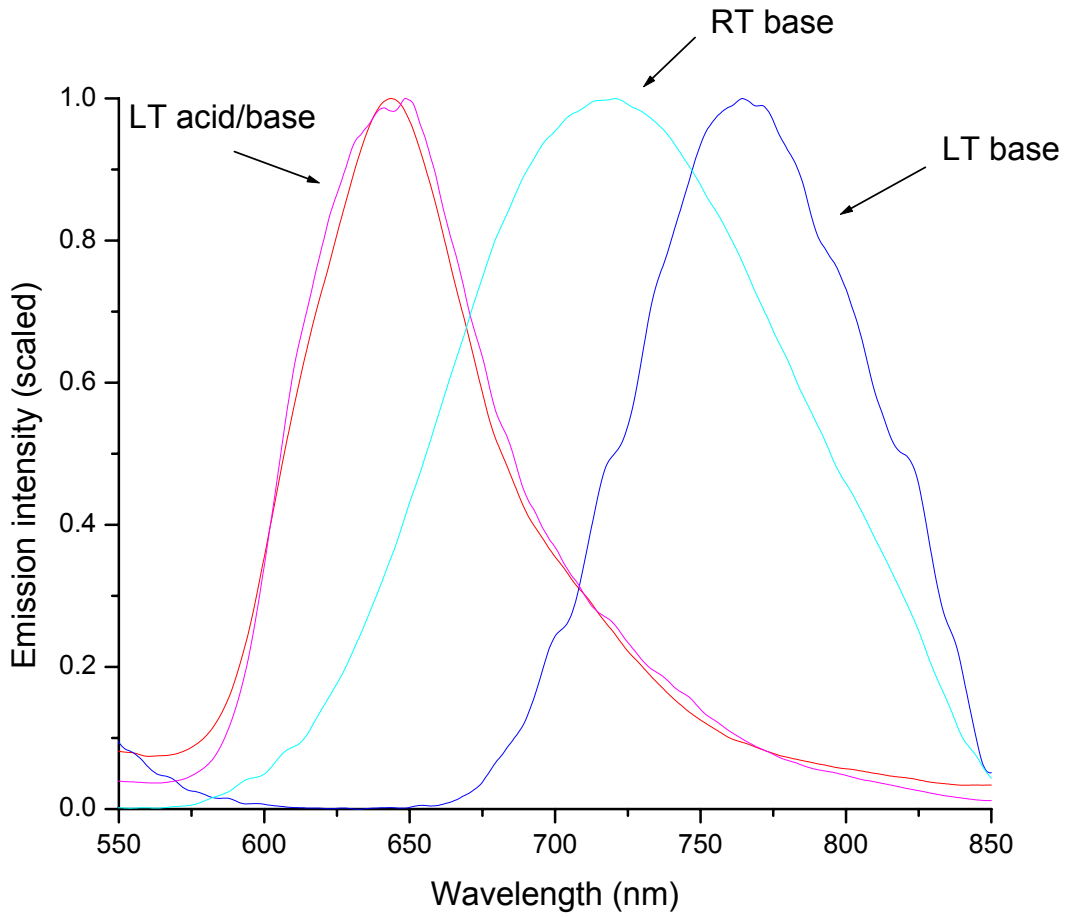

Figure A.13 – The uncorrected emission spectrum of 1 **at room temperature (RT) and at 77K (LT), in EtOH/MeOH (4:1, v/v). An excitation wavelength of 450nm was used. One drop of tetrafluoroacetic acid was added to create the acidic solutions, and one drop of triethylamine was added to create the basic solutions. The spectra are normalised to an emission maximum of 1.0.**

Room temperature and low temperature (77K) emission spectra for **1** are shown in Figure A.13. The spectra were measured in EtOH/MeOH (4:1, v/v) in acidic and basic solution. The peaks are listed in Table A.1.

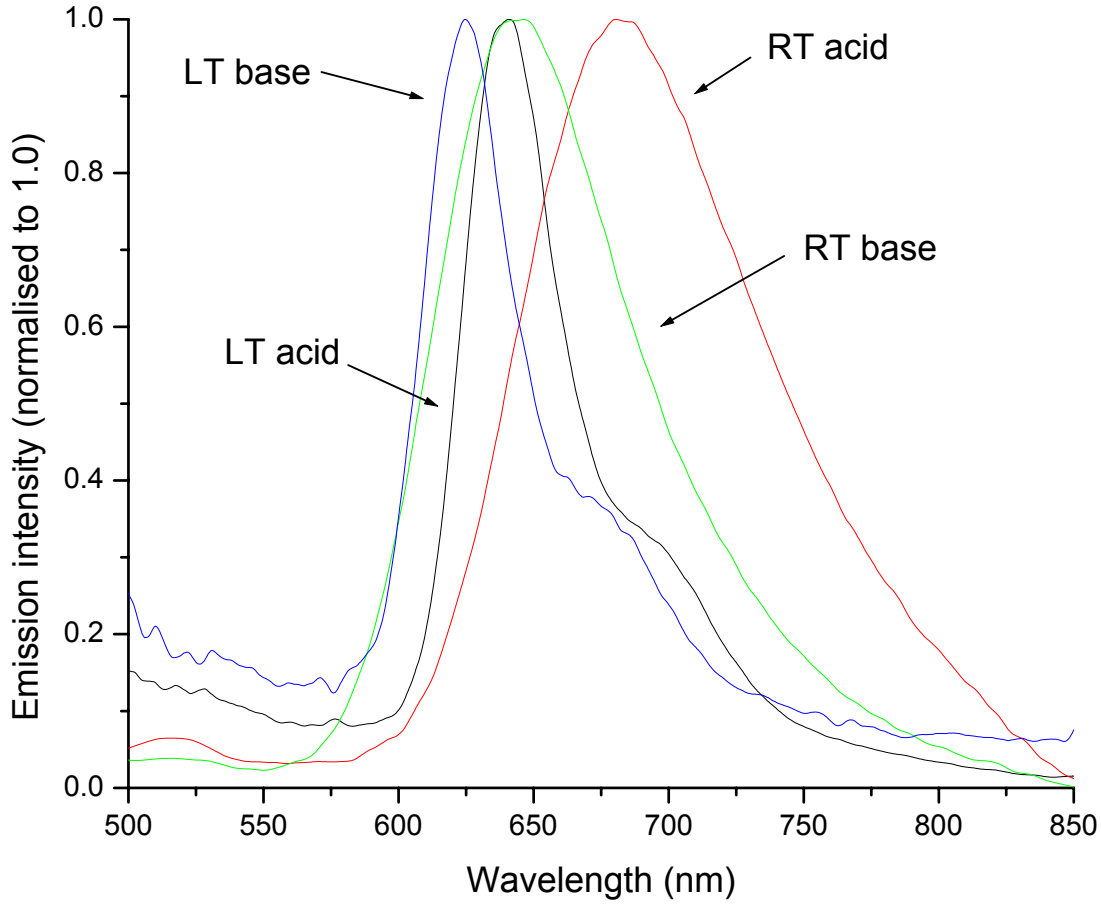

Figure A.14 – The uncorrected emission spectrum of RuRu **at room temperature (RT) and at 77K (LT), in EtOH/MeOH (4:1, v/v). An excitation wavelength of 450nm was used. One drop of tetrafluoroacetic acid was added to create the acidic solutions, and one drop of triethylamine was added to create the basic solutions. The spectra are normalised to an emission maximum of 1.0.**

Room temperature and low temperature (77K) emission spectra for **RuRu** are shown in Figure A.14. The spectra were measured in EtOH/MeOH (4:1, v/v) in acidic and basic solution. The peaks are listed in Table A.1.

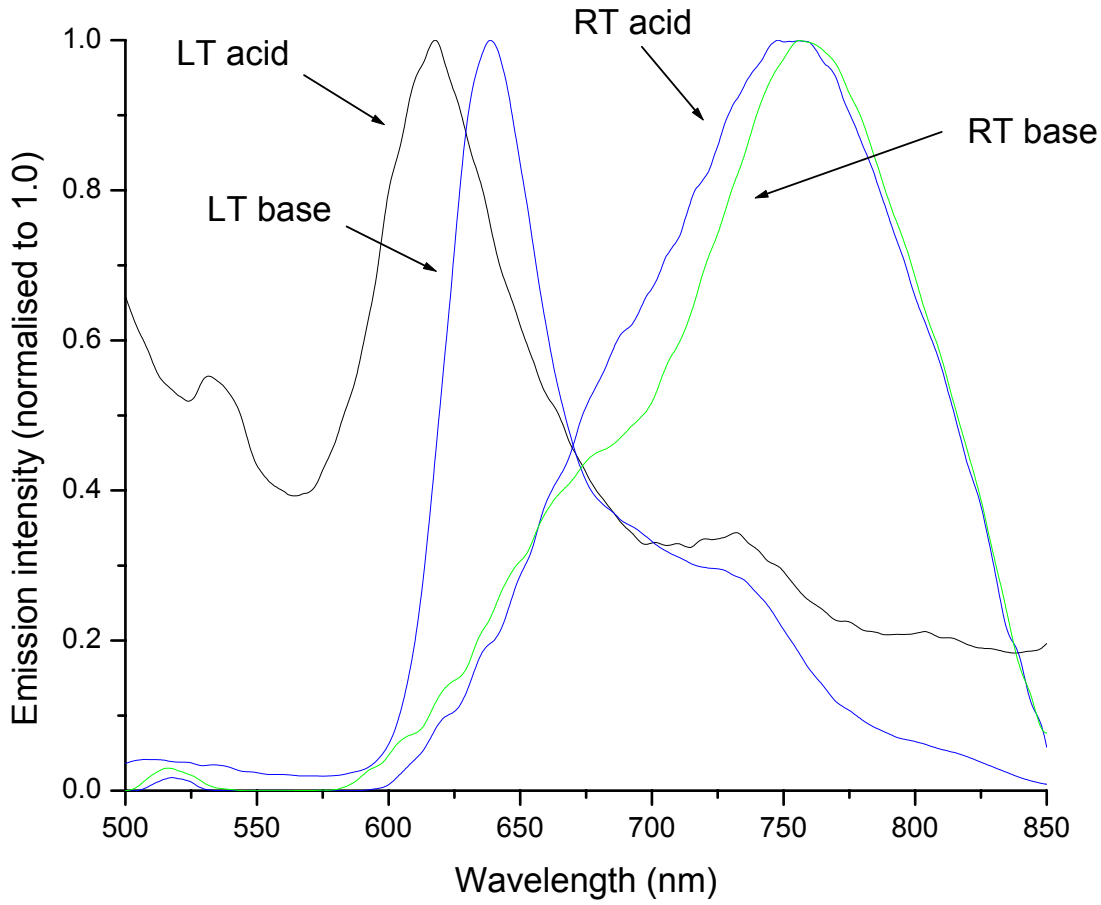

Figure A.15 – The uncorrected emission spectrum of RuOs **at room temperature (RT) and at 77K (LT), in EtOH/MeOH (4:1, v/v). An excitation wavelength of 450nm was used. One drop of tetrafluoroacetic acid was added to create the acidic solutions, and one drop of triethylamine was added to create the basic solutions. The spectra are normalised to an emission maximum of 1.0.**

Room temperature and low temperature (77K) emission spectra for **RuOs** are shown in Figure A.15. The spectra were measured in EtOH/MeOH (4:1, v/v) in acidic and basic solution. The peaks are listed in Table A.1.

A.5 Photophysical studies on TiO_2

The stability of the dye-sensitised TiO_2 was investigated by repeated emission scans in MeCN. Figure A.16 shows the result of the dye desorbing from the surface over time. Although the dye continues to emit in solution, due to the decrease of dye molecules in the light path, and perhaps also due to a change in the quantum yield of emission, the overall emission is reduced. The graph of the reduction in emission intensity with scan number (which is approximately proportion to time) is similar in shape to a exponential decay.

Figure A.17 shows the result of monitoring a TiO_2/**3** slide at a single wavelength (638nm) over a period of 3 hours. Between readings, illumination was cut off using black card. A linear dependence of desorption on time is observed.

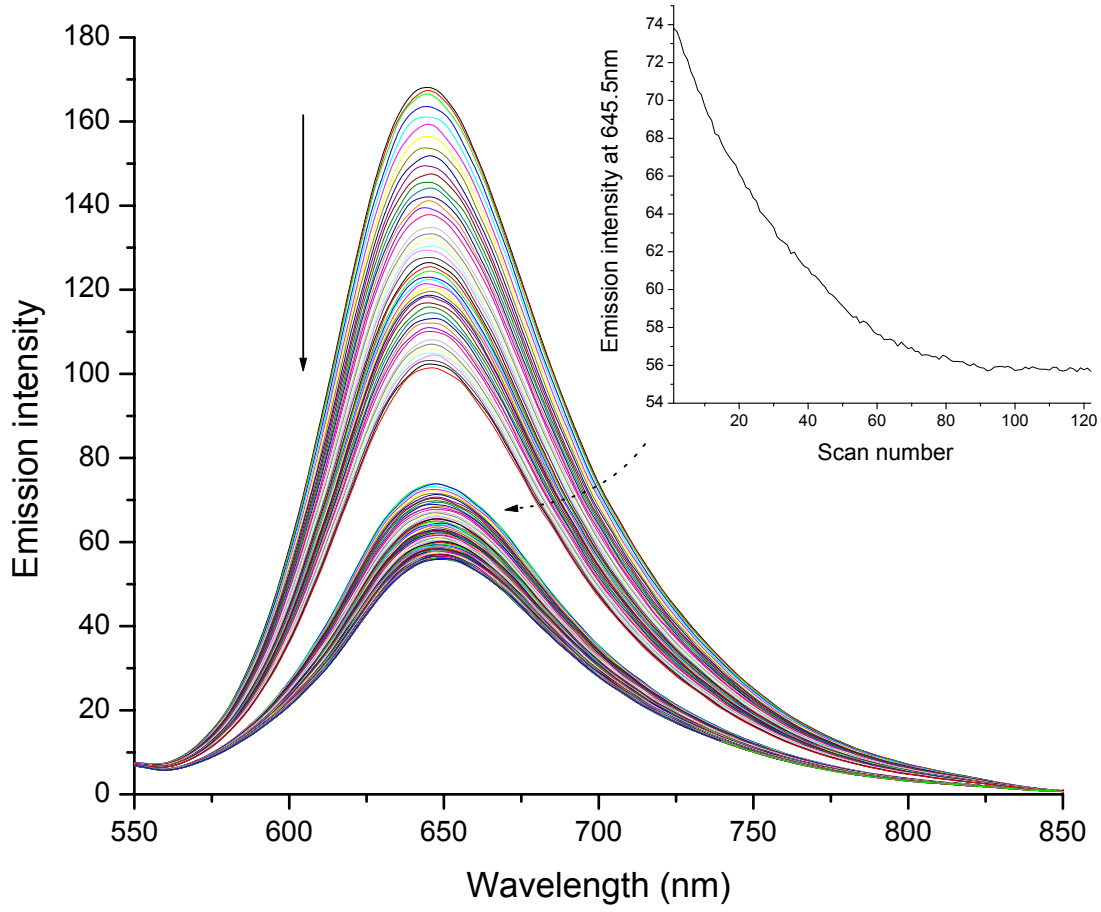

Figure A.16 – Emission intensity for a TiO2 layer sensitised with 3. The excitation wavelength is 450nm. The initial set of 50 scans were taken at 60s intervals. The second set of 122 scans were taken at intervals of 200s. The arrow shows the direction of change of the emission intensity with time. The inset shows a plot of intensity at 645nm versus scan number, for the second set of scans.

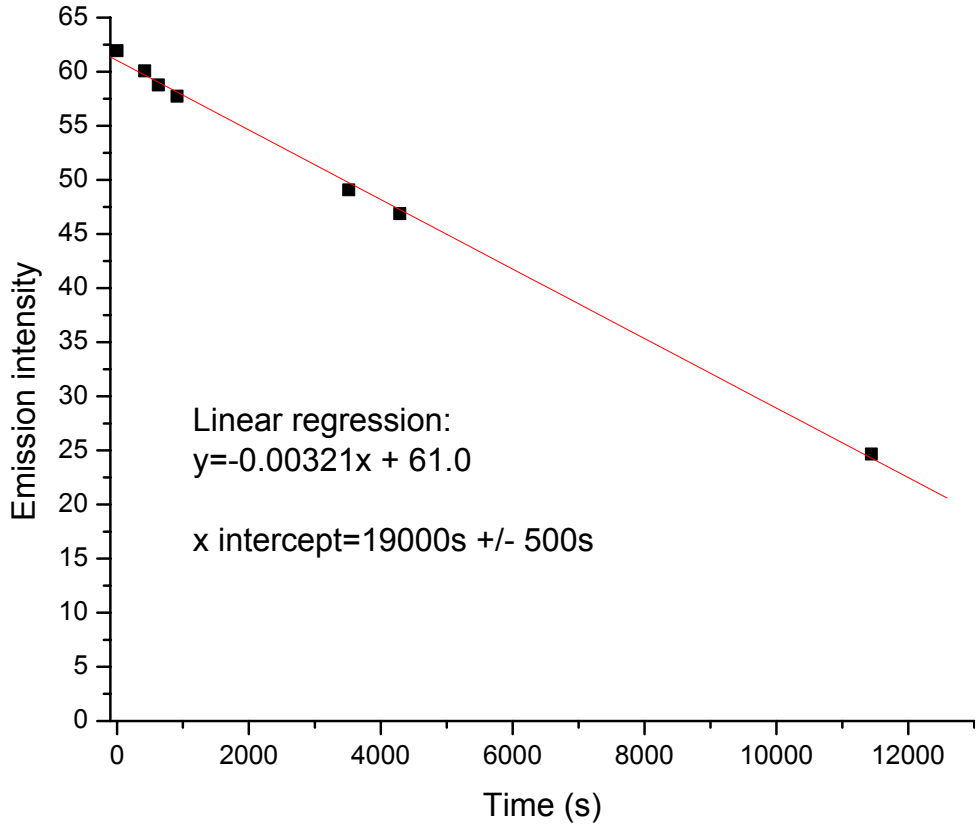

Figure A.17 –The decrease in emission intensity with time for a TiO_2/3 system, monitored at 683nm. The excitation wavelength was 450nm.

In order to investigate the effect of $LiClO_4$ concentration on emission intensity, three solutions of $LiClO_4$ in MeCN were prepared, corresponding to dilute, medium concentrated, and highly concentrated (the exact concentrations used in a particular experiment, where relevant, are quoted in the corresponding figure). At the start of the experiment, an initial volume of $1cm^3$ MeCN was placed in the cuvette containing the glass slide. An autopipette was used to add aliquots of the dilute $LiClO_4$ of between 10μl and 100μl, in increasing volume. After this, aliquots of the medium concentrated solution were added, and finally, aliquots of the highly concentrated solution.

Figure A.18 shows the effect of this addition between 0 and 400s: the step-like appearance of the graph in this region is due to sudden decreases in emission intensity on addition of aliquots of $LiClO_4$. A point of the emission intensity versus $LiClO_4$ concentration is shown in Figure A.19 for a TiO_2/**3** system, Slide A. The values for emission intensity were recorded immediately after addition of each aliquot.

At point ‘B’ in Figure A.18, the solvent was removed and replaced with pure MeCN. This was repeated several times, and then the solution was allowed to stand (point ‘C’) for some time. The solvent was replaced once more (point ‘D’), before the experiment was terminated.

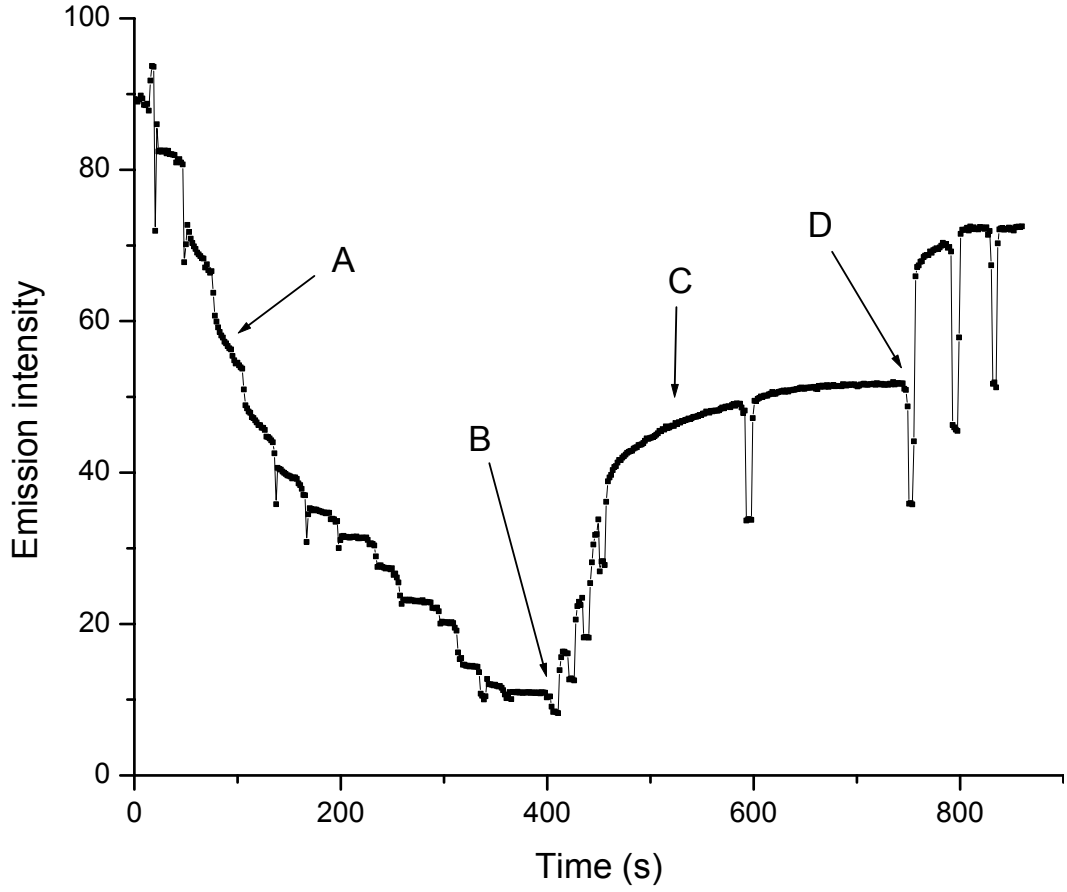

Figure A.18 – An initial study of the effect of $LiClO_4$ on the emission of a TiO_2/3 system in MeCN. An excitation wavelength of 450nm was used, and the emission was monitored at 670nm. ‘A’ indicates the slow equilibration of the emission intensity after addition of an aliquot of $LiClO_4$. ‘B’ marks the starting point for replacement of the solvent by pure MeCN. ‘C’ shows the slow recovery of emission in pure MeCN. ‘D’ indicates the last replacement of the solvent by pure MeCN.

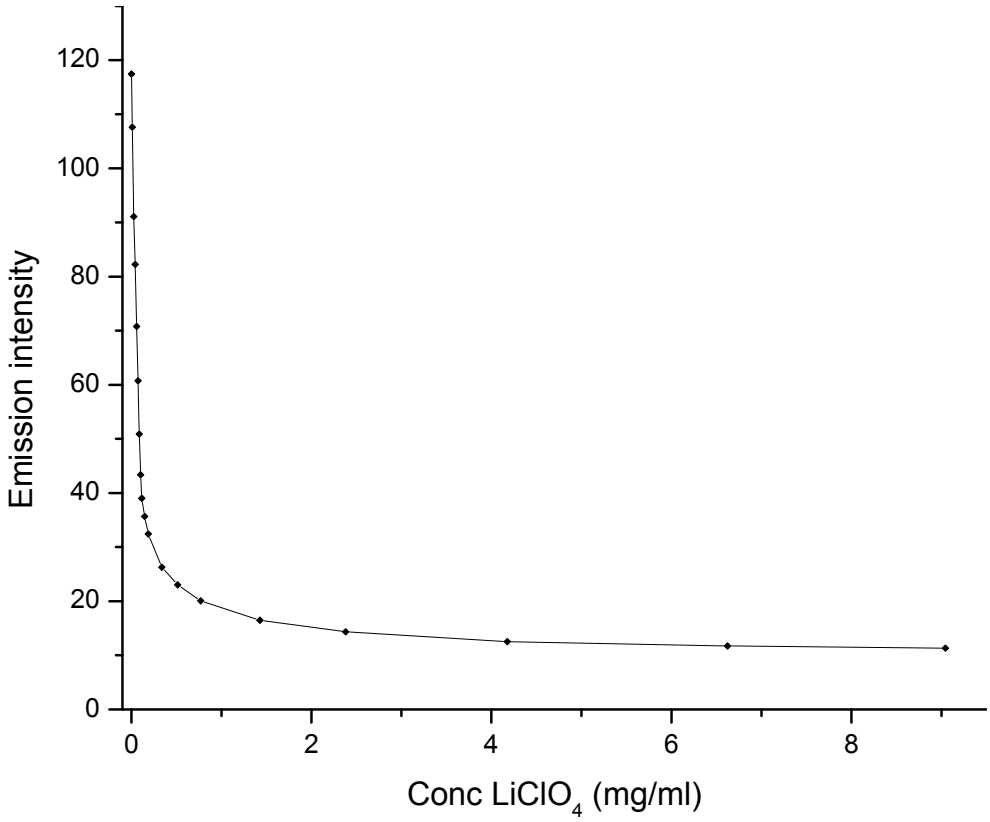

Figure A.19 – Plot of the emission intensity at 670nm versus $LiClO_4$ concentration for a TiO_2/3 system in MeCN, Slide A. The excitation wavelength was 450nm. The emission intensity was recorded immediately after addition of an aliquot of $LiClO_4$ solution.

In initial experiments, no mixing was performed during addition of aliquots of $LiClO_4$ – that is, the added aliquots were simply allowed to diffuse throughout the solution. However, equilibrium was not reached very quickly, as shown by 'A' in Figure A.18. After these initial experiments, the solution was mixed using a glass pipette. Mixing was performed immediately after addition of an aliquot, and about once a minute until equilibrium was reached (indicated by a levelling off of the decrease in emission intensity). The effect of mixing is shown in Figure A.20.

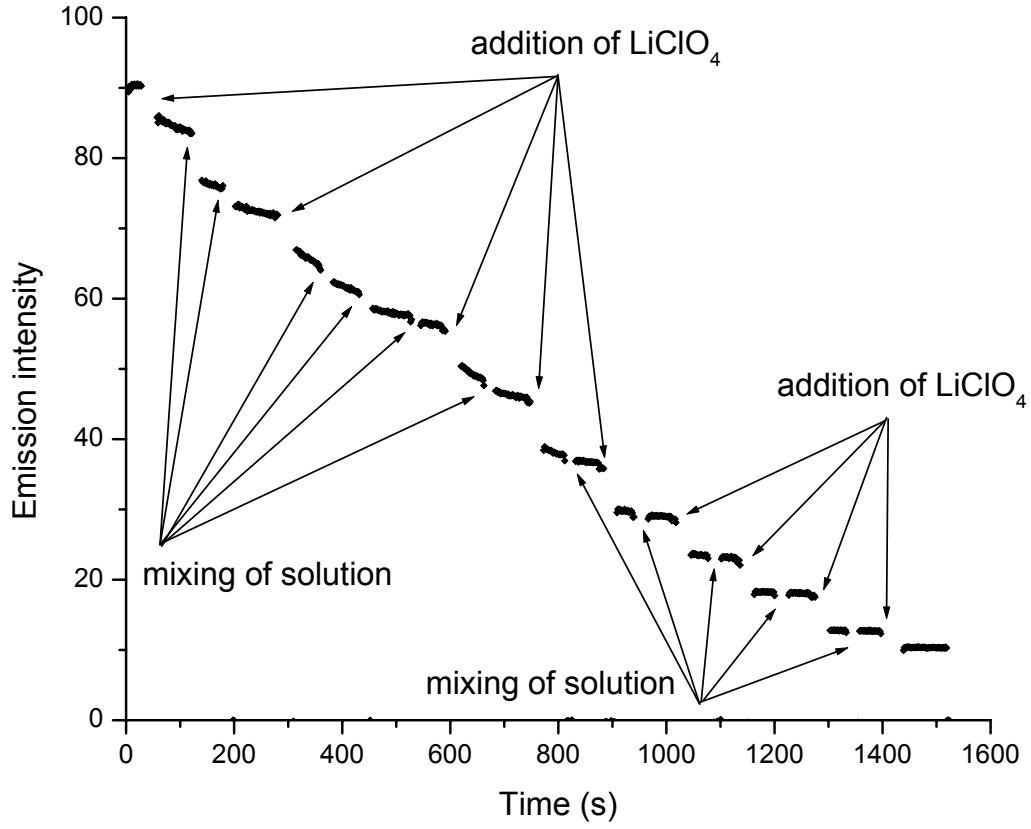

Figure A.20 – Plot of emission intensity versus time for a TiO_2/3 system in MeCN, showing the effect of $LiClO_4$ addition and mixing using a glass pipette. An excitation wavelength of 450nm was used, and the emission was monitored at 670nm.

Figure A.21 and Figure A.22 show, for Slides B and C respectively, the effect of $LiClO_4$ on the emission intensity. The values for the emission intensity at a certain concentration were obtained after equilibration.

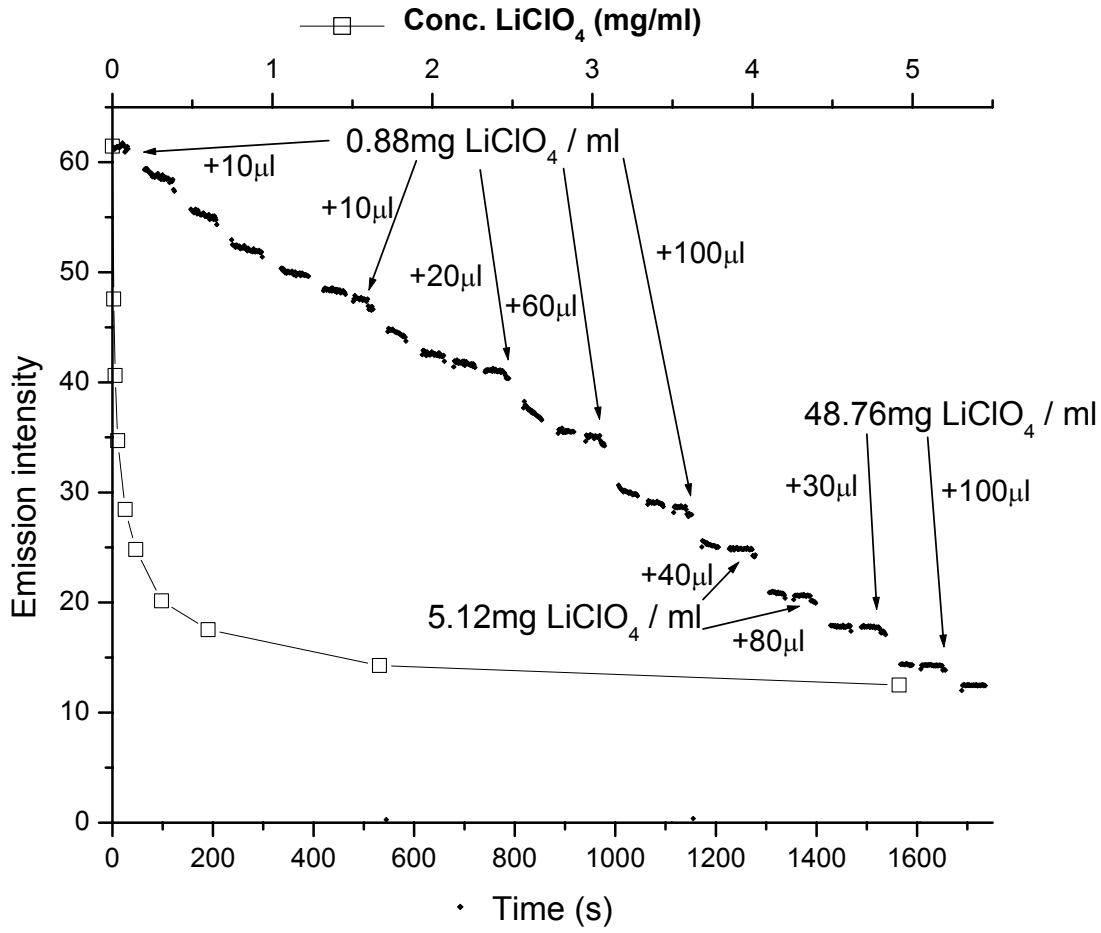

Figure A.21 – The effect of addition of $LiClO_4$ on the emission intensity of a TiO_2/3 system, Slide B. The raw data are shown versus time on the lower axis. The upper axis corresponds to a plot of emission intensity versus $LiClO_4$ concentration.

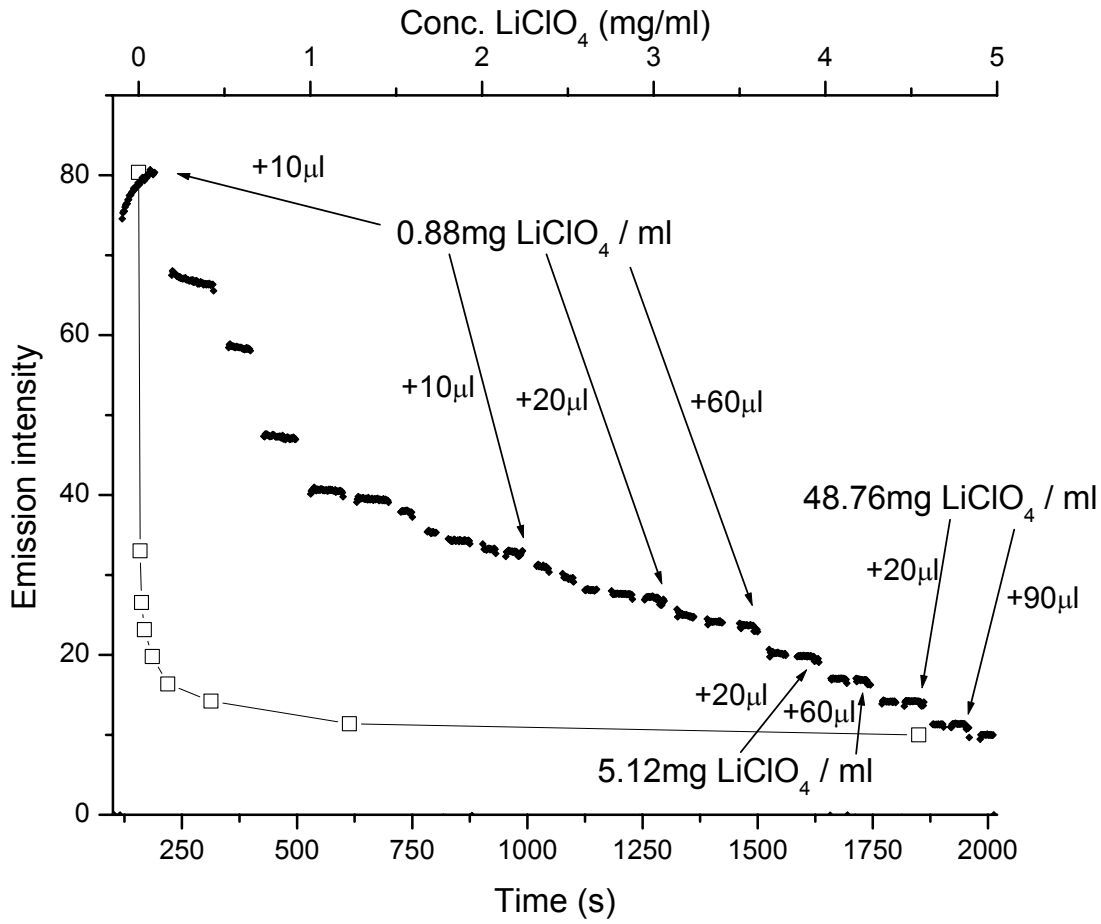

Figure A.22 – The effect of addition of $LiClO_4$ on the emission intensity of a TiO_2/3 system, Slide C. The raw data are shown versus time on the lower axis. The upper axis corresponds to a plot of emission intensity versus $LiClO_4$ concentration.

The effect of $LiClO_4$ on the emission of a TiO_2/**RuRu** and TiO_2/**RuOs** system is shown in Figure A.23 and Figure A.24, respectively. Two measurements were made, corresponding to before and after addition of an aliquot of concentrated $LiClO_4$ solution. The figures show the difference between these two measurements, which corresponds to the emission of the dinuclear complex in free solution.

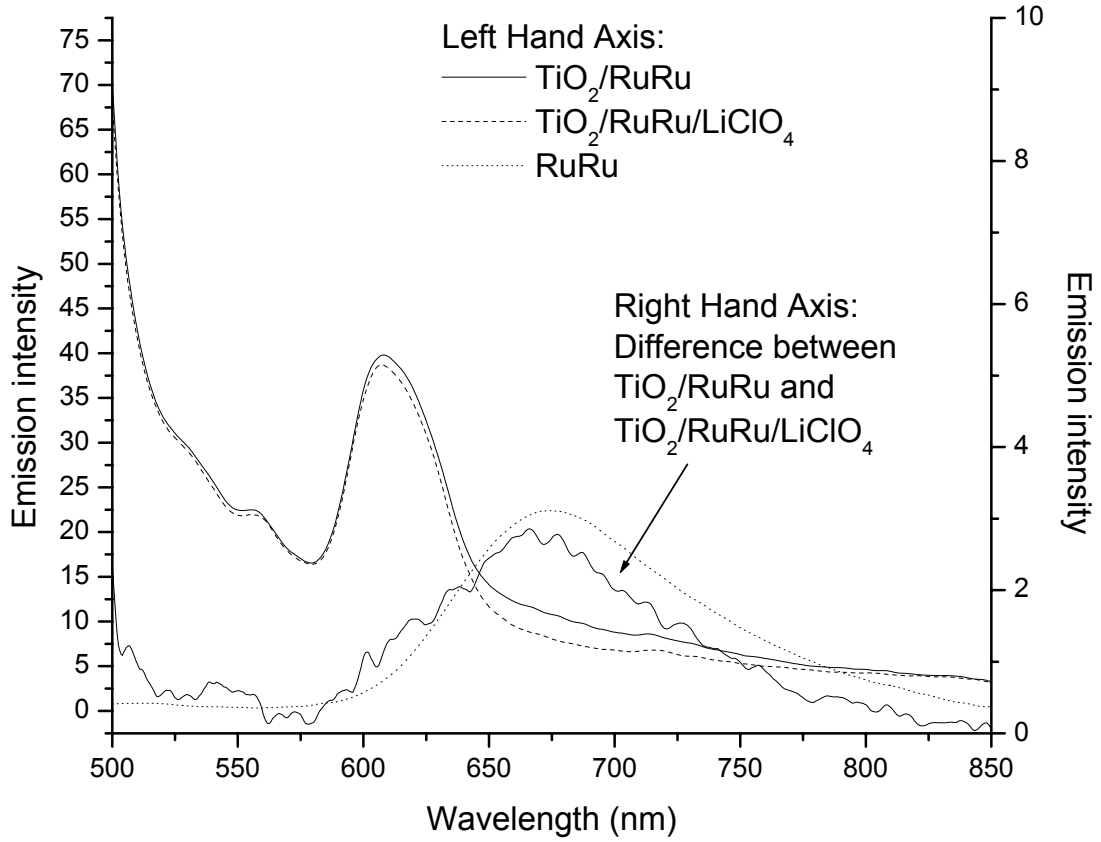

Figure A.23 – The effect of $LiClO_4$ on a TiO_2/RuRu system. The difference between the spectra before and after addition of $LiClO_4$ is compared to the emission spectrum of RuRu **in solution.**

When **RuRu** is adsorbed on TiO_2, it has a very weak emission. Addition of $LiClO_4$ quenches this weak emission as shown in Figure A.23. The difference between the two spectra is shown to correspond to the solution emission spectrum of **RuRu**.

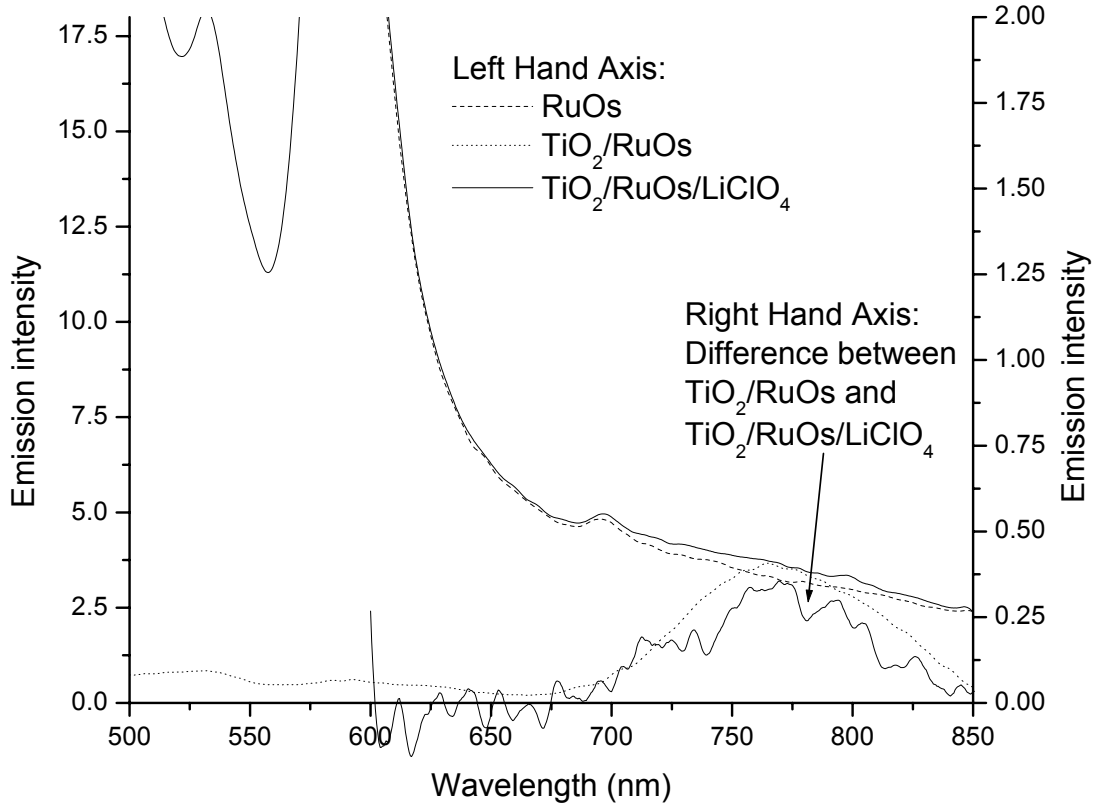

Figure A.24 – The effect of $LiClO_4$ on a TiO_2/RuOs **system. The difference between the spectra before and after addition of $LiClO_4$ is compared to the emission spectrum of** RuOs **in solution.**

When **RuOs** is adsorbed on TiO_2, it has a very weak emission. Addition of $LiClO_4$ quenches this weak emission as shown in Figure A.24. The difference between the two spectra is shown to correspond to the solution emission spectrum of **RuOs**.

A.6 Discussion

For a complex containing H_2dcb, the protonation state plays an important part in determining its physical and photophysical properties. This is highlighted in the pH titrations of the absorption and emission spectra of **2**, shown in Figure A.11 and Figure A.12. A fit of the absorption at 293nm with a sigmoidal curve gives an inflection point at a pH of 2.44. This agrees well with the pK_a value of 2.50 found by Nazeeruddin and Kalyanasundaram[17]. They also found another pK_a value of 1.80, but our method is not sensitive to pK_a values within one pH unit of each other. In the same study, excited state pK_a values of 4.40 and 1.75 were found. In our study, a fit of the emission intensity at 625nm between pH 4.87 and 3.16 gave a value of 4.6+/-0.3. These titrations confirm that in basic or neutral solutions, the complexes are fully deprotonated.

The photophysical properties of complexes **1**, **RuRu** and **RuOs** in solution have been briefly described by Lees *et al.*[8] The following discussion provides greater information on the photophysical behaviour of these complexes in acid and base, and how these properties change at 77K.

The room temperature and low temperature emission data for complexes **1**, **RuRu** and **RuOs** (Figure A.13, Figure A.14 and Figure A.15) are summarised in Table A.1. H_2dcb is a better π-acceptor than bpy and Hbpt. This means that the excited state will be based on the H_2dcb, in general. Deprotonation of the complex, whether or not it removes all of the protons of the 4 carboxy groups, will decrease the π-acceptor strength of the H_2dcb. If the excited state is still based on the dcb^{2-} ligand, then a shift to higher energy will be observed for the emission.

This shift to higher energy is observed for **1** and **RuRu** at RT, and also for **RuRu** at LT. At LT, protonation seems to have no effect on the emission of **1**. This may be because at LT, the system sometimes 'freezes into' a particular configuration, either acid or base, despite the initial concentration of protons.

Emission in the **RuOs** dimer occurs from the osmium centre at RT. The osmium-centred ^{3}MLCT excited state is at lower energy than the ruthenium-centred ^{3}MLCT excited state. This is due to the lower oxidation potential of osmium complexes, compared to their ruthenium analogues: although the π* level of the H_2dcb (attached

to the Ru) may be at lower energy than that of the bpy (attached to the Os), the d orbitals of the osmium are at higher energy than those of ruthenium. As a result, protonation has little effect on the emission at RT, since the protonated site is not involved in the emission.

The situation changes at LT for **RuOs**. Emission, both for the protonated and deprotonated complexes, occurs mainly from the ruthenium centre, although a small peak due to osmium emission is also observed. The reason for this is unknown????

		Protonated	Deprotonated
1	RT	765	721
	LT (77K)	~648	649
RuRu	RT	681	646
	LT (77K)	641	625
RuOs	RT	752	756
	LT (77K)	618	639

Table A.1 – Room and low temperature emission data for complexes 1**,** RuRu **and** RuOs**. Experimental conditions are described under Figure A.13, Figure A.14 and Figure A.15, respectively.**

In all of the experiments involving TiO_2-coated glass slides, it is important to take into account the stability of the dye-sensitised layer. A large variation occurred in the stability of these layers: some showed no sign of a reduction in emission intensity with time (at least, over a few minutes), whereas others showed a notable decrease in intensity.

Some of this lack of stability may be due to photoassisited or photochemically-assisted desorption. When the sample was under constant illumination, a decay similar to an exponential decay occurred (Figure A.16). However, when the illumination was interrupted between successive measurements, a linear dependence on time was observed (Figure A.17). It must be noted, however, that although both samples involved the same dye and solvent, the actual slide used was different (each slide was used only once).

For the slide whose results are shown in Figure A.17, a 5% decrease in emission from the initial value took just over 15 minutes. This means that it is possible to get

useful information from emission studies provided that the timescale of the experiment is around 15 minutes.

The initial studies on the effect of $LiClO_4$ on the emission intensity of a TiO_2/**3** system showed some interesting results. Intercalation of Li^+ ions into the nanocrystalline structure is a slow process, occurring on a timescale of minutes, rather than seconds. For example, at point A in Figure A.18, the emission intensity decreases steadily over a period of about 30 seconds after addition of an aliquot of $LiClO_4$ solution, without any signs of levelling off. It is clear from this experiment, as well as from others performed, that equilibration is a particular problem in the early stages of addition of $LiClO_4$ solution. The reverse process of removal of Li^+ ions from the TiO_2 occurs on a similar, or longer, timescale. After rinsing the cuvette four times with pure MeCN, the emission starts to recover, but leaching of Li^+ from the TiO_2 is slow (see point 'C' in Figure A.18), and further rinsing is required (point 'D'). Despite the potential reversibility of this process, slides were not reused for further experiments.

Mixing was found to increase the rate of equilibration (Figure A.20). This is especially true for low concentrations of $LiClO_4$ (see Figure A.22, in particular). At these concentrations, the rate of equilibration may be diffusion-controlled.

The graphs of emission intensity versus $LiClO_4$ concentration initially appeared to be exponential. However, they could not be fit with any simple function. This means that comparisons between the characteristic graphs for a particular dye on a TiO_2 surface were only possible visually. Figure A.25 compares these graphs for Slide A, B and C (data taken from Figure A.19, Figure A.21 and Figure A.22). Note that the data for Slide A was noted immediately *after* addition of the $LiClO_4$ aliquot, without allowing time for equilibration. Each of the graphs were scaled to have the same starting point, and approximately same end point. The graphs for Slides B and C are initially steeper than that of A: equilibration causes the emission intensity to fall further for B and C at low concentrations. At higher concentrations the graphs of B and C are quite similar and have a more gentle transition from a vertical slope to a horizontal slope.

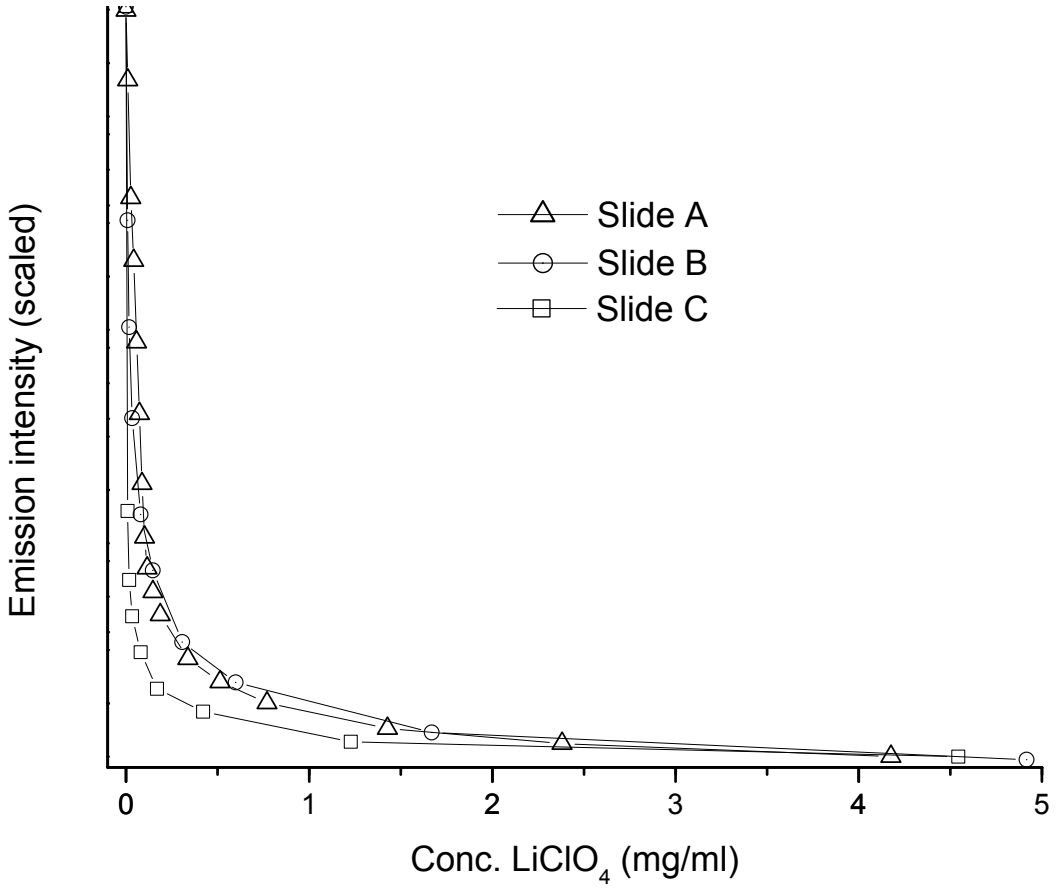

Figure A.25 – Comparison of plots of emission intensity versus $LiClO_4$ concentration for Slides A, B and C.

Little information is available on the effect of $LiClO_4$ concentration on the flatband potential, V_{fb}. A study by Redmond and Fitzmaurice[18] of nanocrystalline TiO_2 electrodes in dry MeCN showed a rapid increase in V_{fb} at $LiClO_4$ concentrations between 10^{-3}M and 10^{-2}M (0.1mg/ml and 1.1mg/ml). At concentrations less than 10^{-3}M they found a very gradual change, which they attribute to specific adsorption of Li^+ on the electrode surface. The rapid increase which followed was attributed to intercalation of Li^+ into the lattice structure of TiO_2.

Although our main interest was in the effect of $LiClO_4$ concentration on the emission from TiO_2/**RuRu** and TiO_2/**RuOs** systems, the emission from these systems prior to addition of $LiClO_4$ is very small (Figure A.23 and Figure A.24). Hence, it is impossible to investigate in detail the changes that occurs at different

concentrations. The results show that, although very small, the emission on TiO_2 occurs at the same wavelength as the emission in solution.

The excited state of these dinuclear complexes are at high enough energy relative to the Fermi level of the TiO_2 that they can easily inject an electron into the surface, rather than deactivating through emission of a photon. For this reason, lowering the Fermi level further, by intercalation with Li^+ ions, has little effect. For complex **3**, the energy of the excited state is lower, and hence substantial emission occurs. Li^+ intercalation reduces the energy of the Fermi and favours electron injection rather than emission: hence the emission decreases.

A.7 Conclusions

Little study has been done on the effect of different concentrations of Li^+ ion on rates of interfacial charge transfer. The study described in this chapter shows that the emission intensity decreases almost exponentially with increase in Li^+ concentration. This is due to the decrease in the energy of the conducting band as the accumulated charge is neutralised by adsorbed or intercalated Li^+.

Typical studies on dye-sensitised solar cells use a 0.2M Li^+ concentration. Such studies should take into account the fact that lower concentrations of Li^+ might still ensure adequate quantum efficiencies of injection, while allowing other beneficial process to increase their rates.

The photophysical characteristics of **RuRu** and **RuOs** were measured at room temperature and at 77K. A shift in the location of the emitting state occurs for **RuOs**.

A.8 References

1. Grätzel, M., *Nature*, **2001**, *414*, 338.

2. O'Regan, B. and Grätzel, M., *Nature*, **1991**, *353*, 737.

3. Tachibana, Y., Haque, S.A., Mercer, I.P., Durrant, J.R. and Klug, D.R., *J. Phys. Chem. B*, **1997**, *101*, 6799.

4. Hannappel, T., Burfeindt, B., Storck, W. and Willig, F., *J. Phys. Chem. B*, **1997**, *101*, 6799.

5. Kuciauskas, D., Freund, M.S., Gray, H.B., Winkler, J.R. and Lewis, N.S., *J. Phys. Chem. B*, **2001**, *105*, 392.

6. Haque, S.A., Tachibana, Y., Willis, R.L., Moser, J.E., Grätzel, M., Klug, D.R. and Durrant, J.R., *J. Phys. Chem. B*, **2000**, *104*, 538.

7. Clifford, J.N., Palomares, E., Nazeeruddin, Md.K., Grätzel, M., Nelson, J., Li, X., Long, N.J. and Durrant, J.R., *J. Am. Chem. Soc.*, **2004**, *126*, 5225.

8. Lees, A.C., Kleverlaan, C.J., Bignozzi, C.A. and Vos, J.G., *Inorg. Chem.*, **2001**, *40*, 5343.

9. Farzad, F., Thompson, D.W., Kelly, C.A. and Meyer, G.J., *J. Am. Chem. Soc.*, **1999**, *121*, 5577.

10. Sprintschnik, G., Sprintschnik, H.W., Kirsch, P.P. and Whitten, D.G., *J. Am. Chem. Soc.*, **1977**, *99*, 4947.

11. Ghosh, P.K. and Spiro, T.G., *J. Am. Chem. Soc.*, **1980**, *102*, 5543.

12. Oki, A.R. and Morgan, R.J., *Synth. Commun.*, **1995**, *25*, 4093.

13. Browne, W., PhD Thesis, Dublin City University, **2002**.

14. Hughes, D., PhD Thesis, Dublin City University, **1999**.

15. Liska, P., Vlachopoulos, Nazeeruddin, M.K., Comte, P. and Grätzel, M., *J. Am. Chem. Soc.*, **1988**, *110*, 3686.

16. Geldard, J.F. and Lions, F., *J. Org. Chem.*, **1965**, *30*, 318.

17. Nazeeruddin, Md. K. and Kalyanasundaram, K., *Inorg. Chem.*, **1989**, *28*, 4251.

18. Redmond, G. and Fitzmaurice, D., *J. Phys. Chem.*, **1993**, *97*, 1426.

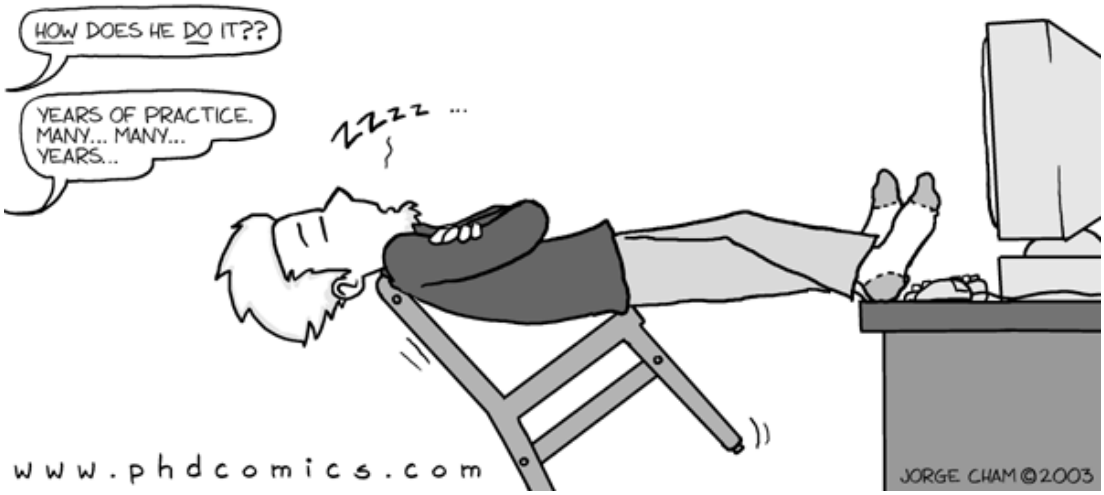
HOW DOES HE DO IT??
YEARS OF PRACTICE. MANY... MANY... YEARS...
ZZZZ ...
www.phdcomics.com
JORGE CHAM ©2003

Appendix B
Brief guide to use of Gaussian and GaussView

Both Gaussian and GaussView come with an extensive collection of manuals and help files which describe in detail the various capabilities and features of each. The purpose of this appendix is to describe some methods and features which I have found very useful when preparing job files for Gaussian.

B.1 Preparation of input structure

The initial Gaussian job files (or GJFs) were always prepared using GaussView. GaussView is a graphical user interface which allows visualisation and editing of molecules and results. It has further extensive capabilities, among the most useful of which is the enforcement of symmetry (see below).

In our group, we are mostly concerned with ruthenium polypyridyl type molecules. When preparing a new geometry optimisation, it is best to proceed by modifying the output of a previous geometry optimisation of a related structure. Otherwise, there may be problems with the initial SCF convergence. If the ligand is of a completely new structure, you should at least ensure that the Ru-N bond length is set to a reasonable length based on previous calculations of complexes with similar ligands.

For example, in my initial study of **trisbpy**, I imported the crystal structure into GaussView and set the Ru-N bond length close to that obtained in previous DFT studies.

GaussView allows you to rotate one ring with respect to another ring (using the bond torsion tool). Sometimes, GaussView refuses to rotate the ring. In these cases, temporarily breaking a bond in one of the rings often allows rotation to proceed. Unbonded ligands can be moved independently of the rest of the molecule by holding down ALT, in combination with the usual mouse buttons (LEFT=turn, MIDDLE=move, RIGHT=rotate).

For molecules with symmetry, it is of great importance that Gaussian uses that symmetry. The presence of any symmetry element (apart from the identity) will reduce computation time by half. Although a molecule may appear symmetric, it is necessary to perfectly symmetrise the molecule before submitting it to Gaussian. Fortunately this is easily achieved within GaussView: choose “Point Group” from the Edit menu and tick “Enable Point Group Symmetry”. If the current point group does not have the desired symmetry, choose the desired point group from the “Approximate higher-order point groups” list (usually you should choose the most symmetric group) and click “Symmetrize”.

If GaussView does not pick up on the symmetry you wish, you could try one of the following. You can start the geometry optimisation and open the checkpoint file after a number of steps. If it picks up on the symmetry at this stage, kill Gaussian and restart the calculation using a newly prepared GJF containing the symmetrised coordinates. You could also try and edit a molecule which already has the desired symmetry.

Once the molecule’s structure has been prepared, you should save the job as a GJF.

B.1.1 Tips

- It is possible to run Gaussian from within GaussView, but I have avoided doing this as it may result in a decrease in speed and available memory.

- GJFs and output files (.out) should be set to automatically open in Notepad, if double-clicked. This is set by right clicking on the file, choosing “Open with”, and “Notepad”. Make sure you tick the “Always open file with this program” box.

- Before using Gaussian, it is worthwhile to change the display preferences. Go to “File”, “Preferences”. Untick the “Motif Look” box. The use of Motif seems to be incompatible with Windows XP, and can cause strange effects to window menus. You may also wish to change the “Input” folder to “C:\Gaussian\Scratch”.

B.2 Preparing the Gaussian Job File (GJF)

Start Gaussian and open the GJF using “File”, “Open”. If Gaussian closes immediately, it means that there was an error in the structure of the input file. This usually means a missing blank line at the end of the file. If there were no problems, the GJF opens in the Edit Window.

The first part of the GJF contains lines which begin with a percent sign. This is referred to as the Link 0 section, since these commands are processed by the Gaussian subroutine Link 0. This section will usually be the same for every job, except for the checkpoint file name:

`%chk=benzene`	checkpoint file name (.chk will be added by Gaussian)
`%mem=100MB`	the amount of memory allocated to Gaussian
`%nproc=1`	the number of processors to be used

The amount of memory allocated should be less than the total amount of physical RAM available on the machine. For example, if the machine has 1GB (1024MB) of RAM and you specify `%mem=1024MB` you may find it runs *very* slowly. This is because Windows needs memory to stay afloat, and a lot of time will be spent swapping various processes to disk because there isn’t enough memory to go around. A balance must be found between the amount of memory required to run Gaussian as fast as possible, while at the same time keeping Windows happy. You should also bear in mind whether you are going to be using the computer for running other processes at the same time as Gaussian. Even if you pause Gaussian, it doesn’t relinquish control over the memory it has been given.

In the case of ruthenium complexes, the amount of memory allocated to Gaussian has little effect on performance. This is because the basis set size is so large that it cannot all fit into memory in any case. This may not be the case for calculations on ligands, where an increase in the memory allocated may cause a substantial increase in speed. I have not investigated this to any great degree though. I use `%mem=800MB` for the computer with 1024MB memory. If you add extra memory to the machine, make sure to reset the Windows swap file size to optimal for that memory and to adjust the %mem value accordingly.

During the course of calculations, a read-write file (RWF) is created. Gaussian has a restriction of 2GB on the size of the RWF. In some instances, e.g. a Raman frequency calculation on a large asymmetric molecule, it is necessary to circumvent this limit. This can be done by use of the `%rwf` statement in the route section, which can used to specify a number of RWFs along with their maximum size (which cannot be more than 2GB):

```
%rwf=1.rwf,2000MB,2.rwf,2000MB,3.rwf,2000MB
```

B.3 A method for organising GJFs and results

All GJFs, output files and checkpoint files related to a particular molecule should be stored in a single folder with the name of the molecule. When carrying out a calculation, the GJF should be copied to the C:\Gaussian\Scratch folder. Afterwards the results should be moved back to the original folder. You should retain the original checkpoint file from the geometry optimisation and use a copy of it to absorb the results from TD and Freq calculations. This is because the checkpoint file increases greatly in size due to TD and frequency information. Files for geometry optimisation should be named benzene.gjf, benzene_b.gjf, etc. where the files with the suffix are continuations of the geometry optimisation. For the frequency and TD calculations, job names like benzene_td.gjf and benzene_freq.gjf should be used.

B.4 The route section

The line beginning with a hash symbol is the route section. This section tells Gaussian what calculation to carry out. The following subsections give examples of some common routes. Further details on each of the keywords is available in the Gaussian manual.

B.4.1 Geometry optimisation

```
#p rb3lyp/lanl2dz opt
```

(molecule specification)

Note: the use of the ‘r’ before b3lyp will force Gaussian to abort if it thinks the calculation should be unrestricted. This is usually due to the use of an incorrect charge.

Continuing a geometry optimisation from a checkpoint file

```
#p rb3lyp/lanl2dz opt=readfc geom=allcheck guess=read
```

If the geometry optimisation has reached a shallow valley (indicated by low rms and max force, but high rms and max displacement) it may be useful to accurately calculate the force constants and use these to make the next step in the geometry optimisation (be warned: it takes a while to calculate the force constants):

```
#p rb3lyp/lanl2dz opt=calcfc geom=allcheck guess=read
```

If the geometry optimisation has reached an impasse, for example, the energy keeps oscillating between two values, then a finer integration grid may be necessary:

```
#p rb3lyp/lanl2dz opt(readfc) geom=allcheck guess=read int=ultrafine
```

Note: there will be a slight slowdown in the speed. In addition, energy values calculated using different integration grids can not be compared.

If tight geometry optimisation is required, as it may be for Raman calculations, then an ultrafine grid is recommended:

```
#p rb3lyp/lanl2dz opt=(tight,readfc) geom=allcheck guess=read
int=ultrafine
```

There may sometimes be a problem with SCF convergence, especially at the initial step of a geometry optimisation. If this happens, it is possible to use the slower but more robust quadratic convergence method to ensure convergence:

```
#p rb3lyp/lanl2dz opt scf=qc
```

Note: after it has converged, you may find it faster to kill the job and continue from the checkpoint file with the default convergence method.

B.4.2 Calculations at the stationary point

All of the following calculations should be carried out using the same route as for the corresponding geometry optimisation, except that the ‘opt’ keyword is replaced by the indicated keywords.

- Population analysis for input to GaussSum

  ```
  pop=full iop(3/33=1,3/36=-1)
  ```

- TD-DFT

```
td(singlets,nstates=30) iop(9/45=2)
```

- IR and Raman frequencies

```
freq=raman
```

- Wavefunction stability

```
Stable
```

B.4.3 Other points to note:

Make sure the charge on the molecule is correct. In general all your calculations will be on closed-shell systems, i.e. the multiplicity will be 1 (singlet). If Gaussian exits with an error complaining about the multiplicity or saying the calculation should be unrestricted, you probably have the wrong charge.

When the job begins, check the symmetry of the molecule and make sure it is correct.

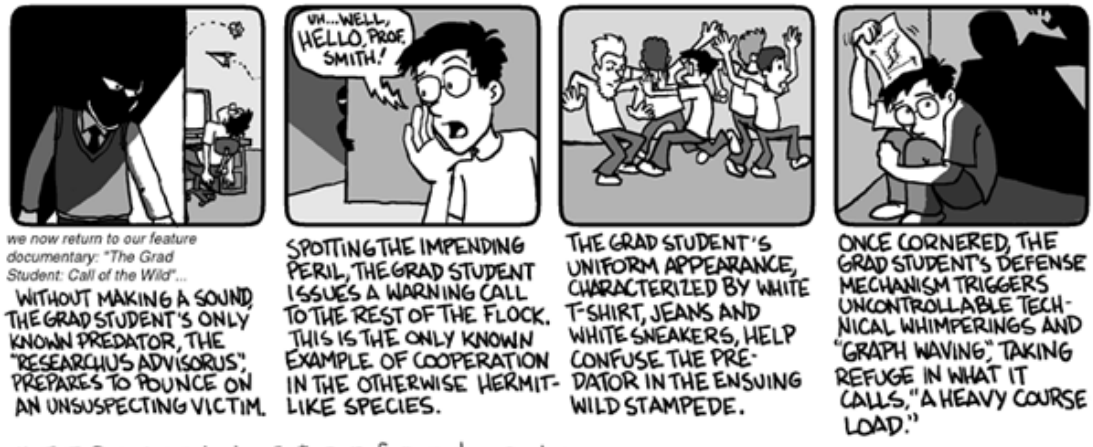
we now return to our feature documentary: "The Grad Student: Call of the Wild"...
WITHOUT MAKING A SOUND, THE GRAD STUDENT'S ONLY KNOWN PREDATOR, THE "RESEARCHUS ADVISORUS", PREPARES TO POUNCE ON AN UNSUSPECTING VICTIM.
UH... WELL, HELLO, PROF. SMITH!
SPOTTING THE IMPENDING PERIL, THE GRAD STUDENT ISSUES A WARNING CALL TO THE REST OF THE FLOCK. THIS IS THE ONLY KNOWN EXAMPLE OF COOPERATION IN THE OTHERWISE HERMIT-LIKE SPECIES.
THE GRAD STUDENT'S UNIFORM APPEARANCE, CHARACTERIZED BY WHITE T-SHIRT, JEANS AND WHITE SNEAKERS, HELP CONFUSE THE PREDATOR IN THE ENSUING WILD STAMPEDE.
ONCE CORNERED, THE GRAD STUDENT'S DEFENSE MECHANISM TRIGGERS UNCONTROLLABLE TECHNICAL WHIMPERINGS AND "GRAPH WAVING," TAKING REFUGE IN WHAT IT CALLS, "A HEAVY COURSE LOAD."
HTTP://phd.stanford.edu
JORGE CHAM ©THE STANFORD DAILY

Appendix C

Calculated structures not included in thesis

The electronic structures of the following compounds, although not discussed in this thesis, have also been calculated using B3LYP/LanL2DZ.

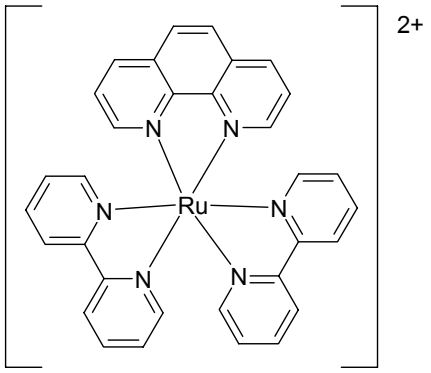

$[Ru(bpy)_2(phen)]^{2+}$

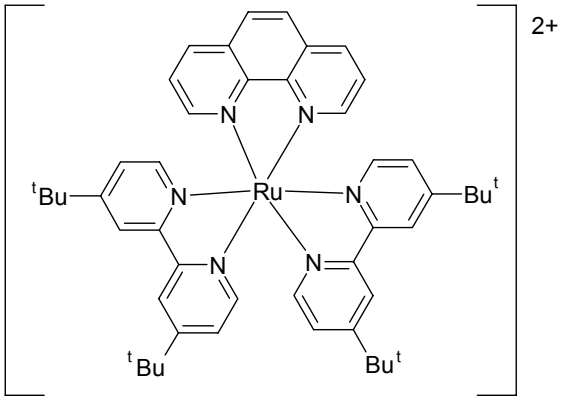

$[Ru(4,4'\text{-bis}^t\text{Bu-bpy})_2(phen)]^{2+}$

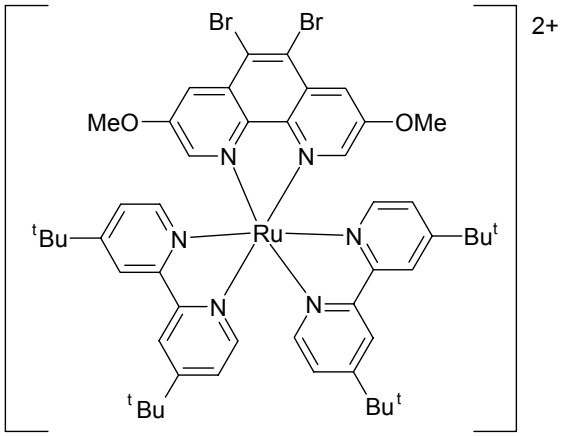

$[Ru(4,4'\text{-bis}^t\text{Bu-bpy})_2(3,8\text{-diOMe-}5,6\text{-diBr-phen})]^{2+}$

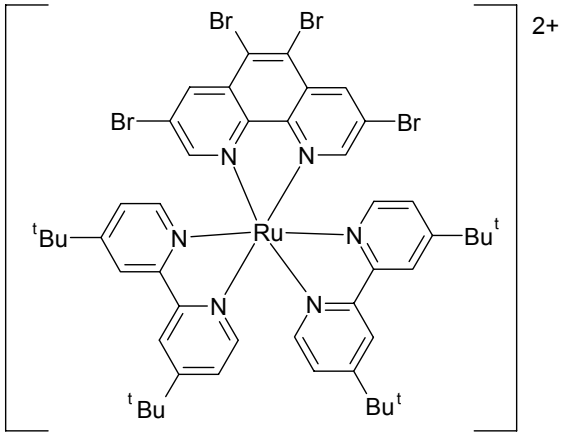

$[Ru(4,4'\text{-bis}^t\text{Bu-bpy})_2(3,5,6,8\text{-tetraBr-phen})]^{2+}$

Figure C.1 – Complexes related to work by Dr. Sven Rau, University of Jena, Germany.

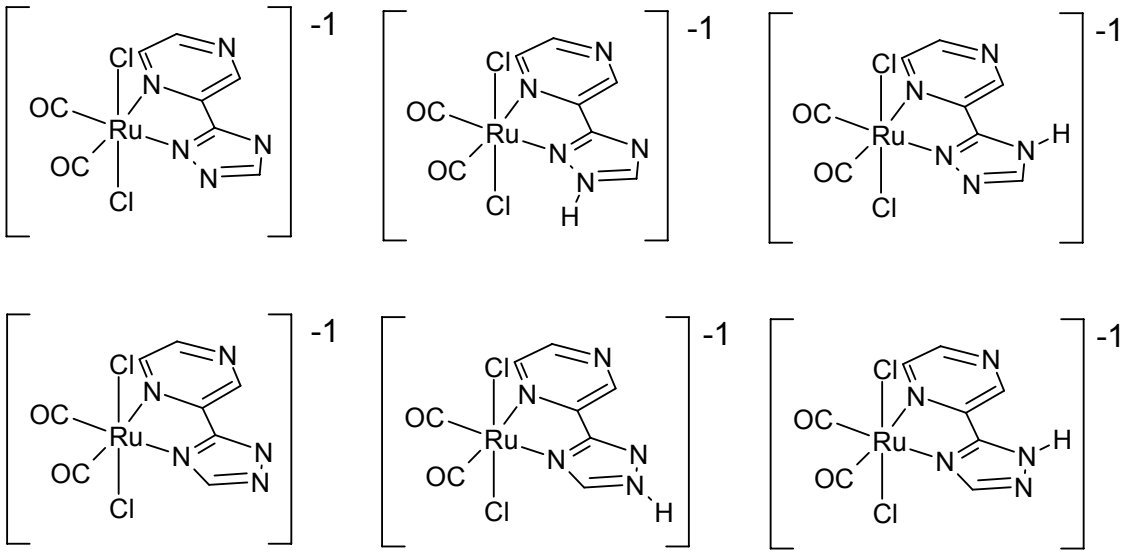

Figure C.2 – Complexes related to work by Dr. Declan Mulhern, formerly of Dublin City University.

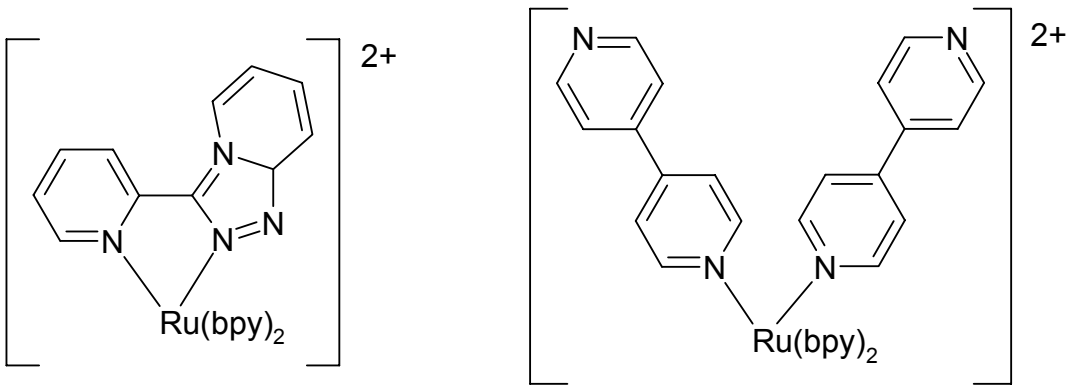

$[Ru(bpy)_2(JNN)]^{2+}$ $[Ru(bpy)_2(P0P)_2]^{2+}$

Figure C.3 – Complexes related to work by Dr. Adrian Guckian, Dublin City University.

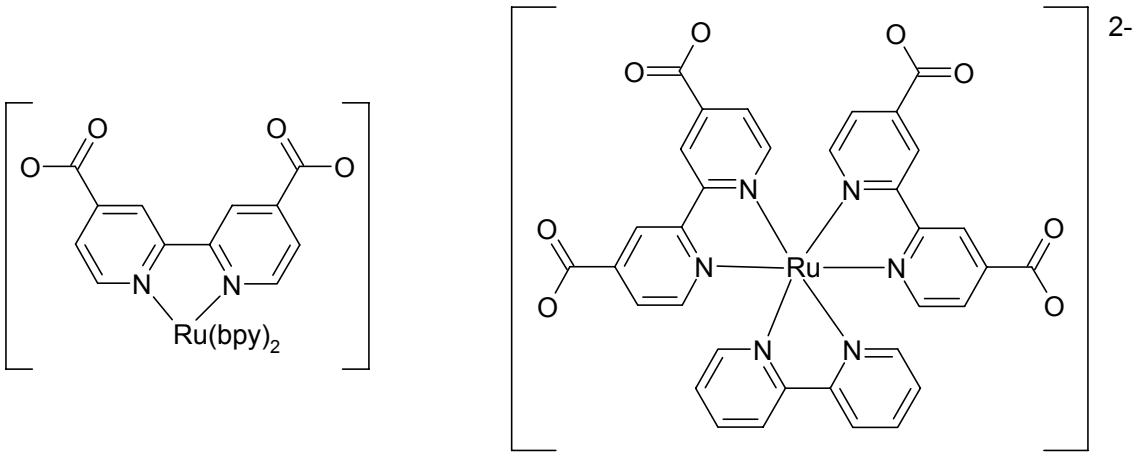

Figure C.4 – Complexes related to solar cell studies.

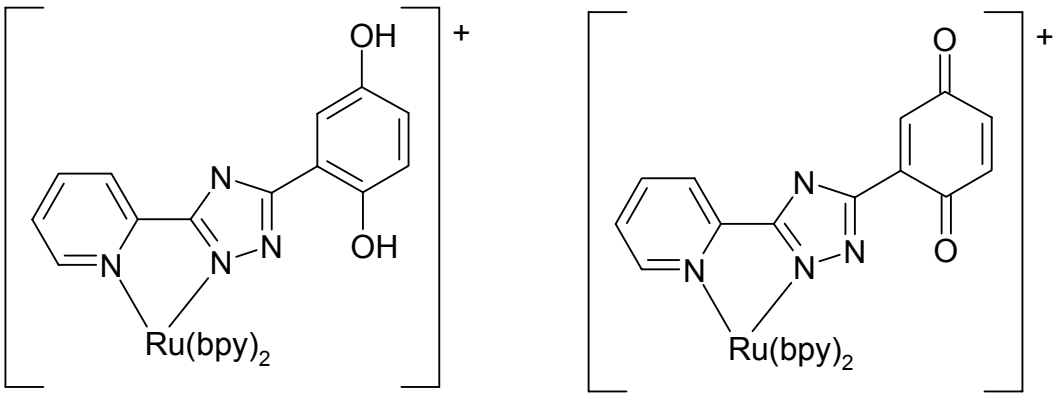

Figure C.5 – Complexes related to work by Fiona Lynch, Dublin City Univeristy


CLICK
YES!!
FINISHED ANOTHER PARAGRAPH, DID WE?
I AM A WRITING GOD!
JORGE CHAM © 2003
www.phdcomics.com


CLICK
YES!!
FINISHED ANOTHER PARAGRAPH, DID WE?
I AM A WRITING GOD!
JORGE CHAM © 2003
www.phdcomics.com

Dalton
www.rsc.org/dalton

Synthesis and characterisation of ruthenium complexes containing a pendent catechol ring †

Luke O'Brien,[a] Marco Duati,[a] Sven Rau,[b] Adrian L. Guckian,[a] Tia E. Keyes,[a] Noel M. O'Boyle,[a] Andreas Serr,[a,c] Helmar Görls[b] and Johannes G. Vos*[a]

[a] *National Centre for Sensor Research, School of Chemical Sciences, Dublin City University, Dublin 9, Ireland. E-mail: johannes.vos@dcu.ie; Fax: +353 1 7005503; Tel: +353 1 7005307*

[b] *Institut für Anorganische und Analytische Chemie, Friedrich-Schiller-University, 07743, Jena, Germany. E-mail: Sven.Rau@uni-jena.de; Fax: +49 3641 948102; Tel: +49 3641 948113*

[c] *Fakultät für Chemie, Universität Bielefeld, D-33615 Bielefeld, Germany. E-mail: Andreas.Serr@uni-bielefeld.de*

Received 26th September 2003, Accepted 23rd December 2003
First published as an Advance Article on the web 20th January 2004

A series of $[Ru(bipy)_2L]^+$ and $[Ru(phen)_2L]^+$ complexes where L is 2-[5-(3,4-dimethoxyphenyl)-4*H*-1,2,4-triazol-3-yl]pyridine (**HL1**) and 4-(5-pyridin-2-yl-4*H*-1,2,4-triazol-3-yl)benzene-1,2-diol (**HL2**) are reported. The compounds obtained have been characterised using X-ray crystallography, NMR, UV/Vis and emission spectroscopies. Partial deuteriation is used to determine the nature of the emitting state and to simplify the NMR spectra. The acid-base properties of the compounds are also investigated. The electronic structures of $[Ru(bipy)_2\mathbf{L1}]^+$ and $Ru(bipy)_2\mathbf{HL1}]^{2+}$ are examined using ZINDO. Electro and spectroelectrochemical studies on $[Ru(bipy)_2(L2)]^+$ suggest that proton transfer between the catechol and triazole moieties on **L2** takes place upon oxidation of the **L2** ligand.

Introduction

The hydroquinone/quinone redox couple plays an essential role as electron mediator in the charge separation processes in photosynthesis.[1] As a result there has been extensive interest in the redox properties of quinone containing metal complexes and in their potential to act as electron acceptors or donors.[2] In these studies catechol based ligands are coordinated to a wide range of metals.[3] Much less attention has been paid to the interaction between metal centres and pendent hydroquinone/quinone groupings, although such materials may participate in light induced electron transfer reactions.[4] We are presently involved in a systematic study of the electrochemical and photophysical properties of ruthenium complexes containing pendent hydroquinone/quinones.[5,6] In an earlier study on ruthenium polypyridyl complexes incorporating pyridyltriazole ligands with free hydroquinone groupings, electrochemically induced intramolecular protonation of the ruthenium centre was observed upon oxidation of the hydroquinone moiety.[6] In this contribution the synthesis and deprotection of the methoxy complexes $[Ru(bipy)_2(L1)]PF_6 \cdot 5H_2O$ and $[Ru(phen)_2(L1)]PF_6 \cdot 2H_2O$ (where **HL1** is 2-[5-(3,4-dimethoxyphenyl)-4*H*-1,2,4-triazol-3-yl]pyridine) to produce the catechol type complexes with the ligand **HL2** 4-(5-pyridin-2-yl-4*H*-1,2,4-triazol-3-yl)-benzene-1,2-diol are described (for ligand structures see Fig. 1). The partially deuteriated analogues $[Ru(d_8\text{-bipy})_2(L1)]^+$ and $[Ru(d_8\text{-phen})_2(L1)]^+$ are also described. The materials obtained have been characterised by X-ray crystallography and ^{1}H-NMR spectroscopy. The absorption, emission, photophysical and electrochemical properties of the complexes are also examined. To aid interpretation of the results obtained, semi-empirical calculations using ZINDO were carried out on $[Ru(bipy)_2(HL1)]^{2+}$ and $[Ru(bipy)_2(L1)]^+$, where the triazole moieties are in the protonated and deprotonated states respectively.

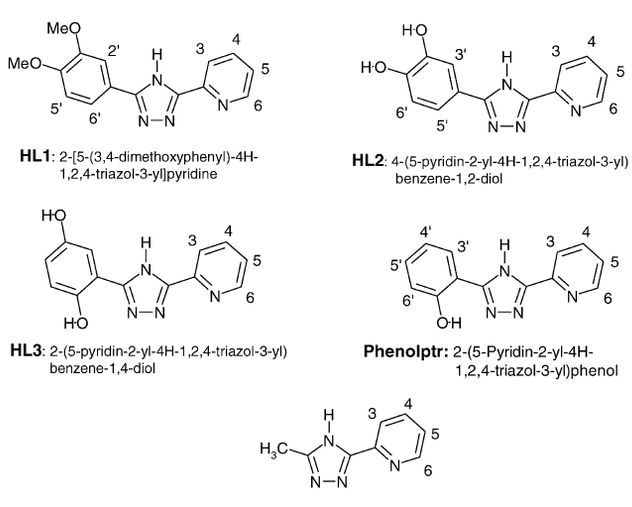

Fig. 1 Structures and labelling scheme for ^{1}H NMR of ligands.

Experimental

All synthetic reagents were of commercial grade and used without further purification. The solvents used in spectroscopic measurements were HPLC grade. Perdeuteriated 1,10-phenanthroline (d_8-phen) and perdeuteriated 2,2′-bipyridyl (d_8-bipy) were obtained using established methods.[7] *cis*-$[Ru(bipy)_2Cl_2] \cdot 2H_2O$, *cis*-$[Ru(d_8\text{-bipy})_2Cl_2] \cdot 2H_2O$, *cis*-$[Ru(phen)_2Cl_2] \cdot 2H_2O$ and *cis*-$[Ru(d_8\text{-phen})_2Cl_2]$ were synthesised using literature methods.[8]

2-[5-(3,4-dimethoxyphenyl)-4*H*-1,2,4-triazol-3-yl]pyridine (**HL1**). A solution of 2-picolylamhydrazone 0.01 mol (1.36 g) and 0.015 mol (1.5 g) triethylamine in 30 cm^3 of dry THF was vigorously stirred and cooled to 0 °C with an ice bath. 3,4-Dimethoxy-benzoylchloride 0.01 mol (2.005 g) in 10 cm^3 THF was added dropwise to this solution and the reaction mixture was heated at reflux for a further 5 min. The volume was reduced to half *in vacuo*. An equal amount of water was added and the flask stored overnight at 4 °C. The white precipitate was collected by filtration, washed with water and dried under vacuum.

† Electronic supplementary information (ESI) available: Fig. S1: molecular structure of $[Ru(phen)_2(L1)]^+$ showing atomic numbering; Fig. S2: pH dependence of the emission spectra of $[Ru(phen)_2(L2)]^+$; Table S1: energy and % contribution of atomic orbitals to each molecular orbital in the frontier region for (a) $[Ru(bipy)_2(L1)]^+$ and (b) $[Ru(bipy)_2(HL1)]^{2+}$. See http://www.rsc.org/suppdata/dt/b3/b311989k/

DOI: 10.1039/b311989k

The solid obtained was recrystallised from ethylene glycol : water to yield 1.7 g (70%). ^{1}H NMR in d_6-dmso 8.73 (1H,d,H^6), 8.19 (1H,d,H^3), 8.01 (1H,dd,H^4), 7.68 (1H,s,H$^{2'}$), 7.66 (1H,d,H$^{6'}$), 7.52 (1H,dd,H^5), 7.11 (1H,d,H$^{5'}$), 3.87 (3H,s,OMe), 3.83 (3H,s,OMe), mp = 186–188 °C.

[Ru(bipy)$_2$(L1)]PF$_6$·H$_2$O 0.395 g (1.41 mmol) of **HL1** was dissolved in 50 cm^3 ethanol : water (1 : 1 v/v) and the mixture was heated at reflux until the ligand was fully dissolved. 0.520g (1 mmol) *cis*-[Ru(bipy)$_2$Cl$_2$]·2H$_2$O was added and the reaction allowed to reflux for 8 h. The reaction was monitored by analytical HPLC. After cooling the reaction mixture was filtered and the volume reduced to *circa* 15 cm^3. The complex was precipitated by addition of a concentrated aqueous solution of ammonium hexafluorophosphate. The precipitate was filtered and washed with water. The crude complex was recrystallised from acetone/water (2 : 1 v/v) to which a few drops of aqueous NH_3 were added. The complex was further purified by column chromatography on neutral alumina using acetonitrile as eluent and recrystallised as outlined above. ^{1}H-NMR in d_3-acetonitrile for coordinated L1; 8.08 (1H,d,H^3); 7.89 (1H,dd,H^4); 7.10 (1H,dd,H^5); 7.46 (1H,d,H^6); 7.49 (1H,s,H$^{2'}$); 7.48 (1H,d,H$^{6'}$) 6.88 (1H,d,H$^{5'}$). Yield = 0.53 g (60%). Calcd. for $RuC_{35}H_{31}N_8O_3PF_6$: C: 49.00; H: 3.60; N: 13.10%. Anal. found: C: 48.58; H: 3.34; N: 12.66%.

[Ru(phen)$_2$(L1)]PF$_6$·H$_2$O was prepared and purified as described for [Ru(bipy)$_2$(L1)]PF$_6$·H$_2$O. ^{1}H NMR in d_3-acetonitrile for coordinated L1; 8.14 (1H,d,H^3); 7.87 (1H,dd,H^4); 7.01 (1H,dd,H^5); 7.49 (1H,d,H^6); 7.47 (1H,s,H$^{2'}$); 7.40 (1H,d,H$^{6'}$) 6.86 (1H,d,H$^{5'}$). Yield = 0.45 g (50%). Calcd. for $RuC_{39}H_{31}N_8O_3PF_6$: C: 51.72; H: 3.45; N: 12.37%. Anal. found: C: 52.12; H: 3.54; N: 12.17%.

[Ru(d_8-bipy)$_2$(L1)]PF$_6$·H$_2$O was prepared and purified as reported for [Ru(bipy)$_2$(L1)]PF$_6$·H$_2$O. ^{1}H NMR in d_3-acetonitrile for coordinated L1; 8.13 (1H,d,H^3); 7.88 (1H,dd,H^4); 7.14 (1H,dd,H^5); 7.47 (1H,d,H^6); 7.52 (1H,s,H$^{2'}$); 7.49 (1H,d,H$^{6'}$); 6.90 (1H,d,H$^{5'}$). Yield = 0.46 g (54%). Calcd. for $RuC_{35}H_{15}D_{16}N_8O_3PF_6$: C: 48.11; H: 3.55; N: 12.82%. Anal. found: C: 47.90; H: 3.48; N: 12.49%.

[Ru(d_8-phen)$_2$(L1)]PF$_6$·H$_2$O was prepared and purified as described for [Ru(bipy)$_2$(L1)]PF$_6$·H$_2$O. ^{1}H NMR in d_3-acetonitrile for coordinated L1; 8.12 (1H,d,H^3); 7.84 (1H,dd,H^4); 6.99 (1H,dd,H^5); 7.45 (1H,d,H^6); 7.42 (1H,s,H$^{2'}$); 7.39 (1H,d,H$^{6'}$) 6.83 (1H,d,H$^{5'}$). Yield = 0.52 g (56%). Calcd. for $RuC_{39}H_{15}D_{16}N_8O_3PF_6$: C: 50.80; H: 3.39; N: 12.16%. Anal. found: C: 50.75; H: 3.42; N: 11.91%.

[Ru(bipy)$_2$(L2)]PF$_6$·5H$_2$O was prepared by demethylation of [Ru(bipy)$_2$(L1)]$^+$ with boron tribromide.[9] 0.523 g (0.61 mmol) of [Ru(bipy)$_2$(L1)]PF$_6$·H$_2$O was dissolved and stirred in 20 cm^3 dry dichloromethane under N_2. The flask was placed in a toluene/liquid nitrogen bath (−78 °C) and allowed to equilibrate for at least 20 min. 12 cm^3 (ten fold molar excess) of 1.0 M boron tribromide in dichloromethane was slowly added to the reaction flask. The reaction was left stirring at −78 °C for at least one hour under N_2 and allowed to warm to room temperature overnight. The reaction was quenched by slow addition of iced water to the reaction flask. The reaction mixture was neutralised by adding an aqueous solution of concentrated sodium carbonate. The deep red product was precipitated using saturated aqueous NH_4PF_6. The product was washed with diethyl ether and recrystallised from acetone/water (2 : 1). ^{1}H NMR resonances of coordinated L2 in d_3-acetonitrile 8.25 (1H,d,H^3); 7.96 (1H,dd,H^4); 7.28 (1H,dd,H^5); 7.54 (1H,d,H^6); 7.34 (1H,s,H$^{3'}$); 7.26 (1H,d,H$^{5'}$); 6.84 (1H,d,H$^{6'}$). Yield = 0.351 g (64%). Calcd. for $RuC_{33}H_{35}N_8O_7PF_6$: C: 43.96; H: 3.91; N: 12.42%. Anal. found: C: 43.83; H: 4.00; N: 12.24%.

[Ru(phen)$_2$(L2)]PF$_6$·2H$_2$O [Ru(phen)$_2$(L1)]$^+$ was deprotected to form [Ru(phen)$_2$(L2)]PF$_6$·2H$_2$O using BBr_3 in a similar reaction to that described for [Ru(bipy)$_2$(L2)]PF$_6$·5H$_2$O. ^{1}H-NMR resonances of L2 in d_3-acetonitrile 8.19 (1H,d, H^3); 7.87 (1H,dd,H^4); 7.01 (1H,dd,H^5); 7.42 (1H,d,H^6); 7.30 (1H,s,H$^{3'}$); 7.18 (1H,d,H$^{5'}$); 6.85 (1H,d,H$^{6'}$). Yield = 0.535 g (83%). Calcd. for $RuC_{37}H_{29}N_8O_4PF_6$: C: 49.62; H: 3.26; N: 12.51%. Anal. found: C: 49.86; H: 3.26; N: 12.17%.

Instrumental methods

^{1}H and ^{1}H COSY spectra were recorded on a Bruker AC400 (400 MHz) instrument. Peak positions are relative to residual solvent peaks. UV/Visible spectra were obtained using a Shimadzu UV3100 UV-Vis-NIR spectrophotometer interfaced to an Elonex PC433 personal computer. Extinction coefficients are accurate to 5%. Emission spectra were obtained on a Perkin-Elmer LS50-B luminescence spectrometer equipped with a red sensitive Hamamatsu R928 detector, interfaced to an Elonex PC466 personal computer employing Perkin-Elmer FL WinLab custom built software. Excitation and emission slit widths of 10 nm were used. The spectra were not corrected for photomultiplier response. HPLC grade acetonitrile was used as a solvent. To ensure protonation/deprotonation, 50 μL perchloric acid or diethylamine solution were added to the sample. pK_a values were determined in Britton-Robinson buffer (0.04 M boric acid, 0.04 M acetic acid, 0.04 M phosphoric acid). The pH was adjusted by adding conc. NaOH or conc. H_2SO_4 and was measured using a Corning 240 digital pH meter. The pK_a values were determined from the point of inflection of the absorbance *versus* pH plot. Excited state acid–base equilibria were measured from the changes in the emission intensity as a function of pH (*vide infra*). A suitable isosbestic point in the absorption titration curves was taken as excitation wavelength.

Luminescence lifetime measurements were obtained using an Edinburgh Analytical Instruments (EAI) Time-Correlated Single-Photon Counting apparatus (TCSPC). Samples were deaerated for 20 min using Ar gas before measurements were carried out, followed by repeated deaeration to ensure total oxygen exclusion. Emission lifetimes were calculated using a single exponential fitting function; Levenberg–Marquardt algorithm with iterative reconvolution (Edinburgh instruments F900 software) and are ±10%. The $\chi 2$ and residual plots were used to judge the quality of the fits. Measurements were performed in spectroscopic grade acetonitrile. The protonation state of the triazole rings was controlled as outlined above.

Cyclic voltammetry and square wave voltammetry were carried out using a CHInstrument Model 660 potentiostat electrochemical workstation interfaced to an Elonex 486 PC. 0.1 M tetraethylammonium perchlorate (TEAP) in acetonitrile was used as electrolyte. A Ag/AgCl reference electrode, a 3 mm diameter teflon shrouded glassy carbon working electrode and a platinum gauze counter electrode were employed. TFA was added to ensure protonation of the complexes when needed. Samples were N_2 purged prior to measurements. Spectroelectrochemistry was carried out using electrochemical equipment as outlined above with a home-made pyrex glass thin layer cell (1 mm), a platinum gauze working electrode, a *pseudo*-Ag/AgCl reference electrode and a platinum wire counter electrode. Spectra were recorded in 0.1 M TEAP in CH_3CN with a Shimadzu 3100 UV/Vis/NIR spectrometer interfaced to an Elonex PC433 computer.

HPLC experiments were carried out using a Waters HPLC system, consisting of a model 501 pump, a 20 μl injector loop, a Partisil SCX steel column and a 990 photodiode array detector. The mobile phase used was 0.08 M $LiClO_4$ in 80 : 20 acetonitrile : water, the flow rate 1.8 cm^3 min^{-1}. C,H,N elemental analyses were carried out by the Microanalytical laboratories at University College Dublin.

X-ray crystallography. Intensity data were collected on a Nonius KappaCCD diffractometer, using graphite-monochromated Mo-Kα radiation. Data were corrected for Lorentz and polarisation effects, but not for absorption.[10] The structures were solved by direct methods (SHELXS[11]) and refined by

full-matrix least squares techniques against F_o^2 (SHELXL-97[12]). The hydrogen atoms of the structures were included at calculated positions with fixed thermal parameters. The PF_6^- groups of $[Ru(phen)_2(L1)]^+$ and $[Ru(d_8\text{-bipy})_2(L1)]^+$ are disordered, but this disorder could be solved. All non-hydrogen atoms were refined anisotropically.[12] XP (SIEMENS Analytical X-ray Instruments, Inc.) was used for structure representations.

Crystal data for $[Ru(phen)_2(L1)]^+$: $C_{39}H_{29}F_6N_8O_2PRu$, M_r = 887.74 g mol^{-1}, red–brown prism, size 0.38 × 0.32 × 0.28 mm^3, monoclinic, space group $P2_1/c$, a = 11.6379(9), b = 19.473(2), c = 16.879(1) Å, β = 102.944(7)°, V = 3728.0(5) Å^3, T = −90 °C, Z = 4, ρ_{calcd} = 1.582 g cm^{-3}, μ(Mo-Kα) = 5.42 cm^{-1}, $F(000)$ = 1792, 7896 reflections in $h(-14/14)$, $k(-24/0)$, $l(0/21)$, measured in the range 2.43° ≤ Θ ≤ 26.42°, completeness Θ_{max} = 99.4%, 7631 independent reflections, R_{int} = 0.029, 4848 reflections with $F_o > 4\sigma(F_o)$, 508 parameters, 0 restraints, $R1_{obs}$ = 0.053, wR^2_{obs} = 0.142, $R1_{all}$ = 0.116, wR^2_{all} = 0.155, GOOF = 0.997, largest difference peak and hole: 0.996/−0.558 e Å^{-3}.

Crystal data for $[Ru(d_8\text{-bipy})_2(L1)]^+$: $C_{35}H_{13}D_{16}F_6N_8O_2PRu\cdot H_2O$, M_r = 848.71 g mol^{-1}, colourless prism, size 0.32 × 0.30 × 0.20 mm^3, red–brown, space group $P2_1/n$, a = 9.1165(9), b = 18.068(1), c = 21.424(1) Å, β = 96.599(6)°, V = 3505.5(4) Å^3, T = −90 °C, Z = 4, ρ_{calcd} = 1.608 g cm^{-3}, μ(Mo-Kα) = 5.73 cm^{-1}, $F(000)$ = 1716, 7296 reflections in $h(-11/11)$, $k(-22/0)$, $l(0/26)$, measured in the range 2.34° ≤ Θ ≤ 26.31°, completeness Θ_{max} = 99.8%, 7106 independent reflections, R_{int} = 0.026, 4811 reflections with $F_o > 4\sigma(F_o)$, 482 parameters, 0 restraints, $R1_{obs}$ = 0.054, wR^2_{obs} = 0.153, $R1_{all}$ = 0.102, wR^2_{all} = 0.167, GOOF = 0.995, largest difference peak and hole: 1.216/−0.691 e Å^{-3}.

CCDC reference numbers 213441 ($[Ru(phen)_2(L1)]^+$) and 213442 ($[Ru(d_8\text{-bipy})_2(L1)]^+$).

See http://www.rsc.org/suppdata/dt/b3/b311989k/ for crystallographic data in CIF or other electronic format.

Calculations. INDO/1 and INDO/S semi-empirical calculations used the ZINDO method and HyperChem[13] on an Intel Pentium IV 1.6 GHz PC. Geometry optimisations were performed using the ZINDO/1 method. The default parameters for ruthenium as suggested by Anderson *et al.*[14] were used, apart from a value for the resonance integral, β(4d), of −20.0 eV as suggested by Gorelsky *et al.*[15] The overlap weighting factors σ–σ and π–π for ZINDO/1 calculations were both set at 1. Convergence was assumed when a gradient went below 5 cal mol^{-1} Å^{-1}. Molecular orbital calculations were performed with ZINDO/S using the Krogh–Jespersen bases for ruthenium.[16] However, the electronic energy of the isolated atom was adjusted to the standard value for ZINDO/1. Values of 0.0, 0.9, and 0.1 respectively, were used for the fractional contributions of the $d^{n-2}s^2$, $d^{n-1}s(p)$ and d^n configurations to the core integrals.[17] The overlap weighting factors σ–σ and π–π for ZINDO/S calculations were set at 1.265 and 0.585 as suggested by Ridley and Zerner.[18] Density of states spectra were constructed from the calculated ZINDO/S molecular orbital energies by convolution with gaussians of unit height and FWHM of 0.5 eV.

Results and discussion

Synthetic procedures

The synthesis of the complexes based on **HL1** follows well-established preparation methods. As has been observed with other pyridyltriazole complexes the ligand **HL1** deprotonates upon coordination to the metal centre to form $\mathbf{L1}^-$ and the complexes are therefore obtained as monocations upon the addition of excess PF_6^-. To ensure that deprotonated complexes are obtained the products were recrystallised in the presence of a few drops of aqueous ammonia. The method applied for the deprotection of the methoxy compounds is a modification of literature methods, however,[9] longer reaction times were needed to ensure complete demethylation. Successful demethylation was verified by HPLC and ^{1}H-NMR (*vide infra*).

X-ray crystallography

A feature of many pyridyltriazole ligands is the possibility of coordination *via N2* and *N4* of the triazole (See Fig. 2 for 1,2,4-triazole labelling scheme). In a study carried out by Ryan *et al.* it was found that for ligands with a substituent on the triazole 5-position coordination occurred *via* both *N4* and *N2* in a ratio of approximately 9 : 1,[19] while the ratio of isomers is 1 : 1 when the 5-position is occupied by a hydrogen atom.[20] With **HL1** only one major product was obtained in all cases. To unambiguously determine the coordination mode of the triazole ring in these compounds the X-ray structural analysis of two compounds was performed. The crystallographic parameters are given in the Experimental. A projection of the structure of $[Ru(d_8\text{-bipy})_2(L1)]^+$ is shown in Fig. 3. The structural details obtained for $[Ru(phen)_2(L1)]^+$ are very similar (see Fig. S1 †). Selected bond lengths and angles are listed in Table 1. The data for the complexes $[Ru(bipy)_2(5Mptr)]PF_6\cdot 4H_2O$[21] and $[Ru(bipy)_2(phenolptr)]PF_6\cdot CH_3COCH_3$[22] (see Fig. 1) are added for comparison. In both, the pyridyltriazole ligand is coordinated *via* the *N2* atom of the triazole ring. The deprotonated state of the ring is confirmed by the presence of one PF_6 counter ion per ruthenium centre. The Ru–N distances and the bite angles for the compounds are similar to those observed for other similar compounds.[23–26] One significant difference between the two complexes is the position and orientation of the phenyl ring. In $[Ru(phen)_2(L1)]^+$ the OMe unit at C2 is orientated away from the neighbouring 1,10-phenanthroline ligand, whereas in $[Ru(d_8\text{-bipy})_2(L1)]^+$ it is orientated towards the coordinated 2,2′-bipyridine. This corresponds to a rotation

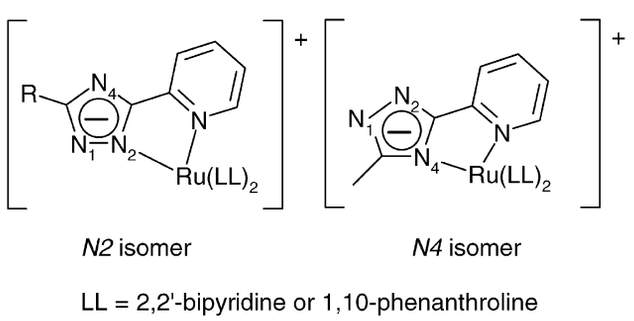

Fig. 2 *N2* and *N4* binding modes in complexes described in text.

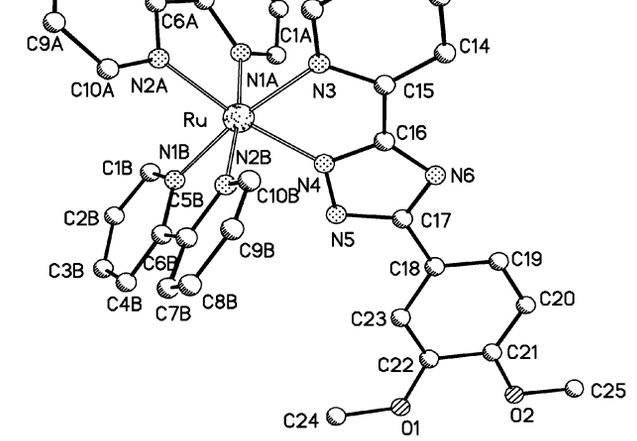

Fig. 3 Molecular structure of $[Ru(d_8\text{-bipy})_2(L1)]^+$ showing atomic numbering (*nb.* the crystallographic atom labelling scheme is different to that employed in the text to refer to the coordination mode of the 1,2,4-triazole, see Fig. 2).

Table 1 Selected bond distances (Å) and angles (°) of $[Ru(d_8\text{-bipy})_2(L1)]^+$ and $[Ru(phen)_2(L1)]^+$ and some related compounds

	$[Ru(d_8\text{-bipy})_2(L1)]^+$	$[Ru(phen)_2(L1)]^+$	**Ru5Mptr**[a]	**Ruphenolptr**[a]
Bond distances/Å				
Ru–N4	2.038(4)	2.036(4)	2.050(5)	2.051(3)
Ru–N3	2.109(4)	2.089(4)	2.086(4)	2.085(3)
Ru–N1B	2.044(4)	2.057(4)	2.055(4)	2.056(3)
Ru–N2B	2.044(4)	2.054(4)	2.042(5)	2.056(3)
Ru–N2A	2.043(4)	2.071(4)	2.060(4)	2.063(3)
Ru–N1A	2.062(4)	2.054(4)	2.056(4)	2.049(3)
Bond angles/°				
N4–Ru–N3	77.86(15)	78.16(15)	78.0(2)	77.9(1)
N4–Ru–N1B	94.29(15)	96.42(15)	96.1(2)	92.3(1)
N4–Ru–N1A	96.11(15)	93.73(16)	96.5(5)	91.8(1)
N4–Ru–N2B	89.88(15)	92.47(15)	87.4(2)	97.6(1)
N3–Ru–N2B	96.25(17)	95.88(17)	95.0(2)	94.3(1)
N3–Ru–N2A	94.88(15)	94.66(15)	95.9(2)	90.7(1)
N3–Ru–N1A	86.28(15)	90.17(16)	90.9(2)	96.3(1)
N1B–Ru–N2B	79.00(17)	79.86(17)	79.4(2)	79.9(1)
N1B–Ru–N2A	93.29(15)	91.19(15)	90.5(2)	97.8(1)
N2B–Ru–N2A	95.48(16)	94.59(16)	98.0(2)	90.9(1)
N2A–Ru–N1A	78.73(16)	79.83(15)	78.7(2)	78.7(1)

[a] **Ru5Mptr** = $[Ru(bipy)_2(5Mptr)]PF_6\cdot 4H_2O$[21] and **Ruphenolptr** = $[Ru(bipy)_2(phenolptr)]PF_6\cdot CH_3COCH_3$.[22]

of the dimethoxy substituted phenyl ring around the C_{phenyl}–$C_{triazole}$ bond. Both dimethoxy substituted phenyl rings are twisted out of plane of the pyridine triazole unit. For $[Ru(d_8\text{-bipy})_2(L1)]^+$ the torsion angle is 20.8°, while for the phen compound a value of 25.9° is obtained. In the $[Ru(d_8\text{-bipy})_2(L1)]^+$ solid-state structure there are several intermolecular hydrogen bonds. The oxygen of the methoxy group (labelled O2) serves as hydrogen bond acceptor for a water molecule (O2–O_{water} = 2.971(10) Å). The same water molecule is also a hydrogen bond donor for the N6 atom of the triazole ring of a neighbouring molecule (N6–O_{water} = 2.863(10) Å). This supramolecular association leads to the formation of one-dimensional chains consisting of alternating ruthenium complexes and water molecules and these chains are stacked upon each other as depicted in Fig. 4. The resulting packing diagram is shown in Fig. 5. $[Ru(phen)_2(L1)]^+$ contains no water molecules even though the complex was obtained in an identical manner as $[Ru(d_8\text{-bipy})_2(L1)]^+$. In the solid state relatively weak intermolecular CH–N hydrogen bonds can be observed. N5 of the triazole moiety serves as hydrogen bond acceptor for a C5–H bond of a phenanthroline from a neighbouring complex (C5B–N5 = 3.285(10) Å, angle C5B–H5B–N5 = 139.9(3)). In both molecular structures no significant influence of the hydrogen bonding network on the coordination geometry can be observed.

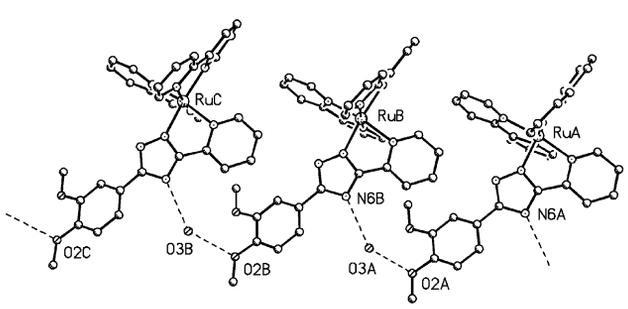

Fig. 4 Schematic representation of the inter-molecular interaction in $[Ru(d_8\text{-bipy})_2(L1)]^+$.

^{1}H NMR spectroscopy

The ^{1}H NMR data for the complexes are listed in the Experimental. The resonances observed for the bipy and phen ligands are as expected and are not included. The assignment of the signals was carried out with the help of 2D ^{1}H COSY spectra and the use of partial deuteriation of the complexes (See Fig. 6). These spectra clearly show the presence of only one isomer. Fig. 6b shows that selective deuteriation greatly simplifies the

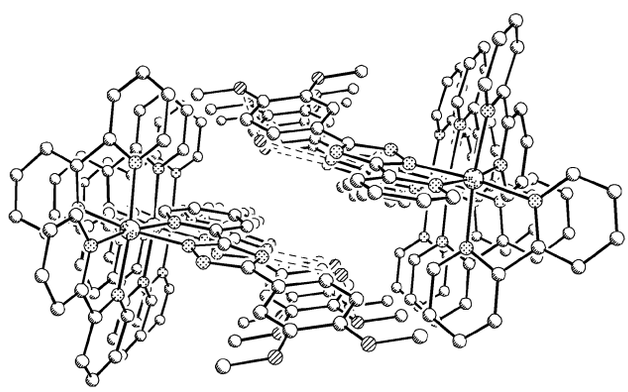

Fig. 5 Packing diagram for $[Ru(d_8\text{-bipy})_2(L1)]^+$.

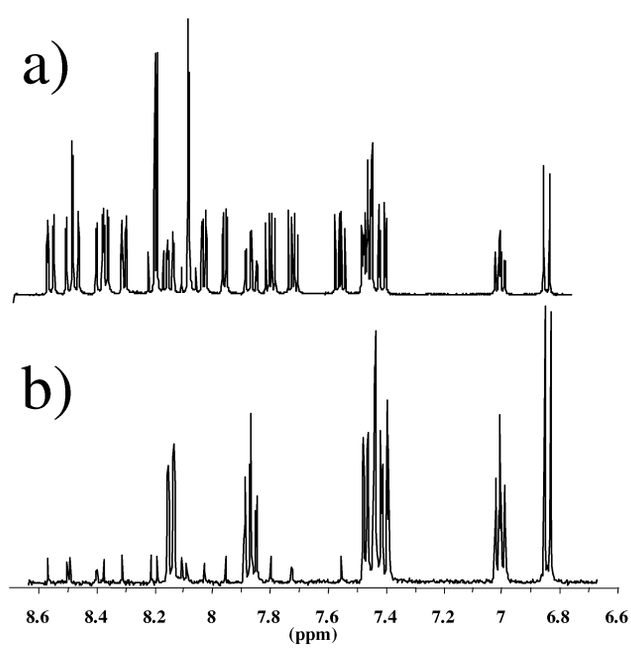

Fig. 6 ^{1}H-NMR spectrum in d_3-acetonitrile of (a) $[Ru(phen)_2(L1)]^+$ and (b) $[Ru(d_8\text{-phen})_2(L1)]^+$.

spectra. From this spectrum the deuteriation of the phen ligands is estimated to be better than 95%. The quantitative demethylation of $[Ru(bipy)_2(L1)]^+$ and $[Ru(phen)_2(L1)]^+$ to form $[Ru(bipy)_2(L2)]^+$ and $[Ru(phen)_2(L2)]^+$ respectively, can be verified by the absence of the –OMe resonances between 3.7 and 3.9 ppm. In addition, there are also small but significant changes in the position of the proton resonances for the coordinated **L2**$^-$ moiety compared to the methoxy precursor ligand. Proton resonances for the deprotected ligand are shifted to higher field by about 0.1–0.2 ppm. The effect is largest for the phenyl protons.

Electronic and photophysical properties

UV-Visible spectra of the complexes are consistent with those observed for other pyridyltriazole compounds[5,21,27] and are listed in Table 2. The spectra are dominated in the visible region (300–500 nm) by dπ–π* metal-to-ligand-charge-transfer (MLCT) transitions, while the UV spectrum is dominated by intense π–π* transitions associated with the different ligands. On protonation of the triazole ring the ^{1}MLCT absorption bands of the complexes undergo a blue shift (see Table 2) as a result of the reduced electron donor properties of the triazole ring.

All compounds exhibit emission at 298 K with the λ_{max} of the deprotonated complexes occurring at lower energy than observed for $[Ru(bipy)_3]^{2+}$ (605 nm).[28] This is explained by the strong σ-donor properties of the anionic triazole ligand. As with the absorption spectra, protonation of the triazole ring in the complexes results in a blue shift of the emission maxima. The emission lifetimes of the deprotonated species are listed in Table 2. The lifetimes for the protonated species are <10 ns (*i.e.* shorter than the limit of the detection system employed). The lifetimes obtained for $[Ru(phen)_2(L1)]^+$ and $[Ru(d_8\text{-phen})_2(L1)]^+$ are considerably longer than those found for the analogous bipy-based compounds. The significant increase in emission lifetime upon deuteriation[29] of the bipy and phen ligands, from 70 to 90 ns and from 365 to 500 ns respectively, suggests that the emitting state is based on the polypyridyl ligands rather than the pyridyl–triazole based ligands.[30] The emission lifetimes of $[Ru(bipy)_2(L1)]^+$ and $[Ru(bipy)_2(L2)]^+$ are very similar (see Table 2). However, the lifetime observed for $[Ru(phen)_2(L2)]^+$ (225 ns) is shorter than found for $[Ru(phen)_2(L1)]^+$ (365 ns). This suggests that there is a significant quenching by the catechol moiety in the phen analogue, most likely *via* an electron transfer mechanism. A comparison of the two lifetimes suggests that the quenching rate is about 2×10^6 s^{-1}.[31] This relatively slow rate is not expected to have a significant effect on the excited state lifetime of the bipy analogue. A detailed study on the photophysical properties of these and of related hydroquinone (**HL3,** see Fig. 1) compounds is in progress.

Acid–base properties

The effect of protonation and deprotonation of the triazole ring on the λ_{max} of absorption and emission spectra is illustrated in Table 2. The acid–base behaviour of the compounds was studied by recording the pH dependence of these spectra. A typical ground-state titration is shown in Fig. 7. For all compounds clear isosbestic points are observed and all changes are reversible in the pH range 1–8. However in the pH range 8–12, under aerobic conditions, the spectroscopic changes observed for $[Ru(bipy)_2(L2)]^+$ and $[Ru(phen)_2(L2)]^+$ are not reversible probably because of the formation of semiquinone intermediates. The pK_a values obtained for the coordinated triazole ring are shown in Table 2. Information about the excited state acidity can be obtained from the pH dependence of the emission spectra. A typical titration showing the pH dependence of the emission of $[Ru(phen)_2(L2)]^+$ is shown in Fig. S2.† The changes observed may allow for determination of the location of the

Table 2 Spectroscopic and electrochemical data for complexes described in text and related complexes

Complex	Abs[a] λ_{max}(log ε)/nm		Em[a] λ_{max}/nm[b](τ/ns)						[c]pK_a* (± 0.1)	[d]Anodic $E_{1/2}$/V	[d]Cathodic $E_{1/2}$/V
			Protonated		Deprotonated		[c]pK_a (± 0.1)				
	Protonated	Deprotonated	300 K	77 K	300 K	77K				Deprotonated	Deprotonated
$[Ru(bpy)_3]^{2+}$ [e]		452			615(1100)					1.21	−1.38
$[Ru(bpy)_2(5Mprt)]^+$	438	467(3.92)	612	587	660	610	4.9		—	0.75	−1.52, −1.79
$[Ru(bipy)_2(L1)]^+$	435	482(4.00)	616	578	692(70)	618	4.1		1.7	0.71, 1.25 (irr)	−1.35, −1.56
$[Ru(d_8\text{-bipy})_2(L1)]^+$	440	478(4.00)	620	582	689(90)	617	4.2		2.2	0.71, 1.25 (irr)	−1.35, −1.57
$[Ru(bipy)_2(L2)]^+$	440	476(4.01)	622	577	689(65)	625	4.2		1.4	0.82 (irr), 1.00 (irr), 1.22 (irr)	—
$[Ru(phen)_3]^{2+}$ [e]		442			604(460)					1.35	−1.46
$[Ru(phen)_2(L1)]^+$	420	427(4.13)	607	569	681(365)	608	4.4		2.0	0.76, 1.25 (irr)	−1.48 (irr), −1.55 (irr)
$[Ru(d_8\text{-phen})_2(L1)]^+$	418	426(4.13)	607	570	680(500)	606	4.0		1.8	0.78	−1.49 (irr), −1.59 (irr)
$[Ru(phen)_2(L2)]^+$	418	426(4.13)	607	568	663(225)	609	4.0		1.5	0.86, 1.05, 1.24 (irr)	—

[a] All measurements at 300 K were performed in acetonitrile. [b] Values in brackets are emission lifetimes in ns. Samples for lifetime measurements were degassed using N_2. The lifetimes of the protonated complexes are too short to be measured with the equipment available. All measurements at 77 K were performed in ethanol/methanol 4 : 1 v/v. [c] Ground- and excited-state pK_a values were obtained in Britton–Robinson buffer. [d] Electrochemical data for deprotonated complexes in V *vs.* Ag/AgCl in acetonitrile with 0.1 M TEAP (scan rate: 100 mV s^{-1}). [e] Values obtained from ref. 29*a*, no acid/base chemistry observed for these two compounds so protonation/deprotonation labels not relevant.

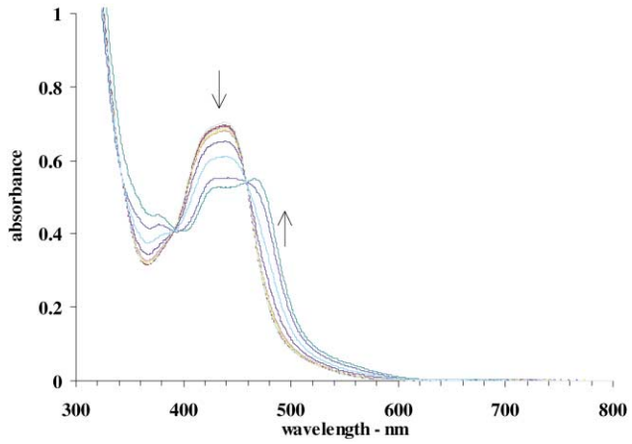

Fig. 7 pH dependence of the absorption spectrum of $[Ru(bipy)_2(L2)]^+$ (5×10^{-5} M) in an aqueous Britton–Robinson buffer at pH 1.44, 1.79, 2.09, 2.55, 2.95, 3.13, 3.70, 4.18, 4.92 and 6.66.

excited state.[32] Excited state pK_a values (pK_a*) were evaluated using the Förster method [33] as shown in eqn. (1):

$$pK_a^* = pK_a + (0.625/T)(\nu_{B-} - \nu_{HB}) \quad (1)$$

where ν_{B-} and ν_{HB} are the E_{0-0} values (in cm^{-1}) of the deprotonated and protonated complexes respectively. These values are taken from the λ_{max} of the emission spectra at 77 K as they are the most accurate means of obtaining an estimate for the energy difference involved in the 0–0 transitions. This equation gives an estimate of the excited state acidity of the compound. A more reliable method is based on the measurement of the emission lifetimes of both the protonated and the deprotonated species.[33] However, for the compounds reported here the emission of the protonated compounds is well below 10 ns, which prevents the formation of equilibrium in the excited state. This lack of equilibrium in the excited state limits the physical meaning of the pK_a* values obtained using eqn. (1). The trend observed is nevertheless significant and the increased acidity in the excited state indicates that formation of the ^{3}MLCT excited state involves transfer of charge from Ru(II) to a polypyridyl rather than the triazole based ligand.[32,34] This observation is in agreement with the dependence of the emission lifetime on deuteriation as outlined above.

Electrochemical properties

Complexes based on the HL1 ligand. The oxidation and reduction potentials of the complexes are presented in Table 2. Between 0 V to 1.0 V *vs.* Ag/AgCl the complexes $[Ru(bipy)_2(L1)]^+$ and $[Ru(phen)_2(L1)]^+$, feature a reversible oxidation process at ~0.8 V *vs*. Ag/AgCl (see Fig. 8). An irreversible oxidation is observed at potentials close to 1.2 V. To further investigate the nature of these two redox processes spectroelectrochemical measurements were carried out. Bulk oxidation of $[Ru(bipy)_2(L1)]^+$ at 1.00 V *vs*. Ag/AgCl leads to the appearance of new bands in the region 400–1600 nm. The analogous $[Ru(phen)_2(L1)]^+$ complex shows similar results. The new bands have been assigned as ligand-to-metal charge transfer (LMCT) bands on the basis of their energy and intensity and by comparison with structurally related complexes.[34–36] The expected depletion of ^{1}MLCT absorption bands is masked by the concomitant growth of bands at 435, 478 and 1167 nm for the bipy complex (see Fig. 9) and 420 and 1166 nm for the phen complex. A full recovery of the original spectrum was observed upon electrochemical reduction of the oxidised species, confirming the reversibility of the first oxidation process and allowing it to be attributed to a metal centred oxidation process. Oxidation at potentials above 1.2 V results in further changes in the absorption spectrum. These changes are however irreversible and

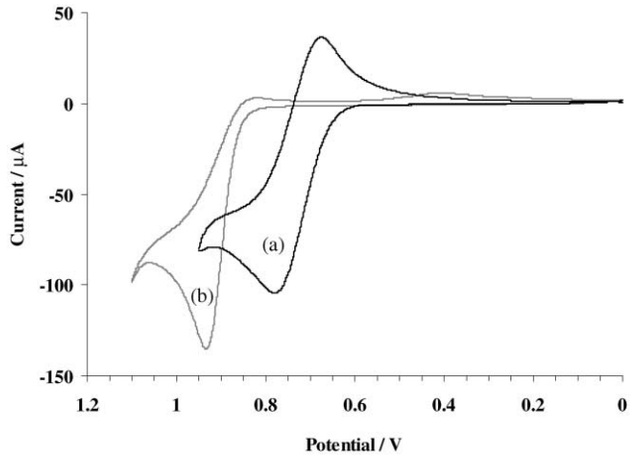

Fig. 8 Cyclic voltammogram of (a) $[Ru(bipy)_2(L1)]^+$ and (b) $[Ru(bipy)_2(HL1)]^{2+}$ (1×10^{-3} M) in acetonitrile with 0.1 M TEAP (a few drops of TFA were added to ensure protonation of the triazole ring) (scan rate: 100 mV s^{-1}).

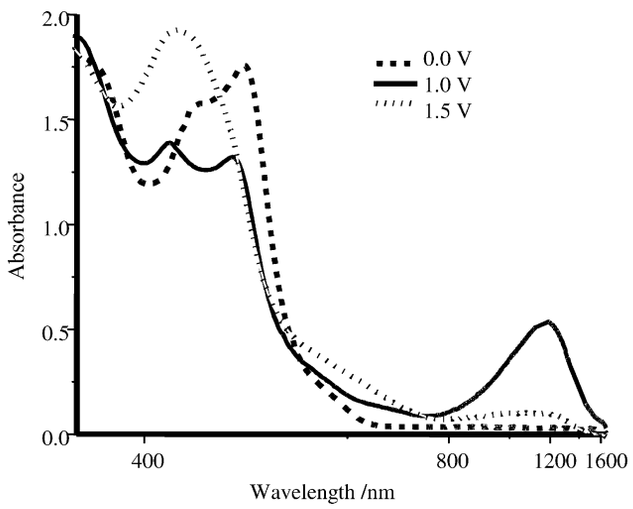

Fig. 9 Spectroelectrochemistry of $[Ru(bipy)_2(L1)]^+$ in acetonitrile with 0.1 M TEAP at 0 V, 1.00 V and 1.50 V *vs.* Ag/AgCl (ordinate axis is set on non-linear scale for clarity).

therefore no further detailed electrochemical experiments were carried out. The irreversibility of the second oxidation process suggests that this process is related to the presence of methoxy groups.[5] This assignment is further addressed in the Calculations section below.

The LMCT spectra of Ru(III) complexes have received relatively little attention, in part due to their low intensity (*e.g.* $\varepsilon \leq 500$ M^{-1} cm^{-1} for $[Ru(bipy)_3]^{3+}$) and also because of their non-emissive nature. It is clear, however that both the energy and intensity of LMCT bands can vary greatly,[37] with a direct correlation between the σ-donor strength of the ligands and band intensity. LMCT bands of moderate intensity in the red/near IR region have previously been observed in the mixed-ligand complexes of Ru(III) containing electron-rich donor ligands such as bisbenzimidazole [38] and bispyridinetriazoles.[35] The position and intensity of these LMCT bands correlate well with those found here. The intense LMCT bands for $[Ru(bipy)_2(L1)]^{2+}$ and $[Ru(phen)_2(L1)]^{2+}$ complexes are, therefore, not unexpected considering the electron rich nature of the deprotonated triazole ligand.

In related complexes, protonation of the triazole ring shifts the reversible metal based oxidation about 400 mV more positive.[5a] Surprisingly Fig. 8 shows that the anodic shift is less than expected and also that an irreversible signal is obtained. The lack of reversibility observed for the oxidation process upon protonation of the ligand is possibly best explained by an

overlap between the, still reversible, metal oxidation and the irreversible methoxy based redox process. The ZINDO calculations do indeed indicate that the methoxy and metal-based oxidation processes are expected to be much closer when the triazole is protonated (*vide infra*). Unfortunately the irreversibility of the redox wave and in particular fouling of the electrode did prevent more detailed studies. The reduction waves observed are by comparison with other polypyridyl complexes assigned to bipy or phen based reductions.[5] The reduction processes are not well defined due to surface adsorption effects and become irreversible by protonation and deprotonation effects initiated by the reduction processes.[39] This prevents a detailed investigation of the reduction processes.

Complexes based on the HL2 ligand. The cyclic voltammogram of the complex $[Ru(bipy)_2(L2)]^+$ is shown in Fig. 10. Between 0.0 and 1.4 V *vs*. Ag/AgCl the compound shows three oxidation waves and a number of poorly defined reduction processes. None of the processes appear reversible but considering the complexity of the hydroquinone/quinone redox couple this is not unexpected. Several attempts were made to improve the quality of the CV. One approach involved pre-treatment of the electrode as described by Cabaniss *et al*.[40] This treatment involves anodisation of the glassy carbon electrode by placing it in 0.1 M H_2SO_4 at a potential of 1.80 V for 1 min. This did not significantly improve the behaviour obtained and the results reported in Fig. 10 are the best obtained. Similar problems were observed for the oxidative chemistry of the analogous complex $[Ru(bipy)_2(L3)]^+$ (see Fig. 1). However, for this compound electrode anodisation led to a much improved CV and three well-defined redox processes were observed in the anodic region. Based on spectroelectrochemical investigations, the first process at 0.74 V was assigned to the oxidation of the hydroquinone group to the semiquinone species. The result of this oxidation process is that the adjacent triazole group is protonated. This results in a quasi-reversible oxidation wave with a $E_{1/2}$ of 1.18 V. The semiquinone/quinone oxidation is observed at 1.01 V. The pattern observed for $[Ru(bipy)_2(L2)]^+$ and $[Ru(phen)_2(L2)]^+$ is not unlike that observed for $[Ru(bipy)_2(L3)]^+$ but as expected the electrochemistry of the catechol grouping is much less well-defined.[41] As a result spectroelectrochemical measurements did not yield unambiguous results. It seems likely however that the redox waves observed at 0.82 and 1.00 V are best described as a two step oxidation of the catechol moiety to the quinone. The last oxidation step at 1.22 V is best explained by the oxidation of the quinone complex in which the triazole ring is protonated. This process is not expected to be intramolecular in nature as proposed for $[Ru(bipy)_2(L3)]^+$, but is most likely caused by an increase in the acidity of the solution following proton release upon oxidation of the catechol ring.

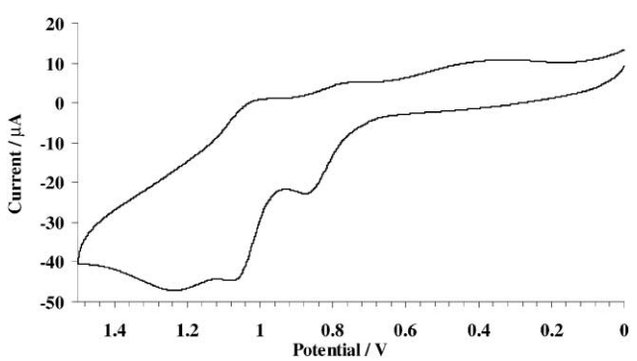

Fig. 10 Cyclic voltammogram of $[Ru(bipy)_2(L2)]^+$ (1×10^{-3} M) in acetonitrile with 0.1 M TEAP (scan rate: 100 mV s^{-1}).

Calculations

To better understand the electrochemical behaviour of the methoxy compounds the electronic structures of $[Ru(bipy)_2(HL1)]^{2+}$ and $[Ru(bipy)_2(L1)]^+$, were calculated using ZINDO/S. The structures of both complexes were geometry optimised before ZINDO/S calculations were performed. The ZINDO/1 optimised structure of this compound shows good agreement with the X-ray structure reported for the d_8-bipy analogue discussed above. For the protonated complexes, protonation may occur either at the *N1* or *N4* position of the triazole tring. ZINDO/S calculations on each isomer gave very similar results. The results for the *N4* isomer will be discussed here. The HOMO and LUMO levels of $[Ru(bipy)_2(HL1)]^{2+}$ and $[Ru(bipy)_2(L1)]^+$ are shown in Fig. 11, with corresponding information on their relative energies and atomic orbital contributions. Values for atomic orbital contributions of the pyridyltriazole (*pytrz*), and dimethoxyphenyl (*ph*), moieties of **L1** have been determined separately.

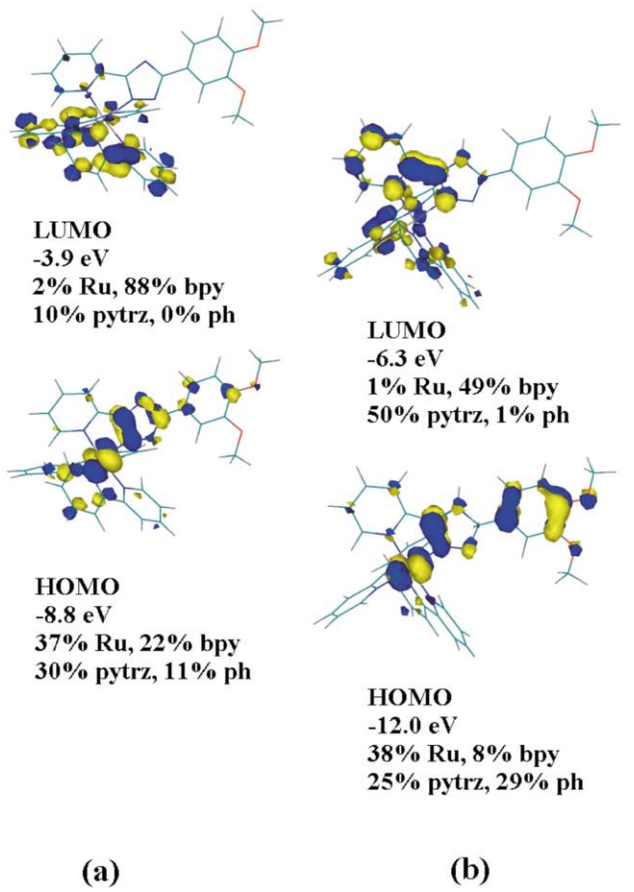

Fig. 11 Isosurface drawings of the HOMO and LUMO levels of (a) $[Ru(bipy)_2(L1)]^+$ in which the triazole ring is deprotonated and (b) $[Ru(bipy)_2(HL1)]^{2+}$, in which the triazole ring is protonated Also shown are the energies of the levels in eV and the % contribution of the metal and ligands to the molecular orbital, based on the contributions of the individual atomic orbitals to the molecular orbital. The contribution of both **HL1** and $\mathbf{L1}^-$, the protonated and the deprotonated pyridyltriazole ligands, is divided into a pyridinetriazole component, *pytrz* and a contribution from the dimethoxyphenyl moiety, *ph*.

The HOMO of the deprotonated complex contains significant contributions from each of the ligand and metal-based components considered in the calculation. However, the value for *ph* is about one-third of that for the *pytrz* portion (11% *vs.* 30%). This situation is changed in the protonated complex, where the contribution of the *ph* moiety to the HOMO is slightly greater than that of *pytrz* (29% *vs.* 25%). The metal centre contributes equally to the HOMOs of both complexes. The LUMO of the deprotonated complex is almost completely bipy-based (88%). On protonation, both bipy and *pytrz* make a 50 : 50 contribution to the LUMO.

Calculated density of states (DOS) spectra have been shown to be a useful method to visualise the spatial distribution of the electronic structure of complexes.[42] In particular, where there are several close-lying energy levels in the frontier region, DOS spectra give a better picture of the contributions of the various moieties to the HOMO and LUMO, compared to examination of individual energy levels.

DOS spectra calculated for $[Ru(bipy)_2(L1)]^+$ and its protonated form are shown in Fig. 12. For the deprotonated form, we can clearly see that though the *ph* moiety makes a large contribution to H-2, H-3 and H-4, it contributes little to HOMO and H-1, which are somewhat separate in energy from the others. The highest occupied molecular orbital levels of the protonated complex are closely spaced, resulting in a peak, which shows a large contribution from the Ru, and then similar contributions from the other three moieties though with *pytrz* contributing the least. On protonation, a significant difference in the LUMOs is apparent also. They change from bipy-based to having an equally large contribution from the bipy and *pytrz* moieties.

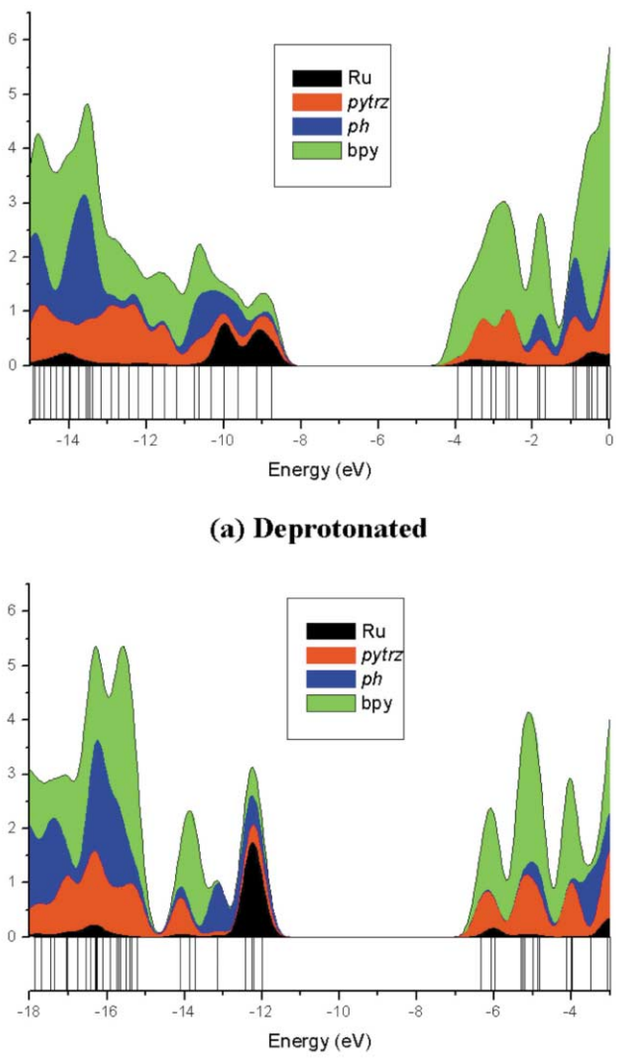

Fig. 12 Calculated density of states (DOS) diagram showing contributions from the metal centre, the ligands for (a) $[Ru(bipy)_2(L1)]^+$ in which the triazole ring is deprotonated and (b) $[Ru(bipy)_2(HL1)]^{2+}$, where the triazole ring is protonated. The contribution of both **HL1** and $\mathbf{L1^-}$, the protonated and the deprotonated pyridyltriazole ligands, is divided into a pyridinetriazole component, *pytrz* and a contribution from the dimethoxyphenyl moiety, *ph*. The contributions are shown stacked upon one another. The bars at the bottom of each graph represent the ZINDO/S calculated energy levels. See text for details.

According to Koopmans' theorem, electrochemical oxidation of the complex is equivalent to the removal of an electron from the HOMO. The observed differences in the electrochemical behaviour of $[Ru(bipy)_2(HL1)]^{2+}$ and $[Ru(bipy)_2(L1)]^+$ agree qualitatively with the calculated differences in their electronic structures. The calculations show the electronic structure of the highest occupied molecular orbitals to be that of a typical triazole, containing significant contributions from the metal centre, bipy and *pytrz* moieties. Experimentally a reversible peak at 0.8 V is found due to the oxidation of the metal centre. On protonation, it is found that the methoxy group is oxidised at a potential close to that of the expected oxidation potential of the metal. The DOS spectra support these results, showing that the *ph* moiety makes a significant contribution to the highest occupied molecular orbitals on protonation of the complex.

Concluding remarks

The results obtained show that deprotection of dimethoxy precursors is an effective route to the synthesis of ligands containing catechol type pending groups. The spectroscopic, electrochemical and acid–base properties of the compounds obtained are in agreement with those obtained for ruthenium compounds based in similar pyridyltriazole ligands. Electrochemical evidence seems to suggest that upon oxidation of the catechol group a partial protonation of the triazole moiety takes place. ZINDO calculations provide a good qualitative description of the electronic properties of the methoxy compounds and confirm the assignments made for the two oxidations observed at ~1.0 V. This highlights the usefulness of ZINDO type calculations in the investigation of ruthenium polypyridyl complexes. The emission lifetime data suggest that although the interaction between the hydroquinone group and the polypyridyl based excited state is weak, the change in lifetime observed for the phen analogue is significant. Based on the redox properties of the hydroquinone grouping is seems most likely that this quenching is caused by a photoinduced electron transfer process. At present further photophysical studies are taking place, investigating the properties of the catechol complexes. Preliminary results have shown that the catechol moiety can bind a range of first row transition metal ions and that binding can strongly affect the emitting properties of the ruthenium core. The compounds have therefore potential applications as metal ion sensors and can act as models for the investigation of photoinduced energy and electron transfer reactions. Results on these studies will be reported in a subsequent paper.

Acknowledgements

This research was partly funded by Enterprise Ireland and the European Communities Programmes, Training and Mobility of Researchers, under Contract 96CT-0076 and the Human Potential Programme under Contract HPRN-CT-2002-00185.

References

1 R. K. Clayton, *Photosynthesis; Physical methods and chemical patterns*, Cambridge University Press, 1st edn., 1980.
2 (*a*) D. Gust, T. A. Moore, P. A. Liddell, G. A. Nemeth, L. R. Makings, A. L. Moore, D. Barrett, P. J. Pessiki, R. V. Benasson, M. Rougee, C. Chachaty, F. C. De Schryver, M. van der Auweraer, A. R. Hotzwarth and J. S. Connolly, *J. Am. Chem. Soc*, 1987, **109**, 846; (*b*) R. Foster M. I. Foreman, in *The Chemistry of Quinone Compounds*, ed. Spatai, Wiley and Sons, Chichester, 1988, ch. 6.
3 M. Ebadi and A. B. P. Lever, *Inorg. Chem.*, 1999, **38**, 467.
4 V. Goulle, A. Harriman and J-M Lehn, *J. Chem. Soc., Chem. Commun.*, 1993, 1034.
5 (*a*) P. Passaniti, W. R. Browne, F. C. Lynch, D. Hughes, M. Nieuwenhuyzen, P. James, M. Maestri and J. G. Vos, *J. Chem. Soc., Dalton Trans.*, 2002, 1740; (*b*) F. M. Weldon and J. G. Vos, *Inorg. Chim. Acta*, 2000, **307**, 13.

6 R. Wang, T. E. Keyes, R. Hage, R. H. Schmehl and J. G. Vos, *J. Chem. Soc., Chem. Commun.*, 1993, 1652.
7 W. R. Browne, C. M. O'Connor, J. S. Killeen, A. L. Guckian, M. Burke, P. James, M. Burke and J. G. Vos, *Inorg. Chem.*, 2002, **41**, 4245.
8 B. P. Sullivan, D. J. Salmon and T. J. Meyer, *Inorg. Chem.*, 1978, **17**, 3334.
9 (*a*) E. H. Vickery, L. F. Pahler and E. J. Eisenbraun, *J. Org. Chem.*, 1979, **44**, 4444; (*b*) J. F. W. McOmie, M. L. Watts and D. E. West, *Tetrahedron*, 1968, **24**, 2289; (*c*) B. Whittle, N. S. Everest, C. Howard and M. D. Ward, *Inorg. Chem.*, 1995, **34**, 2025; (*d*) C. A. Howard and M. D. Ward, *Angew. Chem. Int. Ed. Engl.*, 1992, **31**, 1028.
10 (*a*) COLLECT, Data Collection Software; Nonius B. V., The Netherlands, 1998; (*b*) Z. Otwinowski and W. Minor, "Processing of X-Ray Diffraction Data Collected in Oscillation Mode", in Methods in Enzymology, vol. 276, Macromolecular Crystallography, part A, ed. C. W. Carter and R. M. Sweet, Academic Press 1997, p. 307.
11 G. M. Sheldrick, *Acta Crystallogr., Sect. A*, 1990, **46**, 467.
12 G. M. Sheldrick, SHELXL-97, Program for refinement of crystal structures, University of Göttingen, Germany, 1997.
13 HyperChem for Windows, Release 5.11 Standard Version, Hypercube, Inc., Gainesville, FL, USA, 1997.
14 W. P. Anderson, T. R. Cundari, R. S. Drago and M. C. Zerner, *Inorg. Chem.*, 1990, **29**, 1.
15 S. I. Gorelsky, E. S. Dodsworth, A. B. P. Lever and A. A. Vlcek, *Coord. Chem. Rev.*, 1998, **174**, 469.
16 K. Krogh-Jespersen, J. D. Westbrook, J. A. Potenza and H. J. Schugar, *J. Am. Chem. Soc.*, 1987, **109**, 7025.
17 A. B. P. Lever, University of York, Toronto, Canada, private communication.
18 J. E. Ridley and M. C. Zerner, *Theor. Chim. Acta.*, 1976, **42**, 223.
19 E. M. Ryan, R. Wang, J. G. Vos, R. Hage and J. G. Haasnoot, *Inorg. Chim. Acta*, 1993, **208**, 49.
20 B. E. Buchanan, R. Wang, J. G. Vos, R. Hage, J. G. Haasnoot and J. Reedijk, *Inorg. Chem.*, 1990, **29**, 3263.
21 B. E. Buchanan, J. G. Vos, M. Kaneko, W. J. M. van der Putten, J. M. Kelly, R. Hage, R. A. G. de Graaff, R. Prins, J. G. Haasnoot and J. Reedijk, *J. Chem. Soc., Dalton Trans.*, 1990, 2425.
22 R. Hage, J. G. Haasnoot, J. Reedijk, R. Wang, E. M. Ryan, J. G. Vos, A. L. Spek and A. J. M. Duisenberg, *Inorg. Chim. Acta*, 1990, **174**, 77.
23 R. Hage, J. G. Haasnoot, H. A. Nieuwenhuis, J. Reedijk, D. J. A. De Ridder and J. G. Vos., *J. Am. Chem. Soc.*, 1990, **112**, 9245.
24 D. P. Rillema, D. G. Taghdiri, D. S. Jones, L. A. Worl, T. J. Meyer, H. A. Levy and C. D. Keller, *Inorg. Chem.*, 1987, **26**, 578.
25 D. P. Rillema, D. S. Jones and H. A. Levy, *J. Chem. Soc., Chem. Commun.*, 1979, 849.
26 D. S. Eggleston, K. A. Goldsby, D. J. Hodgson and T. J. Meyer, *Inorg. Chem.*, 1985, **24**, 4573.
27 W. R. Browne, C. M. O'Connor, H. P. Hughes, R. Hage, O. Walter, M. Doering, J. F. Gallagher and J. G. Vos, *J. Chem. Soc., Dalton Trans.*, 2002, 1740–1746.
28 (*a*) A. Juris, V. Balzani, F. Barigelletti, S. Campagna, P. Belser and A. von Zelewsky, *Coord. Chem. Rev.*, 1988, **84**, 85; (*b*) J. V. Caspar and T. J. Meyer, *J. Am. Chem. Soc.*, 1983, **105**, 5583.
29 The level of deuteriation is determined by ^{1}H NMR spectroscopy. For the complexes, biexponential emission from different isotopomers is not observed since 95% deuteriation results in at most 1 in ~20 positions not being exchanged with deuterium. Hence every second molecule will have one proton not exchanged and 1 in 20 molecules having two protons not exchanged *etc*. It has been shown that the effect of one proton not being exchanged is normally relatively minor and hence a monoexponential lifetime is observed {ref. 31}.
30 (*a*) T. E. Keyes, F. Weldon, E. Müller, P. Pechy, M. Grätzel and J. G. Vos, *J. Chem. Soc., Dalton Trans.*, 1995, 2705; (*b*) T. E. Keyes, C. M. O'Connor, U. O'Dwyer, C. C. Coates, P. Callaghan, J. J. McGarvey and J. G. Vos, *J. Phys. Chem. A*, 1999, **103**, 8915; (*c*) W. R. Browne and J. G. Vos, *Coord. Chem. Rev.*, 2001, **219**, 761.
31 This value has been obtained using the equation; $k_{el} = 1/\tau_{complex} - 1/\tau_{model}$, where $/\tau_{complex}$ is the lifetime of $[Ru(phen)_2(L2)]^+$ and τ_{model} is the lifetime of $[Ru(phen)_2(L1)]^+$, R. J. Forster, T. E. Keyes and J. G. Vos, *Interfacial Supramolecular Assemblies*, Wiley, Chichester, 2003, p. 47.
32 J. G. Vos, *Polyhedron*, 1992, **11**, 2285.
33 J. F. Ireland and P. A. H. Wyatt, *Adv. Phys. Org. Chem.*, 1976, **12**, 131.
34 H. A. Nieuwenhuis, J. G. Haasnoot, R. Hage, J. Reedijk, T. L. Snoeck, D. J. Stufkens and J. G. Vos, *Inorg. Chem.*, 1991, **30**, 48.
35 (*a*) S. Fanni, C. Di Pietro, S. Serroni, S. Campagna and J. G. Vos, *Inorg. Chem. Commun.*, 2000, **3**, 42; (*b*) C. Di Pietro, S. Serroni, S. Campagna, T. Gandolfi, R. Ballardini, S. Fanni, W. R. Browne and J. G. Vos, *Inorg. Chem.*, 2002, **41**, 2871.
36 W. R. Browne, F. Weldon, A. L. Guckian and J. G. Vos, *Collect. Czech. Chem. Commun.*, 2003, **68**, 1467.
37 M. K. Nazeeruddin, S. M. Zakeeruddin and K. Kalyanasundaram, *J. Phys. Chem.*, 1993, **97**, 9607.
38 (*a*) M. A. Haga, *Inorg. Chim. Acta*, 1980, **45**, L183; (*b*) P. Rillema, R. Sahai, P. Matthews, A. K. Edwards, R. J. Shaver and L. Morgan, *Inorg. Chem.*, 1990, **29**, 167; (*c*) M. A. Haga, M. M. Ali, S. Koseki, K. Fujimoto, A. Yoshimura, K. Nozaki, T. Ohno, K. Nakajima and D. J. Stufkens, *Inorg. Chem.*, 1996, **35**, 3335; (*d*) T. Ohno, K. Nozaki and M. A. Haga, *Inorg. Chem.*, 1992, **31**, 4256.
39 R. Hage, R. Prins, J. G. Haasnoot, J. Reedijk and J. G. Vos, *J. Chem. Soc., Dalton Trans.*, 1987, 1389.
40 G. E. Cabaniss, A. A. Diamantis, W. Rorer Murphy, Jr. R. W. Linton and T. J. Meyer, *J. Am. Chem. Soc.*, 1985, **107**, 1845.
41 A. D. Shukla, B. Whittle, H. C. Bajaj, A. Das and M. D. Ward, *Inorg. Chim. Acta*, 1999, **285**, 89.
42 H. Rensmo, S. Lunell and H. Siegbahn, *J. Photochem. Photobiol. A*, 1998, **114**, 117.

FULL PAPER

Dalton
www.rsc.org/dalton

Assessment of intercomponent interaction in phenylene bridged dinuclear ruthenium(II) and osmium(II) polypyridyl complexes†

Adrian L. Guckian,[a] Manfred Doering,[b] Michael Ciesielski,[b] Olaf Walter,[b] Johan Hjelm,[a] Noel M. O'Boyle,[a] William Henry,[a] Wesley R. Browne,[a] John J. McGarvey[c] and Johannes G. Vos*[a]

[a] *National Centre for Sensor Research, School of Chemical Sciences, Dublin City University, Glasnevin, Dublin 9, Ireland. E-mail: han.vos@dcu.ie; Fax: 00353-1-7005503; Tel: 00353-1-7005307*

[b] *ITC-CPV, Forschungszentrum Karlsruhe, PO Box 3640, 76021, Karlsruhe, Germany*

[c] *School of Chemistry, Queen's University Belfast, Belfast, Northern Ireland, UK BT9 5AG*

Received 16th June 2004, Accepted 11th October 2004
First published as an Advance Article on the web 3rd November 2004

The synthesis and characterisation of $[Ru(bipy)_2(\mathbf{L1})]^{2+}$ and the homodinuclear complexes $[M(bipy)_2(\mathbf{L1})M(bipy)_2]^{4+}$ (where M = Ru or Os), employing the ditopic ligand, 1,4-phenylene-bis(1-pyridin-2-ylimidazo[1,5-*a*]pyridine) (**L1**), are reported. The complexes are identified by elemental analysis, UV/Vis, emission, resonance Raman, transient resonance Raman and ^{1}H NMR spectroscopy, mass spectrometry and electrochemistry. The X-ray structure of the complex $[Ru(bipy)_2(\mathbf{L1})(bipy)_2Ru](PF_6)_4$ is also reported. DFT calculations, carried out to model the electronic properties of the compounds, are in good agreement with experiment. Minimal communication between the metal centres is observed. The low level of ground state electronic interaction is rationalized in terms of the poor ability of the phenyl spacer in facilitating superexchange interactions. Using the electronic and electrochemical data a detailed picture of the electronic properties of the **RuRu** compound is presented.

Introduction

The design and synthesis of polynuclear transition metal complexes containing electro-active and photo-active units are topics of continuing interest due to their potential usage as building blocks for supramolecular assemblies and molecular devices.[1] Ruthenium(II) and osmium(II) polypyridine complexes are playing a key role in the development of compounds capable of performing photo- and/or redox-triggered useful functions in charge separation devices for photochemical solar energy conversion[2] and information storage.[1,3] In particular, species featuring photophysical properties and redox behaviour, which can undergo controlled modification with external stimuli, are of interest.[3,4] For example, reversible electrochemical switching of emission energy shows potential in applications such as electronic displays.[5] The role played by the bridging ligand in determining intercomponent interaction is well recognised.[6,7] Since the late 1970s, ground and excited state intercomponent interactions in dinuclear Ru(II) complexes containing polytopic bridging ligands employing imidazoles,[8] triazoles,[9] pyrazine,[10] 4,4′-bipyridyl,[11] 2,2′-bipyrimidine,[12] tetrazine,[13] have received considerable attention. The incorporation of spacer units (*i.e.*, phenylene,[14] dimethoxyphenyl,[9b] thienyl,[9c] *etc.*) has allowed for further control over the degree of interaction between metal centres in multinuclear complexes.

In this contribution the structural, photophysical and electrochemical characterisation of two symmetrical, phenylene bridged complexes of the form $[M(bipy)_2(\mathbf{L1})M(bipy)_2](PF_6)_4$ (where M = Ru(II) or Os(II) and **L1** = 1,4-phenylene-bis(1-pyridin-2-ylimidazo[1,5-*a*]pyridine)) are reported (see Fig. 1). Selective deuteriation is employed to facilitate interpretation of ^{1}H NMR, luminescence and resonance Raman spectra. DFT calculations are described for **RuRu**. A detailed description of the electronic properties of this compound is presented based on these calculations and the results obtained are compared with experimental data. Furthermore, the results obtained are discussed in the context of earlier studies on related complexes.

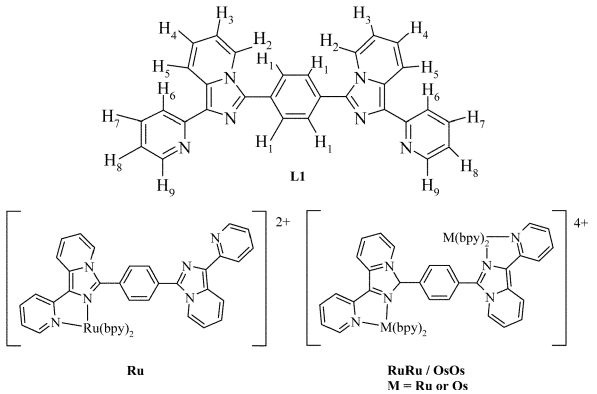

Fig. 1 Structure of the mononuclear and dinuclear complexes and **L1**.

Experimental

All reagents were of HPLC grade or better and used as received. Spectroscopic grade (UVASOL) solvents were employed for all spectroscopic measurements. d_8-2,2′-bipyridyl (d_8-bipy) (Complex Solutions, Dublin, Ireland) was used as received, *cis*-$[Ru(bipy)_2Cl_2]\cdot 2H_2O$, its deuteriated analogue *cis*-$[Ru(d_8\text{-}bipy)_2Cl_2]\cdot 2H_2O$ [15] and *cis*-$[Os(bipy)_2Cl_2]\cdot 2H_2O$[16] were prepared by previously reported procedures.

Syntheses

$[Ru(bipy)_2(L1)](PF_6)_2\cdot 2H_2O$ (Ru). **L1** (102 mg, 0.219 mmol) was heated at reflux in 300 cm^3 of a 1 : 1 EtOH/H_2O mixture. *cis*-$[Ru(bipy)_2Cl_2]\cdot 2H_2O$ (114 mg, 0.219 mmol) in 20 cm^3 EtOH

† Electronic supplementary information (ESI) available: Fig. S1: ^{1}H NMR spectra of **Ru** and **RuRu**. Fig. S2: Resonance Raman spectra of ***d*Ru*d*Ru**, **RuRu** and **OsOs**. Fig. S3: Reductive and oxidative electrochemistry of **Ru**. Fig. S4: Frontier orbitals of **RuRu**. Table S1: ^{1}H NMR spectra of L^1 and L^1 in ***d*Ru*d*Ru**. Table S2: Selected bond distances. Table S3: Selected bond angles. Table S4: Calculated data for the frontier orbitals of **RuRu**. See http://www.rsc.org/suppdata/dt/b4/b409189b/

DOI: 10.1039/b409189b

was added over 90 min. After 3 h the reaction was allowed to cool and the volume reduced *in vacuo*. The solution was filtered to remove unreacted ligand. 10 cm^3 of a saturated aqueous solution of ammonium hexafluorophosphate was added to the filtrate yielding an orange–brown precipitate, which was isolated by filtration, washed with 25 cm^3 of water, 25 cm^3 of diethyl ether and air-dried. The compound was purified by column chromatography (silica gel, 0.05 M KNO_3 acetonitrile–water (80/20 v/v)). The first orange band eluted, yielded the desired product. The acetonitrile was removed *in vacuo* and an excess of NH_4PF_6 added to precipitate the product. The precipitate was filtered, washed with 25 cm^3 cold water and 25 cm^3 diethyl ether. Yield 95 mg (37%). Mass spectrometry: *m/z* calculated for [**Ru**]$(PF_6)^{1+}$: 1023.2. Found: 1023.3. ^{1}H NMR spectrum (400 MHz, d_6-DMSO) δ 6.95 (dd, 1H), 7.24 (m, 4H), 7.44 (m, 2H), 7.60 (m, 7H), 7.78 (d, 1H), 7.82 (d, 1H), 7.88 (m, 2H), 7.97 (d, 1H), 8.14 (m, 7H), 8.29 (d, 1H), 8.53 (m, 5H), 8.66 (d, 1H), 8.74 (m, 3H). Elemental analysis for $C_{50}H_{40}N_{10}Ru_1O_2P_2F_{12}$: Calc. C 50.04, H 3.17, N 11.68. Found C 49.45, H 3.01, N 11.19%.

[Ru(bipy)$_2$(L1)Ru(bipy)$_2$](PF$_6$)$_4$·4H$_2$O (RuRu). **L1** (200 mg, 0.43 mmol) and *cis*-[Ru(bipy)$_2$Cl$_2$]·2H$_2$O (492 mg, 0.946 mmol) were heated at reflux in 30 cm^3 (1 : 1) EtOH–H_2O for 16 h. The solution was cooled to r.t., reduced *in vacuo* and filtered to remove unreacted ligand. 5 cm^3 of a saturated aqueous solution of ammonium hexafluorophosphate was added to the filtrate to yield an orange–brown precipitate, which was filtered off, washed with 25 cm^3 water and 25 cm^3 diethyl ether. The compound was purified by column chromatography (as for **Ru**). The second orange band to elute yielded the desired product. Yield 650 mg (81%). Mass spectrometry: *m/z* calculated for [**RuRu**]$(PF_6)_3^+$: 1727.15. Found: 1727.3. ^{1}H NMR spectrum (400 MHz, d_6-DMSO) δ 6.75 (dd, 1H), 6.94 (dd, 1H), 7.24 (m, 8H), 7.43 (m, 7H), 7.60 (m, 10H), 7.80 (d, 1H), 7.90 (d, 1H), 8.16 (m, 12H), 8.40 (d, 1H), 8.63 (m, 6H), 8.75 (m, 4H). Elemental analysis for $C_{70}H_{60}N_{14}Ru_2O_4P_4F_{24}$: Calc.: C 43.43, H 2.90, N 10.13. Found: C 43.11, H 3.08, N 10.01%.

[Ru(d_8-bipy)$_2$(L1)Ru(d_8-bipy)$_2$](PF$_6$)$_4$·4H$_2$O (*d*Ru*d*Ru). As for **RuRu** except **L1** (50 mg, 0.107 mmol) and *cis*-[Ru(d_8-bipy)$_2$Cl$_2$]·2H$_2$O (127 mg, 0.237 mmol) were heated at reflux in 20 cm^3 of 1 : 1 EtOH–H_2O. Yield 112 mg (55%). Mass spectrometry: *m/z* calculated for [***d*Ru*d*Ru**]$(PF_6)_3^+$: 1759.2. Found: 1758.3 [M^+]. ^{1}H NMR spectrum (400 MHz, d_6-DMSO) δ 7.27 (m, 3H), 7.41 (d, 2H), 7.60 (m, 2H), 8.05 (dd, 1H), 8.63 (m, 2H). Elemental analysis for $C_{70}H_{28}N_{14}D_{32}Ru_2O_4P_4F_{24}$: Calc.: C 42.73, H 2.85, N 9.97. Found C 43.21, H 2.98, N 9.51%.

[Os(bipy)$_2$(L1)Os(bipy)$_2$](PF$_6$)$_4$·4H$_2$O (OsOs). As for **RuRu** except **L1** (200 mg, 0.43 mmol) and *cis*-[Os(bipy)$_2$Cl$_2$]·2H$_2$O (523 mg, 0.946 mmol) were heated at reflux in 20 cm^3 of 1 : 1 ethylene glycol–H_2O for 72 h. Yield 549 mg (62%). Mass spectrometry: *m/z* calculated for [**OsOs**]$(PF_6)_3^+$: 1907.3. Found: 1908.1 [M^+]. ^{1}H NMR spectrum (400 MHz, d_6-acetone) δ 6.81 (dd, 2H), 7.06 (dd, 1H), 7.25 (m, 7H), 7.53 (m, 13H), 7.74 (d, 1H), 7.94 (m, 14H), 8.26 (d, 1H), 8.40 (d, 1H), 8.46 (m, 2H), 8.65 (m, 10H). Elemental analysis for $C_{70}H_{60}N_{14}Os_2O_4P_4F_{24}$: Calc.: C 39.77, H 2.65, N 9.28. Found C 39.44, H 2.39, N 9.41%.

X-Ray crystallography

Data for **RuRu** were collected on a Siemens SMART 1000 CCD-diffractometer fitted with a molybdenum tube (Mo-Kα, λ = 0.71073 Å) and a graphite monochromator. A full sphere of data was collected with the irradiation time of 4 s per frame. The structures were solved with direct methods and all non hydrogen atoms refined anisotropically with the SHELX-97 program[17] (refinement by least-squares against F^2). *Crystal data*: **RuRu**: [Ru(bipy)$_2$(**L1**)Ru(bipy)$_2$](PF$_6$)$_4$, $C_{75.1}H_{52}F_{24}N_{14}P_4O_{1.7}$ Ru_2; M_r = 1959.73; monoclinic, $P2_1/c$, a = 15.0193(15), b = 24.332(3), c = 21.810(2) Å, β = 96.956(2), V = 7911.9 Å^3; D_c = 1.645 Mg m^{-3}, data collection range: h −20 to 19, k = −30 to 32, l = −26 to 28; reflections collected: 85840, reflections unique: 19449, reflections observed ($I > 2\sigma I$): 8985, final R-values: $R1 = 0.054$ ($I > 2\sigma I$), $wR2 = 0.156$ (all data).

CCDC reference number 230287.

See http://www.rsc.org/suppdata/dt/b4/b409189b/ for crystallographic data in CIF or other electronic format.

Physical methods

^{1}H NMR spectra were recorded on a Bruker Avance 400 (400 MHz) instrument. The chemical shifts are relative to residual solvent peaks. UV/Visible spectra were recorded using a Shimadzu UV3100 UV-Vis-NIR spectrophotometer interfaced with an Elonex PC433 personal computer (Molar absorptivities (ε) ±5%). Emission spectra were recorded on a Perkin-Elmer LS50-B spectrofluorimeter equipped with a red-sensitive Hamamatsu R928 detector, interfaced to an Elonex PC466 personal computer employing Perkin Elmer FL Winlab custom built software. Excitation and emission slit widths were 10 nm. The spectra are not corrected for photo multiplier response. Luminescence lifetime measurements were obtained using an Edinburgh Analytical Instruments Time Correlated Single Photon Counting apparatus.[9d] Excitation employed the 337 nm N_2 emission line of the nanosecond flashlamp. Cyclic voltammetry (100 mV s^{-1}) and DPV (step height: 50 mV, increment: 4 mV, pulse duration: 60 ms, sampling interval: 20 ms, frequency: 5 Hz were carried out in acetonitrile with 0.1 M $TBABF_4$. A conventional three-electrode cell was used. A 2 mm Pt disk electrode sealed in Kel-F (purchased from CH Instruments) was used as the working electrode, the counter (auxiliary) electrode was a coiled Pt-wire, and a Ag/Ag$^+$ (10 mM $AgNO_3$, 0.1 M $TBABF_4$ in acetonitrile) half-cell was used as reference electrode. The solutions were deoxygenated with argon and a blanket of argon was maintained over the solutions during the experiments. Glassware used was dried in a vacuum oven at 80 °C overnight or flamed using a Bunsen burner prior to preparing solutions. The $TBABF_4$ salt was dried in the vacuum oven overnight at 80 °C. The electrodes were polished on a soft polishing pad (Struers, OP-NAP) with an aqueous slurry of 0.3 micron alumina (Buehler) and sonicated for at least 5 min in MQ-water to remove any remaining polishing material from the surface of the electrode. The working electrodes were rinsed thoroughly with acetone and dried in air before insertion into the cell. The reference electrode was calibrated externally by carrying out cyclic voltammetry (also at 100 mV s^{-1}) in solutions of ferrocene of similar concentration as that of the complexes (0.4–2 mM) in the same electrolyte at the end of each day of experiments. Bulk electrolysis was carried out in a three-compartment, three-electrode cell. The reference electrode was Ag/Ag$^+$, the working electrode was a cylinder of Pt gauze, 1 cm × 1 cm (52 mesh) and the counter electrode used was a coiled Pt wire. Spectroelectrochemistry[18] was carried out in 0.1 M TEAP acetonitrile (anhydrous, Aldrich). The potential was controlled using a EG&G PARC Model 362 scanning potentiostat. A platinum/rhodium gauze working electrode, Ag/Ag$^+$ reference electrode (calibrated against the Fc/Fc$^+$ standard prior to each experiment) and platinum wire counter electrode was employed. All references are quoted relative to Fc/Fc$^+$ using the relevant conversion factor.[19,20] Absorption spectra of the species generated in the optically transparent thin layer electrode (OTTLE) cell were recorded on a Shimadzu 3100 UV-Vis/NIR spectrophotometer (*vide supra*). Elemental analysis was carried out by the Microanalytical Laboratories at University College Dublin.

Ground-state resonance Raman spectra of the complexes were recorded at 457.9, 488 and 514 nm using an argon ion laser (Spectra Physics model 2050) as the excitation source.[21] The laser power at the sample was typically 30–40 mW. The Raman backscatter was focused onto the entrance slit of a single stage spectrograph (JY Horiba HR640), which was coupled to a CCD

detector (Andor Technology DV420-OE). The spectra were run in quartz cuvettes and were not corrected for detector response. Transient resonance Raman spectra were recorded using the single-colour pump and probe method in which the leading edge of the pulse excites the molecules and the trailing edge probes the resultant Raman scattering.[22] The excitation source was a pulsed laser (Spectra Physics Q-switched Nd:YAG, GCR-3) at 354.7 nm with a typical pulse energy of approx. 3 mJ at the sample. The Raman backscatter was focused onto the entrance slit of a double-stage spectrograph (Spex 1870), which was coupled to an ICCD (Andor Technology DH501). Typically, spectra were collected as a summation of 6000 accumulations.

Density functional theory (DFT) calculations were carried out using Gaussian03.[23] Becke's 3-parameter hybrid functional[24] was used with the correlation functional of Lee, Yang and Parr[25] (B3LYP). The effective core potential basis set LanL2DZ[26] was used for all atoms. Although the crystallographic structure of the dimer was of C_1 symmetry, due to the size of the system it was necessary to reduce the computational cost by imposing C_2 symmetry during the geometry optimisation. The homochiral $\Delta\Delta$ isomer was studied. The resulting electronic structure is not expected to differ significantly for the other stereoisomers. GaussSum[27] was used to calculate the contributions from groups of atoms to each molecular orbital and to convolute the molecular orbital data to create a partial density of states (PDOS) spectrum. The contributions were calculated within the framework of a Mulliken population analysis. The PDOS was convoluted with Gaussian curves of FWHM of 0.3 eV and unit height.

Results and discussion

The very low solubility of **L1** in comparison with the mononuclear complex (**Ru**) results in the rapid formation of the binuclear complex once the mononuclear complex forms. To overcome this, **Ru** was prepared by slow addition of *cis*-[Ru(bipy)$_2$Cl$_2$] to a large volume of solvent saturated with **L1**, heated at reflux. **RuRu** and **OsOs** were prepared by direct reaction of two equivalents of *cis*-[M(bipy)$_2$Cl$_2$] (where M = Ru(II) or Os(II)) with one equivalent of **L1** in ethanol–water and ethylene glycol–water, respectively.

X-Ray crystallography

The molecular structure of **RuRu** is shown in Fig. 2. Selected bond angles and lengths are listed in Tables S1 and S2 (ESI†). **RuRu** co-crystallized with 1.7 molecules of acetone per unit cell and four hexafluorophosphate counter anions, (three of which are disordered). From the crystal structure it is clear that **L1** is coordinated to Ru1 *via* the N1 and N3 atoms and the Ru2 atom *via* the N4 and N6 atoms. The bite angle of the N(1)–Ru(1)–N(3) is 78.65(16)° and N(4)–Ru(2)–N(6) is 78.63(16)° which corresponds well with the bite angle of 77.9(1)° obtained by Hage *et al.* for [Ru(bipy)$_2$(3-(2-hydroxyphenyl)-5-(pyridin-2-yl)-1,2,4-triazole)]PF$_6$·CH$_3$COCH$_3$.[28] Bite angles of between 79.35(16) and 78.86(17)° for bipyridine ligands and Ru–N distances of 2.045(4)–2.068(4) Å are also comparable to those found in other complexes.[9,14,28] One factor contributing to the increased length of the Ru(1)–N(1) and Ru(2)–N(4) bond lengths (2.080(4) and 2.086(4) Å, respectively) is the limited π-backbonding to the electron rich bridging ligand from the metal centre. The N1–Ru1–N8, N3–Ru1–N10 and N7–Ru1–N9 angles are 174.81(15), 175.85(16) and 176.44(16)°, respectively, while the *trans* angular bond angles around the Ru2 atom are 169.22(16), 175.74(16) and 172.83(17)° for N4–Ru2–N12, N6–Ru2–N14 and N11–Ru2–N13, respectively. This deviation from octahedral geometry is due to the acute bite angles of both the 2,2′-bipyridyl and the **L1** ligand. The internuclear (Ru···Ru) separation is 9.06 Å and the orientation of the phenyl ring of **L1** is distorted from planarity (by 61.1°) with respect to the imidazole rings.

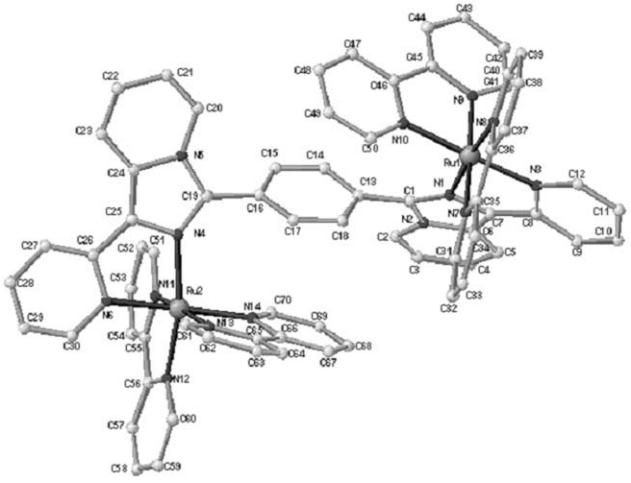

Fig. 2 X-Ray crystal structure of **RuRu** showing the atomic numbering used. The PF_6^- ions, acetone molecules and hydrogen atoms have been omitted for clarity.

^{1}H NMR Spectroscopy

The ^{1}H NMR spectroscopic data of all the complexes are given in the Experimental section (see Table S3 and Fig. S1. ESI†). As expected the protons of the **L1** ligand are shifted downfield upon coordination. The symmetry of **L1** is retained upon addition of the two equivalent metal centres, which greatly simplifies the spectra of the homonuclear (**RuRu** and **OsOs**) complexes.[29] Deuteration of the bipy ligands allowed for the identification of the **L1** protons in the ***d*Ru*d*Ru** complex.[30]

Electronic and photophysical properties

The absorption spectra of **Ru** and **RuRu** are similar, differing only in that the molar absorptivity of the dinuclear compound is almost twice that of the mononuclear complex (Table 1). The electronic data of **L1** are shown in Fig. 3(c). The ligand shows a number of features in the visible part of the spectrum, with absorption maxima at 277, 330 and 372 nm. At room temperature an emission is observed at 455 nm. The UV/Vis absorption spectra of the complexes (Fig. 3) are reminiscent with those observed for related Ru(II) and Os(II) imidazole and benzimidazole based complexes reported by Haga and co-workers.[8] The visible region of the spectra is dominated by dπ→π* MLCT transitions, while π→π* (bipy) and π→π* (**L1**) transitions are located at *ca.* 290 and 350 nm, respectively (*vide infra*). The metal-to-ligand-charge-transfer (^{1}MLCT) bands for the Ru(II) complexes are close in energy to the transition observed for [Ru(bipy)$_3$]$^{2+}$ and are assigned as dπ→π$_{bipy}$* ^{1}MLCT, based on electrochemical and resonance Raman data (*vide infra*). In the mixed-metal complex, **OsOs**, absorption bands between 580 and 700 nm are assigned to formally spin forbidden dπ→π* (bipy) (^{3}MLCT) transitions. Comparison of the spectroscopic properties of the binuclear complexes with the parent [M(bipy)$_3$]$^{2+}$ (where M = Ru or Os) indicates that transitions involving the bridging ligand **L1** are responsible for the absorption features at around 350 nm. The nature of this band is further discussed in the resonance Raman section.

All compounds are luminescent in acetonitrile at room temperature and in butyronitrile glass at 77 K. As for the absorption spectra only a modest (~15 nm) red shift in the emission spectrum with respect to [M(bipy)$_3$]$^{2+}$ (M = Ru or Os) is observed (Table 1) and, typical of ^{3}MLCT emission, the emission undergoes a blue shift on cooling to 77 K.[31] The luminescence lifetimes of **Ru** (690 ns) and **RuRu** (506 ns) in deaerated acetonitrile are comparable to the luminescence lifetimes of related complexes (*e.g.*, benzimidazoles, triazoles *etc.*).[8,32] Deuteriation of the bipyridyl ligands leads to an increase

Table 1 Photophysical and electrochemical data in CH_3CN

	Abs, λ_{max}/nm ($10^{-4}\varepsilon$/M^{-1} cm^{-1})[a]	Lum. λ_{max}/nm 298 K (τ/ns)[b]	Lum. λ_{max}/nm 77 K (τ/μs)[b]	Oxid.[c]/V	Red.[c]/V
Ru	290 (7.73), 365 (3.67), 454 (1.135)	628 (690)	598	0.79, 1.42 *irr*[d]	−1.78, −2.01
RuRu	290 (12.97), 357 (4.62), 457 (1.95)	625 (506)	602	0.79, 1.41 *irr*[d]	−1.76, −2.03
***d*Ru*d*Ru**		625 (940)	602		
OsOs	293 (13.5), 359 (4.73), 484 (1.79), 624 (0.72)	753 (39)	738	0.36, 1.41 *irr*[d]	−1.77, −1.99
$[Ru(bipy)_3]^{2+}$ [e]	452	620 (1000)	590 (5100)	0.88	−1.82, −2.01, −2.26
$[Os(bipy)_3]^{2+}$ [f]	640	723 (62)	940	0.45	−1.65

[a] In CH_3CN. [b] In butyronitrile. [c] *vs.* Fc/Fc^+. [d] Ligand oxidations are sensitive to conditions. [e] Ref. 36. [f] Ref. 37.

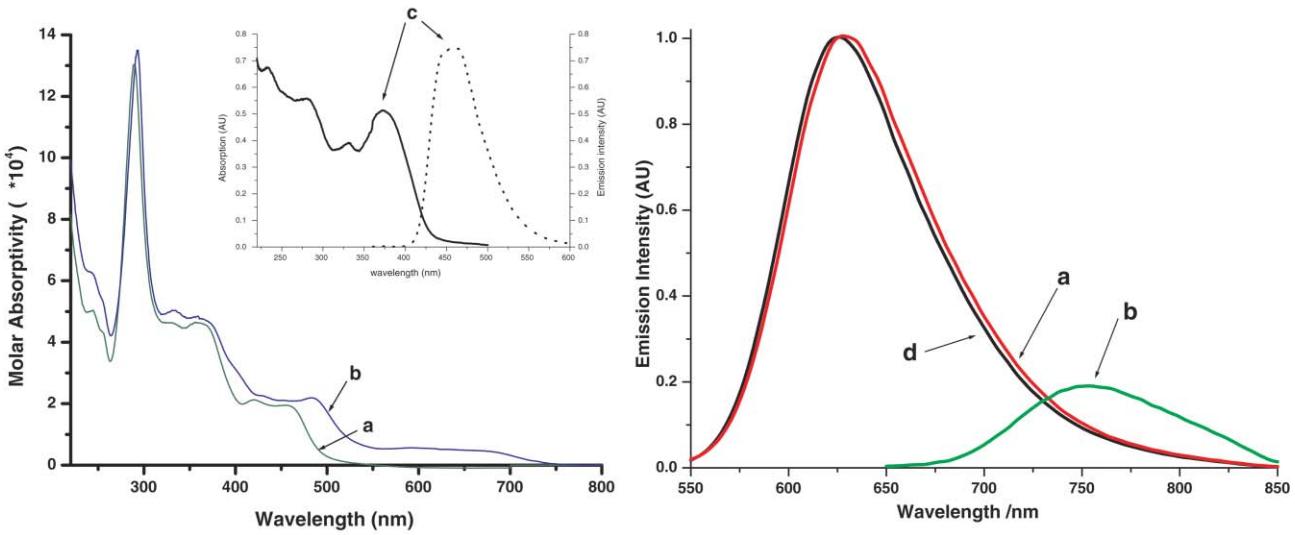

Fig. 3 Absorption (left) and emission (right) spectra in acetonitrile: (a) **RuRu**, (b) **OsOs** and (d) **Ru** [inset: absorption and emission spectra of (c) **L1**].

in the emission lifetime of the **RuRu** complex from 506 to 940 ns (185%), suggesting that the lowest emissive excited state is ^{3}MLCT(bipy) in nature and not ^{3}MLCT (L1).[33]

Resonance Raman and transient Resonance Raman spectroscopy

Resonance Raman (rR) spectroscopy enables the assignment of the optical transitions in the visible region of the absorption spectrum. Using excitation wavelengths coincident with absorption bands results in resonant enhancement of vibrational modes of the chromophore by several orders of magnitude. This allows for assignment of optical transitions. The ground and excited state rR spectra of the **L1** based complexes are complicated by the overlap of resonant chromophores in the visible region, *e.g.* the M(dπ) or **L1**(π) → **L1**(π*) and M(dπ) → bipy(π*) MLCT transitions. In the case of the Os(II) based complexes the spectra are further complicated by the presence of formally spin forbidden ^{3}MLCT transitions. Resonance Raman spectra recorded at 457.9 and 488 nm excitation for all complexes reveal only vibrational modes associated with M(dπ)→bipy(π*) ^{1}MLCT absorption bands, this conclusion is confirmed by isotopic shift observed for ***d*Ru*d*Ru**, as shown in Fig. S2, ESI.† It would be anticipated therefore that emission is ^{3}MLCT(bipy) based, an assignment supported by the observation that, upon deuteriation of the bipy ligands, the emission lifetime observed almost doubles.

Excited state (or transient) resonance Raman spectroscopy (TR^2) proves to be an invaluable tool in confirming the nature of the emissive ^{3}MLCT state. The observation of features characteristic of bipy$^-$* anion radical (*i.e.* bands at 1212 and 1285 cm^{-1}) in the TR^2 spectrum at 354.67 nm excitation, indicate a bipy-based ^{3}MLCT excited state is present.[34] However, as shown in Fig. 4 the presence of a strong **L1** based transition at 350 nm complicates the transient rR spectrum obtained at 354.5 nm excitation, with **L1** ligand modes being observed. The presence of vibrational features due to **L1** raises the possibility that the bands at 1212 and 1285 cm^{-1} are **L1** bands. It is in assigning vibrational modes that deuteriation becomes invaluable. Upon deuteriation the principle marker bands for bipy$^-$* (1212 and 1285 cm^{-1}) disappear and a feature at 1186 cm^{-1} tentatively assigned to d_8-bipy$^-$* is observed (the 1334 cm^{-1} band of d_8-bpy$^-$* is masked by **L1** vibrations), confirming that these bands are bipy based. Since the **L1** based 350 nm absorption is independent of the nature of the metal, it has been assigned as an interligand π−π* transition.

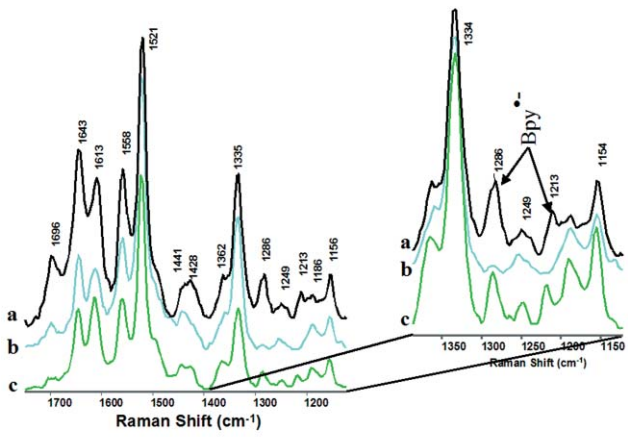

Fig. 4 TR^2 spectra at 354.67 nm of (a) **RuRu**, (b) ***d*Ru*d*Ru** and (c) **OsOs** in H_2O–acetone (95/5 v/v) (spectra normalized to the 1521 cm^{-1} band).

These results demonstrate that excitation of the complexes results in vibrational features which can be assigned to excited state bipy, and hence support the assignment of the lowest emitting ^{3}MLCT state as being bipy based.

Electrochemical properties

The oxidation and reduction potentials of **Ru**, **RuRu** and **OsOs** are presented in Table 1, differential pulse and cyclic voltammograms for the dinuclear complexes are shown in Fig. 5 (for **Ru** see Fig. S3, ESI†). The assignment of the oxidation processes observed is not straightforward due to the presence of the **L1** ligand, which undergoes irreversible oxidation. Assignment of the metal based redox processes is, however, possible by comparison with $[Ru(bipy)_3]^{2+}$ and $[Os(bipy)_3]^{2+}$. The fact that **L1** is oxidised at relatively low anodic potentials suggests that it is electron rich and is supported by the DFT calculations (*vide infra*). The **OsOs** complex displays a single oxidation wave at 0.36 V *vs.* Fc/Fc^+ which is 90 mV lower than that observed for $[Os(bipy)_3]^{2+}$. The stabilisation of the Os(III) oxidation state in this compound with respect to $[Os(bipy)_3]^{2+}$ is indicative of the presence of a stronger electron donating ligand (relative to bipy) in the inner coordination sphere of the Os ion. Similarly, for **Ru** and **RuRu** the metal redox potentials are 90 mV more cathodic than $[Ru(bipy)_3]^{2+}$. The two equivalent Os centres undergo simultaneous one electron oxidations which indicates that any metal–metal interactions are relatively weak. This is further supported by the absence of mixed valence charge transfer transitions (*vide infra*). Attempts to resolve the metal centred redox wave of the **OsOs** compound using differential pulse voltammetry were unsuccessful (Fig. 5). The value of $n = 1.92$ determined by bulk electrolysis carried out on the **OsOs** compound confirms the bielectronic nature of the first oxidation wave. **RuRu** behaves similarly with a single metal oxidation wave being observed at 0.79 V and an irreversible feature at 1.42 V. The absence of separation between the first and second metal oxidation steps in the dinuclear complexes, is in agreement with other systems of similar internuclear separation and is due to the minimal electrostatic interactions observed over these distances.[9c,35]

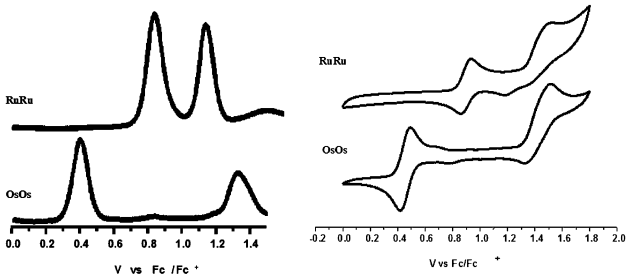

Fig. 5 DPV (left) and cyclic voltammograms (right) of **OsOs** and **RuRu** *vs.* Fc/Fc^+ with 0.1 M $TBABF_4$ in CH_3CN.

Based on the difference in formal potential of $[Ru(bipy)_3]^{2+}$ and $[Os(bipy)_3]^{2+}$, a potential difference of *ca.* 430 mV is expected between analogous Ru and Os metal centres. This compares well with the observed potential difference for the compounds reported of 430 mV.[36,37] The irreversible processes observed at more anodic potentials are attributed to oxidation of the bridging **L1** ligand. These redox processes are ill defined and their potential is very dependent on the conditions employed, with variation in the anodic potentials of up to 200 mV being observed. The reasons for this are at present not fully understood. The reduction potentials are as expected and are in agreement with a bipy based LUMO.

Spectroelectrochemistry

Electrochemical studies discussed above indicate that for **RuRu** and **OsOs** communication between the metal centres in the ground state is, at best, weak (comproportionation constant, $K_c \sim 4$).[38] To gain a better understanding of the true strength of the delocalisation of the SOMO in the mixed valence complex ($M^{II}M^{III}$) and hence internuclear communication, the spectroscopic properties of mixed valence dinuclear complexes were investigated. For the homonuclear complexes the single bielectronic metal oxidation process makes generation of the mixed valence species more difficult. Nevertheless spectroelectrochemistry has proven useful in determining the degree of intercomponent interaction in related dinuclear systems exhibiting single bielectronic metal redox processes.[35] A typical example of such spectroelectrochemical studies is shown in Fig. 6 for the compound **RuRu**. For the dinuclear complexes reversible spectral changes were observed at potentials below 1 V, however, bulk electrolysis at higher potentials results in irreversible spectral changes, which were not investigated further. Oxidation at 0.7 V *vs.* Fc/Fc^+ results in a gradual disappearance of the MLCT bands and a decrease in the intensity and red-shift in the $\pi \rightarrow \pi^*$ transition around 280 nm. Bleaching of the MLCT band continues at potentials higher than 0.7 V *vs.* Fc/Fc^+. At these potentials a concurrent increase in the intensity of band in the region 500 to 800 nm, which can is expected to be ligand-to-metal-charge-transfer (LMCT) in nature. Importantly, neither complex show any evidence for the presence of an intervalence band in the mixed valence state, indicating little or no communication between the two metal centres in the ground state.

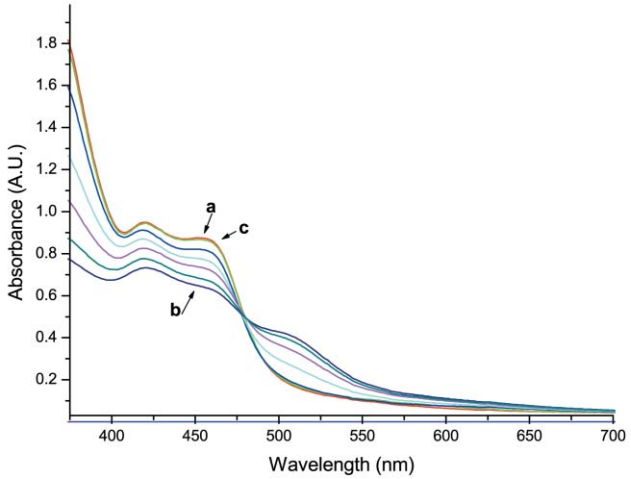

Fig. 6 Spectroelectrochemistry of the mixed metal complex **RuRu** in MeCN with 0.1 M TEAP at intervals from (a) 0 V to (b) 0.9 V and (c) after re-reduction at 0 V (*vs.* Fc/Fc^+)

DFT Calculations

The geometry optimisation of the dimer gave results in good agreement with the crystal structure. B3LYP has a tendency to overestimate the Ru–N bond length[39] (typically by 0.05 Å for the $Ru–N_{bipy}$ bonds). From crystallographic data (*vide supra*) it is seen that for **RuRu** the $Ru–N_{py}$ bond is longer than the $Ru–N_{imid}$ bond (see Table S2. ESI†) but in the calculated structure the reverse is found (with the $Ru–N_{imid}$ bond overestimated by 0.07 Å). The distortion from planarity of the phenyl ring with respect to the imidazole rings is reproduced by the calculations, although the dihedral angle is also overestimated by 7°. The calculated energies of the frontier orbitals are shown in Table S4 (ESI†). Each molecular orbital has been broken down in terms of a percentage contribution from the metal centres, *Ru*, the bipyridine ligands, *bipy*, the central phenyl ring of the **L1** ligand, *L1-ph*, and a moiety comprising the pyridine and fused rings of the **L1** ligand, *L1-py*. These data have been plotted in the form of a PDOS spectra in Fig. 7.[40]

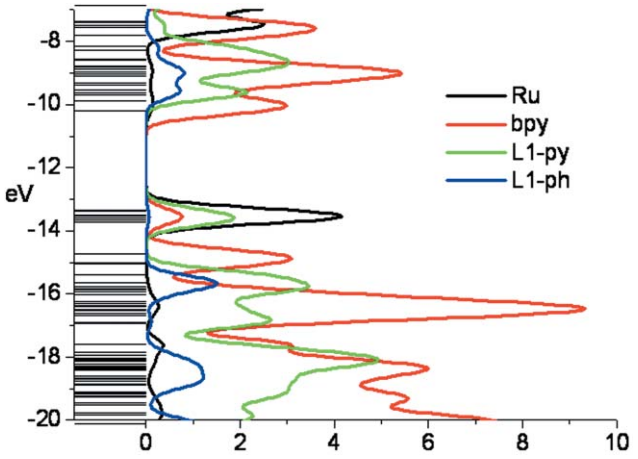

Fig. 7 Partial density of states (PDOS) spectrum of **RuRu** showing the percentage contributions of *Ru*, *bipy*, *L1-py* and *L1-ph* (see text) to the molecular orbitals.

The highest occupied metal orbitals are largely metal-based, but also contain a significant contribution from *L1-py* (See Fig. 8 and Table S4, ESI†). This agrees with the electrochemical results, which show that the first oxidation is metal-based but that oxidation of the ligand **L1** is also expected. The lowest unoccupied metal orbitals are bipyridine-based (see Fig. 8).

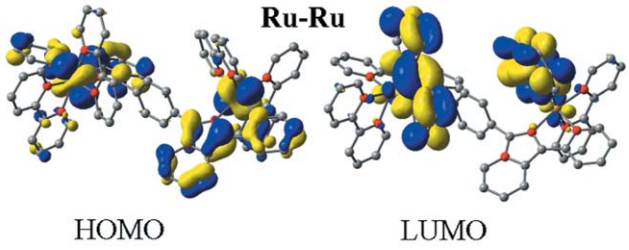

Fig. 8 Calculated HOMO and LUMO orbitals for **RuRu**.

Based on these ground state results, it is expected that the first reduction is bipy-based. It is worth noting also that the two moieties of **L1** are at best only weakly electronically coupled: for example, *L1-ph* does not contribute to the HOMO, in contrast to *L1-py*. This suggests that delocalisation of molecular orbitals across **L1** is unlikely to be significant.

A comparison of the molecular orbital data in Table S4 (and Fig. S4), ESI,† and the energy level diagram of Fig. 9, which is based on the experimental results, shows some interesting parallels. The bipy $\pi \rightarrow \pi^*$ is reproduced using the ground state data (H-8 → LUMO; 36000 cm^{-1}) although the energy of the L1 $\pi \rightarrow \pi^*$ transition is overestimated (H-7 → L+4; 32 000 cm^{-1}). The oxidation difference between Ru and **L1** can be estimated using the HOMO to H-7 distance as 2400 cm^{-1}, in good agreement with experiment. The HOMO → LUMO distance (26000 cm^{-1}), on the other hand, does not agree with the experimental value. Accurate calculation of these values, including the inclusion of solvent was outside the scope of this experiment, but the estimates nevertheless give a satisfactory representation of the experimentally obtained parameters. The discrepancies observed are most likely due to the limitations of using ground state molecular orbital data to represent excited state systems, and to the fact that mixing of orbitals of the same symmetry has been neglected.

Conclusion

In the present study, intercomponent communication in dinuclear complexes is explored. Despite the relatively moderate internuclear separation, no detectable interaction between the metal centres is observed. It seems likely that the lack of communication can be rationalised by considering the inability of the phenyl ring to mediate such an interaction (both the X-ray data and the DFT calculations show that there is a significant deviation from planarity). In the absence of through-bond interaction, through-space interaction over the distance between to the $M(bipy)_2$ moieties is likely to be very weak, however this in itself does not account for the absence of any excited state interaction. The location of the lowest excited ^{3}MLCT state on the peripheral bipy ligands and not on the bridging ligand increases the effective energy/electron transfer distance.

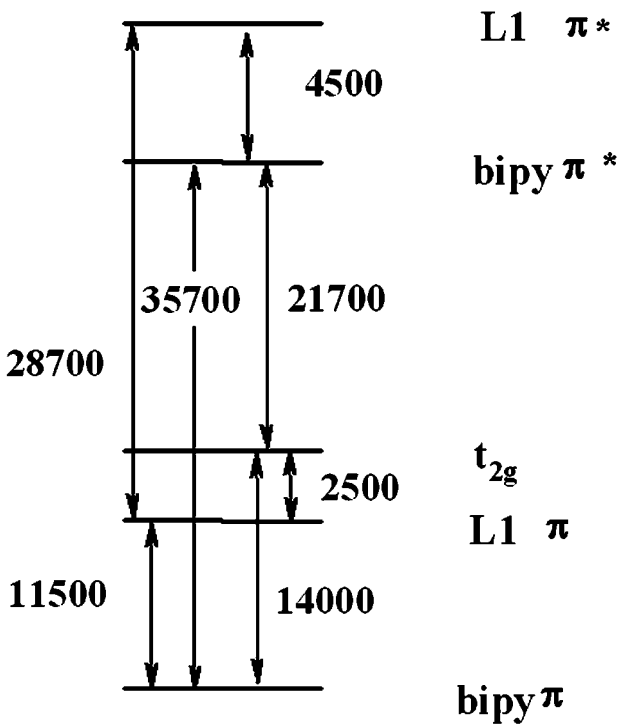

Fig. 9 Relative energy of energy levels in **RuRu**. Data used; bipy ππ* 280 nm (35700 cm^{-1}); L1 ππ* 350 nm (28700 cm^{-1}). Lowest energy ^{1}MLCT 460 nm (21700 cm^{-1}); difference between oxidation of Ru(II) and **L1** in is 310 mV (2500 cm^{-1}).

Acknowledgements

This work was partly supported by Enterprise Ireland (Grant Number SC/2003/74) and by the Improving Human Potential Programme (Grant Number HPRN-2002-00185).

References

1 (*a*) L. A. Worl, G. F. Strouse, J. N. Younathan, S. M. Baxter and T. J. Meyer, *J. Am. Chem. Soc.*, 1990, **112**, 7571; (*b*) V. Balzani, *Tetrahedron*, 1992, **48**, 10443; (*c*) V. Balzani, S. Campagna, G. Denti, A. Juris, S. Serroni and M. Venturi, *Acc. Chem. Res.*, 1998, **31**, 26; (*d*) V. Balzani and F. Scandola, *Supramolecular Photochemistry*; Horwood, Chichester, UK, 1991; (*e*) F. Scandola, M. T. Indelli, C. Chiorboli and C. A. Bignozzi, *Top. Curr. Chem.*, 1990, **158**, 73.

2 (*a*) K. Kalyanasundaram, *Coord. Chem. Rev.*, 1982, **46**, 159; (*b*) J.-M. Lehn, *Angew. Chem., Int. Ed. Engl.*, 1988, **27**, 89; (*c*) V. Balzani, S. Campagna, G. Denti, A. Juris and M. Ventura, *Coord. Chem. Rev.*, 1994, **132**, 1; (*d*) V. Balzani, A. Juris, M. Venturi, S. Campagna and S. Serroni, *Chem. Rev.*, 1996, **96**, 759; (*e*) C. A. Slate, D. R. Striplin, J. A. Moss, P. Chen, B. W. Erickson and T. J. Meyer, *J. Am. Chem. Soc.*, 1998, **120**, 4885; (*f*) Y.-Z. Hu, S. Tsukiji, S. Shinkai, S. Oishi and I. Hamachi, *J. Am. Chem. Soc.*, 2000, **122**, 241; (*g*) J.-P. Sauvage, J.-P. Collin, J.-C. Chambron, S. Guillerez, C. Coudret, V. Balzani, F. Barigelletti, L. De Cola and L. Flamigni, *Chem. Rev.*, 1994, **94**, 993; (*h*) E. R. Carraway, J. N. Demas, B. A. DeGraff and J. R. Bacon, *Anal. Chem.*, 1991, **63**, 337.

3 (*a*) *Supramolecular Photochemistry*, ed. V. Balzani, Reidel, Dordrecht, 1997; (*b*) J.-M. Lehn, *Supramolecular Chemistry*, Wiley-VCH, Weinheim, 1995.

4 (*a*) P. D. Beer, F. Szemes, V. Balzani, C. M. Salá, M. G. Drew, S. W. Dent and M. Maestri, *J. Am. Chem. Soc.*, 1997, **119**, 11864; (*b*) O. Waldmann, J. Hassmann, P. Müller, G. S. Hanan, D. Volkmer, U. S. Schubert and J.-M. Lehn, *Phys. Rev. Lett.*, 1997, **78**, 3390; (*c*) E. Zahavy and M. A. Fox, *Chem. Eur. J.*, 1998, **4**, 1647; (*d*) V. Balzani, A. Credi and M. Venturi, *Curr. Opin. Chem. Biol.*, 1997, **1**, 506.

5 S. Welter, K. Brunner, J. W. Hofstraat and L. De Cola, *Nature*, 2003, **421**, 54.

6 Y. Kim and C. M. Lieber, *Inorg. Chem.*, 1989, **28**, 3990.

7 F. Barigelletti, L. Flamigni, V. Balzani, J.-P. Collin, J.-P. Sauvage, A. Sour, E. C. Constable and A. M. W. C. Thompson, *J. Chem. Soc., Chem. Commun.*, 1993, 942.

8 (*a*) M. Haga, M. M. Ali, H. Sato, H. Monojushiro, K. Nozaki and K. Kano, *Inorg. Chem.*, 1998, **37**, 2320; (*b*) M. A. Haga, M. Ishizuya, T. Kanesugi, T. Yubaka, D. Sakiyama, J. Fees and W. Kaim, *Indian J. Chem., Sect. A*, 2003, **42**, 2290; (*c*) M. Haga, T. Takasugi, A. Tomie, M. Ishizuga, T. Yamada, M. D. Hossain and M. Inoue, *Dalton Trans.*, 2003, 2069; (*d*) M. D. Hossain, M. Haga, B. Gholamkhass, K. Nozaki, M. Tsushima, N. Ikeda and T. Ohno, *Collect. Czech. Chem. Commun.*, 2001, **66**, 307; (*e*) M. D. Hossain, R. Ueno and M. Haga, *Inorg. Chem. Commun.*, 2000, **3**, 35; (*f*) M. M. Ali, H. Sato, M. A. Haga, K. Tanaka, A. Yoshimura and T. Ohno, *Inorg. Chem.*, 1998, **37**, 6176.

9 (*a*) R. Hage, J. G. Haasnoot, H. A. Nieuwenhuis, J. Reedijk, D. J. A. De Ridder and J. G. Vos, *J. Am. Chem. Soc.*, 1990, **112**, 9245; (*b*) P. Passaniti, W. R. Browne, F. C. Lynch, D. Hughes, M. Nieuwenhuyzen, P. James, M. Maestri and J. G. Vos, *J. Chem. Soc., Dalton Trans.*, 2002, 1740; (*c*) W. R. Browne, F. Weldon, A. L. Guckian and J. G. Vos, *Collect. Czech. Chem. Commun.*, 2003, **68**, 1467; (*d*) W. R. Browne, C. M. O'Connor, C. Villani and J. G. Vos, *Inorg. Chem.*, 2001, **40**, 5461.

10 (*a*) C. H. Braunstein, A. D. Baker, T. C. Strekas and H. D. Gafney, *Inorg. Chem.*, 1984, **23**, 857; (*b*) Y. Fuchs, S. Lofters, T. Dieter, W. Shi, R. Morgan, T. C. Strekas, H. D. Gafney and A. D. Baker, *J. Am. Chem. Soc.*, 1987, **109**, 2691; (*c*) W. R. Murphy, K. J. Brewer, G. Gettliffe and J. D. Petersen, *Inorg. Chem.*, 1989, **28**, 81; (*d*) K. Kalyanasundaram and Md. K. Nazeeruddin, *Inorg. Chem.*, 1990, **29**, 1888; (*e*) R. M. Berger, *Inorg. Chem.*, 1990, **29**, 1920; (*f*) G. Denti, S. Campagna, L. Sabatino, S. Serroni, M. Ciano and V. Balzani, *Inorg. Chem.*, 1990, **29**, 4750.

11 C. Creutz, *Prog. Inorg. Chem.*, 1963, **30**, 1.

12 (*a*) E. V. Dose and L. J. Wilson, *Inorg. Chem.*, 1978, **17**, 2660; (*b*) R. Sahai, D. P. Rillema, R. Shaver, S. van Wallendael, D. C. Jackman and M. Boldaji, *Inorg. Chem.*, 1989, **28**, 1022.

13 (*a*) W. Kaim, *Coord. Chem. Rev.*, 2002, **230**, 127; (*b*) W. Kaim, A. Klein and M. Glöckle, *Acc. Chem. Res.*, 2000, **33**, 755; (*c*) B. Sarker, W. Kaim, A. Klein, B. Schwederski, J. Fiedler, C. Duboc-Toia and G. K. Lahiri, *Inorg. Chem.*, 2003, **42**, 6172.

14 (*a*) J. M. de Wolf, R. Hage, J. G. Haasnoot, J. Reedijk and J. G. Vos, *New J. Chem.*, 1991, **15**, 501; (*b*) H. E. B. Lempers, J. G. Haasnoot, J. Reedijk, R. Hage, F. Weldon and J. G. Vos, *Inorg. Chim. Acta.*, 1994, **225**, 67; (*c*) F. Barigelleti, L. Flamigni, V. Balzani, J-P. Collin, J. P. Sauvage, A. Sour, E. C. Constable and A. M. W. Cargill Thompson, *J. Am. Chem. Soc.*, 1994, **116**, 7692; (*d*) M. T. Indelli, F. Scandola, J-P. Collin, J-P. Sauvage and A. Sour, *Inorg. Chem.*, 1996, **35**, 303; T. Ohno, K. Nozaki and M. Haga, *Inorg. Chem.*, 1992, **31**, 4256; (*e*) M. Haga, M. M. Ali, S. Koseki, K. Fujimoto, A. Yoshimura, K. Nozaki, T. Ohno, K. Nakajima and D. J. Stufkens, *Inorg. Chem.*, 1996, **35**, 3335; (*f*) D. P. Rillema, R. Sahai, P. Matthews, A. K. Edwards, R. J. Shaver and L. Morgan, *Inorg. Chem.*, 1990, **29**, 167.

15 B. P. Sullivan, D. J. Salmon and T. J. Meyer, *Inorg. Chem.*, 1978, **17**, 3334.

16 D. A. Buckingham, F. P. Dwyer, H. A. Goodwin and A. M. Sargeson, *Aust. J. Chem.*, 1964, **17**, 325.

17 G. M. Sheldrick, *SHELX-97*, Universität Göttingen, 1997.

18 W. R. Heineman, *J. Chem. Educ.*, 1983, **60**, 4.

19 J. P. Chang, E. Y. Fung and J. C. Curtis, *Inorg. Chem.*, 1986, **25**, 4233.

20 N. G. Connelly and W. E. Geiger, *Chem. Rev.*, 1996, **96**, 877.

21 D. S. Jones, A. F. Brown, A. D. Woolfson, A. C. Dennis, L. J. Matchett and S. E. J. Bell, *J. Pharm. Sci.*, 2000, **89**, 563–571.

22 (*a*) C. G. Coates, L. Jacquet, J. J. McGarvey, S. E. J. Bell, A. H. R. Al-Obaidi and J. M. Kelly, *J. Am. Chem. Soc.*, 1997, **119**, 7130; (*b*) C. G. Coates, J. Olofsson, M. Coletti, J. J. McGarvey, B. Onfelt, P. Lincoln, B. Norden, E. Tuite, P. Matousek and A. W. Parker, *J. Phys. Chem. B*, 2001, **105**, 12653–12664.

23 *Gaussian 03, Revision B.04*, M. J. Frisch, G. W. Trucks, H. B. Schlegel, G. E. Scuseria, M. A. Robb, J. R. Cheeseman, J. A. Montgomery, Jr., T. Vreven, K. N. Kudin, J. C. Burant, J. M. Millam, S. S. Iyengar, J. Tomasi, V. Barone, B. Mennucci, M. Cossi, G. Scalmani, N. Rega, G. A. Petersson, H. Nakatsuji, M. Hada, M. Ehara, K. Toyota, R. Fukuda, J. Hasegawa, M. Ishida, T. Nakajima, Y. Honda, O. Kitao, H. Nakai, M. Klene, X. Li, J. E. Knox, H. P. Hratchian, J. B. Cross, C. Adamo, J. Jaramillo, R. Gomperts, R. E. Stratmann, O. Yazyev, A. J. Austin, R. Cammi, C. Pomelli, J. W. Ochterski, P. Y. Ayala, K. Morokuma, G. A. Voth, P. Salvador, J. J. Dannenberg, V. G. Zakrzewski, S. Dapprich, A. D. Daniels, M. C. Strain, O. Farkas, D. K. Malick, A. D. Rabuck, K. Raghavachari, J. B. Foresman, J. V. Ortiz, Q. Cui, A. G. Baboul, S. Clifford, J. Cioslowski, B. B. Stefanov, G. Liu, A. Liashenko, P. Piskorz, I. Komaromi, R. L. Martin, D. J. Fox, T. Keith, M. A. Al-Laham, C. Y. Peng, A. Nanayakkara, M. Challacombe, P. M. W. Gill, B. Johnson, W. Chen, M. W. Wong, C. Gonzalez, and J. A. Pople, Gaussian, Inc., Pittsburgh PA, 2003.

24 A. D. Becke, *J. Chem. Phys.*, 1993, **98**, 5648.

25 C. Lee, W. Yang and R. G. Parr, *Phys. Rev. B*, 1988, **37**, 785.

26 (*a*) T.H. Dunning, Jr. and P. J. Hay, in, *Modern Theoretical Chemistry*, ed. H. F. Schaefer III, Plenum, New York, 1976, vol. 3, p. 1; (*b*) P. J. Hay and W. R. Wadt, *J. Chem. Phys.*, 1985, **82**, 270; (*c*) P. J. Hay and W. R. Wadt, *J. Chem. Phys.*, 1985, **82**, 284; (*d*) P. J. Hay and W. R. Wadt, *J. Chem. Phys.*, 1985, **82**, 299.

27 N. M. O'Boyle and J. G. Vos, *Gauss Sum 0.8*, Dublin City University, 2004. Available at http://gausssum.sourceforge.net.

28 (*a*) R. Hage, J. G. Haasnoot, J. Reedijk, R. Wang, E. M. Ryan, J. G. Vos, A. L. Spek and A. J. M. Duisenberg, *Inorg. Chim. Acta*, 1990, **174**, 77; (*b*) D. P. Rillema, D. S. Jones, C. Woods and H. A. Levy, *Inorg. Chem.*, 1992, **31**, 2935; (*c*) R. Hage, J. P. Turkenburg, R. A. G. de Graaf, J. G. Haasnoot, J. Reedijk and J. G. Vos, *Acta Crystallogr., Sect. C*, 1980, **45**, 381; (*d*) D. P. Rillema, D. S. Jones and H. A. Levy, *J. Chem. Soc., Chem. Commun.*, 1979, 849.

29 F. Weldon, L. Hammarström, E. Mukhtar, R. Hage, E. Gunneweg, J. G. Haasnoot, J. Reedijk, W. R. Browne, A. L. Guckian and J. G. Vos, *Inorg. Chem.*, 2004, **43**, 4471.

30 W. R. Browne, C. M. O'Connor, H. P. Hughes, R. Hage, O. Walter, M. Doering, J. F. Gallagher and J. G. Vos, *J. Chem. Soc., Dalton Trans.*, 2002, 4048.

31 (*a*) W. J. Vining, J. V. Caspar and T. J. Meyer, *J. Phys. Chem.*, 1985, **89**, 1095; (*b*) M. Wrighton and D. L. Morse, *J. Am. Chem. Soc.*, 1974, **96**, 996; (*c*) A. Juris, V. Balzani, F. Barigelletti, S. Campagna, P. Belser and A. von Zelewsky, *Coord. Chem. Rev.*, 1988, **84**, 85.

32 S. Fanni, F. Weldon, L. Hammarström, E. Muktar, W. R. Browne, T. E. Keyes and J. G. Vos, *Eur. J. Inorg. Chem.*, 2001, 529.

33 W. R. Browne and J. G. Vos, *Coord. Chem. Rev.*, 2001, **219**, 761, and references therein.

34 (*a*) K. Maruszewski, K. Bajdor, D. P. Strommen and J. R. Kincaid, *J. Phys. Chem.*, 1995, **99**, 6286; (*b*) P. K. Mallick, G. D. Danzer, D. P. Strommen and J. R. Kincaid, *J. Phys. Chem.*, 1988, **92**, 5628; (*c*) D. P. Strommen, P. K. Mallick, G. D. Danzer and R. S. Lumpkin, *J. Phys. Chem.*, 1990, **94**, 1357.

35 (*a*) A. C. Ribou, J.-P. Launay, K. Takahashi, T. Nihira, S. Tarutani and C. W. Spangler, *Inorg. Chem.*, 1994, **33**, 1325; (*b*) P. Laine, V. Marvaud, A. Gourdon, J.-P. Launay, M. L. Sachtleben, H. Li and C. W. Spangler, *Inorg. Chem.*, 1996, **35**, 3735.

36 E. Krausz, G. Moran and H. Riesen, *Chem. Phys. Lett.*, 1990, **165**, 401.

37 E. M. Kober, B. P. Sullivan, W. J. Dressick, J. V. Caspar and T. J. Meyer, *J. Am. Chem. Soc.*, 1980, **102**, 7385.

38 D. E. Richardson and H. Taube, *Inorg. Chem.*, 1981, **20**, 1278.

39 S. I. Gorelsky and A. B. P. Lever, *J. Organomet. Chem.*, 2001, **635**, 187.

40 This representation gives a better overview of the nature of the frontier orbitals, especially where neighbouring orbitals are closely-spaced.